ABSTRACT

CHATTOPADHYAY, RITWIK. Three Port Transformer Isolated Phase Shifted DC-DC Converter Design & Control for Renewable Energy Source and Energy Storage Integration. (Under the Direction of Dr. Subhashish Bhattacharya).

Recent advancements of wide bandgap (WBG) semiconductor devices have created abundant scope of research for Renewable Energy Source(RES) integration into Medium Voltage(MV) utility grid. WBG semiconductor devices of rating 1200V & 1700V have been commercially available for a long time and their applications are directed towards low voltage(around 1kV) power converters. Renewable energy source converters require high efficiency, low cost & volume. Therefore, the use of WBG SiC devices provides tremendous opportunity to reduce the size of magnetic components, thereby reducing the overall converter volume. MV grid tied inverters like Cascaded H-bridge(CHB) or Modular Multilevel Converter(MMC) converters are suitable for RES grid integration at MV level. However, CHB requires an input dc source for each modular unit and MMC requires a high voltage dc bus at its input. The research work in this paper focuses into three port converter system, that can be used as an input to each modular unit of a CHB or a number of which can be series connected to develop a Medium Voltage DC or MVDC bus. Use of SiC Mosfet devices of the ratings 1200V & 1700V provides the possibility of high switching frequency for the three-port dc-dc converter, which thus demands suitable high frequency magnetics.

Several high Frequency switching converters for dc-dc conversion have been proposed by researchers over years. One of the critical property that makes dc-dc conversion attractive to designers is the soft-switching capability. Switching devices like IGBTs & MOSFETs if operated under soft-switching provides high efficiency for the converter. SiC Mosfet devices provide negligible switching loss under Zero Voltage Switching(ZVS) conditions. Phase-shifted

dc-dc Dual Active Bridge(DAB) or Triple Active Bridge(TAB) converters exhibit their inherent ZVS turn-on property due to their operating nature, which makes them lucrative for use with Mosfet. The dissertation work presented here focuses on three port phase shifted converter like TAB converter and its associated magnetics. The dissertation work focuses on operating TAB converter for 10kW/50kW power level at 50kHz or higher switching frequencies, while using ferrite core transformers. In addition, tape wound core based transformers have also been discussed here for frequencies around 20kHz switching frequencies.

Phase shifted dc-dc converters use the leakage inductance of transformer or series inductors as the energy transferring element. Design of high frequency magnetics is crucial as it demands specific optimum leakage inductance or series inductances for rated operation. A significant part of the thesis work presented here focuses on leakage inductance modelling and optimized design of transformers for phase shifted converters. In addition, high switching speed of semiconductor devices produce significant dv/dt noise signals, which are primary sources for common mode noises. The inter-winding coupling capacitance plays an important role as it provides the impedance to the common mode noise path. Therefore, significant attention has been paid to selecting transformer topologies & designing transformers with low inter-winding coupling capacitances. Using tape wound core transformers for phase-shifted converters provide a challenge to converter designers as the leakage flux induces eddy current and creates losses in the laminations. A different approach for tape wound core transformers has been suggested in this dissertation work to address the leakage flux issues for tape wound core transformers.

The dissertation work includes high frequency transformer current control techniques for eliminating dc biases from transformer current during phase change and provides a decoupling of control variables. The current control method is used to control the dc powers at the converter

input & output ports independently of each other, which provides the path to independent control of converters for series connection of converter units. Lastly, a generalized phase shift technique has been suggested to eliminate dc shifts in transformer currents & core fluxes during transients. The proposed method has been applied across different cases to verify its generality.

Three Port Transformer Isolated Phase Shifted DC-DC Converter Design & Control for Renewable Energy Source and Energy Storage Integration

by
Ritwik Chattopadhyay

A dissertation submitted to the Graduate Faculty of
North Carolina State University
in partial fulfillment of the
requirements for the degree of
Doctor of Philosophy

Electrical Engineering

Raleigh, North Carolina
2018

APPROVED BY:

Dr. Subhashish Bhattacharya (Committee Chair)	Dr. Srdjan Lukic
Dr. David Lubkeman	Dr. Gregory Buckner

BIOGRAPHY

The author was born in Kolkata, India on December 15, 1983. He received his Bachelor of Engineering (B.E.) degree in Electrical Engineering in the year 2006 from Jadavpur University, Kolkata, India. He received his Master of Technology (M.Tech.) degree in 2012 from Indian Institute of Technology, Bombay in the year 2012 at Mumbai, India. He has worked at IBM India Pvt Ltd, Robert Bosch Engineering in India. The author has been joined North Carolina State University (NCSU) at Raleigh, NC, USA for pursuing his Ph.D. in Electrical Engineering from January 2013. During his PhD study, he worked for the ABB Inc at Raleigh, NC as a graduate intern for four months. His research interests include High Frequency Power Converters, High Frequency Magnetics Design, SiC Devices Characterization & Gate Driver designs, Converter control etc.

ACKNOWLEDGMENTS

This work has been done at the Department of Electrical and Computer Engineering at North Carolina State University and at NSF FREEDM Engineering Research Center. I would like to express my sincere gratitude to my advisor Professor Subhashish Bhattacharya for his guidance and support throughout the course of this work. His constant encouragement and advice have helped me develop as a researcher and an electrical engineer over the duration I have worked here. He has always strived to provide us with the best working environment and state-of-the-art equipment for research. I would also like to thank other faculty members of FREEDM Systems Centre for being a constant source of inspiration and new ideas. It has been a great pleasure to work at the National Science Foundation funded Future Renewable Electric Energy Delivery and Management (FREEDM) Systems Center.

I would like to express my gratitude to Dr. Paul R. Ohodnicki from NETL,CMU, Mark A. Juds, Cheng Luo from Eaton Corparation Corporate Research & Technology(CRT-Milwaukee) for having precious and fruitful brainstorming discussions with me, which have provided me the opportunity to think beyond regular practices. I would like to acknowledge the effort of all the FREEDM faculty members and staffs to create and maintain an excellent research and education environment. My sincere gratitude goes to all my colleagues at the FREEDM center for providing a nice and friendly atmosphere for research. I would like to thank my colleagues Sayan, Sachin, Kasu, Byron, Anup, Vishnu, Srinivas, Ashish, Suyash for having numerous fruitful & helping discussions. I would also like to thank Arun, Awneesh, Samir, Ankan, Souvik, Ali, Mahsa, Urvir, Tanvir & many others for their support and help. I would also like to thank FREEDM System Centre Lab manager Hulgize Kassa for a being a great helping hand in the lab and providing with all the support that are needed. I would also like to thank post-doctoral

fellows Dr. Ghanshyam Gohil, Dr. Viju Nair, Dr. Sudhin Roy, Dr. Dhaval patel, Dr. Krishna Mainali for their help and having useful discussions on research. I would also like to thank my parents back in India and my wife Hiya, staying with me at Raleigh, for their numerous sacrifices and patience.

TABLE OF CONTENTS

LIST OF TABLES

LIST OF FIGURES

Chapter 1. Introduction

Renewable energy sources like Solar, Wind, Tidal, Wave Energy have been continuously growing in demand over the years due to their zero carbon footprint, efficiency and lower initial cost compared to thermal or hydro power installations. Technologies enabling the transformation of natural renewable energy into usable electrical energy form, is one of the key components behind renewable energy's growing development. The transformation from renewable energy to electrical energy is generally achieved in two stages. First stage is the conversion of renewable energy in some form of non-usable uncontrolled electrical energy form, such as using Photovoltaic Cells for PV, Rotating Machines for Wind, Tidal and Wave energies etc. Second stage of power conversion involves converting the raw, non-usable form of electrical energy to usable form such as feeding electrical power in compliance with low or medium voltage utility grid, off grid electrical loads and other. This second stage of power conversion heavily depends upon power electronic state of the art technology. Solar Energy or Photovoltaics has been one of the cleanest form of energy sources, which is finding increasing acceptance worldwide. Power electronic technology enabling the installation of large Photovoltaic(PV) plants, are growing in demand and evolving with time due to enhancements and inventions in technology. The state of art of power electronic technology is also coming across rapid advances with the invention of Wide Band Gap(WBG) devices such as Silicon Carbide(SiC) and Gallium Nitride(GaN) semiconductor devices. Large scale commercial Photovoltaic installations generally use a power electronic inverter, which is using Silicon technology, filters and a low frequency 50Hz/60Hz transformer for grid connection at medium voltages(few kV levels). The primary function of low frequency transformer is to isolate the low voltage(less than 1kV) PV and power electronics from

medium voltage(4.16kV-13.8kV) utility grid. The low frequency transformer in such installations are bulky and costly in nature since they carry the full power feeding to grid. With new age SiC and other WBG devices, there is an increasing demand to eliminate the low frequency transformer and use the power electronics technology with high frequency galvanic isolation, as a direct interface block between PV panels/modules and grid. The thesis work presented here discusses and focuses on isolated power electronic converter systems suitable for large scale PV integration.

1.1. Traditional System Architecture for Large Scale PV with Low Frequency Transformer

Integration of renewable energy sources like PV, Wind into electric power utility grid, has been the research interest for quite a long period of time. Renewable energy integration using Silicon-technology semiconductor device based power electronic solutions have been in practice and has been accepted by industry standards and are implemented for small scale to large scale installations in significant numbers for renewable energy integration. Integration of renewable energy sources(RES) has been mostly carried out at low voltage levels(around 1kV or lower) for renewable source and the grid side voltages vary from 480V to medium voltage levels of 13.8kV. Several medium voltage utility grids in US are in the range starting from 4kV to 35kV voltage level class. Traditional Si based power electronics have used low voltage power-electronics of voltage levels around 1kV and have used a step-up low frequency transformer for connecting to medium voltage grid. System architectures for large scale PV installations as defined by leading power electronic industries like ABB, Siemens are shown in figures 1.1 and 1.2([1]-[4]). A short summary of the power levels and efficiency standards for PV central

inverters and MW level isolating step-up transformers, are shown in table 1 and 2. The sources for these data are obtained from ([1]-[13]).

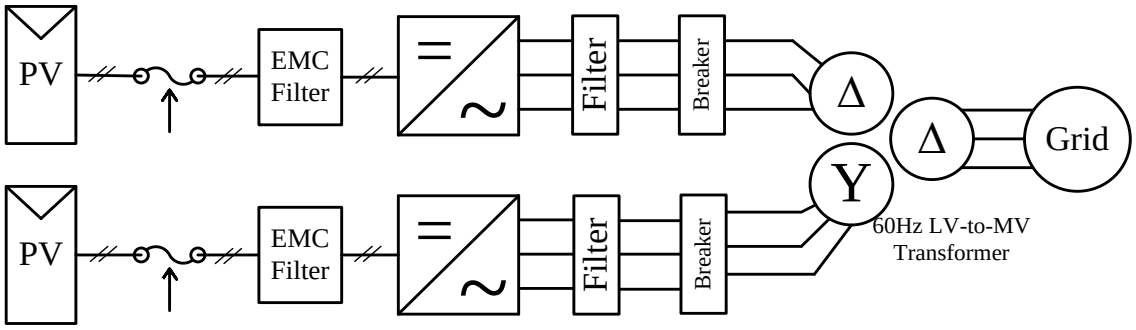

Figure 1.1. 1MW PV Inverter PVS800-MWS-1000kW-20 from ABB.

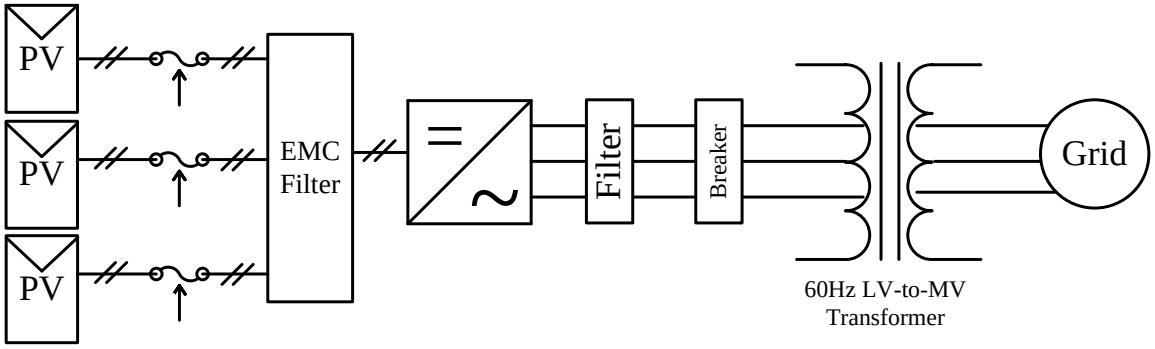

Figure 1.2. 350kW SINVERT PVS Central Inverters from Siemens.

Typical Si-based system architecture for PV installation, as shown in figures 1.1-1.2, a low frequency step-up transformer is used which serves two purposes, (i) steps up the inverter voltage level to match with grid voltage and (ii) provides isolation between ac side and PV side. The dc voltage of PV varies typically around 400V to 1000V. Similar system architecture has been in use for commercial solutions, as developed by other leading industries as well. The step up low frequency transformer is a key element with traditional system architecture for large scale PV, but it has a huge weight and volume which makes the overall solution expensive and bulky. The commercial inverters shown above has typical efficiencies around 98.5% and low frequency

transformers also have efficiencies above 99%, which puts the total system efficiency in the range of 97% to 98%. The main motivation behind this thesis work aims at achieving an alternative solution which does not uses the bulky low frequency transformer, while it maintains the efficiency standard of the aforementioned commercially available solutions.

Table 1. Few Commercial PV Central Inverters

Product Series	DC Voltage	AC Voltage	Power level	Max Efficiency
PVS800 series/ ABB	600V~1100V	300V~400V	0.5MW~2.7MW	98.5%-98.8%
GE LV5 Series	600V~1500V	400V~550V	0.7MW~4MW	98.25~98.5%
SINVERT series/Siemens	500V~900V	230V~400V	0.1kW~1.7MW	96.1%~96.3%
Conext Core XC series / Schneider Electric	440V~1000V	300V~380V	0.54MW~0.68MW	98.3%~98.7%
SanRex 900V series	400V~900V	380V~420V	0.1MW~0.5MW	96%

Table 2. Commercial Step-Up Medium Voltage Transformers

Source	Voltage Level/Power	Efficiency	Weight
HPS Dry Type Transformer	208V-416V-600V/2.5kV-15kV 0.5MVA-7.5MVA	99.1~99.2%	2800 LBS to 60600 LBS
Energy Star Market Industry Scoping Report	480V/14.4kV, upto 2MVA	Upto 99.2%	5000 LBS to 10000 LBS

1.2. System Architecture for Large Scale PV without Low Frequency Transformer

Renewable Energy Sources'(RES) integration into medium voltage grids(4.16kV to 13.8kV) without the low frequency step-up transformer is quite challenging as the voltage step-up action

needs to be addressed in the converter architecture and also the isolation between PV side and grid side is required. In order to investigate converter architectures that can provide solutions for large scale PV installations such as discussed in (14)-(16), the important component for such solutions is the grid-integrated inverter for medium voltage applications. The most in-demand and widely acceptable converter topologies for medium voltage(MV) grid-tie applications are given as follows

- Modular Multilevel Converter(MMC)
- Cascaded H-bridge Converter(CHB)

The operation, control and working principle of MMC and CHB converters have been widely discussed in literatures for PV installations([17]-[28]). For MMC based architecture, a very high voltage input dc bus is needed, which provides all the required power to the ac side. Instead of using MMC as the grid-tie inverter unit, two/three level inverters using high-voltage SiC devices, can also be used if a high voltage dc bus is available. With series PV string, as shown in figure 1.3, large number of individual PV modules are needed to be connected in series, which curtails the PV power availability during partial shading[18]. Also, a single module dysfunction will reduce the available power by huge margin.

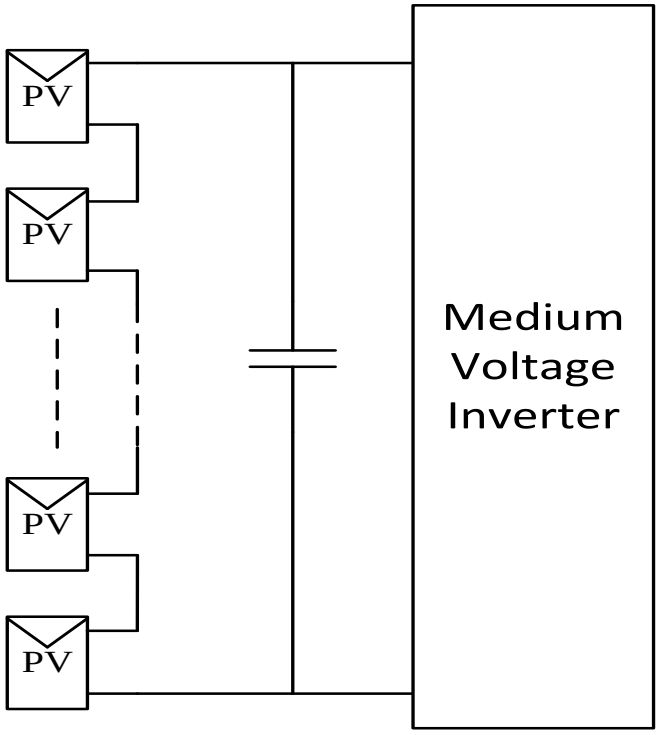

Figure 1.3. Solar String Based Inverter.

The Cascaded H-bridge topology for large scale PV installation([17]-[23]) require an isolated dc-dc converter that performs MPPT for each modular dc-dc block, as shown in figure 1.4. In this type of configuration, the H-bridge modules require high capacitance or additional control action to reduce the second harmonic oscillation effect on individual module's dc bus([19],[20]).

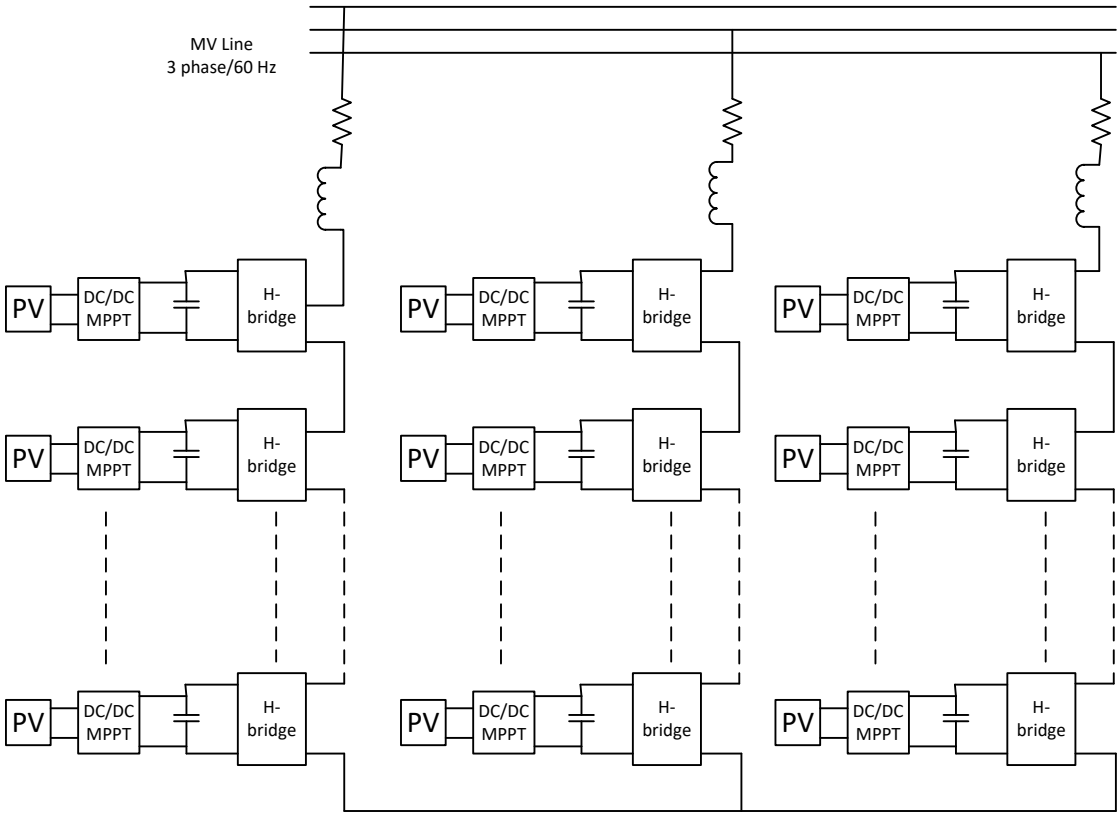

Figure 1.4. Cascaded H-bridge Topology.

While using MMC type inverter or medium voltage inverter([24]-[26]) for grid connection, the drawbacks of string inverter and CHB can be removed by a having a higher voltage dc bus architecture, as shown in figure 1.5. In this configuration, the individual dc buses from modular dc-dc converters, make up a high voltage dc bus which acts as an input dc bus to medium voltage inverter. In MMC topology, for the case of one modular converter block failure or PV shading for one block, rest of the modular blocks can operate successfully provided the minimum overall dc bus voltage requirement is met. In MMC applications, the number of series strings installed can be more in number than that required for the MV grid-tied inverter. One drawback is the voltage balancing for each individual dc-dc block([29]-[36]) in the series dc string, when the dc-dc converters are required to operate as MPPT converter. In this scenario, passive balancing requirement is required for balancing individual dc bus voltages for the modular converter blocks.

For MMC inverter, the total dc bus voltage is controlled by the inverter, while the dc-dc blocks perform MPPT. The inverter has the disadvantage that it cannot operate in P-Q control mode.

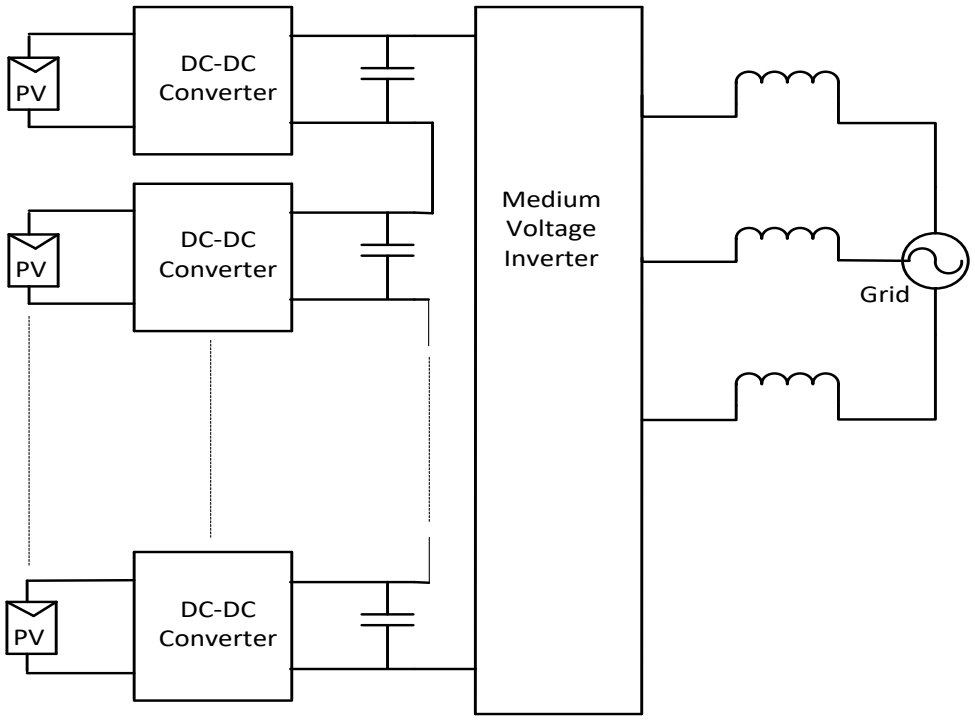

Figure 1.5. Series Connected DC-DC Converter with Medium Voltage Inverter.

1.3. Energy Storage Requirement for Large Scale PV Integration

Renewable energy sources like PV undergoes interruptions due to varying weather conditions and other effects environmental effects. PV installations often suffer from shading effects and undergo fluctuations in output power. In addition to that, PV based grid-tied architectures as explained above, the grid tied inverter can only do power feed through and cannot perform P-Q control. In order to smoothen out the output power, and to enable the grid tied inverter to operate in P-Q control mode under certain operating conditions, an energy storage is required to be integrated with the PV. Energy storages like battery bank can smoothen out the power output,

storing extra energy during excess PV power generation and delivering extra required power during low PV power generation([35]-[38]).

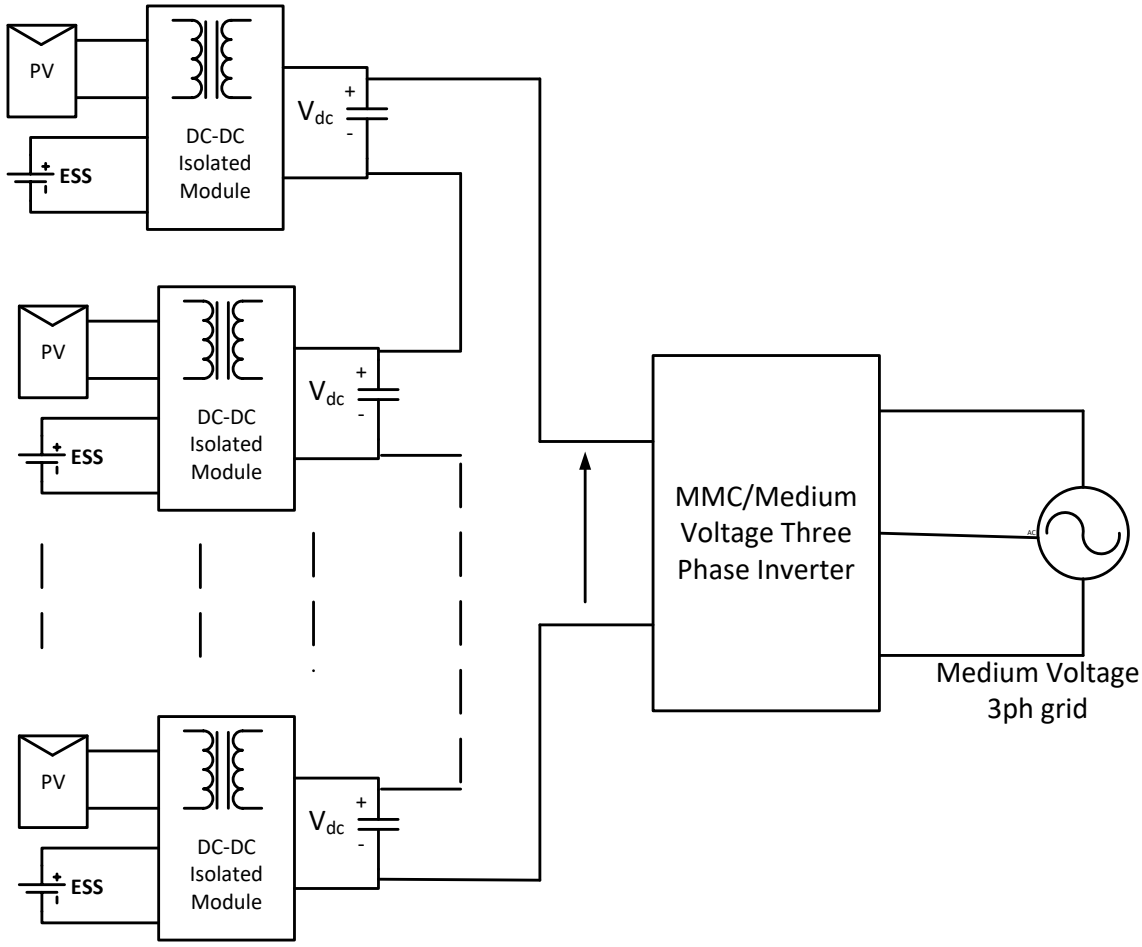

Figure 1.6. PV/ ES Integrated DC-DC Converter Based MV Architecture.

Integration of ES with PV at dc side provides the flexibility to control the power output of each modular DC-DC block[38,39]. Integration of the whole Energy Storage System using a separate DC-AC stage provides the power smoothening/energy storage control at the plant level but the controllability at modular level is not present in this case. In the thesis work here, a single power electronic converter, using a high frequency transformer providing isolation between all the three ports(PV,ES and dc output) is discussed. Using isolated DC-DC converter integrating PV and ES,

large scale medium voltage inverter based solution is shown in figure 1.6. The dc-dc converters are connected in series to create the dc bus for medium voltage inverter. In order to meet the power rating of the inverter power flow requirement, multiple series connected structures of dc-dc converters can be connected in parallel. In this thesis work, the PV and ES integrated isolated dc-dc converter module, as a building block for large scale architecture, is discussed.

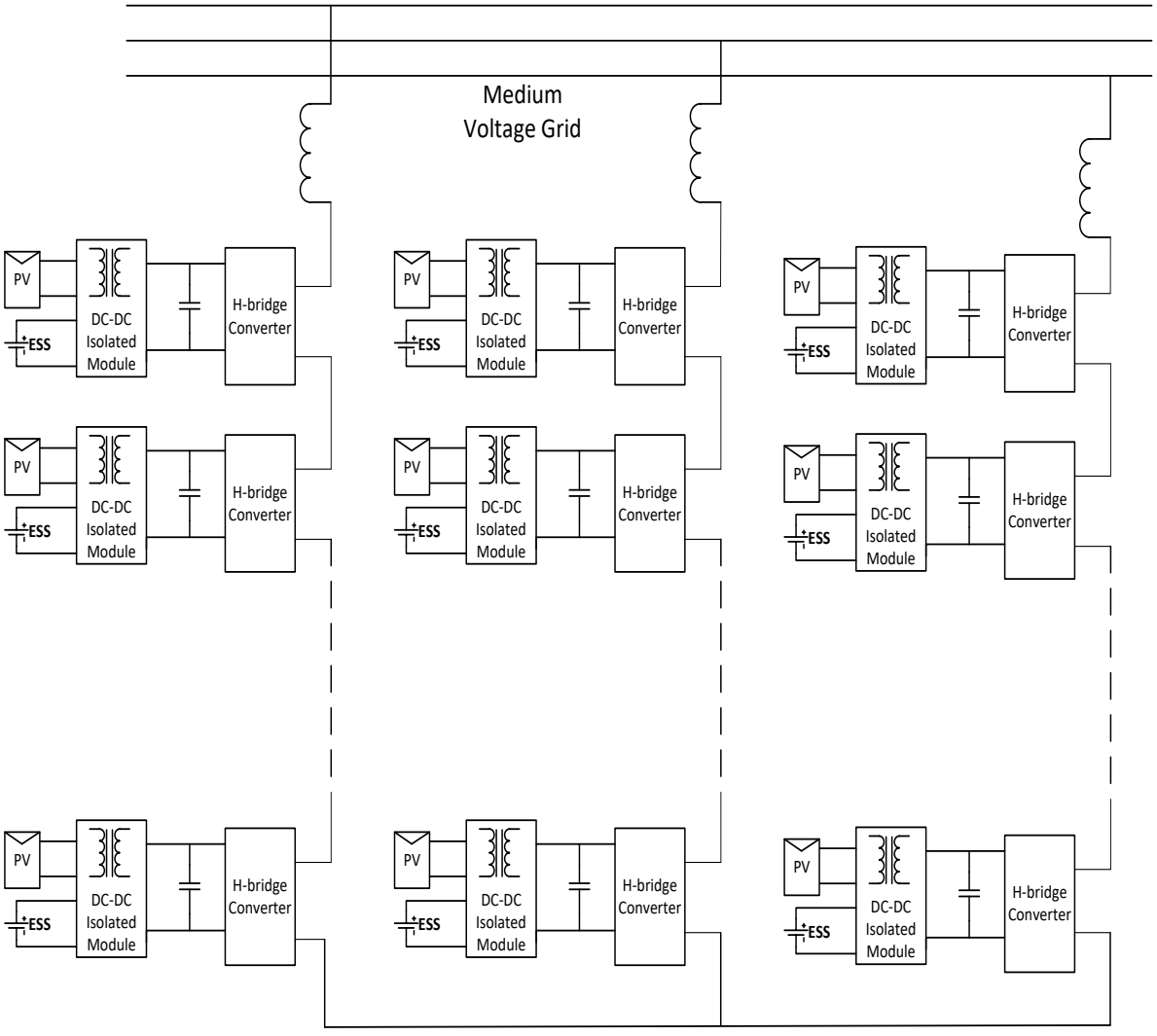

Figure 1.7. PV/ES Integrated DC-DC Converter Based CHB Architecture.

Instead of using PV and ES integrated isolated dc-dc converter module, single stage isolated dc-ac converter module using four quadrant switches, can also be used as modular building block.

The inverter architecture using isolated dc-ac converter module is shown in figure 1.8, where multiple dc-ac modules are connected in series for each phase.

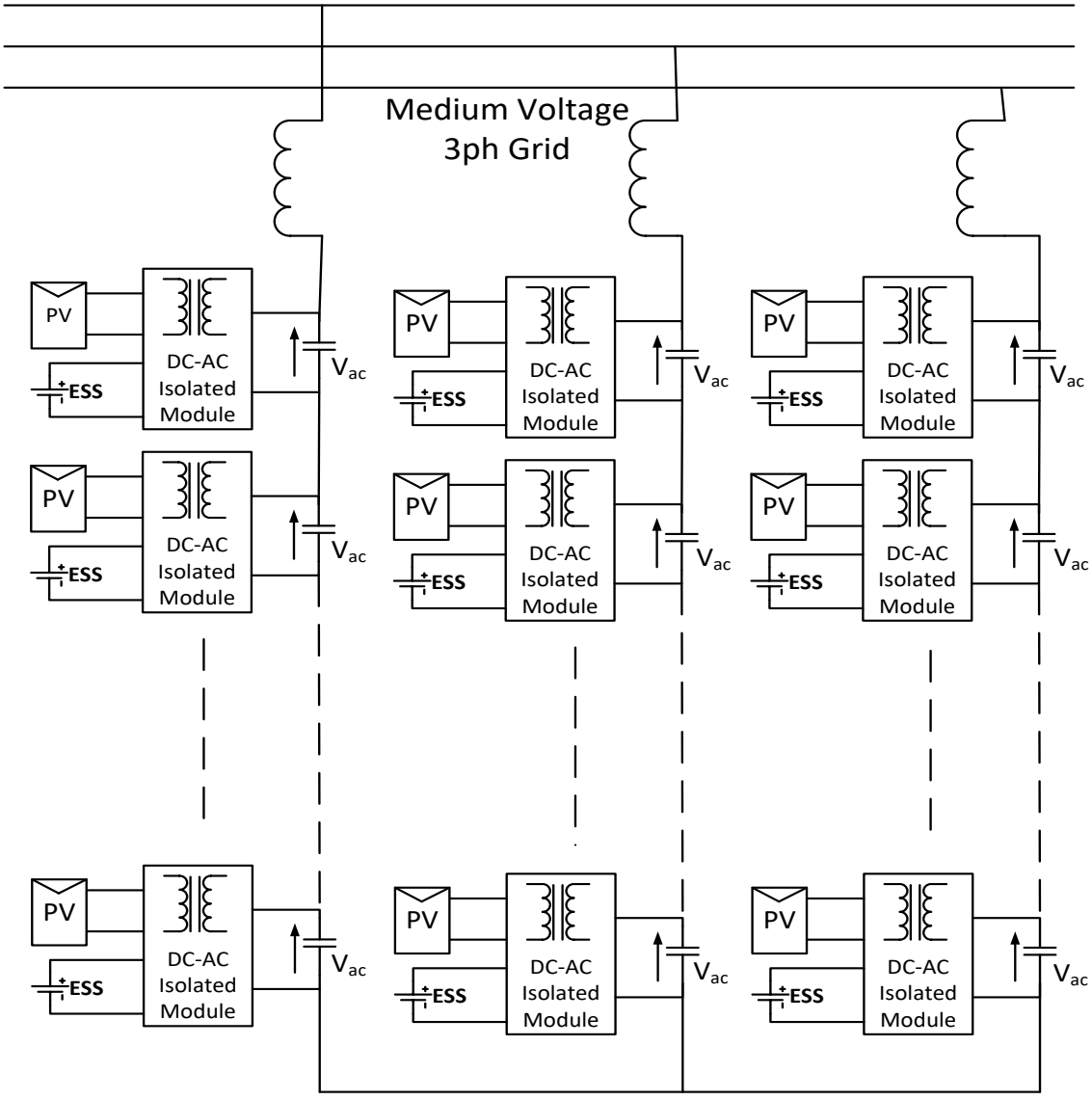

Figure 1.8. PV and ES Integrated DC-AC Converter Module Based Configuration.

1.4. Impact of Wide Band Gap High Frequency Silicon-Carbide Devices

With the emergence of post-Si Wide Bandgap technology such as SiC and GaN technology, there has been increasing research work across the globe to replace Si based power electronic architecture with SiC based power electronics for medium voltage levels[40]-[46]. The new age

SiC devices come in different voltages classes such as 1200V, 1700V, 3.3kV, 10kV and upto 15kV. However, the only 1200V and 1700V SiC devices are available till date as commercial component, the other higher voltage SiC devices are still not available for commercial purpose of use. Typically, 1200V SiC devices can withstand 800V~900V dc bus voltage[44] and operate successfully, while 1700V SiC devices are capable of operating successfully at voltage levels of 1kV-1.4kV[43].

The SiC technology offers the advantage of higher switching frequency([39]) than Si technology for voltage levels starting from 600V and higher upto few kVs. In other words, using SiC technology, for a specific frequency, the operating voltage that can be reached within device's thermal operating limits, is much higher. Hence the use of SiC technology provides the feasibility of higher voltages and higher power densities for power electronic converters.

The very high voltage fast switching devices for the range of 10kV or higher have much limitation in terms of reliability and robustness, which encourages the use of series connected multiple dc buses of the type shown in figure 1.6, to achieve a high voltage dc link. The work presented in this paper involves the use of 1200V and 1700V SiC Mosfet based multiport dc-dc converter suitable for RES integration.

1.5. Objective, Key Findings and Contributions

The main objective of this thesis work is to investigate efficient three port converter that can act as modular building block and can provide all the required functions, with a target efficiency around 98.5% and above. The key contributions from the thesis work are as follows

- Overview of different three port converter systems and their usability for RES & PV integrated systems for high power three port system for medium voltage applications.

- Modelling & analysis of key properties, advantages & disadvantages for different transformer topologies for three port operation.
- Leakage integrated three port transformer design with leakage and parasitic capacitance modelling.
- Phase shift control technique & Modulation based control technique for three winding transformers.
- Optimized design of leakage integrated three port transformer for three port phase shifted operation. Design & operation of 10kW & 50kW ferrite core three port transformer.
- Nano crystalline based three winding transformer design & operation. Leakage integrated two winding transformer designs.
- High frequency transformer current control techniques & power control. Series connection & independent control of multiple dc-dc converters.
- Generalized Phase shift technique for phase shifted converters

1.6. Organization

In Chapter 1, the state-of-art renewable energy integration architecture is discussed and how for medium voltage applications, series connected three port dc-dc converters can be used as medium voltage dc grid. Each of the three port converter unit acts as an independent modular building block.

In Chapter 2, different state-of-art three port converter cells/units are exemplified and their properties are discussed. The three port phase shifted converter unit provides several advantages over other converters like ZVS operation, reduced magnetic component, bidirectional power

flow etc. The impact of low inter-winding parasitic capacitances over high parasitic inter-winding capacitances have also been discussed in this section.

In Chapter 3, modelling & equivalent circuit analysis of three limb three port high frequency transformer has been done along with leakage inductance modelling & parasitic capacitance modelling. The modelling results from analytical methods are compared & matched with FEA simulation results and actual measurement results.

In Chapter 4, three port converter operation using phase shift control technique and modulation technique has been discussed & analyzed. The drawbacks of three port converter while using three limb transformer has been addressed in this chapter and possible corrective measures have been proposed.

In Chapter 5, split-winding type transformer has been proposed for three port converter operation. Modelling, equivalent circuit analysis and operation of three port converter using split-winding type transformer has been discussed.

In Chapter 6, optimized design of a 10kW split-winding type transformer has been discussed which focuses on loss-volume optimization of the transformer, along with converter results and validations. Also, a 50kW split-winding transformer has been designed for three port operation and its results are demonstrated.

In Chapter 7, the usability of tape wound core transformers has been discussed for three port phase shifted operation. Issues related to leakage flux in tape wound core transformers are addressed and possible corrective measures are suggested. A three port 50kW tape wound core transformer and a two port 50kW leakage integrated transformer design and demonstrations are shown.

In Chapter 8, the high frequency transformer current control technique along with decoupling of control variables has been proposed and investigated for three port phase shifted converter. Three different techniques are discussed in this chapter along with their advantages, drawbacks etc. The proposed control technique has been applied to closed loop control of individual converters of series connected closed loop converter units.

In Chapter 9, a generalized phase shift control technique has been suggested for two port & three port phase shifted converters. The proposed control technique has been verified across different case scenarios for its applicability and generalization.

In chapter 10, conclusions from the research work are drawn and future works are proposed.

Chapter 2. DC-DC Converter For Photovoltaic (PV) And Energy Storage (ES) Integration

2.1. Architecture of DC-DC Converter for PV and ES Integration

The dc-dc converter for integrating dc-dc Photovoltaics(PV) and Energy Storage(ES) is a crucial part of the large scale power conversion system architecture, as discussed in previous chapter. Large scale conversion systems like series connected dc-dc architecture or cascaded converter structure would need some form of galvanic isolation for the dc-dc conversion block. DC-DC converters with galvanic isolation has the advantage of having all the PV modules and Energy Storage units(from modular converter architecture types shown in chapter 1) to be at placed at same reference level from the ground. Also, the high frequency transformer in dc-dc converter provides the opportunity to select desired voltage gain in case of the large voltage difference between low voltage PV/ES side and the output dc bus side. The converter architecture can be of different types depending on the installation of energy storage along with PV. A summary of energy storage integration with a renewable source is discussed in [47]. The energy storage can be integrated with grid using a separate DC-AC stage, directly connected to the grid at PCC, in parallel with PV inverter. In this case, total power fed to the grid can be easily controlled by using energy storage but the low frequency bulky transformer needs to be connected to the grid. In other method, the energy storage can be integrated at the dc side using several methods, (a) it can be integrated to the output dc bus with a separate converter, (b) it can integrated at the PV terminals with a bidirectional converter, or (c) it can be integrated with PV in a single converter, as shown in figures 2.1-2.3.

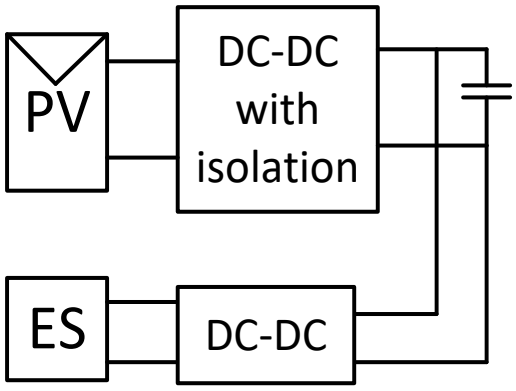

Figure 2.1. PV and ES Converters Connected at Output DC Bus.

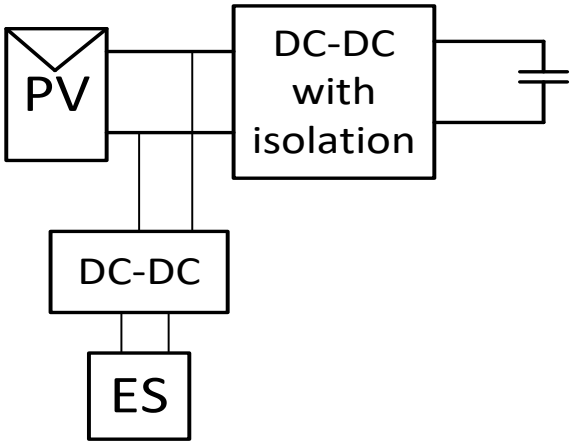

Figure 2.2. PV and ES Converters Connected at PV Terminal.

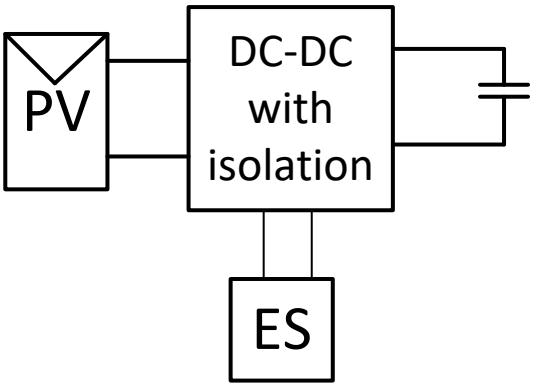

Figure 2.3. PV and ES Converters Integrated Using Single Converter.

The energy storage(ES) block can be integrated at the dc-dc conversion stage using the three aforementioned converter architectures[47]. The selection of converter architecture or configuration depends on application type, power requirement etc. PV panels & converters have high common mode leakage current flowing through the ground due to presence of parasitic capacitance between panel and frame([57]-[58]). The isolated topology using ideal high frequency transformer, provides a blockage to this leakage current path from flowing into other parts of the converter circuit. However, due to inherent non-idealities of high frequency transformer, inter-winding capacitances exist in transformers and propagate the leakage current from one winding to other windings of the transformer[58]. Using non-isolated topologies, this leakage current sees much lower impedance paths compared to isolated topologies and the common mode leakage current flows through other parts of converter circuit. If PV and ES do not have galvanic isolation between them, this leakage current flows through the circuit components connecting PV and ES. Using isolated topology, the leakage current flow is reduced compared to non-isolated topologies, but it largely depends on the inter-winding capacitance value. The requirement of isolation between PV and ES is not very critical, but providing an isolation between them, provides the flexibility of having wide differences between voltage levels of PV and ES.

2.2. DC-DC Converter and Transformers for High Frequency Isolation

The isolated dc-dc converter for PV and ES integration is the critical element of power conversion architecture. The dc-dc converter for PV and ES integration has the following primary tasks

- Performing MPPT for PV module to extract maximum power available from PV
- Control the output dc bus voltage
- Store extra power generated by PV into ES during low load requirement

- Deliver extra power required by load from ES during high load requirement
- Deliver power from ES to grid when PV is off
- Deliver power from grid to ES when PV is off

Clearly the power directions from the ES and grid are bidirectional in nature and from PV the power flow in unidirectional. The possible power flow cases for the three port converter are shown in figures 2.4-2.9.

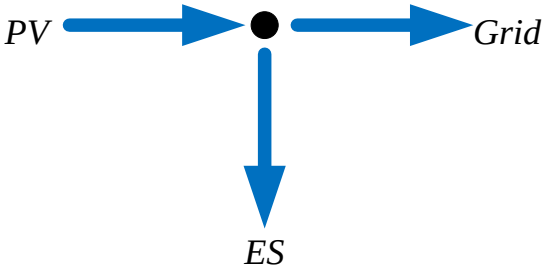

Figure 2.4. PV Delivering Power to ES and Grid.

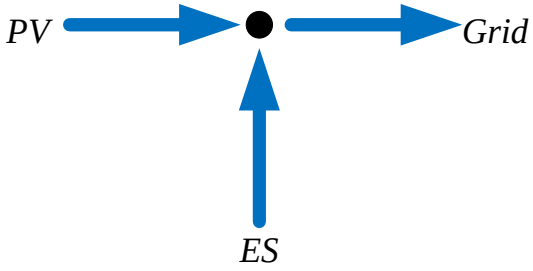

Figure 2.5. PV and ES Delivering Power to Grid.

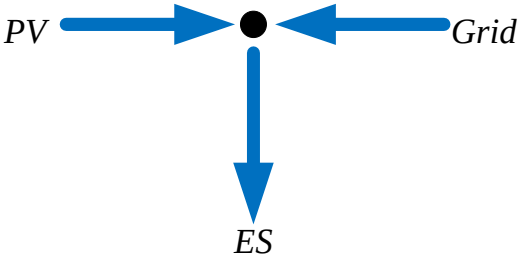

Figure 2.6. PV and Grid Delivering Power to ES.

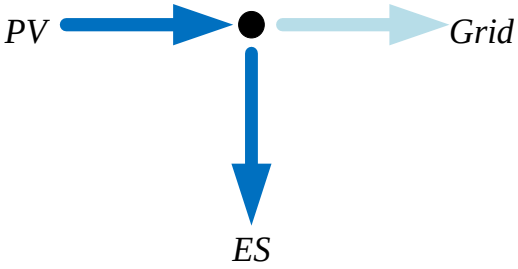

Figure 2.7. PV Delivering Power to ES, Grid Unavailable.

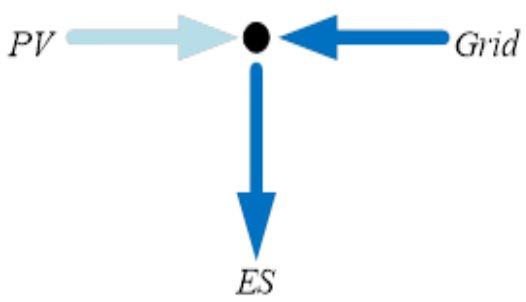

Figure 2.8. PV Unavailable, Grid Delivering Power to ES.

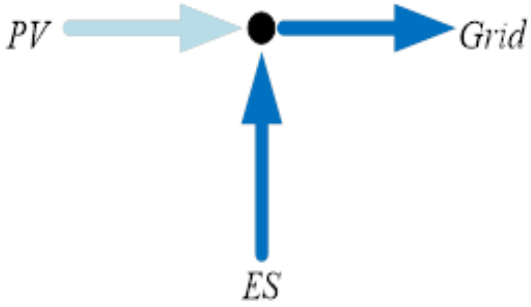

Figure 2.9. PV Unavailable, ES Delivering Power to Grid.

The converter architecture of dc-dc converter requires a bidirectional converter for Energy Storage(ES) and Grid side, while for PV side, an unidirectional power converter is sufficient. The dc-dc converter integrating PV, ES and grid side dc bus needs to have a three port converter configuration type as has been discussed in literature. Series of non-isolated topologies integrating three dc ports are discussed in [47]-[56]. In this thesis work, all the three ports are considered to be galvanically isolated from each other, so that the PV leakage current effect on other ports are minimal and the voltage differences between different ports can be wide. The isolation between different ports are provided with a transformer of high/medium frequency type depending on power level. The three port isolated dc-dc converters with isolation between all the three ports have been a subject of interest for researchers. A brief summary of isolated three port dc-dc converters are presented here.

2.3. Different Converter Cell/Blocks for Three Port Isolated DC-DC Converter

The isolated dc-dc converters presented in different literatures, mostly work on phase shift or duty cycle control techniques. Several different converters have been proposed by researchers for different applications, power levels & operating scenarios. One of the most simple topology for

isolated dc-dc converter is Dual Active Bridge Converter[60], which has inherent Zero Voltage Switching(ZVS) in it providing the capability to switch at higher frequency. Several other converters have also been developed been researchers, which can be broadly categorized as phase shifted converters[60],[47]-[56]. There are three most widely used type of converter cell/blocks for phase shifted converters [47]-[56]. Figures 2.10-2.13 show the four converter cells as given below.

- Boost Cell
- Boost Isolated Cell
- Half Bridge Cell
- Full Bridge Cell

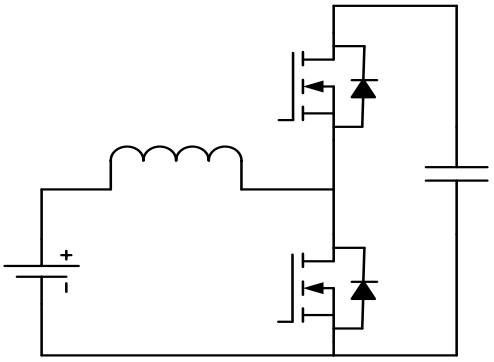

Figure 2.10. Bidirectional Boost Cell.

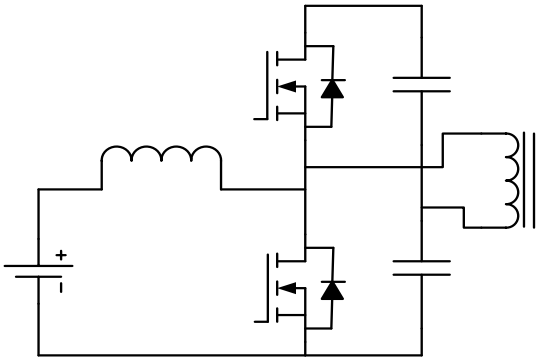

Figure 2.11. Bidirectional Boost Isolated Cell.

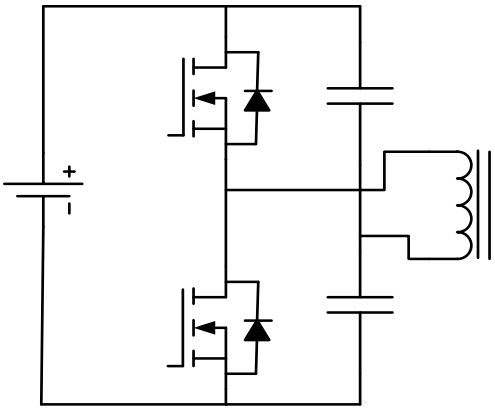

Figure 2.12. Half Bridge Cell.

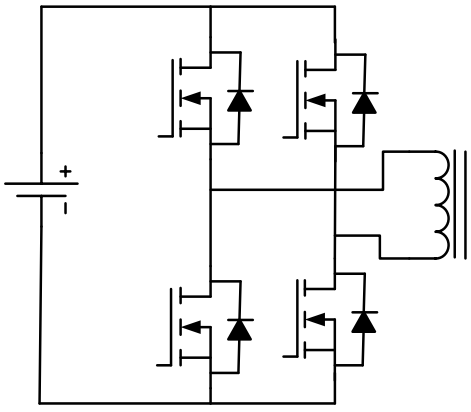

Figure 2.13. Full Bridge Cell.

The converter cell blocks in figures 2.10-2.13 can act as single converter unit for different ports of a three port or multi-port converter system. Using the boost cell unit and boost half bridge cell units, the dc sources act as current sources whereas using the half bridge and full bridge cell units, the dc sources act as voltage sources. Different converter architectures have been reported in literature for three port isolated dc-dc converter with a high frequency transformer isolation. Figures 2.14 and 2.15 show the converter schematic using boost cell and half bridge boost cell units. These two converter systems have non-isolated PV and Energy Storage ports, which entails their dc voltage levels to be close to each other, around 1.5-2.5 times for boost converter, and also requires extra inductor(s) and a two winding high frequency transformer[47]. However, one of the switches in each of the switching legs in primary side operate in hard switching manner while the other switch operates in soft switching manner. In figure 2.15, the primary side dc bus is connected across the source which results in loss of direct current control for storage[47-56].

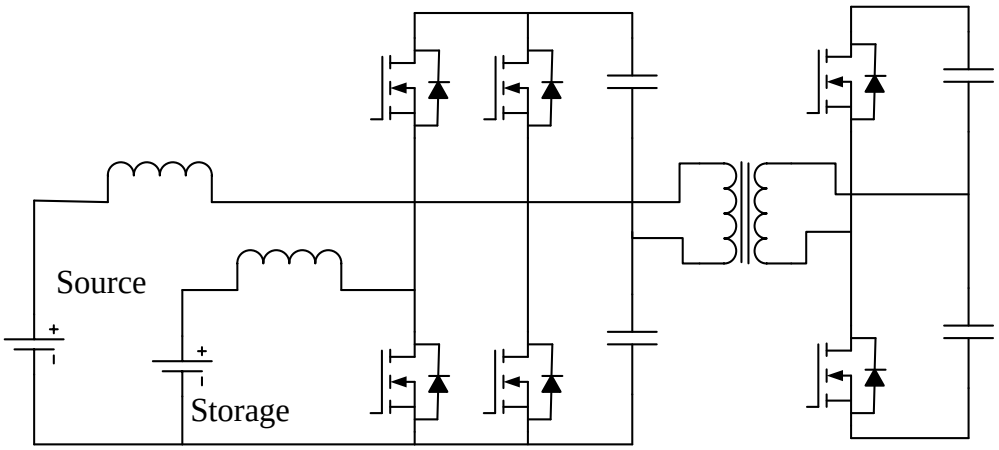

Figure 2.14. Converter Using Boost Cell, Half Bridge Boost Cell, Half Bridge Cell.

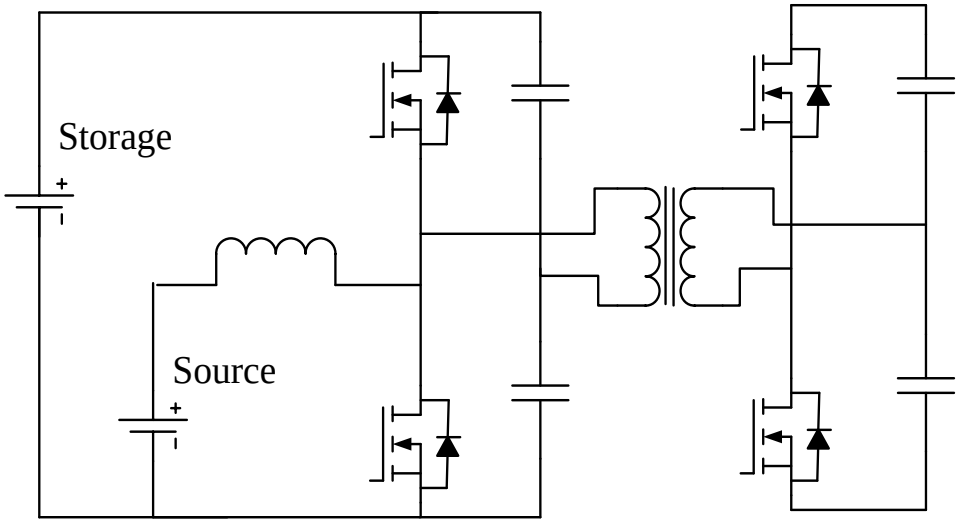

Figure 2.15. Converter Using Half Bridge Boost Cell and Half Bridge Cell.

Figure 2.16 shows the three winding converter architecture with two voltage fed ports and one current fed port. In this configuration, current stress on the semiconductors and current ripple on one dc port is reduced. However, with varying voltage source, the duty cycle adjustment can be provided with boost cell. Figure 2.17 shows another three winding architecture with two current fed ports and one voltage fed port[40]. Using this configuration, provides the flexibility to control the current ripple for both the dc source and storage, however, two separate inductors are required for the two boost half bridge cells, and the hard-switching is present for two of the boost switching legs.

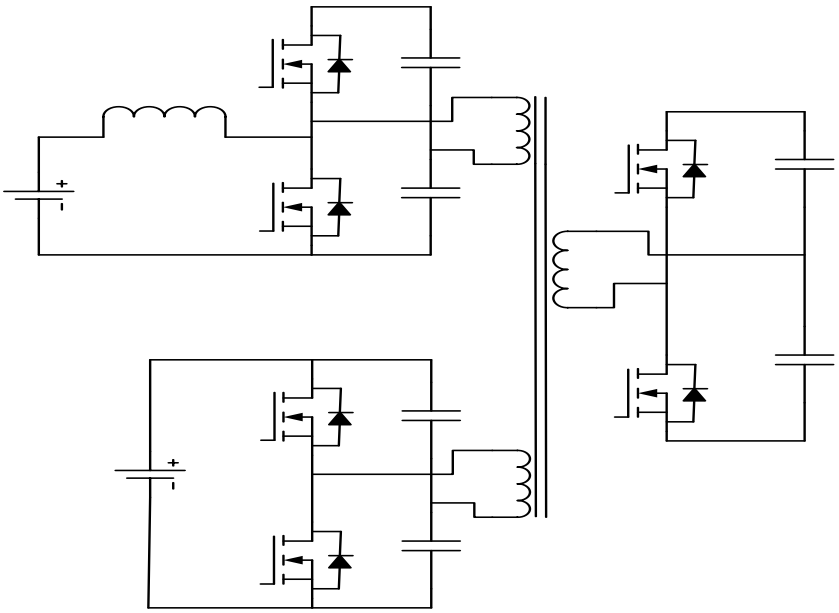

Figure 2.16. Isolated Bidirectional Three Port Converter.

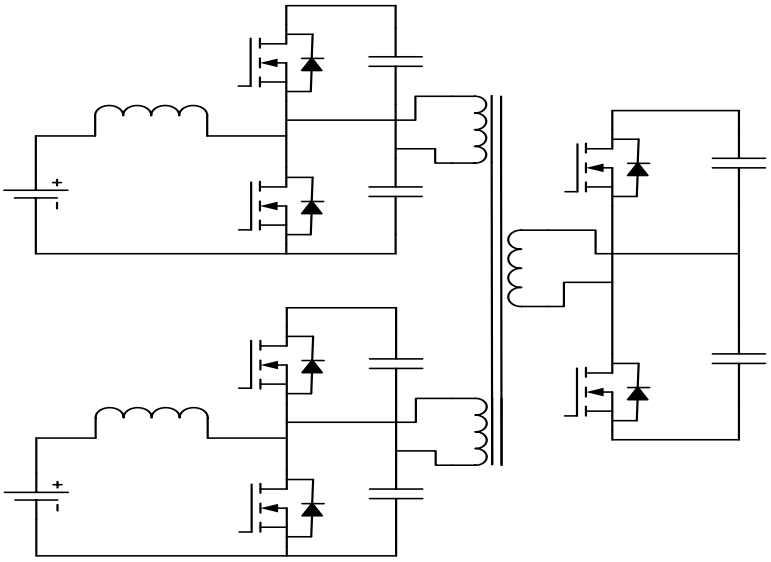

Figure 2.17. Isolated Bidirectional Three Port Converter.

Figures 2.18 and 2.19 show the three port voltage fed converter system using a single magnetic structure of three winding transformer[48][49]. The topologies shown in figures 2.18 and 2.19 are known as Triple Active Bridge(TAB) converters. Figure 2.18 show the three port TAB converter architecture using three half bridge cell units and figure 2.19 show the same architecture using

three full bridge cell units. The full bridge cell units have higher number of device counts but for high power application, the current stresses on the switches are reduced, and also full bridge architecture provides the flexibility of phase shift control and duty cycle control of winding voltages while the half bridge architecture provides only phase shift control technique. The operation of Triple Active Bridge(TAB) converter has first been proposed in [56], which is similar to the working principle of Dual Active Bridge(DAB) converter. Therefore, the use of duty cycle control similar to that used for DAB control([61],[62]) can also be applied to TAB converter and the advantages of higher ZVS operating ranges and optimum operation can be achieved for TAB converter. For the thesis work presented here, the focus has been to develop a high power dc-dc unit, integrating PV and ES, for 10kW & 50kW applications. Since the full bridge converter architecture of figure 2.19 provides extra degree of control freedom, the work presented in this report has pursued the full bridge converter architecture.

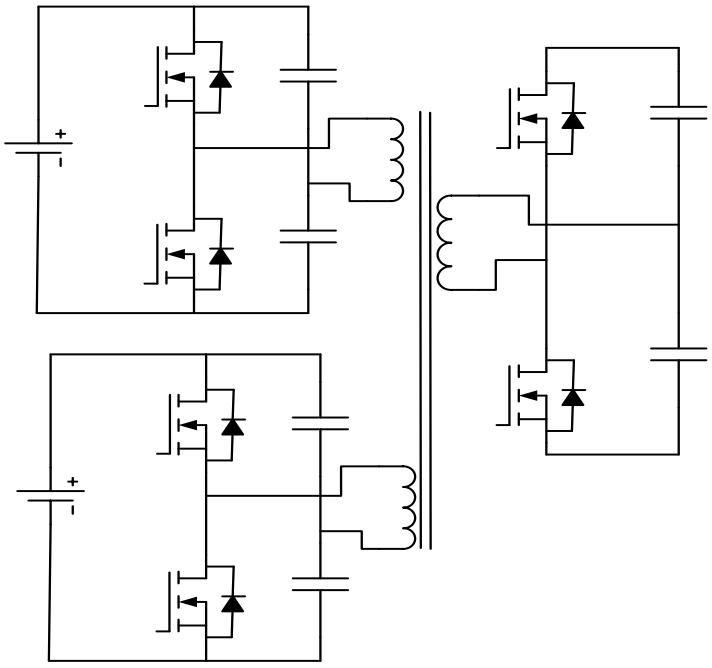

Figure 2.18. Converter Using Three Half Bridges and Three Winding Transformer.

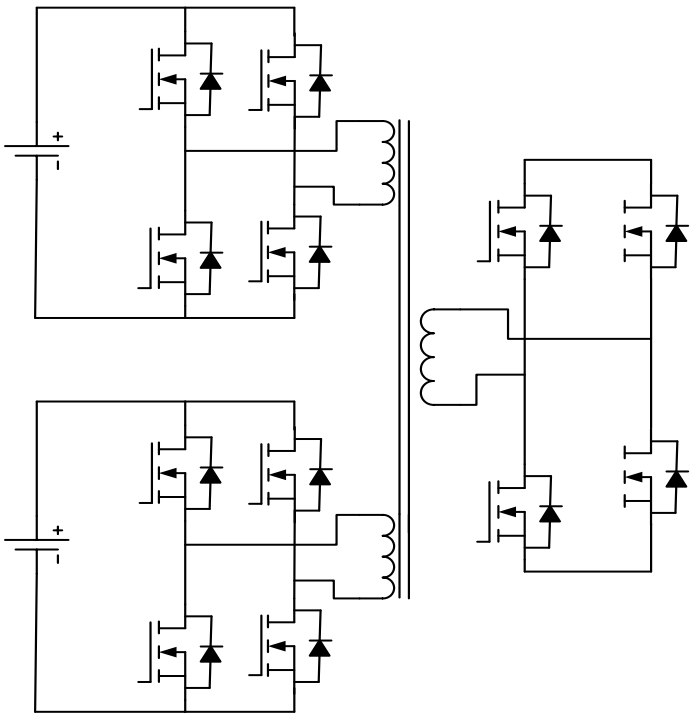

Figure 2.19. Converter Using Three Full Bridges and Three Winding Transformer.

2.4. Three Port High Frequency Transformer Isolated Triple Active Bridge DC-DC Converter

The Triple Active Bridge converter of figure 2.19, is a three port converter where every port is bidirectional in nature. The converter has inherent Zero Voltage Switching(ZVS) during device turn-on which provides low switching losses. The ZVS criteria makes it suitable to be used with SiC MOSFETs, which has very low switching losses compared to similar rated Si IGBTs. Therefore, TAB converter using SiC MOSFETs is a preferable approach to have lower semiconductor losses(due to ZVS switching at turn-on & low switching loss during turn-off) and higher efficiencies. A schematic of the TAB converter is shown in figure 2.20, where a single high frequency transformer unit with its leakage inductances, acts as the energy transferring element. The equivalent circuit of the general three winding transformer is shown in figure 2.21.

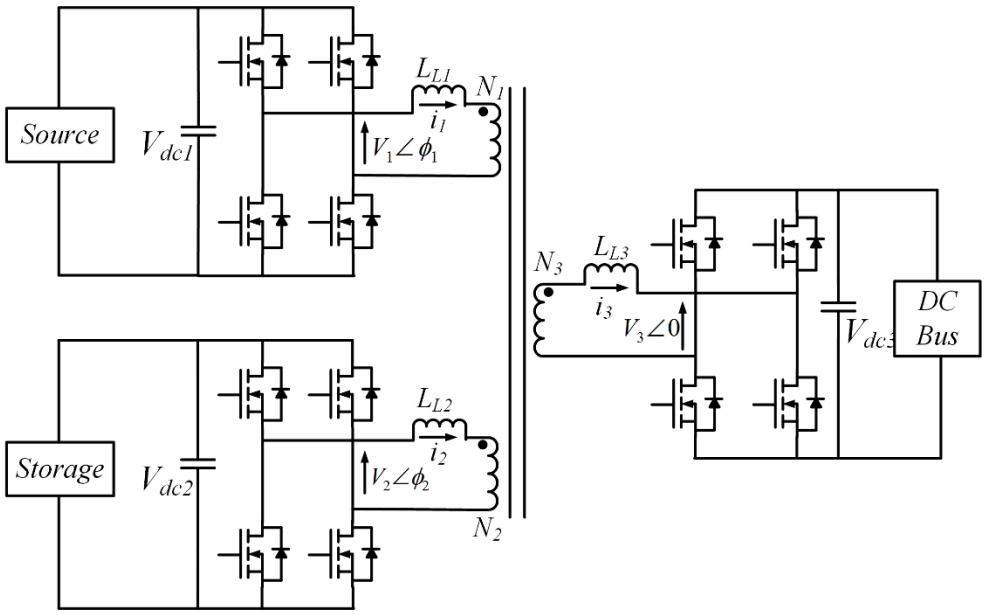

Figure 2.20. Triple Active Bridge Converter.

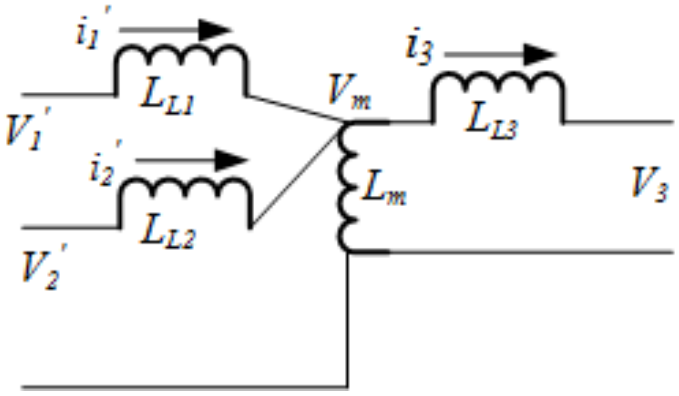

Figure 2.21. Equivalent Circuit of Transformer for TAB Converter.

The advantages of Triple Active Bridge converter lies within the inherent properties such as (1) All ports are bidirectional in nature, (2) Zero Voltage Switching(ZVS) for Mosfets, (3) Single High Frequency Magnetic component, (4) Leakage Inductance acting as energy transferring element, (4) Magnetizing Current sharing by different ports, which depends on the leakage inductances of different ports, resulting in reduction of core losses. The Triple Active Bridge

converter thus can be used as a general purpose three port converter for other three port applications such as battery-grid-load integration, integrating different dc grids etc.

There have been considerable research efforts being directed towards triple active bridge converter of figure 2.20 over the years. A great deal of effort has been directed towards achieving ZVS range extension, power decoupling, power flow control, however the high frequency transformer current control suitable for avoiding dc transients, for three port converter has not been addressed in literature([87],[88],[91],[92],[96],[97]). Few of the research motivations have been directed towards topology modification, using half bridge cells in place of full bridge cells[88], use of series resonant tank in addition with series inductors[90], using the dc-dc converter for bipolar dc grid applications[94] and using two transformers in place of one single three port transformer[95]. Majority of the research efforts have been towards development of low power converter prototypes[91,93]. A three port three phase transformer base high power three port transformer has been proposed in [89], but the proposed topology increases the component count of the converter. The research efforts towards the three port phase shifted converter have not addressed the three port transformer design aspects and have not investigated different three port transformers for TAB converters. The research work presented in this paper has addressed use of ferrite core based transformers for high frequency operation[50kHz-100kHz] and use of nano-crystalline or tape wound core transformer for 10kHz-20kHz applications. The advent of SiC devices has prompted the use of high frequency converters for high/medium power applications, which need suitable magnetics for operation.

2.5. High Frequency Transformer for Isolated DC-DC Converter

High frequency transformer is the one of the most important element of isolated dc-dc converter. As mentioned before, the isolation transformer provides isolation, voltage gain and

reduces the common mode leakage current. In any transformer isolated converter topology, the common mode leakage current flows through the transformer's inter-winding parasitic capacitances[59] and its value depends on the inter-winding parasitic capacitance values. The transformer inter-winding parasitic capacitance is affected by winding and core geometry. The leakage impedance of high frequency transformer act as energy transferring element for phase shifted converters. The parasitic capacitance and leakage inductance are in general inversely related to each other, the parasitic capacitance is high when leakage inductance is low, and the parasitic capacitance is low when leakage inductance is high. This is explained by the field theory as follows - the electric field is high and the leakage flux is low if two energized current carrying windings are close to each other, while the electric field is low and the leakage flux is high if two energized current carrying windings are placed far from each other. Several transformer geometries have been in use for transformer design based on different core type and winding type configurations. Few of the commonly used geometry types are mentioned below which are used for high frequency transformers.

- Core type winding transformers
- Shell type winding transformers
- Concentric winding transformers
- Planar type transformers
- Co-axial winding type transformers

From the list of above mentioned transformers, the inter-winding capacitances vary based on the geometry and winding arrangement. A comparative evaluation of winding parasitic capacitance is carried out between a core type transformer and a concentric winding transformer

using cores of same size and windings for same number of turns. Figures 2.22 and 2.23 show the three winding transformers using core type arrangement and concentric type arrangement.

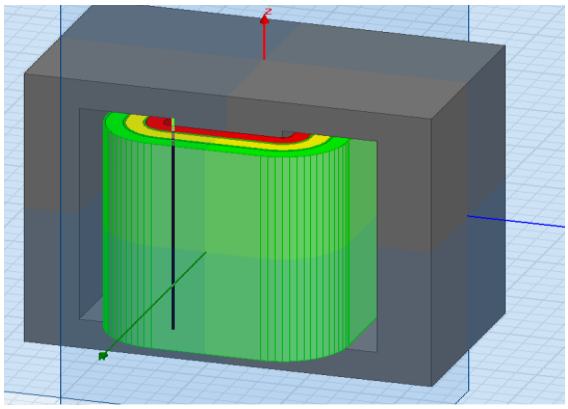

Figure 2.22. Concentric Type Winding.

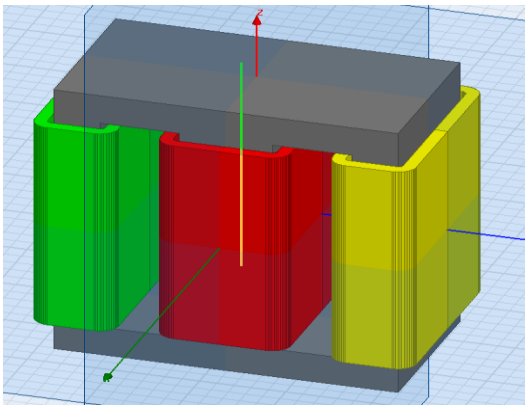

Figure 2.23. Core Type Winding.

Table 3. Comparison of Inter-winding Parasitic Capacitance

Concentric Type Winding Arrangement	Core Type Winding Arrangement
$C_{inter\text{-}winding}$: 300-400 pF	$C_{inter\text{-}winding}$: 20-30 pF

A comparison of the effect of the inter-winding parasitic transformer is carried out using MATLAB/PLECS simulation platform, where a three winding model of [49] is considered for circuit simulation and inter-winding capacitances are placed as follows. Figures 2.24 shows the winding current waveforms when the inter-winding capacitances are around 20pF and figure 2.25 show the current waveforms when the capacitances are around 200pF. It can be observed that the winding currents for high inter-winding capacitances have high ringing on the current. A more dominant effect of current ringing due to inter-winding parasitic capacitances have been explained in [59], where the switching frequency is very close to resonance peak of transformer open circuit impedance due to inter-winding capacitances of range 1nF. The simulation scenarios

is recreated with a 20 times higher magnetizing inductance and the winding current waveforms are observed, as shown in figure 2.26.

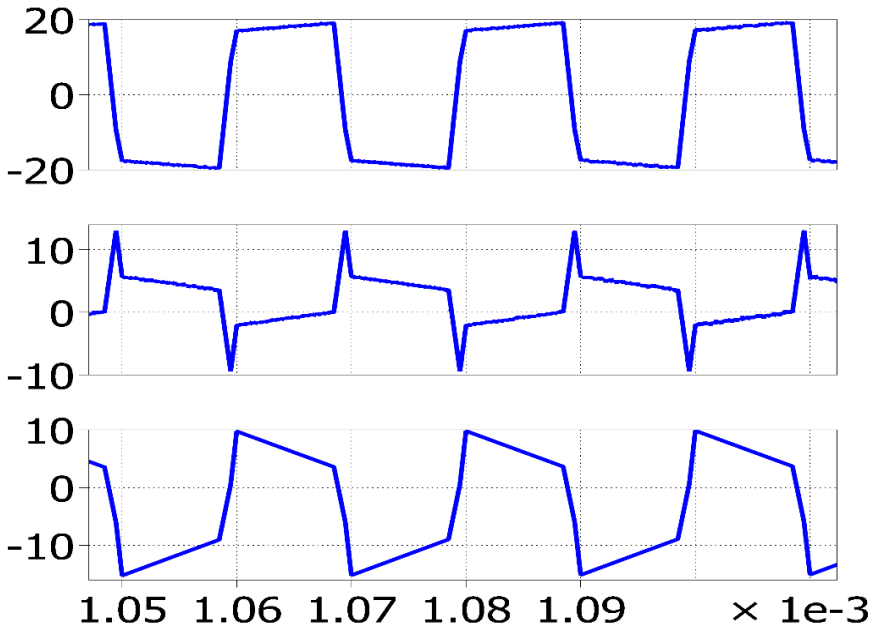

Figure 2.24. Transformer Winding Currents for 20pF Inter-Winding Capacitances.

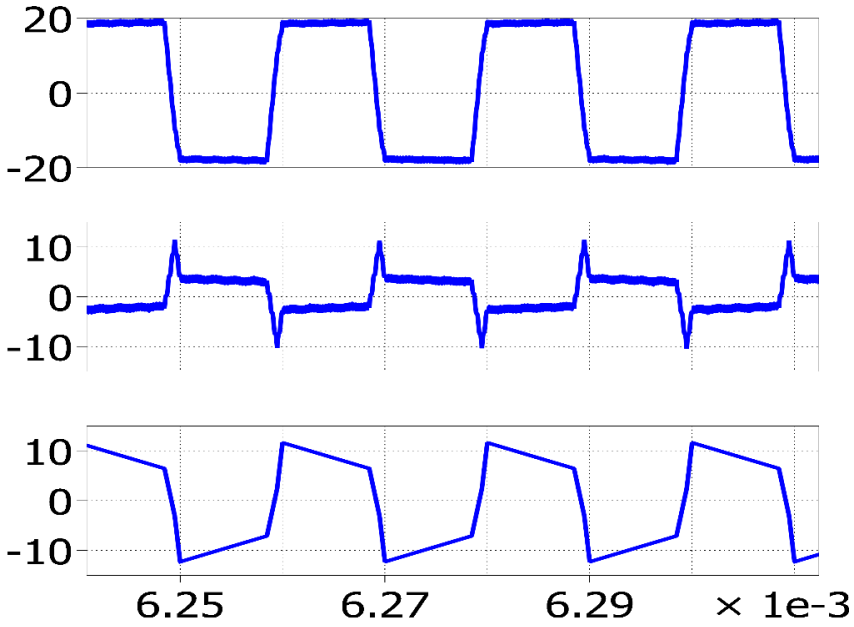

Figure 2.25. Transformer Winding Currents for 200pF Inter-Winding Capacitances.

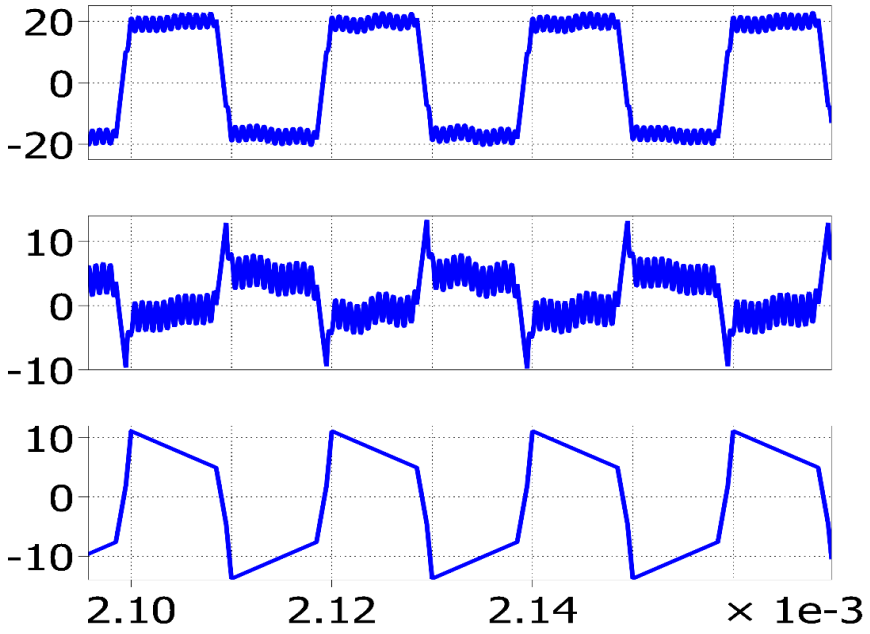

Figure 2.26. Transformer Winding Currents for 1nF Inter-Winding Capacitances.

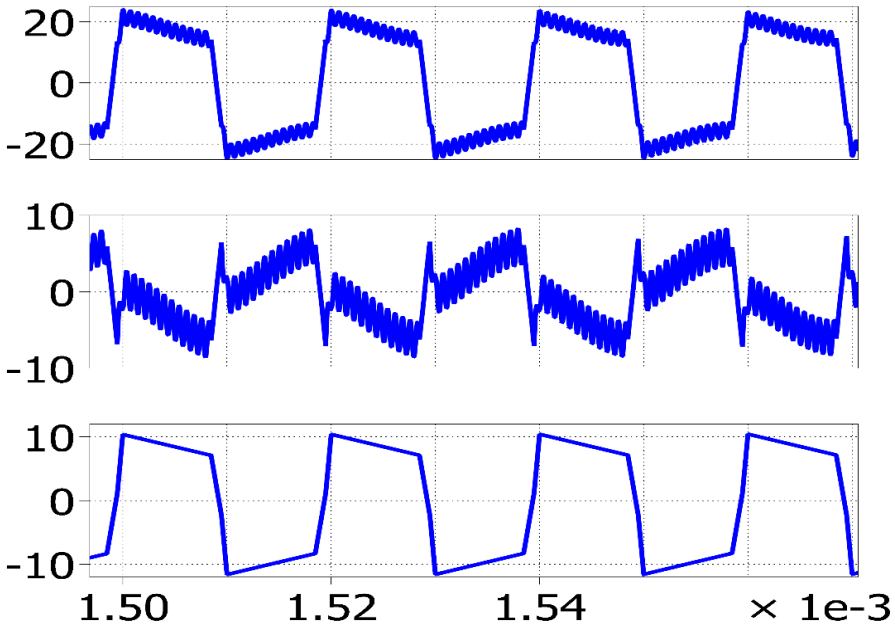

Figure 2.27. Transformer Winding Currents for High Magnetizing Inductace and 1nF Interwinding Capacitances.

The above figures of transformer waveforms indicate the ringing in winding currents due to inter-winding capacitances' effects. As the capacitance grows higher, the ringing and oscillation increases. The transformer waveforms for figure 2.24-2.27 are for 50kHz switching frequency, where the switching frequency is low enough compared to ringing frequency. But for the case in figure 2.27, the oscillation is dominant and distorts the current waveform heavily. The thesis work presented in this report, focuses on low parasitic based high frequency transformer analysis, understanding and experimental performance evaluation for PV and ES integration.

2.6. Conclusion

The dc-dc converter is the most crucial element of three port phase-shift controlled dc-dc converter. Three port isolated converter provides isolation between all three dc ports using a three-winding transformer. From above discussion, it is clear that the core type topology for high frequency transformer provides lower inter-winding parasitic capacitance than concentric type winding. The three-limb core type transformer is discussed in this thesis work for having lower inter-winding parasitic capacitance, ease of construction, lesser requirement of insulation for medium voltage prototype.

Chapter 3. Three Limb Three Winding Transformer

3.1. Magnetic Circuit and Equivalent Inductance Matrix Derivation

The magnetic circuits for magnetic components in power electronic circuits are important for proper and detailed understanding and analysis of power electronic converters. In order to derive the magnetic circuit model for three limb transformer, each winding is considered to have its own leakage inductance. When a voltage is applied on a transformer winding, part of the applied volt-seconds or induced flux flows through the core and links with other winding(s), known as mutual flux, while rest of it does not link with other winding(s), which mainly flows through air, core window volume and winding volume. Figure 3.1 shows the magnetic flux paths for three limb three winding transformer, where leakage fluxes are shown to flow through outside the core volume and mutual fluxes flow through the core. In the magnetic equivalent circuit of figure 3.1, the leakage fluxes are considered to be distributed among different windings. The leakage flux paths are assumed to be dominant around the winding regions only and leakages around yoke portions are neglected as the transformer core has much higher permeability than the air.

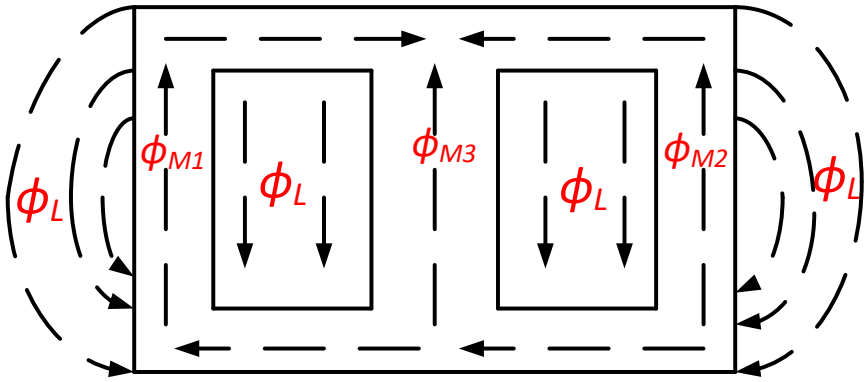

Figure 3.1. Flux Flow path for Mutual and Leakage Fluxes.

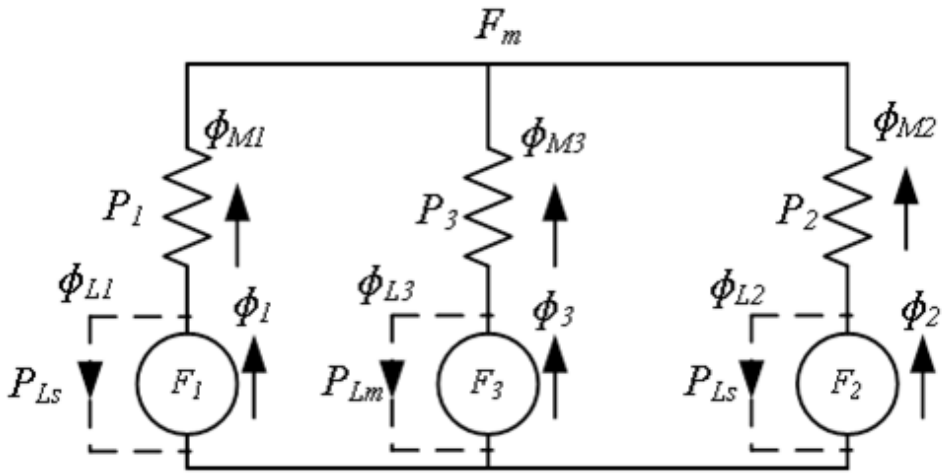

Figure 3.2. Magnetic Equivalent Circuit Model for Three Limb Transformer.

In figure 3.1, the MMF and permeance based magnetic circuit model for the three limb transformer is shown. In MMF based model, a winding is replaced by a MMF source and the transformer core is replaced by reluctance or permeance. The three MMF sources are F_1, F_2 and F_3 and the fluxes produced by the winding currents are denoted by ϕ_1, ϕ_2 and ϕ_3, which are equivalent to applied volt-seconds per turn. The fluxes ϕ_{M1}, ϕ_{M2} and ϕ_{M3} denote the fluxes that flow through each limb of the transformer core and link other windings. The leakage flux ϕ_L is divided among the three windings as ϕ_{L1}, ϕ_{L2} *and* ϕ_{L3}. The permeances for each flux path in the core limbs are given by P_1, P_2, P_3 and the permeances for leakage path are given by P_{Ls} *and* P_{Lm}. The leakage path permeances for the side limb windings are considered to be same. From figure 3.2, it can be observed that the sum of the instantaneous fluxes from the three limbs is zero, as shown by equation 3.1-3.2.

$$\phi_{M1} + \phi_{M2} + \phi_{M3} = 0 \quad (3.1)$$

$$(\phi_1 - \phi_{L1}) + (\phi_2 - \phi_{L2}) + (\phi_3 - \phi_{L3}) = 0 \quad (3.2)$$

Considering zero leakage fluxes, the expression for Fm is given as shown in equation 3.3.

$$F_m = \frac{F_1P_1 + F_2P_2 + F_3P_3}{P_1 + P_2 + P_3} \qquad (3.3)$$

Now, ϕ_{M1}, ϕ_{M2} and ϕ_{M3} can be expressed in terms of MMFs F_1, F_2 and F_3 as given in equation 3.4-3.6.

$$\phi_{M1} = (F_1 - F_m)P_1 \quad (3.4), \quad \phi_{M2} = (F_2 - F_m)P_2 \quad (3.5), \quad \phi_{M3} = (F_3 - F_m)P_3 \quad (3.6)$$

Replacing Fm with (3.3), the three fluxes ϕ_1, ϕ_2 and ϕ_3 can be expressed as follows.

$$\begin{bmatrix} \phi_{M1} \\ \phi_{M2} \\ \phi_{M3} \end{bmatrix} = \frac{1}{(P_1+P_2+P_3)} \begin{bmatrix} (P_2+P_3)P_1 & -P_1P_2 & -P_1P_3 \\ -P_1P_2 & (P_1+P_3)P_2 & -P_3P_2 \\ -P_1P_3 & -P_3P_2 & (P_1+P_2)P_3 \end{bmatrix} \begin{bmatrix} F_1 \\ F_2 \\ F_3 \end{bmatrix} \qquad (3.7)$$

Now the fluxes ϕ_{M1}, ϕ_{M2} and ϕ_{M3} can be related to the leakage fluxes as given in equations 3.8-3.10.

$$\phi_{M1} = \phi_1 - \phi_{L1} \quad (3.8), \quad \phi_{M2} = \phi_2 - \phi_{L2} \quad (3.9), \quad \phi_{M3} = \phi_3 - \phi_{L3} \quad (3.10)$$

Now ϕ_{L1}, ϕ_{L2} and ϕ_{L3} can be related to their leakage flux path permeances P_{L1}, P_{L2} and P_{L3} as given in equation 3.11-3.13. Equation (3.7) is modified as given in (3.14).

$$\phi_{L1} = P_{L1}F_1 \quad (3.11), \quad \phi_{L2} = P_{L2}F_2 \quad (3.12), \quad \phi_{L3} = P_{L3}F_3 \quad (3.13)$$

$$\begin{bmatrix} \phi_1 \\ \phi_2 \\ \phi_3 \end{bmatrix} = \frac{1}{(P_1+P_2+P_3)} \begin{bmatrix} (P_2+P_3)P_1 & -P_1P_2 & -P_1P_3 \\ -P_1P_2 & (P_1+P_3)P_2 & -P_3P_2 \\ -P_1P_3 & -P_3P_2 & (P_1+P_2)P_3 \end{bmatrix} \begin{bmatrix} F_1 \\ F_2 \\ F_3 \end{bmatrix} + \begin{bmatrix} P_{L1} & 0 & 0 \\ 0 & P_{L2} & 0_2 \\ 0 & 0 & P_{L3} \end{bmatrix} \begin{bmatrix} F_1 \\ F_2 \\ F_3 \end{bmatrix} \qquad (3.14)$$

The fluxes ϕ_1, ϕ_2 and ϕ_3 are respective winding voltages' volt-seconds per turn. Considering the side limb windings being similar their core and leakage permeances are considered same, thus $P_{L1}=P_{L2}=P_{Ls}$, and $P_{L3}=P_{Lm}$ and $P_1=P_2=P_s$, $P_3=P_m$.

$$\begin{bmatrix}\phi_1\\ \phi_2\\ \phi_3\end{bmatrix}=\frac{1}{(2P_s+P_m)}\begin{bmatrix}(P_s+P_m)P_s & -P_s^2 & -P_sP_m\\ -P_s^2 & (P_s+P_m)P_s & -P_sP_m\\ -P_sP_m & -P_sP_m & 2P_sP_m\end{bmatrix}\begin{bmatrix}F_1\\ F_2\\ F_3\end{bmatrix}+\begin{bmatrix}P_{Ls} & 0 & 0\\ 0 & P_{Ls} & 0_2\\ 0 & 0 & P_{Lm}\end{bmatrix}\begin{bmatrix}F_1\\ F_2\\ F_3\end{bmatrix} \quad (3.15)$$

The above equation (3.15) can be expressed in terms of winding voltages and currents as follows in (3.16).

$$\begin{bmatrix}\frac{1}{N_1}\int V_1dt\\ \frac{1}{N_2}\int V_2dt\\ \frac{1}{N_3}\int V_3dt\end{bmatrix}=\frac{1}{(2P_s+P_m)}\begin{bmatrix}(P_s+P_m)P_s & -P_s^2 & -P_sP_m\\ -P_s^2 & (P_s+P_m)P_s & -P_sP_m\\ -P_sP_m & -P_sP_m & 2P_sP_m\end{bmatrix}\begin{bmatrix}N_1i_1(t)\\ N_2i_2(t)\\ N_3i_3(t)\end{bmatrix}+\begin{bmatrix}P_{Ls} & 0 & 0\\ 0 & P_{Ls} & 0_2\\ 0 & 0 & P_{Lm}\end{bmatrix}\begin{bmatrix}N_1i_1(t)\\ N_2i_2(t)\\ N_3i_3(t)\end{bmatrix} \quad (3.16)$$

Differentiating both sides w.r.t time parameter ‘t’, the winding voltage expressions are obtained as given in (3.17), which can be simplified into an inductance matrix form given in (3.18).

$$\begin{bmatrix}V_1\\ V_2\\ V_3\end{bmatrix}=\begin{bmatrix}\frac{N_1^2(P_s+P_m)P_s}{(2P_s+P_m)}+N_1^2P_{Ls} & \frac{-N_1N_2P_s^2}{(2P_s+P_m)} & \frac{-N_1N_3P_sP_m}{(2P_s+P_m)}\\ \frac{-N_1N_2P_s^2}{(2P_s+P_m)} & \frac{N_2^2(P_s+P_m)P_s}{(2P_s+P_m)}+N_2^2P_{Ls} & \frac{-N_2N_3P_sP_m}{(2P_s+P_m)}\\ \frac{-N_1N_3P_sP_m}{(2P_s+P_m)} & \frac{-N_2N_3P_sP_m}{(2P_s+P_m)} & \frac{2N_3^2P_mP_s}{(2P_s+P_m)}+N_3^2P_{Lm}\end{bmatrix}\begin{bmatrix}\frac{d}{dt}i_1(t)\\ \frac{d}{dt}i_2(t)\\ \frac{d}{dt}i_3(t)\end{bmatrix} \quad (3.17)$$

$$\begin{bmatrix}V_1\\ V_2\\ V_3\end{bmatrix}=\begin{bmatrix}L_{11} & -L_{12} & -L_{13}\\ -L_{21} & L_{22} & -L_{23}\\ -L_{31} & -L_{32} & L_{33}\end{bmatrix}\begin{bmatrix}\frac{d}{dt}i_1(t)\\ \frac{d}{dt}i_2(t)\\ \frac{d}{dt}i_3(t)\end{bmatrix} \quad (3.18)$$

$$L_{11} = \frac{N_1^{\,2}(P_s + P_m)P_s}{(2P_s + P_m)} + P_{Ls} \quad (3.19), \qquad L_{22} = \frac{N_2^{\,2}(P_s + P_m)P_s}{(2P_s + P_m)} + P_{Ls} \quad (3.20)$$

$$L_{21} = L_{12} = \frac{N_1 N_2 P_s^{\,2}}{(2P_s + P_m)} \quad (3.21), \quad L_{31} = L_{13} = \frac{N_1 N_3 P_s P_m}{(2P_s + P_m)} \quad (3.22)$$

$$L_{32} = L_{23} = \frac{N_2 N_3 P_s P_m}{(2P_s + P_m)} \quad (3.23), \quad L_{33} = \frac{2N_3^{\,2} P_m P_s}{(2P_s + P_m)} + P_{L3} \quad (3.24)$$

3.2. Equivalent Electrical Circuit Derivation

The equivalent electrical circuit for three limb transformer is derived in this section based on the magnetic circuit. The leakage inductance and magnetizing inductance based electrical equivalent circuit is derived in this section. From figure 3.2, the magnetic circuit for three limb transformer provides the relation given in 3.17. The leakage fluxes of transformer windings are related to the winding currents and respective number of turns. The leakage fluxes ϕ_{L1}, ϕ_{L2} and ϕ_{L3} can be written in terms of winding currents as given in 3.25-3.27.

$$\phi_{L1} = \frac{\lambda_{L1}}{N_1} = \frac{L_{L1} I_1}{N_1} \quad (3.25), \quad \phi_{L2} = \frac{\lambda_{L2}}{N_2} = \frac{L_{L2} I_2}{N_2} \quad (3.26), \quad \phi_{L3} = \frac{\lambda_{L3}}{N_3} = \frac{L_{L3} I_3}{N_3} \quad (3.27)$$

In the equation (3.2), the fluxes ϕ_1, ϕ_2 and ϕ_3 are written in terms of volt-seconds and leakage fluxes are written in terms of leakage inductances and winding currents. Differentiating the equation w.r.t. time gives the equation 3.28, which represents three voltage sources in series connection. The equivalent electrical circuit is thus represented by three transformers whose secondary windings are in series, as shown in figure 3.3. The polarity of V_3 is taken as opposite to that mentioned in equation 3.28. From figure 3.3, it can be observed that three transformers have same secondary current i_s. Neglecting the magnetizing inductance current, the three

windings have the following relation given in 3.28, representing same MMF across all the windings.

$$\frac{1}{N_1}(V_1 - L_{L1}\frac{di_1}{dt}) + \frac{1}{N_2}(V_2 - L_{L2}\frac{di_2}{dt}) + \frac{1}{N_3}(V_3 - L_{L3}\frac{di_3}{dt}) = 0 \quad (3.28)$$

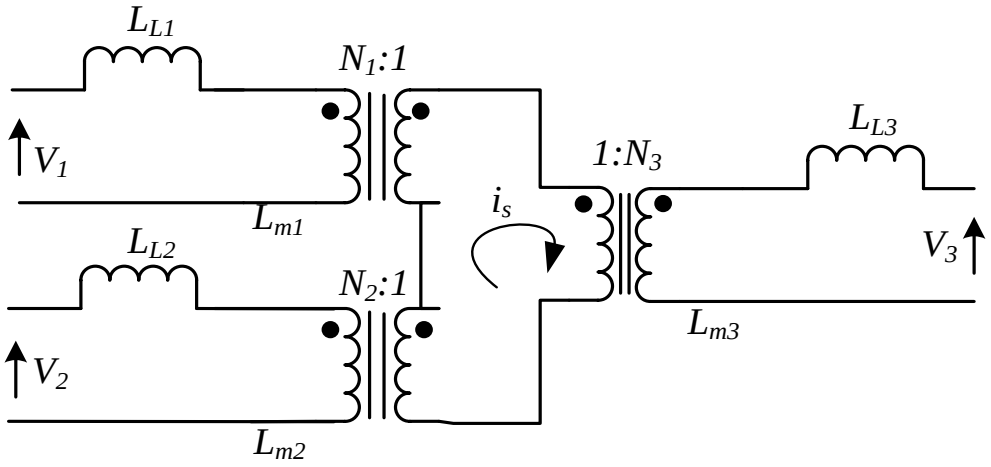

Figure 3.3. Eq. Circuit for Three Limb Transformer neglecting L_m.

$$N_1 i_1 = N_2 i_2 = N_3 i_3 = i_s \quad (3.29)$$

From the equation (3.17), the self-inductance terms have a leakage component and a magnetizing component. It can be observed that the magnetizing component of L_{33} is sum of the of L_{31} and L_{32} multiplied by respective turns ratio square, given in (3.30). Considering the magnetizing inductance current, the MMF relation can be expressed as shown in (3.31). The equivalent circuit representing the three limb transformer using L_{m3} is shown in figure 3.4. Referring the magnetizing inductance to side limb windings, the magnetizing inductance can be split up as shown in figure 3.5. The magnetizing inductance in the circuit shown in figure 3.4 represents the measured open circuit inductance seen from the middle winding of three limb transformer.

$$L_{m3} = L_{33} - L_{L3} = (\frac{N_3}{N_1})^2 L_{31} + (\frac{N_3}{N_2})^2 L_{32} = \frac{2N_3{}^2 P_m P_s}{(2P_s + P_m)} \quad (3.30)$$

$$N_1(i_1 - i_{m1}) = N_2(i_2 - i_{m2}) = N_3(i_3 - i_{m3}) = \mathrm{i_s} \quad (3.31)$$

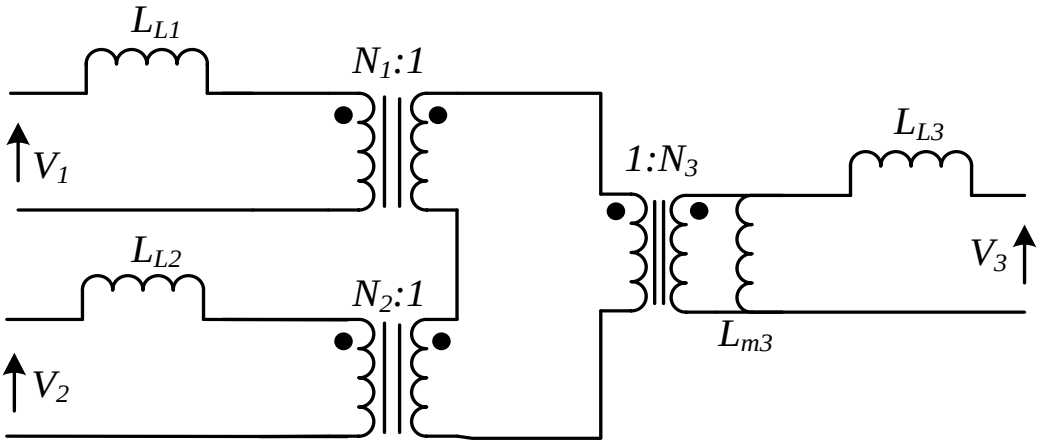

Figure 3.4. Eq. Circuit for Three Limb Transformer With L_{m3}.

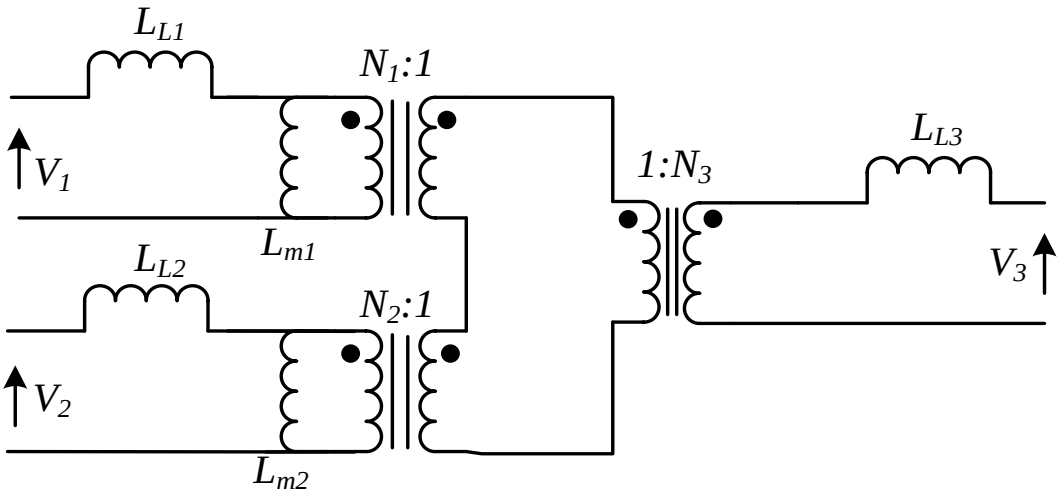

Figure 3.5. Electrical Equivalent Circuit With L_{m1} and L_{m2}.

Considering the circuit of figure 3.3, while neglecting magnetizing inductance, the three transformer model can be simplified into two transformer based model, as shown in figure 3.6,

where L_{eq} is the leakage inductance seen from middle limb winding. R_s is the series resistance measured from middle winding. From figure 3.6, the leakage inductances L_{L1} and L_{L2} can be referred to middle winding using turns ratio and since the circuit is series in nature, they can be added together as shown in equation (3.32).

$$L_{eq} = L_{L3} + (\frac{N_3}{N_1})^2 L_{L1} + (\frac{N_3}{N_2})^2 L_{L2} = N_3{}^2 (P_{Lm} + 2P_{Ls}) \quad (3.32)$$

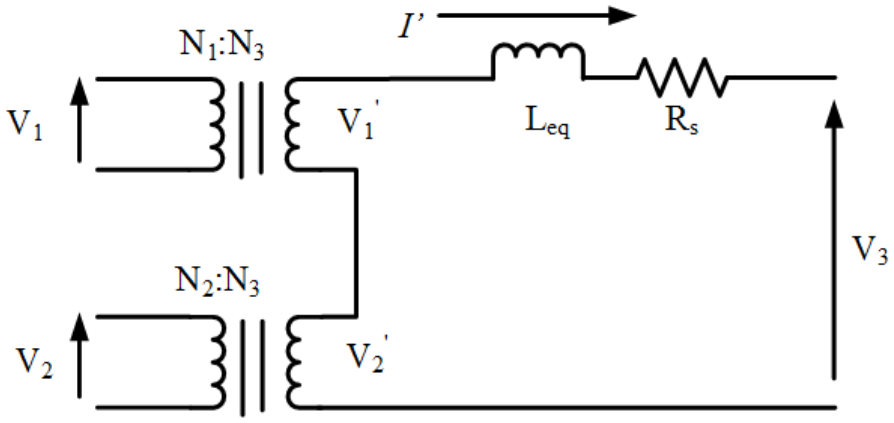

Figure 3.6. Reduced order Electrical Equivalent Circuit for Three Limb Transformer.

3.3. Leakage Inductance and Parasitic Capacitance Estimation for Three Limb Three Winding Transformer

Estimation of parasitic elements such as leakage inductance and coupling capacitance of high frequency transformers are important, specially for applications similar as Dual Active Bridge(DAB) Converters where the semiconductor dV/dT transient(generated due to fast switching of devices) is seen by the winding on the magnetic core. For DAB applications, the leakage inductance acts as the power transferring element, higher the power required, lower should be the leakage inductance. The leakage inductance also acts as a key element for enabling ZVS turn-on of switching devices, therefore the leakage inductance should have a significant

value so that it has enough energy to discharge the parasitic capacitance of the device within the dead-time interval[53] of a switching leg. Hence estimation of leakage inductance is a key factor for designing of high frequency transformer. The coupling capacitance plays an important role in common mode and EMI considerations. For isolated PV systems, the PV parasitic capacitance between PV terminals and ground has significant value. In order to minimize its effects, the inter-winding parasitic capacitance of the transformer should be low enough so that it offers high impedance to the common mode current path of the system. In this section, analytical estimation of leakage inductance and coupling capacitance of transformer is presented along with FEA models and experimental measurements. The analytical models are represented in terms of transformer core geometry parameters. The leakage inductance is expressed in terms of core dimensions and winding dimensions. Wire dimensions' effects are neglected here. The research work presented here has mostly used litz wires for transformer designs. Therefore the current distribution inside window area of transformer is considered uniform, which leads to consideration of MMF distribution as linear across the winding width. The front view and side view of a three limb three winding transformer is shown in figure 3.7.

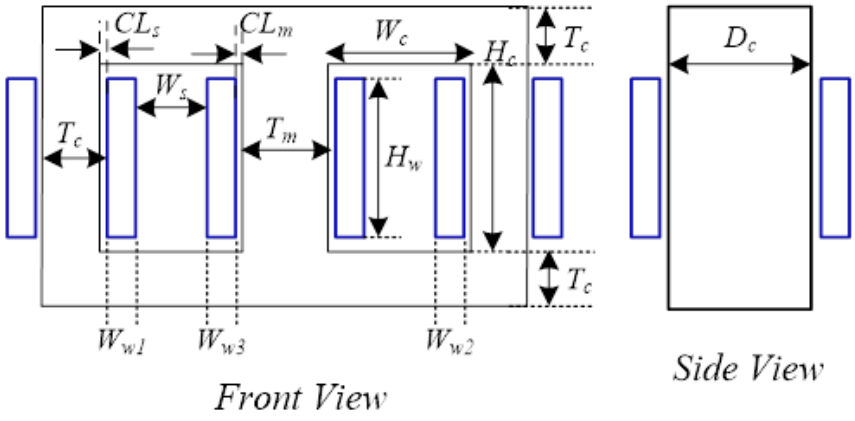

Figure 3.7. Dimensional View for Three Limb Three Winding Transformer.

Dc = core depth

Hc = window height

Wc = window width

Tc = side limb and yoke thickness

Tm = the middle limb thickness

W_{W1} = winding 1 thickness

W_{W2} = winding 1 thickness

W_{W3} = winding 1 thickness

CL_s and CL_m = clearance between windings and the core

Hw = same height for all the windings

Analytical methods for leakage inductance estimation for concentric type windings and sandwich type windings have been carried out in [63]-[64], which considers the flux distribution along the winding volume only. Leakage inductance estimation for core-type transformers have been done in [65] but the presented models are not discussed in detail. An approximate method of finding the pemeances for different geometrical shapes and volumes have been presented in [66], which have been more precisely detailed & explained in [67]. In order to estimate the leakage inductances of three limb transformers, the methods presented for permeance estimation in [66]-[67], is followed.

The leakage inductance of the aforementioned three limb transformer is estimated by evaluating the permeances of different leakage paths. The leakage paths considered here are shown in figures 3.8-3.12. Figure 3.8 shows the leakage volumes PL_1, PL_2, PL_4 across the core as seen from the front view. Figure 3.9 shows the leakage volume across the core from side view. The permeance P_{L1} is represented by the volume inside the core, permeance P_{L4} is represented by

the half hollow cylindrical volume across the core yoke both in front view and side view. The permeance P_{L2} is represented by the half cylinder volume across the window portion only. The permeance P_{L3} is represented by the hollow quarter spherical volume as shown in figure 3.10. The windings are considered rectangular blocks, hence the permeances across the windings are represented by two type of volumes, P_{L5} which is a hollow half cylindrical volume representing the leakage flux across a portion of winding, along the length of winding and R_{L2} which is hollow quarter spherical leakage flux volume across the winding corner portions.

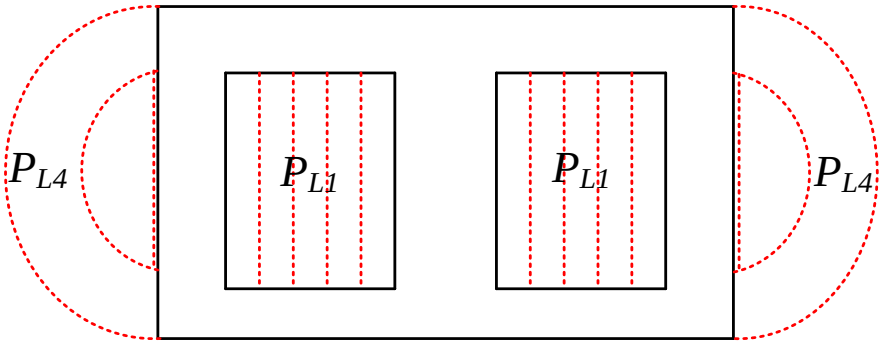

Figure 3.8. Leakage Paths for three Limb Transformer from the Front View.

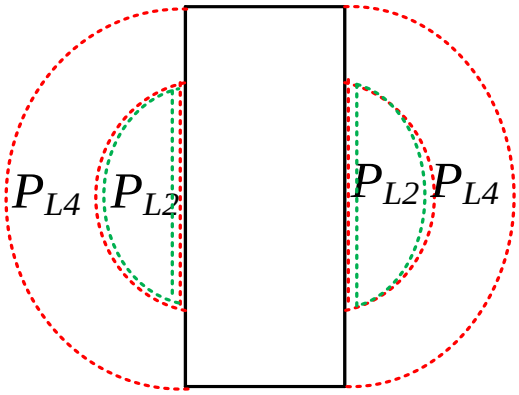

Figure 3.9. Leakage Path for Core from Side View.

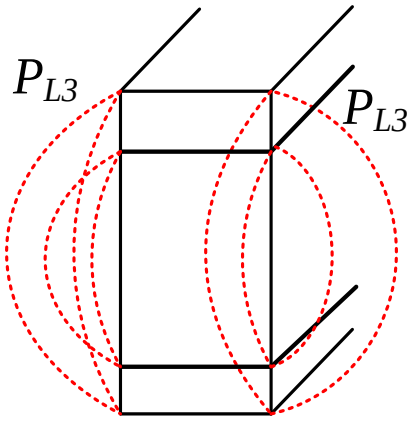

Figure 3.10. Leakage Path for Core from Corner View.

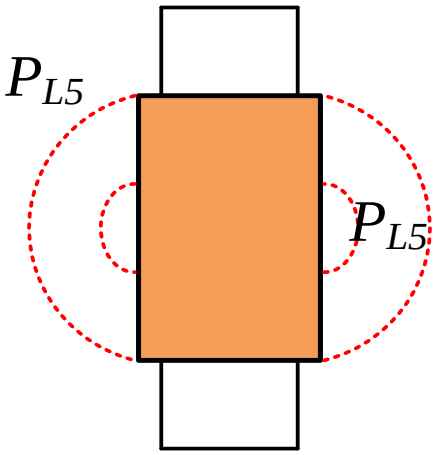

Figure 3.11. Leakage Path for Winding along its Length.

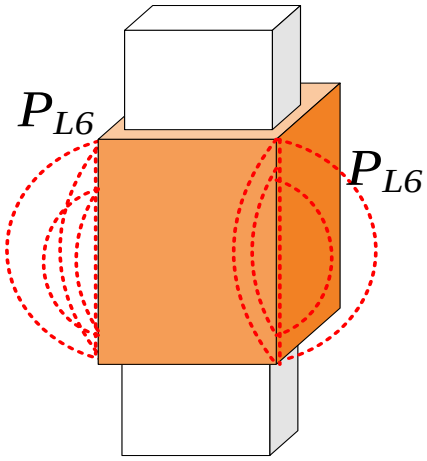

Figure 3.12. Leakage Path for Winding from Corner.

The permeance expressions for these volumes are represented as follows in expression (3.33). The leakage inductance is expressed as sum of all individual permeances, as given in (3.34). The individual leakage inductances evaluated following (3.33) and are given in (3.35)-(3.41).

$$P_L = \mu_0 \frac{A}{L} = \mu_0 \frac{A.L}{L^2} = \mu_0 \frac{V}{L^2} \quad (3.33) \qquad L_l = N^2 \sum P_L \quad (3.34)$$

$$P_{L1} = 2(\mu_0 \frac{D_c W}{H_c}) \quad (3.35), \quad P_{L2} = 4(0.24\mu_0 W_c) \quad (3.35), \quad P_{L3} = 4\mu_0 \frac{T_c}{\pi} \quad (3.36)$$

where $W = (W_s + \frac{W_{w1,2}}{3} + \frac{W_{w3}}{3})$ (3.37), $P_{L4} = \frac{2\mu_0}{\pi}(2(W_c + T_c) + D_c + T_m)\ln(1 + \frac{2T_c}{H_c})$ (3.38)

$$P_{L5\_1,2} = \frac{\mu_0}{\pi}(2T_c + D_c)\ln(1 + \frac{2H_{w1,2}/3}{H_{w1,2}/3}) \quad (3.39),$$

$$P_{L5\_3} = \frac{\mu_0}{\pi}(2T_m)\ln(1+\frac{2H_{w3}/3}{H_{w3}/3}) \quad (3.40), \quad P_{L6\_1,2,3} = \frac{4\mu_0 H_{w1,2,3}}{3\pi} \quad (3.41)$$

$$L = N^2(\sum_{i=1}^{4} P_{Li} + \sum_{j=1}^{3} P_{L5\_j} + \sum_{k=1}^{3} P_{L6\_k}) \quad (3.42)$$

The leakage inductance of three limb transformer can be estimated using finite element analysis tool Ansys Maxwell. The individual leakage inductances L_{L1}, L_{L2}, L_{L3} for the equivalent circuit shown in figure 3.5, can be estimated from the L matrix of (3.18), which is obtained from finite element analysis of the 3D FEA model(figure 3.13). The expressions for L_{L1}, L_{L2}, L_{L3} are given in (3.43)-(3.45). Considering L_m to be very high compared to individual leakages, the total leakage inductance of the three limb transformer, referred to middle limb winding, is given by (3.46).

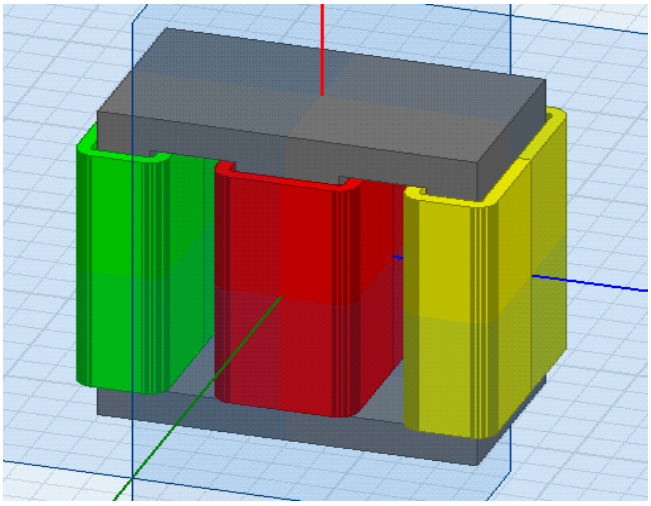

Figure 3.13. 3D Model of Three Limb Three Winding Transformer.

$$L_{L1} = N_1^2 P_{Ls} = L_{11} - (\frac{N_1}{N_2})L_{12} - (\frac{N_1}{N_3})L_{13} \quad (3.43)$$

$$L_{L2} = N_2^2 P_{Ls} = L_{22} - (\frac{N_2}{N_1})L_{12} - (\frac{N_2}{N_3})L_{23} \quad (3.44)$$

$$L_{L3} = N_3{}^2 P_{Lm} = L_{33} - (\frac{N_3}{N_1})\mathrm{L}_{13} - (\frac{N_3}{N_2})\mathrm{L}_{23} \qquad (3.45)$$

The above three equations are derived considering the two side limbs and their respective windings are same in dimensions, but the equations are applicable for any core and winding dimensions.

$$L_L = L_{L3} + ((\frac{N_3}{N_1})^2)\mathrm{L}_{L1} + ((\frac{N_3}{N_2})^2)\mathrm{L}_{L2} \qquad (3.46)$$

The inter-winding parasitic capacitance model is derived from the transformer geometry shown in figure 3.14. In analyzing the capacitance model, two capacitances are taken in consideration, (a) the capacitance C_{core} between transformer winding and core, (b) capacitance C_{coil} between two faces of windings on two separate limbs. An assumption is made that the core is equipotential causing no drop in electric field intensity around the core. Hence it can be inferred that the capacitances C_{core1},C_{core3} are in series, C_{core2},C_{core3} are in series and C_{core1},C_{core2} are in series. The expressions for inter-winding capacitances C_{12}, C_{13}, C_{23} are given in (3.47)-(3.49) in terms of C_{core} and C_{coil}. The expressions for C_{core} and C_{coil} are given in (3.50)-(3.52).

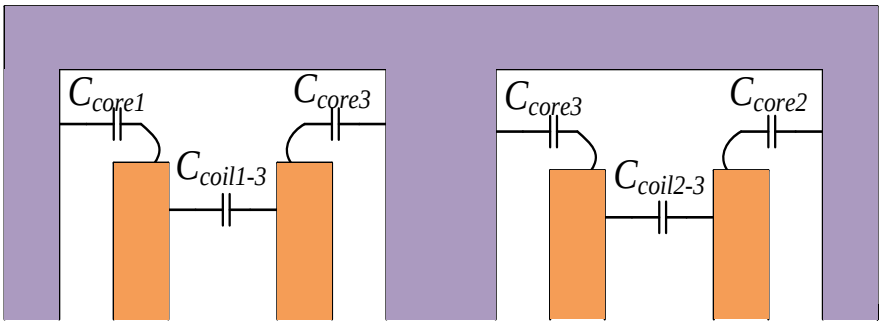

Figure 3.14. Parasitic Capacitance Model of Three Limb Transformer.

$$C_{13} = C_{coil1-3} + \frac{C_{core1} * C_{core3}}{C_{core1} + C_{core3}} \quad (3.47), \qquad C_{23} = C_{coil2-3} + \frac{C_{core2} * C_{core3}}{C_{core2} + C_{core3}} \quad (3.48),$$

$$C_{12} = \frac{C_{core1} * C_{core2}}{C_{core1} + C_{core2}} \quad (3.49), \qquad C_{coil} = \frac{\varepsilon_0 D_c H_w}{W_s} \quad (3.50)$$

$$C_{core1,2} = \frac{\varepsilon_0 2(T_c + D_c) H_{w1,2}}{CL_s} \quad (3.51), \qquad C_{core3} = \frac{\varepsilon_0 2(T_m + D_c) H_{w3}}{CL_m} \quad (3.52)$$

The inter-winding capacitances can also be verified using finite element analysis tool Ansys Maxwell. The off-diagonal elements of C matrix, as given in (3.53), obtained from FEA analysis provide the inter-winding capacitances.

$$[C] = \begin{bmatrix} C_{11} & C_{12} & C_{13} \\ C_{21} & C_{22} & C_{23} \\ C_{31} & C_{32} & C_{33} \end{bmatrix} \quad (3.53)$$

3.4. Transformer Prototypes and Verification of Leakage Inductance and Parasitic Capacitance Estimation for Three Limb Three Winding Transformer

Verification of the leakage and parasitic capacitances for three limb three winding transformer has been carried out by comparing the parameter values obtained from FEA analysis and analytical method with values measured using Precision Impedance Impedance Analyzer Keysight 4294A. For the aforementioned three limb transformer, a design approach using E cores is considered, where the middle limb has twice cross-sectional area than side limbs. The number of turns for each limb is calculated using the voltage equation given in (3.54), where V is peak of applied voltage, K_f is the form factor(K_f = 1 for square wave voltages), K_s is the stacking factor of cores(K_s = 0.98 for ferrites), N is the number of turns, B_m is the maximum flux density, A_c is the core area and f_s is the switching frequency.

$$V = 4K_f K_s N A_c B_m f_s \qquad (3.54)$$

Transformer power rating is targeted at 10kW with side limb winding voltages at 700V, and 1200V for middle limb winding voltage at 50kHz operating frequency with peak flux density of 0.2T. For the transformer, 3C90 based ferrite core E-100/60/28 is chosen, where two E-cores are joined to form three limb configuration and two back to back E-100/60/28 cores are stacked to increase cross-sectional area. The middle limb has twice the cross-sectional area than side limbs. Litz wire of type 2 with configuration 600/38 is used for windings. In this design, the middle limb has twice cross-sectional area than the side limbs, hence the fluxes from the side limb add up together in the middle limb and double the voltage of side limb winding voltages can be obtained using same number of turns on middle limb. Here, the side limb windings are designed at 700V and the middle limb winding is designed at 1200V. Figures 3.16 show the laboratory prototype of the three limb transformer. Table 4 below shows the transformer configuration details with operating frequency of 50kHz and flux density of limbs at 0.2T.

Figure 3.15. Designed Transformer Prototype.

Table 4. Three Limb Transformer Dimensional Data

Side limb no of turns	24
Middle limb no of turns	20
Clearance+Bobbin thickness CL_s and CL_m	2.5 mm each
Core depth D_c	55mm
Window height H_c	93mm
Window width W_c	22.5 mm
Side limb and yoke thickness T_c	13.75 mm
Middle Limb Thickness T_m	27.5 mm
Winding 1 thickness W_{w1}	4.5 mm
Winding 2 thickness W_{w2}	4.5 mm
Winding 2 thickness W_{w3}	4.5 mm

3.5. Transformer Parameter Measurement and Analysis

For the transformer prototype shown in figure 3.15, the parameters are measured using Keysight Precision Impedance Analyzer 4294. For the transformer, the leakage inductances are measured by measuring the short-circuit inductances and the inter-winding capacitances are measured by measuring capacitance between windings with each winding being shorted. Leakage inductances and inter-winding capacitances values are listed in table 3 for the designed transformer prototype. Figures 3.16 shows the relative distribution for each of the leakage permeance components from equations (10)-(18) for the prototype transformers. It can be clearly inferred that for the designed transformer, 70% of total leakage permeance is due to winding and 45% of total permeance is due to the winding heights.

Table 5. Three Limb Transformer Parameter Comparison

	Analytical	FEA	Measured
Leakage from Middle Winding	131μH	129μH	134μH
Leakage from PV Winding	189μH	188μH	174μH
Leakage from ES Winding	189μH	188μH	176μH
Capacitance between PV-HV	27pF	26pF	24pF
Capacitance between ES-HV	27pF	26pF	23pF
Capacitance between ES-PV	23pF	22pF	20pF

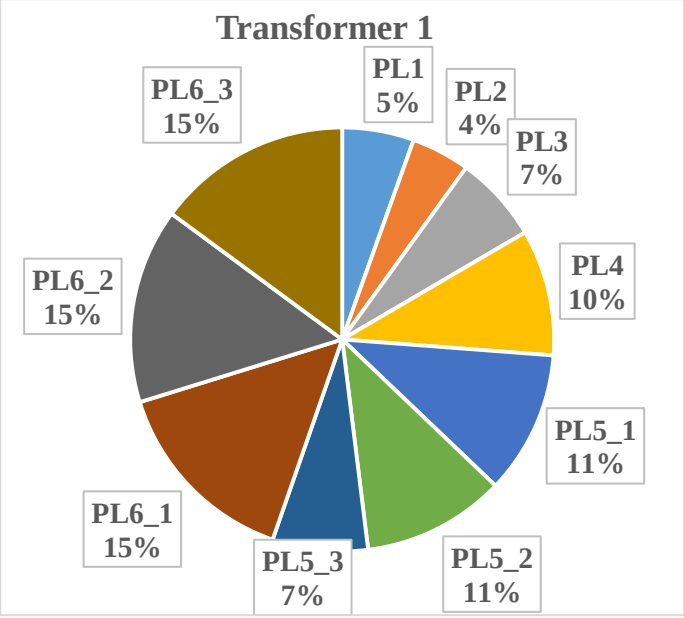

Figure 3.16. Relative Distribution of Leakage Permeances.

Open circuit and short circuit impedance plots of high frequency magnetic devices are important to infer about the resonant frequencies of the transformer. Typically, the open circuit resonant frequency is lower than short circuit resonant frequency for a high frequency

transformer. The operating frequency of high frequency transformers should not be in close proximity to resonant frequencies in order to have a proper operation of the transformer. The operating frequency should be much lower than resonant frequency, in the linear inductive range of impedance vs frequency plots, in order to ensure stable operation of the converter.

Figures 3.19 shows the open circuit impedance plot vs frequency for the aforementioned transformer. It can be observed that the impedance is linear almost upto 1MHz range beyond which capacitive effect becomes dominant, resulting in resonance peaks. Around the switching frequency range, the magnetizing impedance, as seen from middle limb winding, dominates and the resonant capacitance, seen from the middle limb winding, can be obtained from the first resonance frequency point. Similar to the open circuit impedance plot, short circuit impedance as seen from the middle limb winding, is plotted in figures 3.21. It can be observed that the short circuit impedance is linear almost upto 4-5MHz range beyond which capacitive effect comes into effect. From the open circuit plots, the magnetizing inductance L_m values are obtained as 1.53mH. The leakage inductance value as obtained from the short circuit plots is 131µH. The capacitance as seen from the middle limb windings are obtained from the impedance plot portion beyond first resonance point, where impedance falls with increasing frequency.

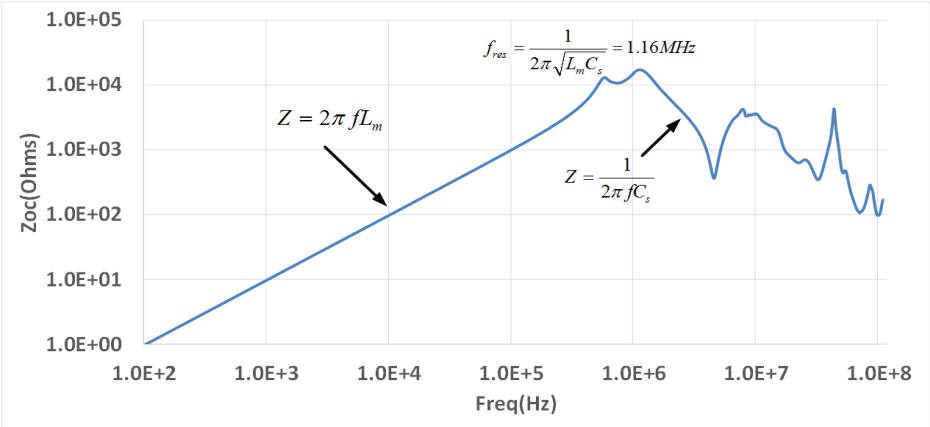

Figure 3.17. Open Circuit Impedance Plot from Middle Limb Winding.

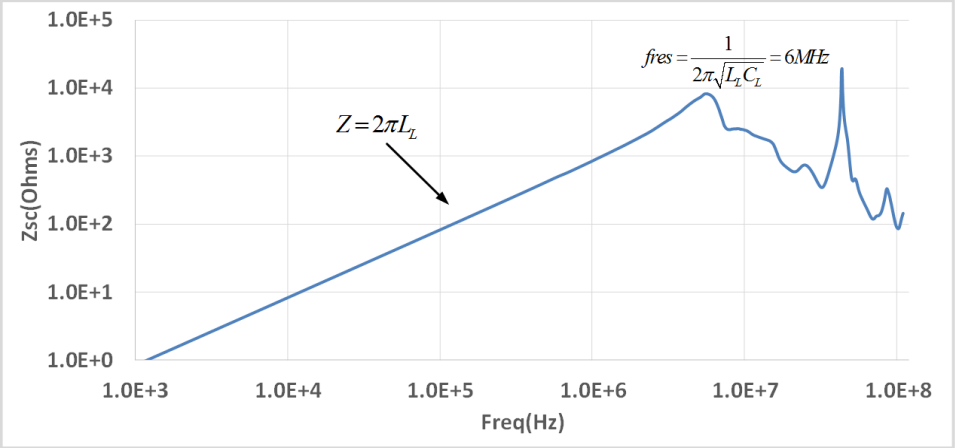

Figure 3.18. Short Circuit Impedance Plot from Middle Limb Winding.

Table 6. Measured Self Capacitance

Self capacitance C_1	6.8pF
Self capacitance C_2	10pF
Self capacitance C_3	8pF

The measured capacitances as seen from the middle limb winding represent self-capacitance and the capacitances in parallel with self-capacitance. The parallel path capacitance is neglected and the measured capacitance is considered as the self-capacitance. For the two designs, the measured self-capacitances are listed in table 6.

3.6. Experimental Results

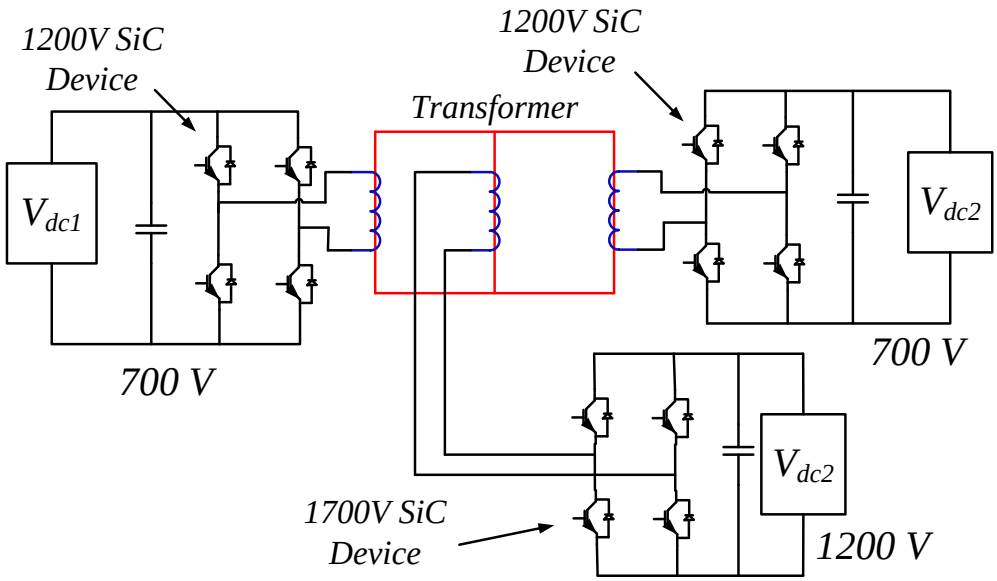

Figure 3.19. Experimental Setup Schematic.

In order to verify the effectiveness of the three limb three winding transformer, experimental studies have been performed with the high frequency transformers designed above with the setup shown in figure 3.19. The side limb ports have H-bridges using 1200V devices with a rated dc voltage of 700V and the middle limb port has H-bridge using 1700V devices with a rated dc voltage of 1200V.

The effects of transformer parasitic capacitances are observed by investigating the winding currents at different power levels. Figures 3.20 shows the transformer current waveforms for 9kW of power at 50kHz switching frequency. Figures 3.21 shows the transformer current waveforms for 6kW of power at 50kHz switching frequency. From figures 3.22-3.23, almost negligible ringing currents due to parasitic capacitance and device dv/dt, can be observed during switching transition. Moreover, the fundamental component of transformer current waveform is free of ringing and unaffected by transformer capacitances, there is no ringing component of current

imposed on the fundamental component of current. In order to investigate more into the effect of parasitic capacitances, the two designed transformers are run at lower power and transformer current wave forms are analyzed in expanded display.

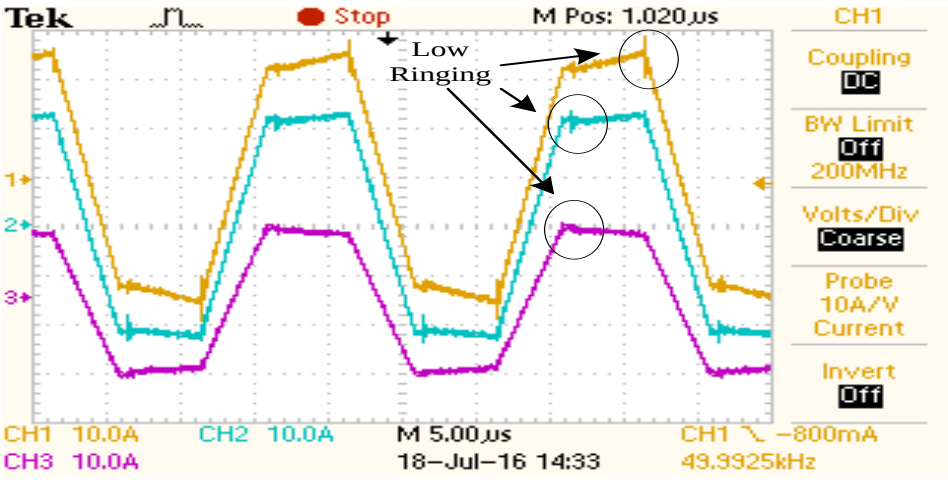

Figure 3.20. Three Limb Transformer Current Waveform at 9kW, 50kHz.

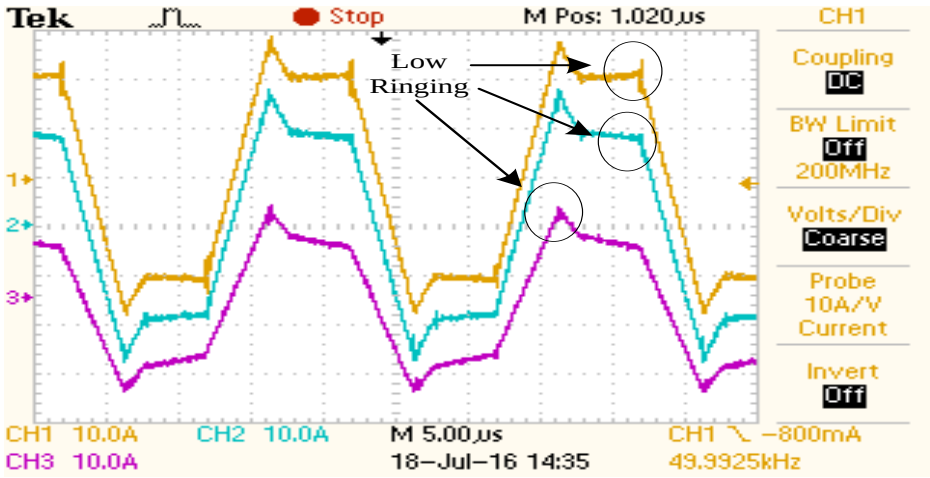

Figure 3.21. Three Limb Transformer Current Waveform at 6kW, 50kHz.

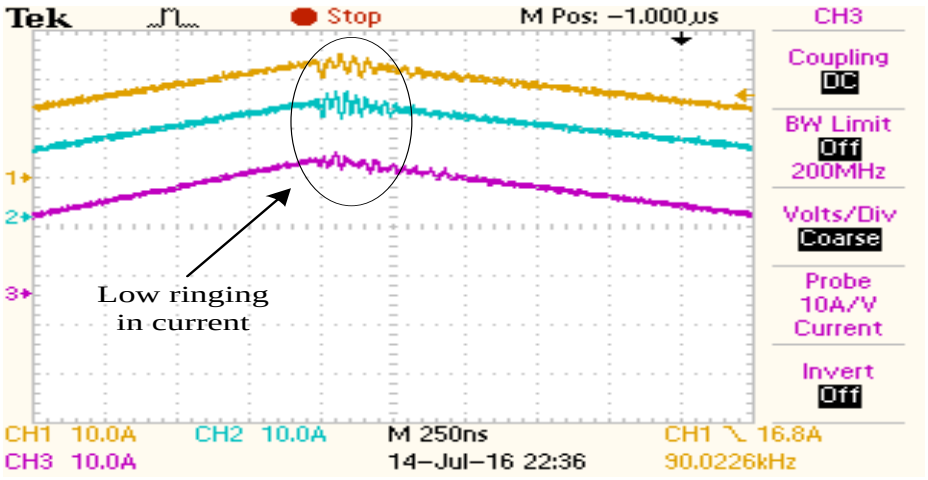

Figure 3.22. Ringing Current for Three Limb Transformer at 10kW, 50kHz.

In order to have a more detailed understanding of the ringing effect, the current waveforms at switching instants are observed in an expanded manner, as shown in figures 3.22-3.23. Figure 3.22 show the transformer currents during 10kW of power, which has very low ringing compared to the line current. Figure 3.23 shows transformer current waveforms during switching transients, for 3kW power at 50kHz, where current ringing is significant as line current is lower. The ringing in transformer line current seems higher as the line current magnitude is lower than 10kW. The ringing effect mostly remains unchanged with power level since the ringing is affected mostly by voltage levels of switching waveforms, dV/dT of switching transients, power and gate loop inductances.

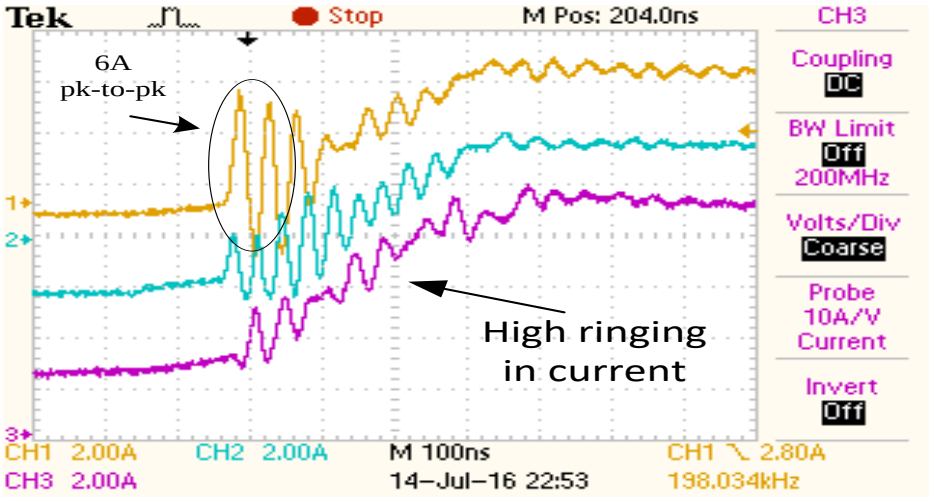

Figure 3.23. Ringing Current for Three Limb Transformer at 3kW, 50kHz.

3.7. Conclusion

From the analysis of three limb three winding transformer as discussed above, the equivalent circuit is series in nature and have been established using the experimental waveform of transformer winding currents. The leakage inductance and parasitic capacitance models are close to FEA and actual values. The designed three limb transformers offer quite low current ringing due to parasitic effects, which are slightly dominant during voltage level transition.

Chapter 4. Triple Active Bridge Converter Operation With Three Limb Transformer And ZVS Analysis

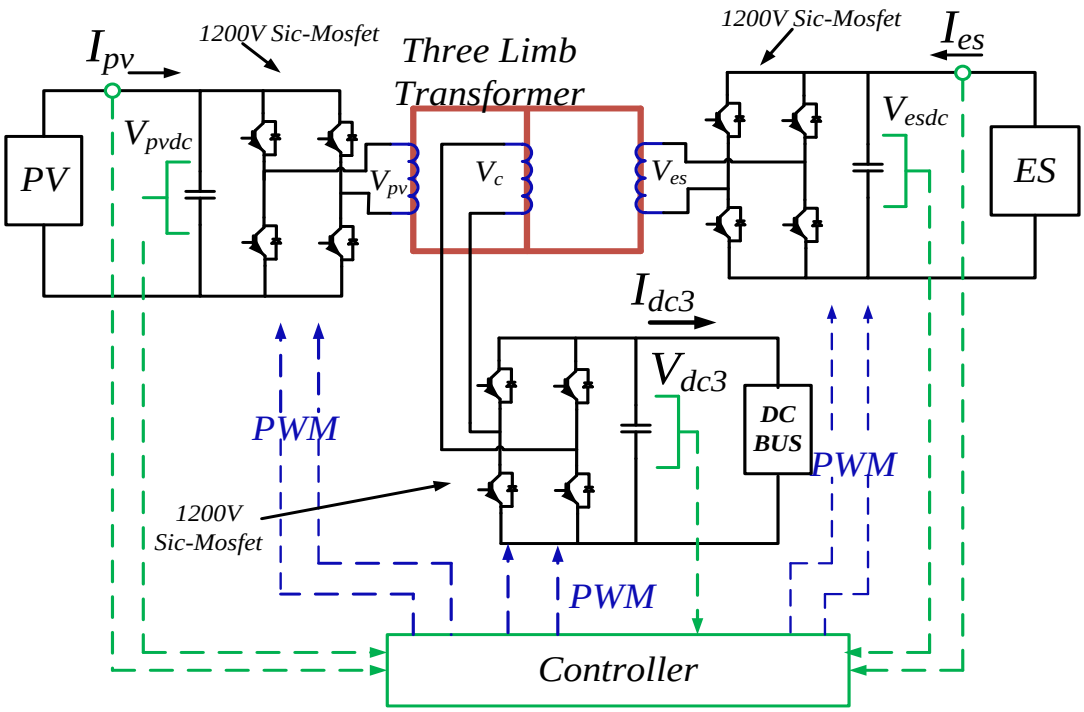

Figure 4.1. Three port DAB Converter using Three Limb Three Winding Transformer.

This chapter focuses in power flow control for three port triple active bridge converter using three limb three winding transformer. Figure 4.1 shows the converter schematic using three limb three winding transformer, where the PV and ES port has H-bridges connected to the two side limb windings and higher voltage dc bus, which is output bus for this case, and it has another H-bridge connected to the middle limb winding. The PV and ES side H-bridges has a dc voltage rating of 700V and the output dc bus has a voltage rating of 1200V. The PV and ES side bridges use 1200V SiC-Mosfets and the H-bridge connected to middle limb winding use 1700V SiC-Mosfets.

4.1. Three-Limb Transformer Power Flow Based on Equivalent Circuit

From the discussions on magnetic and electrical equivalent circuit of three limb high frequency transformer, the power flow expressions are developed here for triple port active bridge converter. From previous chapter, the equivalent circuit of figure 4.2 is referred in this section, which can be simplified as shown below in figure 4.3. Also, considering the side limb portions to have same cross-sectional area, the magnetizing inductance seen from the side limb windings can be considered to be equal. From the reduced order circuit of figure 4.2, winding currents of PV and ES can be considered to be same.

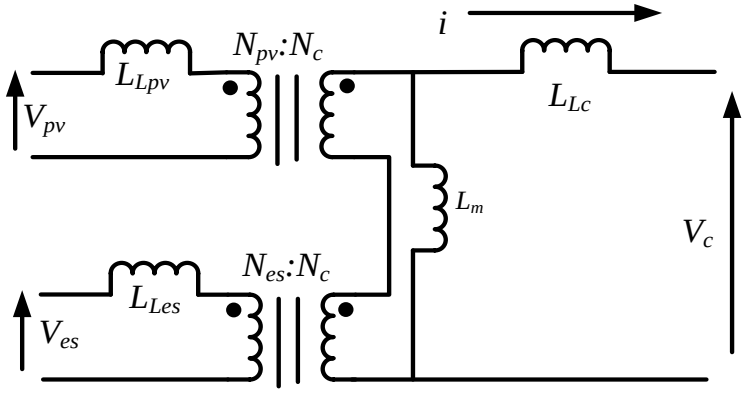

Figure 4.2. Electrical Equivalent Circuit for Three Limb Transformer.

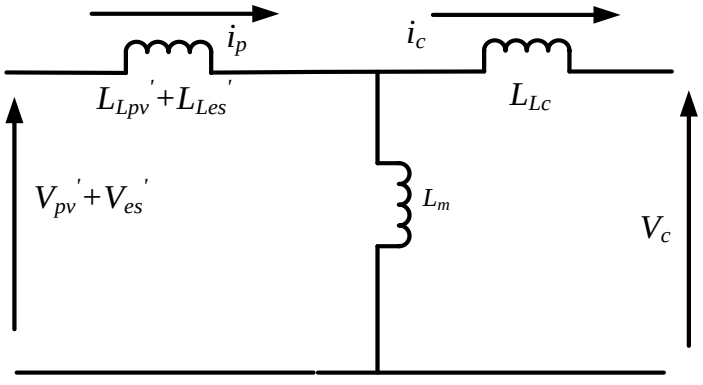

Figure 4.3. Reduced Order Electrical Eq. Circuit for Three Limb Transformer.

For the phase shift control of the three limb high frequency transformer, the power flow of each port will depend on the phase differences between the winding voltages. The four possible positions of the winding voltages are shown in figure 4.4. The voltage on the middle limb winding voltage V_c is considered to be the reference, and the magnitude and phase differences of winding voltages V_{pv} and V_{es} are referred to V_c. Depending on the phase shifts, the rms values of winding currents and the currents during switching instants change. The expressions for winding current values at different switching transitions are given in (4.8)-(4.16).

$$r_{12} = \frac{N_{pv}}{N_{es}} \text{ (4.1)}, r_{13} = \frac{N_{pv}}{N_c} \text{ (4.2)}, \ r_{31} = \frac{N_c}{N_{pv}} \text{ (4.3)}, \ r_{32} = \frac{N_c}{N_{es}} \text{ (4.4)}, \ L_{m1} = r_{13}{}^2 L_m \text{ (4.4)},$$

$$L_{Ls} = L_{Lpv} + r_{12}{}^2 L_{Les} \text{ (4.5)}, \ L_{Ls3} = r_{31}{}^2 L_{Ls} \text{ (4.6)}, \ \ L_{n3}{}^2 = L_{Lc}L_{Ls3} + L_{Lc}L_m + L_{Ls3}L_m \text{ (4.7)},$$

$$i_{pv}(\phi_{pv}) = \left(\frac{N_c}{N_{pv}}\right)\left(\frac{-r_{31}V_{pvdc}(L_{Lc}+L_{m3})\pi - r_{32}V_{esdc}(L_{Lc}+L_{m3})(\pi - 2|\phi_{pv}-\phi_{es}|) + V_{dcm}L_{m3}(\pi - 2|\phi_{pv}|)}{2\omega L_{n3}{}^2}\right) \text{(4.8)}$$

$$i_{pv}(\phi_{es}) = \left(\frac{N_c}{N_{pv}}\right)\left(\frac{-r_{31}V_{pvdc}(L_{Lc}+L_{m3})(\pi - 2|\phi_{pv}-\phi_{es}|) - r_{32}V_{esdc}(L_{Lc}+L_{m3})\pi + V_{dcm}L_{m3}(\pi - 2|\phi_{es}|)}{2\omega L_{n3}{}^2}\right) \text{(4.9)}$$

$$i_{pv}(0) = \left(\frac{N_c}{N_{pv}}\right)\left(\frac{-r_{31}V_{pvdc}(L_{Lc}+L_{m3})(\pi - 2|\phi_{pv}|) - r_{32}V_{esdc}(L_{Lc}+L_{m3})(\pi - 2|\phi_{es}|) + V_{dcm}L_{m3}\pi}{2\omega L_{n3}{}^2}\right) \text{(4.10)}$$

$$i_{es}(\phi_{pv}) = \frac{N_{pv}i_{pv}(\phi_{pv})}{N_{es}} \text{ (4.11)}, \quad i_{es}(\phi_{es}) = \frac{N_{pv}i_{pv}(\phi_{es})}{N_{es}} \text{ (4.12)}, \ i_{es}(0) = \frac{N_{pv}i_{pv}(0)}{N_{es}} \text{ (4.13)}$$

$$i_c(\phi_{pv}) = \frac{-r_{31}V_{pvdc}L_{m3}\pi - r_{32}V_{esdc}L_{m3}(\pi - 2|\phi_{pv}-\phi_{es}|) + V_{dcm}(L_{Ls3}+L_{m3})(\pi - 2|\phi_{pv}|)}{2\omega L_{n3}{}^2} \text{ (4.14)}$$

$$i_c(\phi_{es}) = \frac{-r_{31}V_{pvdc}L_{m3}(\pi - 2|\phi_{pv}-\phi_{es}|) - r_{32}V_{esdc}L_{m3}\pi + V_{dcm}(L_{Ls3}+L_{m3})(\pi - 2|\phi_{es}|)}{2\omega L_{n3}{}^2} \text{ (4.15)}$$

$$i_c(0) = \frac{-r_{31}V_{pvdc}L_{m3}(\pi - 2|\phi_{pv}|) - r_{32}V_{esdc}L_{m3}(\pi - 2|\phi_{es}|) + V_{dcm}(L_{Ls3} + L_{m3})\pi}{2\omega {L_{n3}}^2} \quad (4.16)$$

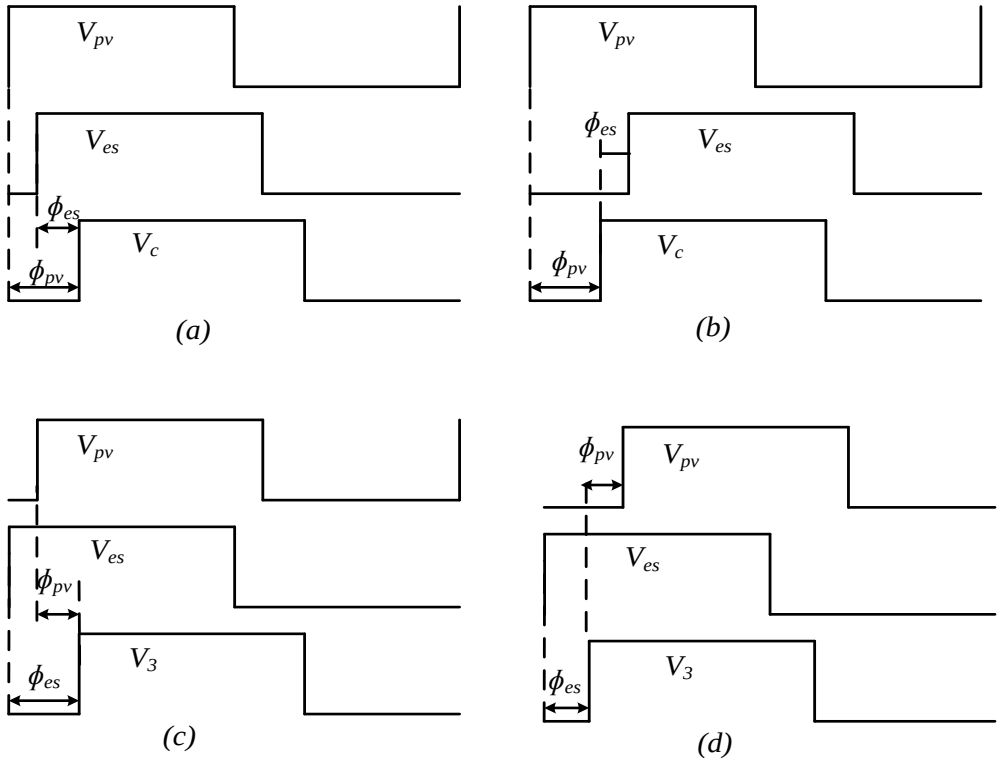

Figure 4.4. Four Possible Positions of Winding Voltages for Three Limb Transformer.

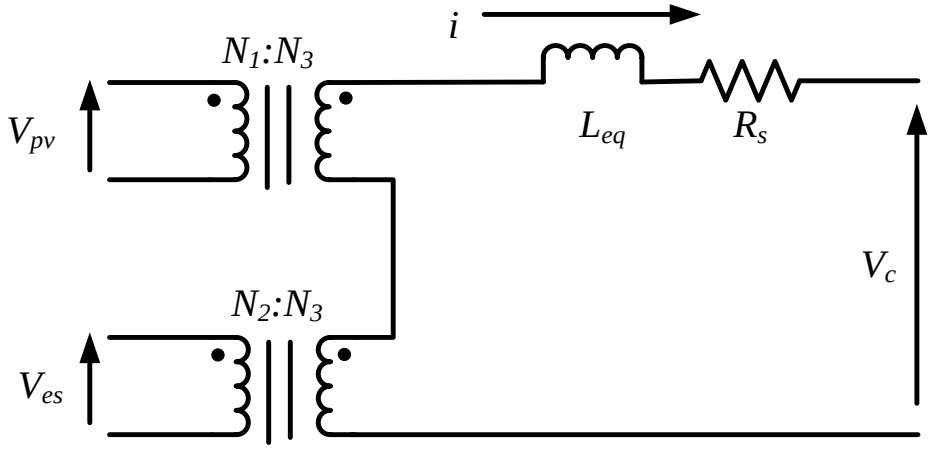

Figure 4.5. Ideal Electrical Eq. Circuit for Three Limb Transformer.

For the four power flow scenarios shown in figure 4.4, the phase shift angles ϕ_1, ϕ_2 are positive when V_{pv} and V_{es} are leading w.r.t. V_c, whereas the phase shift angles ϕ_1, ϕ_2 are negative when V_{pv} and V_{es} are lagging V_c. The power flowing out of PV and ES ports and the power flowing into port 3 are calculated by averaging the instantaneous power of each port over half switching cycle. Neglecting the magnetizing inductance effects, for ideal circuit of figure 4.5, the expressions for P_{pv}, P_{es} and P_{middle} are shown in equations (4.17-4.19)

$$P_{pv} = \frac{-(r_{31}V_{pvdc})(r_{32}V_{esdc})(\phi_{pv}-\phi_{es})\left(\pi-\left|\phi_{pv}-\phi_{es}\right|\right)+r_{31}V_{pvdc}V_{dcm}\phi_{pv}\left(\pi-\left|\phi_{pv}\right|\right)}{\pi\omega L_{eq}} \quad (4.17)$$

$$P_{es} = \frac{(r_{31}V_{pvdc})(r_{32}V_{esdc})(\phi_{pv}-\phi_{es})\left(\pi-\left|\phi_{pv}-\phi_{es}\right|\right)+r_{32}V_{esdc}V_{dcm}\phi_{es}\left(\pi-\left|\phi_{es}\right|\right)}{\pi\omega L_{eq}} \quad (4.18)$$

$$P_{middle} = \frac{r_{31}V_{pvdc}V_{dcm}\phi_{pv}\left(\pi-\left|\phi_{pv}\right|\right)+r_{32}V_{esdc}V_{dcm}\phi_{es}\left(\pi-\left|\phi_{es}\right|\right)}{\pi\omega L_{eq}} \quad (4.19)$$

From the equations, it can be evidently observed that $P_{pv}+P_{es}=P_{middle}$. The first part of equations 4.17 and 4.18 denote the power flowing from PV port to ES port, which can be represented as in (4.20). The second part of equations (4.17),(4.18) represent the power flowing from PV and ES port to middle port, which are given in (4.21) and (4.22).

$$\left|P_{pves}\right| = \frac{V_{pvdc}r_{12}V_{esdc}}{\pi\omega L_{eq}}\left|\left[(\phi_{pv}-\phi_{es})\left(\pi-\left|\phi_{pv}-\phi_{es}\right|\right)\right]\right| \quad (4.20)$$

$$\left|P_{pv-middle}\right| = \frac{V_{pvdc}r_{13}V_{dcm}}{\pi\omega L_{eq}}\left|\left[\phi_{pv}\left(\pi-\left|\phi_{pv}\right|\right)\right]\right| \quad (4.21)$$

$$\left|P_{es-middle}\right| = \frac{V_{esdc}r_{23}V_{dcm}}{\pi\omega L_{eq}}\left|\left[\phi_{es}\left(\pi-\left|\phi_{es}\right|\right)\right]\right| \quad (4.22)$$

The transformer prototype described in chapter 3, is referred here to analyze and to look into the operating ranges for the three port converter. The power flow ranges of each port for the two

types of three limb transformer, described above, are shown in figures 4.6-4.7 for phase shifts varying from $-\pi/2$ to $+\pi/2$.

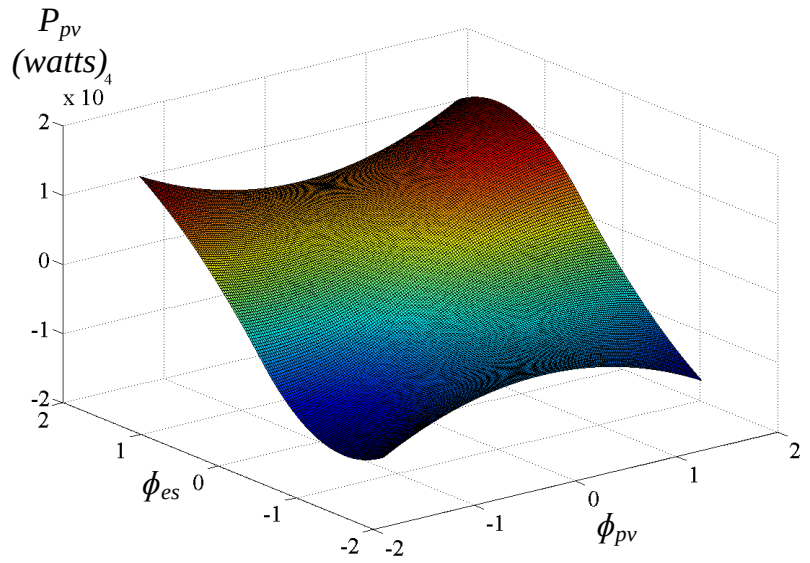

Figure 4.6. PV Port Power for Three Limbs Transformer.

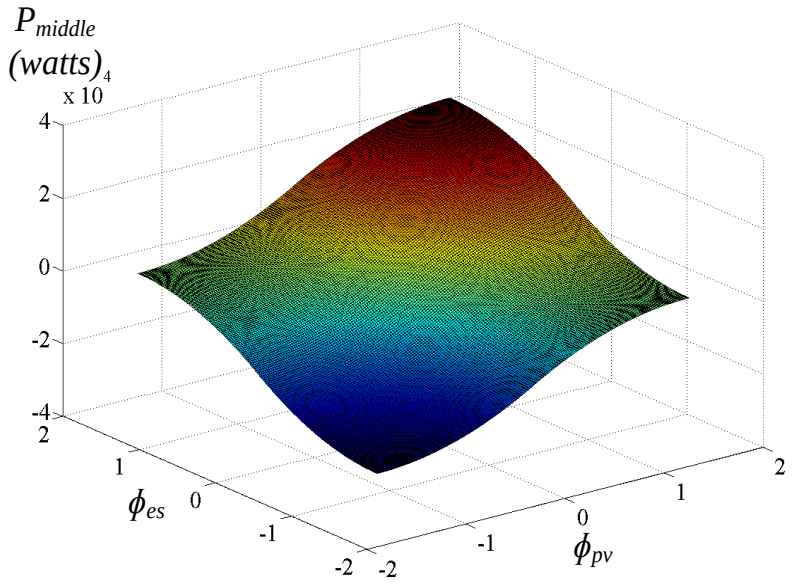

Figure 4.7. Middle Port Power for Three Limbs Transformer.

The feasible operating points for positive power output of PV and positive and negative power output for ES port is shown in figure 4.8.

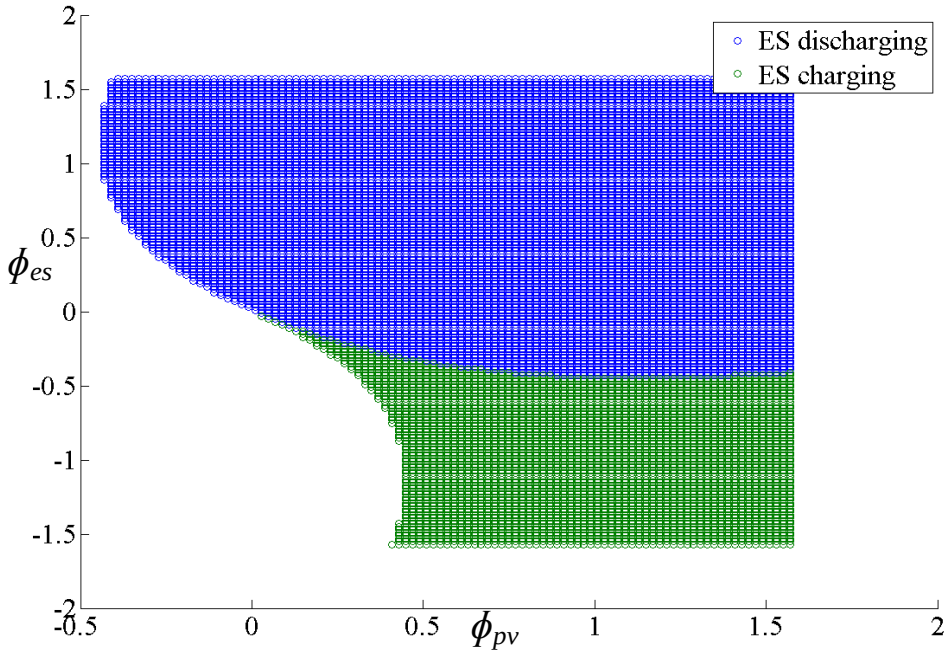

Figure 4.8. Operating Points for 3Port Converter.

4.2. Decoupled Power Flow Control Strategy

The three port converter system of figure 4.1 has two degrees of freedom ϕ_{pv} and ϕ_{es}. Henceforth, power flow of only two of the three ports can be controlled. The average power expression for PV and ES ports are given in equations (4.17)-(4.19), which are coupled expressions of ϕ_{pv} and ϕ_{es}. Decoupling of P_{pv} and P_{es} over the operating power range can be done by pre-computing several operating points such that the set of pre-computed values of ϕ_{pv} and ϕ_{es} are exhaustive in nature to cover the range of power flow for each port[49]. With pre-computation of operating phase angles, for any operating point in the converter operation, the values of ϕ_{pvA} and ϕ_{esA} are available for a point A which is in close vicinity to the actual desired

operating point. In this case the power flow controller only has to adjust ϕ_{pv} and ϕ_{es} over a very small range[49]. For this kind of control, linearized model of the power flow expressions of each port are required for any arbitrary operating point A. Linearizing equations (4.17) and (4.18) over point A gives the following expressions for small changes in power

$$\Delta P_{pvA} = G_{11A}\Delta\phi_{pvA} + G_{12A}\Delta\phi_{esA} \qquad (4.22)$$

$$\Delta P_{esA} = G_{12A}\Delta\phi_{pvA} + G_{22A}\Delta\phi_{esA} \qquad (4.23)$$

Where G_{11A}, G_{12A}, G_{21A}, G_{22A} are functions of ϕ_{pvA} and $\phi_{esA.}$ The expressions for G_{11A}, G_{12A}, G_{21A}, G_{22A} are given in equations (4.24) – (4.26).

$$G_{11A} = -\frac{(r_{31}V_{pvdc})(r_{32}V_{esdc})}{\pi\omega L_{eq}}(\pi - 2|\phi_{pv} - \phi_{es}|) + \frac{(r_{31}V_{pvdc})V_{dcm}}{\pi\omega L_{eq}}(\pi - 2|\phi_{pv}|) \qquad (4.24)$$

$$G_{12A} = G_{21A} = \frac{(r_{31}V_{pvdc})(r_{32}V_{esdc})}{\pi\omega L_{eq}}[\pi - 2|\phi_{pv} - \phi_{es}|] \qquad (4.25)$$

$$G_{22A} = -\frac{(r_{31}V_{pvdc})(r_{32}V_{esdc})}{\pi\omega L_{eq}}(\pi - 2|\phi_{pv} - \phi_{es}|) + \frac{(r_{32}V_{esdc})V_{dcm}}{\pi\omega L_{eq}}(\pi - 2|\phi_{es}|) \qquad (4.26)$$

The small changes in power can be expressed in matrix form as follows

$$\begin{bmatrix} \Delta P_{pvA} \\ \Delta P_{esA} \end{bmatrix} = \begin{bmatrix} G_{11A} & G_{12A} \\ G_{21A} & G_{22A} \end{bmatrix} \begin{bmatrix} \Delta\phi_{pvA} \\ \Delta\phi_{esA} \end{bmatrix} = G \begin{bmatrix} \Delta\phi_{pvA} \\ \Delta\phi_{esA} \end{bmatrix} \qquad (4.27)$$

The interaction between two power flow expressions can be eliminated for any arbitrary operating point A using equation 4.27. While for other operating points around its close vicinity, the decoupling can be achieved using a decoupling matrix **H,** as explained similarly in [49], which decomposes a coupled multivariable system into a linearized independent system. The control structure required using matrix **H** is given below.

$$\begin{bmatrix} \Delta P_{pvA} \\ \Delta P_{esA} \end{bmatrix} = GH \begin{bmatrix} \Delta\lambda_{pvA} \\ \Delta\lambda_{esA} \end{bmatrix} \quad (4.28), \quad \text{where} \quad \begin{bmatrix} \Delta\phi_{pvA} \\ \Delta\phi_{esA} \end{bmatrix} = H \begin{bmatrix} \Delta\lambda_{pvA} \\ \Delta\lambda_{esA} \end{bmatrix} \quad (4.29)$$

To achieve independent control loops, the structure of the matrix multiplication should be diagonal[4.30], therefore the decoupling matrix **H** can be calculated as $\mathbf{H=G^{-1}}$. The system controller for the independent power flow control of two ports 1 and 2 are shown below in figure 4.14.

$$H = G^{-1} = \begin{bmatrix} H_{11A} & H_{12A} \\ H_{21A} & H_{22A} \end{bmatrix}$$

$$H = \frac{1}{(G_{11A}G_{22A} - G_{12A}G_{21A})} \begin{bmatrix} G_{22A} & -G_{12A} \\ -G_{21A} & G_{11A} \end{bmatrix} \quad (4.30)$$

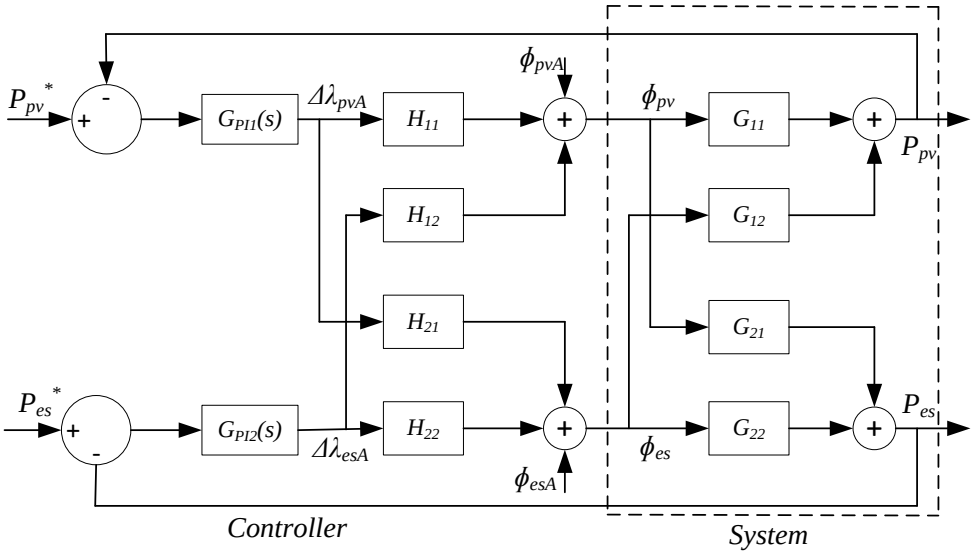

Figure 4.9. Control Loop for Decoupled Power Flow Control.

4.3. Simulation Results for Decoupled Control

The aforementioned control strategy for three port DAB converter has been implemented and verified in MATLAB/PLECS simulation environment. Designed three port transformer's

parameters from chapter 3 has been referred in the simulation model. The PV and ES voltages are kept at 700V and V_{dc3} has been kept at 1200V. Equations (4.17) and (4.18) are solved for $I_1(I_{PV})$ varying from 1A to 12A and $I_2(I_{ES})$ is varied from -12A to 12A. The solution points are obtained for each combination of I_1 and I_2, using a scale of 1A between two consecutive points. The obtained values of ϕ_1 and ϕ_2 are used to calculate the **H** matrix for each combination of I_1 and I_2. All the solution points of ϕ_1 and ϕ_2, indexed by I_1 and I_2, together with the corresponding H matrix element are loaded into a look up table. The control schematic of figure 4.14 is implemented here, where for any reference of I_{1A} and I_{2A}, corresponding ϕ_{1A} and ϕ_{2A} and the H matrix elements are fetched from the look-up table to control the reference power.

4.3.1. Constant PV Power with Change in Port 3 Power

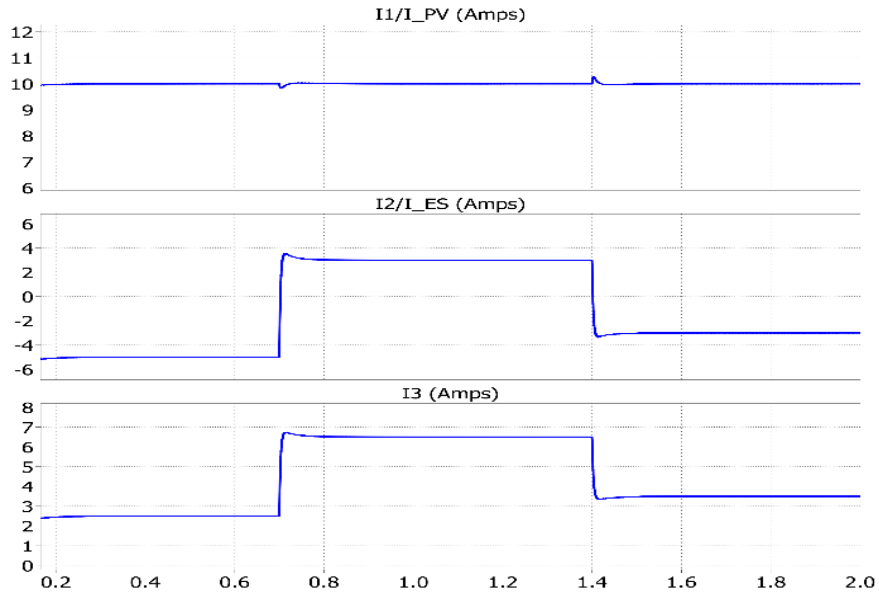

Figure 4.10. ES Power Change Under Constant PV Power.

Figure 4.10 shows the input dc current changes for I_{pv} and I_{es} and output I_{dc3} current for port 3 when PV is delivering a constant current of 10A and port 3 power intake undergoes changes. Under this scenario ES power inflow changes to outflow mode to feed the extra port 3 power

demand. In figure 4.10, initially ES is charging itself with 5A, now as port 3 power demand changes, it discharges to provide the extra power requirement while I_1 remains unchanged due to decoupled control of figure 4.9. Next, as port 3 power demand falls, ES comes back from discharging to charging mode again.

4.3.2. Zero ES Power with PV Power Changing

In this scenario PV power output changes as solar irradiation changes but ES continue to remain in idle, without taking in or feeding out any power. In figure 4.11, PV output current I_1 changes from 7A to 12A, and then again back to 5A, without disturbing the ES idle condition of zero power.

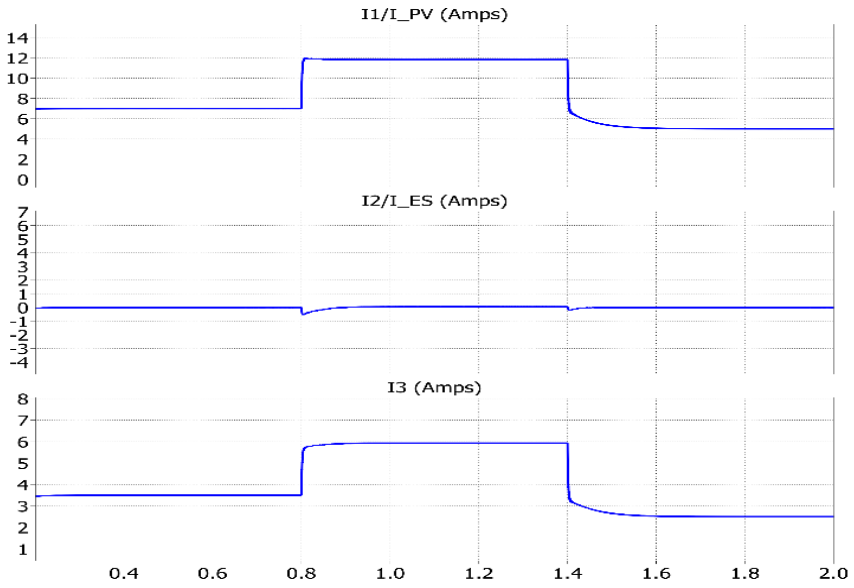

Figure 4.11. PV Power Change Under Zero ES Power.

4.3.3. Constant ES Charging with PV Power Changing

In this scenario PV power output changes as solar irradiation changes but ES continue to charge itself under constant current. In figure 4.12, PV output current I_1 falls from 7A to 1A, and

then again jumps to 12A, while the current control of figure 4.9 continues to charge ES at constant current. When PV current is 1A, the extra power required for ES charging is fetched from port 3 constant dc bus.

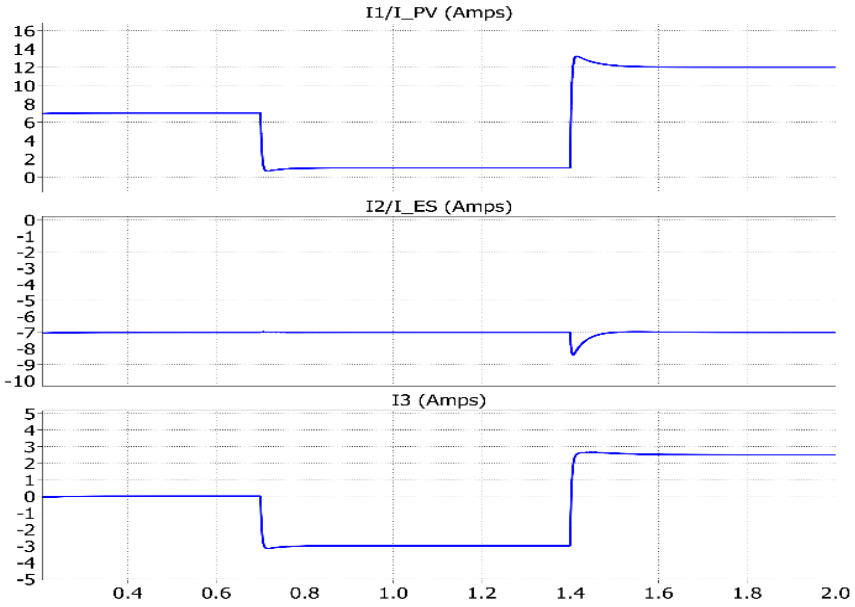

Figure 4.12. PV Power Change Under Constant Current ES Charging.

4.3.4. Zero Port3 Power Constant ES Charging with PV Power Changing

In this scenario, port 3 remains idle at zero power condition while ES charges itself with all the power that is generated by PV. In figure 4.13, as PV output current I_1 is 5A, ES charges with 5A. As I_1 changes from 5A to 12 A, ES charges with 12A. As I_1 falls to 7A, ES charging current also falls to 7A. In this scenario, the decoupled current control shows it can control the port 3 dc current I_3 as well, in an indirect manner by controlling I_1 and I_2 at same level.

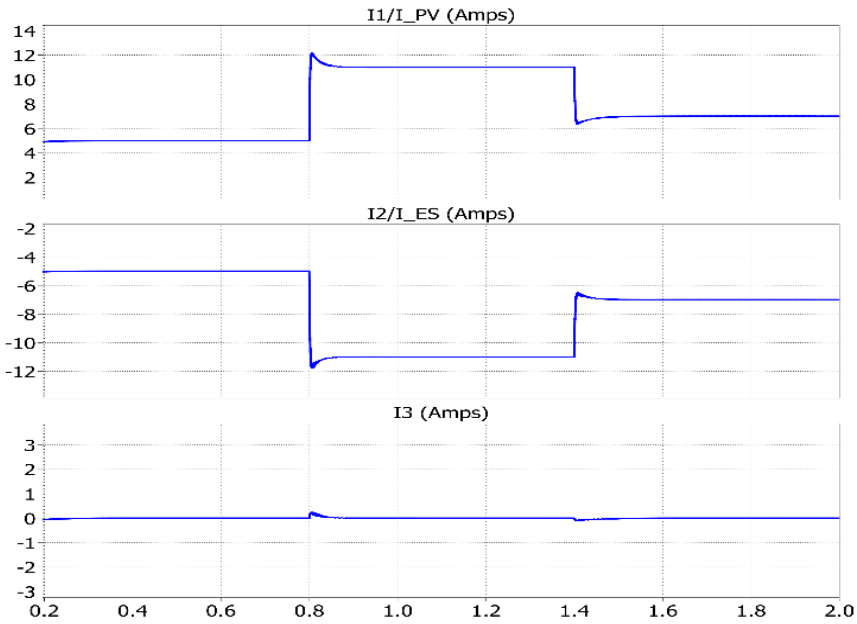

Figure 4.13. PV and ES Power Change Under Zero Port 3 Power.

4.3.5. Constant Port3 Power Demand as PV Power Changes

In this case in figure 4.14, the port 3 has a constant power demand or current demand of 6kW for 5A current at 1200V output voltage. While PV power undergoes variation due to solar irradiation, the ES changes its output current to feed extra power demand or take in extra PV power generated. In figure 4.14, initially PV delivers 12A, while ES charges itself with 2A. When PV current drops to 10A, ES takes zero current. When PV output current falls to 2A, ES output current jumps to 8A to provide constant demand of 6kW. When PV current rises up to 7A, ES output current falls to 3A to keep the port3 power demand unchanged.

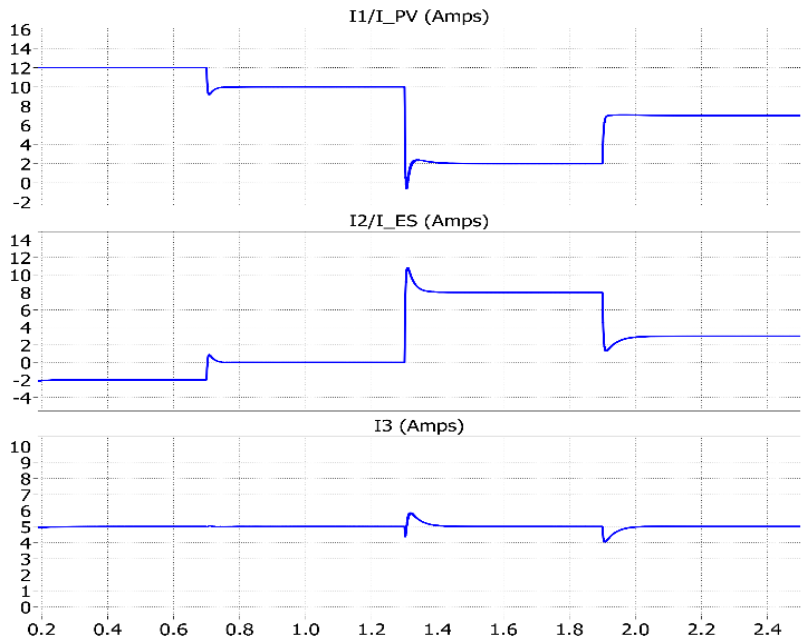

Figure 4.14. Constant Port 3 Power Under PV power Variation.

4.4. Discussion on ZVS Operation for Three Limb Three Winding Transformer enabled Triple Active Bridge Converter Operation under Phase Shift Control

Natural Zero Voltage Switching turn-on or ZVS turn-on operation for high frequency switching based two-port DAB converters[53], is a significant advantage over other hard-switched converters. For converters using Mosfet devices, ZVS turn-on is important for higher switching frequency as most of the Mosfet switching loss takes place during hard turn-on. However, with the advent of SiC Mosfet devices, hard turn-on operation of converter can be allowed to some extent provided converter efficiency target is met. For the three port DAB converter of figure 4.1 with the phase shift control technique, the ideal ZVS scenarios are analyzed and discussed in this section.

For a switching device like a Mosfet or IGBT + anti-parallel diode, natural ZVS turn-on takes place when prior to the turn on of a device, the current is flowing through the body diode or anti-

parallel diode in an opposite direction to the positive channel conduction direction of the device. In other words, before the devices turn on, the circuit current flows through the body diode or anti-parallel diode when the positive gate signal is applied to the device. For a switching leg of an H-bridge with a series inductance at switching node, carrying a continuous current, the conduction of current through anti-parallel diode also depends on dead-band time, value of the output capacitance of the device, magnitude of inductance and magnitude of current[53]. For this discussion, the change in ZVS operating region is due to device capacitance is neglected and only direction of current flowing out of the corresponding switching node is considered. The prototype transformer details for 10kW power in chapter 3 are shown below.

Table 7. Transformer Parameters for Three Limb Transformer

Design Type 1 Transformer
V_{pv}:V_{es}:V_c = 1:1:2
L_{lc}=59.3µH
L_m=1.53mH
L_{l1}=51.64µH
L_{l2}=51.68µH

For the different winding voltage positions shown in figures 4.4, ideal case of ZVS requirement is stated as outgoing current from the switching leg should be negative during $-V_{dc}$ to $+V_{dc}$ transition. Based on the assumption, the ZVS operating constraint for the three limb transformer model of figure 4.4, are givens below. The ZVS operating regions in the range of (-π/2 to π/2), are shown in figures 4.15-4.18.

$$i_{pv}(\phi_{pv}) < 0 \ , \ i_{es}(\phi_{es}) < 0 \ , \ i_c(0) > 0$$

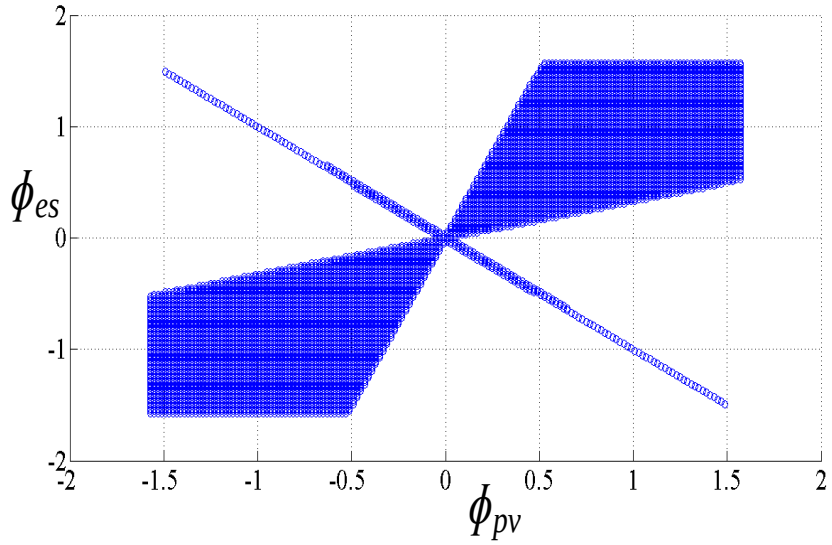

Figure 4.15. ZVS Operating Region for Three Port Converter.

The figures 4.15 clearly indicates there is a loss of ZVS for the converters for a considerable portion of operating range of the two high frequency transformers. Figures 4.16-4.18 show the individual port ZVS operating ranges for the two transformers. The ZVS operating ranges are verified through simulation of three port converter using the aforementioned two transformers.

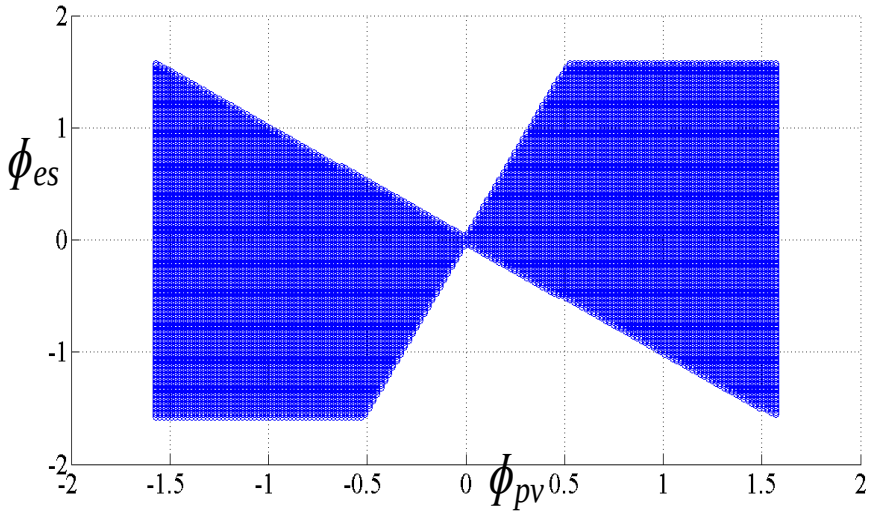

Figure 4.16. ZVS Operating Region for PV Port.

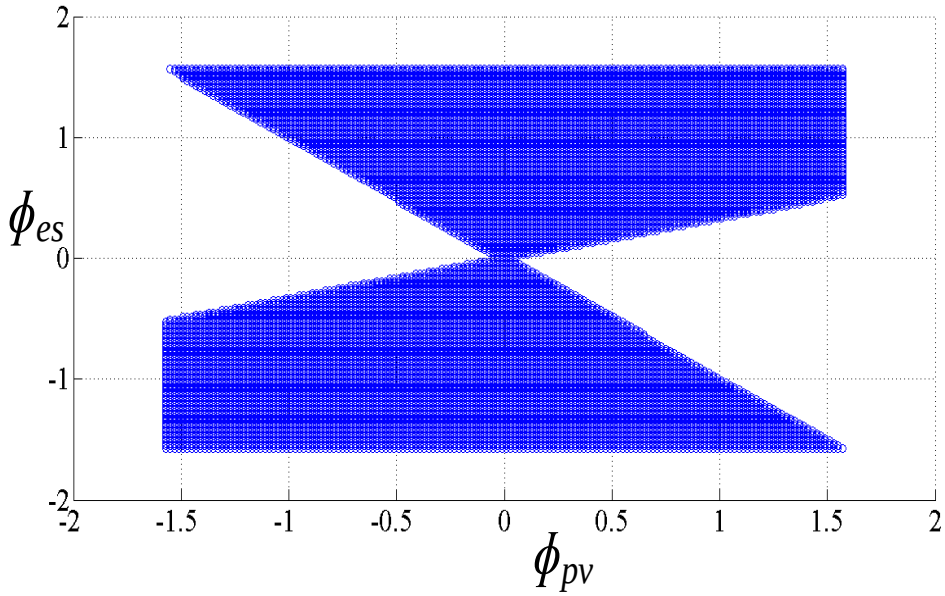

Figure 4.17. ZVS Operating Region for ES Port.

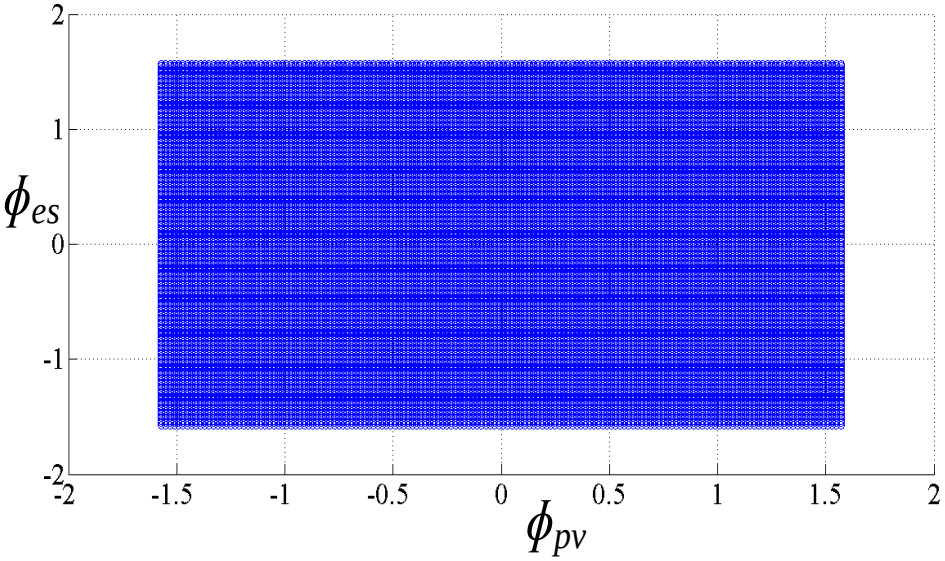

Figure 4.18. ZVS Operating Region for Middle Port.

From the above plots of ZVS operating ranges, it can be found that for the three limb transformer, both PV and ES converter has loss of ZVS over significant operating region, while the middle port converter has ZVS over full operating region. The ZVS scenarios have been

verified using simulation in MATLAB/PLECS environment by creating a simulation model of converter system shown in figure 4.1. Figure 4.19 shows three limb transformer winding waveforms for the converter when all the three ports have natural ZVS turn-on, since all the three ports have lagging current, as during $-V_{dc}$ to $+V_{dc}$ transition, the outgoing currents for PV and ES port is negative, while the incoming current for middle port is positive. Figure 4.20 shows the scenario when ES port has ZVS but PV port has no ZVS, as the outgoing current for PV port is positive and the outgoing current of ES port is negative. Figure 4.21 shows the transformer winding waveforms when PV port has ZVS and ES port has no ZVS, as the outgoing current for PV port is negative and the outgoing current of ES port is positive. The incoming current to middle port is positive in both figures 4.20 and 4.21.

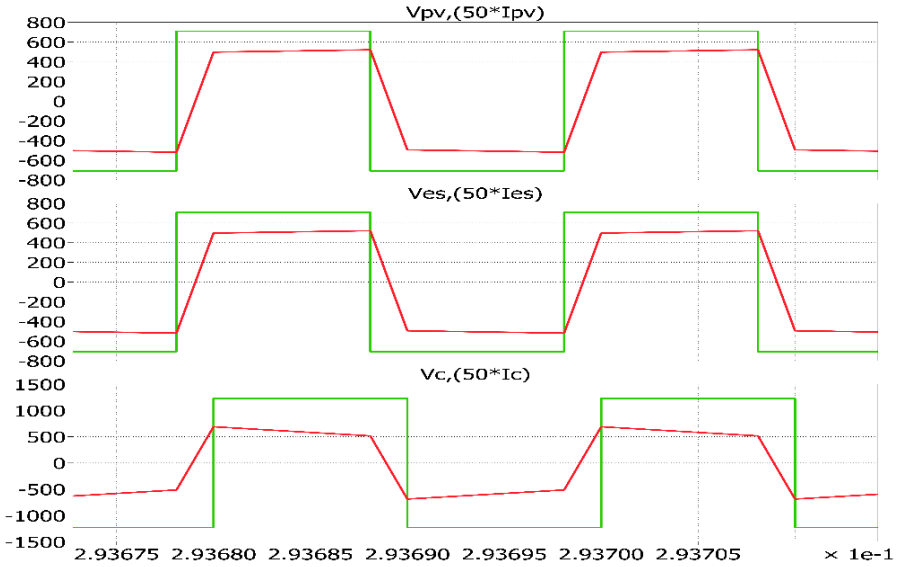

Figure 4.19. Transformer Voltages and Currents for ϕ_{pv} =0.6 rad and ϕ_{es} = 0.6 rad.

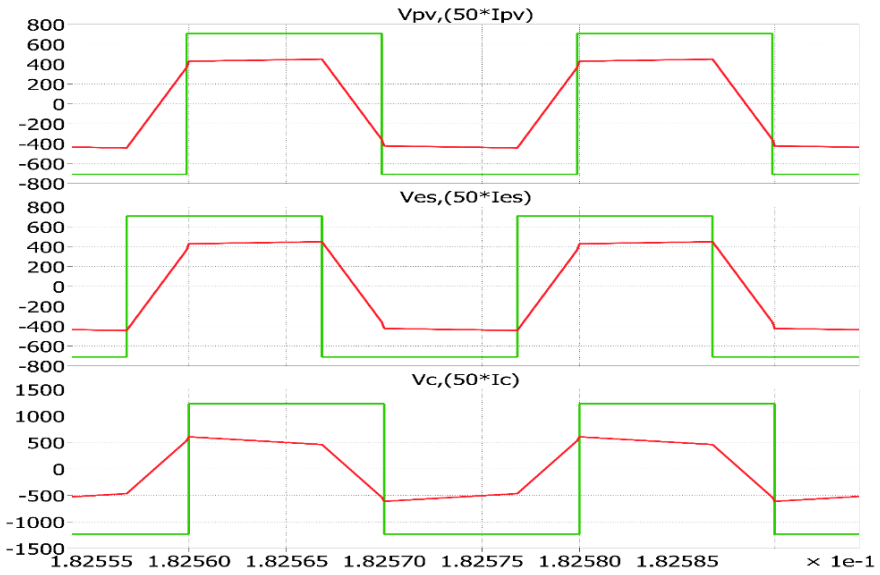

Figure 4.20. Transformer Voltages and Currents for ϕ_{pv} =0.1 rad and ϕ_{es} = 1 rad.

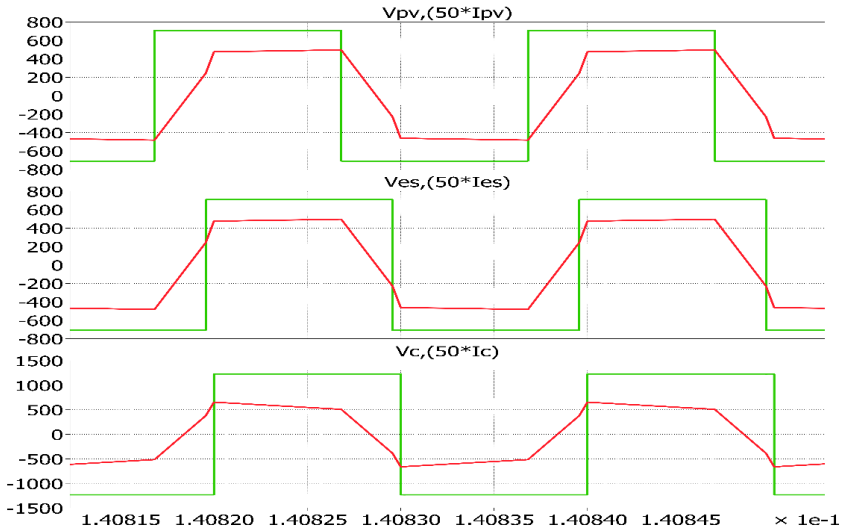

Figure 4.21. Transformer Voltages and Current for ϕ_{pv} =1 rad and ϕ_{es} = 0.2 rad.

4.5. Experimental Study of Three Port Converter

The ZVS scenarios for three port converter using three limb transformer are observed using experimental study. The PV and ES side converters use 1200V/60A SiC Mosfet device and the middle port converter uses 1700V/45A SiC Mosfet. The three port converter has been run at

50kHz switching frequency, using the two types of three limb transformers discussed before. Different ZVS scenarios are observed for three port operation with prototype transformer. Figures 4.22-4.24 show the ZVS and non-ZVS scenarios for the three port converter using design type 1 transformer.

In figure 4.22, the PV and ES winding voltages have lagging currents as the winding currents are negative during $-V_{dc}$ to $+V_{dc}$ transition. For the middle port winding voltage, the incoming winding current is leading and positive during $-V_{dc}$ to $+V_{dc}$ transition. The three ports have natural ZVS turn-on in figure 4.22. In figure 4.23, the PV winding voltage has negative and lagging current during $-V_{dc}$ to $+V_{dc}$ transition, while the ES winding voltage has positive and leading current during $-V_{dc}$ to $+V_{dc}$ transition. The middle winding voltage has incoming leading current to the middle bridge. In figure 4.24, PV and middle port converter has natural ZVS turns-on, while ES port has no natural ZVS.

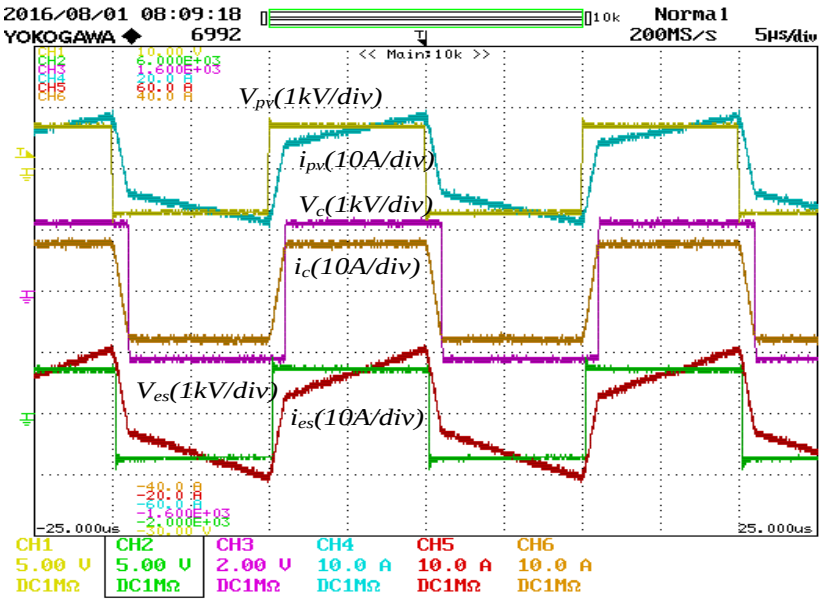

Figure 4.22. Transformer Waveforms for All Three Ports having ZVS Turn-On.

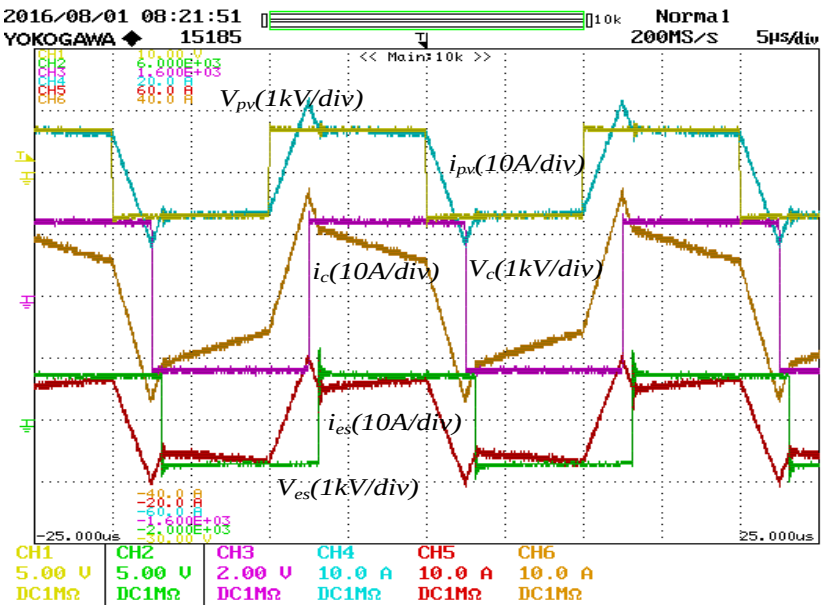

Figure 4.23. PV and Middle Port having ZVS Turn-On, ES port having no ZVS.

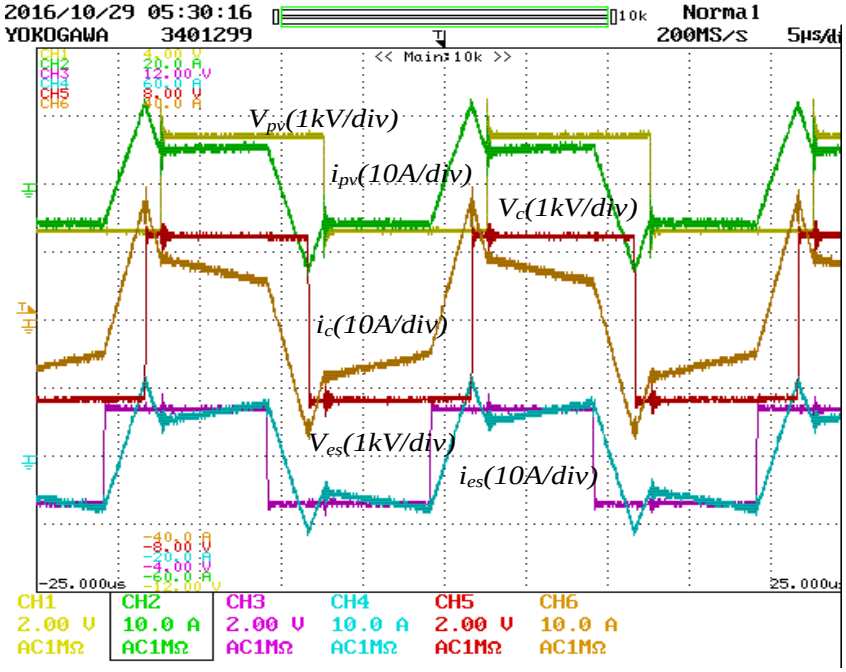

Figure 4.24. ES and Middle Port having ZVS Turn-On, PV port having no ZVS.

In figure 4.24, the ES winding voltage has negative and lagging current during $-V_{dc}$ to $+V_{dc}$ transition, while the PV winding voltage has positive and leading current during $-V_{dc}$ to $+V_{dc}$

transition. The middle winding voltage has incoming leading current to the middle bridge. In figure 4.24, ES and middle port converter has natural ZVS turns-on, while PV port has no natural ZVS.

The efficiency measurement for three port dc-dc converter with three limb transformer using phase shift control has been carried out using Power Analyzer WT3000, as shown in figure 4.25. Both ES charging and discharging scenarios have been carried out for efficiency measurements. The experimental schematic is shown in figure 4.25.

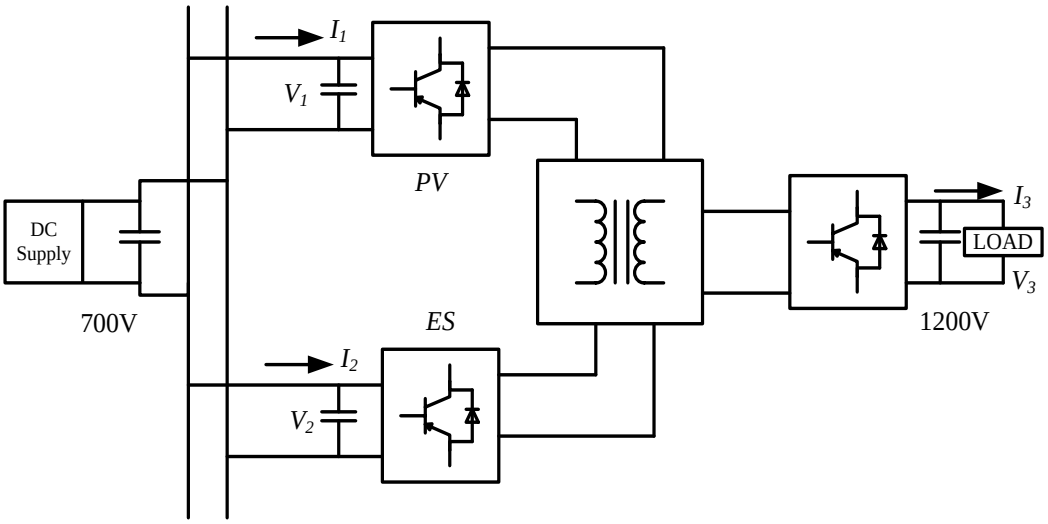

Figure 4.25. Experimental Setup Schematic with Split-Winding Transformer.

The efficiency of the three port converter for different operating conditions, is measured by measuring the total input and output power of the setup shown in figure 4.39. The total input and output power of the converter defined as follows.

$$P_{pv} = V_1 I_1 ,\ P_{es} = V_2 I_2 ,\ P_c = V_3 I_3$$

When ES is delivering power, then $P_{in} = P_{pv} + |P_{es}|$, $P_{out} = P_c$

And when ES is charging, then $P_{in} = P_{pv}$, $P_{out} = P_c + |P_{es}|$

The efficiency of the converter is defined as $\eta = P_{out}/P_{in}$, the efficiency plot of the converter system is shown below in figure 4.26. The data for efficiency calculation is measured for 5 minute continuous run for each of the operating point. The peak efficiency has been found to be around 97.9%.

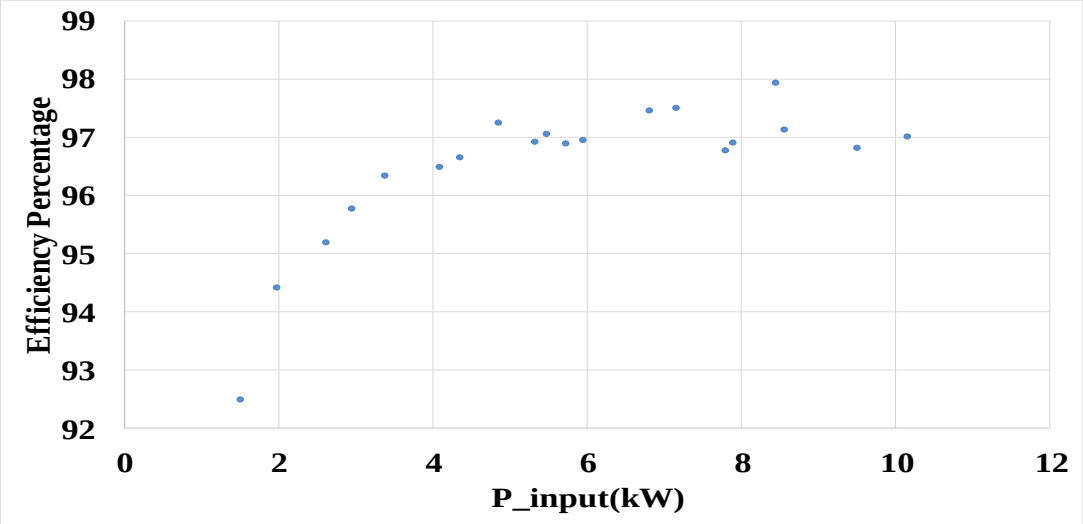

Figure 4.26. Three Port DC-DC Converter System Efficiency Plot.

4.6. Operating Three Limb Three Winding Transformer with One Port Idle

One of the most important aspects of operating a three port converter, is its successful operation under the condition of 'one port idle condition'. Under the scenario of idle condition operation for one port, the corresponding converter is kept switched off or the corresponding winding can be kept open, in which case an open circuit voltage develops across the winding. In 'switched off' condition, all the semiconductor switches are turned off, as shown in figure 4.27-4.28, and the dc source/storage may or may not be available to the converter dc bus capacitance. During idle condition, when one winding is open, then the corresponding winding do not provide any excitation to the core, hence the reluctance offered is very low and as a result the

corresponding limb acts as a short to the flux path. As a consequence, the mmf sources from the other two limbs, see a low reluctance path through the third limb with open winding, and majority of their fluxes flow through the low reluctance path. A very small portion of flux links the two active windings. This phenomenon is shown in figure 4.29-4.30.

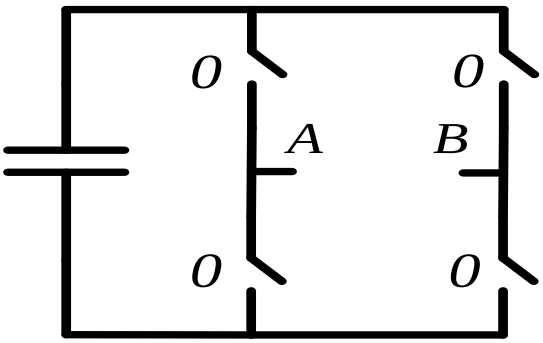

Figure 4.27. Converter in 'Switched Off' Condition.

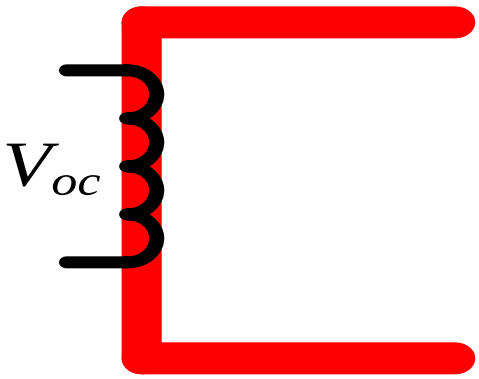

Figure 4.28. Winding in Open Condition.

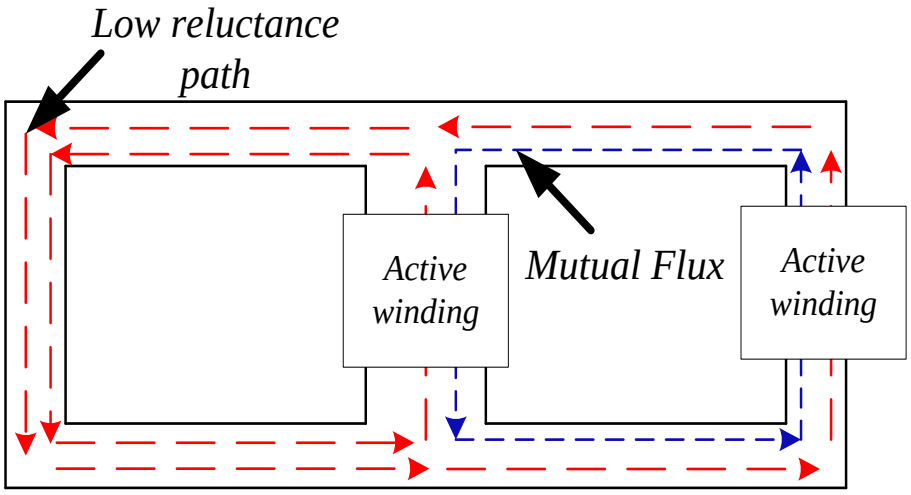

Figure 4.29. Flux paths of Three Limb Transformer when One Side Port is Idle.

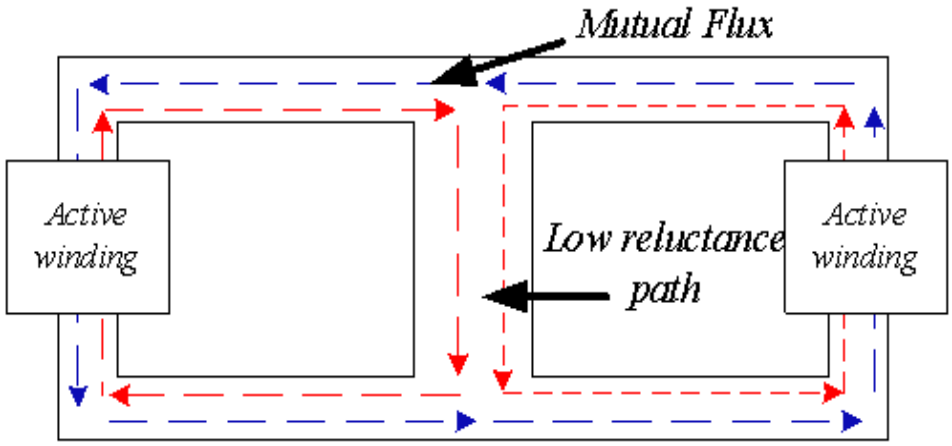

Figure 4.30. Flux paths of Three Limb Transformer when Middle Port is Idle.

In ideal transformer, in presence of zero air gaps in limbs, the fluxes from both the windings add up and flow through the limb with open circuit, and mutual flux is almost zero. In case of limbs with small air gaps, very small mutual flux cuts through the active windings. MATLAB/PLECS simulation has been performed to verify this phenomenon.

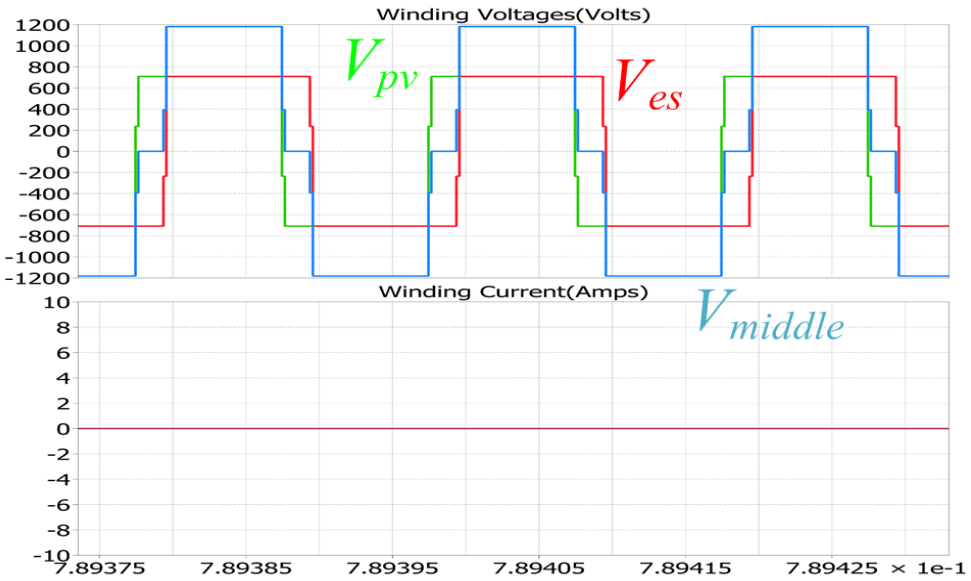

Figure 4.31. Ideal Transformer's Voltages & Currents with Open Middle Winding.

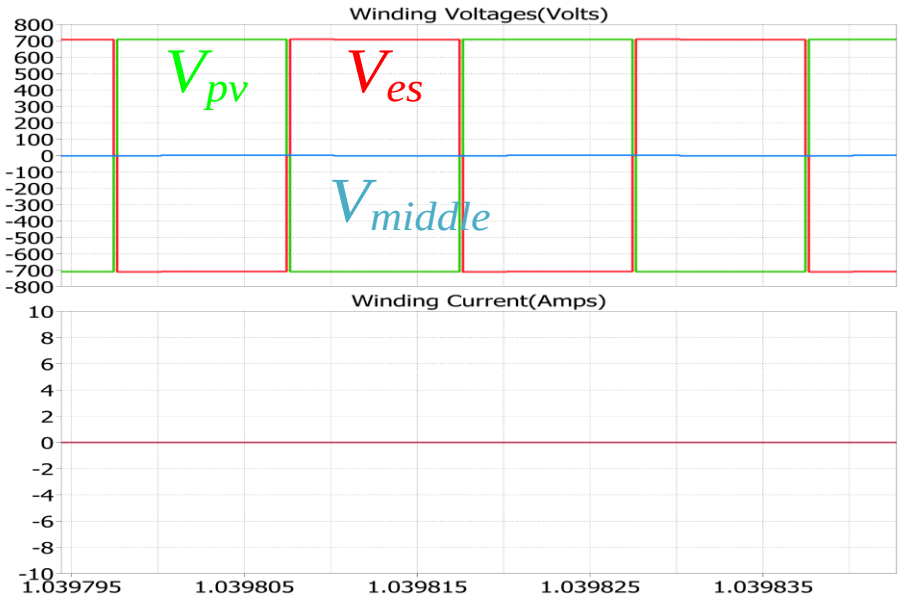

Figure 4.32. Ideal Transformer's Voltages and Currents with Open Side Winding.

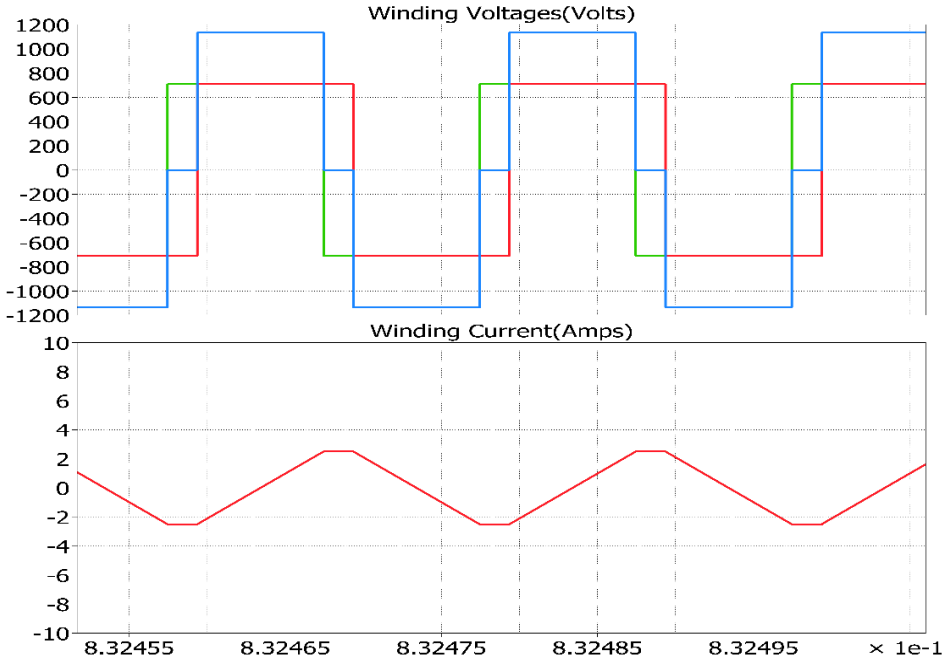

Figure 4.33. Actual Transformer's Voltages and Currents with Open Middle Winding.

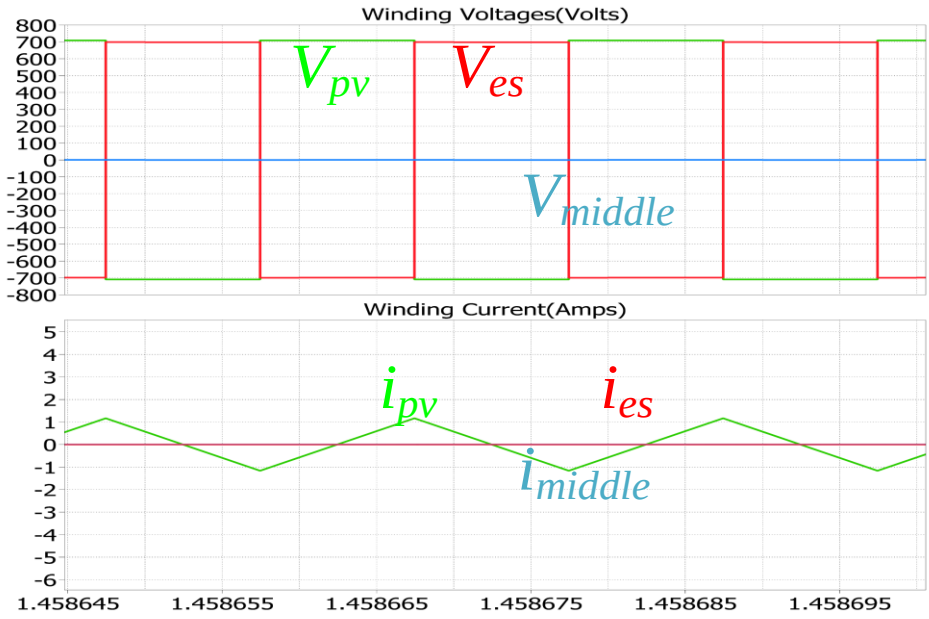

Figure 4.34. Actual Transformer's Voltages and Currents with Open Side Winding.

For ideal transformer, the magnetizing inductance is infinite, hence no winding current flows through any of the windings in figure 4.31-4.32. With actual transformer, a small air gap is considered, which causes a considerable magnetizing inductance. As a result, magnetizing current flows through the windings in figure 4.33-4.34. When a side port(PV/ES) is idle, zero current flows through the idle port as the dc bus gets charged through the diodes during initial current rush, and sits at the peak value of induced winding voltage, thus causing no power to flow in side limb winding. Majority of the fluxes thus flow through side limb winding, and small flux flows through middle limb, causing a very small voltage to get induced, when the middle limb has a load attached. When the middle port is connected to a constant voltage dc bus, the middle winding gets a very small current flowing through it and a large voltage is developed across side limb winding, which is much higher than the rated voltage and can cause failure of transformer and semiconductor devices. The reason behind very high induced voltage is the addition of fluxes from the other two side limbs. The transformer winding waveforms are shown

in figure 4.35. In this case, though the middle port winding and the side port winding, which are active, the winding currents are reactive in nature and the average dc current of the three ports are zero, as shown in figure 4.36.

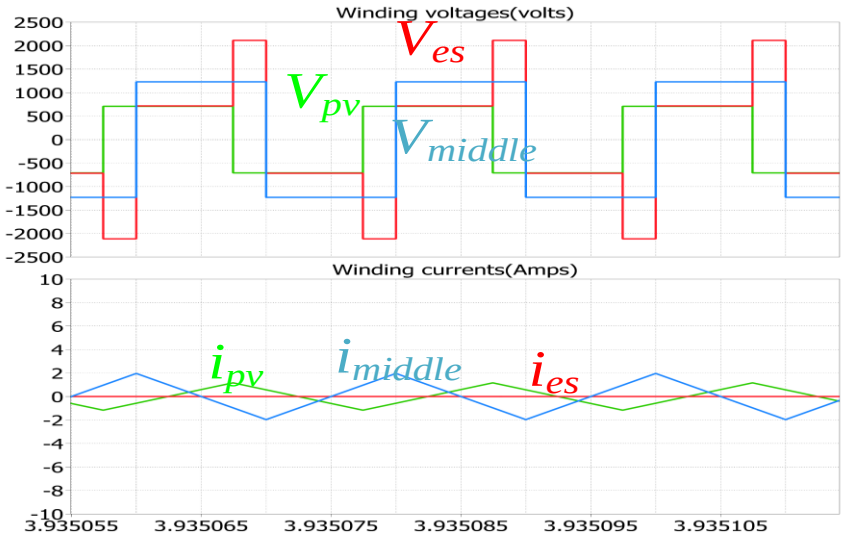

Figure 4.35. Transformer's Winding Voltages and Currents with Open Side Winding.

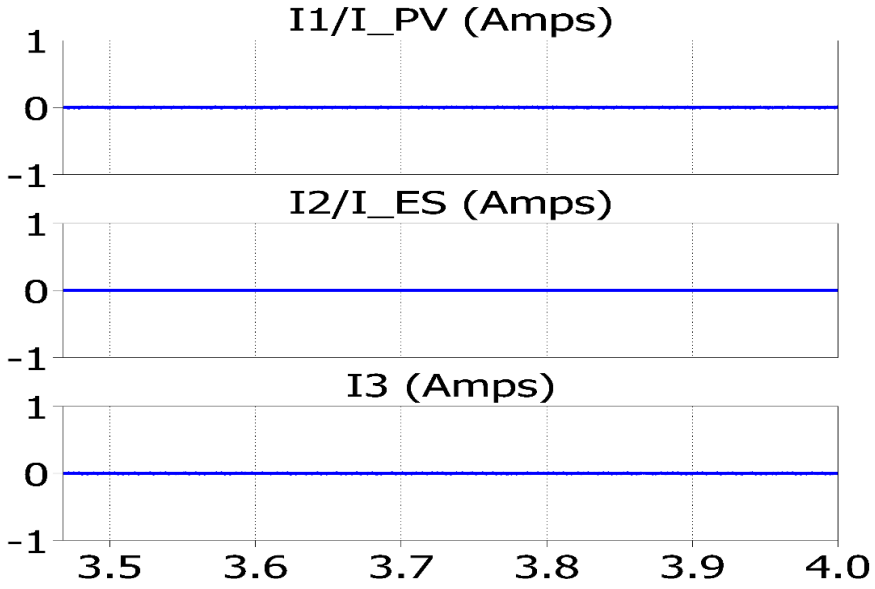

Figure 4.36. Average DC Currents of Three Ports when Side Winding is Open.

The shortcomings of three port three limb converter in ‘one port idle’ operation is verified with laboratory experiments with the prototypes discussed above. The corresponding port, which is kept idle, has all semiconductor switches turned off by pulling down PWM signals to zero. For the PV or ES ports, when one is in idle condition, only the PWM signals are put off for one and the dc sources are kept on, while the other side port switches are active and the middle port is loaded with resistive loads. Figure 4.37 show the transformer winding waveforms when PV port is idle and figure 4.38 shows the transformer waveforms when ES port is idle. It can be observed that in both the cases, the side limb windings carry mainly reactive currents and a very small power is transferred to port 3, since the middle winding develops a small voltage. Hence it can be inferred that most of the flux from the active side limb links the other idle side limb and a very small portion links the middle port. In figure 4.39, the middle port is kept idle, with resistive loads removed from its dc bus. It can be observed that the side limbs carry mainly reactive current, while middle winding carries zero current with high ringing in winding voltages, which is caused by leakage inductance and dc bus capacitance.

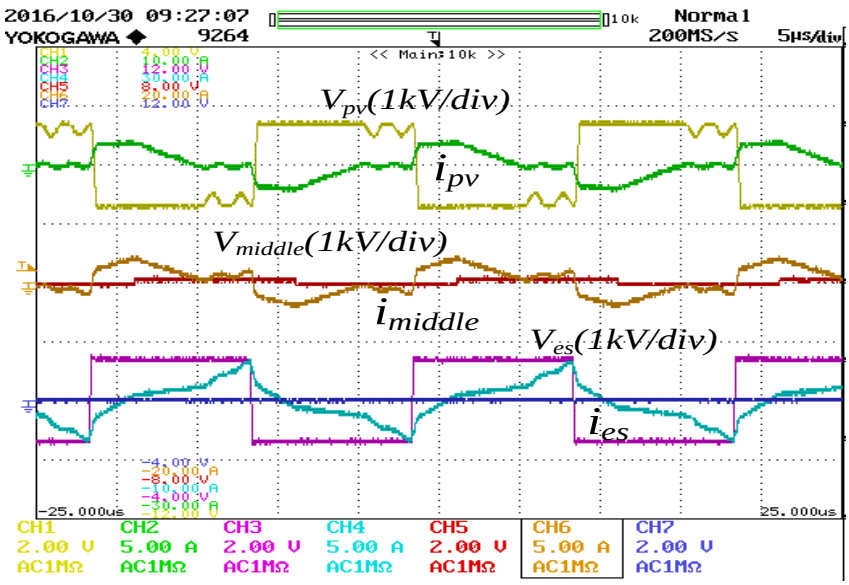

Figure 4.37. Transformer Waveforms When PV port is Idle.

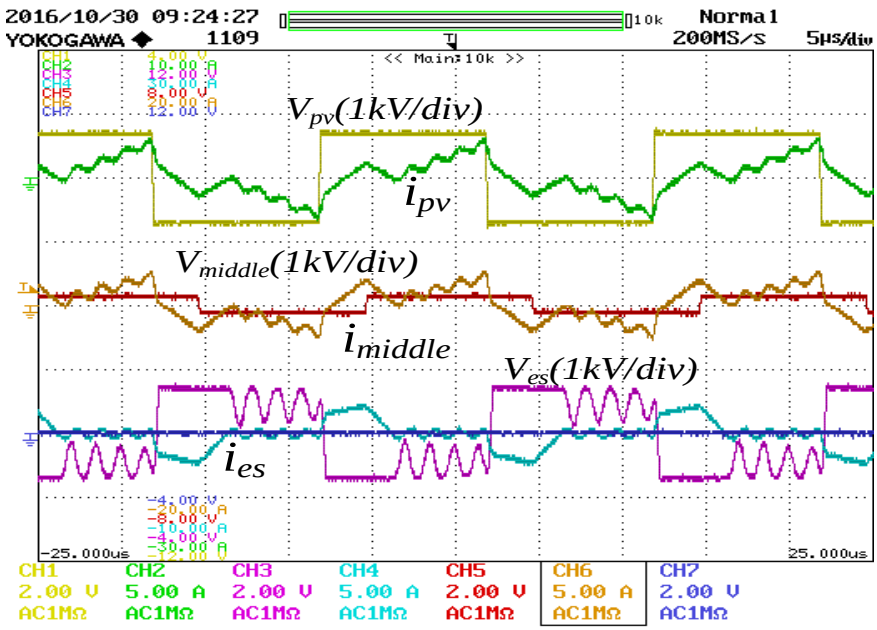

Figure 4.38. Transformer Waveforms When ES port is Idle.

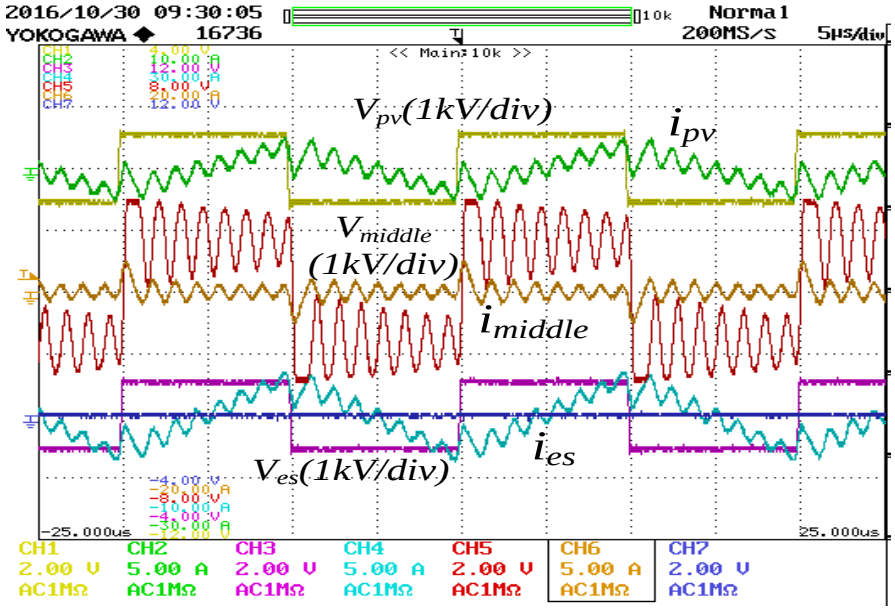

Figure 4.39. Transformer Waveforms When Middle port is Idle.

4.7. Possible Techniques for Operating Three Limb Three Winding Transformer with One Port Idle

Two possible techniques have been analyzed and suggested here so that the three limb three winding transformer can be operated successfully when one port is to be kept idle. The first method includes use of a crowbar switch to short the idle port winding, so that enough magnetic field is present along the limb cross section area. Schematic of the three limb three winding transformer using a shorted winding is shown in figures 4.40, 4.41.

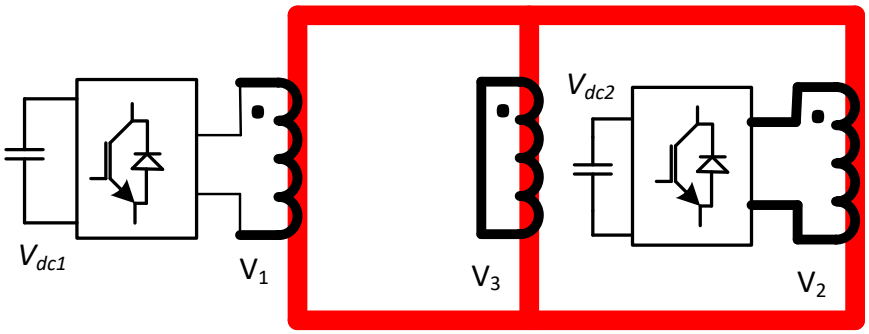

Figure 4.40. Three Limb Transformer with Shorted Middle Port.

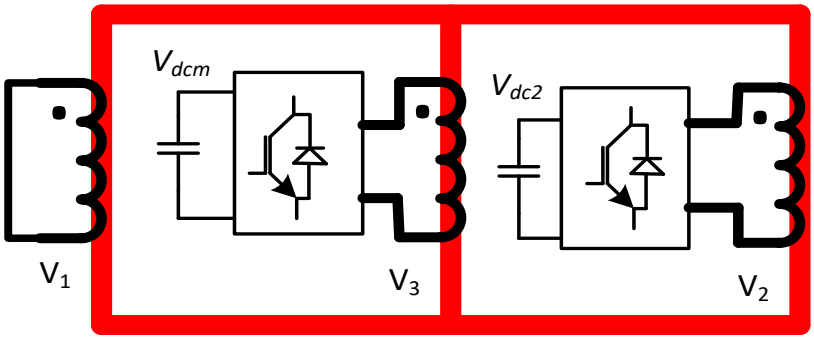

Figure 4.41. Three Limb Transformer with Shorted Side Port.

The second method includes use of a double throw switch so that the idle port winding can be connected in parallel with one of the active windings. The schematic of the three limb transformer using this method under one port idle condition is shown in figure 4.42, 4.43.

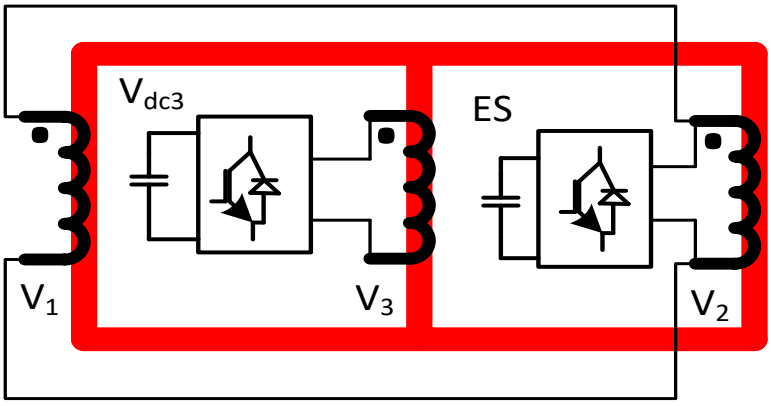

Figure 4.42. Three Limb Transformer with Parallel Connected Side Ports.

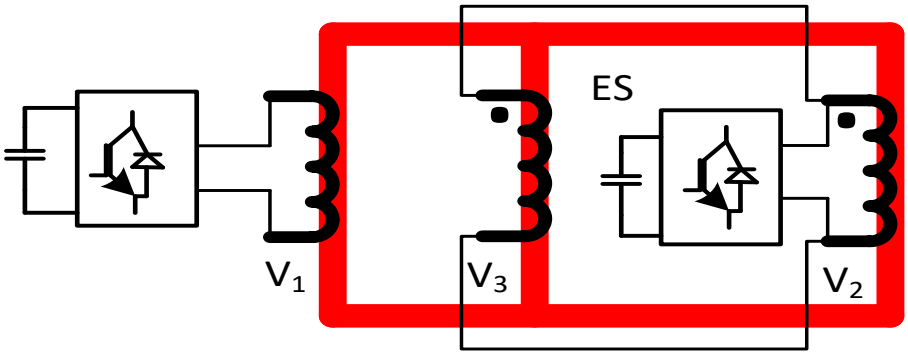

Figure 4.43. Three Limb Transformer with Parallel Connected Side & Middle Ports.

4.8. Decoupled Power Flow for Triple Active Bridge Converter Operation with Modulation Control Technique and ZVS Scenarios

The phase shift control discussed above, have shown how non-linear control method is applied to the PV and Energy Storage(ES) power flow control. The non-linear method requires pre-estimation of operating points and requires memory storage for implementing in hardware. Moreover, the ZVS operating region for the three limb transformer is limited for both the types of transformers. In this chapter, modulation control based linear control method is applied to PV and ES power flow control. The ZVS operating scenarios for the whole converter system and for the

individual converters of PV, ES and middle ports are discussed here. A discussion on ZVS operating regions is carried out to analyze ZVS operating regions.

The equivalent circuit of three limb three winding transformer derivation has been done in chapter 3. The reduced order equivalent circuit, neglecting magnetizing inductance, is derived in chapter 3. The derived equivalent circuit is shown in provided in figure 4.44. The power flows from one side limb H-bridge to another side limb H-bridge of the three port DAB converter can be realized by circuit analysis of equivalent circuit of figure 4.44. The possible voltage levels that can be applied to the winding voltages by an H-bridge are V_{dc}, 0, $-V_{dc}$, as shown in figure 4.45.

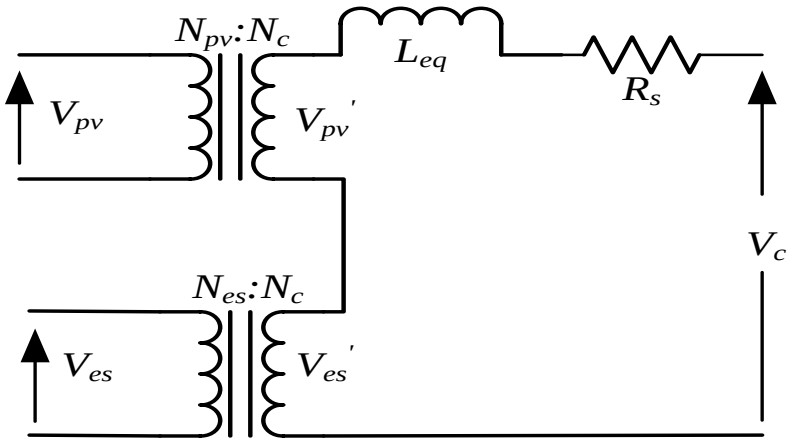

Figure 4.44. Equivalent circuit of Three Limb Three Winding Converter.

The power flow from one port to another port of the three port dc-dc converter of figure 4.44 can be realized by circuit analysis of equivalent circuit of figure 4.44. Each port of three limb transformer has H-bridges connected to them. The three possible voltage levels that can be produced at the output ac terminals of an H-bridge, are V_{dc}, 0, $-V_{dc}$, as shown in figure 4.45.

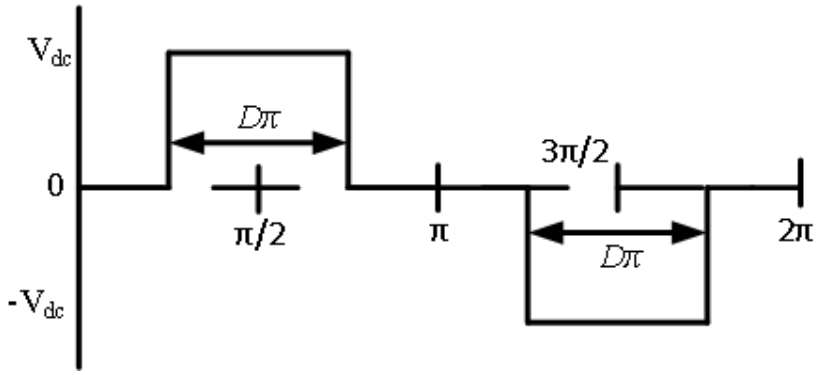

Figure 4.45. Three Level Voltage Output of an H-Bridge.

The fourier representation of three level voltage of figure 4.45 is given by equation (4.32).

$$v(t) = \sum_{n=odd} \frac{4V_{dc}}{n\pi} \sin\frac{nD\pi}{2} \sin n\omega t \quad (4.32)$$

The three winding voltages of three limb transformer equivalent circuit of figure 4.45, can be represented in the same way as given by fourier representation in equation (4.32). The three winding voltages are represented in fourier series as given in equations (4.33)-(4.35). In these equations, the middle winding voltage is the reference and the PV and ES winding voltages are having phase differences of δ_{pv} and δ_{es} w.r.t. the middle winding voltage.

$$V_{pv}'(t) = \sum_{n=odd} \frac{4(N_c/N_{pv})V_{pvdc}}{n\pi} \sin\frac{nD_{pv}\pi}{2} \sin(n\omega t + \delta_{pv}) \quad (4.33)$$

$$V_{es}'(t) = \sum_{n=odd} \frac{4(N_c/N_{es})V_{esdc}}{n\pi} \sin\frac{nD_{es}\pi}{2} \sin(n\omega t + \delta_{es}) \quad (4.34)$$

$$V_c'(t) = \sum_{n=odd} \frac{4V_{dcm}}{n\pi} \sin\frac{nD_c\pi}{2} \sin(n\omega t) \quad (4.35)$$

From the equivalent circuit, which neglects the magnetizing inductance, the winding current is same in shape and phase in all the windings, only the magnitude differs based on number of turns.

Hence, analyzing the current referred to middle winding can provide the power equations. The RMS current expression for nth component of middle current is given by equation (4.36), where δ_{pv} and δ_{es} are the phase angle differences of fundamental component of side limb winding voltages w.r.t. fundamental component of middle limb winding voltage. For power flow from side limb sources to middle limb source, the phase angles are leading while for power flow from middle limb source to side limb sources, the phase angle is lagging.

$$i_n = \frac{V_{pvn}\angle n\delta_{pv} + V_{esn}\angle n\delta_{es} - V_{cn}\angle 0}{Z_n\angle\theta_n} \quad (4.36)$$

$$P_k = \sum_{n=1,3,5}^{\infty} P_{kn} = \sum_{n=1,3,5}^{\infty} \text{Real}(V_{kn} \times i_n^{*}) \quad (4.37)$$

$$P_{kn} = \frac{V_{kn}^{\,2}\cos\theta_n}{Z_n} + \frac{V_{kn}V_{jn}\cos(\text{n}\,\delta_k - \text{n}\,\delta_j + \theta_n)}{Z_n} - \frac{V_{kn}V_{cn}\cos(\text{n}\,\delta_k + \theta_n)}{Z_n} \quad (4.38)$$

where k=pv,es

The power flowing from one side limb winding of the three limb transformer is given by equation (4.37), which is sum of real powers due to each harmonic components of the voltage and current, where V_{kn} is the RMS voltage of nth harmonic component of kth winding. Real power due to nth harmonic components of the voltage and current for kth winding is given by equation (4.38), where V_{jn} is the RMS voltage of the other side limb winding. The expressions for winding impedance parameters Z_n and θ_n are given in equations (4.39) and (4.40).

$$Z_n = \sqrt{R_s^{\,2} + (n\omega L_{eq})^2} \quad (4.39) \qquad \theta_n = \tan^{-1}\left(\frac{n\omega L_{eq}}{R_s}\right) \quad (4.40)$$

For a high frequency transformer $n\omega L_{eq} >> R_s$, hence $\theta_n \approx \pi/2$, hence the expression for P_{kn} changes as follows.

$$P_{kn} = \frac{V_{kn}V_{jn}\sin(\mathrm{n}\,\delta_j - \mathrm{n}\,\delta_k)}{n\omega L_{eq}} + \frac{V_{kn}V_{cn}\sin(\mathrm{n}\,\delta_k)}{n\omega L_{eq}} \quad (4.41)$$

Analyzing the equation (4.41), it can be inferred that the first term represent the coupling between the two side limb winding voltages and the second term represent the power flowing to/from middle limb winding from/to one of the side limb windings. To decouple the power flow of each side limb ports, three options are feasible to make to the coupling term zero. First option is to make the side limb winding voltages lead at same angle, $\delta_{pv} = \delta_{es}$, and the second option is to place them 180 degree apart, $\delta_{pv} \sim \delta_{es} = \pi$. Clearly, from the equation (4.41), if the two side limbs' winding voltages are placed at same leading angle w.r.t. V_c, the side ports will deliver power and if they are placed 180 degree apart, one will deliver while the other will consume power. Hence, when PV and ES both are delivering, their respective winding voltages can be placed at the same phase shift angle of δ(leading), and when PV is delivering and ES is charging, PV voltage can lead V_c by phase shift angle δ, and ES voltage can lag V_c by phase shift (π-δ). A third option for decoupling the side limb port power flows, during ES charging, PV voltage leads V_c by δ and the ES voltage lags V_c by π. Using method 2, ES can charge from both V_{dcm} bus and PV, while, using method 3, ES can charge only from PV.

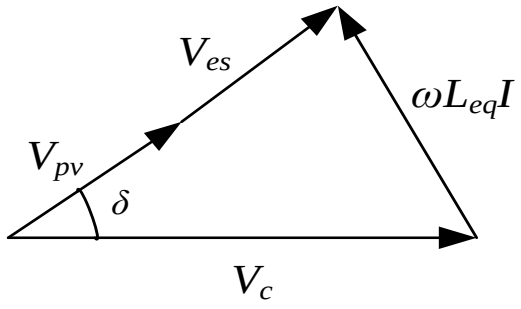

Figure 4.46. Method 1: PV and ES delivering.

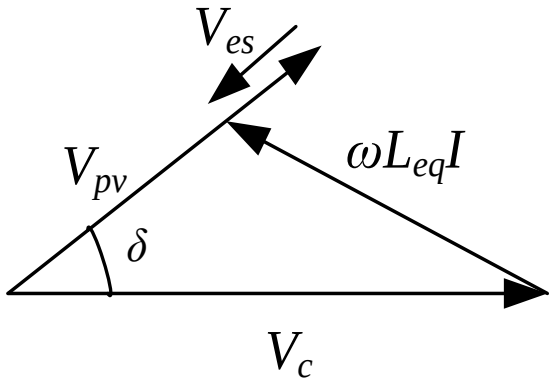

Figure 4.47. Method 2: PV delivering, ES charging.

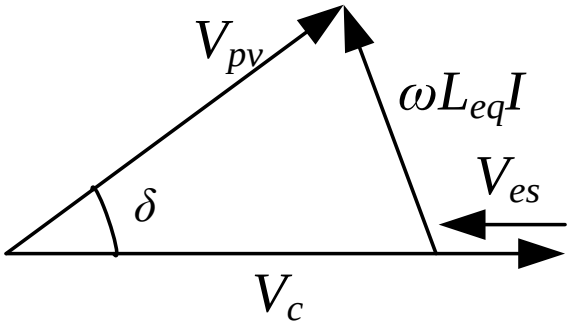

Figure 4.48. Method 3: PV delivering, ES charging.

The power flow expressions for the three ports under the different methods can be evaluated from equation 4.41. Power flow of each port is expressed here as sum of active power components due to each individual harmonic component. Equations (4.42-4.50) give the average power flow expressions for the three ports(output power for PV and ES and power flowing into middle port).The power flow expressions for the three ports are functions of winding voltages, phase shift angle and total series leakage inductance,

a) Method 1: , $\delta_{pv} = \delta_{es} = \delta$; PV and ES delivering

$$P_{pv} = \sum_{n=1,3,5}^{\infty} \frac{(N_c / N_{pv}) V_{pvn} V_{cn} \sin(n\delta)}{n\omega L_{eq}} \quad (4.42), \quad P_{es} = \sum_{n=1,3,5}^{\infty} \frac{(N_c / N_{es}) V_{esn} V_{cn} \sin(n\delta)}{n\omega L_{eq}} \quad (4.43)$$

$$P_c = \sum_{n=1,3,5}^{\infty} \frac{(N_c / N_{pv}) V_{pvn} V_{cn} \sin(n\delta)}{n\omega L_{eq}} + \sum_{n=1,3,5}^{\infty} \frac{(N_c / N_{es}) V_{esn} V_{cn} \sin(n\delta)}{n\omega L_{eq}} \quad (4.44)$$

b) Method 2: , $\delta_{pv} = \delta$, $\delta_{es} = \pi - \delta$; PV delivering and ES charging

$$P_{pv} = \sum_{n=1,3,5}^{\infty} \frac{(N_c / N_{pv}) V_{pvn} V_{cn} \sin(n\delta)}{n\omega L_{eq}} \quad (4.45), \quad P_{es} = -\sum_{n=1,3,5}^{\infty} \frac{(N_c / N_{es}) V_{esn} V_{cn} \sin(n\delta)}{n\omega L_{eq}} \quad (4.46)$$

$$P_c = \sum_{n=1,3,5}^{\infty} \frac{(N_c / N_{pv}) V_{pvn} V_{cn} \sin(n\delta)}{n\omega L_{eq}} - \sum_{n=1,3,5}^{\infty} \frac{(N_c / N_{es}) V_{esn} V_{cn} \sin(n\delta)}{n\omega L_{eq}} \quad (4.47)$$

c) Method 3: , $\phi_{pv} = \phi$, $\phi_{es} = \pi$; PV delivering and ES charging

$$P_{es} = -\sum_{n=1,3,5}^{\infty} \frac{(N_c / N_{pv}) V_{pvn} (N_c / N_{es}) V_{esn} \sin(n\delta)}{n\omega L_{eq}} \quad (4.48),$$

$$P_{pv} = \sum_{n=1,3,5}^{\infty} \frac{(N_c / N_{pv}) V_{pvn} V_{cn} \sin(n\delta)}{n\omega L_{eq}} \quad (4.49),$$

$$P_{es} = \sum_{n=1,3,5}^{\infty} \frac{(N_c / N_{pv}) V_{pvn} (N_c / N_{es}) V_{esn} \sin(n\delta)}{n\omega L_{eq}} + \sum_{n=1,3,5}^{\infty} \frac{(N_c / N_{pv}) V_{pvn} V_{cn} \sin(n\delta)}{n\omega L_{eq}} \quad (4.50)$$

From the power flow expressions above, it can be inferred that all expression are functions of phase shift angle δ, hence decoupled power flow control is not feasible by controlling the phase shift angle. However, individual port powers can be independently controlled by keeping the phase shift angle δ fixed at a pre-selected value and controlling the output ac voltage of each converter. The rms or average value of converter output voltages can be controlled by controlling duty cycles of output square wave or quasi square wave voltages. From equations 4.33-4.35, the three winding voltages can be expressed as functions of D_{pv}, D_{es}, D_c.

Using method 1, when both PV and ES are delivering, the PV and ES winding voltages are kept at a fixed leading phase shift angle δ, and their output power can be controlled by controlling their individual duty cycles, as given in equation 4.41. It can be observed that method 2 is same as method 1, only the polarity of ES winding voltage changes, hence the same equations for method 1 are applicable to method 2.

Method 1, 2: $P_{pv} = f(D_{pv})$ (4.51), $|P_{es}| = f(D_{es})$ (4.52), $P_c = P_{pv} + P_{es}$ (4.53)

Using method 3, the ES and middle port winding voltages are kept at reference phase angle and PV winding voltage is made to lead the reference by δ. The power going into middle port is controlled by controlling duty cycle of middle winding voltage, while power going into ES port is also controlled in similar way by controlling duty cycle of ES winding voltage.

Method 3: $P_c = f(D_c)$ (4.54), $|P_{es}| = f(D_{es})$ (4.55), $P_{pv} = P_c + P_{es}$ (4.56)

Using method 2, the ES can be charged at a higher power when PV output power is very low, by taking extra charging power from middle port dc bus, while using method 3, the ES can only be charged from PV.

4.9. Switching Technique for Duty Cycle Control Method

The typical three level winding voltage waveform during a full switching cycle period for the H-bridge converter is shown in figure 4.45. Two different kind of switching techniques are possible for getting the three level voltage waveforms. First technique is to switch every H-bridge leg at 50% duty cycle and shift the two switching legs of the same H-bridge by some angle to create a three level voltage output. Figure 4.49 shows the switching technique for this method, where S_1, S_2 are switches of one leg and S_3,S_4 are switches for another leg. For this switching technique with 50% duty cycle, one switching leg of the H-bridge connected to middle limb winding is taken as reference and the phase leading/lagging angles of the switching legs of other H-bridge are calculated using ϕ, D_{pv}, D_{es}, D_c.

Switching technique 2, as shown in figure 4.50, has unequal duty cycle for switches. In this technique, one leg has a carrier signal proportional to D, and the other leg has a carrier signal proportional to (1-D). The switching logic for both the legs are opposite to each other or complimentary to each other, which has been shown in figure 4.50. In this method a single carrier wave is used for a bridge, while the phase differences between the winding voltages is created by shifting the corresponding carrier waves by the required phase shift angles.

The difference between the two switching techniques is unequal switch conduction. For technique 1, neglecting the deadband time, the current flows through the Mosfet channels for the whole switching period, while for technique 2 the current flows through body diode of mosfets during some portion of the switching cycle, when the switch is off. As a consequence, in switching technique 1, all the mosfets have equal conduction losses while in technique 2, all the mosfets do not have equal conduction loss, mosfets remaining on for lower time has higher

conduction loss as conduction through body diode of SiC-Mosfets creates more losses than conduction through channel.

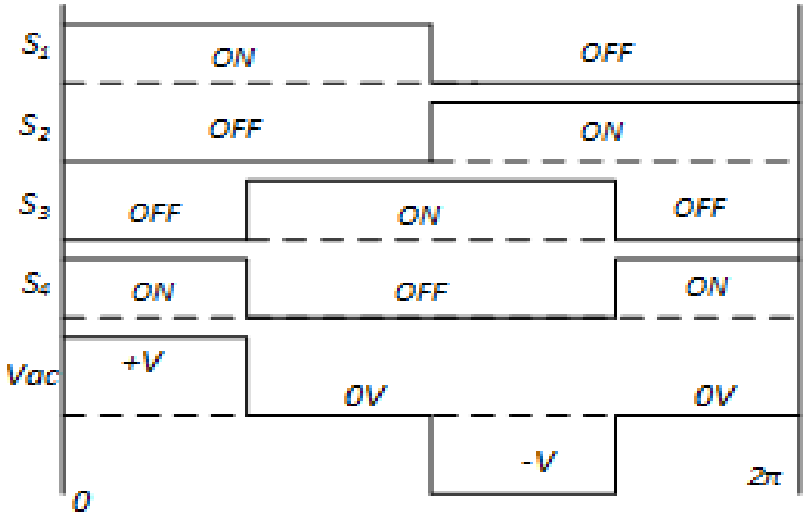

Figure 4.49. Switching Technique 1 with 50% duty Cycle and Phase Shift.

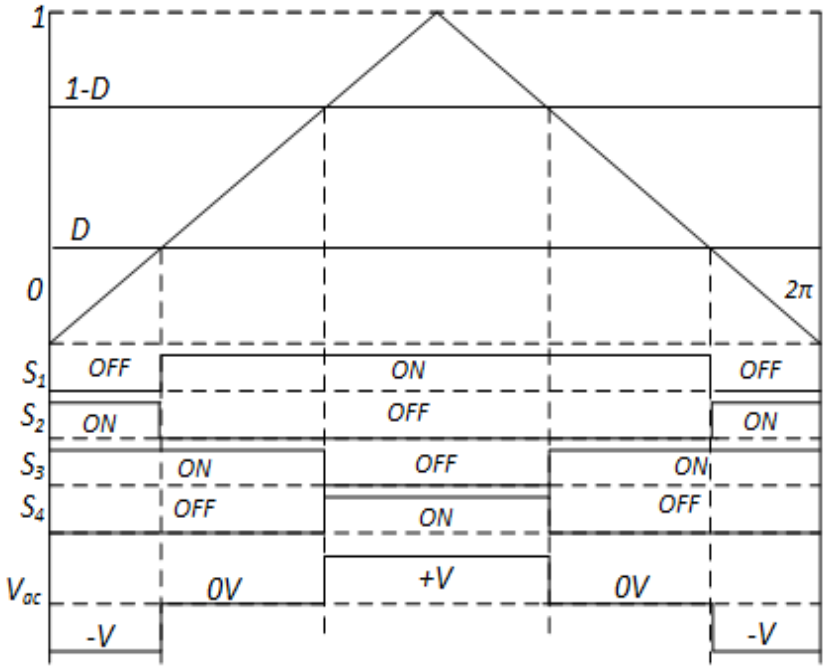

Figure 4.50. Switching Technique 2 with Asymmetrical Duty Cycle.

4.10. Triple Active Bridge Converter Turn-on ZVS operating Regions

Power switches such as Mosfets and IGBTs have natural ZVS turn-on depending on the line current value and direction flow during switching transition[60]. The ZVS turn-on takes place when the switch to be turned on has zero voltage across it, when the gate pulse is applied, which happens due to current flowing through the anti-parallel diode of the switch. Dual active bridge converters and triple active bridge converters generally has natural ZVS turn-on characteristics for outgoing lagging current and incoming leading current. The switching node current varies depending on different values of phase shift angle and zero voltage duration of winding voltages. Using modulation control technique 1, when PV and ES both deliver power, there are twelve possible cases or modes of positioning of winding voltage transitions, which are shown in figures 4.51-4.62, where V_1, V_2, V_3 represent the winding voltages V_{pv}, V_{es} and V_c.

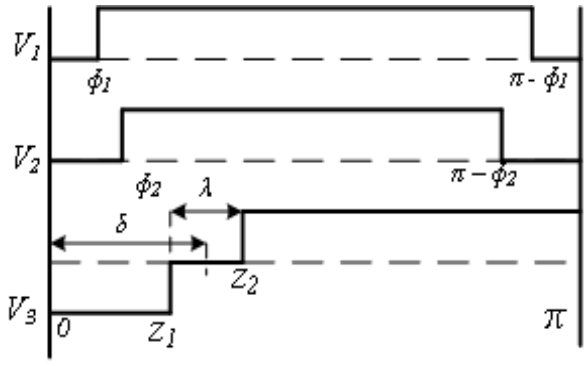

Figure 4.51. Strategy 1: Mode 1.

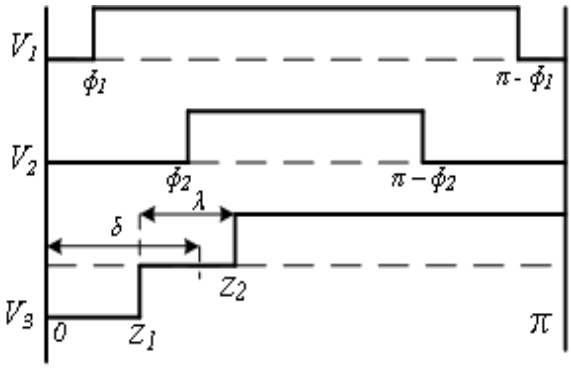

Figure 4.52. Strategy 1: Mode 2.

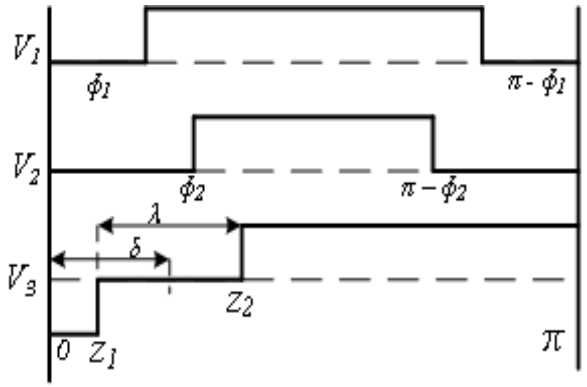

Figure 4.53. Strategy 1: Mode 3.

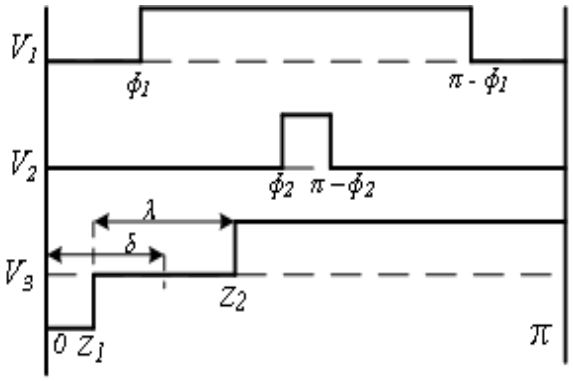

Figure 4.54. Strategy 1: Mode 4.

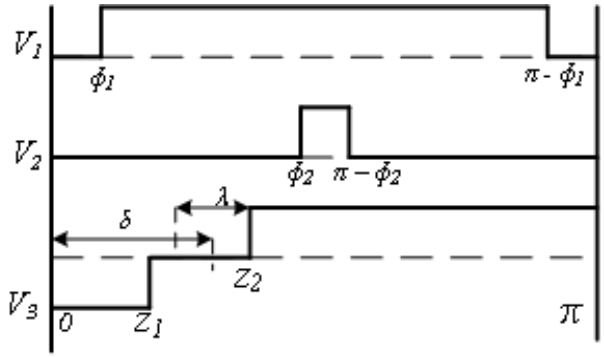

Figure 4.55. Strategy 1: Mode 5.

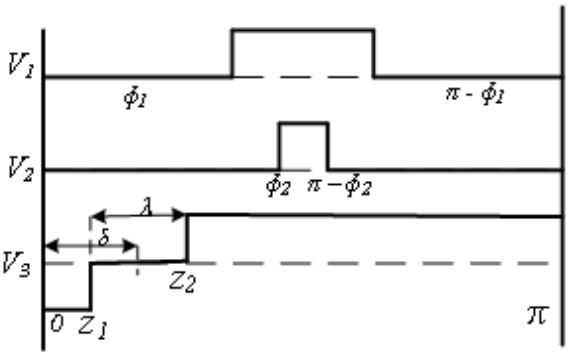

Figure 4.56. Strategy 1: Mode 6.

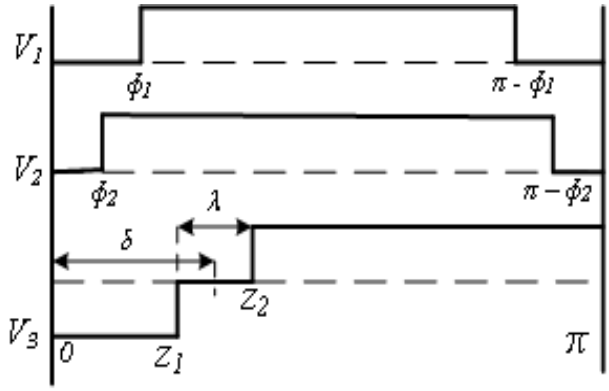

Figure 4.57. Strategy 1: Mode 7.

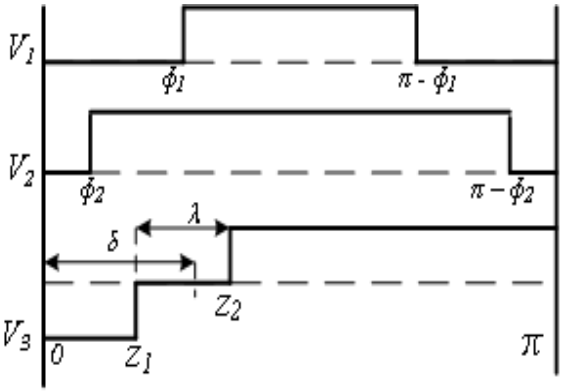

Figure 4.58. Strategy 1: Mode 8.

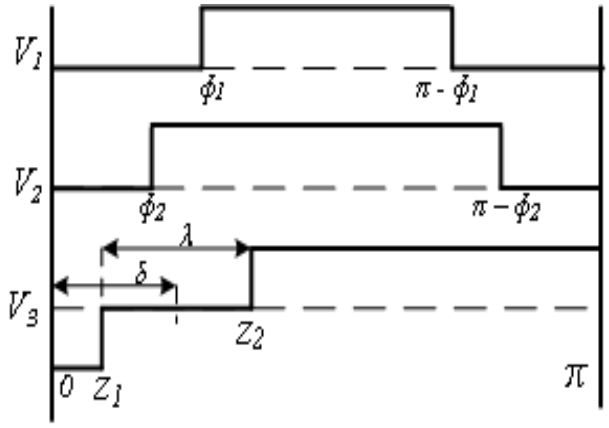

Figure 4.59. Strategy 1: Mode 9.

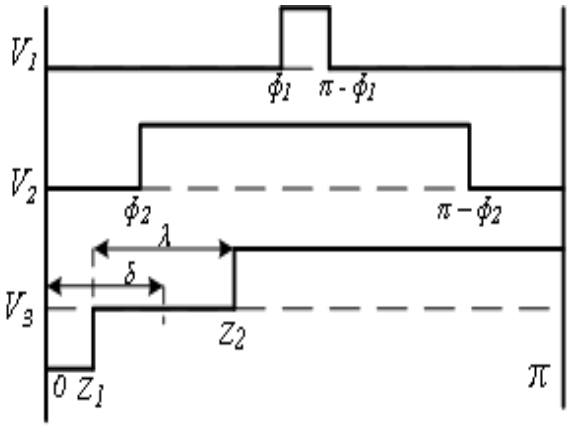

Figure 4.60. Strategy 1: Mode 10.

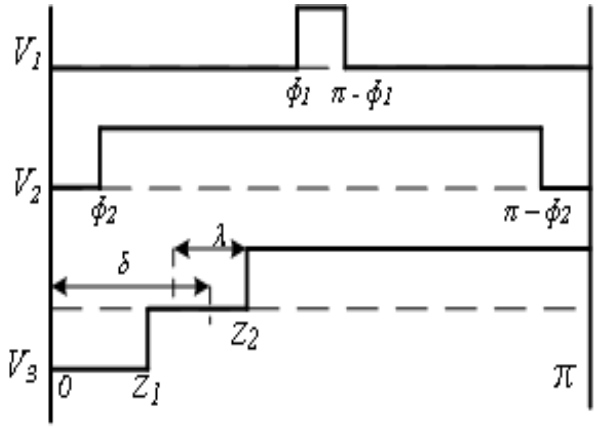

Figure 4.61. Strategy 1: Mode 11.

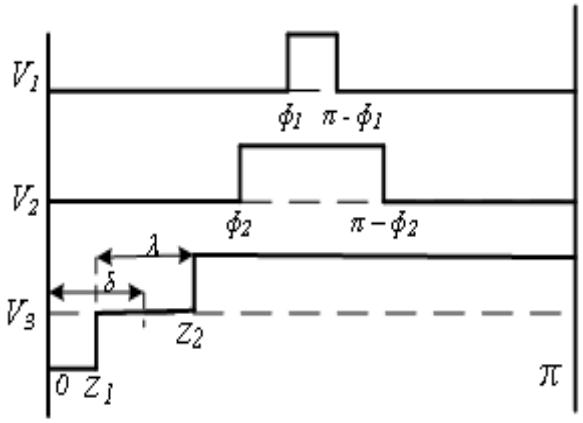

Figure 4.62. Strategy 1: Mode 12.

Using modulation control technique 2, when PV delivers and Energy Storage gets charged, there are twelve possible cases or modes of positioning of winding voltage transitions, which are shown in figures 4.63-4.74.

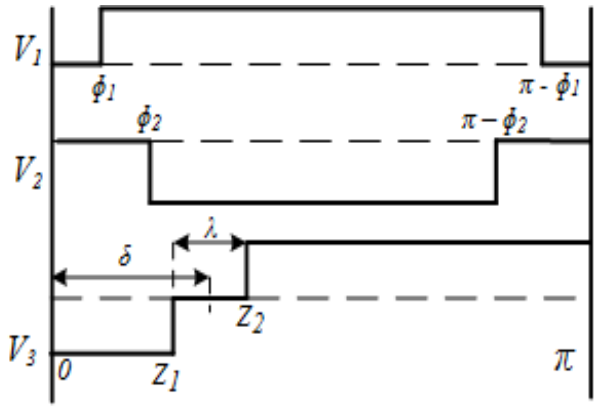

Figure 4.63. Strategy 2: Mode 1.

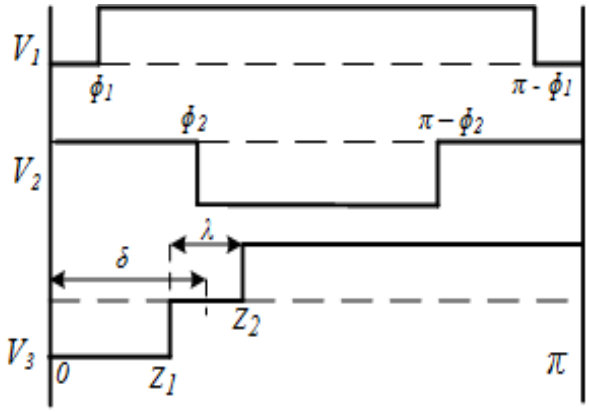

Figure 4.64. Strategy 2: Mode 2.

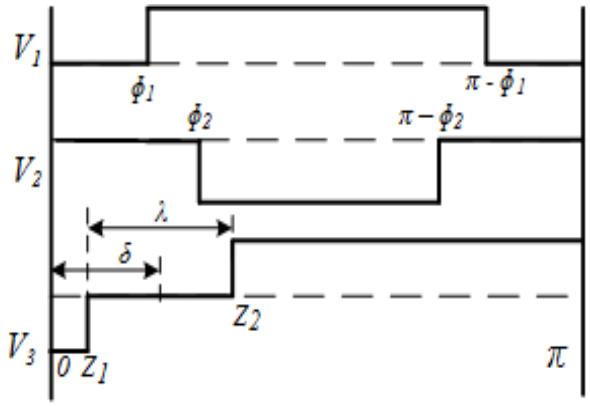

Figure 4.65. Strategy 2: Mode 3.

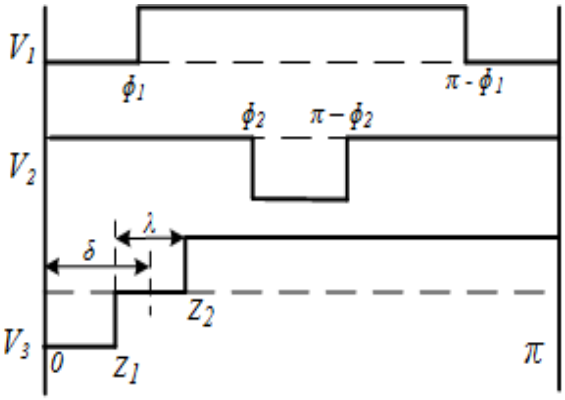

Figure 4.66. Strategy 2: Mode 4.

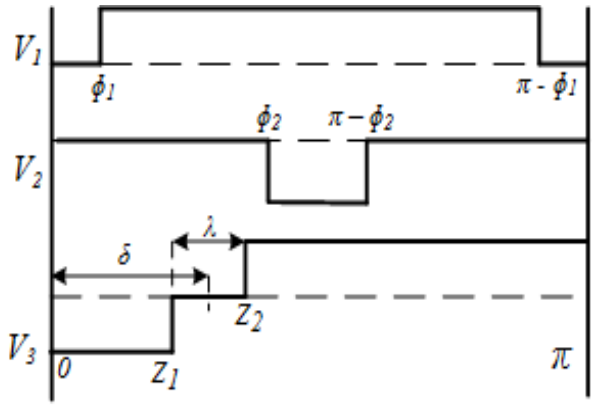

Figure 4.67. Strategy 2: Mode 5.

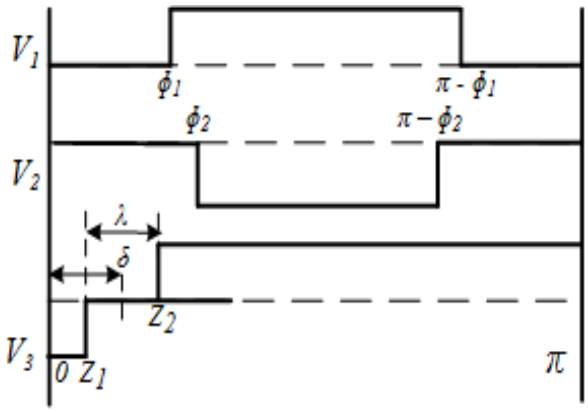

Figure 4.68. Strategy 2: Mode 6.

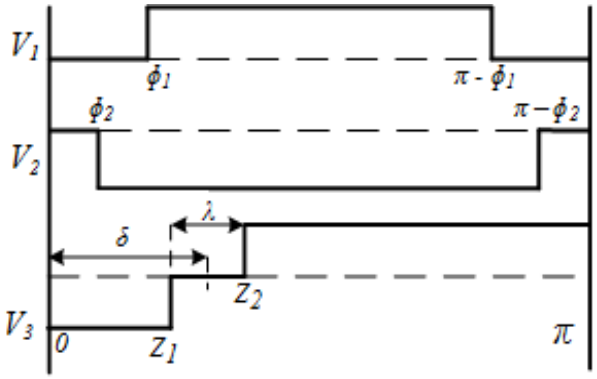

Figure 4.69. Strategy 2: Mode 7.

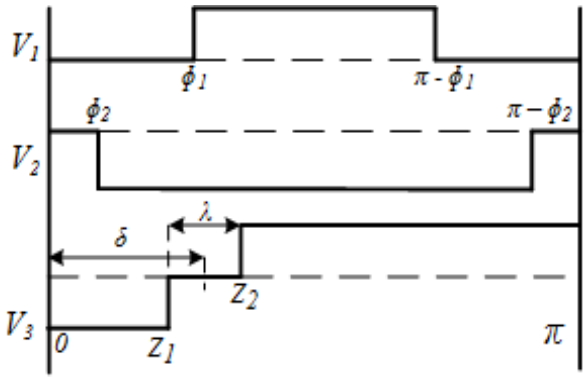

Figure 4.70. Strategy 2: Mode 8.

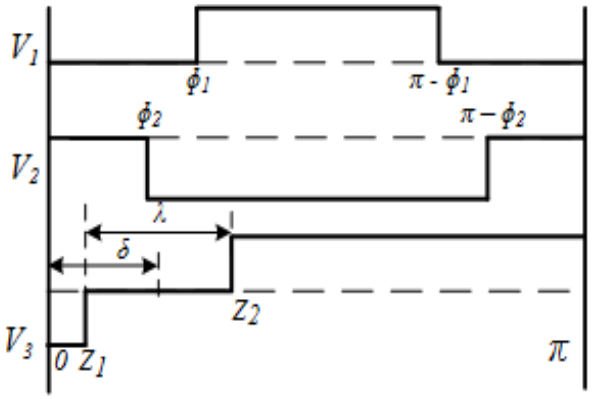

Figure 4.71. Strategy 2: Mode 9.

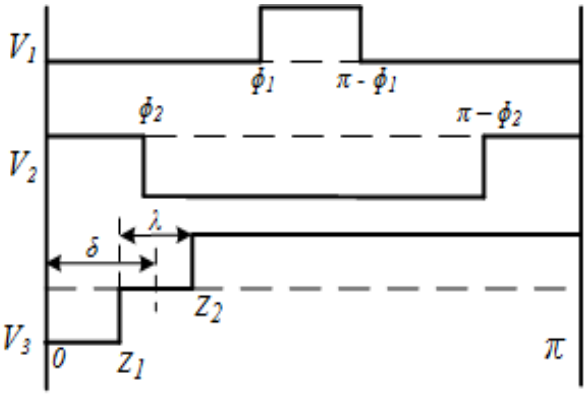

Figure 4.72. Strategy 2: Mode 10.

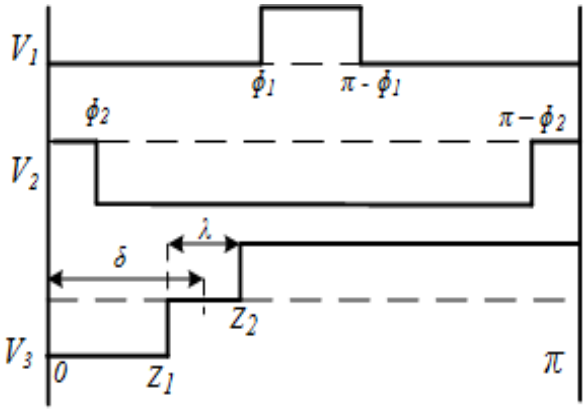

Figure 4.73. Strategy 2: Mode 11.

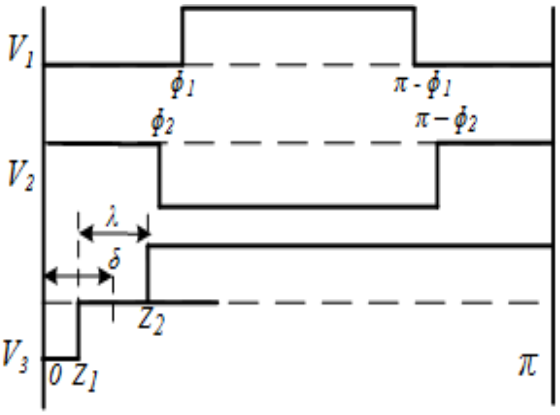

Figure 4.74. Strategy 2: Mode 12.

Using modulation control technique 3, when PV delivers and Energy Storage gets charged, there are ten possible cases or modes of positioning of winding voltage transitions, which are shown in figures 4.75-4.84.

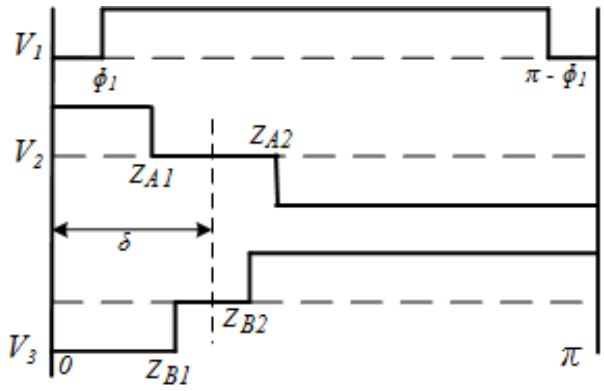

Figure 4.75. Strategy 3: Mode 1.

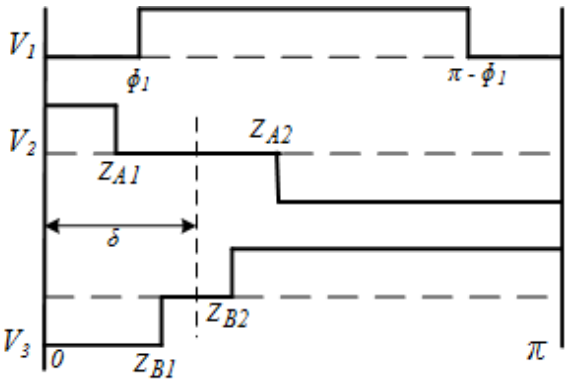

Figure 4.76. Strategy 3: Mode 2.

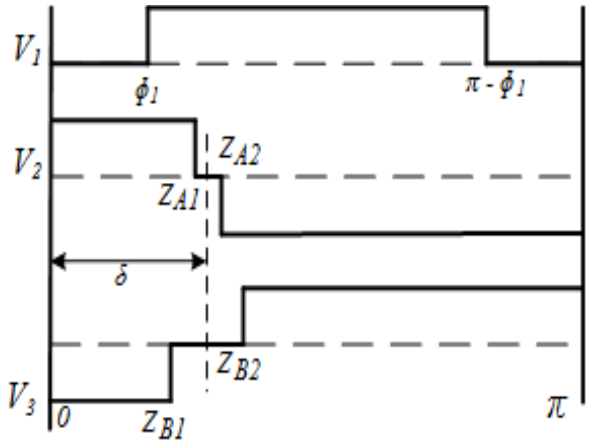

Figure 4.77. Strategy 3: Mode 3.

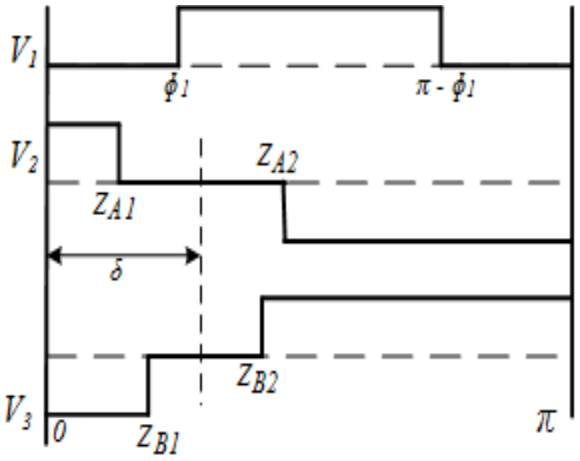

Figure 4.78. Strategy 3: Mode 4.

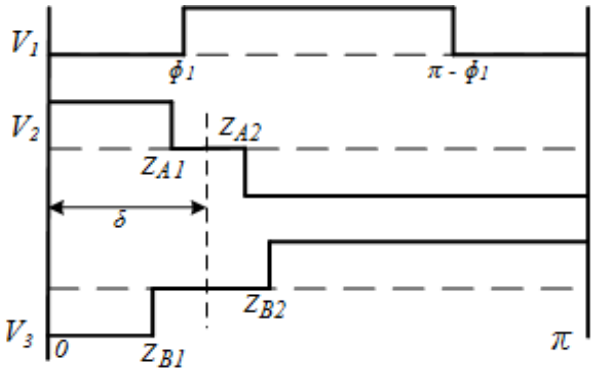

Figure 4.79. Strategy 3: Mode 5.

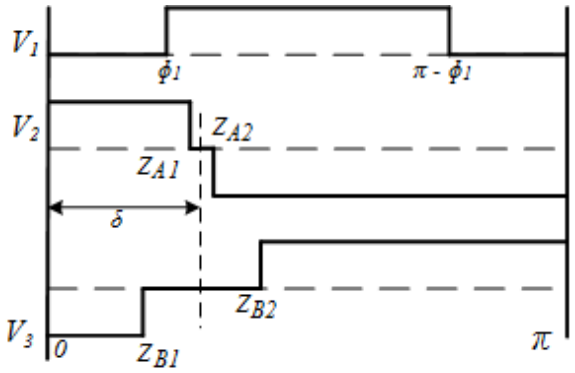

Figure 4.80. Strategy 3: Mode 6.

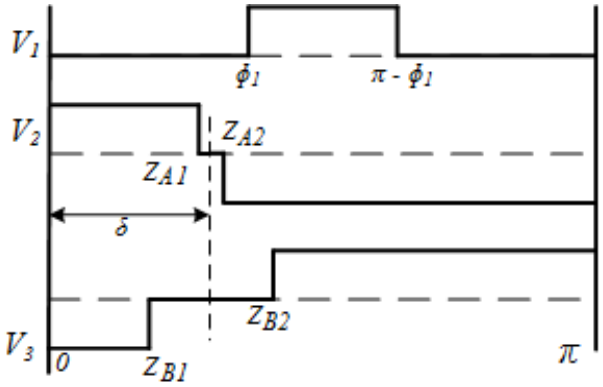

Figure 4.81. Strategy 3: Mode 7.

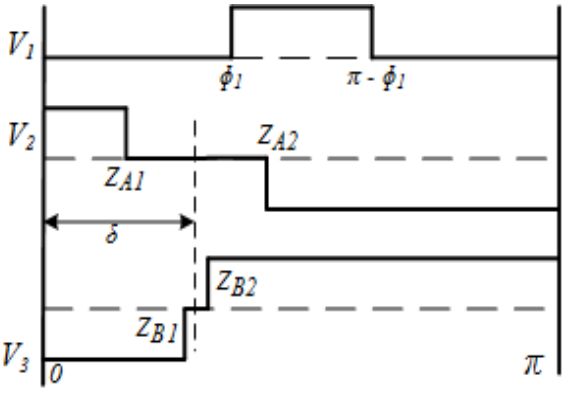

Figure 4.82. Strategy 3: Mode 8.

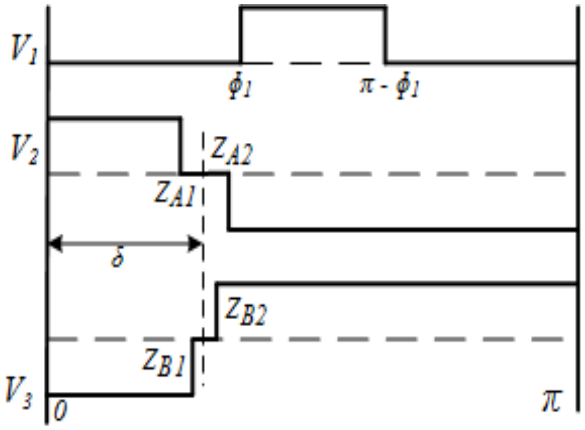

Figure 4.83. Strategy 3: Mode 9.

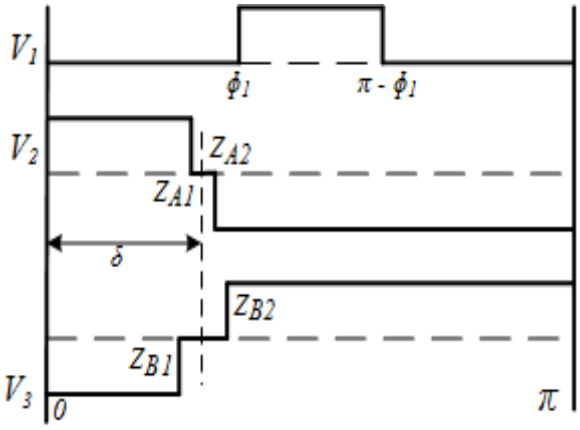

Figure 4.84. Strategy 3: Mode 10.

Using the three control strategies, the ZVS operating regions for the triple active bridge converter can be evaluated by determining the line current value and direction during the different switching transition instants. For determining the ZVS operating points, it is assumed that the effect of device capacitance is negligible and sufficient dead-band time is available for the ZVS transition to take place. In other words, the ZVS operating region discussed here pertains to ideal ZVS operating cases, where a small negative current present in the line is enough to discharge the device capacitance and the effect of transformer magnetizing inductance is neglected. The winding current is evaluated as given in equation (4.57), neglecting the effect of magnetizing inductance.

$$i_L(\omega t) = \frac{1}{\omega L_{eq}} \int \{ \frac{N_{pv}}{N_c} V_{pv}(\mathrm{D}_{pv}, \mathrm{t}, \delta) + \frac{N_{es}}{N_c} V_{es}(\mathrm{D}_{es}, \mathrm{t}, \delta) - V_c(\mathrm{D}_c, \mathrm{t}, \delta) \} \mathrm{dt} \quad (4.57)$$

The i_L as evaluated from (4.57), is used to check the current direction during the switching instants shown in figures 4.51-4.84. During control strategy 1,2 and 3, the criteria being used for ZVS operating point determination is given below.

ZVS Criteria for Control Strategy 1

$i_L(\phi_1) < 0$ (4.58), $i_L(\phi_2) < 0$ (4.59), $i_L(Z_1) > 0$ (4.60), $i_L(Z_2) > 0$ (4.61),

$i_L(\pi - \phi_1) > 0$ (4.62), $i_L(\pi - \phi_2) > 0$ (4.63)

ZVS Criteria for Control Strategy 2

$i_L(\phi_1) < 0$ (4.64), $i_L(\phi_2) > 0$ (4.65), $i_L(Z_1) > 0$ (4.66), $i_L(Z_2) > 0$ (4.67),

$i_L(\pi - \phi_1) > 0$ (4.68), $i_L(\pi - \phi_2) < 0$ (4.69)

ZVS Criteria for Control Strategy 3

$i_L(\phi_1) < 0$ (4.70), $i_L(Z_{a1}) > 0$ (4.71), $i_L(Z_{a2}) > 0$ (4.72), $i_L(Z_{b1}) > 0$ (4.73), $i_L(Z_{b2}) > 0$ (4.74), $i_L(\pi - \phi_2) < 0$ (4.75)

Clearly, control strategy 1 is the only feasible method for PV and ES both to deliver. Therefore, control strategy 1 and 2 is a combination of operating PV and ES in power outflow/inflow scenarios, while control strategy 1 and 3 is the other possible scenario for PV and ES integration. Using the ZVS criteria listed above, the ZVS operating points for the three limb transformer based triple active bridge converter is evaluated as below. Clearly the ZVS operating points are functions of the phase shift δ, duty cycle D_{pv}, D_{es} and D_c. For the analysis presented here, two values of phase shift δ are considered, δ=π/3 and δ=π/6. The duty cycle D_c for the middle winding voltage is varied over range of ($0<D_c<1$) for variation of D_{pv} and D_{es} over the ranges ($0<D_{pv}<1$) and ($-1<D_{es}<1$) respectively.

4.10.1. ZVS Operating Point Ranges with Control Strategy 1 and 2

Using control strategy 1 for PV and ES delivering conditions and using control strategy 2 for PV delivering and ES charging condition, figure 4.85 shows the full converter ZVS operating points for the three port converter.

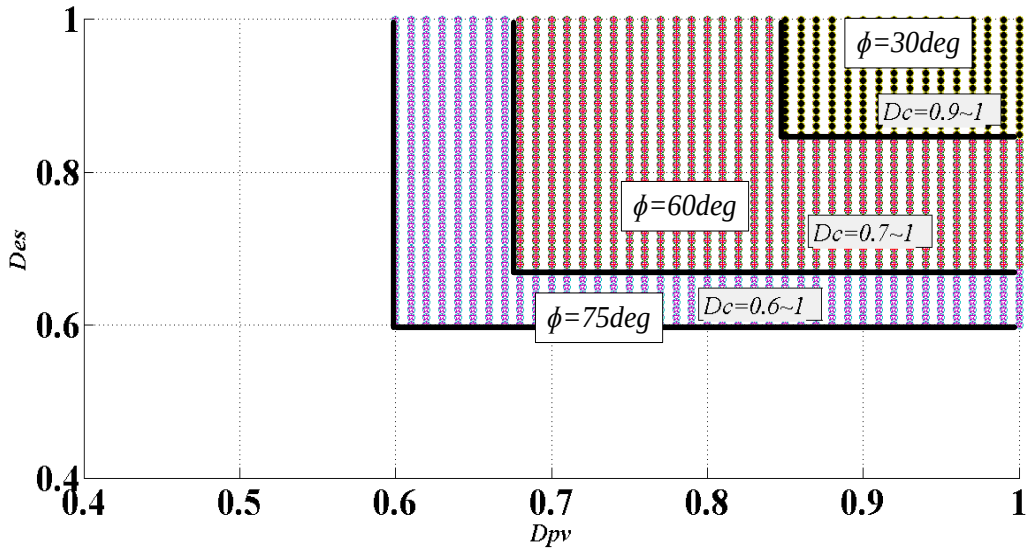

Figure 4.85. Converter ZVS Operating Points for Three Limb Transformer.

It can be observed that for phase shift values around 30 to 60 degree, using transformer type 2, the converter has much higher ZVS operating points than using transformer type 2. However, it can be observed that for both the converters, no ZVS operating points are there when D_{es} is negative, i.e. the during ES charging, the converter system doesn't have ZVS. To investigate more into the ZVS of converter, individual H-bridge ZVS operating points are evaluated. Figures 4.86-4.87 show the PV and ES converter ZVS operating points for δ=30 degree.

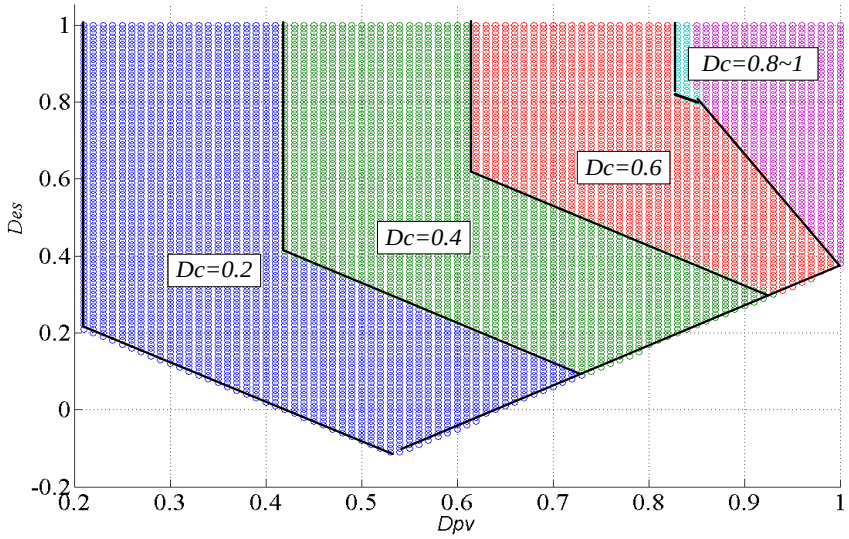

Figure 4.86. PV Converter ZVS Operating Points at δ=30 degree.

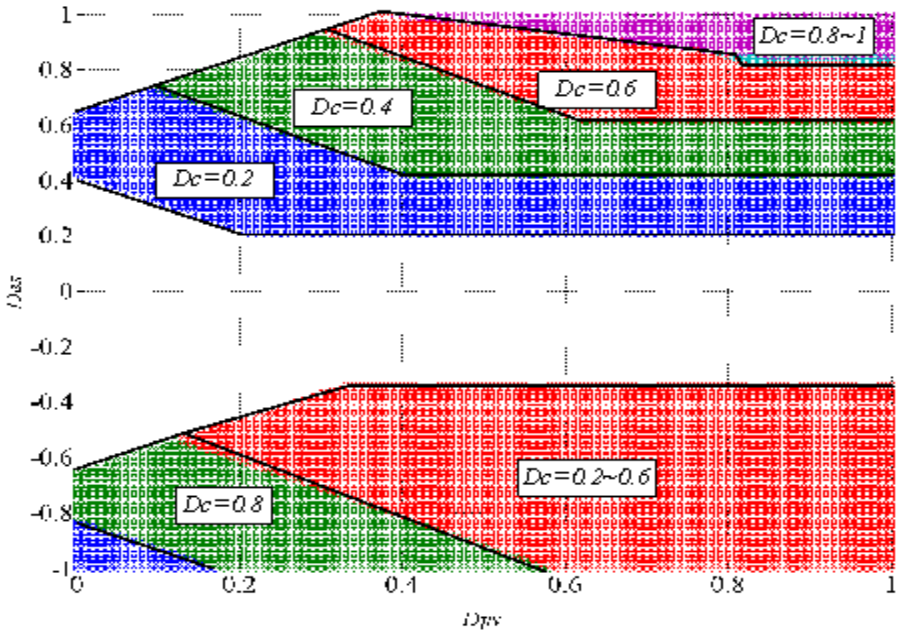

Figure 4.87. ES Converter ZVS Operating Points at δ=30 degree.

It can be observed that there are no overlapping ZVS operating points for δ=30 degree in the negative D_{es} region, which rules out the possibility of converter ZVS during ES charging.

However, the ES converter has considerably large ZVS operating points. Figures 4.88-4.89 show the ZVS operating points for δ=60 degree.

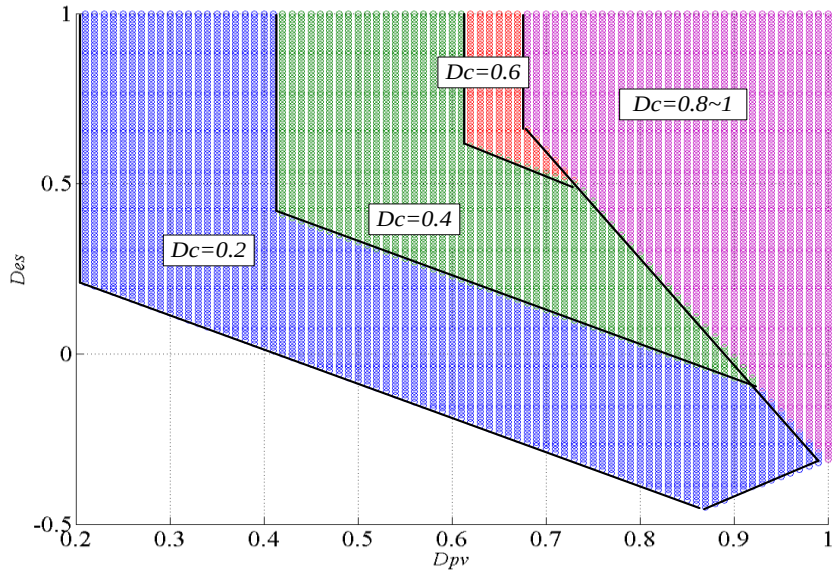

Figure 4.88. PV Converter ZVS Operating Points at δ=60 degree.

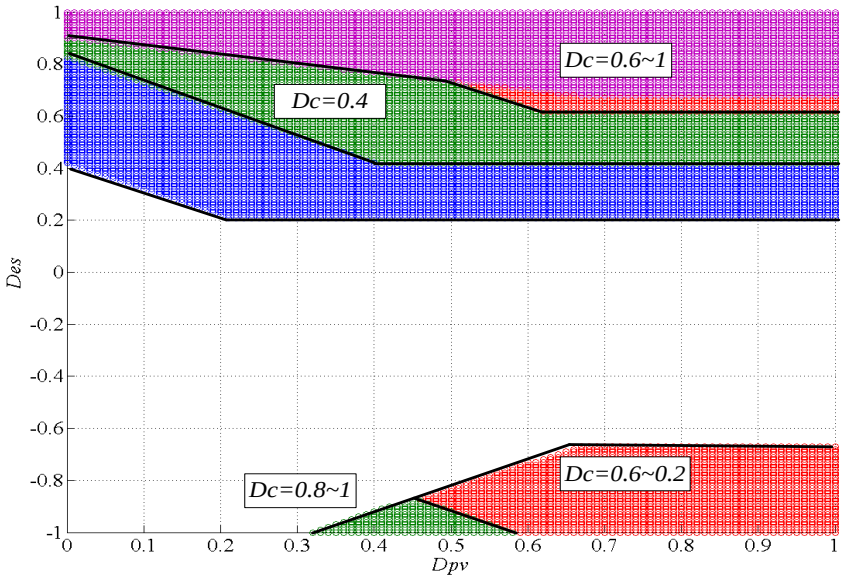

Figure 4.89. ES Converter ZVS Operating Points at δ=60 degree.

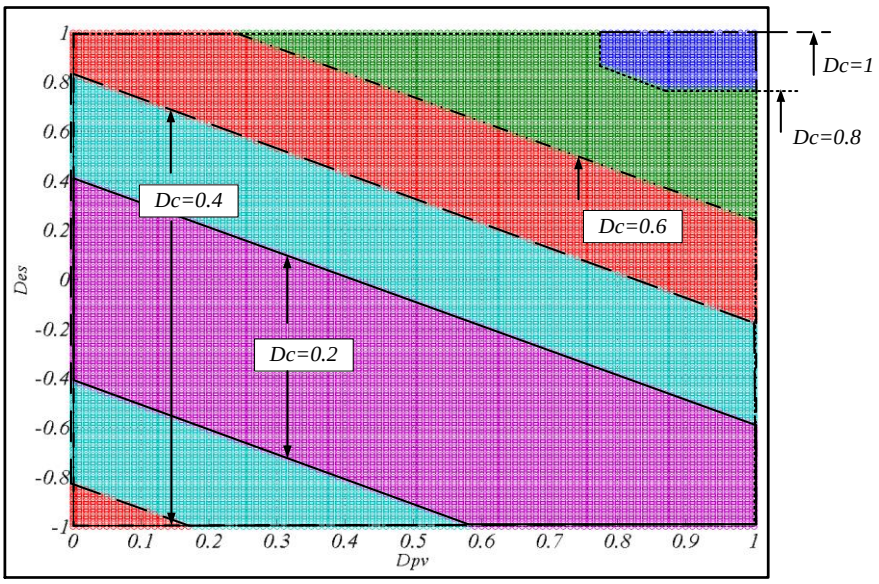

Figure 4.90. Middle Port Converter ZVS Operating Points at δ=30 degree.

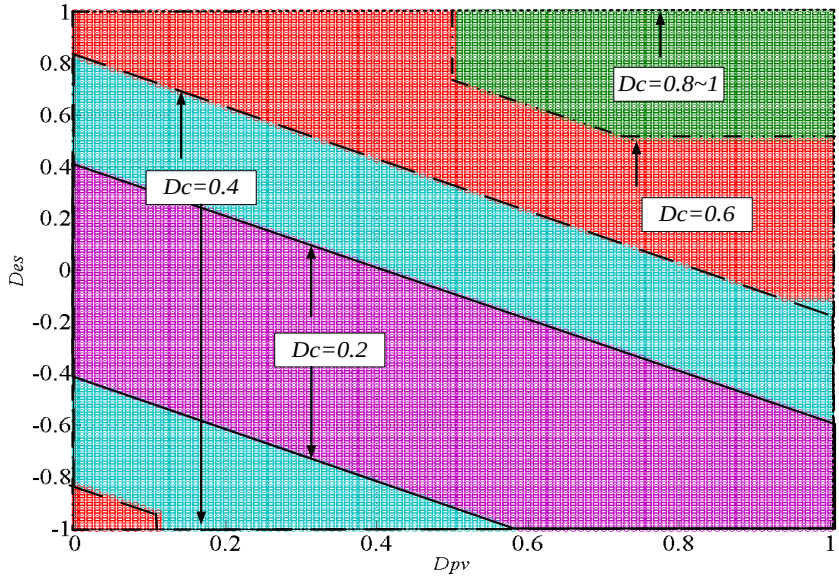

Figure 4.91. Middle Port Converter ZVS Operating Points at δ=60 degree.

Figures 4.90-4.91 show the middle port converter ZVS operating points, where it can be observed that for a particular phase angle, the ZVS region increases with increasing value of duty cycle D_c. Also, for higher phase shift angle, the ZVS range is higher for fixed duty cycle D_c.

4.10.2. ZVS Operating Point Ranges with Control Strategy 1 and 3

Using control strategy 1 for PV and ES delivering and using control strategy 3 for PV delivering and ES charging, figures 4.92 and 4.93 show the full converter ZVS operating points with the transformer type for δ=30 degree and δ=60 degree.

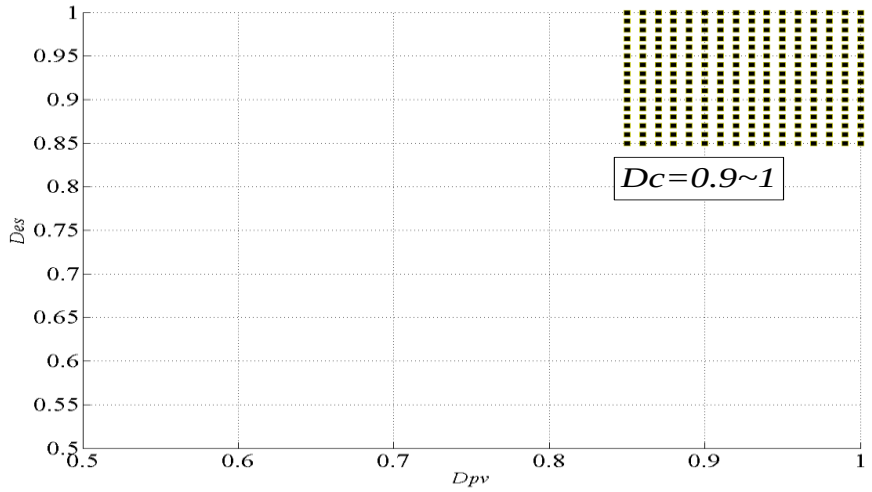

Figure 4.92. Full Converter ZVS Operating Points at δ=30 degree.

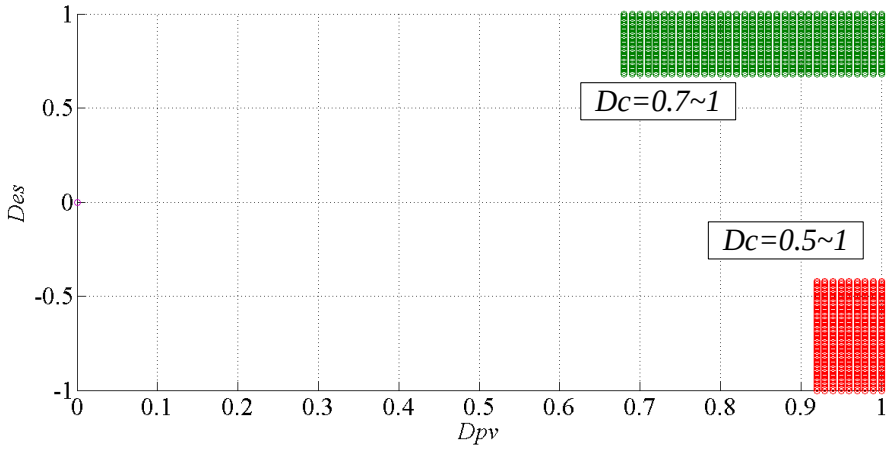

Figure 4.93. Full Converter ZVS Operating Points at δ=60 degree.

It can be observed from figures that for this control strategy of 1 and 3 that the full ZVS operating points include some ES charging portions for phase shift angle of 60 degree, which is not present for full ZVS operating points of control strategy 1 and 2. Also, using control strategy 3, a slightly greater range of ZVS operating points are obtained for the full converter system. The ZVS operating ranges for individual converter ports are analyzed and evaluated as shown below. Figures 4.94-4.95 show the PV converter ZVS operating regions for phase shift angles of 30 degree and 60 degree.

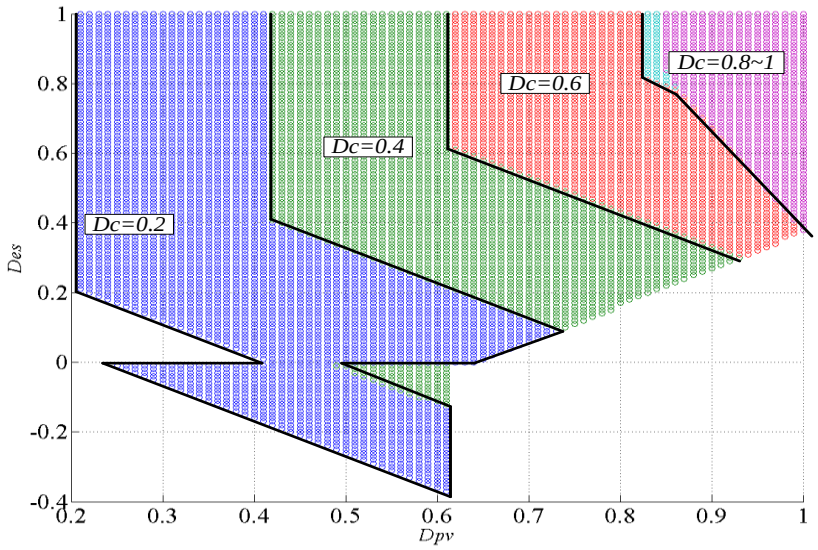

Figure 4.94. PV Converter ZVS Operating Points at δ=30 degree.

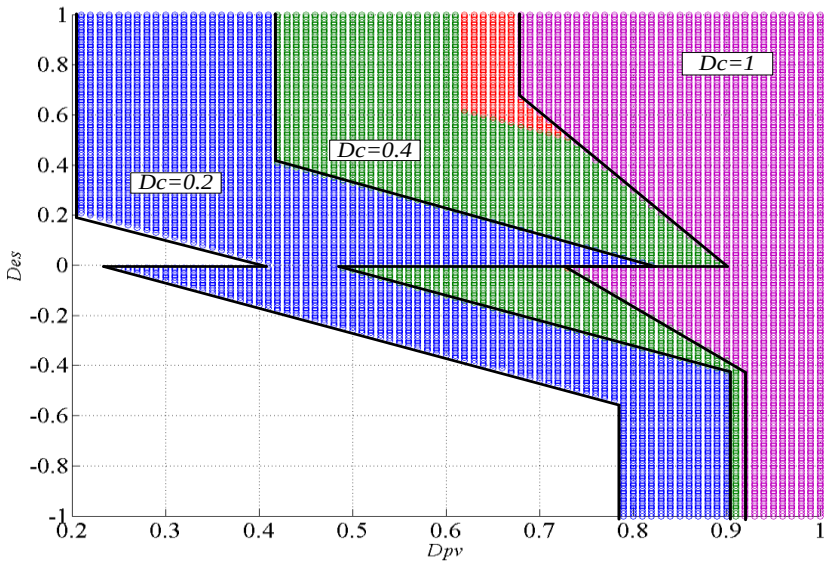

Figure 4.95. PV Converter ZVS Operating Points at δ=60 degree.

From the above figures, it can be observed that for both the transformers, the ZVS operating points vary with the three duty cycles, and ZVS operating points are higher for ES discharging scenarios compared to ES charging scenarios. The ZVS operating points for ES converter are shown in figures 4.96-4.97 for the two transformers for two different phase angles.

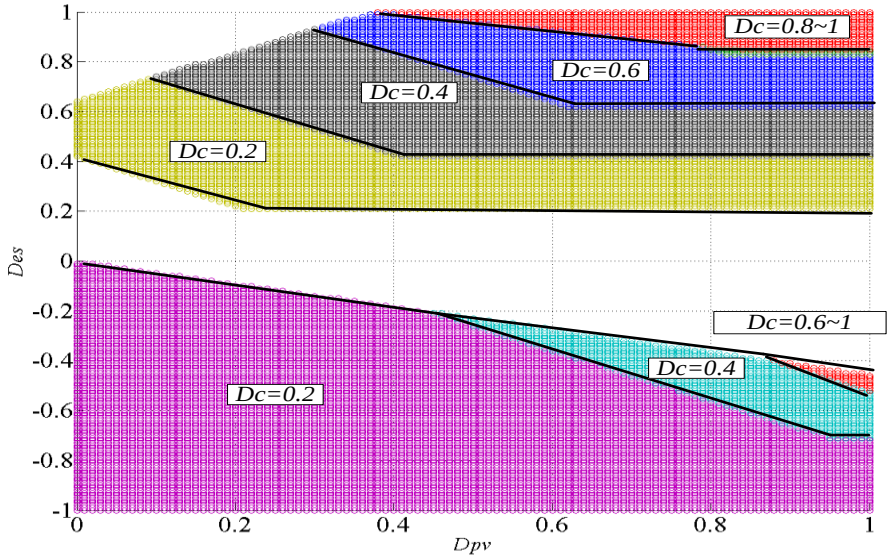

Figure 4.96. ES Converter ZVS Operating Points at δ=30 degree.

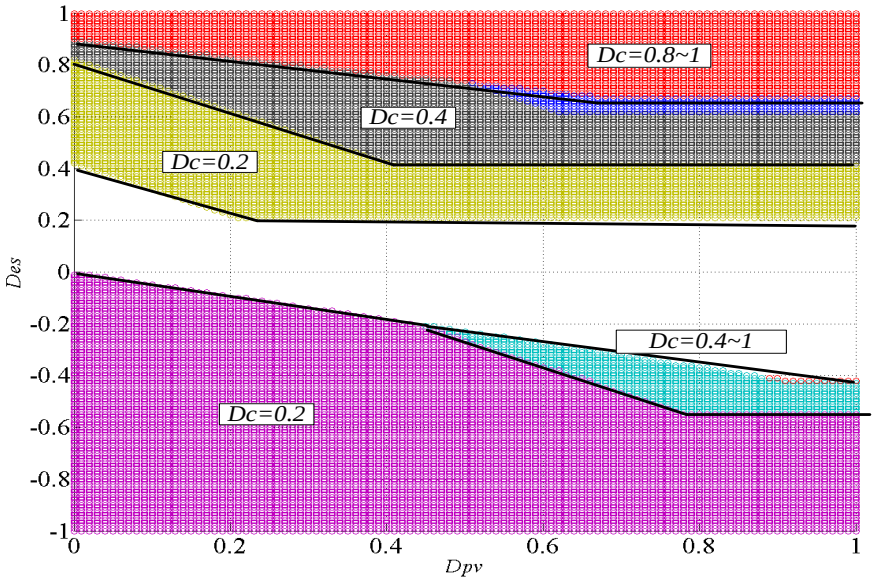

Figure 4.97. ES Converter ZVS Operating Points at δ=60 degree.

From the figures 4.96-4.97 for ZVS operating region of ES converter, it can be observed that ES converter has high ZVS operating points with both the transformers compared to control strategy 2. Figures 4.98-4.99 show the ZVS operating points for middle port converter using the two transformer design types for two different phase shift angles.

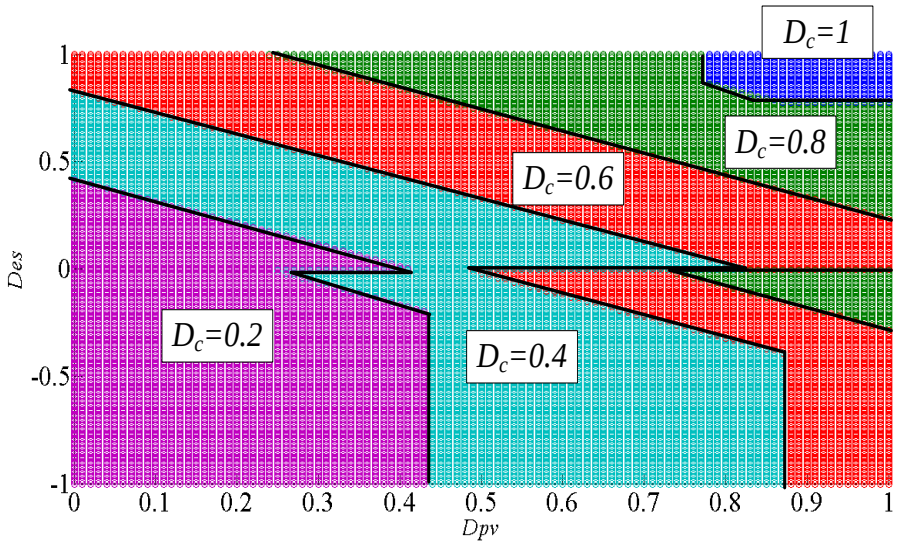

Figure 4.98. Middle Port Converter ZVS Operating Points at δ=30 degree.

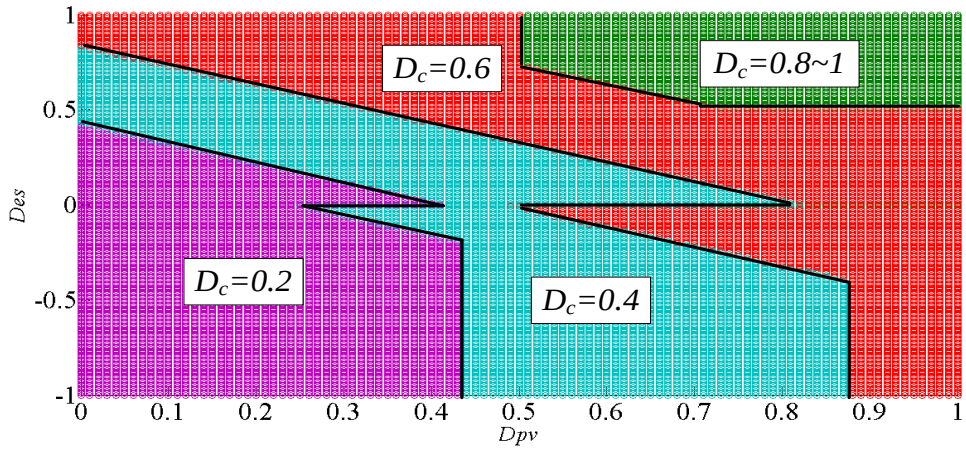

Figure 4.99. Middle Port Converter ZVS Operating Points at δ=60 degree.

The ZVS operating point plot for the two transformer types using control strategy 1 and 3, provides a wide range of operating points for different values of duty cycles. It can be inferred that using transformer type 1 provides a high range of ZVS operating points than using transformer type 2.

4.11. Experimental Study with Modulation Control of Three Port Converter

In order to verify the decoupled power control using modulation control, the dc current of source PV is controlled at a reference value and the dc current of source ES is controlled as well to control the power flowing into port 3. The ES port power controls the dc bus voltage of middle port at a fixed value. For experimental purpose, the input dc voltages for PV and ES are kept at 500V and the HV dc voltage is controlled at 1000V.

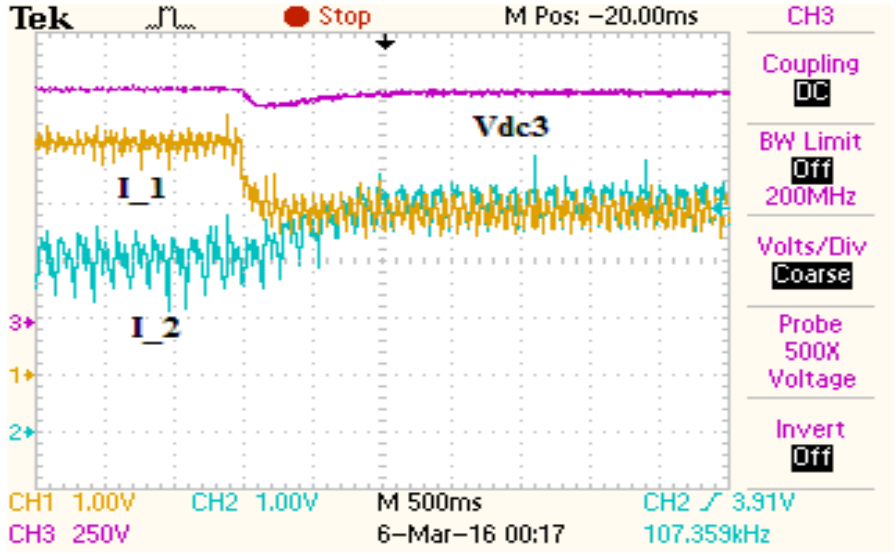

Figure 4.100. Closed Loop Power Control of Three Port Converter.

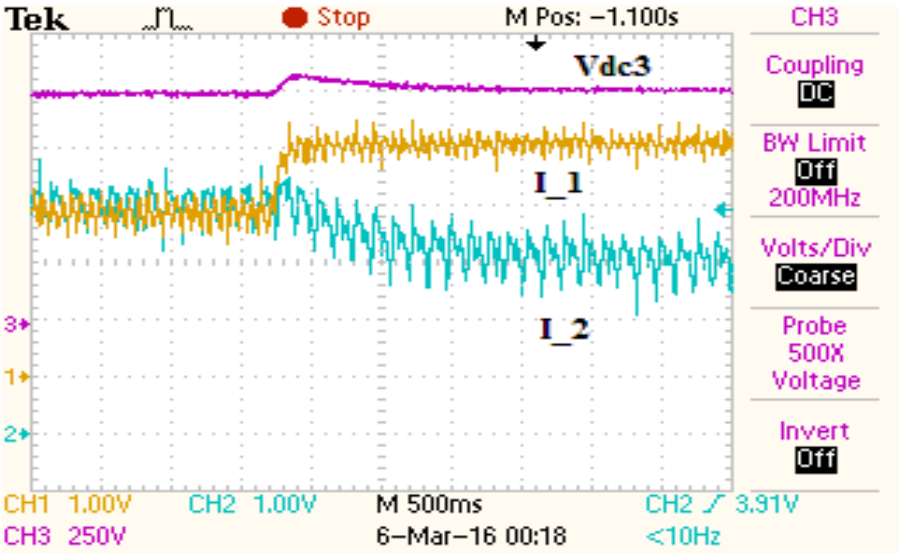

Figure 4.101. Closed Loop Power Control of Three Port Converter.

Figure 4.100 shows the scenario when I_1 changes from 10A to 7A due to change in I_1 reference current which is set through s DSP controller, the dc voltage V_{dc3} falls which initiates increase in current I_2 to feed in more power from ES to restore the dc voltage V_{dc3}. Similarly, figure 4.101 shows the scenario when current I_1 increases from 10A to 7A due to change in I_1 reference, resulting in increase in V_{dc3}, which initiates the current I_2 to fall to restore V_{dc3} to

1000V. Few cases of ZVS and loss of ZVS scenarios are shown below for three port converter using three limb three winding transformer with Modulation control in figures 4.102-4.104.

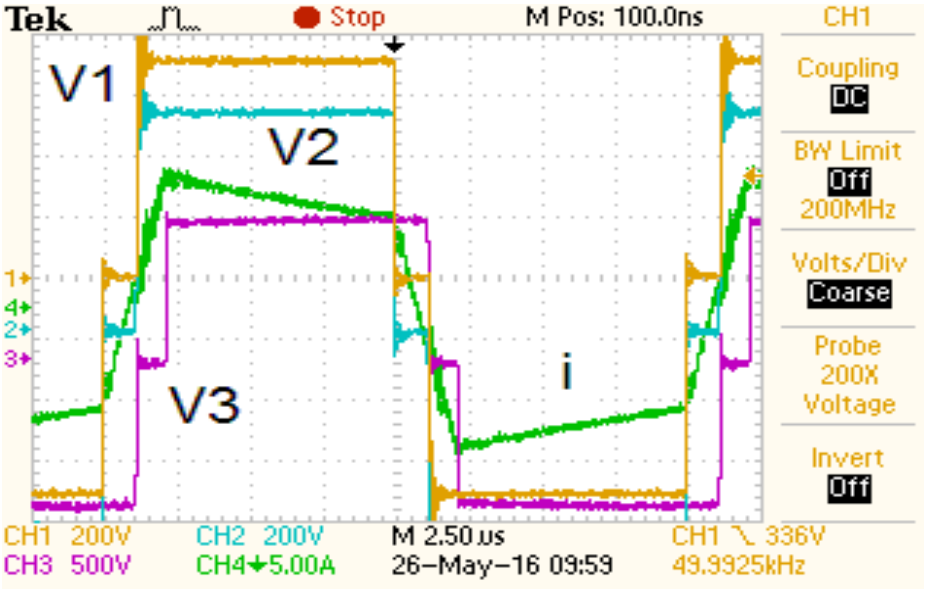

Figure 4.102. Winding Waveforms Using Control Strategy 1.

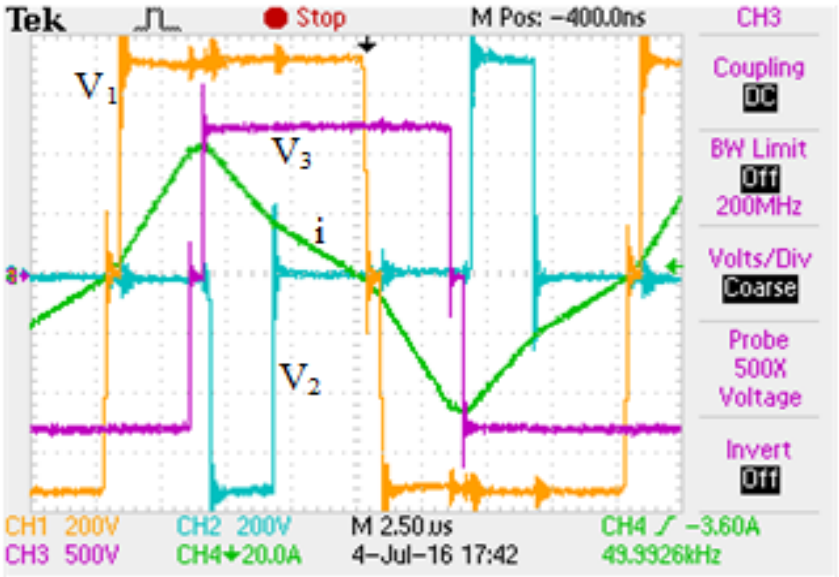

Figure 4.103. Winding Waveforms Using Control Strategy 2.

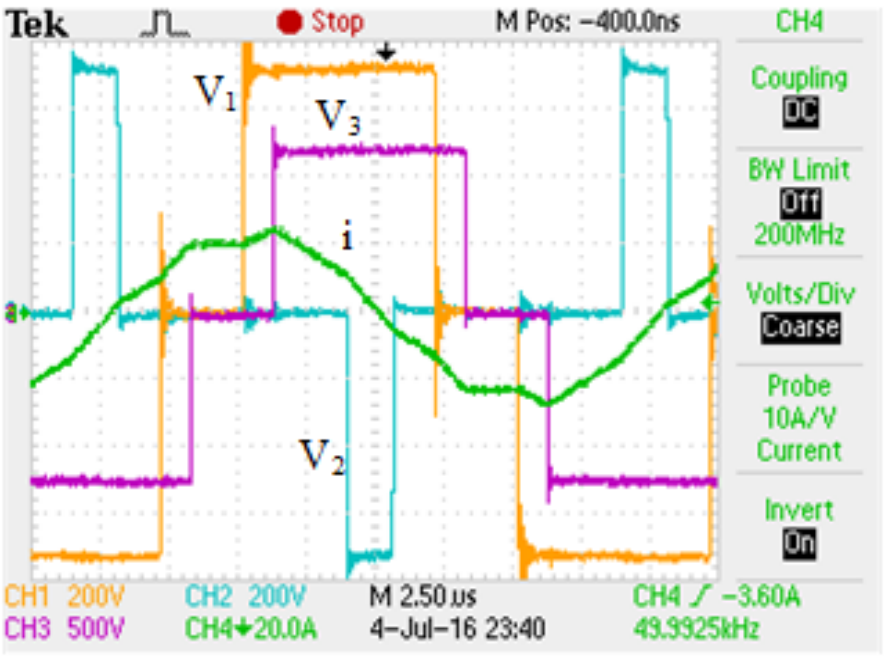

Figure 4.104. Winding Waveforms Using Control Strategy 3.

Using the modulation control, each of the three the converters undergo different ZVS and no-ZVS scenarios or partial ZVS scenarios, when one leg of the corresponding H-bridge has natural ZVS turn-on but the other switching leg has hard turn-on.

4.12. Conclusion

The phase shift control method provides a low ZVS operating range for the converters. Using three limb transformer provides a high ZVS range for middle port H-bridge but low ZVS region for PV and ES port bridges. The efficiency achieved with phase shift control is not very high for as compared to phase shifted converter. The one port idle condition thus provides a major drawback for the designer to use extra connecting/disconnecting switches for successful operation in ZVS. The modulation control method for three port dc-dc converter offers simpler control of power flow associated with each port, it has a varying natural ZVS operating region depending on

the chosen value of phase shift angle. Determining the optimum phase shift angle and modulation duty cycle while having ZVS for all the three converters is a quite complex process. The modulation control provides a partial ZVS turn-on scenario where one leg of a H-bridge gets ZVS but the other leg does not have natural turn-on ZVS. One major disadvantage with modulation control is the high reactive power flow for either PV or ES port at certain scenarios, which can be observed from the waveforms shown above.

Chapter 5. Three Limb Split-Winding Transformer

The three limb three winding type transformer as discussed in previous chapters, has few drawbacks as mentioned above while being operated for three port triple active bridge configuration. One of the major shortcomings is case of power flow among two ports during idle conditions, when the converter connected to one port is switched off and the dc link source is inactive. Secondly, the three limb three winding transformer while being operated as Dual Active Bridge converter has low ZVS operating points for all the converters, the H-bridges connected to PV and ES side has lower ZVS operating region, as discussed in above chapters. Loss of ZVS operating points at high switching frequency leads to lower efficiency. In order to overcome these shortcomings, a split-winding type three limb transformer is proposed in this chapter, using which the problems of open circuit condition and loss of ZVS operating points are overcome. In this transformer, the middle winding is kept same as in case of three limb three winding transformer while the PV and ES windings are split up into two sections each, which are put into two side limbs and are connected in series, as shown in figure 5.1. The transformer shown in figure 5.1 is re-arrangement of three limb three wnding transformer discussed in chapter 3 & 4, which provides significant advantages in terms of ZVS operation, one port idle operation, efficicency etc., which will be discussed in detail in this chapter. The split-winding transformer of figure 5.1 has equal core volume, core cross-section and copper requirement while comparing with three limb three winding transformer.

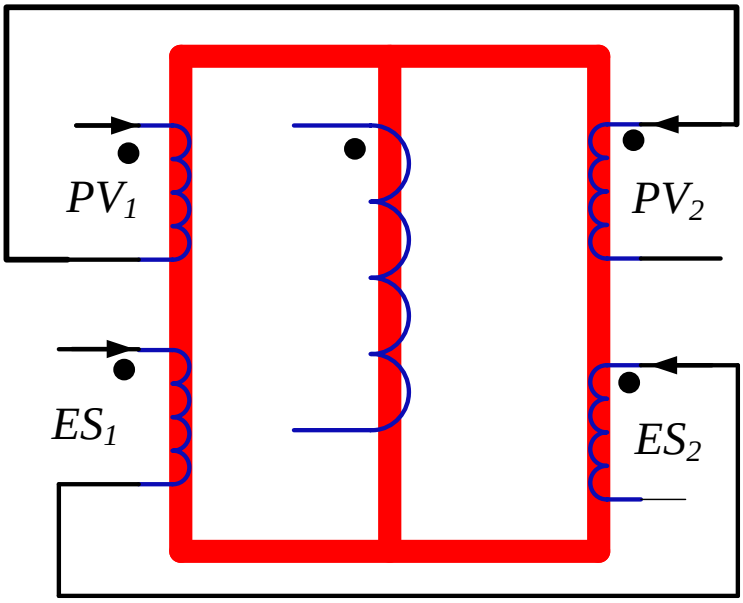

Figure 5.1. Schematic for Split-Winding Type Three Limb Transformer.

5.1. Magnetic Circuit and Equivalent Inductance Matrix Derivation

In order to analyze the effectiveness of split-winding type three limb transformer, it is essential to have a proper model derivation for magnetic circuit of the transformer. For power electronic circuit analysis, understanding of magnetic circuit s important in order to obtain a proper electrical circuit model. In order to analyze the magnetic circuit of split-winding type transformer, the leakage inductances are modeled as parallel flux paths through the air across the windings, windings are replaced by MMF sources and magnetic core is represented with reluctances or permeances. In figure 5.2, the MMF and permeance based magnetic circuit model for the split-winding type three limb transformer is shown. All the parameters related to side limbs are related by suffixes '*a*' and '*b*', the middle limb parameters are denoted by suffix '*c*'. Permeances of the two side limbs with the yoke portions are P_a and P_b and permeance of the middle limb is P_c. Each winding is replaced by an MMF source with a parallel leakage path. The

windings on the left hand side limb has two MMF sources F_{a1}, F_{a2} together with two parallel paths P_{La1}, P_{La2} for leakage fluxes ϕ_{La1} and ϕ_{La2}. The applied volt-seconds on each winding portion of left hand side limb is represented by ϕ_{a1} and ϕ_{a2}. The windings on the right hand side limb has two MMF sources F_{b1}, F_{b2} together with two parallel paths P_{Lb1}, P_{Lb2} for leakage fluxes ϕ_{Lb1} and ϕ_{Lb2}. The applied volt-seconds on each winding portion of left hand side limb is represented by ϕ_{b1} and ϕ_{b2}. The middle limb winding has a MMF source F_c with parallel path P_{Lc} for leakage flux ϕ_{Lc}. The applied volt-seconds on the middle limb winding is represented by ϕ_c. The fluxes that flow through the three limbs are represented by ϕ_{Ma}, ϕ_{Mb} and ϕ_{Mc}.

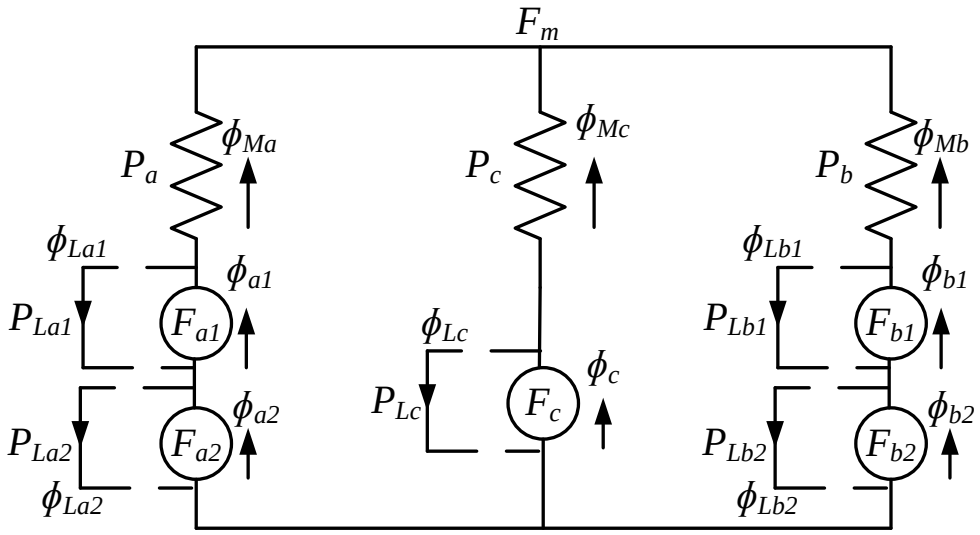

Figure 5.2. Magnetic Equivalent Circuit Model for Three Limb Transformer.

From the above figure 5.2 of three limb transformer, the sum of the instantaneous fluxes from the three limbs is zero, as given by equations (5.1) and (5.2). The expression for fictitious mmf F_m is given in equation (5.3).

$$\phi_{Ma} + \phi_{Mb} + \phi_{Mc} = 0 \qquad (5.1)$$

$$(F_{a1} + F_{a2} - F_m) * \mathrm{P}_a + (F_{b1} + F_{b2} - F_m) * \mathrm{P}_b + (F_c - F_m) * \mathrm{P}_c = 0 \qquad (5.2)$$

$$F_m = \frac{(F_{a1} + F_{a2}) * P_a + (F_{b1} + F_{b2}) * P_b + F_c P_c}{P_a + P_b + P_c} \qquad (5.3)$$

Now, ϕ_{M1}, ϕ_{M2} and ϕ_{M3} can be expressed in terms of MMFs F_1, F_2 and F_3 as given in equation 5.4-5.6.

$$\phi_{Ma} = (F_{a1} + F_{a2} - F_m)P_a \quad (5.4), \quad \phi_{Mb} = (F_{b1} + F_{b2} - F_m)P_b \quad (5.5),$$

$$\phi_{Mc} = (F_c - F_m)P_c \qquad (5.6)$$

Replacing F_m with (5.3), the three fluxes ϕ_{Ma}, ϕ_{Mb} and ϕ_{Mc} can be expressed as follows.

$$\begin{bmatrix} \phi_{Ma} \\ \phi_{Mb} \\ \phi_{Mc} \end{bmatrix} = \frac{1}{(P_a + P_b + P_c)} \begin{bmatrix} P_a(P_b + P_c) & P_a(P_b + P_c) & -P_a P_b & -P_a P_b & -P_a P_c \\ -P_a P_b & -P_a P_b & P_b(P_a + P_c) & P_b(P_a + P_c) & -P_b P_c \\ -P_c P_a & -P_c P_a & -P_c P_b & -P_c P_b & P_c(P_a + P_b) \end{bmatrix} \begin{bmatrix} F_{a1} \\ F_{a2} \\ F_{b1} \\ F_{b2} \\ F_c \end{bmatrix} \quad (5.7)$$

The fluxes ϕ_{Ma}, ϕ_{Mb} and ϕ_{Mc} can be related to the leakage fluxes as given in equations 5.8-5.10. The applied volt seconds for each winding can be expressed as functions of core flux and leakage fluxes, given in equations (5.8)-(5.10).

$$\phi_{Ma} = \phi_{a1} - \phi_{La1} = \phi_{a2} - \phi_{La2} \quad (5.8), \quad \phi_{Mb} = \phi_{b1} - \phi_{Lb1} = \phi_{b2} - \phi_{Lb2} \quad (5.9),$$

$$\phi_{Mc} = \phi_c - \phi_{Lc} \quad (5.10)$$

The leakage fluxes for all the windings can be related to their leakage flux path permeances P_{La1}, P_{La2}, P_{Lb1}, P_{Lb2} and P_{Lc} as given in equations (5.11)-(5.15). Using equations (5.11)-(5.15) in equations (5.4)-(5.6) changes the 3x5 matrix of equation (5.7) into a 5x5 matrix expression as shown in equation (5.16).

$$\phi_{La1} = P_{La1}F_{a1} \quad (5.11), \quad \phi_{La2} = P_{La2}F_{a2} \quad (6.12), \quad \phi_{Lb1} = P_{Lb1}F_{b1} \quad (5.13),$$

$$\phi_{Lb2} = P_{Lb2}F_{b2} \quad (5.14), \quad \phi_{Lc} = P_{Lc}F_{c} \quad (5.15),$$

$$\begin{bmatrix} \phi_{a1} \\ \phi_{a2} \\ \phi_{b1} \\ \phi_{b2} \\ \phi_{c} \end{bmatrix} = \frac{1}{(P_a + P_b + P_c)} \begin{bmatrix} P_a(P_b+P_c) & P_a(P_b+P_c) & -P_aP_b & -P_aP_b & -P_aP_c \\ P_a(P_b+P_c) & P_a(P_b+P_c) & -P_aP_b & -P_aP_b & -P_aP_c \\ -P_aP_b & -P_aP_b & P_b(P_a+P_c) & P_b(P_a+P_c) & -P_bP_c \\ -P_aP_b & -P_aP_b & P_b(P_a+P_c) & P_b(P_a+P_c) & -P_bP_c \\ -P_cP_a & -P_cP_a & -P_cP_b & -P_cP_b & P_c(P_a+P_b) \end{bmatrix} \begin{bmatrix} F_{a1} \\ F_{a2} \\ F_{b1} \\ F_{b2} \\ F_{c} \end{bmatrix}$$
$$+ \begin{bmatrix} P_{La1} & & & & \\ & P_{La2} & & & \\ & & P_{Lb1} & & \\ & & & P_{Lb2} & \\ & & & & P_{Lc} \end{bmatrix} \begin{bmatrix} F_{a1} \\ F_{a2} \\ F_{b1} \\ F_{b2} \\ F_{c} \end{bmatrix} \tag{5.16}$$

The fluxes ϕ_{a1}, ϕ_{a2}, ϕ_{b1}, ϕ_{b2} and ϕ_c are respective winding voltages' volt-seconds per turn. Expressing the fluxes in terms of volt-seconds and the mmf sources in terms of ampere-turns, equation (5.16) is expressed as shown in (5.17).

$$\begin{bmatrix} \frac{1}{N_{a1}}\int V_{a1}dt \\ \frac{1}{N_{a2}}\int V_{a2}dt \\ \frac{1}{N_{b1}}\int V_{b1}dt \\ \frac{1}{N_{b2}}\int V_{b2}dt \\ \frac{1}{N_{c}}\int V_{c}dt \end{bmatrix} = \frac{1}{(P_a + P_b + P_c)} \begin{bmatrix} P_a(P_b+P_c) & P_a(P_b+P_c) & -P_aP_b & -P_aP_b & -P_aP_c \\ P_a(P_b+P_c) & P_a(P_b+P_c) & -P_aP_b & -P_aP_b & -P_aP_c \\ -P_bP_a & -P_bP_a & P_b(P_a+P_c) & P_b(P_a+P_c) & -P_bP_c \\ -P_bP_a & -P_bP_a & P_b(P_a+P_c) & P_b(P_a+P_c) & -P_bP_c \\ -P_cP_a & -P_cP_a & -P_cP_b & -P_cP_b & P_c(P_a+P_b) \end{bmatrix} \begin{bmatrix} N_{a1}i_{a1}(t) \\ N_{a2}i_{a2}(t) \\ N_{b1}i_{b1}(t) \\ N_{b2}i_{b2}(t) \\ N_{c}i_{c}(t) \end{bmatrix} \tag{5.17}$$
$$+ \begin{bmatrix} P_{La1} & & & & \\ & P_{La2} & & & \\ & & P_{Lb1} & & \\ & & & P_{Lb2} & \\ & & & & P_{Lc} \end{bmatrix} \begin{bmatrix} N_{a1}i_{a1}(t) \\ N_{a2}i_{a2}(t) \\ N_{b1}i_{b1}(t) \\ N_{b2}i_{b2}(t) \\ N_{c}i_{c}(t) \end{bmatrix}$$

Differentiating the above equation w.r.t time parameter ‘t’, the winding voltage expressions are obtained as given in (5.18), which can be simplified into an inductance matrix form given in (6.19).

$$\begin{bmatrix} V_{a1} \\ V_{a2} \\ V_{b1} \\ V_{b2} \\ V_c \end{bmatrix} = \begin{bmatrix} \frac{N_{a1}^2 P_a(P_b+P_c)}{(P_a+P_b+P_c)} + N_{a1}^2 P_{La1} & \frac{N_{a1}N_{a2}P_a(P_b+P_c)}{(P_a+P_b+P_c)} & \frac{-N_{a1}N_{b1}P_aP_b}{(P_a+P_b+P_c)} & \frac{-N_{a1}N_{b2}P_aP_b}{(P_a+P_b+P_c)} & \frac{-N_{a1}N_cP_aP_c}{(P_a+P_b+P_c)} \\ \frac{N_{a2}N_{a1}P_a(P_b+P_c)}{(P_a+P_b+P_c)} & \frac{N_{a2}^2 P_a(P_b+P_c)}{(P_a+P_b+P_c)} + N_{a2}^2 P_{La2} & \frac{-N_{a2}N_{b1}P_aP_b}{(P_a+P_b+P_c)} & \frac{-N_{a2}N_{b2}P_aP_b}{(P_a+P_b+P_c)} & \frac{-N_{a2}N_cP_aP_c}{(P_a+P_b+P_c)} \\ \frac{-N_{b1}N_{a1}P_bP_a}{(P_a+P_b+P_c)} & \frac{-N_{b1}N_{a2}P_bP_a}{(P_a+P_b+P_c)} & \frac{N_{b1}^2 P_b(P_a+P_c)}{(P_a+P_b+P_c)} + N_{b1}^2 P_{Lb1} & \frac{N_{b1}N_{b2}P_b(P_a+P_c)}{(P_a+P_b+P_c)} & \frac{-N_{b1}N_cP_bP_c}{(P_a+P_b+P_c)} \\ \frac{-N_{b2}N_{a1}P_bP_a}{(P_a+P_b+P_c)} & \frac{-N_{b2}N_{a2}P_bP_a}{(P_a+P_b+P_c)} & \frac{N_{b2}N_{b1}P_b(P_a+P_c)}{(P_a+P_b+P_c)} & \frac{N_{b2}^2 P_b(P_a+P_c)}{(P_a+P_b+P_c)} + N_{b2}^2 P_{Lb2} & \frac{-N_{b2}N_cP_bP_c}{(P_a+P_b+P_c)} \\ \frac{-N_cN_{a1}P_aP_c}{(P_a+P_b+P_c)} & \frac{-N_cN_{a2}P_aP_c}{(P_a+P_b+P_c)} & \frac{-N_cN_{b1}P_bP_c}{(P_a+P_b+P_c)} & \frac{-N_cN_{b2}P_bP_c}{(P_a+P_b+P_c)} & \frac{N_c^2 P_c(P_a+P_b)}{(P_a+P_b+P_c)} + N_c^2 P_{Lc} \end{bmatrix} \frac{d}{dt} \begin{bmatrix} i_{a1}(t) \\ i_{a2}(t) \\ i_{b1}(t) \\ i_{b2}(t) \\ i_c(t) \end{bmatrix} \quad (5.18)$$

$$\begin{bmatrix} V_{a1} \\ V_{a2} \\ V_{b1} \\ V_{b2} \\ V_c \end{bmatrix} = \begin{bmatrix} L_{a1a1} & L_{a1a2} & -L_{a1b1} & -L_{a1b2} & -L_{a1c} \\ L_{a2a1} & L_{a2a2} & -L_{a2b1} & -L_{a2b2} & -L_{a2c} \\ -L_{b1a1} & -L_{b1a2} & L_{b1b1} & L_{b1b2} & -L_{a1c} \\ -L_{b2a1} & -L_{b2a2} & L_{b2b1} & L_{b2b2} & -L_{b2c} \\ -L_{ca1} & -L_{ca2} & -L_{cb1} & -L_{cb2} & L_{cc} \end{bmatrix} \begin{bmatrix} \frac{d}{dt} i_1(t) \\ \frac{d}{dt} i_2(t) \\ \frac{d}{dt} i_3(t) \end{bmatrix} \quad (5.19)$$

From equations (5.18), the individual leakage inductances can be expressed as given in 5.20-5.24.

$$L_{La1} = N_{a1}^2 P_{La1} = L_{a1a1} - (\frac{N_{a1}}{N_{a2}}) L_{a1a2} \quad (5.20) \qquad L_{La2} = N_{a2}^2 P_{La2} = L_{a2a2} - (\frac{N_{a2}}{N_{a1}}) L_{a2a1} \quad (5.21)$$

$$L_{Lb1} = N_{b1}^2 P_{Lb1} = L_{b1b1} - (\frac{N_{b1}}{N_{b2}}) L_{b1b2} \quad (5.22) \qquad L_{Lb2} = N_{b2}^2 P_{Lb2} = L_{b2b2} - (\frac{N_{b2}}{N_{b1}}) L_{b2b1} \quad (5.23)$$

$$L_{Lc} = N_c^2 P_{Lc} = L_{cc} - (\frac{N_c}{N_{a1}}) L_{ca1} - (\frac{N_c}{N_{b1}}) L_{cb1} = L_{cc} - (\frac{N_c}{N_{a2}}) L_{ca2} - (\frac{N_c}{N_{b2}}) L_{cb2} \quad (5.24)$$

5.2. Equivalent Electrical Circuit Derivation

The equivalent electrical circuit for split-winding type three limb transformer is derived in this section based on the magnetic circuit. The equivalent circuit of split-winding type transformer is similar to that discussed in chapter 3, with modifications for multiple windings. From figure 5.2, the magnetic circuit for three limb transformer provides the relation given in 5.18. The leakage fluxes of transformer windings are related to the winding currents and respective number of turns. The leakage fluxes ϕ_{La1}, ϕ_{La2}, ϕ_{Lb1}, ϕ_{Lb2} and ϕ_{Lc} can be written in terms of winding currents as given in (5.25)-(5.29).

$$\phi_{La1} = \frac{\lambda_{La1}}{N_{a1}} = \frac{L_{La1} I_{a1}}{N_{a1}} \quad (5.25), \quad \phi_{La2} = \frac{\lambda_{La2}}{N_{a2}} = \frac{L_{La2} I_{a2}}{N_{a2}} \quad (5.26), \quad \phi_{Lb1} = \frac{\lambda_{Lb1}}{N_{b1}} = \frac{L_{Lb1} I_{b1}}{N_{b1}} \quad (5.27)$$

$$\phi_{Lb2} = \frac{\lambda_{Lb2}}{N_{b2}} = \frac{L_{Lb2} I_{b2}}{N_{b2}} \quad (5.28), \quad \phi_{Lc} = \frac{\lambda_{Lc}}{N_{c}} = \frac{L_{Lc} I_{c}}{N_{c}} \quad (5.29)$$

The electrical equivalent circuit of three limb three winding transformer is series in nature as discussed in chapter 3, as the fluxes add up from the three limbs to give a series electrical equivalent circuit. Similarly, for the split-winding type transformer, the equation for the middle winding voltage can be written as given in equation (5.30).

$$\frac{1}{N_c}\left(V_c - L_c \frac{di_c(t)}{dt}\right) = \phi_c = \phi_{Ma} + \phi_{Mb} \quad (5.30)$$

For single core based three winding transformers, the electrical equivalent circuit is parallel in nature[56], since all the windings cut across the same mutual flux. For the side limbs of split-winding type transformer, same mutual flux is enclosed by the two windings. The windings on the side limbs of the split-winding transformer can be put in parallel to each other while the middle winding can be in series with two set of parallel windings from both the side limbs. The

voltage equations for the side limb fluxes are shown in equations (5.31) and (5.32). The resulting equivalent circuit is shown in figure 5.3. The magnetizing inductance of the transformer is referred to the middle limb winding, as in case of three limb three winding transformer. Neglecting the magnetizing current, the mmf equation for the split-winding type transformer is shown in equation (5.33).

$$\frac{1}{N_{a1}}(V_{a1} - L_{a1}\frac{di_{a1}(t)}{dt}) = \frac{1}{N_{a2}}(V_{a2} - L_{a2}\frac{di_{a2}(t)}{dt}) = \phi_{Ma} \quad (5.31)$$

$$\frac{1}{N_{b1}}(V_{b1} - L_{b1}\frac{di_{b1}(t)}{dt}) = \frac{1}{N_{b2}}(V_{b2} - L_{b2}\frac{di_{b2}(t)}{dt}) = \phi_{Mb} \quad (5.32)$$

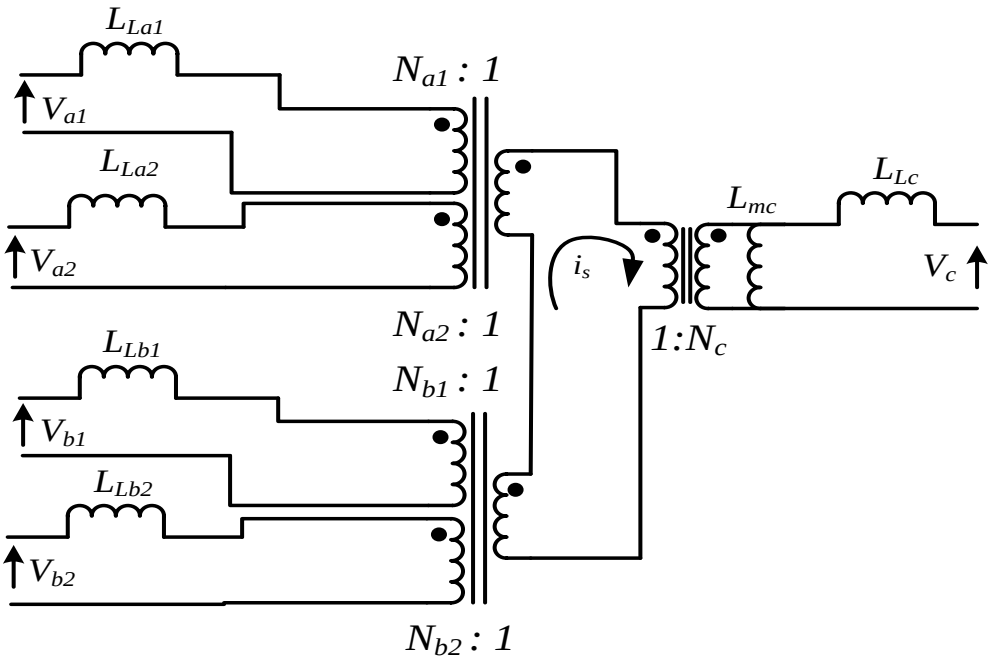

Figure 5.3. Electrical Equivalent Circuit for Split-Winding Transformer.

$$N_{a1}i_{a1} + N_{a2}i_{a2} = N_{b1}i_{b1} + N_{b2}i_{b2} = N_c i_c = i_s \quad (5.33)$$

5.3. PV and ES integration with Split Winding Type Three Limb Transformer

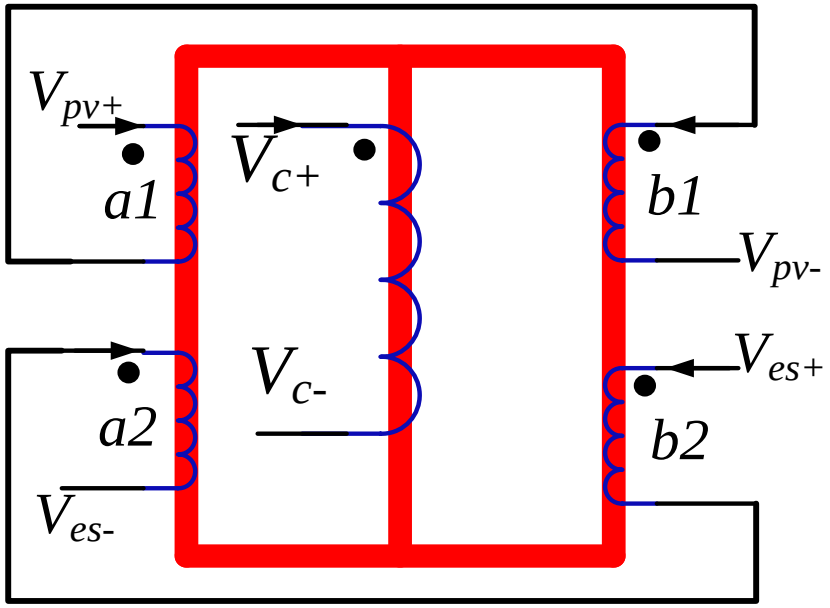

Figure 5.4. PV and ES Connection for Split-Winding Transformer.

The split-winding type transformer discussed above is analyzed in this section for PV and Energy Storage(ES) integration. In order to use the split winding type transformer for PV and ES integration for a three port application, one winding from each of the two side limbs are selected and are connected in series. The connection diagram for split winding type transformer is shown in figure 5.4 and the equivalent electrical circuit is shown in figure 5.5. The sections a1 and b1 are connected in series with opposite polarity terminals being joined, so that the voltages of the series connected windings, get added. In a similar way, sections a2 and b2 are joined together in series. Figure 5.4 shows the connection diagram for equivalent electrical circuit. For PV and ES integration using split-winding type configuration, it is convenient to split the PV and ES into two identical windings on two side limbs, i.e. the side limb winding sections have equal number of turns, winding height. Also, cross section of the two side limb sections are considered to be equal.

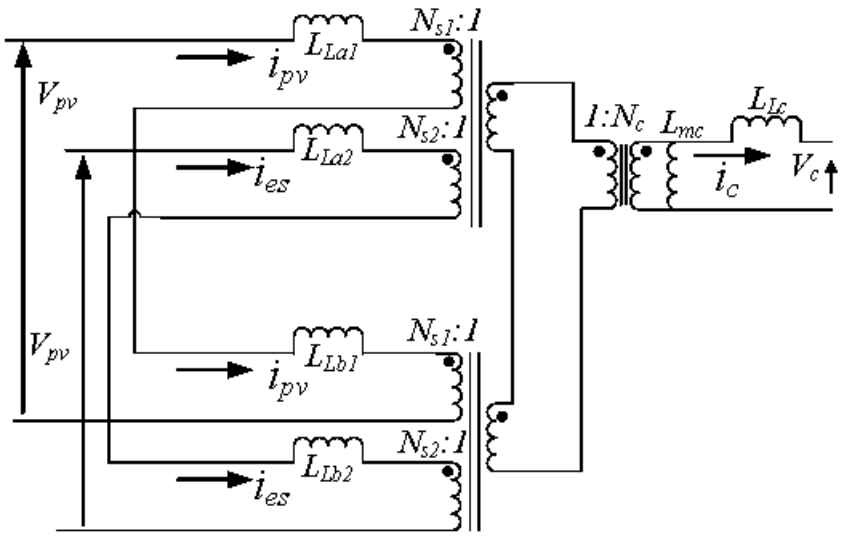

Figure 5.5. PV and ES Connection with Electrical Equivalent Circuit.

From the above two figures of split winding transformer configuration for PV and ES integration, the equation (5.19) needs to be modified to reflect three winding voltages and currents. An assumption is made that both the PV and ES windings are each split into two equal halves on the two side limbs. The two equal halves for PV and ES have equal number of turns and also the geometric dimensions of the two side limbs are same. Hence, $N_{a1}=N_{b1}=N_{s1}$, $N_{a2}=N_{b2}=N_{s2}$ and $P_a=P_b=P_s$ and $P_c=P_m$. For the PV and ES integration, $V_{pv} = V_{a1} + V_{b1}$, $V_{es} = V_{a2} + V_{b2}$, $i_{a1} = i_{b1} = i_{pv}$, $i_{a2} = i_{b2} = i_{es}$. Replacing the parameters of equation (5.19) with these values provides the equation (5.34), which can be written as shown in equation (5.35).

$$\begin{bmatrix} V_{pv} \\ V_{es} \\ V_c \end{bmatrix} = \begin{bmatrix} \frac{2N_{s1}^{\,2}P_sP_c}{2P_s+P_c} + N_{s1}^{\,2}(P_{La1}+P_{Lb1}) & \frac{2N_{s1}N_{s2}P_sP_c}{2P_s+P_c} & \frac{-2N_{s1}N_cP_sP_c}{2P_s+P_c} \\ \frac{2N_{s1}N_{s2}P_sP_c}{2P_s+P_c} & \frac{2N_{s2}^{\,2}P_sP_c}{2P_s+P_c} + N_{s2}^{\,2}(P_{La2}+P_{Lb2}) & \frac{-2N_{s2}N_cP_sP_c}{2P_s+P_c} \\ \frac{-2N_{s1}N_cP_sP_c}{2P_s+P_c} & \frac{-2N_{s2}N_cP_sP_c}{2P_s+P_c} & \frac{2N_c^{\,2}P_sP_c}{2P_s+P_c} + N_c^{\,2}P_{Lc} \end{bmatrix} \frac{d}{dt}\begin{bmatrix} i_{pv}(t) \\ i_{es}(t) \\ i_c(t) \end{bmatrix} \quad (5.34)$$

$$\begin{bmatrix} V_{pv} \\ V_{es} \\ V_c \end{bmatrix} = \begin{bmatrix} L_{pvpv} & L_{pves} & -L_{cpv} \\ L_{pves} & L_{eses} & -L_{ces} \\ -L_{cpv} & -L_{ces} & L_{cc} \end{bmatrix} \frac{d}{dt} \begin{bmatrix} i_{pv}(t) \\ i_{es}(t) \\ i_c(t) \end{bmatrix} \quad (5.35)$$

From figure 5.5, the two winding sections of PV and ES ports are connected in series, hence for equally split windings, PV and ES voltages are divided equally across the two windings, hence the reflected voltages, as seen from the middle winding are given as $2*0.5*(N_c/N_{s1})*V_{pv}$ and $2*0.5*(N_c/N_{s2})*V_{es}$. Hence, the reflected voltages for PV and ES ports are multiplied by ratio equal to number of turns on middle winding to number of turns on any one section of split windings. The equivalent circuit can thus be reduced to a more simple form as shown in figure 5.6.

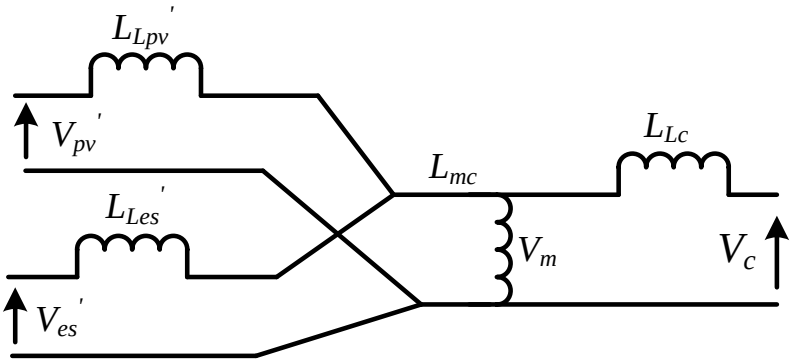

Figure 5.6. Reduced order Electrical Equivalent Circuit.

In figure 5.6, all parameters are referred to the middle limb winding, the parameters are listed out below.

$$L_{Lpv}' = (\frac{N_c}{N_{s1}})^2 (L_{La1} + L_{Lb1}) \quad (5.36), \qquad L_{Les}' = (\frac{N_c}{N_{s2}})^2 (L_{La2} + L_{Lb2}) \quad (5.37)$$

$$V_{pv}' = (\frac{N_c}{N_{s1}})V_{pv} \quad (5.38), \qquad V_{es}' = (\frac{N_c}{N_{s2}})V_{es} \quad (5.39)$$

5.4. Triple Active Bridge Operation with Split Winding Type Three Limb Transformer

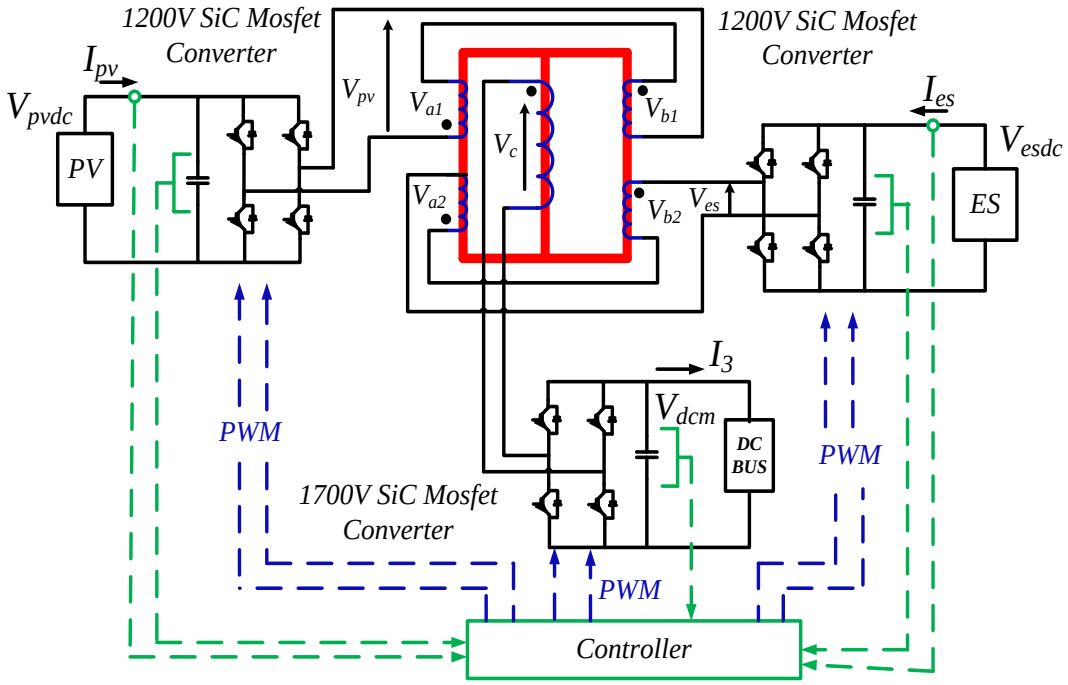

Figure 5.7. Triple Active Bridge Converter Using Split-Winding Transformer.

The three port split-winding transformer is the transformer for three port dc-dc converter or triple active bridge converter as shown in figure 5.7. The power flow expression for triple active bridge converter or three port DAB converter can be derived from the reduced order equivalent circuit of figure 5.6. Neglecting the magnetizing inductance, the power flow equation for such a star network modeled three port transformer has been derived in [56], where the star connected model is transformed to delta model as shown in figures 5.8-5.9 and the power flow equation

between any two ports is derived. Conversion of leakages from star to delta model are given in equation (5.40)-(5.42).

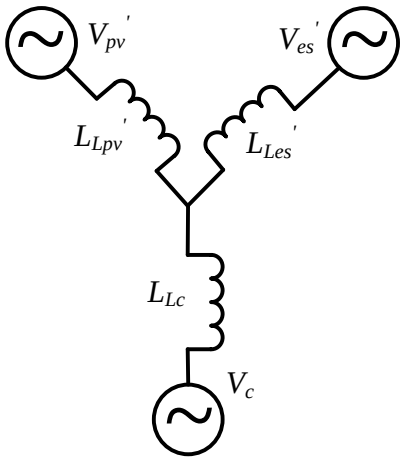

Figure 5.8. Star Network Model

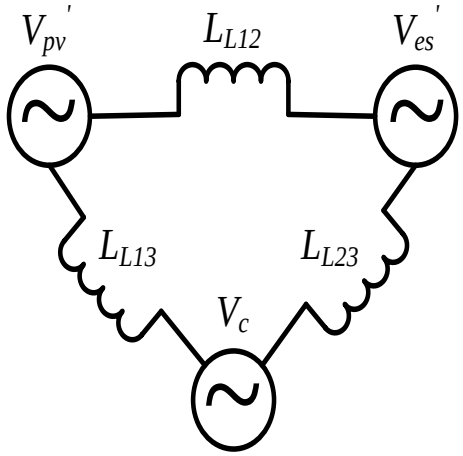

Figure 5.9. Delta Network Model

$$L_{L12} = L_{Lpv}' + L_{Les}' + \frac{L_{Lpv}' L_{Les}'}{L_{Lc}} \quad (5.40) \qquad L_{L13} = L_{Lpv}' + L_{Lc} + \frac{L_{Lpv}' L_{Lc}}{L_{Les}'} \quad (5.41)$$

$$L_{L23} = L_{Les}' + L_{Lc} + \frac{L_{Les}' L_{Lc}}{L_{Lpv}'} \quad (5.42)$$

In this discussion, V_c is considered as the reference voltage and V_{pv} and V_{es} are shifted by angles ϕ_{pv} and ϕ_{es}. Considering 50% duty cycle switching for all the three winding voltages, i.e. 180 degree on-time for each switching device, the power flow between any two ports are expressed as follows in (5.43)-(5.45). Individual power flow associated with each port is obtained by algebraically summing up the power coming and going out of each port. The power flowing out of PV and ES ports and going into middle port are given in (5.46)-(5.48).

$$P_{PV-ES} = \frac{(\frac{N_c}{N_{s1}})(\frac{N_c}{N_{s2}})V_{pvdc}V_{esdc}(\phi_{pv}-\phi_{es})(\pi-|\phi_{pv}-\phi_{es}|)}{\pi\omega L_{12}} \quad (5.43)$$

$$P_{PV-middle} = \frac{(\frac{N_c}{N_{s1}})V_{pvdc}V_{dcm}\phi_{pv}(\pi-|\phi_{pv}|)}{\pi\omega L_{13}} \quad (5.44), \quad P_{ES-middle} = \frac{(\frac{N_c}{N_{s2}})V_{esdc}V_{dcm}\phi_{es}(\pi-|\phi_{es}|)}{\pi\omega L_{23}} \quad (5.45)$$

$$P_{PV} = \frac{(\frac{N_c}{N_{s1}})V_{pvdc}V_{dcm}\phi_{pv}(\pi-|\phi_{pv}|)L_{12}+(\frac{N_c}{N_{s1}})(\frac{N_c}{N_{s2}})V_{pvdc}V_{esdc}(\phi_{pv}-\phi_{es})(\pi-|\phi_{pv}-\phi_{es}|)L_{13}}{\pi\omega L_{13}L_{12}} \quad (5.46)$$

$$P_{ES} = \frac{(\frac{N_c}{N_{s2}})V_{esdc}V_{dcm}\phi_{es}(\pi-|\phi_{es}|)L_{12}-(\frac{N_c}{N_{s1}})(\frac{N_c}{N_{s2}})V_{pvdc}V_{esdc}(\phi_{pv}-\phi_{es})(\pi-|\phi_{pv}-\phi_{es}|)L_{23}}{\pi\omega L_{23}L_{12}} \quad (5.47)$$

$$P_{middle} = \frac{(\frac{N_c}{N_{s1}})V_{pvdc}V_{dcm}\phi_{pv}(\pi-|\phi_{pv}|)L_{23}+(\frac{N_c}{N_{s2}})V_{esdc}V_{dcm}\phi_{es}(\pi-|\phi_{es}|)L_{13}}{\pi\omega L_{23}L_{13}} \quad (5.48)$$

In case of a non-ideal transformer, the magnetizing inductance may not be too high to neglect due to presence of intended air-gaps to prevent core-saturation, the magnetizing inductance effects need to be considered for power flow calculation. From the figure 5.6, the voltage induced across the magnetizing inductance L_{mc} is given as shown in (5.49).

$$V_m = \frac{(V_{pv}'L_{Les}'L_{Lc}+V_{es}'L_{Lpv}'L_{Lc}+V_cL_{Lpv}'L_{Les}')L_{mc}}{L_n^{\,3}} \quad (5.49),$$

where $L_n^{\,3} = L_{Lpv}'L_{Les}'L_{Lc}+L_{Lpv}'L_{Les}'L_{mc}+L_{Lpv}'L_{Lc}L_{mc}+L_{Les}'L_{Lc}L_{mc}$

The average current from each winding is given as shown in equations (5.50)-(5.52)

$$i_{pv(avg)} = \frac{1}{\pi\omega L_{Lpv}}\int_0^{\pi}(V_{pv}-(\frac{N_{s1}}{N_c})V_m)d\theta \quad (5.50), \quad i_{es(avg)} = \frac{1}{\pi\omega L_{Les}}\int_0^{\pi}(V_{es}-(\frac{N_{s2}}{N_c})V_m)d\theta \quad (5.51),$$

$$i_{c(avg)} = \frac{1}{\pi\omega L_{Lc}} \int_0^{\pi} (V_m - V_c) d\theta \quad (5.52)$$

Considering 50% duty cycle switching for all the three winding voltages, i.e. 180 degree on-time for each switching device, the average winding voltages for the three winding voltages are equal to their dc link voltage. Average power flow associated to each port is given by multiplication of average port voltage and average current, which are expressed in (5.53)-(5.57).

$$P_{PV} = \frac{V_{pvdc}' V_{dcm} \phi_{pv} (\pi - |\phi_{pv}|) L_{Les}' L_{mc} + V_{pvdc}' V_{esdc}' (\phi_{pv} - \phi_{es})(\pi - |\phi_{pv} - \phi_{es}|) L_{Lc} L_{mc}}{\pi\omega L_n^{\,3}} \quad (5.53)$$

$$P_{ES} = \frac{V_{esdc}' V_{dcm} \phi_{es} (\pi - |\phi_{es}|) L_{Lpv}' L_{mc} - V_{pvdc}' V_{esdc}' (\phi_{pv} - \phi_{es})(\pi - |\phi_{pv} - \phi_{es}|) L_{Lc} L_{mc}}{\pi\omega L_n^{\,3}} \quad (5.54)$$

$$P_{middle} = \frac{V_{pvdc}' V_{dcm} \phi_{pv} (\pi - |\phi_{pv}|) L_{Les}' L_{mc} + V_{esdc}' V_{dcm} \phi_{es} (\pi - |\phi_{es}|) L_{Lpv}' L_{mc}}{\pi\omega L_n^{\,3}} \quad (5.55)$$

where $V_{pvdc}' = (\frac{N_c}{N_{s1}}) V_{pvdc}$ (5.56), $V_{esdc}' = (\frac{N_c}{N_{s2}}) V_{esdc}$ (5.57)

In a PV and ES integrated three port phase-shifted dc-dc converter, the PV always acts as power source or remains idle, while ES port and third port, which if connected to grid, can act both as a source and sink. Considering this set of power flow scenarios, the winding voltages' positions for different possible cases are shown in figures (5.10)-(5.12).

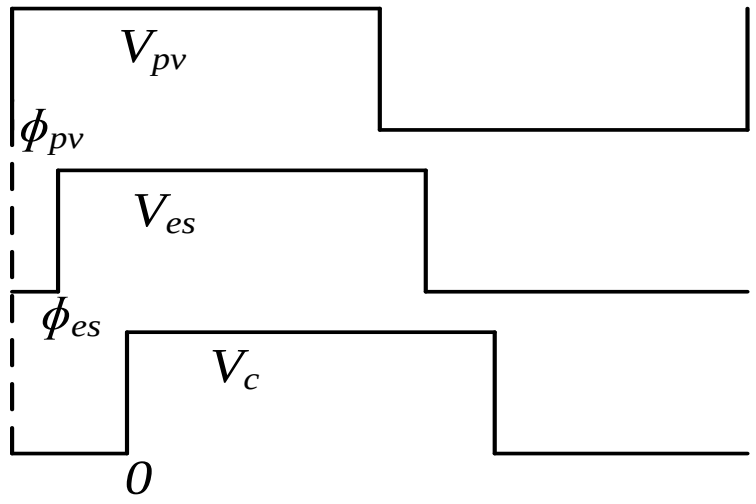

Figure 5.10. V_{PV}, V_{ES} are leading V_C and V_{PV} leading V_{ES}.

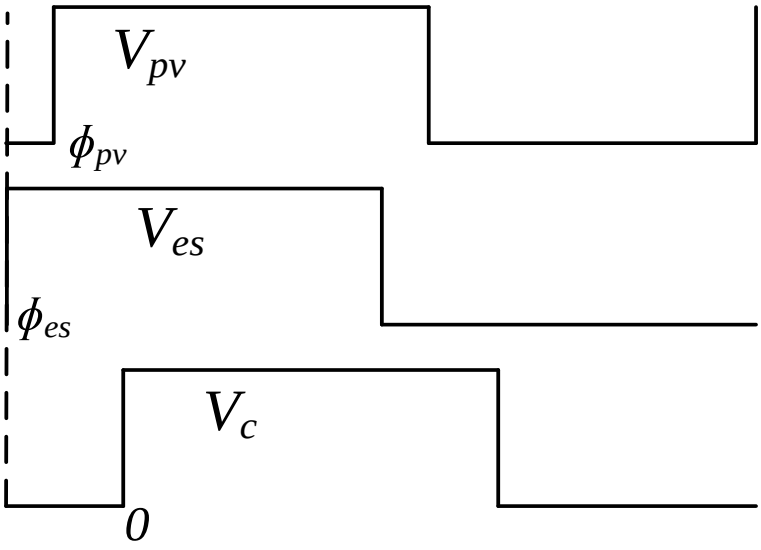

Figure 5.11. V_{PV}, V_{ES} are leading V_C and V_{PV} lagging V_{ES}.

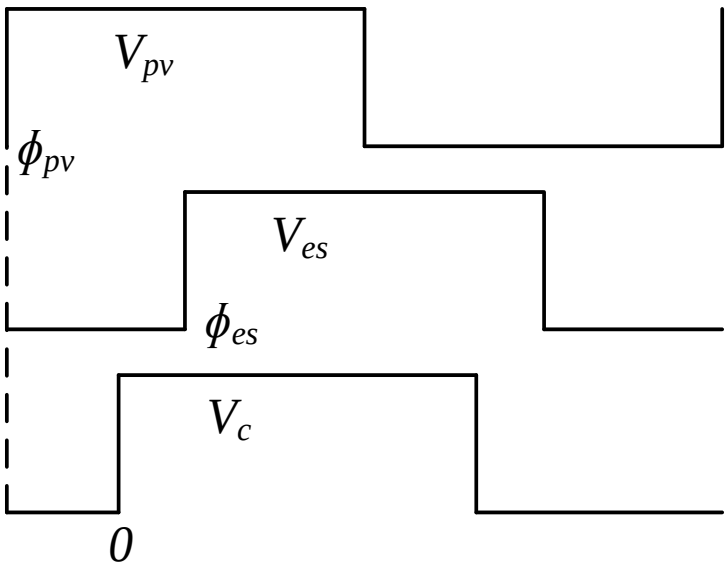

Figure 5.12. V_{PV}, V_C are leading V_{ES} and V_{PV} leading V_C .

The transformer winding voltages and the phase shifts together with the leakage inductances define the winding currents and the ZVS scenarios. Equations (5.76)-(5.84) show the three winding currents' values during the instants ϕ_1, ϕ_2 and 0.

$$r_{12} = \frac{N_{s1}}{N_{s2}} \text{ (5.58)}, \; r_{13} = \frac{N_{s1}}{N_c} \text{ (5.59)}, \; r_{21} = \frac{N_{s2}}{N_{s1}} \text{ (5.60)},$$

$$r_{23} = \frac{N_{s2}}{N_c} \text{ (5.61)}, \; r_{31} = \frac{N_c}{N_{s1}} \text{ (5.62)}, \; r_{32} = \frac{N_c}{N_{s2}} \text{ (5.63)}$$

$$L_{L31} = r_{31}{}^2 L_{Lpv} \text{ (5.64)}, \; L_{L32} = r_{32}{}^2 L_{Les} \text{ (5.65)}, \; L_{L21} = r_{21}{}^2 L_{Lpv} \text{ (5.66)}, \; L_{L23} = r_{23}{}^2 L_{Lc} \text{ (5.67)},$$

$$L_{L12} = r_{12}{}^2 L_{Les} \text{ (5.68)}, L_{L13} = r_{13}{}^2 L_{Lc} \text{ (5.69)}, L_{m1} = r_{13}{}^2 L_{mc} \text{ (5.70)}, L_{m2} = r_{23}{}^2 L_{mc} \text{ (5.71)},$$

$$L_{m3} = L_{mc} \text{ (5.72)}, \; L_{n1}{}^3 = r_{13}{}^3 L_n{}^3 \text{ (5.73)}, \; L_{n2}{}^3 = r_{23}{}^3 L_n{}^3 \text{ (5.74)}, \; L_{n3}{}^3 = L_n{}^3 \text{ (5.75)}$$

$$i_{pv}(\phi_{pv}) = \frac{-V_{pvdc}(L_{12}L_{13} + L_{12}L_{m1} + L_{13}L_{m1})\pi + r_{12}V_{esdc}L_{13}L_{m1}(\pi - 2|\phi_{pv} - \phi_{es}|) + r_{13}V_{dcm}L_{12}L_{m1}(\pi - 2|\phi_{pv}|)}{2\omega L_{n1}{}^3} \text{ (5.76)}$$

$$i_{pv}(\phi_{es}) = \frac{-V_{pvdc}(L_{12}L_{13} + L_{12}L_{m1} + L_{13}L_{m1})(\pi - 2|\phi_{pv} - \phi_{es}|) + r_{12}V_{esdc}L_{13}L_{m1}\pi + r_{13}V_{dcm}L_{12}L_{m1}(\pi - 2|\phi_{es}|)}{2\omega L_{n1}{}^3} \quad (5.77)$$

$$i_{pv}(0) = \frac{-V_{pvdc}(L_{12}L_{13} + L_{12}L_{m1} + L_{13}L_{m1})(\pi - 2|\phi_{pv}|) + r_{12}V_{esdc}L_{13}L_{m1}(\pi - 2|\phi_{es}|) + r_{13}V_{dcm}L_{12}L_{m1}\pi}{2\omega L_{n1}{}^3} \quad (5.78)$$

$$i_{es}(\phi_{pv}) = \frac{-V_{esdc}(L_{21}L_{23} + L_{21}L_{m2} + L_{23}L_{m2})(\pi - 2|\phi_{pv} - \phi_{es}|) + r_{21}V_{pvdc}L_{23}L_{m2}\pi + r_{23}V_{dcm}L_{21}L_{m2}(\pi - 2|\phi_{pv}|)}{2\omega L_{n2}{}^3} \quad (5.79)$$

$$i_{es}(\phi_{es}) = \frac{-V_{esdc}(L_{21}L_{23} + L_{21}L_{m2} + L_{23}L_{m2})\pi + r_{21}V_{pvdc}L_{23}L_{m2}(\pi - 2|\phi_{pv} - \phi_{es}|) + r_{23}V_{dcm}L_{21}L_{m2}(\pi - 2|\phi_{es}|)}{2\omega L_{n2}{}^3} \quad (5.80)$$

$$i_{es}(0) = \frac{-V_{esdc}(L_{21}L_{23} + L_{21}L_{m2} + L_{23}L_{m2})(\pi - 2|\phi_{pv}|) + r_{21}V_{pvdc}L_{23}L_{m2}(\pi - 2|\phi_{es}|) + r_{23}V_{dcm}L_{21}L_{m2}\pi}{2\omega L_{n2}{}^3} \quad (5.81)$$

$$i_{c}(\phi_{pv}) = \frac{V_{dcm}(L_{31}L_{32} + L_{31}L_{m3} + L_{32}L_{m3})(\pi - 2|\phi_{pv}|) - r_{31}V_{pvdc}L_{32}L_{m3}\pi - r_{32}V_{esdc}L_{31}L_{m3}(\pi - 2|\phi_{pv} - \phi_{es}|)}{2\omega L_{n3}{}^3} \quad (5.82)$$

$$i_{c}(\phi_{es}) = \frac{V_{dcm}(L_{31}L_{32} + L_{31}L_{m3} + L_{32}L_{m3})(\pi - 2|\phi_{es}|) - r_{31}V_{pvdc}L_{32}L_{m3}(\pi - 2|\phi_{pv} - \phi_{es}|) - r_{32}V_{esdc}L_{31}L_{m3}\pi}{2\omega L_{n3}{}^3} \quad (5.83)$$

$$i_{c}(0) = \frac{V_{dcm}(L_{31}L_{32} + L_{31}L_{m3} + L_{32}L_{m3})\pi - r_{31}V_{pvdc}L_{32}L_{m3}(\pi - 2|\phi_{pv}|) - r_{32}V_{esdc}L_{31}L_{m3}(\pi - 2|\phi_{es}|)}{2\omega L_{n3}{}^3} \quad (5.84)$$

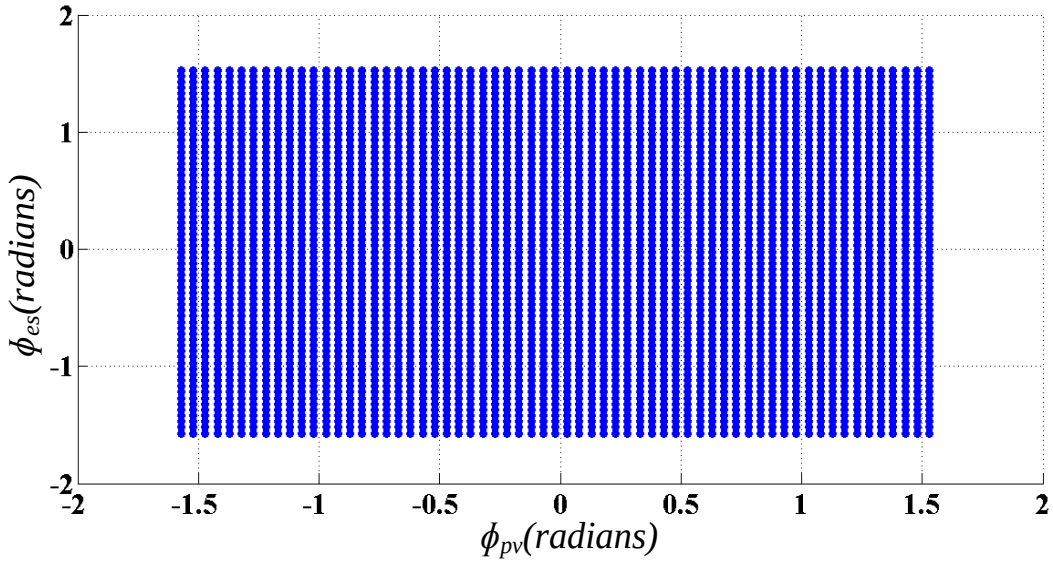

Figure 5.13. Full ZVS Region for TAB Converter with Split-type Transformer.

The full ZVS operation range for the three port triple active bridge converter is shown in figure 5.13 for phase shift angles ϕ_{pv} and ϕ_{es} in the feasible operating range of (-π/2, +π/2) for phase shifted isolated converters. It can be observed that the split-winding transformer provides a large ZVS operating range for the converter, based on the assumption that very small inductor current can discharge the voltage across the device capacitance. The ZVS range is evaluated based on the ideal condition for ZVS, as shown below.

$$i_{pv}(\phi_{pv}) < 0 \quad (5.85), \quad i_{es}(\phi_{es}) < 0 \quad (5.86), \quad i_c(0) > 0 \quad (5.87)$$

5.5. Comparison of Split-Winding Transformer & Two-Limb Three Winding Transformer

The split-winding transformer discussed above is similar in equivalent circuit and functionalities when compared to two limb three winding transformer. The physical structures of two limb three winding structure & its equivalent circuit is shown in figure 5.14.

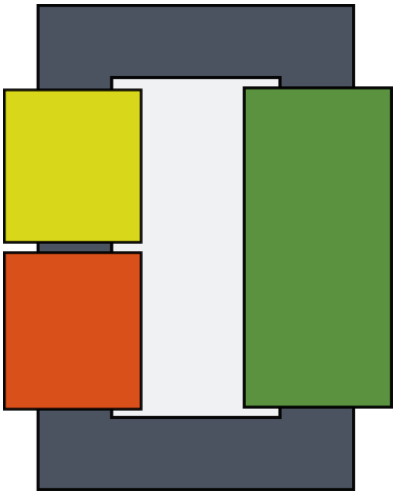

Figure 5.14. Two Limb Three Winding Transformer.

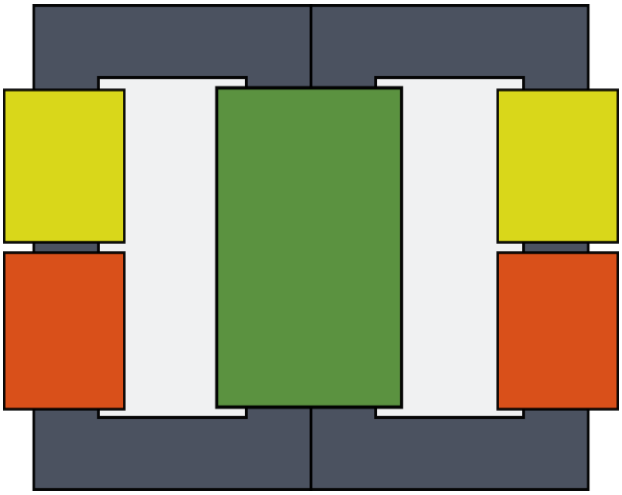

Figure 5.15. Three Limb Three Winding Transformer.

A comparison of the two limb three winding and split-winding type transformer is carried out for same voltage and current ratings. The comparison of the two transformers is based on same amount power rating and same volume of core material and addresses same copper requirement, leakage inductances, core loss and copper losses. Table 8 below shows the comparison between leakage inductance of split-winding transformer and leakage inductance of two limb three winding transformer.

Table 8. Leakage Inductance Comparison

	Two Limb Three Winding Transformer	Split-Winding Transformer
L_{L31}	0.28μH/turns^2	0.44μH/turns^2
L_{L32}	0.28μH/turns^2	0.44μH/turns^2
L_{L12}	0.22μH/turns^2	0.506μH/turns^2

The differences of leakage inductances result in different operating angles. Higher the phase angle, higher is winding current for same operating power level with higher reactive power. Larger operating phase angle also result in lower operating flux density, which results in lower

core losses. Therefore, for phase shifted converters, with higher leakages the core loss goes down with increasing loading/operating phase angle. Figures 5.16-5.17 below shows the operating flux densities for the two different transformers when the ES is charging and ES is discharging.

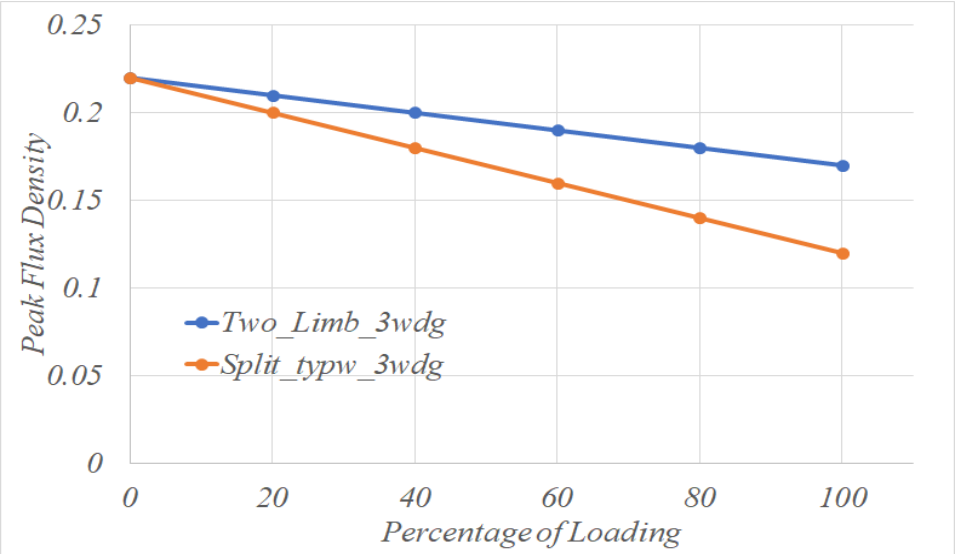

Figure 5.16. Peak Flux Density Comparison for ES Charging.

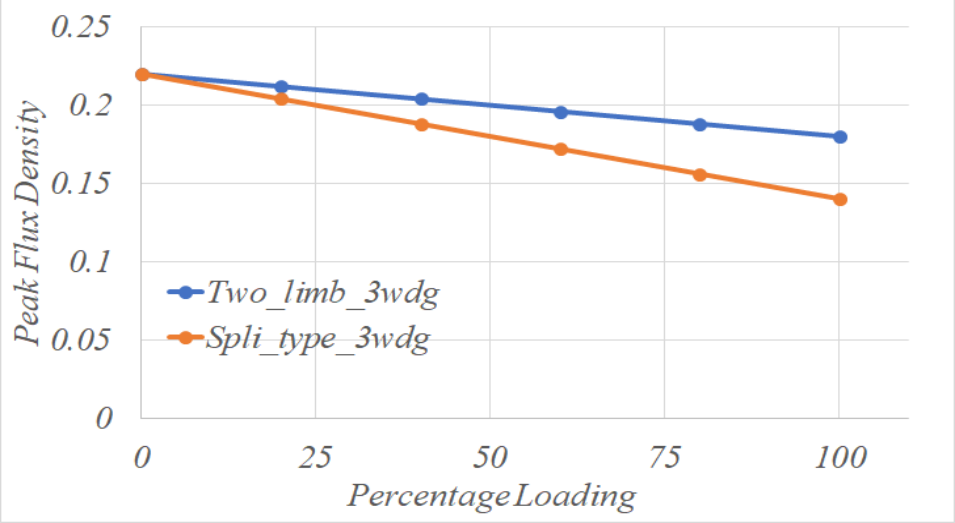

Figure 5.17. Peak Flux Density Comparison for ES Discharging.

5.6. Split-Winding Transformer Leakage Inductance

The leakage inductance of split-winding transformer play an important role in defining the power flow limits for three port dc-dc converter. In this section, analytical evaluation for the leakage inductance of three limb split-winding transformer is derived. The method for deriving leakage inductance of split-winding type transformer is similar to that presented in chapter 3. For split-winding type transformer, with three windings occupying each half of window area, leakage between any two windings are estimated through the permeance method of chapter 3. Deriving the leakage inductances, when three windings are carrying current is not straight-forward, hence considering two windings to be active at any instant, the third winding is considered open. The mmf distribution inside each window half for the three cases are shown in figures 5.18-5.20. In these figures, only the active windings are shown. The transformer core and window dimensions are shown in figure 5.21.

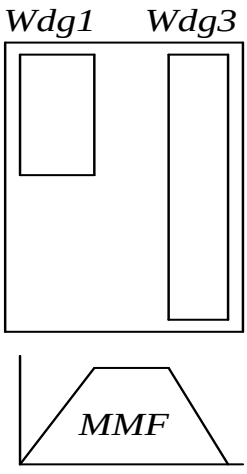

Figure 5.18. Wdg 1-3 active.

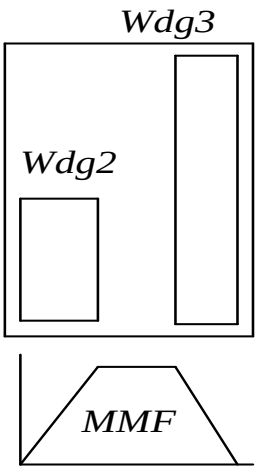

Figure 5.19. Wdg 2-3 active.

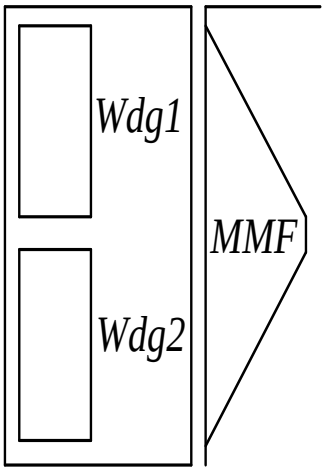

Figure 5.20. Wdg 1-2 active.

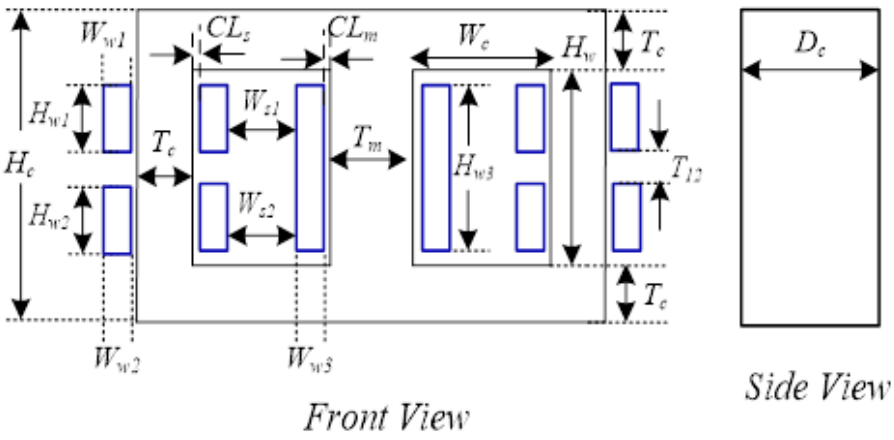

Figure 5.21. Transformer Dimensions.

The leakage fluxes for three limb three winding transformer are across the core volume and winding volumes as shown in chapter 3. In a similar manner, the leakage flux paths or volumes for three limb split-winding transformer are shown in figures 5.22-5.26.

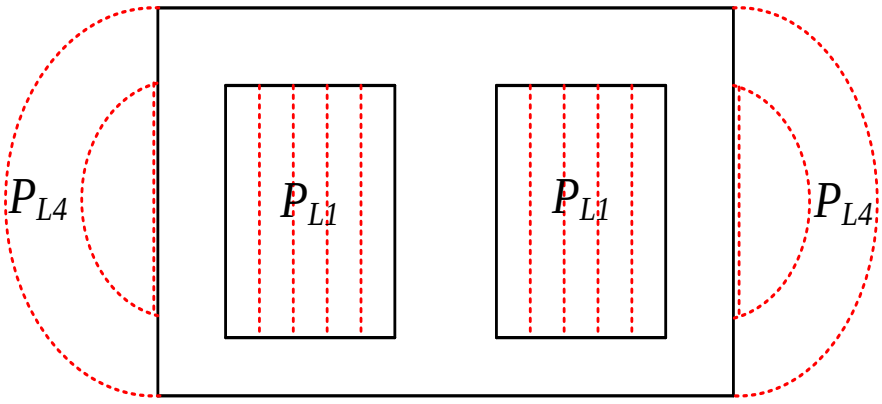

Figure 5.22. Leakage Flux Path across the Core from Front View.

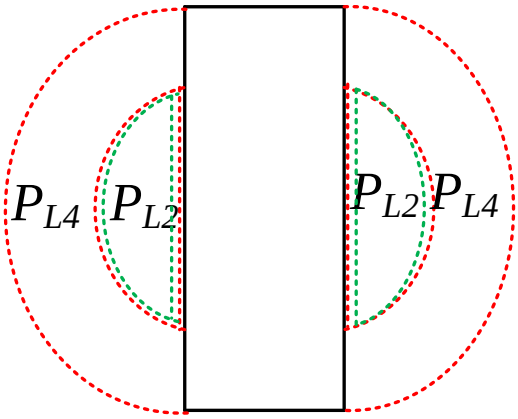

Figure 5.23. Leakage across the Core from Side View.

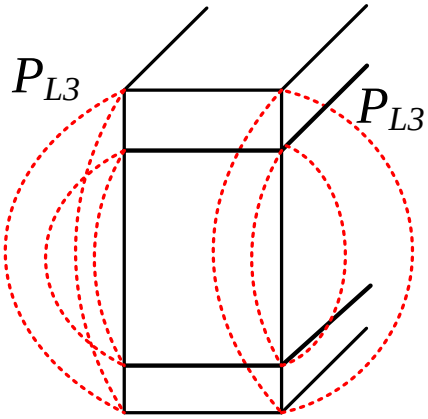

Figure 5.24. Leakage across the Core Corners.

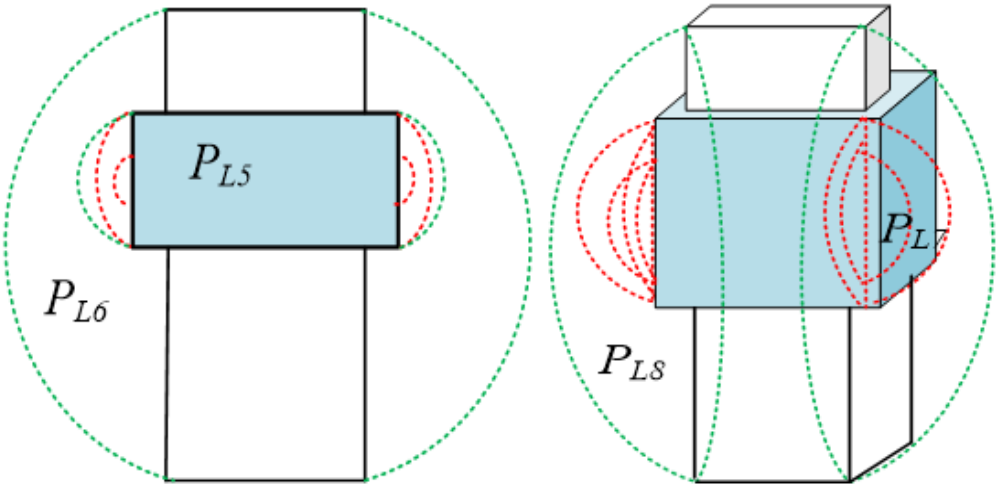

Figure 5.25. Core and Winding Portions Leakage(1-3 or 2-3) for Front/Side and Corner.

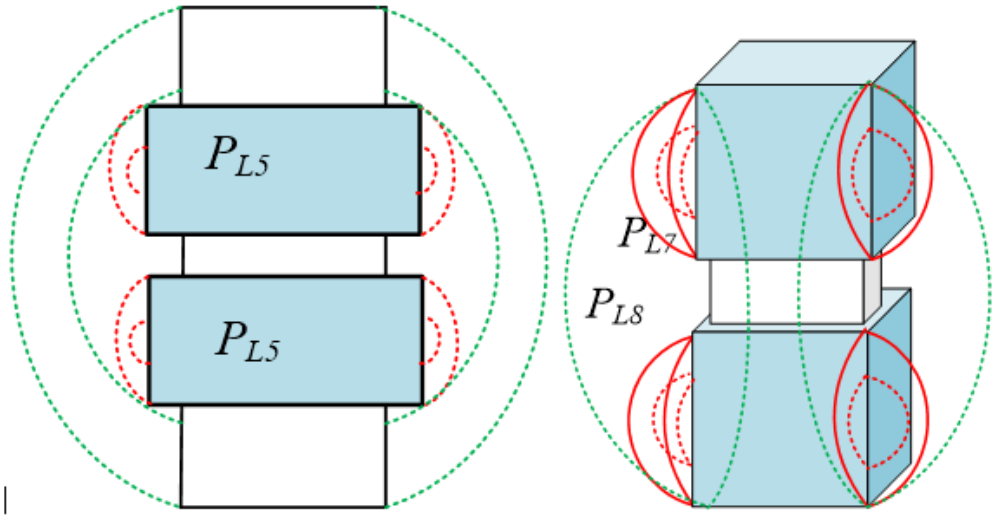

Figure 5.26. Core and Winding Portions Leakage (1-2) for Front/Side and Corner.

The leakage permeance for the paths shown above are of different geometrical nature, e.g. half cylindrical shell structure, quarter spherical shell structure, half solid cylinder, cube. The leakage permeance is considered only due to permeability of air, permeability of core is neglected. The leakage permeance is expressed as follows.

$$L_L = \mu_0 \frac{A}{l} = \mu_0 \frac{Al}{l^2} = \mu_0 \frac{V}{l^2} \qquad (5.88)$$

The mmf inside the window area has a trapezoidal shape, as shown in figures 5.16-5.18, the leakage permeance components for winding-to-winding leakage are expressed as follows.

$$P_{L1(1-3)} = \mu_0 \frac{D_c W_{13}}{H_w} \text{ (cubic shape)} \quad (5.89), \text{ where } W_{13} = \frac{W_{w1}}{3} + \frac{W_{w3}}{3} + W_{s1} \quad (5.90)$$

$$P_{L1(2-3)} = \mu_0 \frac{D_c W_{23}}{H_w} \text{ (cubic shape)} \quad (5.91), \text{ where } W_{23} = \frac{W_{w2}}{3} + \frac{W_{w3}}{3} + W_{s2} \quad (5.92)$$

$$P_{L1(1-2)} = \mu_0 \frac{D_c W_{12}}{W_w} \text{ (cubic shape)} \quad (5.93), \text{ where } W_{12} = \frac{H_{w1}}{3} + \frac{H_{w2}}{3} + T_{12} \quad (5.94)$$

$$P_{L4(window)} = \frac{\mu_0}{\pi}(2W_w)\ln(1+2\frac{T_c}{H_w})$$ (half cylindrical hollow shell) (5.95),

$$P_{L4(side)} = \frac{\mu_0}{\pi}(2T_c + D_c)\ln(1+2\frac{T_c}{H_w})$$ (half cylindrical hollow shell) (5.96)

$$P_{L4(middle)} = \frac{\mu_0}{\pi}(T_m)\ln(1+2\frac{T_c}{H_w})$$ (half cylindrical hollow shell) (5.97),

$$P_{L2(window)} = 0.24(\frac{\mu_0}{\pi})(2W_w)$$ (half cylinder solid) (5.98)

$$P_{L5(wdg1)} = (\frac{\mu_0}{\pi})(2T_c + D_c)(1+2\frac{H_{w1}/3}{H_{w1}/3})$$ (half cylindrical hollow shell) (5.99)

$$P_{L5(wdg2)} = (\frac{\mu_0}{\pi})(2T_c + D_c)(1+2\frac{H_{w2}/3}{H_{w2}/3})$$ (half cylindrical hollow shell) (5.100)

$$P_{L5(wdg3)} = (\frac{\mu_0}{\pi})(2T_m)(1+2\frac{H_{w3}/3}{H_{w3}/3})$$ (half cylindrical hollow shell) (5.101)

$$P_{L6(wdg1)} = \mu_0(\frac{V_{L1}}{L_{avg}^{\ 2}})$$ (quarter spherical hollow shell) , (5.102)

where $V_{L1} = (\frac{\pi}{2})(r_o^{\ 2} - r_{in}^{\ 2})(2T_c + D_c)$ (5.103)

and $L_{avg} = (\frac{\pi}{2})(r_o + r_{in})$ and $r_o = \frac{H_c}{2}$, $r_o = \frac{H_{w1}}{2}$

$$P_{L6(wdg2)} = \mu_0(\frac{V_{L2}}{L_{avg}^{\ 2}})$$ (quarter spherical hollow shell) (5.104),

where $V_{L2} = (\frac{\pi}{2})(r_o^{\ 2} - r_{in}^{\ 2})(2T_c + D_c)$ (5.105)

and $L_{avg} = (\frac{\pi}{2})(\mathrm{r_o} + \mathrm{r}_{in})$ and $r_o = \frac{H_c}{2}$, $r_o = \frac{H_{w2}}{2}$

$$P_{L6(wdg3)} = (\frac{\mu_0}{\pi})(2T_m)(1 + 2\frac{T_c + 2(H_w - H_{w3})}{H_{w3}}) \text{ (half cylindrical hollow shell) (5.106)}$$

$$P_{L7(wdg1)} = \frac{4\mu_0}{\pi}(\frac{H_{w1}}{3}) \text{ (5.107)}, \quad P_{L7(wdg2)} = \frac{4\mu_0}{\pi}(\frac{H_{w2}}{3}) \text{ (5.108)},$$

$$P_{L7(wdg3)} = \frac{4\mu_0}{\pi}(\frac{H_{w3}}{3}) \text{ (5.109)}, \quad P_{L8(wdg1)} = \mu_0(\frac{V_{8\_1}}{L_{avg}^{\ 2}}) \text{ (5.110)}$$

where $V_{L2} = 2(\frac{\pi}{3})(\mathrm{r_o}^3 - \mathrm{r}_{in}^{\ 3})$, $L_{avg} = (\frac{\pi}{2})(\mathrm{r_o} + \mathrm{r}_{in})$, $r_o = \frac{H_c}{2}$, $r_o = \frac{H_{w1}}{2}$

$$P_{L8(wdg2)} = \mu_0(\frac{V_{8\_2}}{L_{avg}^{\ 2}}) \text{ (5.111)}$$

where $V_{L2} = 2(\frac{\pi}{3})(\mathrm{r_o}^3 - \mathrm{r}_{in}^{\ 3})$, $L_{avg} = (\frac{\pi}{2})(\mathrm{r_o} + \mathrm{r}_{in})$, $r_o = \frac{H_c}{2}$, $r_o = \frac{H_{w2}}{2}$

(P_{L7}, P_{L8} are quarter spherical hollow shell)

$$P_{L\_wdg(1-3)} = P_{L5(wdg3)} + P_{L6(wdg3)} + P_{L7(wdg3)} + 2*(P_{L5(wdg1)} + P_{L7(wdg1)} + P_{L6(wdg1)} + P_{L8(wdg1)} + P_{L4(window)} + P_{L2(window)} + P_{L1(1-3)}) \text{ (5.112)}$$

$$P_{L\_wdg(2-3)} = P_{L5(wdg3)} + P_{L6(wdg3)} + P_{L7(wdg3)} + 2*(P_{L5(wdg2)} + P_{L7(wdg2)} + P_{L6(wdg2)} + P_{L8(wdg2)} + P_{L4(window)} + P_{L2(window)} + P_{L1(2-3)}) \text{ (5.113)}$$

$$P_{L\_wdg(1-2)} = 2*(P_{L5(wdg1)} + P_{L7(wdg1)} + P_{L5(wdg2)} + P_{L7(wdg2)} + P_{L4(side)} + P_{L4(window)} + P_{L2(window)} + P_{L4(middle)} + P_{L1(1-2)}) \quad (5.114)$$

The leakage inductances between windings are calculated as follows

$$L_{L31} = N_3^{\ 2} * P_{L\_wdg(1-3)} \text{ (5.115)}, \quad L_{L32} = N_3^{\ 2} * P_{L\_wdg(2-3)} \text{ (5.116)},$$

$$L_{L12} = N_1^{\,2} * P_{L\_wdg(1-2)} \quad (5.117)$$

The leakage inductance from FEA model of split-winding transformer can be estimated from the 5x5 L matrix of equation 5.18, but FEA method considers the leakage between two split portions of same port, whereas being series connected, the leakage between them is not present. The leakage inductance is thus estimated by combining the split-portions together in FEA simulation and deriving the leakage from 3x3 matrix as shown below.

$$L = \begin{bmatrix} L_{11} & L_{12} & L_{13} \\ L_{21} & L_{22} & L_{23} \\ L_{31} & L_{32} & L_{33} \end{bmatrix} \qquad (5.118)$$

$$L_{L31} = L_{33} - \frac{L_{31}^{\,2}}{L_{11}} \quad (5.119), \quad L_{L32} = L_{33} - \frac{L_{32}^{\,2}}{L_{22}} \quad (5.120), \quad L_{L12} = L_{11} - \frac{L_{12}^{\,2}}{L_{22}} \quad (5.121)$$

Where L_{L31} = leakage between 3(middle) and 1(PV) referred to 3(middle)

L_{L32} = leakage between 3(middle) and 2(ES) referred to 3(middle)

L_{L12} = leakage between 1(PV) and 1(ES) referred to 1(PV)

A ferrite core based split-winding transformer is built using stacks of E100/60/28 joined together having the same dimension as the design type 1 transformer of chapter 3. The PV and ES port and the middle port have voltage ratings of 700V and 1200V, same as that for design type 1 transformer in chapter 3. For same peak flux density in limb portions, the split portions of PV and ES winding have half the number of turns as the number of turns in PV and ES windings of design type 1 transformer. Figures 5.27-5.28 show the three limb three winding transformer and split-winding type transformer.

Figure 5.27. Three Limb Transformer.

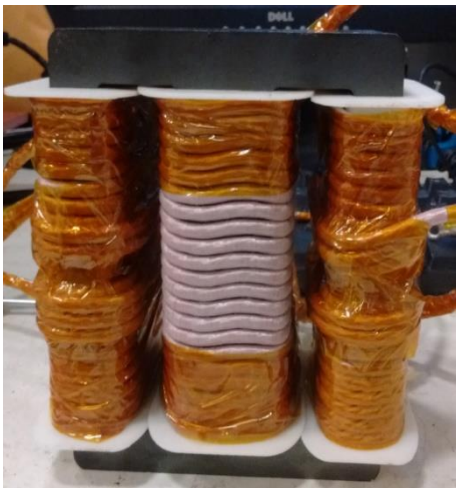

Figure 5.28. Split-WindingTransformer.

The leakage inductance between any two windings of split-winding transformer is measured by keeping the third winding open, keeping the secondary winding short and measuring inductance from the first or primary winding. Following this method, the leakage inductances for the three cases L_{L31}, L_{L32} and L_{L12} are obtained. Table 9 gives the comparison of leakage inductances using analytical method, FEA analysis and actual measurement.

Table 9. Leakage Inductances

	Analytical	FEA Method	Measurement
L_{L31}	162μH	176μH	181μH
L_{L32}	162μH	176μH	188μH
L_{L12}	72μH	73μH	70μH

The leakage inductances L_{L31}, L_{L32} and L_{L12} can be represented by the winding leakage inductances of figure 5.29, as shown below. The relationship between the measured leakage inductances and the equivalent circuit leakage inductances are represented as follows.

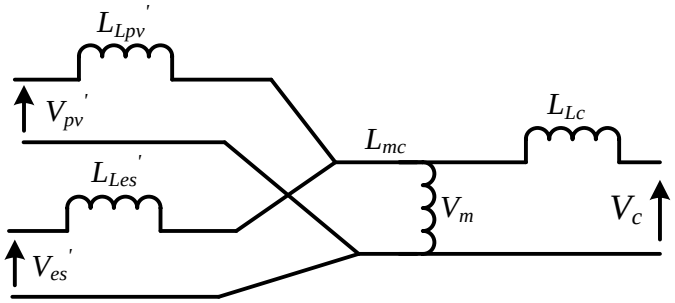

Figure 5.29. Reduced Order Equivalent Circuit of Split-Winding Transformer.

$$L_{L31} = L_{Lc} + L_{Lpv}' \quad (5.121), \quad L_{L32} = L_{Lc} + L_{Les}' \quad (5.122), \quad L_{L12} = L_{Lpv} + \left(\frac{N_{s1}}{N_{s2}}\right)^2 L_{Les} \quad (5.123)$$

Solving the above equations, the values of L_{Lpv}, L_{Les} and L_{Lc} are obtained as follows,

L_{Lpv} = 33µH, L_{Lpv} = 37µH and L_{Lc} = 88µH

The measured magentzing inductance of the transformer is around 1.15mH, which is much lower than estimated by FEA and analytically, due to unwanted air-gap in the core of the transformer.

5.7. Split-Winding Transformer Parasitic Capacitance

The transformer inter-winding parasitic capacitances play an important role in suitable working principle for the transformer. The high dv/dt of SiC devices, together with the inter-winding parasitic capacitance, are the crucial sources of EMI noise. The inter-winding parasitic capacitance of split-winding transformer is estimated using the method as described in chapter 3. The inter-winding capacitance model is shown below. The analytical equations for inter-winding capacitances are given in equations 5.124-5.133. Each winding portion is considered as an equivalent electrical plate and the core is considered equipotential. The concerned capacitances are capacitances between winding and core and between different windings. The inter-winding capacitance values for analytical method, FEA analysis and measured values are given in table

10. The inter-winding capacitance based network model for three limb split-winding transformer, for simulation platforms such as MATLAB/PLECS is given in figure 5.31.

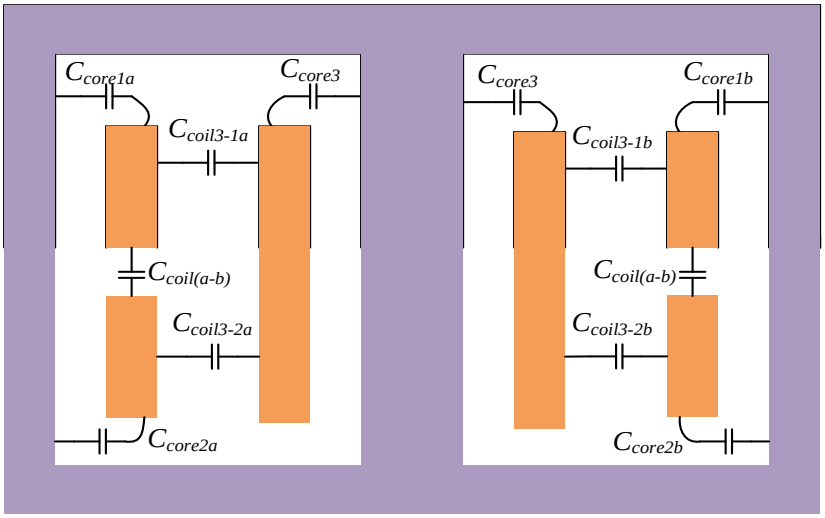

Figure 5.30. Winding-to-Winding and Core-to-Winding Capacitance.

$$C_{core1a} = C_{core1b} = \frac{\varepsilon_0 2(T_c + D_c)H_{w1}}{CL_s} \text{ (5.124)}, \quad C_{core2a} = C_{core2b} = \frac{\varepsilon_0 2(T_c + D_c)H_{w2}}{CL_s} \text{ (5.125)}$$

$$C_{coil3-1a} = C_{coil3-1b} = \frac{\varepsilon_0 D_c H_{w1}}{W_{s1}} \text{ (5.126)}, \quad C_{coil3-2a} = C_{coil3-2b} = \frac{\varepsilon_0 D_c H_{w2}}{W_{s2}} \text{ (5.127)}$$

$$C_{coil(a-b)} = \frac{\varepsilon_0 (2T_c + D_c)0.5*(W_{w1} + W_{w2})}{T_{12}} \text{ (5.128)}$$

$$C_{3-1a} = C_{3-1b} = C_{coil3-1a} + \frac{C_{core1a} * C_{core3}}{C_{core1a} + C_{core3}} \text{ (5.129)}$$

$$C_{3-2a} = C_{3-2b} = C_{coil3-2a} + \frac{C_{core2a} * C_{core3}}{C_{core2a} + C_{core3}} \text{ (5.130)}$$

$$C_{1a-2a} = C_{1b-2b} = C_{coil(a-b)} + \frac{C_{core1a} * C_{core2a}}{C_{core1a} + C_{core2a}} \text{ (5.131)}$$

$$C_{1a-2b} = \frac{C_{core1a} * C_{core2b}}{C_{core1a} + C_{core2b}} \text{ (6.132)}, \quad C_{2a-1b} = \frac{C_{core2a} * C_{core1b}}{C_{core2a} + C_{core1b}} \text{ (5.133)}$$

Table 10. Inter-Winding Parasitic Capacitances

	Analytical	FEA Method	Measurement
$C_{3\text{-}1a}$	13Pf	14pF	17pF
$C_{3\text{-}2a}$	13pF	14pF	18pF
$C_{3\text{-}1b}$	13pF	14pF	14pF
$C_{3\text{-}2b}$	13pF	14pF	16pF
$C_{1a\text{-}2a}$	6pF	6pF	5pF
$C_{1b\text{-}2b}$	6pF	6pF	7pF
$C_{1a\text{-}2b}$	5pF	5pF	3pF
$C_{1b\text{-}2a}$	5pF	5pF	4pF

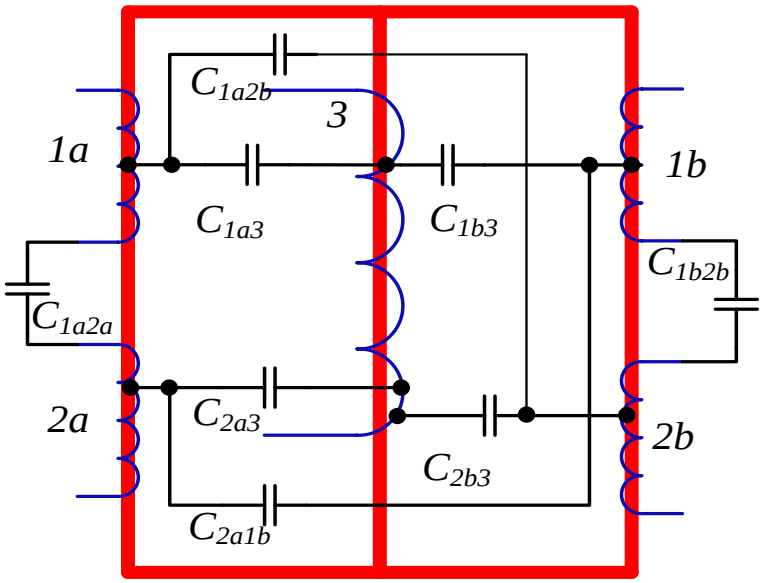

Figure 5.31. Inter-Winding Capacitance with Split-Winding Transformer Model.

The open circuit and short circuit impedance plots vs frequency of the split-winding transformer is measured using Precision Impedance Analyzer 4294A. The open circuit impedance plots for the three ports, are shown in figures 5.32-5.34. The first resonance peaks for the open circuit impedance plots for the three port are around 1MHz and much higher than switching frequency range of 50kHz-100kHz.

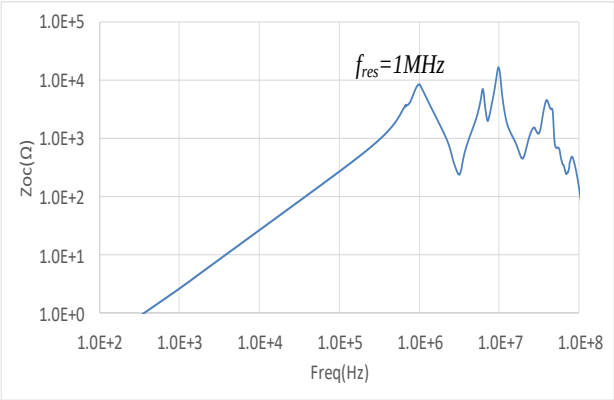

Figure 5.32. Z_{oc} plot from ES winding.

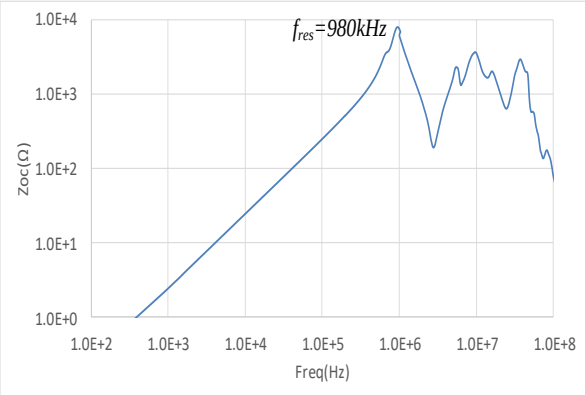

Figure 5.33. Z_{oc} plot from PV winding.

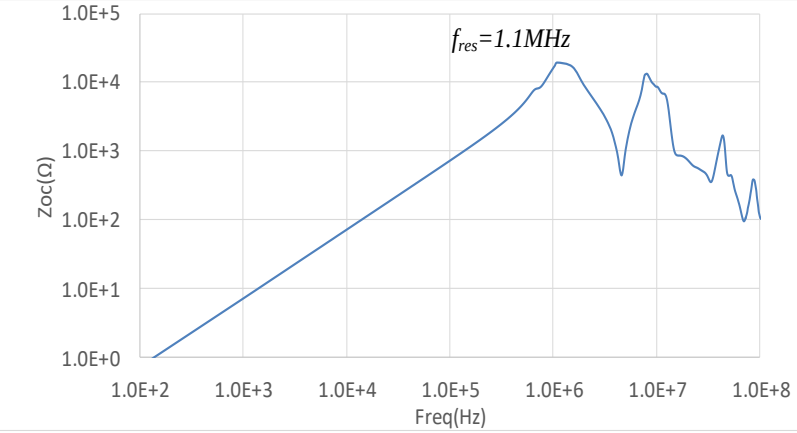

Figure 5.34. Z_{oc} plot from Middle winding.

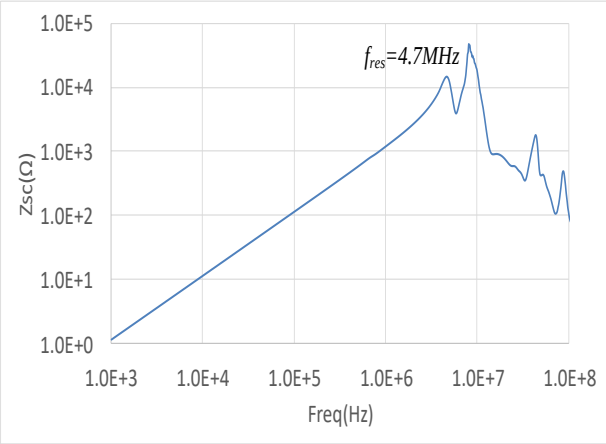

Figure 5.35. Z_{sc} plot from ES winding.

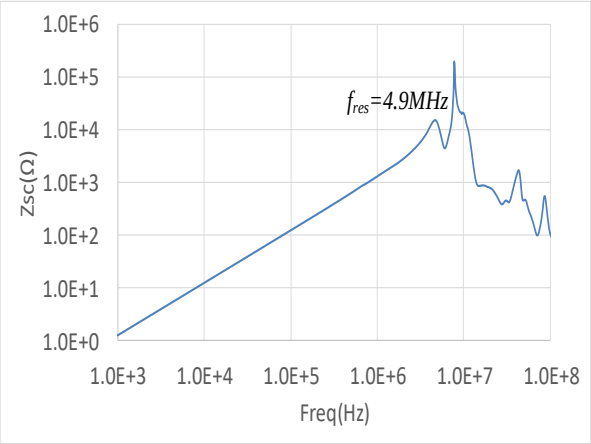

Figure 5.36. Z_{sc} plot from PV winding.

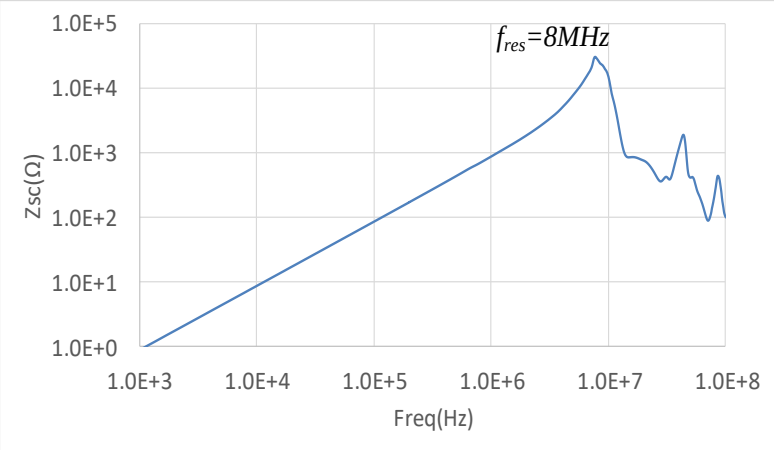

Figure 5.37. Z_{sc} plot from Middle winding.

The short circuit impedance plots for the three ports, are shown in figures 5.35-5.37. The first resonance peaks for the open circuit impedance plots for the three port are around 5MHz and beyond and much higher than switching frequency range of 50kHz-100kHz. The open circuit and short circuit plots of the split-winding transformer clearly indicate the inductive nature of the open circuit impedance and short circuit impedances of the transformer, as the resonance peaks are at a much higher frequency than switching frequency. The transformer has reasonably low inter-winding capacitance to avoid any unwanted ringing in transformer winding currents.

5.8. One Port Idle Operation with SplitWinding Type Three Limb Transformer

Using the split-winding type three limb transformer, the scenarios of one dc port being idle while the other two ports take part in power flow can be successfully executed without shorting the open port winding connecting it in parallel, hence the use of double throw switches as discussed in chapter 3, can be eliminated. For the split-winding type three limb transformer, while PV is idle or ES is idle, the flux flow paths are shown in figures 5.38-5.39, where induced

flux from winding cuts the other winding. In case of a loss of grid, the middle limb dc port can be disconnected and the converter can be switched off, and the power flow can take place between PV and ES, the flux flow path of which is shown in figure 5.40.

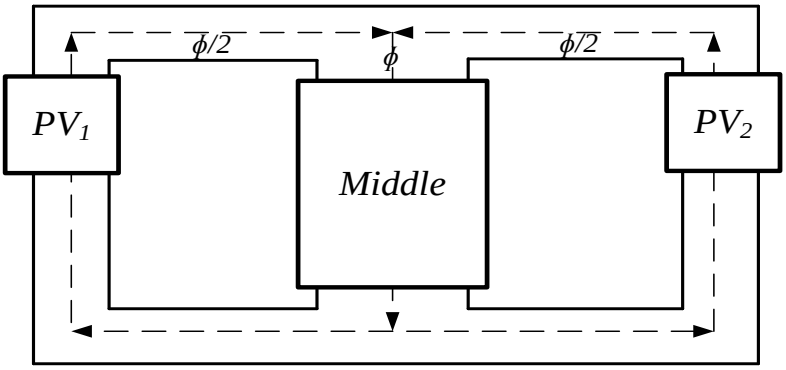

Figure 5.38. Flux flow path when ES winding is open.

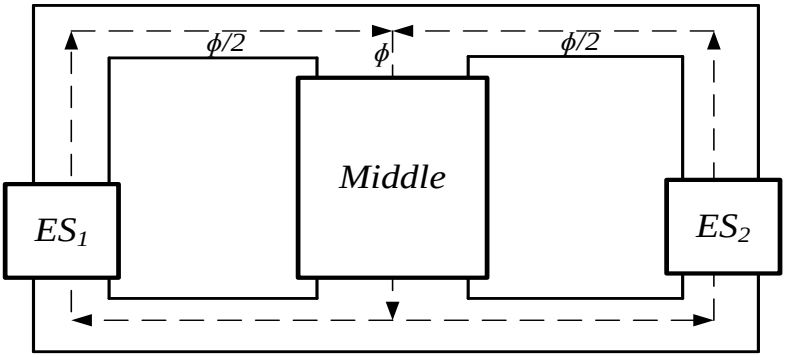

Figure 5.39. Flux flow path when PV winding is open.

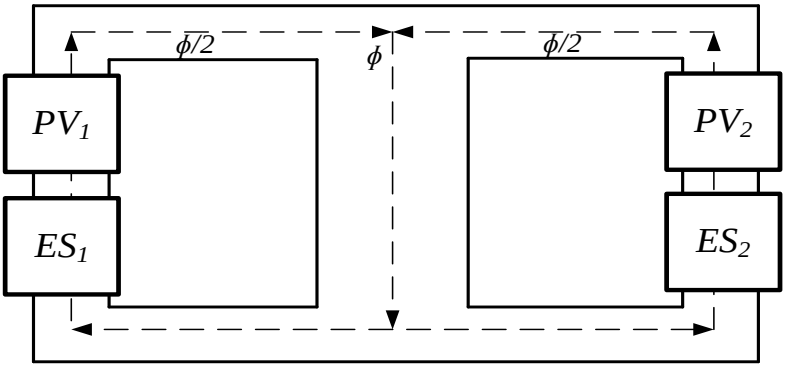

Figure 5.40. Flux flow path when middle winding is open.

The idle condition operation is verified using PLECS simulation platform. Both electrical equivalent circuit model and magnetic circuit models are used for verification. The idle condition is realized by switching off all the pulses to the respective H-bridge converter and disconnecting the source/sink from the dc capacitance of the H-bridge. Figures 5.41-5.43 show the winding voltages and currents for the three windings when one of the three ports are idle, which leads to the conclusion that split-winding type three limb transformer is capable of power transfer from one port to the other when one port is idle.

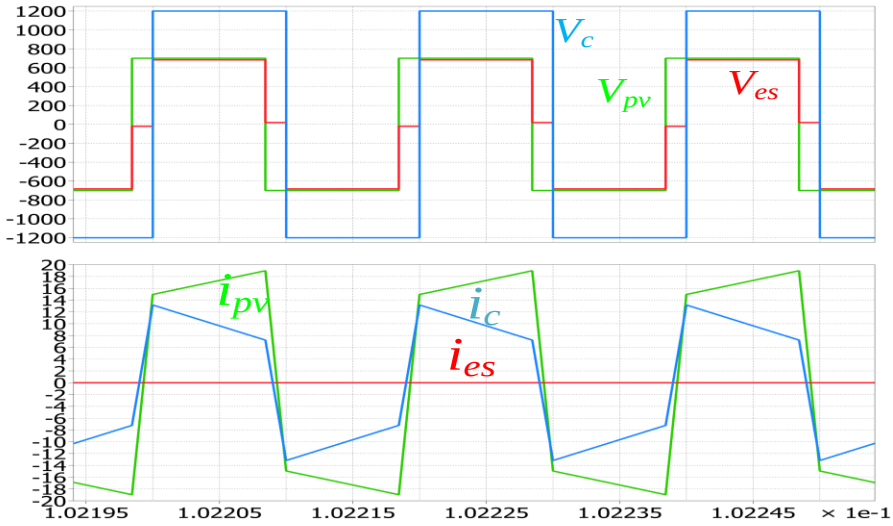

Figure 5.41. Transformer winding voltages and currents with Open ES winding.

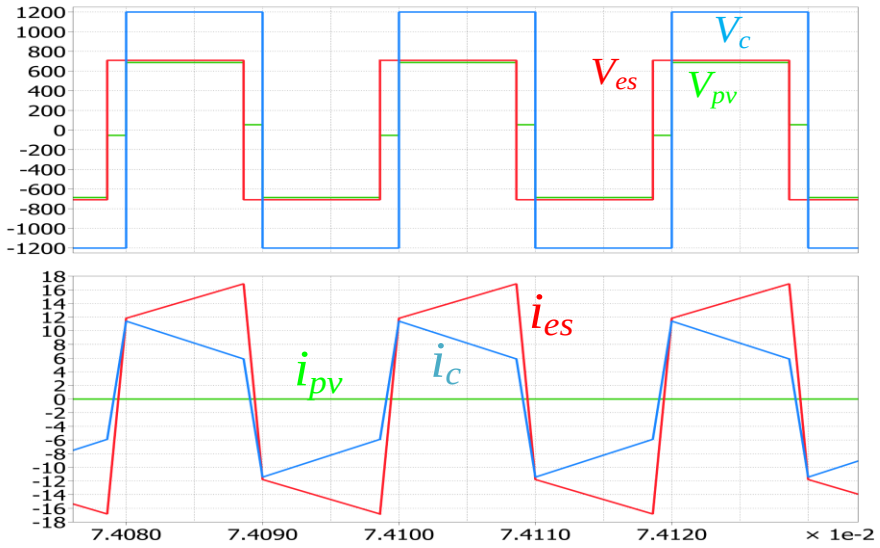

Figure 5.42. Transformer winding voltages and currents with Open PV winding.

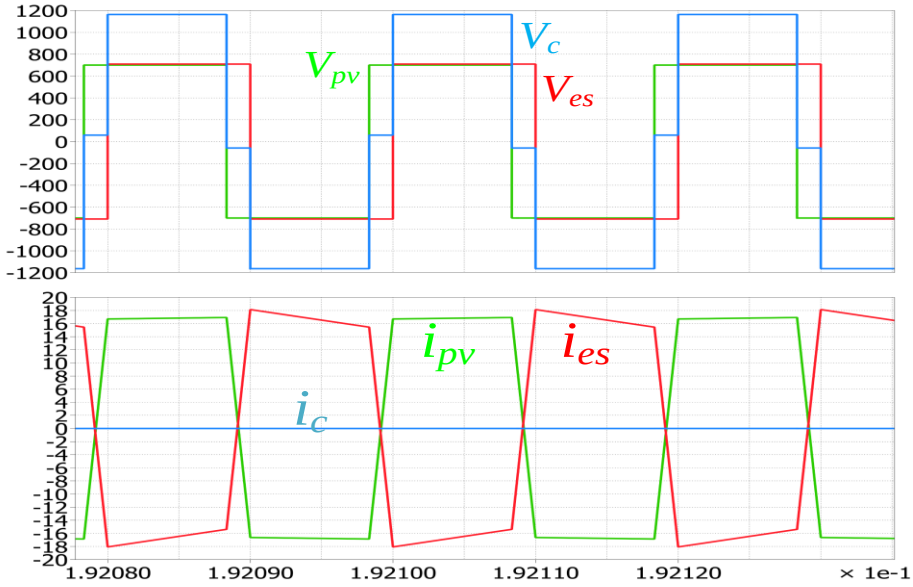

Figure 5.43. Transformer winding voltages and currents with Open Middle winding.

It is observed from figures 5.41-5.43, that the winding attached to the inactive or idle port develops a square voltage waveform because of the flux cutting through the winding. Now for equal volts per turns for each winding, peak or high value of this square wave voltage is close to the rated dc value of the idle port but less than the rated value, hence the diodes are not forward

biased to carry any current. In case of idle ports without any constant voltage dc bus(in case of PV unavailability or loss of grid), initially the dc bus capacitor of the idle port gets charged to the peak value of the induced voltage in the idle winding due to winding current conduction through diodes. Once the capacitors are charged, the diodes are not forward biased any further and conduction through the diodes stops.

5.9. Experimental Study of Split-Winding Transformer

The split-winding transformer prototype discussed above, has been used in experimental study to verify the power flow and ZVS cases. The experimental setup include the same 1200V and 1700V SiC Mosfet based laboratory prototype setup as discussed in previous chapters. The same experimental setup used for experimental study of three limb three winding transformer is used for the split-winding type transformer. The converter system has been run at 50kHz switching frequency for experimental study. Figure 5.44-5.45 show the schematic and the picture for the experimental setup.

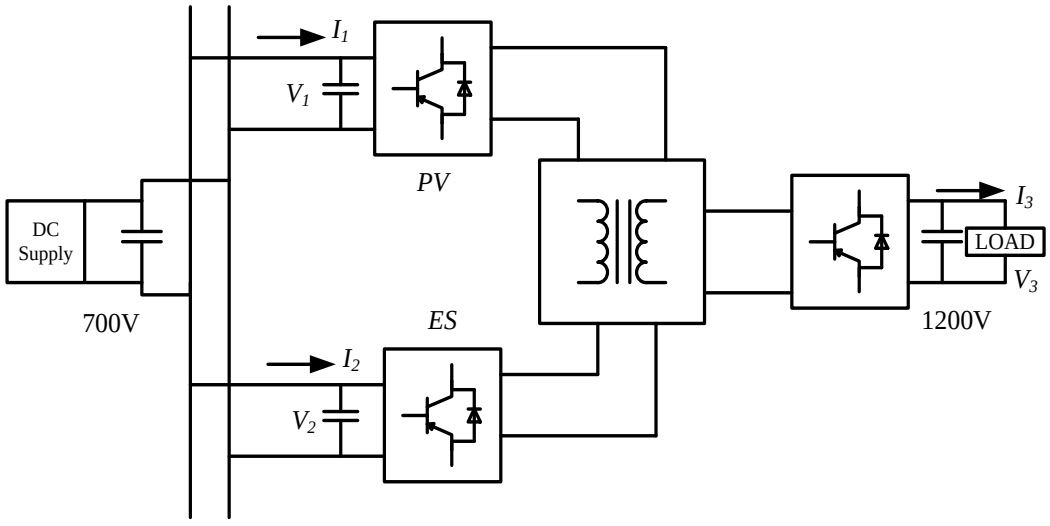

Figure 5.44. Experimental Setup Schematic with Split-Winding Transformer.

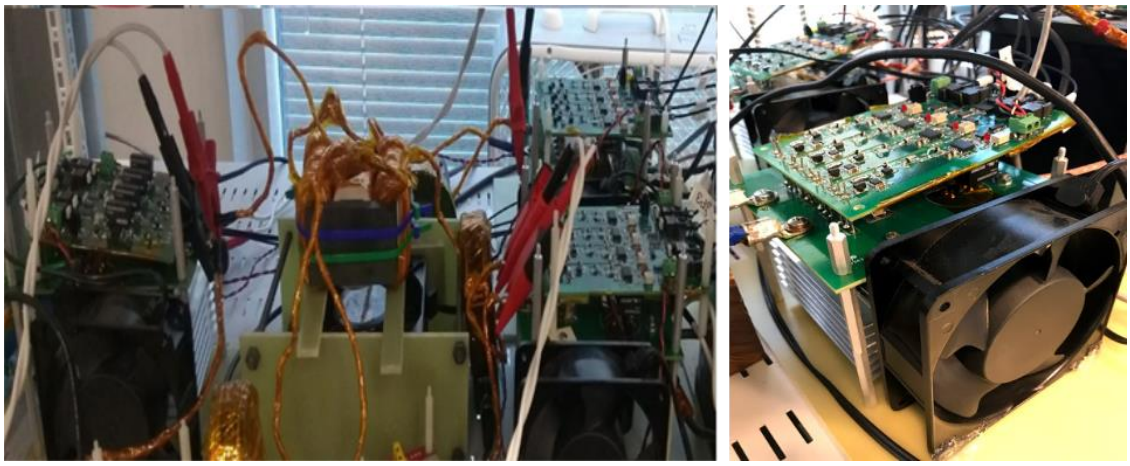

Figure 5.45. Experimental Setup with Split-Winding Transformer.

As can be seen from figure 5.44, the PV and ES ports are fed from same dc bus, which is emulated by a big capacitor, when either PV or ES is idle, the respective converter is switched off. The middle limb winding is connected to a resistive load bank. During idle condition of middle port, the resistive load bank is disconnected and the converter is switched off. The experimental study for one port idle condition is described as follows. Figure 5.46 and 5.47 show the transformer winding waveforms during PV being idle and ES being idle condition. It can be observed that during idle condition, zero current flows into the idle port and the winding develops a voltage, due to the induction of core flux. The peak of winding voltage and voltage across the dc bus capacitance for the idle port are same at 700V, hence no winding current flows through the idle port winding. The same observations can be made for both the cases of PV and ES ports being idle. Figure 5.48 shows the condition of middle port being idle, where it can be observed that the winding voltage in middle port develops a ringing voltage, which is due to the absence of any constant dc source, which are present across PV and ES ports.

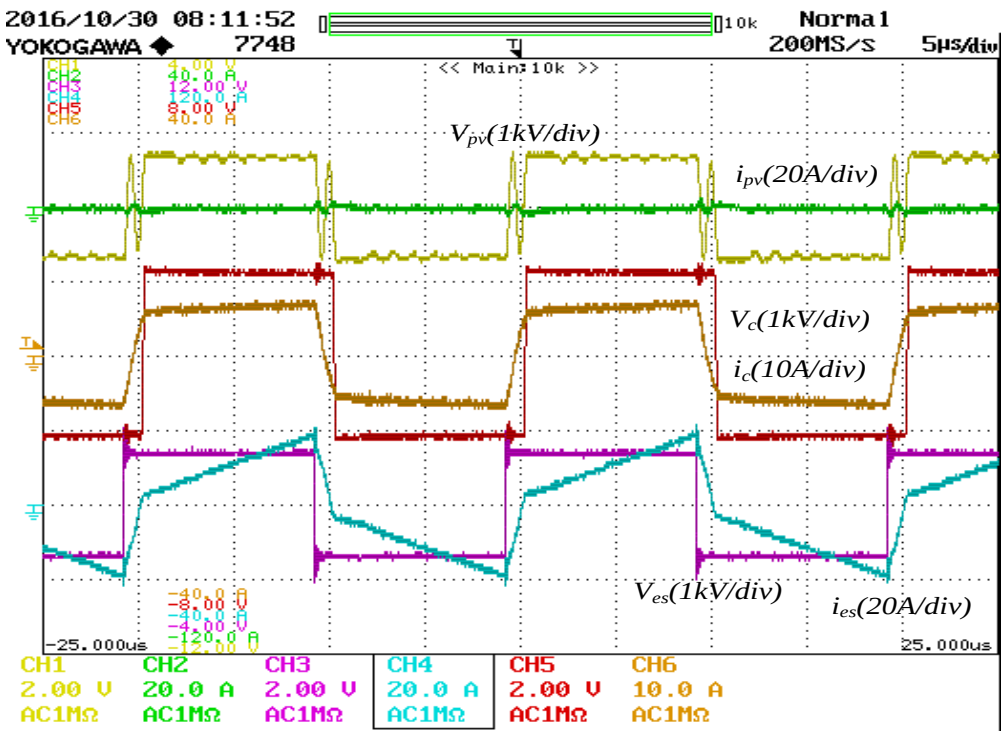

Figure 5.46. Transformer Waveforms when PV Port is Idle.

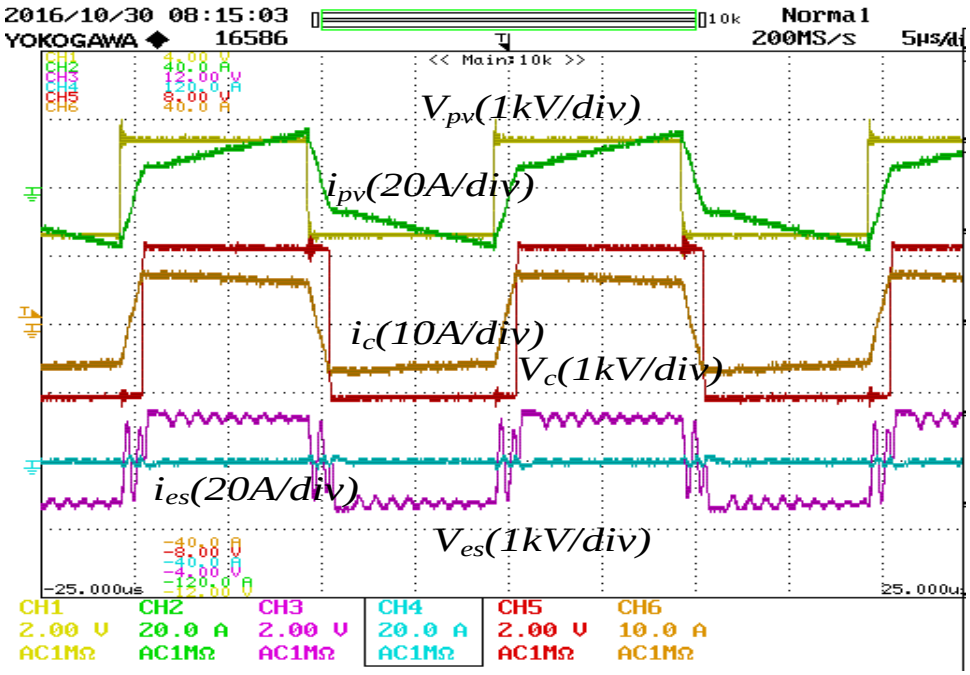

Figure 5.47. Transformer Waveforms when ES Port is Idle.

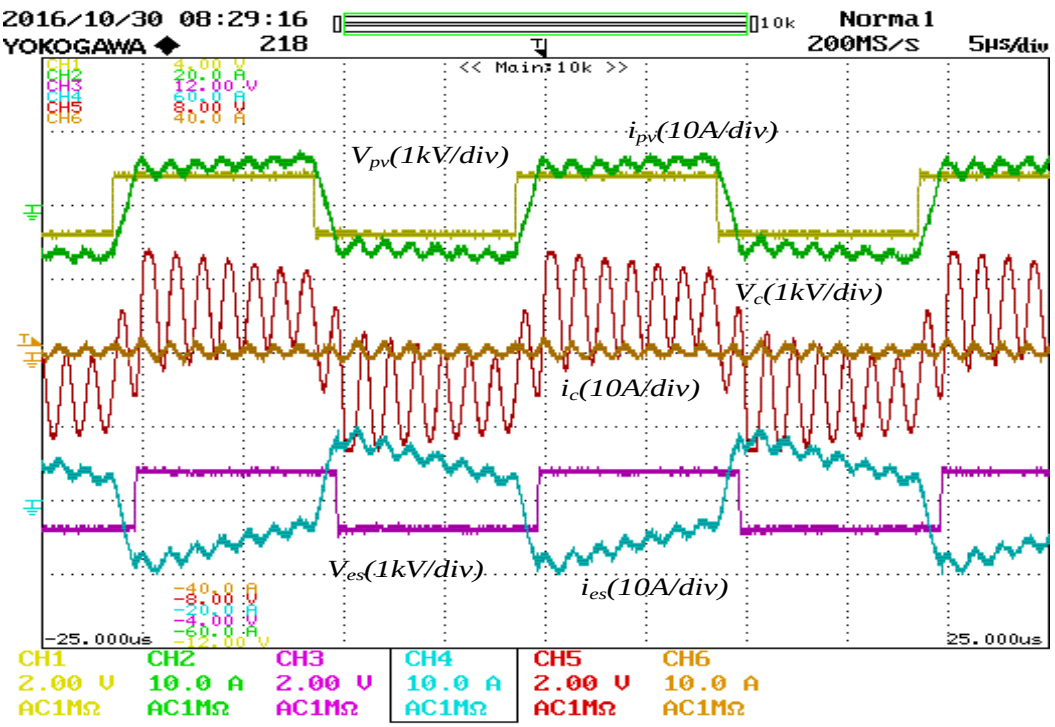

Figure 5.48. Transformer Waveforms when Middle Port is Idle.

Figure 5.49 shows the transformer winding current waveforms for simulation model including parasitic capacitances and figure 5.50 shows the transformer winding waveforms from hardware experiment. The simulation model including parasitics has been created using PLECS magnetic circuit model and by using physical capacitances in the magnetic circuit model. It can be observed that the simulation model waveforms are nearly identical to the hardware waveform and the effect of capacitances are almost negligible.

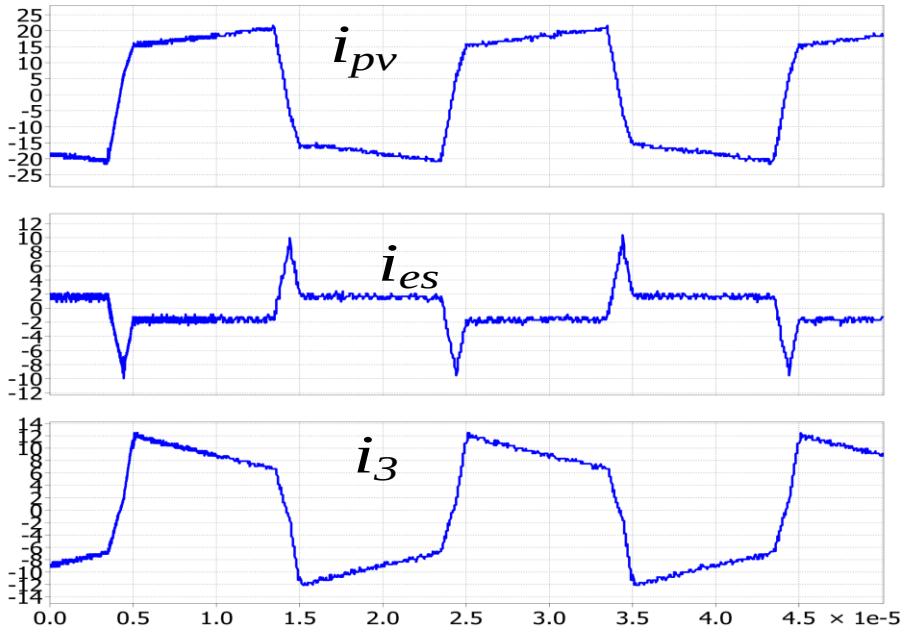

Figure 5.49. Experimental Transformer Winding Currents at 9.4kW, 50kHz.

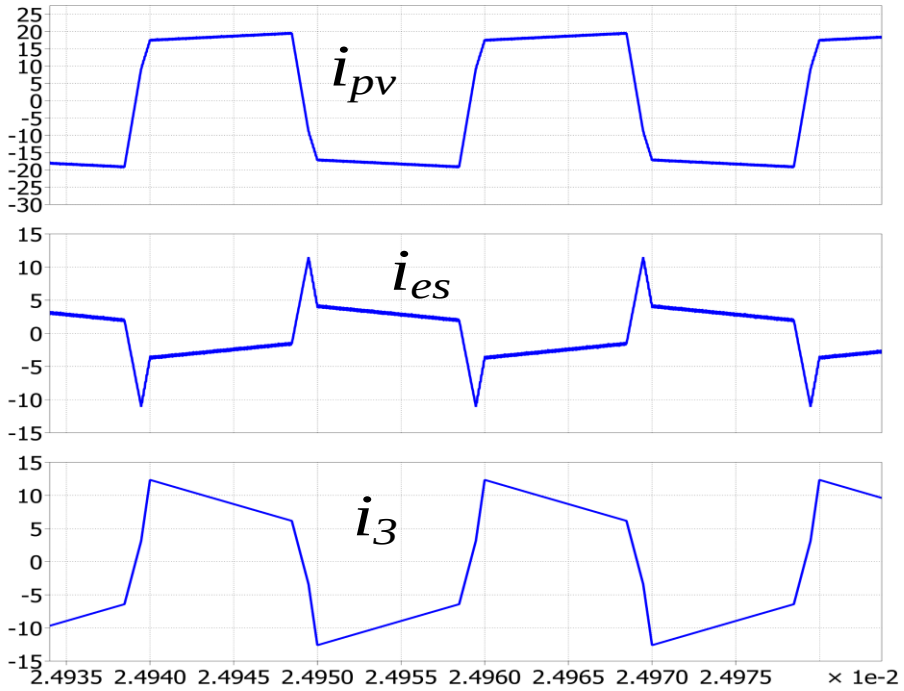

Figure 5.50. Simulation Transformer Winding Currents at 9.4kW, 50kHz.

Different power flow scenarios of PV/ES discharging and charging conditions are experimentally tested for split-winding type three winding transformer. Figure 5.51 show PV delivering and ES charging scenario, when PV is delivering 12.5kW and ES is charging with a power of 2.4 kW, while the load takes a power of 9.4kW. It can be observed that for all the PV and ES winding voltages, the outgoing winding currents are negative when the voltage has a transition from $-V_{dc}$ to $+V_{dc}$, which signified natural ZVS turn-on. For middle winding voltage, the incoming current is leading and positive when the winding voltage undergoes a transition from $-V_{dc}$ to $+V_{dc}$, which results in natural ZVS turn-on scenario. Figure 5.52 represents the case where PV delivers 4.5kW, ES delivers 5kW and the load takes 9.4kW of power. In this scenario as well, the outgoing currents for PV and ES are negative and incoming current for middle bridge is positive during $-V_{dc}$ to $+V_{dc}$ transition.

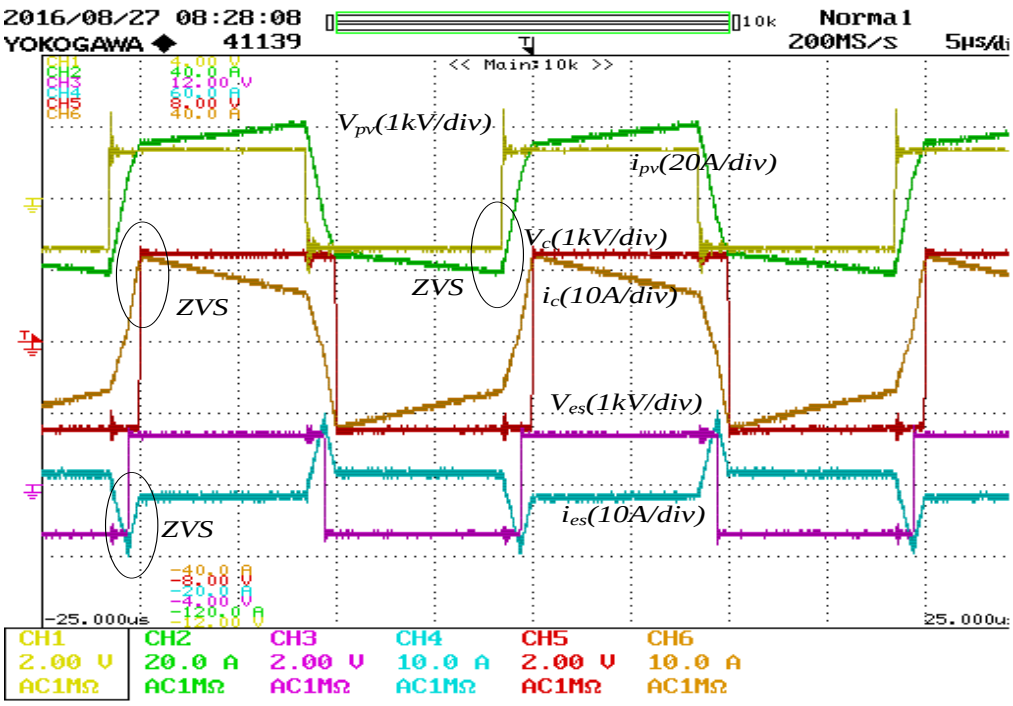

Figure 5.51. PV delivers 12kW, ES charges with 2.4kW and load takes 9.4kW.

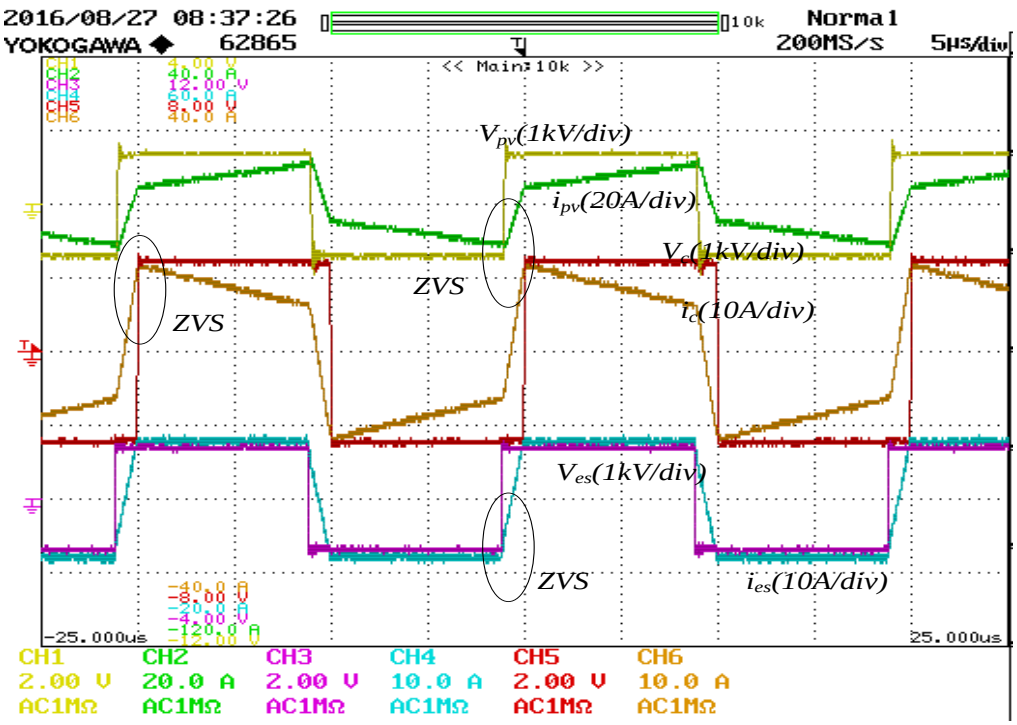

Figure 5.52. PV delivers 4.5kW, ES delivers 5kW and load takes 9.4kW.

When the PV or ES port powers are very low, then the winding currents are investigated for ZVS as shown in figures 5.53 and 5.54. In both the figures it can be observed that for PV and ES port, the outgoing winding current is negative while the bridge voltage goes from $-V_{dc}$ to $+V_{dc}$ transition and the currents are positive during $+V_{dc}$ to $-V_{dc}$ transition. The case, where middle limb winding bridge is delivering low power, is investigated in figure 5.55. In this case as well the conditions for ZVS can be properly observed for the three windings.

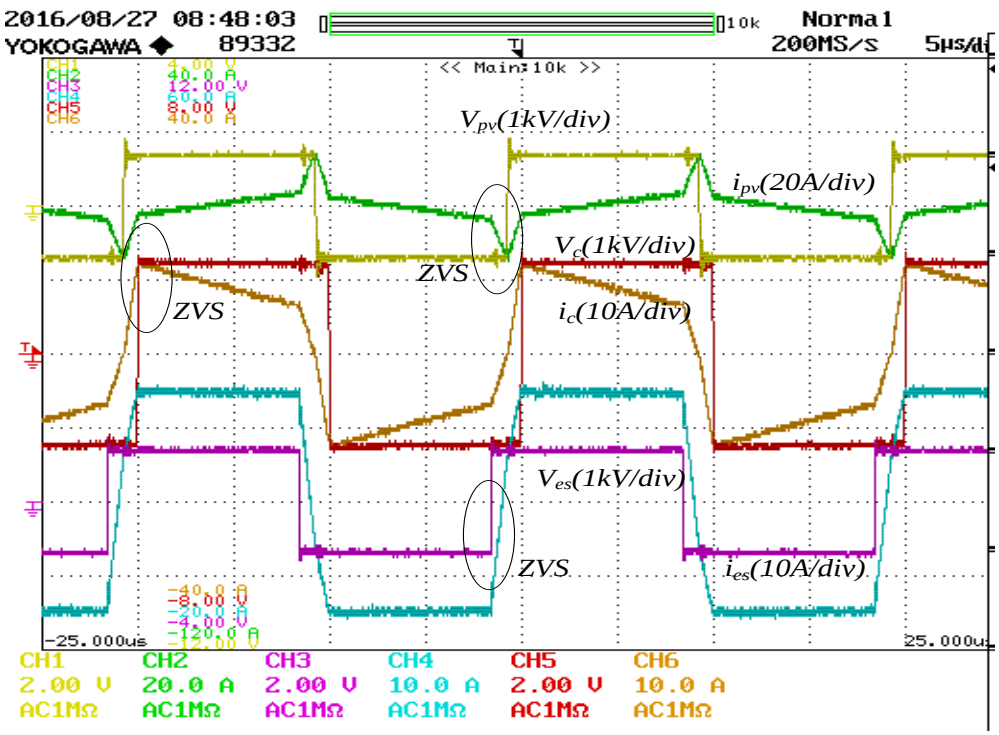

Figure 5.53. PV delivers 1.2kW, ES delivers 8.3kW and load takes 9.4kW.

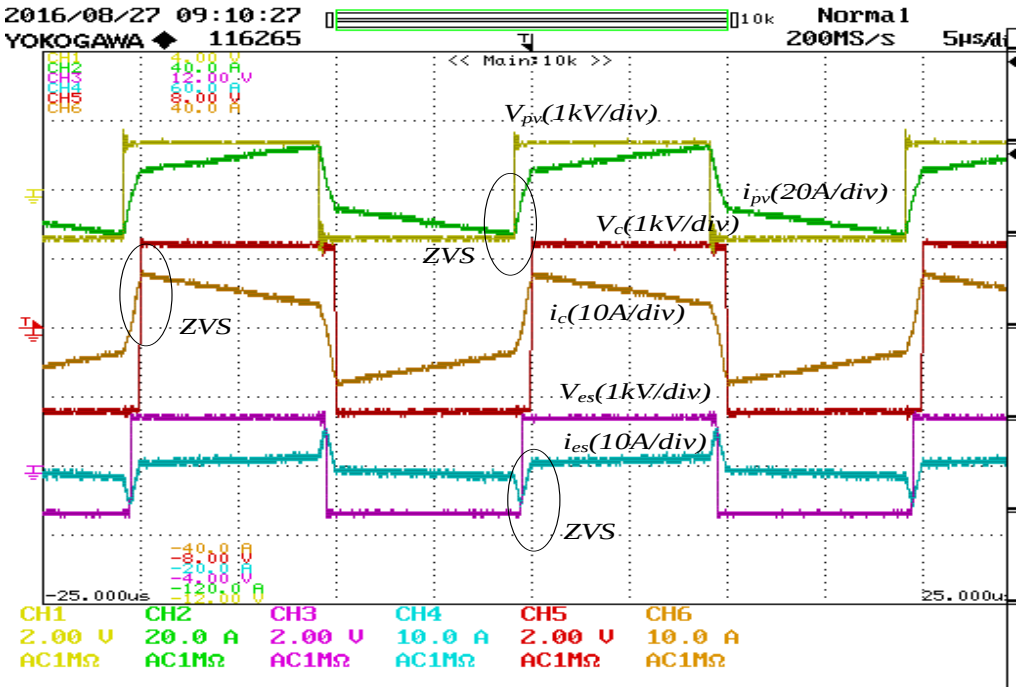

Figure 5.54. PV delivers 5.2kW, ES delivers 1.2kW and load takes 6.3kW.

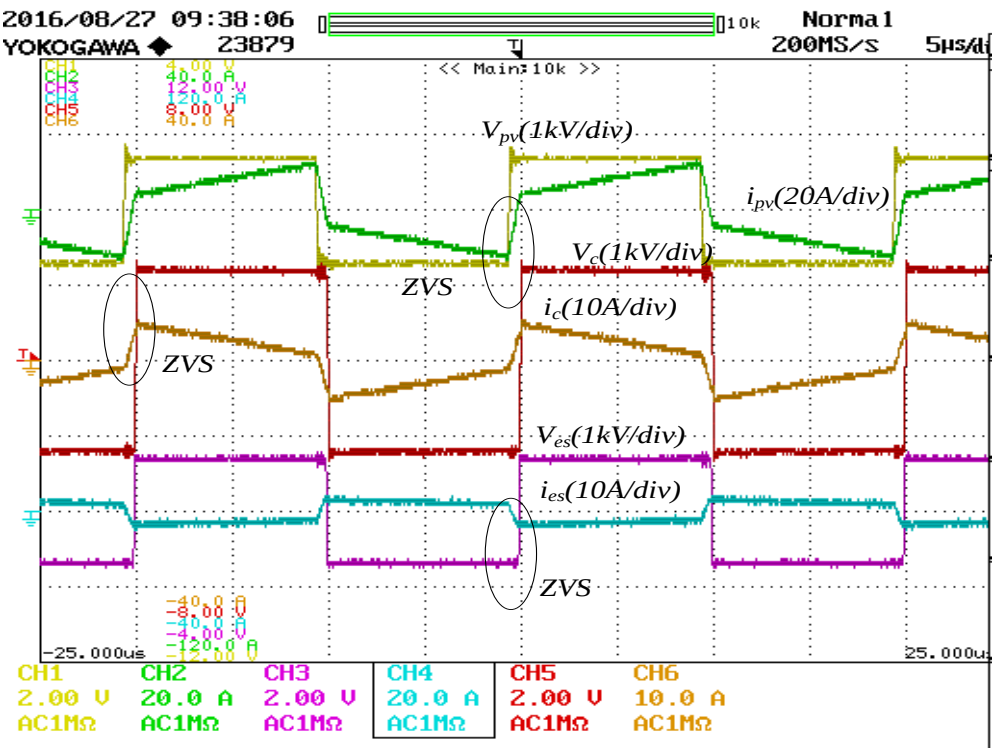

Figure 5.55. PV delivers 5kW, ES takes 1.6kW and load takes 3.3kW.

The efficiency of the three port converter for different operating conditions, is measured by measuring the total input and output power of the setup shown in figure 5.46. The total input and output power of the converter defined as follows.

$$P_{pv} = V_1 I_1 ,\ P_{es} = V_2 I_2 ,\ P_c = V_3 I_3$$

When ES is delivering power, then $P_{in} = P_{pv} + |P_{es}|$, $P_{out} = P_c$

And when ES is charging, then $P_{in} = P_{pv}$, $P_{out} = P_c + |P_{es}|$

The efficiency of the converter is defined as $\eta = P_{out} / P_{in}$, the efficiency plot of the converter system using split-type transformer & three limb transformer is shown below in figure 5.56. The data for efficiency calculation is measured for 5 minutes continuous run for each of the operating point. The peak efficiency has been found to be around 98.7%. The average efficiency of split-

winding transformer based dc-dc converter is around 1% higher than three limb three winding transformer based dc-dc converter of chapter 4.

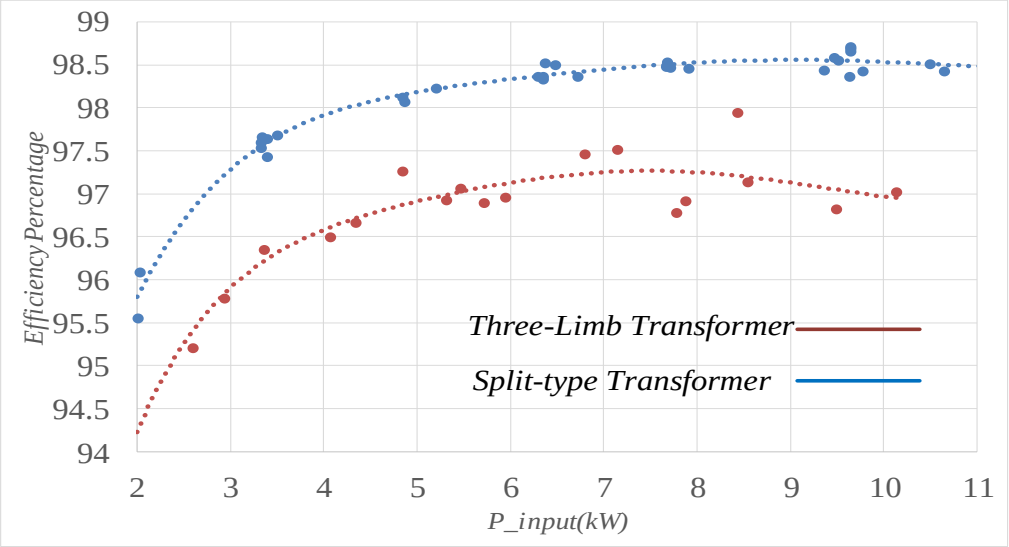

Figure 5.56. Efficiency Comparison for Split-Winding & Three Limb Transformer.

5.10. Conclusion

The proposed split-winding transformer for three port DAB converter has eliminated all the drawbacks of three limb three winding transformer. Using split-winding transformer provides a higher full ZVS range for the converter, higher efficiency and much suitable operation of the converter during 'one port idle' condition. The analytical and FEA model for estimating the leakage inductance and parasitic capacitance of split-winding transformer is quite close. The leakage inductance model varies within 10-15% while the parasitic capacitance model is quite close and the values are too small to comment on the magnitude of variation.

Chapter 6. Optimized Design For Three Port Ferrite Core Transformer

As discussed in chapter 5, the power flow capability of high frequency phase-shifted dc-dc converter depends on transformer leakage inductance and switching frequency. The design of multi-port transformer for three port converter system requires optimized volume and losses with required leakage inductance for rated power flow. Use of fast-switching SiC devices also demand low inter-winding parasitic capacitance for reduced common mode current. The work in this paper focuses on loss-volume optimized design of three port high frequency transformer integrating PV and Energy Storage(ES) based on leakage inductance and parasitic capacitance model. Two laboratory prototypes of 50kHz and 100kHz operating frequency have been designed to verify the actual transformer losses with estimated losses from the optimized design procedures.

6.1. Split-Winding Transformer and Equivalent Circuit

As per the discussion from chapter 5, the split-winding type transformer, for same core size and number of turns, offers higher efficiency than three winding three limb transformer of chapter 4. The split-winding transformer enabled three port phase shifted Triple Active Bridge(TAB) converter, integrating PV and Energy Storage(ES), is shown in figure 6.1, where the PV and ES windings are split into two portion on two limbs and connected together in series. The middle limb has the output winding, which can be designed for medium voltages for higher voltage applications. The work discussed in this paper, focuses on optimized design of split-

winding type three winding transformer based on analytical evaluation of leakage inductances, inter-winding parasitic capacitances and loss analysis.

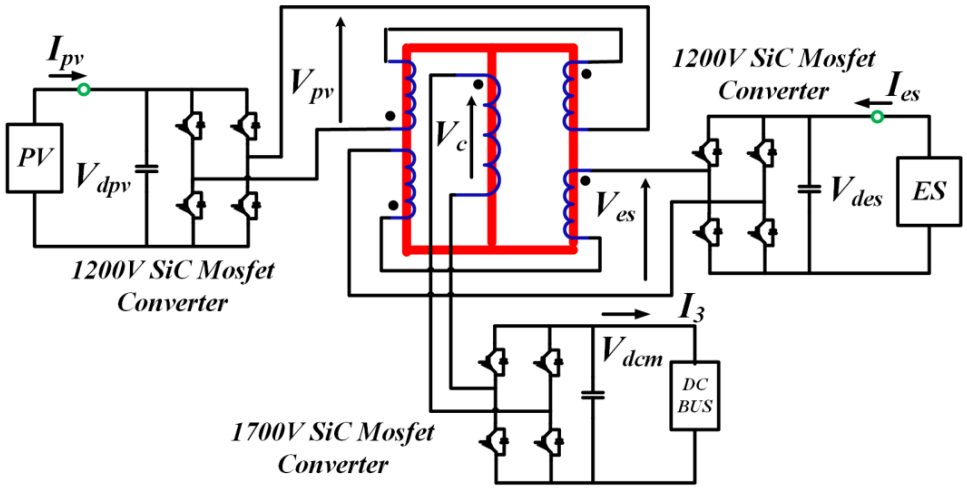

Figure 6.1. Triple Active Bridge(TAB) Converter with Split-Winding Type Three Port Transformer.

The split-winding transformer topology, shown in figure 6.1, has the PV and ES windings split into two parts and each part is placed on two side limbs and are connected in series. The middle limb has the third winding which is a higher voltage winding compared to PV and ES. In this thesis work, the PV and ES voltages are fixed at 800V, which is considered the rated voltage for PV and ES, and the middle winding voltage is rated at 1200V. The electrical equivalent circuit for the transformer of figure 6.1 has been derived in chapter 5 and is shown in figure 6.2. The power flow for Triple Active Bridge(TAB) converter is dependent upon phase shifts among the three winding voltages. Figure 6.3 shows a typical phase-shifted winding voltages' waveform for the TAB converter. The middle winding voltage V_c is the reference voltage and the PV and ES winding voltages V_{pv} and V_{es} are phase shifted w.r.t. V_c by angles ϕ_{pv} and ϕ_{es} respectively.

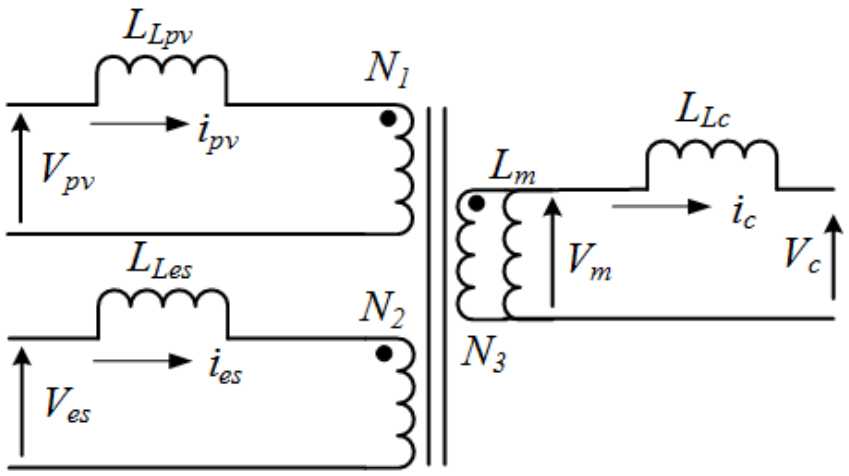

Figure 6.2. Electrical Equivalent Circuit of Split-Winding Transformer.

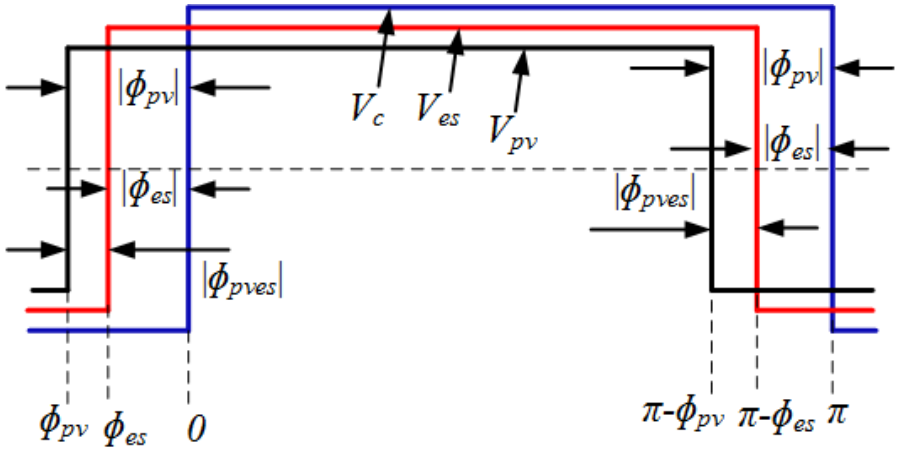

Figure 6.3. Three Port Transformer Winding Voltages.

The transformer winding currents for a TAB converter are piecewise linear in nature[56] and are functions of the phase shift angles ϕ_{pv} and ϕ_{es}. Since PV can only deliver power and Energy Storage can both charge and discharge, there are three possible scenarios for ϕ_{pv} and ϕ_{es}, (a) $\phi_{pv} > \phi_{es} > 0$, (b) $\phi_{es} > \phi_{pv} > 0$, and (c) $\phi_{pv} > 0 > \phi_{es}$. The expressions for the transformer's winding currents at different voltage transition instances(from figure 3) over a half cycle, are derived

using piecewise linear model of [56] and are given in equations (1)-(9), which are derived for the case of $\phi_{pv} < \phi_{es} < 0$, but the piecewise linear model of winding currents have same expressions for the other two cases as well.

$$i_{pv}(\phi_{pv}) = -V_{dpv}K_1^{pv}\pi + V_{des}{}^{pv}K_2^{pv}(\pi - 2|\phi_{pves}|) + V_{dcm}{}^{pv}K_3^{pv}(\pi - 2|\phi_{pv}|) \quad (6.1)$$

$$i_{pv}(\phi_{es}) = -V_{dpv}K_1^{pv}(\pi - 2|\phi_{pves}|) + V_{des}{}^{pv}K_2^{pv}\pi + V_{dcm}{}^{pv}K_3^{pv}(\pi - 2|\phi_{es}|) \quad (6.2)$$

$$i_{pv}(0) = -V_{dpv}K_1^{pv}(\pi - 2|\phi_{pv}|) + V_{des}{}^{pv}K_2^{pv}(\pi - 2|\phi_{es}|) + V_{dcm}{}^{pv}K_3^{pv}\pi \quad (6.3)$$

$$i_{es}(\phi_{pv}) = -V_{des}K_1^{es}(\pi - 2|\phi_{pves}|) + V_{dpv}{}^{es}K_2^{es}\pi + V_{dcm}{}^{es}K_3^{es}(\pi - 2|\phi_{pv}|) \quad (6.4)$$

$$i_{es}(\phi_{es}) = -V_{des}K_1^{es}\pi + V_{dpv}{}^{es}K_2^{es}(\pi - 2|\phi_{pves}|) + V_{dcm}{}^{es}K_3^{es}(\pi - 2|\phi_{es}|) \quad (6.5)$$

$$i_{es}(0) = -V_{des}K_1^{es}(\pi - 2|\phi_{es}|) + V_{dpv}{}^{es}K_2^{es}(\pi - 2|\phi_{pv}|) + V_{dcm}{}^{es}K_3^{es}\pi \quad (6.6)$$

$$i_c(\phi_{pv}) = V_{dcm}K_1^{c}(\pi - 2|\phi_{pv}|) - V_{dpv}{}^{c}K_2^{c}\pi - V_{des}{}^{c}K_3^{c}(\pi - 2|\phi_{pves}|) \quad (6.7)$$

$$i_c(\phi_{es}) = V_{dcm}K_1^{c}(\pi - 2|\phi_{es}|) - V_{dpv}{}^{c}K_2^{c}(\pi - 2|\phi_{pves}|) - V_{des}{}^{c}K_3^{es}\pi \quad (6.8)$$

$$i_c(0) = V_{dcm}K_1^{c}\pi - V_{dpv}{}^{c}K_2^{c}(\pi - 2|\phi_{pv}|) - V_{des}{}^{c}K_3^{es}(\pi - 2|\phi_{es}|) \quad (6.9)$$

The average current over a piecewise linear model is given as follows in (6.10-6.12).

$$i_{pv}(\theta) = i_{pv}(0) + \frac{1}{\omega L_{pv}}\int_0^{\theta}(V_{pv} - V_m)d\theta \quad (6.10), \qquad i_{es}(\theta) = i_{es}(0) + \frac{1}{\omega L_{es}}\int_0^{\theta}(V_{es} - V_m)d\theta \quad (6.11)$$

$$i_c(\theta) = i_c(0) + \frac{1}{\omega L_c}\int_0^{\theta}(V_m - V_c)d\theta \quad (6.12)$$

The constant parameters K_i^{pv}, K_i^{es}, K_i^{c} of equations (6.1-6.9) are functions of the slopes for the piecewise -linear model of winding currents(explained in chapter 8), which can be expressed as functions of leakage and magnetizing inductances L_{Lpv}, L_{Les}, L_{Lc} and L_m. The voltage V_m

across the magnetizing inductance L_m is given in)equation (6.13) where L_n^3 is given in equation (6.14), where the PV and ES winding voltages and inductances are referred to output side winding.

$$V_m = \frac{V_{pv}{}' L_{Les}{}' L_{Lc} + V_{es}{}' L_{Lpv}{}' L_{Lc} + V_c L_{Lpv}{}' L_{Les}{}' L_m}{L_n{}^3} \quad (6.13)$$

$$L_n{}^3 = L_{Lpv}{}' L_{Les}{}' L_{Lc} + L_{Lpv}{}' L_{Les}{}' L_m + L_{Lpv}{}' L_{Lc} L_m + L_{Les}{}' L_{Lc} L_m \quad (6.14)$$

The instantaneous currents and magnetizing voltage equations represented above are used in this chapter to derive the copper loss and core loss model for the split-winding type transformer in this paper.

6.2. Core Loss Modelling for Three Port Transformer

The core loss for three port transformer is derived here using iGSE method[83] as a function of operating phase shift angles ϕ_{pv} and ϕ_{es}. For the three port transformer of figure 6.2, the voltage V_m depends on the polarity of each of the three winding voltages, which are dependent on the following three cases, (a) $\phi_{pv} > \phi_{es} > 0$, (b) $\phi_{es} > \phi_{pv} > 0$, and (c) $\phi_{pv} > 0 > \phi_{es}$. The voltage V_m is a non-linear discontinuous function of ϕ_{pv} and ϕ_{es} over a cycle, however each half cycle can be divided into three linear continuous sub intervals, which are defined by ϕ_{pv} and ϕ_{es}. As per the iGSE method, the expression for core loss per unit volume, between any two instants γ_1 and γ_2 is given in equation 6.15. The $\frac{dB}{dt}$ and ΔB are calculated for each of the continuous

linear interval between 0 to π based on the operating phase shift angle values. The core loss per unit volume for each of the three cases mentioned above are given in equations (6.16)-(6.18).

$$P_v(\gamma_1,\gamma_2)=\frac{1}{\pi}\int_{\gamma_1}^{\gamma_2} k_i\left|\frac{dB}{dt}\right|^{\alpha}(\Delta B)^{\beta-\alpha}\,d\theta \quad (6.15)$$

$Case1:\phi_{pv}>\phi_{es}>0$

$$P_{core}=P_v(0,\pi-|\phi_{pv}|)+P_v(\pi-|\phi_{pv}|,\pi-|\phi_{es}|)+P_v(\pi-|\phi_{es}|,\pi) \quad (6.16)$$

$Case2:\phi_{es}>\phi_{pv}>0$

$$P_{core}=P_v(0,\pi-|\phi_{es}|)+P_v(\pi-|\phi_{es}|,\pi-|\phi_{pv}|)+P_v(\pi-|\phi_{pv}|,\pi) \quad (6.17)$$

$Case3:\phi_{pv}>0>\phi_{es}$

$$P_{core}=P_v(0,|\phi_{es}|)+P_v(|\phi_{es}|,\pi-|\phi_{pv}|)+P_v(\pi-|\phi_{pv}|,\pi) \quad (6.18)$$

6.3. Copper Loss Modelling for Three Port Transformer

The copper losses for the three port transformer, using litz wire, is derived here using the ac resistance modelling method presented in [84]. The ac resistance model presented in [84] is a frequency dependent model, which provides estimation of copper losses for higher harmonics. The instantaneous winding current expressions have been presented in the above sections, which are used to derive the winding rms currents for all the odd harmonics. In this section, only upto 7^{th} harmonic components of winding currents are considered for copper loss calculation. The total copper loss for the three windings are represented in (6.19),where I_{kn} is the fourier coefficient for n^{th} harmonic component of k^{th} winding current, R_{kdc} is the dc resistance for k^{th} winding and $FR_{kn,ac}$ is the ac resistance factor for n^{th} harmonic of k^{th} winding current.

$$P_{cu} = \frac{1}{2}\sum_{k=1}^{3}(\sum_{n=1}^{7} {I_{kn}}^2 R_{k,dc} FR_{kn,ac}) \quad (6.19) \qquad R_{k,dc} = \frac{4\rho_{cu} N (MLT)}{k\pi {d_{str}}^2 N_{str}} \quad (6.20)$$

$$FR_{kn,ac} = A\frac{\sinh(2A)+\sin(2A)}{\cosh(2A)-\cos(2A)} + \frac{1.9(m^2-1)}{3} A\frac{\sinh(A)-\sin(A)}{\cosh(A)+\cos(A)} \quad (6.21)$$

where N is number of turns on winding portion, MLT is the mean length of turn, ρ_{cu} is copper resistivity, d_{str} and N_{str} are the diameter and number of strands in the wire, k is the packing factor of litz wire, taken as 0.5, and m is defined as $m = N_l\sqrt{k}$ where N_l is the number of winding layers. The factor A is defined as $A = (\frac{\pi}{4})^{0.75}(d_{str}/\delta_w)\sqrt{\eta}$, where η (porosity factor) is taken as 0.9. The skin depth factor for litz strand δ_w is defined as $\delta_w = \sqrt{\rho_{cu}/(\pi\mu_0 nf)}$, which is a function of harmonic frequency nf. Harmonic components of each winding current is derived using the fourier coefficients as shown below in equation (6.22).

$${I_{kn}}^2 = \frac{4}{\pi^2}[(\int_0^{\pi} i(\theta)\cos(n\theta)d\theta)^2 + (\int_0^{\pi} i(\theta)\sin(n\theta)d\theta)^2] \quad (6.22)$$

6.4. Optimized Design and Discussions for Three Port Transformer

6.4.1. Genetic Algorithm Based Optimization Procedure

A Genetic Algorithm based optimization procedure using MATLAB's in-built Genetic Algorithm approach is followed here. The design flow for the optimization is shown in figure 6.5. A brief summary of the optimization process is described below. The middle winding parameters are suffixed with 3 and PV and ES winding parameters are suffixed with 1 and 2 respectively.

1. As an input to the optimization procedure for high frequency three port split-winding transformer, the voltage levels for different windings, operating frequency and power ratings are selected. In this paper, kVA rating for each port is taken as 1.4 times of maximum active power transfer rating, in order to account for the reactive power associated with transformer active power flow. Ferrite material of grade 3C97 is selected as the core material and corresponding steinmetz parameters K, α, β are derived from ferrite 3C97 material loss data curve.
2. A set of free variable or parameters are chosen for this design which are maximum operating flux density B_m, maximum current density J, number of layers on middle winding l_3, core depth D_c and number of turns in each layers N_{l1}, N_{l2}, N_{l3}.
3. The middle limb core cross-sectional area A_3 is calculated from voltage relation $V=4N_{l3}l_3fB_m$. The core width T_m is derived from core size and side limb width T_c are taken as half of middle limb width. The number of turns for each split-section of PV and ES winding are calculated by equating the volts per turn of each winding with middle winding.
4. The max current for each port is derived from rms voltage of the port and max kVA rating. In this paper, switching frequencies of the range 50kHz to 100kHz are considered, for which litz wire based design is considered. The number of strands for litz wire is calculated from $N_{str} = 4I_{rms} / (J\pi d_{str}^{\,2})$. For switching frequencies of 50kHz and 100kHz, strand sizes of 38AWG and 40AWG are considered.
5. After core cross-section size and number of strands are calculated, litz wire conductor sizes are determined with a packing factor of 0.5. The winding dimensions are calculated from number of turns per layer and number of layers. The window dimensions and core

dimensions are calculated next from the winding size and core sizes referring to figure 6.4. A minimum gap of 2mm is taken as clearance between inter-windings and between core to winding. Once the core, window and winding dimensions are determined, the leakage inductances and inter-winding parasitic capacitances are determined as explained in previous section.

6. Once the leakage and parasitic capacitances are calculated, a check for limiting values of parasitic capacitances and operating phase angles ϕ_{pv} and ϕ_{es} are considered. A limiting value of 50pF is taken for parasitic capacitances and extreme case operating phase angle limits are taken at $\pm\frac{\pi}{3}$, as shown in the optimization loop in figure 6.5. If the calculated values of phase angles and parasitic capacitances exceed their corresponding set limit, the solution is rejected for that set of free variables. However, if the calculated values of phase angles and parasitic capacitances are within limit, the derived solution for that particular set of free variables is considered acceptable and the corresponding transformer losses & transformer volumes are calculated and stored. The GA algorithm then considers the next set of free variables for optimization. The GA algorithm considers a population size of 200, generation size of 400 and pareto fraction of 0.85.

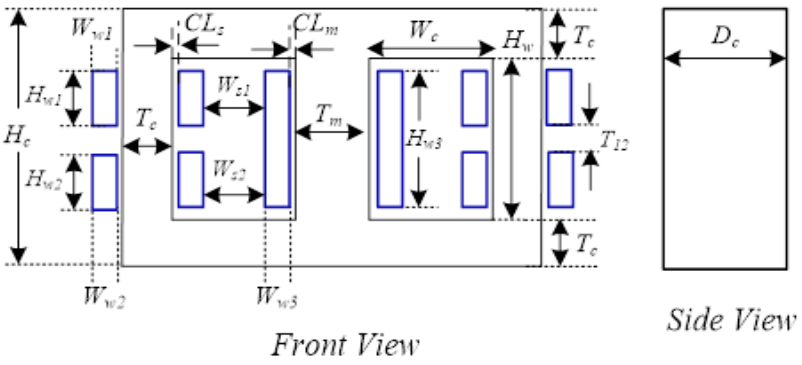

Figure 6.4. Transformer Dimensions.

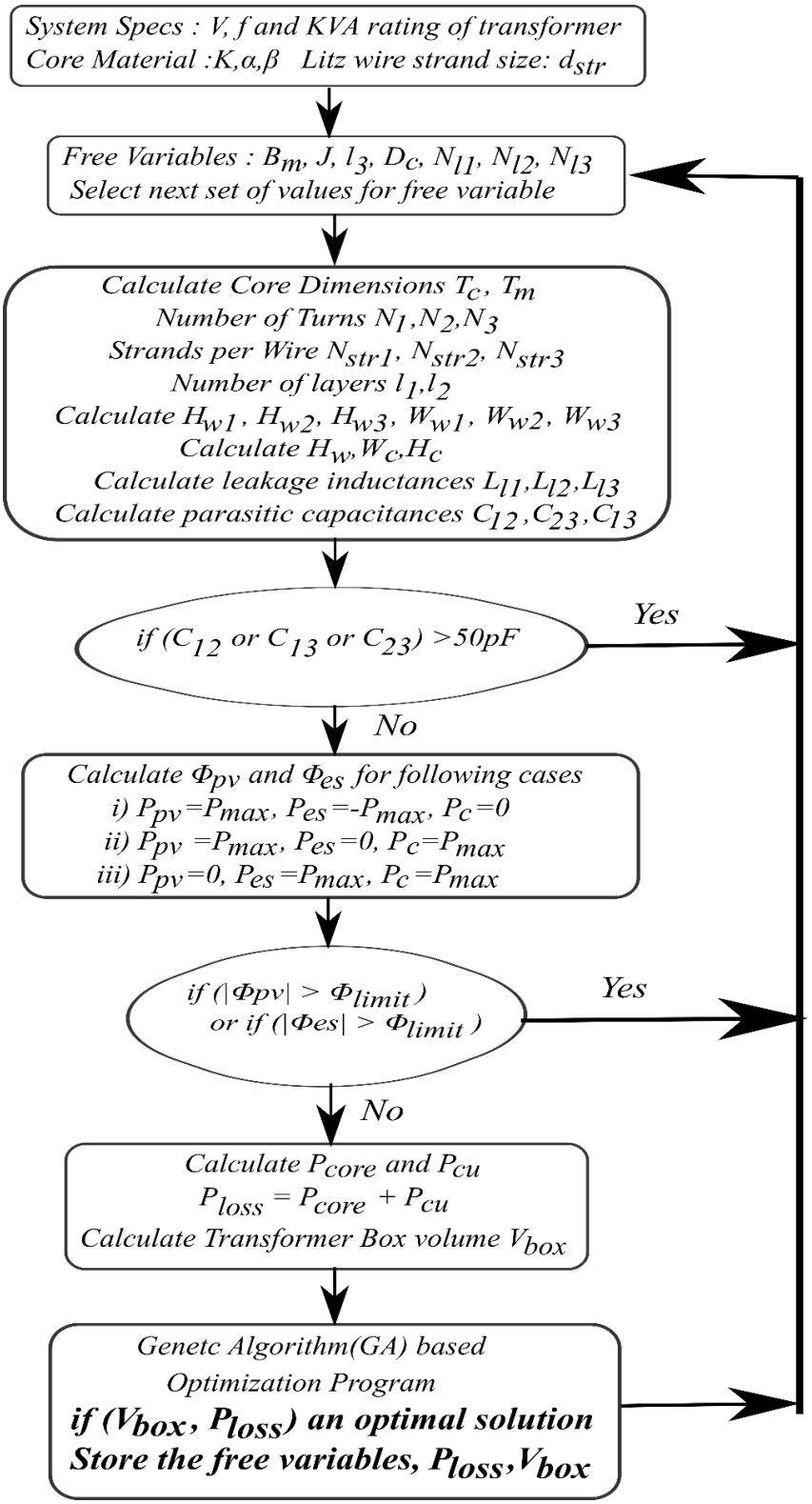

Figure 6.5. Optimization Flow for Transformer Design.

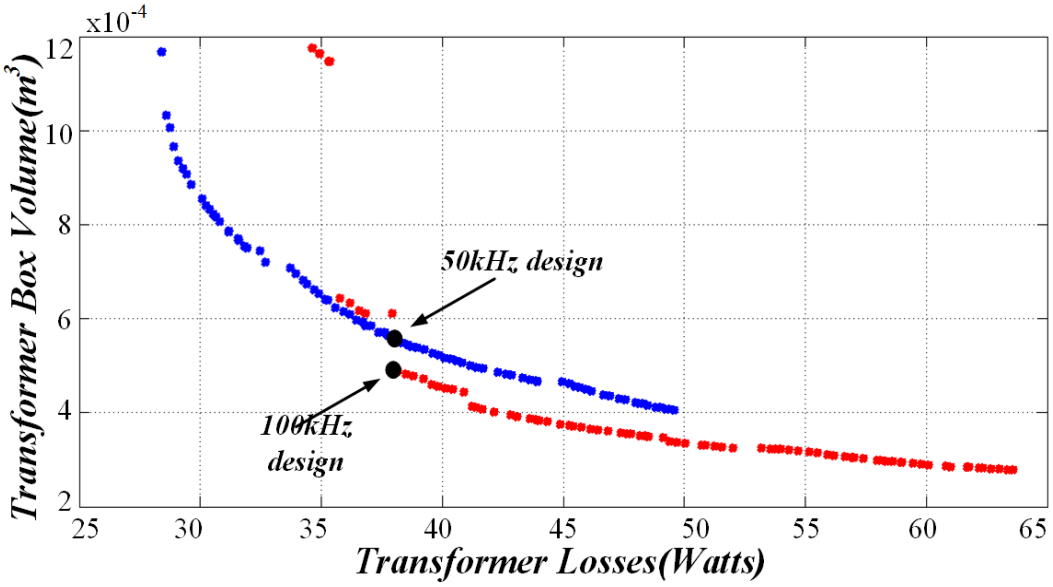

Figure 6.6. Pareto Front Design Plots for 50kHz and 100kHz Designs.

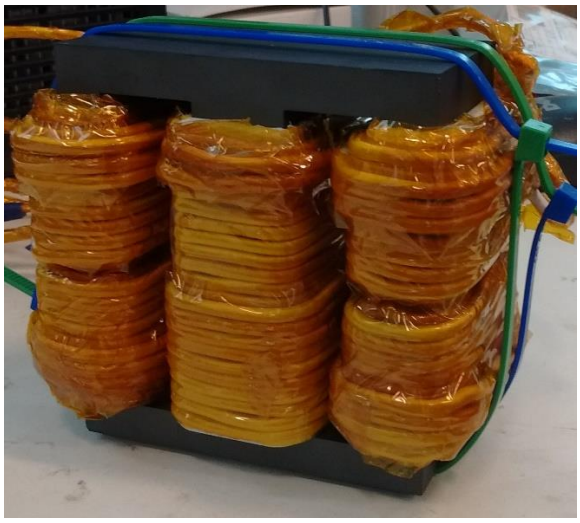

Figure 6.7. 50kHz Transformer.

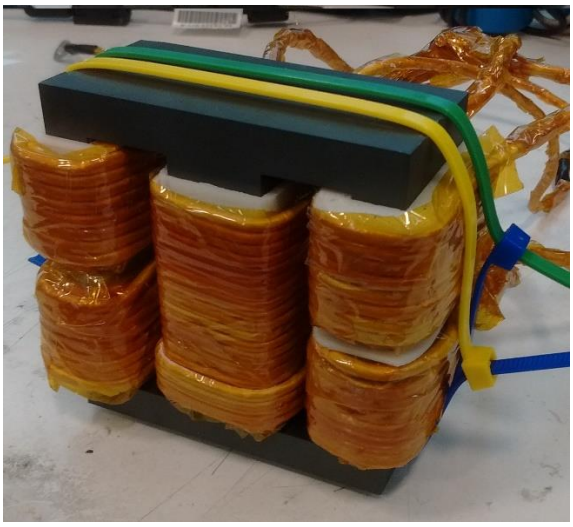

Figure 6.8. 100kHz Transformer.

The design of three port transformer is carried out using the aforementioned optimization process for ferrite based three port transformer design for 10kW active power transfer rating for each port at 50kHz and 100kHz operating frequencies. The rated PV and ES port voltages are 800V and the output middle port has rated voltage of 1200V. In figure 6.6, the pareto front loss-

volume optimized design plots, which are outputs of the optimization process, are shown for 50kHz(blue) and 100kHz(red) designs. The optimized plots provide several locally optimized designs over the range. The pareto front provides two extremes where some designs have low loss & high volume and some designs have high loss & low volume. From practical considerations, some designs are considered optimum designs, which do not have very high losses and the volume is also not high are considered feasible solutions. These optimum designs are in between the two extremes of the pareto front of figure 6.6. The two specific designs for 50kHz and 100kHz are selected near the bend portion of the pareto fronts of figure 6.6, both having equal weighted losses. Two laboratory prototype transformers are built from the design specs of the two above selected designs of figure 6.6. The designed transformer prototypes are shown in figure 6.7-6.8. The transformer parameters for these two transformers are listed in table 11 and the leakage and parasitic capacitances from theoretical, FEA and measured values are shown in tables 12 and 13.

Table 11. Designed Transformer Details

Operating Frequency	50kHz	100kHz
Operating Max. Flux Density	0.22	0.15
Number of Turns for each split PV Winding Portion	22	16
Number of Turns for each split ES Winding Portion	22	16
Number of Turns for Middle Winding	33	24
Magnetizing Inductance(from middle port)	9.17mH	3.4mH
Litz Wire no. of strands for PV & ES Port Winding	420	700
Litz Wire no. of strands for Middle Port Winding	280	435

Table 12. Inductance & Capacitance for 50kHz Designed Transformers

	Analytical	FEA	Measured
L_{Lpv}	88µH	85µH	80µH
L_{Les}	88µH	85µH	105µH
L_{Lc}	124µH	138µH	150µH
$C_{pv\text{-}es}$	20pF	20pF	17pF
$C_{pv\text{-}middle}$	24pF	24pF	26pF
$C_{es\text{-}middle}$	24pF	24pF	22pF

Table 13. Inductance & Capacitance for 100kHz Designed Transformers

	Analytical	FEA	Measured
L_{Lpv}	44µH	40µH	39µH
L_{Les}	44µH	40µH	47µH
L_{Lc}	72µH	80µH	85µH
$C_{pv\text{-}es}$	16pF	16pF	14pF
$C_{pv\text{-}middle}$	22pF	22pF	23pF
$C_{es\text{-}middle}$	22pF	22pF	20pF

6.5. Experimental Study and Loss Analysis

The prototype transformers designed as per the optimization procedures discussed above, are tested for determining performances and efficiency. A 10kW rated laboratory prototype of triple active bridge converter of figure 6.1, is developed using SiC Mosfets. The PV and ES side rated voltages are 800V each, therefore 1200V SiC Mosfets C2M0040120D are used for PV and ES port H-bridges. The output port connected to the middle winding of the three port transformer is rated at 1200V, for which 1700V SiC Mosfets C2M0045170D are used. For experimental purpose, the output port of 1200V is fed to a resistive dc load bank and the output voltage is maintained at 1200V by adjusting phase shift angles. Figures 6.10 and 6.11 show the steady state transformer winding voltage and current waveforms for the 50kHz and 100kHz design prototypes, at 10kW PV power and 9kW output load power, while the ES port takes 1kW charging power. The waveforms are captured using 100MHz bandwidth voltage probes and

120MHz bandwidth current transducers. From the figures 6.10 & 6.11 confirm that the steady state voltage and current waveforms for the transformers are devoid of any higher frequency ringing due to parasitic capacitance effects. The efficiency for the whole converter system is derived from the total dc output power and total dc input power of the three port converter. If ES is charging, then $P_{out} = P_{middle} + P_{es}$ and $P_{in} = P_{pv}$. When ES is discharging then $P_{in} = P_{pv} + P_{es}$ and $P_{out} = P_{middle}$. The efficiency is defined as $\eta = \frac{P_{out}}{P_{in}}$. The whole converter system efficiency plots, using 50kHz and 100kHz prototypes are shown in figure 6.12.

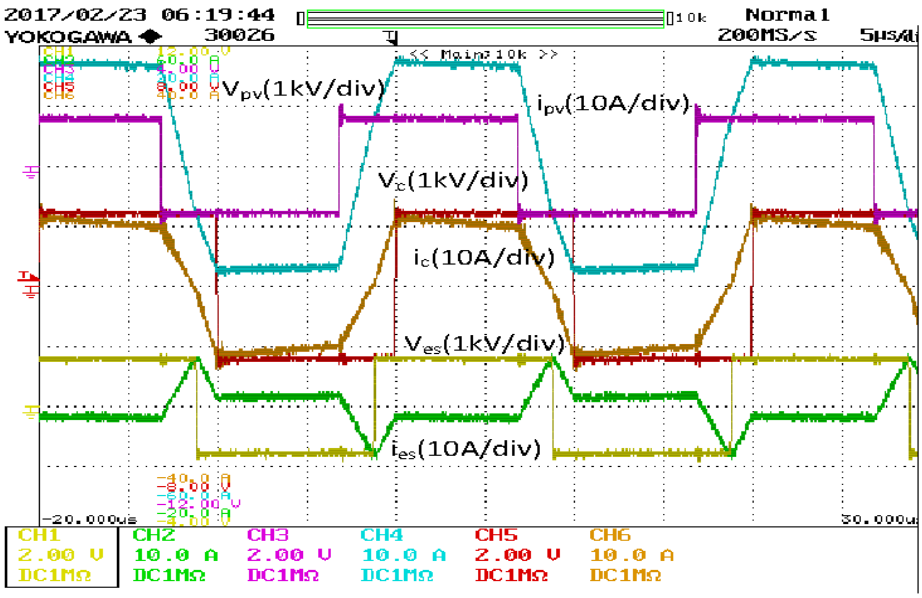

Figure 6.9. Transformer Waveforms for 50kHz Prototype.

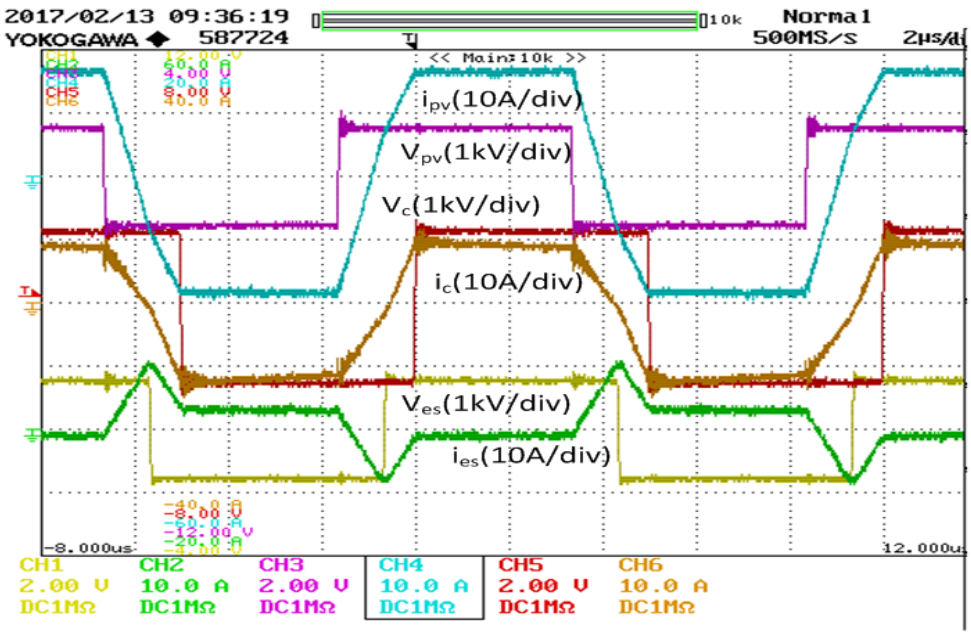

Figure 6.10. Transformer Waveforms for 100kHz Prototype.

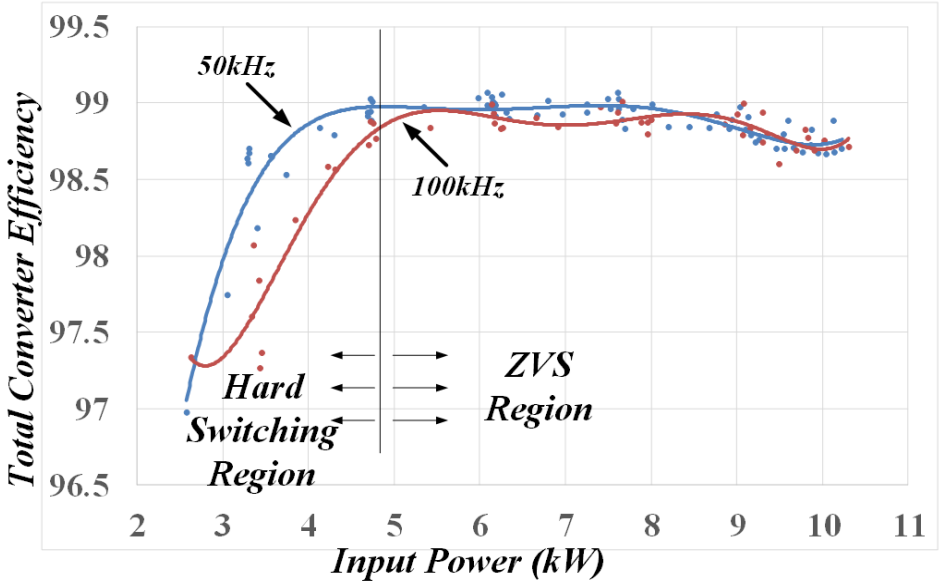

Figure 6.11. Converter Efficiency over Operating Range.

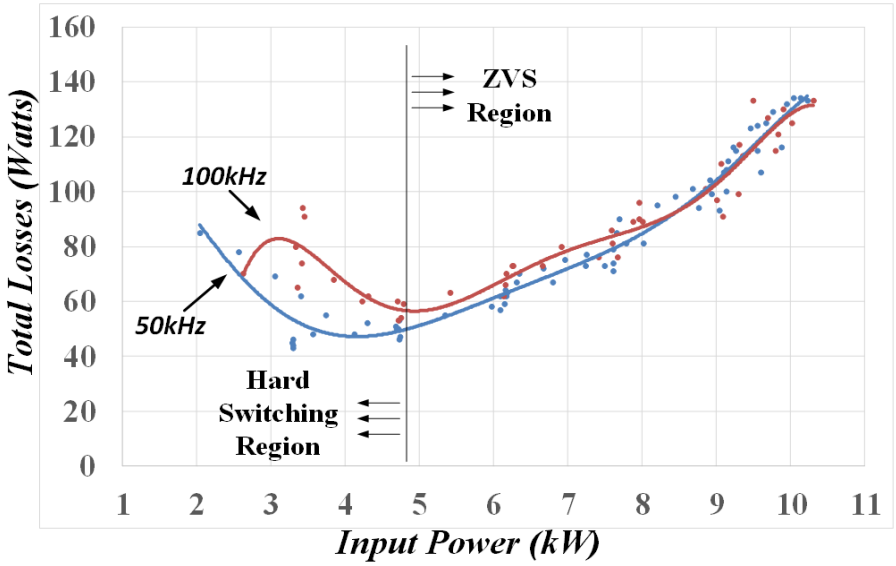

Figure 6.12. Total Converter Losses over Operating Range.

The efficiency plot from figure 6.12, shows that both the designs at 50kHz and 100kHz provide high efficiency around 98.5% to 99% from 5kW to 10kW operating power range. It can be observed that below 5kW region, the efficiency starts falling sharply, which is due to the rise in switching loss resulting from loss of ZVS due to low current in transformer winding and resulting hard switching. For proper ZVS operation, significant line current is required to discharge the MOSFET output capacitance, which is absent during low current operating region, causing hard switching of MOSFETs at high switching frequencies. In order to visualize the losses, the system losses are plotted in figure 6.12, showing the significant increase in losses in the hard switching region. The losses in ZVS region are dominated by MOSFET conduction losses and transformer losses. The transformer losses in ZVS region can thus be estimated by subtracting the MOSFET conduction losses from total losses, $P_{loss,transformer} = P_{loss,total} - P_{MOSFET}$. The MOSFET conduction losses in ZVS region are estimated from PLECS simulation. The temperature dependent PLECS models of the 1200V and 1700V SiC Mosfets, along with the

thermal characteristics for heat sink and thermal pads are incorporated into the PLECS simulation. The PLECS model thus can closely predict the on-state resistance of MOSFET for the particular operating condition and provide closely accurate conduction losses. The transformer losses are thus obtained from subtracting the MOSFET conduction losses from the measured losses, and are now matched with theoretical transformer losses(core loss + copper loss) in figure 6.14. The theoretical transformer losses are derived from the core loss model and copper loss model defined in section 2. Higher order polynomial based trend lines are used to curve fit the different estimated losses and theoretical losses in figure 6.14. There are differences of 5W-15W between the estimated losses and the theoretical losses, which can be attributed to several stray losses in the hardware prototype and in addition to that, ZVS operation of MOSFETs also have some losses which are not considered here. Overall, the pattern of the estimated losses and theoretical losses are similar to each other, increasing over the power range, indicating that the losses are mostly dominated by current.

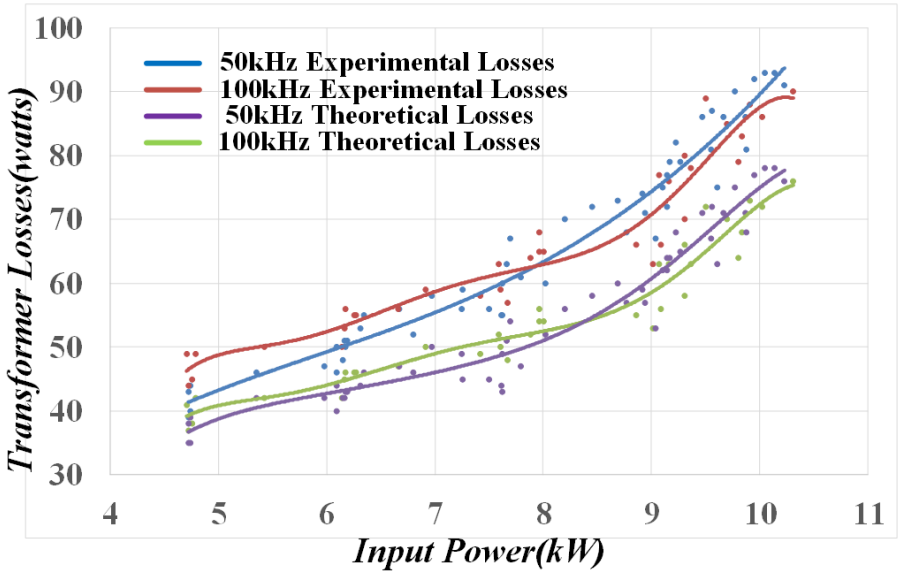

Figure 6.13. Estimated and Theoretical Transformer Losses over ZVS Range.

The transformer design method, for phase shifted converter, using leakage model has provided close experimental results compared to theoretical results. The average leakage model is within 10% to 15% accuracy and the parasitic capacitance model based on equi-potential core and windings also provide close estimation for inter-winding parasitic capacitances. The GA based optimization procedure, using the transformer volume and weighted average loss as objective functions, has proven to provide good optimal designs, as the experimental efficiencies for the converters are around 98.7% to 99% for the half load to full load power range.

6.6. Three Port Phase Shifted Converter Analysis for Quasi-Square Wave Winding Voltages

6.6.1. Harmonic Model Based Winding Currents & Average Power for Three Port Transformer

In this section, analysis for operation of three port phase shifted Triple Active Bridge(TAB) converter using quasi-square wave voltages or square wave voltages with zero voltage duration, is presented. In this section, a reduced model of the equivalent circuit is used, which is obtained by considering the magnetizing inductance $L_m >> L_{L1}, L_{L2}, L_{L3}$ and converting the star connection of leakage inductances into a delta connection as shown in figure 6.15. The equivalent inductances of delta connection can be obtained by converting the leakage inductances in delta form. A typical transformer winding voltages and currents waveform for quasi-square wave voltage operation is shown in figure 6.16.

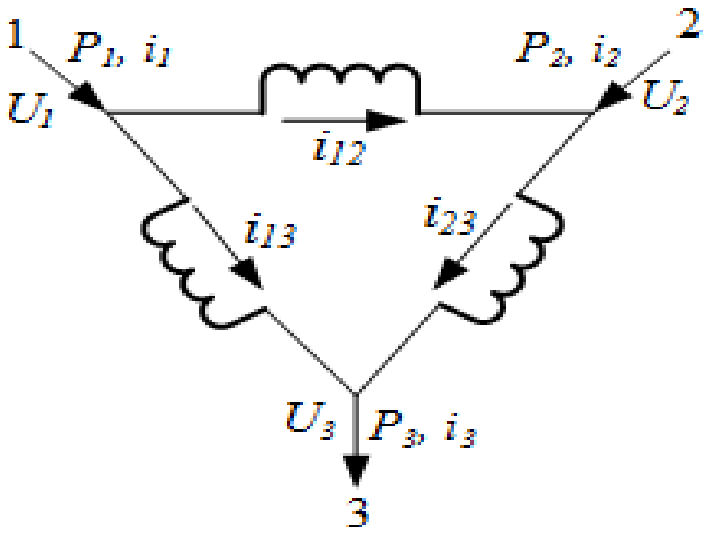

Figure 6.14. Equivalent Circuit of Delta Connected.

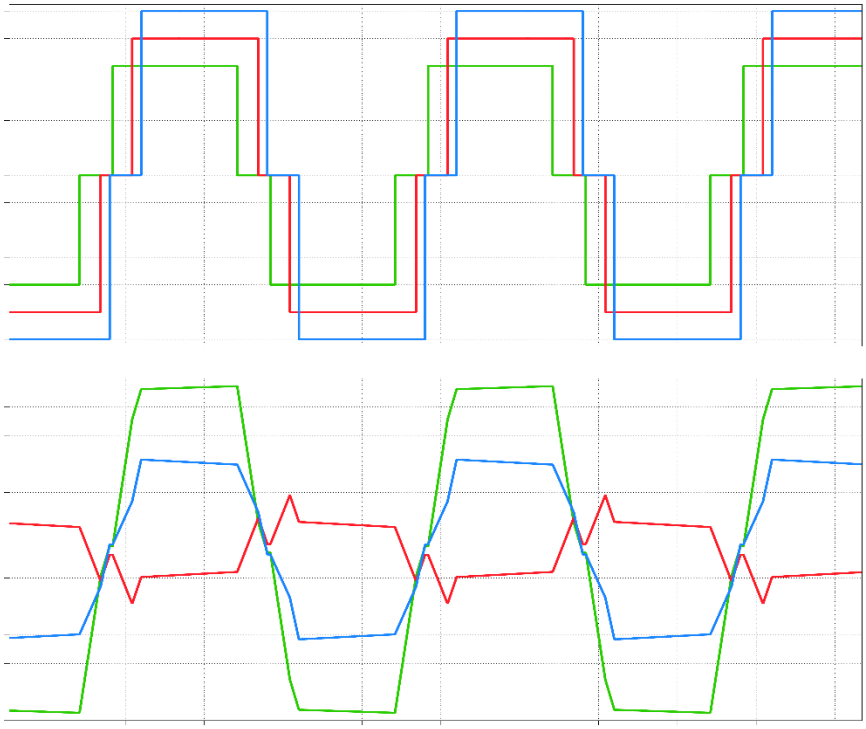

Figure 6.15. Transformer Winding Voltages and Currents.

The winding voltage expressions using harmonic models for each port with quasi-square voltage waveforms are given in equations (6.23)-(6.25). The three winding currents are derived

here using the winding voltage harmonics. The harmonic current vector expressions for any harmonic component 'n', using the voltage vectors, are shown in equations (6.26)-(6.28). The active power flow expressions for each port are derived over a switching cycle and are expressed in (6.29)-(6.31). The current expressions in vector form are derived in terms of different parameters, and are given in equations(6.32)-(6.34). The RMS current expressions are shown in equations (6.35)-(6.37).

$$u_1(\omega t)=\sum_{n=1}^{7}\frac{4V_{dc1}}{n\pi}\sin(\frac{nD_1\pi}{2})\sin(n\omega t+n\phi_1)=\sum_{n=1}^{7}\sqrt{(2)}U_{1n}\sin(n\omega t+n\phi_1) \quad (6.23)$$

$$u_2(\omega t)=\sum_{n=1}^{7}\frac{4V_{dc2}}{n\pi}\sin(\frac{nD_2\pi}{2})\sin(n\omega t+n\phi_2)=\sum_{n=1}^{7}\sqrt{(2)}U_{2n}\sin(n\omega t+n\phi_2) \quad (6.24)$$

$$u_3(\omega t)=\sum_{n=1}^{7}\frac{4V_{dc3}}{n\pi}\sin(\frac{nD_3\pi}{2})\sin(n\omega t)=\sum_{n=1}^{7}\sqrt{(2)}U_{3n}\sin(n\omega t) \quad (6.25)$$

$$I_{1n}=\frac{U_{1n}\angle n\phi_1-U_{2n}\angle n\phi_2}{n\omega L_{12}}+\frac{U_{1n}\angle n\phi_1-U_{3n}\angle 0}{n\omega L_{13}} \quad (6.26)$$

$$I_{2n}=\frac{U_{2n}\angle n\phi_2-U_{1n}\angle n\phi_1}{n\omega L_{12}}+\frac{U_{2n}\angle n\phi_2-U_{3n}\angle 0}{n\omega L_{23}} \quad (6.27)$$

$$I_{3n}=\frac{U_{1n}\angle n\phi_1-U_{3n}\angle 0}{n\omega L_{13}}+\frac{U_{2n}\angle n\phi_2-U_{3n}\angle 0}{n\omega L_{23}} \quad (6.28)$$

$$P_1=\sum_{n=1}^{7}(\frac{U_{1n}U_{2n}\sin n\phi_{12}}{n\omega L_{12}}+\frac{U_{1n}U_{3n}\sin n\phi_{13}}{n\omega L_{13}}) \quad (6.29)$$

$$P_2=\sum_{n=1}^{7}(-\frac{U_{1n}U_{2n}\sin n\phi_{12}}{n\omega L_{12}}+\frac{U_{2n}U_{3n}\sin n\phi_{23}}{n\omega L_{23}}) \quad (6.30)$$

$$P_3=\sum_{n=1}^{7}(\frac{U_{1n}U_{3n}\sin n\phi_{13}}{n\omega L_{13}}+\frac{U_{2n}U_{3n}\sin n\phi_{23}}{n\omega L_{23}}) \quad (6.31)$$

$$I_{1n} = [\frac{U_{1n}\sin(n\phi_1)}{n\omega L_{13}} + \frac{U_{1n}\sin(n\phi_1)}{n\omega L_{12}} - \frac{U_{2n}\sin(n\phi_2)}{n\omega L_{12}}]$$
$$+ j[\frac{U_{3n}}{n\omega L_{13}} + \frac{U_{2n}\cos(n\phi_2)}{n\omega L_{12}} - \frac{U_{1n}\cos(n\phi_1)}{n\omega L_{12}} - \frac{U_{1n}\cos(n\phi_1)}{n\omega L_{13}}] \quad (6.32)$$
$$= A_{1n} + jB_{1n}$$

$$I_{2n} = [\frac{U_{2n}\sin(n\phi_2)}{n\omega L_{12}} + \frac{U_{2n}\sin(n\phi_2)}{n\omega L_{23}} - \frac{U_{1n}\sin(n\phi_1)}{n\omega L_{12}}]$$
$$+ j[\frac{U_{3n}}{n\omega L_{23}} + \frac{U_{1n}\cos(n\phi_1)}{n\omega L_{12}} - \frac{U_{2n}\cos(n\phi_2)}{n\omega L_{12}} - \frac{U_{2n}\cos(n\phi_2)}{n\omega L_{23}}] \quad (6.33)$$
$$= A_{2n} + jB_{2n}$$

$$I_{3n} = [\frac{U_{1n}\sin(n\phi_1)}{n\omega L_{13}} + \frac{U_{2n}\sin(n\phi_2)}{n\omega L_{23}}]$$
$$+ j[\frac{U_{3n}}{n\omega L_{13}} + \frac{U_{3n}}{n\omega L_{23}} - \frac{U_{1n}\cos(n\phi_1)}{n\omega L_{13}} - \frac{U_{2n}\cos(n\phi_2)}{n\omega L_{23}}] \quad (6.34)$$
$$= A_{3n} + jB_{3n}$$

$$I_{1,rms}^2 = \sum_{n=1}^{7} (A_{1n}{}^2 + B_{1n}{}^2) \quad (6.35)$$

$$I_{2,rms}^2 = \sum_{n=1}^{7} (A_{2n}{}^2 + B_{2n}{}^2) \quad (6.36)$$

$$I_{3,rms}^2 = \sum_{n=1}^{7} (A_{3n}{}^2 + B_{3n}{}^2) \quad (6.37)$$

6.6.2. Core Loss Derivation for Quasi-Square Wave Voltage Waveform

The core loss for three port transformer is derived here using the steinmetz equation for core loss. An approximate approach of core loss considering the fundamental component of core flux is considered here. The core flux induced in the transformer core is a function of the voltage V_m

induced across the magnetizing inductance L_m of the equivalent circuit of figure 6.2. The expression of V_m is given in equation (6.44).

$$V_m = [\frac{u_1}{K_1} + \frac{u_2}{K_2} + \frac{u_3}{K_3}]L^2 \quad (6.38)$$

where, $K_1 = L_{31}L_{12}, K_2 = L_{32}L_{12}, K_1 = L_{31}L_{12}$, and $\mathrm{L}^2 = \mathrm{L_{L1}L_{L2}} + \mathrm{L_{L1}L_{L3}} + \mathrm{L_{L3}L_{L2}}$

Considering only fundamental component, the voltage V_m is given as follows,

$$V_m = [\frac{\sqrt{2}U_{11}\sin(\omega t + \phi_1)}{K_1} + \frac{\sqrt{2}U_{21}\sin(\omega t + \phi_2)}{K_2} + \frac{\sqrt{2}U_{31}\sin(\omega t)}{K_3}]L^2 \quad (6.39)$$

the peak value of the fundamental is given in equation(6.40).

$$V_{m,peak} = [\frac{2U_{11}}{K_1^{\,2}} + \frac{2U_{21}}{K_2^{\,2}} + \frac{2U_{31}}{K_3^{\,2}} + \frac{4U_{21}U_{31}\cos(\phi_2)}{K_2K_3} + \frac{4U_{11}U_{31}\cos(\phi_1)}{K_1K_3} + \frac{4U_{11}U_{21}\cos(\phi_1 - \phi_2)}{K_1K_2}]^{\frac{1}{2}} \quad (6.40)$$

The peak value of $V_{m,peak}$ is used to find the peak value of core flux, by considering all the elements from the third port, it can be referred from any other two ports as well. The expression for core loss is derived below, where 'f' is the operating frequency, $\omega = 2\pi f$, A_c is the cross section of the core and l_m is mean length of magnetic flux path.

$$B_{peak} = \frac{V_{m,peak}}{\omega N_3 A_c} \quad (6.41), \qquad P_{core} = KB_{peak}^{\alpha} f^{\beta} A_c l_m \quad (6.42)$$

6.6.3. Copper Loss & Device Conduction losses for Quasi-Square Wave Voltage Waveforms

The copper losses for high frequency transformer and conduction losses for devices are expressed in following equations using the RMS values for winding currents.

$$P_{cu} = \sum_{m=1}^{3}(\sum_{n=1}^{7}(I_{mn})^2 R_{mn,ac}) \quad (6.43)$$

$$P_{device} = 3\sum_{m=1}^{3}\sum_{n=1}^{7} 2(I_{mn}{}^2) R_{ds} \quad (6.44)$$

6.7. Experimental Study and Discussions

6.7.1. Different Operating Methods with ZVS & Minimization of Losses

An experimental study of a 10kW three port converter prototype of figure 6.1 has been carried out for comparing the system efficiencies for different operating schemes. The comparison has been performed for three types of operating mode (a) Fixed frequency operation with square wave winding voltages, (b) Variable frequency operation with square wave winding voltages and (c) Fixed frequency operation with quasi-square wave winding voltages. The operation of three port phase shifted converter using method (a) with fixed frequency and square wave winding voltages provide unique operating points for every value of reference power flow associated to each port. Hence for method (a), solving the following equations provide the solutions for every operating scenario. One of the drawbacks of fixed frequency operation with square wave is observed at low power scenarios, where natural ZVS turn-on of devices is lost due to low transformer winding current, which results into drastic reduction of efficiencies at low power region, as can be seen in previous sections of this chapter. In order to improve the efficiency at low power operating region, achieving natural ZVS turn-on for switching devices is important. This can be achieved by method (b), increasing the frequency of the operating winding voltages, so that the phase shift angle required for same power transfer is higher than that required for operation at nominal design frequency. The higher phase shift angle results in higher reactive power and higher winding current, thus extending the ZVS range for the three

port converter operation at low power. The second method of increasing the ZVS operating range is to use quasi-square wave voltage waveform, which introduces a zero voltage period in winding voltages, enforcing wider phase angle and higher winding current, resulting in increased ZVS range. However, increasing frequency or reducing duty cycle of winding voltage waveforms, results in change of core loss, copper loss and device conduction loss. Hence, determining optimum switching frequency and optimum values of phase shift angles, duty cycles of winding voltages are necessary.

$$P_1 = \frac{V_{dc1} r_{13} V_{dc3} \phi_1 (\pi - |\phi_1|) L_{L21} L_{L31}}{\pi \omega L_{n1}{}^3} + \frac{V_{dc1} r_{12} V_{dc2} (\phi_1 - \phi_2)(\pi - |\phi_1 - \phi_2|) L_{L31} L_{m1}}{\pi \omega L_{n1}{}^3} \quad (6.45)$$

$$P_2 = \frac{V_{dc2} r_{23} V_{dc3} \phi_2 (\pi - |\phi_2|) L_{L12} L_{L32}}{\pi \omega L_{n2}{}^3} - \frac{r_{21} V_{dc1} V_{dc2} (\phi_1 - \phi_2)(\pi - |\phi_1 - \phi_2|) L_{L32} L_{m2}}{\pi \omega L_{n2}{}^3} \quad (6.46)$$

$$P_3 = \frac{r_{31} V_{dc1} V_{dc3} \phi_1 (\pi - |\phi_1|) L_{L23} L_{L3}}{\pi \omega L_{n3}{}^3} + \frac{r_{32} V_{dc2} V_{dc3} \phi_2 (\pi - |\phi_2|) L_{L13} L_{L3}}{\pi \omega L_{n3}{}^3} \quad (6.47)$$

The turn-on ZVS criteria for any switching leg is explained in [60], where the outgoing current needs to lag the phase voltage. For negative to positive transition of winding voltage for any port, the current flowing into the winding, should have a negative minimum value during the transition instant. The required minimum value of the negative current is given in equation (6.48), where k is the winding port for which ZVS is evaluated, and C_{ds} is the drain-source device capacitance for the switching device.

$$I_{k,min} = 2\sqrt{\frac{C_{ds}}{L_{Lk}} V_k V_m} \quad (6.48)$$

The evaluation of optimum switching frequency for three port converter operation with square wave winding voltages, is obtained by varying the frequency over a range and finding the

minimum value of system losses over the frequency range. A MATLAB routine is created to evaluate the optimum switching frequency, which uses the core loss, copper loss and device loss models from section 2 to evaluate the total system dominant losses. The ZVS conditions are checked by using the current expressions of (6.1-6.9) and the ZVS criterion of equation (6.48).

Evaluation of optimum values of winding voltages' duty cycles are carried out by using the duty cycles D_1, D_2, D_3 as free variables for MATLAB minimization routine 'fmincon'. The minimization routine checks for each combination of the duty cycles over the range of upper bound and lower bound values, solves the operating phase shift angles ϕ_1, ϕ_2 using equations (6.29-6.31), checks for ZVS conditions, evaluates the total dominant system losses by summing up core loss, copper loss \& device conduction loss models from section 3. The ZVS condition is checked using equation (6.48), where the harmonic components of winding currents are added to get the instantaneous winding current values during transition, as given in equation (6.49).

$$i_k(\phi_k) = \sum_{n=1}^{7} \sqrt{{A_{kn}}^2 + {B_{kn}}^2} \sin(n\phi_k + \tan^{-1}\frac{B_{kn}}{A_{kn}}) \quad (6.49)$$

6.7.2. Study for Efficiency Improvement with Frequency Variation

The different operating methods of three port Triple Active Bridge converter mentioned above, are experimentally verified with a 10kW SiC-Mosfet based three port converter. The experimental prototype converter uses 1200V/60A SiC-Mosfets for port 1 & 2, and 1700V/45A SiC-Mosfets for port 3. The three port high frequency transformer used is made of ferrite cores with litz wire. Figure 6.17 shows one of the three H-bridges for three port converter and figure 6.18 shows the 50kHz/10kW high frequency transformer. The converter has been run over 2kW to 10kW power range. The voltages for three port converters are defined as $V_{dc1} = V_{dc2} = 800V$,

$V_{dc3} = 1200V$. The frequency range chosen for frequency variation method is from 50kHz to 100kHz. The duty cycle range chosen for the quasi-square wave winding voltage waveforms, is from 0.7 to 1. Figures (6.17)-(6.20) show the transformer winding voltages and currents for different cases.

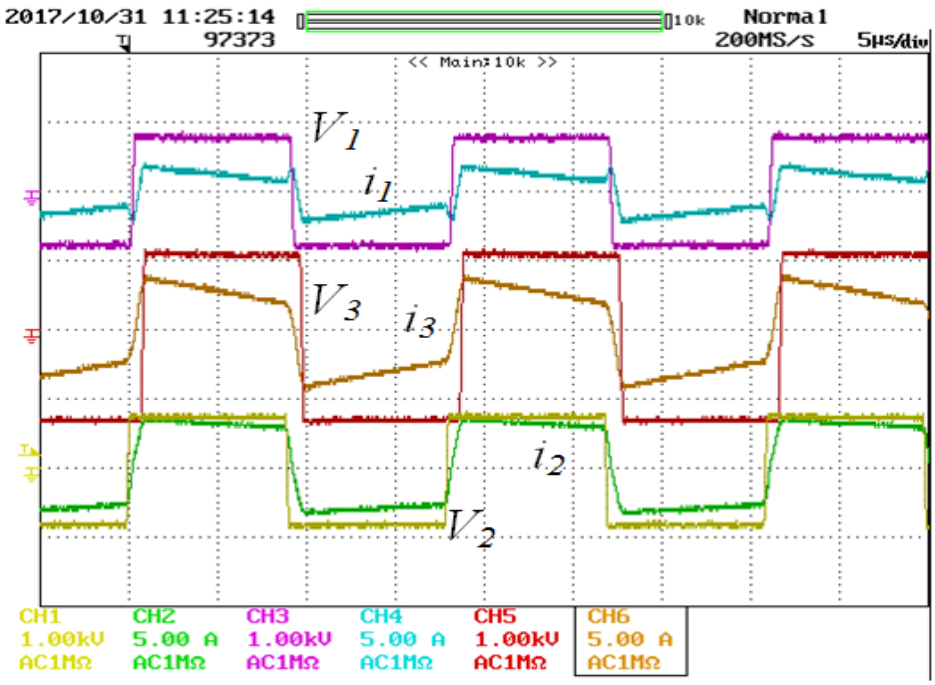

Figure 6.16. Fixed Frequency Operation at 50kHz.

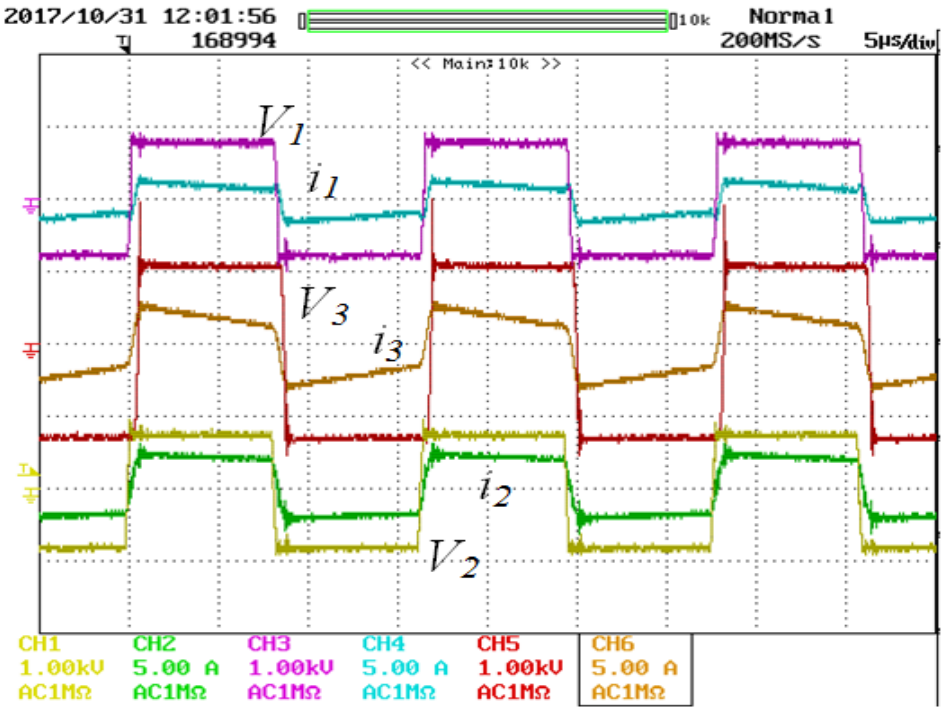

Figure 6.17. Variable Frequency Operation at 62kHz.

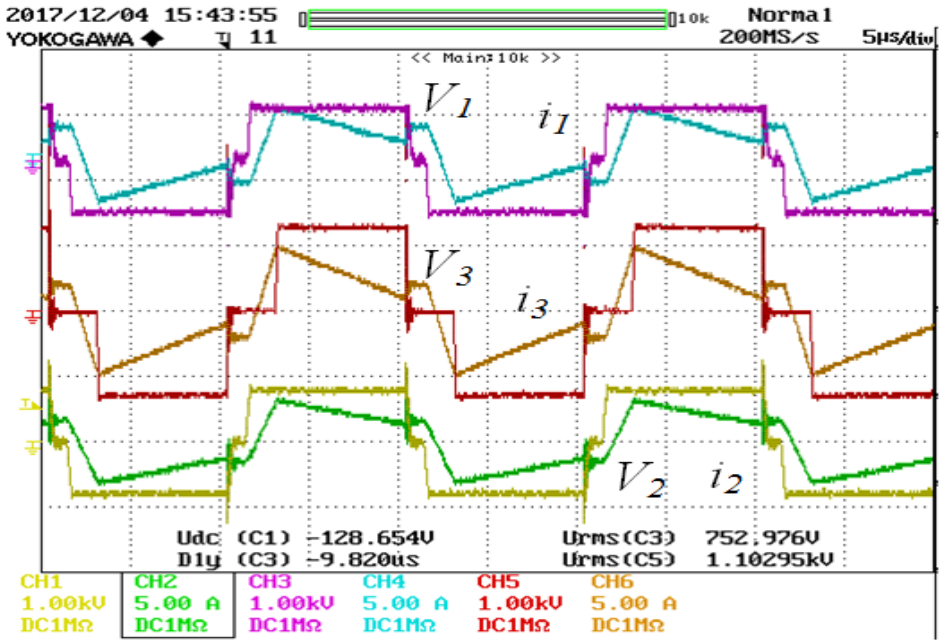

Figure 6.18. Quasi-Square Wave Operation for 2kW Operation.

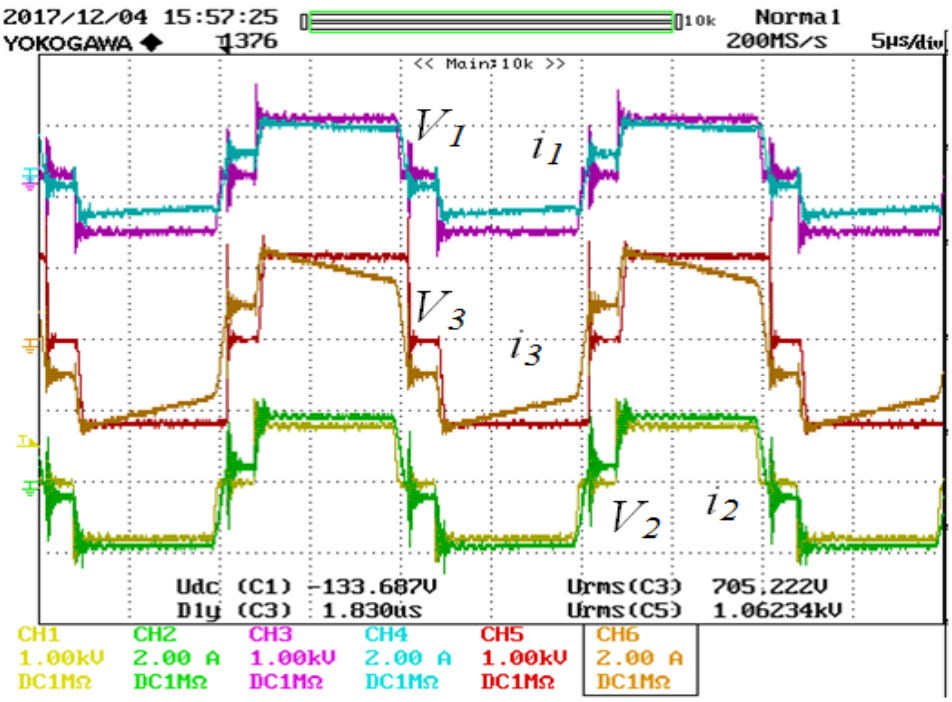

Figure 6.19. Quasi-Square Wave Operation for 1.2kW Operation.

The efficiency of the converter is measured using power analyzer WT3000. The efficiency is defined as $\eta = \frac{P_{out}}{P_{in}}$. If the RES and ESS both are delivering power, then $P_{in} = P_1 + P_2$ and $P_{out} = P_3$. If the RES is delivering power and ESS is charging then $P_{out} = P_3 + P_2$ and $P_{in} = P_1$. It can be observed that using frequency variation, the improvement in efficiency is achieved by a small margin. Using the duty cycle variation method at fixed frequency of 50kHz, the improvement in efficiency achieved is quite considerable. However, the efficiency improvement is achieved around the low power region, while for mid power to full power region, all the three methods provide almost the same efficiency. In figure 6.19 and 6.20, it can be observed that few ports have loss of ZVS at very low power region, where only one leg of the converter experiences natural ZVS turn-on.

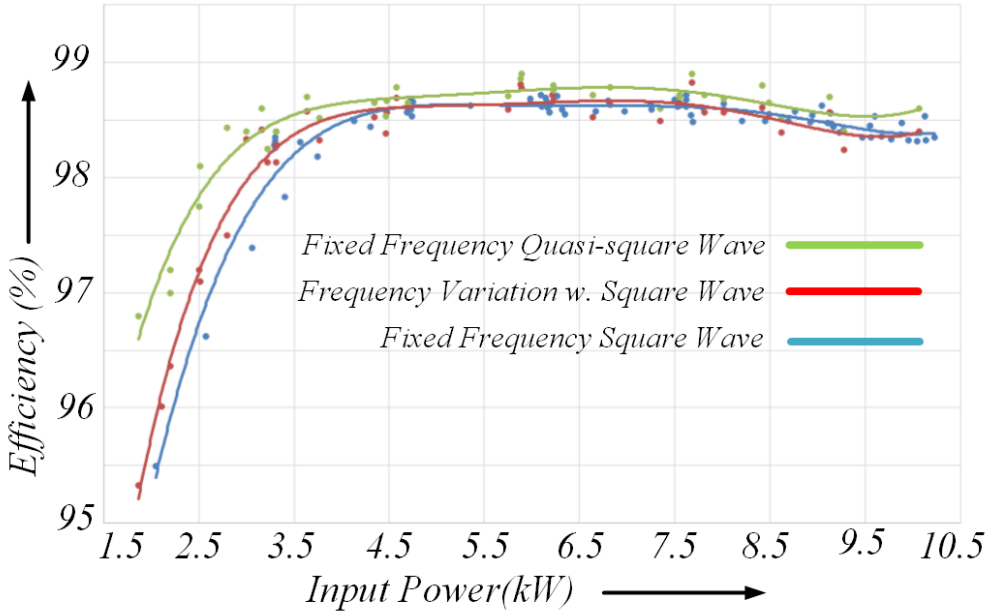

Figure 6.20. Converter Efficiency with Different Methods.

The different methods of operating the three port converter system have been successfully tested using the laboratory prototype. The converter models for power flow and loss calculations have been comprehensively defined in sections 2 and 3. The three operating methods provide almost equal efficiency between mid to high power region. The duty cycle variation method provides relatively higher efficiency at low power operating region compared to frequency variation method.

6.8. 50kW High Frequency Three Port Split-Winding Transformer for Three Port Phase Shifted Converter

This section of the chapter presents experimental studies for a three port 50kW ferrite core transformer for three port phase shifted converter. The transformer is designed using off-the-shelf ferrite U cores, instead of using a custom design. The design process uses an optimization to select the designs which has leakage inductances low enough for 50kW power transfer. The

designed transformer uses 8 pieces of U93/76/30 ferrite cores for the three port transformer. Four pieces of U93/76/30 cores are arranged in E-E format to create a three limb structure and then another four pieces of U93/76/30 cores are arranged in similar manner and stacked with the first E-E shape to create the three port split-winding transformer. The dimensions of the three port transformer and the winding details are given below.

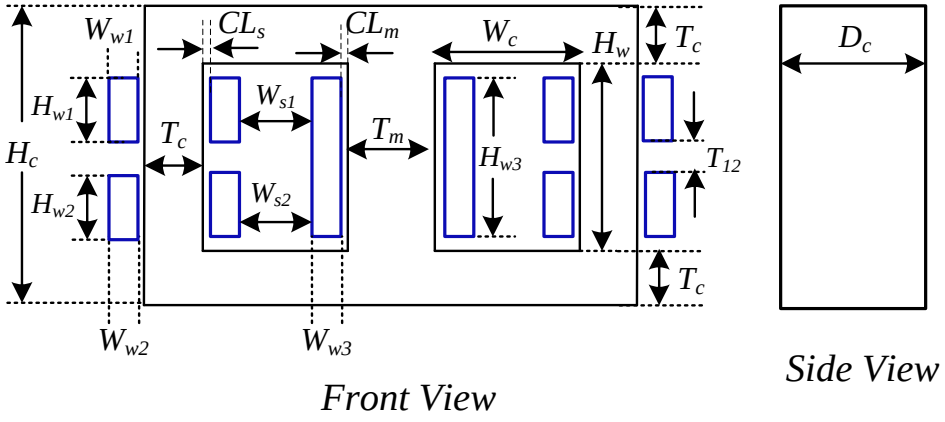

Figure 6.21. Transformer Dimensions.

Figure 6.22. 50kW Ferrite Core Transformer Prototype.

Table 14. 50kW Transformer Dimensions

Core Height H_c	150mm
Core Depth D_c	60mm
Side Limb Thickness T_c	30mm
Middle Limb Thickness T_m	60mm
Window width W_c	35mm
Window height	90mm
Clearances CL_s, CL_m	3mm
Side Limb Winding height $H_{w1,2}$	42mm-44mm
Middle Limb Winding Height H_{w3}	65mm
Side limb number of turns	6
Middle winding number of turns	9
Side winding litz wire	2500/38
Middle winding litz wire	2500/38
Designed Flux density at 50kHz	0.18
Rated voltage for side winding sections/total	400V/800V
Middle winding rated voltage	1200V
Port 1 (PV) Leakage Inductance L_{L1}	8.5µH
Port 2 (PV) Leakage Inductance L_{L2}	9.67µH
Port 3 (Middle) Leakage Inductance L_{L3}	34.25µH
Magnetizing Inductance L_{m3} from middle winding	1.7mH
Capacitance C_{1-3}	56pF
Capacitance C_{2-3}	51pF
Capacitance C_{1-2}	42pF

6.9. Experimental Study for 50kW SiC Enabled Three Port Converter Prototype

The 50kW three port converter prototype is built using 1200V/325A and 1700V/225A SiC Mosfet modules. Figures 6.23 & 6.24 show the schematic and actual prototype of 50kW three port converter. The converter system uses the same gate driver technology as used for 10kW prototype. The PV & ES ports use 1200V/325A SiC Mosfets & the output port use 1700V/225A

SiC Mosfets. The ferrite core 50kW transformer designed above is used as the three port transformer with these converter system. The efficiency of the converter system is measured by measuring the dc input power to the system and output dc power of the system. The input & output powers are measured by power analyzer Yokogawa WT3000. The voltage levels of the converter match the maximum voltage rating(1000V) of the WT3000 for PV & ES port(800V). The dc voltage of the output port(1200V) is measured by using a resistive divider of two resistors and connecting the individual resistors across the WT3000 voltage measuring inputs. The output dc currents are measured by LEM current sensors and connecting the LEM current sensor outputs to WT3000.

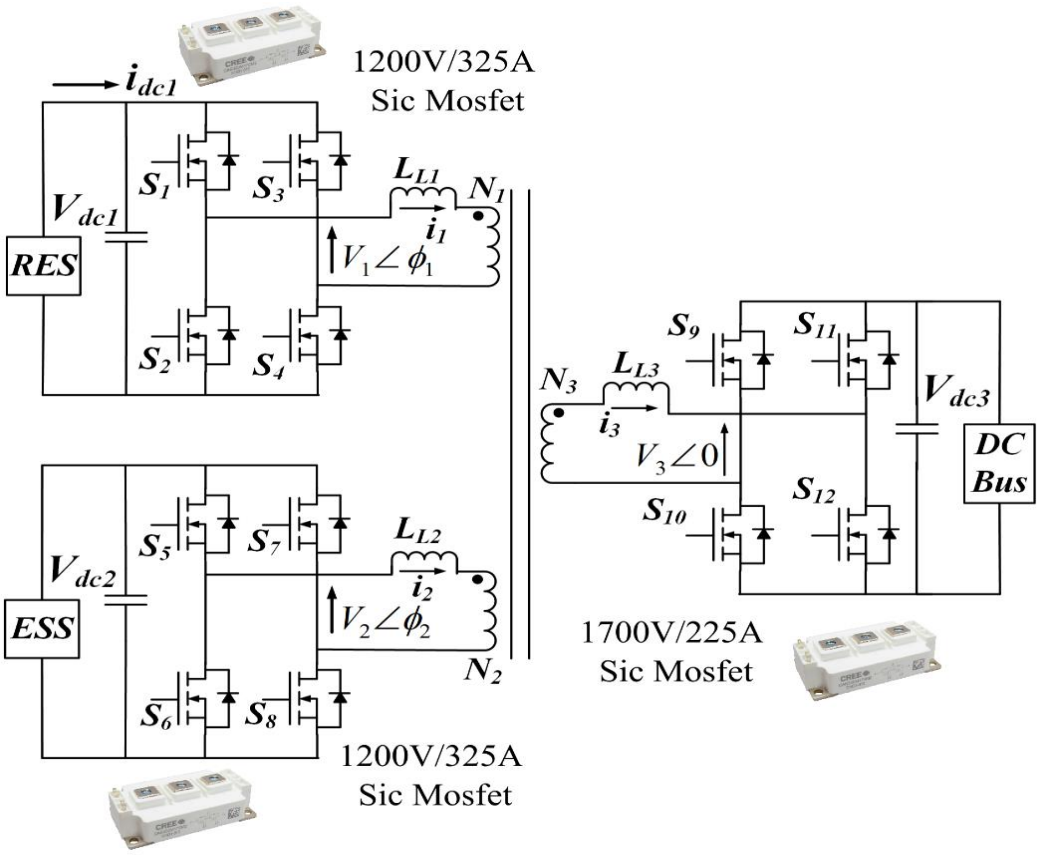

Figure 6.23. Three Port 50kW Converter System.

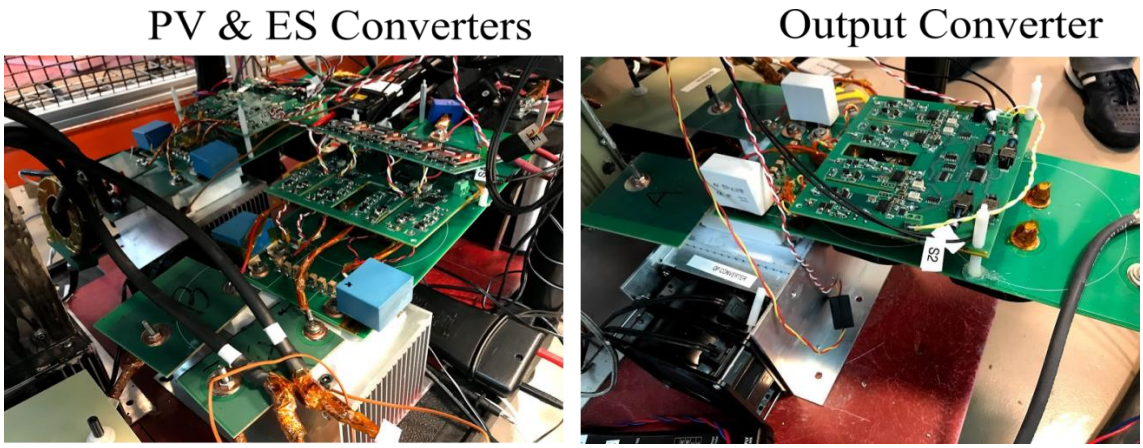

Figure 6.24. 50kW Converter Prototype.

The ferrite core transformer is operated at two different frequencies of 50kHz & 75kHz at different loading conditions. Figures 6.25-6.26 show the transformer winding voltages & currents at two different frequencies of 50kHz & 75kHz. The winding currents & voltages are measured using high bandwidth 100MHz sensors. It can be observed that the winding voltages & currents are devoid of any high frequency MHz level ringing or noise.

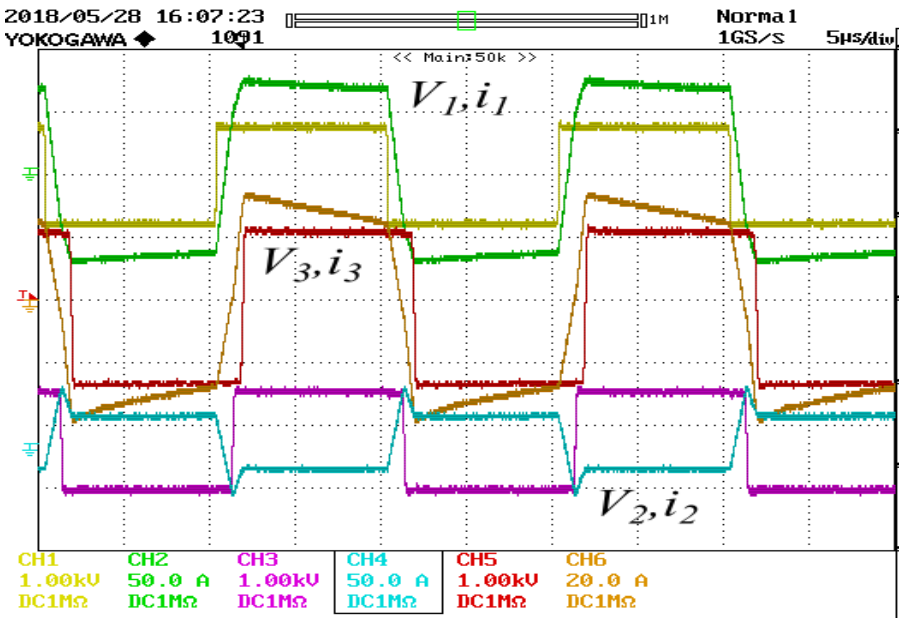

Figure 6.25. Transformer Waveforms at 50kHz.

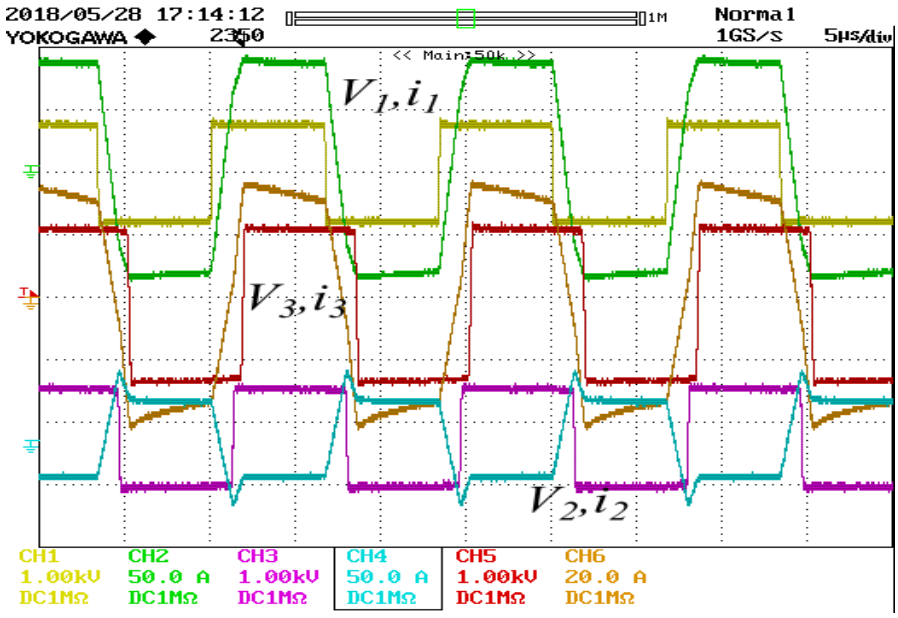

Figure 6.26. Transformer Waveforms at 75kHz.

The converter system efficiencies and losses at 50kHz & 75kHz operating frequencies are shown in figures 6.27 and 6.28, where it can be observed that the efficiency points for 50kHz switching frequency are around the 98.8%-99% marks, whereas for 75kHz switching frequencies, the efficiencies are around 98.4%-98.8%. The efficiency of the converter decreases with loading for 75kHz operation. One reason for this is attributed to the phenomenon that at 75kHz, the transformer winding resistances are higher than those at 50kHz. Also, at 75kHz, the winding currents are higher than 50kHz operation, as the required phase angle at 75 kHz is higher, so it demands a higher reactive component of current. The breakdown of conduction losses for the converter and semiconductor, and the transformer core loss and the other stray losses are shown in figures 6.29 & 6.30.

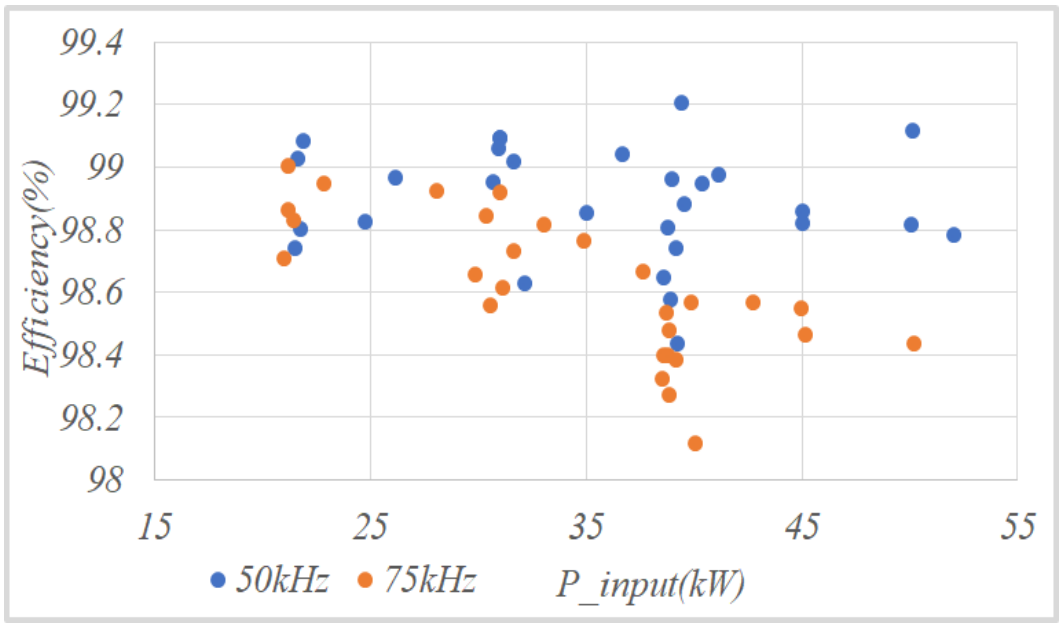

Figure 6.27. Efficiency Plot for 50kW Converter System.

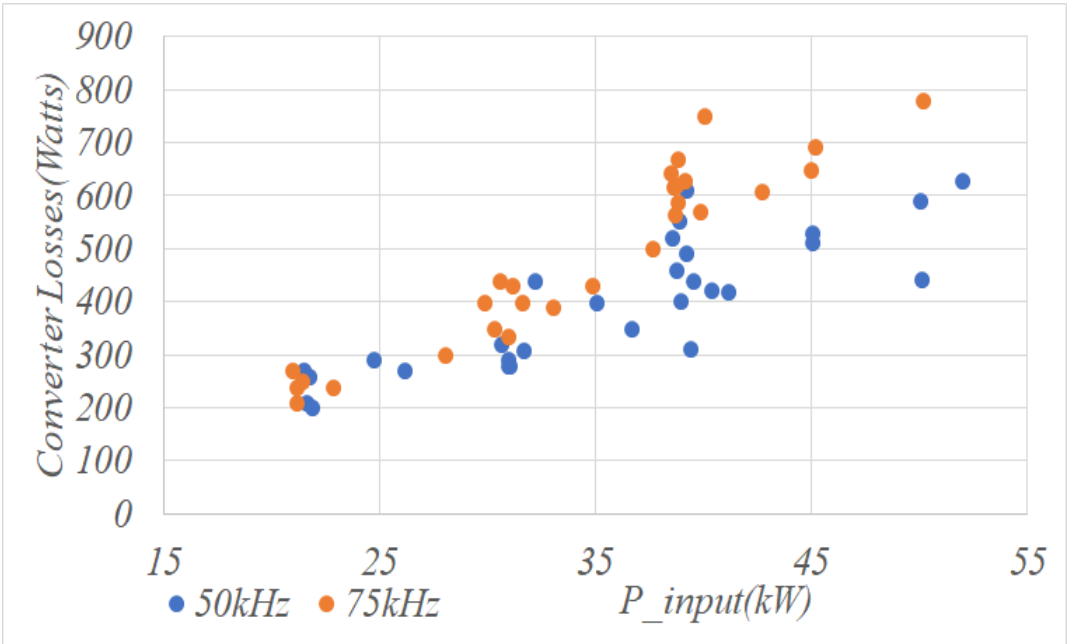

Figure 6.28. Total 50kW Converter System Losses.

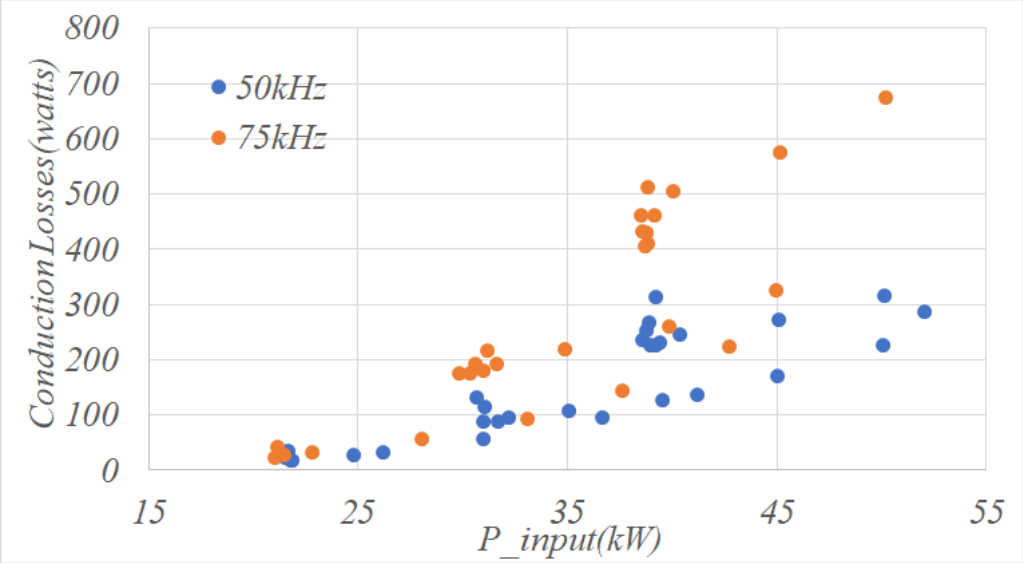

Figure 6.29. Total Mosfet+Transformer Conduction Losses for Converter.

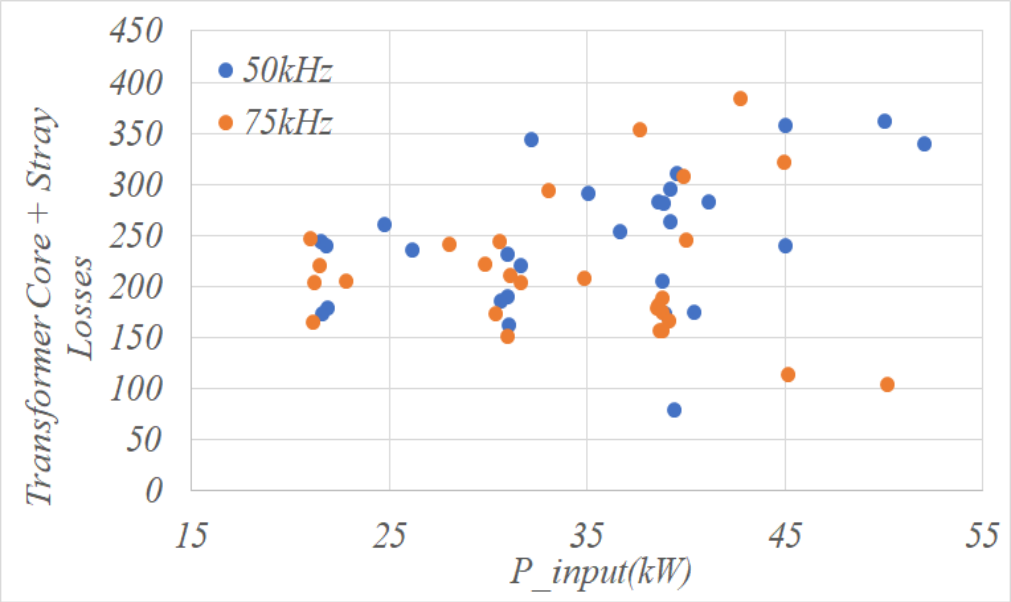

Figure 6.30. Transformer Core+Eddy Current+Stray Losses.

It can be observed that the total losses increase with loading of the converter which explains the dominance of conduction loss over increasing operating power level. However, the total

losses of the converter system increase significantly for 75kHz operation with higher loading, indicating the dominance of conduction losses over other losses.

6.10. Conclusions

The optimized design process of three port split-winding transformer has provided closely matching results for 10kW transformer prototypes. The converter efficiencies are lower at low power operating points using square wave winding voltages than efficiencies for 50% to 100% operating level of power rating. However, using the duty cycle modulation and frequency variation technique, the efficiency of the system is improved by small percentage around the low power operating region. From mid to full power operating region, the efficiency for the 10kW prototypes remain same throughout the operating range. The 50kW prototype demonstrated also has provided efficiencies near the 99% range for the whole converter system. For the 50kW prototype has losses increasing with operating power level for both 50kHz & 75kHz power level, indicating the dominance of conduction losses compared to voltage or switching frequency related losses.

Chapter 7. 50kW Nano Crystalline Material Based Tape-Wound Core Transformers For Phase Shifted DC-DC Converters

7.1. Effect of Leakage Inductances on Nano Crystalline or Tape Wound Core based Transformers

In this section, high frequency transformer design using tape wound core materials such as Nano Crystalline alloy is investigated. The operation of phase shifted DC-DC converters such as Dual Active Bridge(DAB) and Triple Active Bridge(TAB) is based upon storage & transfer of inductive energy using series or leakage inductances. The magnetic flux or magnetic field associated with leakage inductances or series inductances carry the inductive energy and are functions of leakage/series inductances and the load component of transformer winding currents. For the ferrite core based transformers as discussed in previous chapters, the leakage inductance is used as energy transfer element. The leakage fluxes for the ferrite core based transformers, cuts across the ferrite surfaces and moves through the ambient and again comes back into ferrite volume. Ferrite being a homogenous material and being devoid of any laminations, the leakage flux does not induce any eddy currents into ferrite materials. However, the leakage fluxes have significant effects in induced eddy current related losses in case of tape wound core material. The leakage fluxes create additional losses other than hysteresis core losses in tape-wound core material. The magnetic field for a two winding transformer made with laminated tape wound cores, is shown in figure 7.1, where the field lines are spread around the outer volume surrounding the transformer and in the window volume. The magnetic field lines cut across the laminated surfaces, which results is induced voltage in laminations and resulting eddy currents

creating eddy current losses and thus adding to the total core losses. The induced voltages & resulting eddy currents are proportional to the rate of change of leakage flux, which is a function of load component of transformer winding currents. Therefore, higher the load component of current, higher are the induced eddy currents and resulting losses. Therefore, using tape wound material based transformer, the total core losses thus increase with higher load current, whereas in ferrite based transformer, the core loss reduces with higher loading due to lower magnetizing voltages. These continuously increasing high losses with increasing loading due to eddy current causes excessive heating & temperature rise which can result in loss of permeability and saturation of magnetic core. An experimental demonstration of eddy current losses resulting in high core temperature is shown below in figures 7.1. A two winding transformer(shown in figure 7.2) made of VITROPERM500F material is operated at different loading conditions in a Dual Active Bridge[60] configuration, the transformer leakage inductance of the transformer is used as energy transferring element. It can be observed from figures 7.3-7.6, that as loading increases, the temperature of the core over the window portion of the transformer increases. This temperature rise can be explained in the following manner, as the current in the winding increases, the leakage flux cutting increases across the core laminations and the resulting eddy current loss also increases causing increase in core temperature.

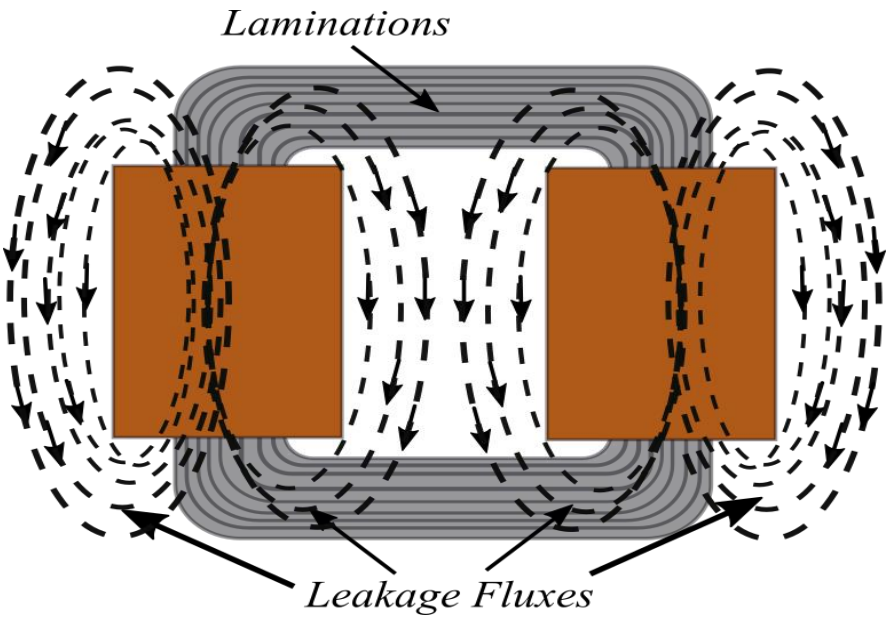

Figure 7.1. Leakage Flux Lines for Core-Type Tape Wound Transformer.

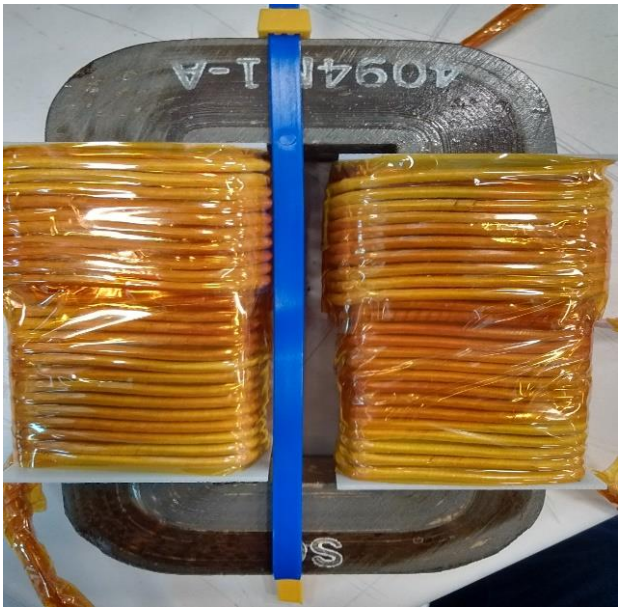

Figure 7.2. 10kW/20kHz 700V:700V Two Winding Transformer.

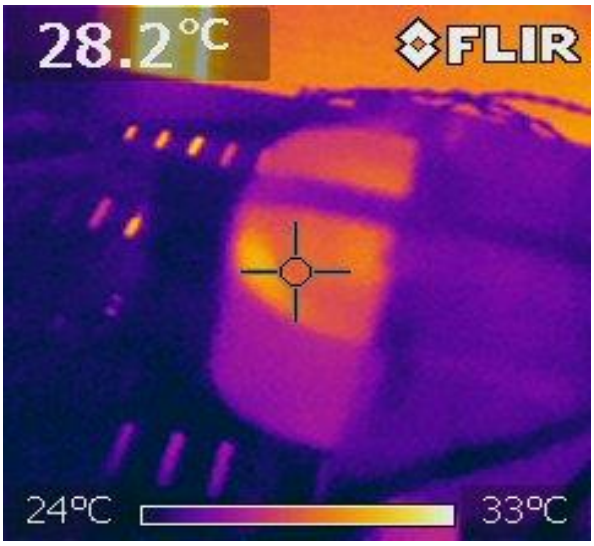

Figure 7.3. Open Circuit Condition(0% Loading).

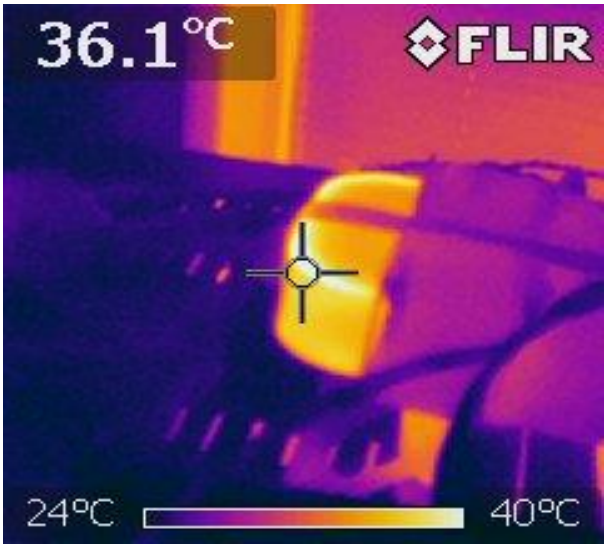

Figure 7.4. 10% Loading Condition.

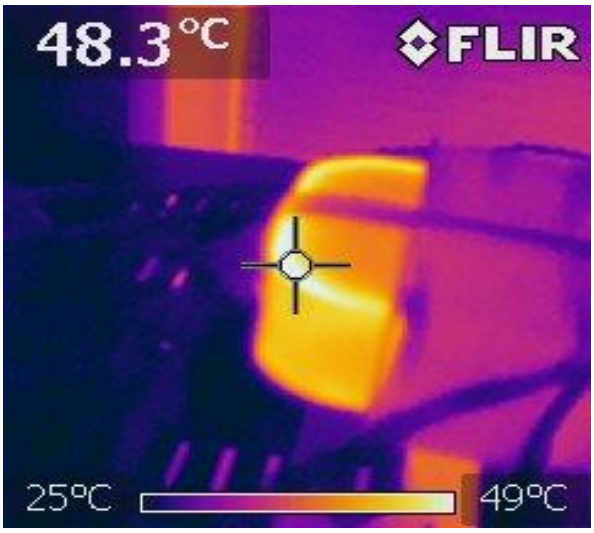

Figure 7.5. 40% Loading Condition.

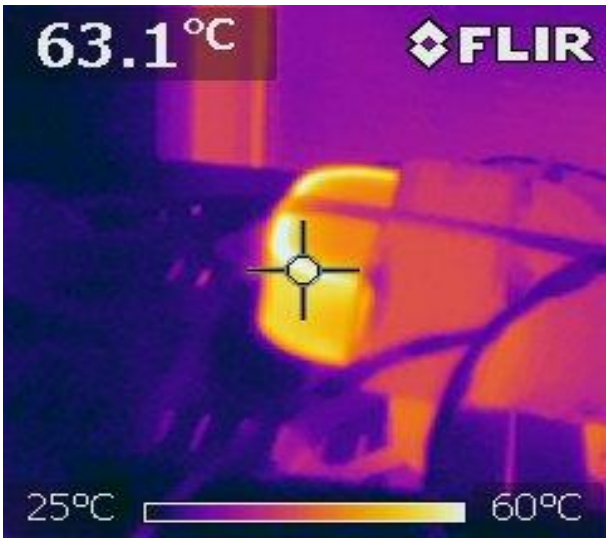

Figure 7.6. 70% Loading Condition.

7.2. Three Port Nano Crystalline Transformer for Three Port Phase-Shifted Converter

In order to avoid or reduce the core heating due to eddy current losses, zero or minimal leakage fluxes should cut across the core laminations, thus reducing the eddy current losses. The

approach taken to solve the problem of leakage flux cutting across the laminations, is to minimize the leakage flux and the leakage inductance. Such a transformer if needed to be used for three port converter, external inductors are required, which would act as energy transferring elements over a switching cycle. Leakage inductances for transformers are minimal if the windings are arranged in concentric and interleaved manner, rather than core type or other distributed manner. A comparison of FEA simulation of core-type winding and concentric windings are carried out in terms of leakage fluxes around the window portion and surrounding volume portion. Figure 7.7 shows the leakage flux for core type transformer of figure 7.2, where the leakage magnetic field is around 10^4-20^4 A/m surrounding the core volume & window. In figures 7.8-7.9 two different concentric winding approaches are shown using the same core material volume for two limb approach(with same window area) and three limb approach(with same window area). It can be observed from the FEA simulations that the leakage magnetic fields are around $5*10^2$-10^3 A/m, which is around 10-20 times lower than core type transformers. Therefore, positioning the transformer windings in a concentric manner reduces the leakage field by almost 20 times compared to using a core type distributed approach.

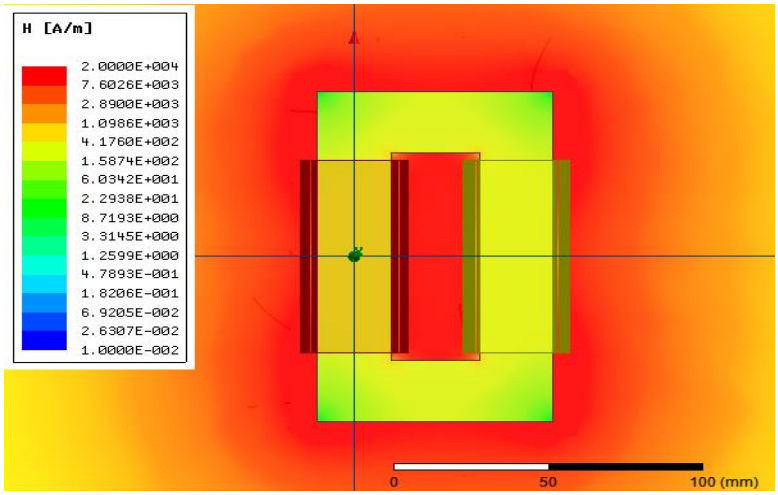

Figure 7.7. Leakage Magnetic Field for Transformer of Figure 7.2.

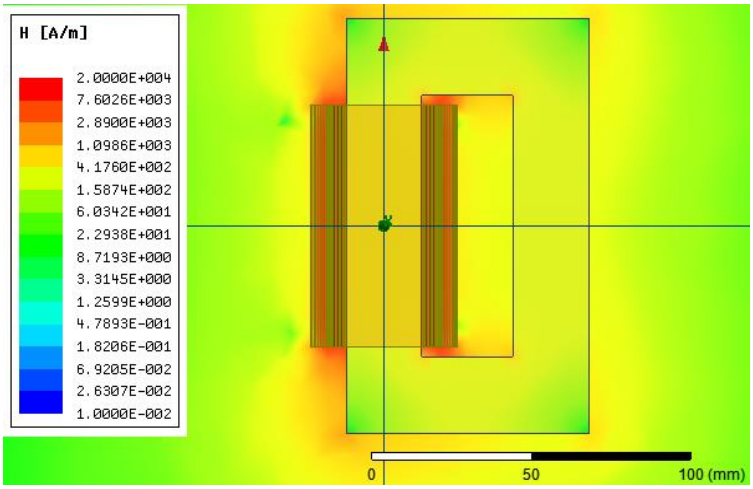

Figure 7.8. Leakage Magnetic Field for Concentric Winding Approach.

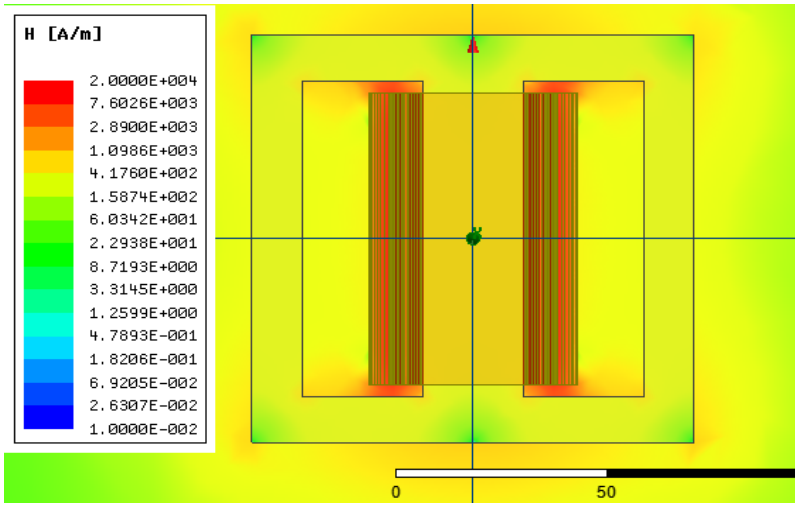

Figure 7.9. Leakage Magnetic Field for Concentric Winding Approach.

In this section, for the three port phase shifted dc-dc converter of 50kW rating, a concentric winding approach is followed for the transformer design using tape wound material. An optimization process is developed to optimize the transformer volume and transformer leakage inductances. In order to have an estimate of the required external series inductances, the power expressions equations are solved for maximum rated power and maximum phase shifts. Since a three port transformer can have three external series inductors. The reflected magnitude of the

inductances are taken equal for the three ports, such that the maximum energy storage $\frac{1}{2}LI_{peak}{}^2$ and total volume of inductors remain same. With equal inductances on the three ports, the power expressions for the three ports are as below, where '*L'* is the required external inductor. Leakage inductance of concentric transformer is considered negligible compared to external inductors. In the expressions 7.1-7.3, all the quantities are referred to port 1. Port 1 is considered as RES port with input voltage 800V, port 2 is considered as ES port with input voltage 800V and port 3 is the output port with 1200V. The typical operating frequency range for tape wound core materials are from medium frequency range(1,2kHz to 25-30kHz). The value of the external inductor L is evaluated from extreme operating cases of (a) $P_1 = P_{\max,}$, $P_2 = -P_{\max}$, $P_3 = 0$, (b) $P_1 = P_{\max}$, $P_2 = 0$, $P_3 = P_{\max}$, (c) $P_1 = 0$, $P_2 = P_{\max}$, $P_3 = P_{\max}$ for a switching frequency of 20kHz and maximum operating angle of 60 degree. The value of '*L*' is selected as 40µH for port 1 and port 2, and referring to output port the required value of inductance is 90µH.

$$P_1 = \frac{V_1 V_2 (\phi_1 - \phi_2)(\pi - |\phi_1 - \phi_2|)}{3L} + \frac{V_1 V_3 (\phi_1)(\pi - |\phi_1|)}{3L} \quad (7.1)$$

$$P_2 = -\frac{V_1 V_2 (\phi_1 - \phi_2)(\pi - |\phi_1 - \phi_2|)}{3L} + \frac{V_2 V_3 (\phi_2)(\pi - |\phi_2|)}{3L} \quad (7.2)$$

$$P_3 = \frac{V_1 V_3 (\phi_1)(\pi - |\phi_1|)}{3L} + \frac{V_2 V_3 (\phi_2)(\pi - |\phi_2|)}{3L} \quad (7.3)$$

The transformer design is carried out using multi-objective optimization procedure for "Leakage-Volume" optimization. A model of concentric winding transformer is shown in figure 7.10. The voltage, number of turns, switching frequency and core area are related as follows in (7.4-7.7). Since the transformer winding currents are high frequency ac in nature, hence litz wire is considered more suitable for design compared to solid conductors. Use of foil winding can

also be investigated for high frequency applications. The effective transformer window area is computed as follows in 7.5. The window height and width are functions of number of turns and number of layers and together with insulation requirement. The winding pattern is considered as a set of three layers, where in each set, each layer is from three different windings. The optimization also finds out number of such three layer sets.

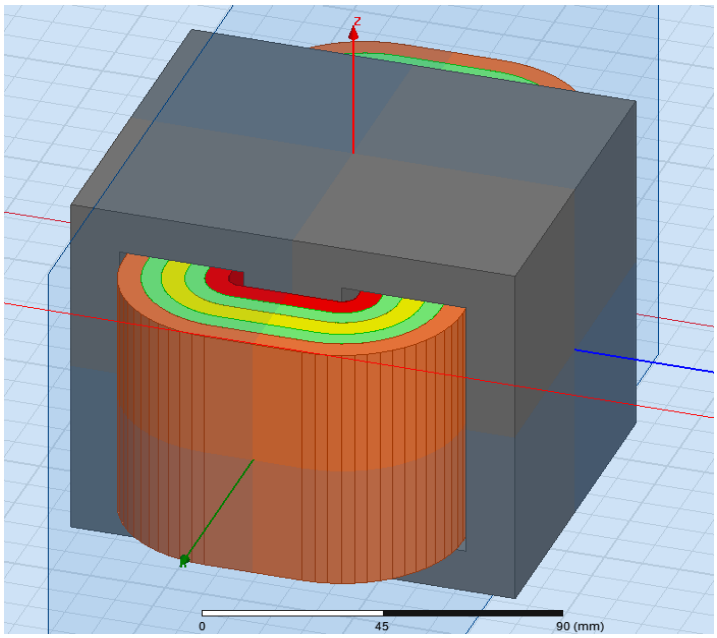

Figure 7.10. Concentric Winding Transformer Model.

$$V_i = 4k_s A_c N_i f_s \quad (7.4) \qquad k_w A_w = N_1 a_{w1} + N_2 a_{w2} + N_3 a_{w3} \quad (7.5)$$

$$H_w = max(N_{L1} d_{w1}, N_{L2} d_{w2}, N_{L3} d_{w3}) + 2*CL \quad (7.6)$$

$$W_w = L(d_{w1} + T_{ins} + d_{w2} + T_{ins} + d_{w3}) + 2*CL \quad (7.7)$$

The leakage model of the concentric winding transformer is given below. For concentric winding transformer, the leakage between the innermost winding and the outer most winding is the highest[68], hence in the optimization, the leakage between the innermost & the outermost

winding is aimed for minimization. The permeances for inner-to-middle and middle-to-outer layer are given below.

$$PL_{inner-middle} = \frac{\mu_0}{H_w}\left(\frac{W_{inner}}{3} MLT_{inner} + W_{gap} MLT_{gap} + \frac{W_{middle}}{3} MLT_{middle}\right) \quad (7.8)$$

$$P_{middle-outer} = \frac{\mu_0}{H_w}\left(\frac{W_{middle}}{3} MLT_{middle} + W_{gap} MLT_{gap} + \frac{W_{outer}}{3} MLT_{outer}\right) \quad (7.9)$$

$$PL_{outer-inner} = PL_{outer-middle} + PL_{middle-inner} \quad (7.10)$$

$$L_{Linner-outer} = N^2 PL_{inner-outer} \quad (7.11)$$

The pareto front output of the optimization procedure is shown below in figure 7.11. A design is selected from the bend of the curve and the corresponding concentric winding transformer design in carried out. The Nano-crystalline material used is FINEMET FT-3L. The designed transformer is shown in figure 7.12 in open frame and figure 7.13 shows the finished epoxy filled closed frame package. The details of the transformer are given in table 15. Litz wire is used for all the three windings.

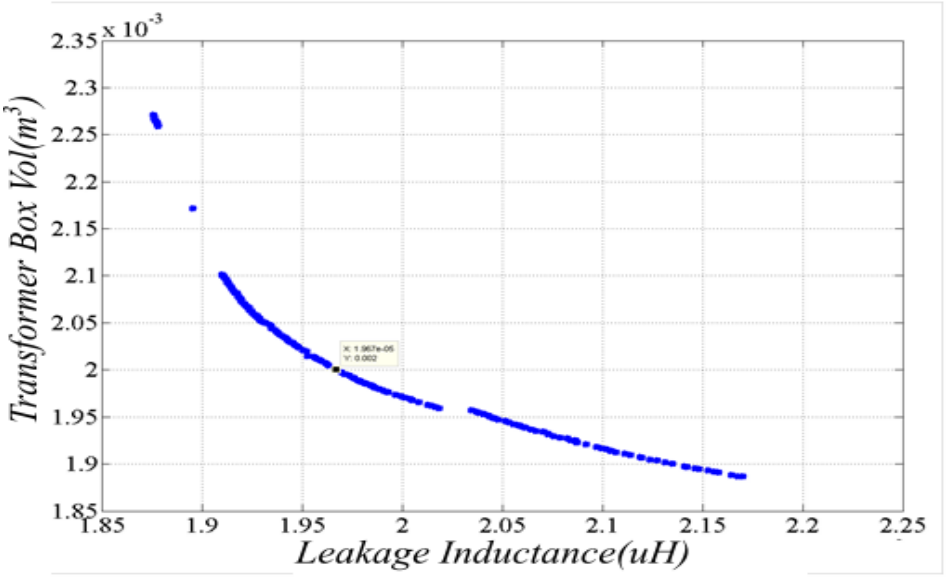

Figure 7.11. Pareto Front for Leakage-Volume Optimization.

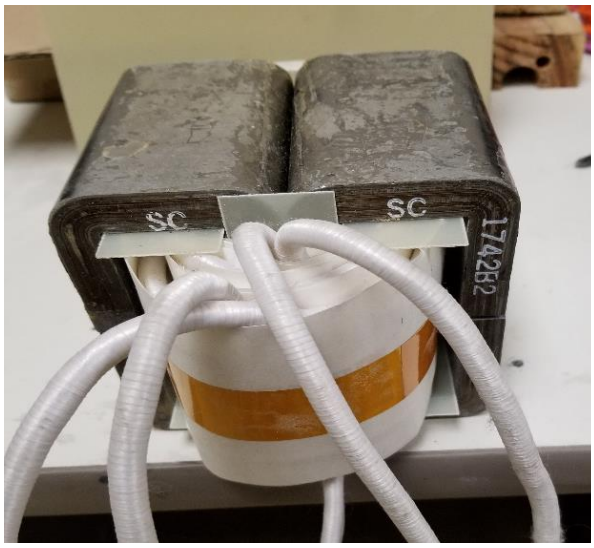

Figure 7.12. Three Port Transformer in Open Frame.

Figure 7.13. Three Port transformer in Closed Frame.

Table 15. Three Port Nano-Crystalline Transformer

Core Depth	96mm
Core Height	106mm
Side Limb thickness	13.5mm
Middle Limb thickness	27mm
RES port No of turns(800V)	8
ES port No of turns(800V)	8
Output port No of turns(1200V)	12
Window (height x width)	79mm x 32mm
Transformer volume	0.002 m^3 = 2 litre
Power density	25 kW/litre = 410W/in^3
Leakage $L_{Linner-outer}$	3 µH
Leakage $L_{Linner-middle}$	1.2 µH
Leakage $L_{Lmiddle-outer}$	2
RES & ES port conductor	Litz wire 2500x38AWG
Output port conductor	Litz wire 1650x38AWG

The core loss for the Nano-crystalline transformer is measured for square wave voltages by applying, a square wave voltage at a certain frequency under open circuit condition. The waveform for the applied square wave voltage is shown in figure 7.14, along with the magnetizing current. The operating flux density B_m is expressed as $B_m = \frac{V_p}{4NA_c f_s}$ for the square wave voltage with peak value V_p. The measured core losses for different flux densities at switching frequencies of 10kHz & 20kHz are shown in figure 7.15. The core loss per weight vs flux densities is given in figure 7.16.

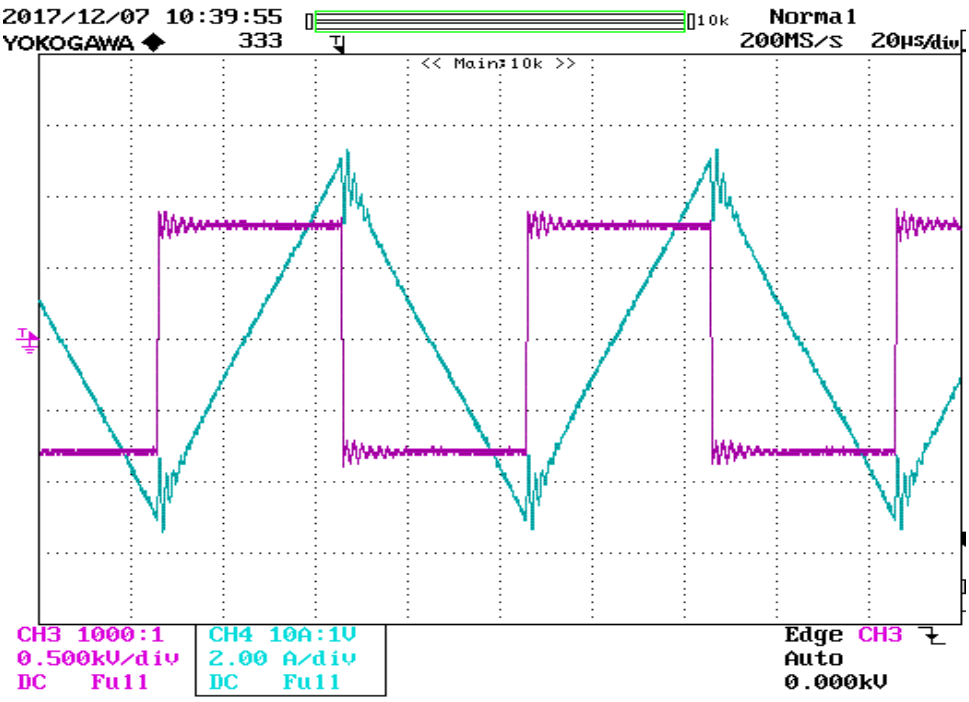

Figure 7.14. Transformer Open Circuit Voltage & Excitation Current.

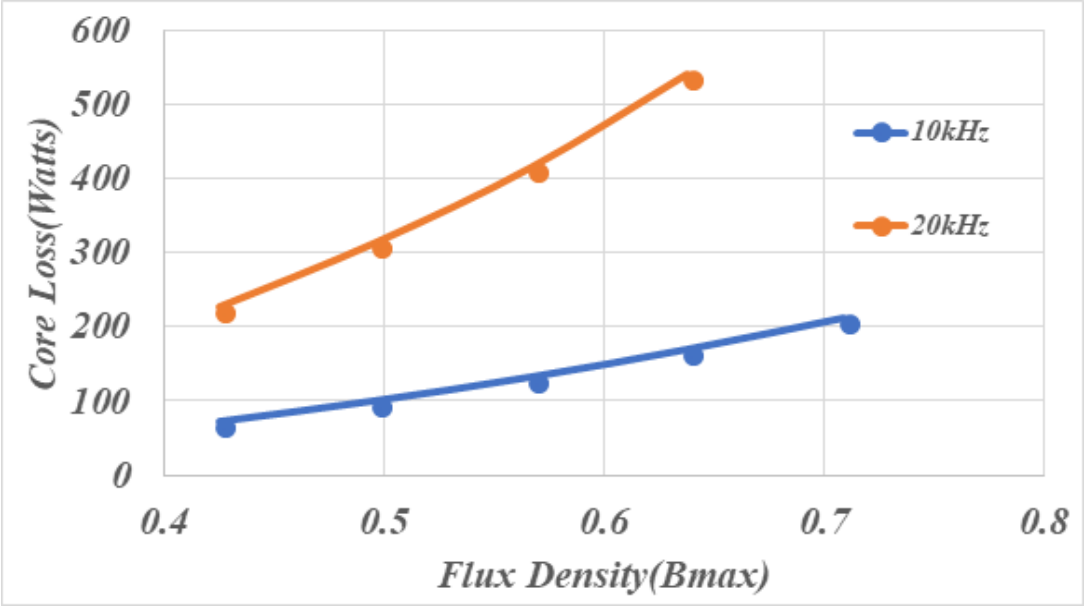

Figure 7.15. Core Loss vs. Flux Density.

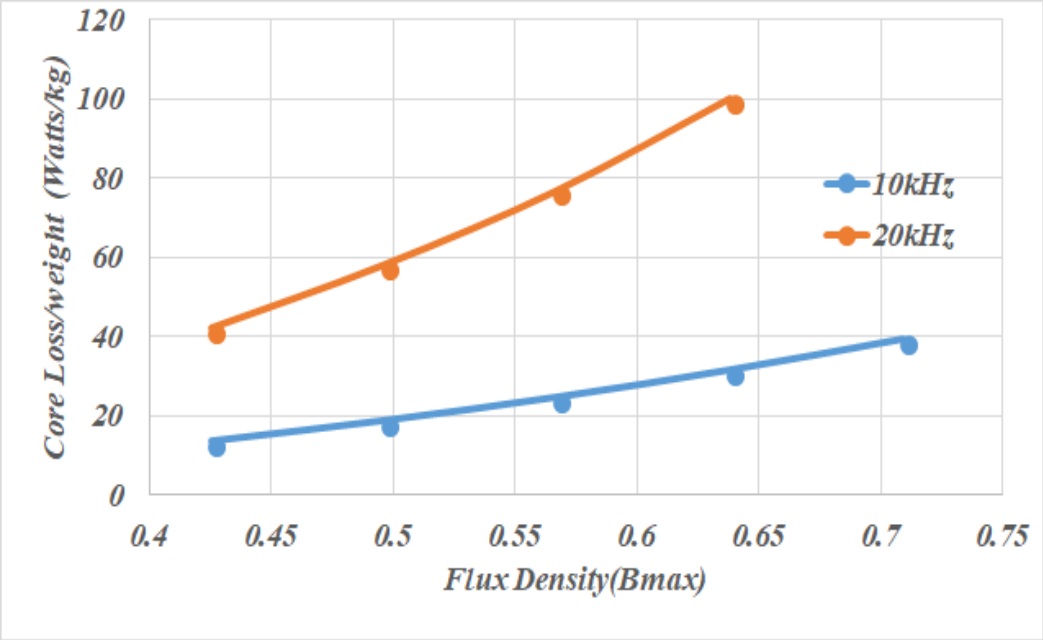

Figure 7.16. Core Loss/Wt vs. Flux Density.

The external inductors are designed using ferrite core materials of grade 3C90 and litz wires. The inductors are designed using the same litz wires as the transformer windings. The ferrite

cores used for each inductor core are U-93/76/30 and U-93/52/30 placed together with air gaps on the legs. Each of the three inductors are designed at same maximum flux density for same value of reflected I_{max}, such that the peak energy stored $\frac{1}{2} L I_{max}^{2}$ is same for all the three inductors, only the number of turns varies. The inductors are shown in figures 7.17-7.18, where it can be observed that the number of turns for each inductor are distributed on two limbs, which is done so that the common mode path(for high speed switching common mode) sees a series capacitance on both the terminals, thus reducing the total series capacitance between any two terminals in the common mode path. The circuit schematic using the external three inductors and the three port transformer is shown in figure 7.19. Figures 7.20-7.21 show the transformer winding voltages and currents for two different operating points for the three port converter at 20kHz switching frequency.

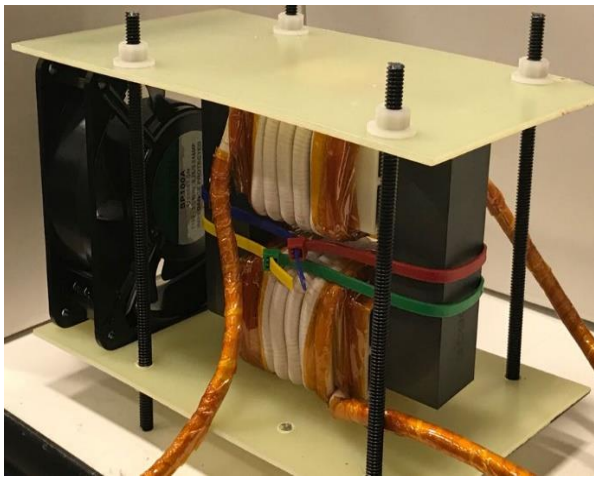

Figure 7.17. RES Port Side Inductor(L_1).

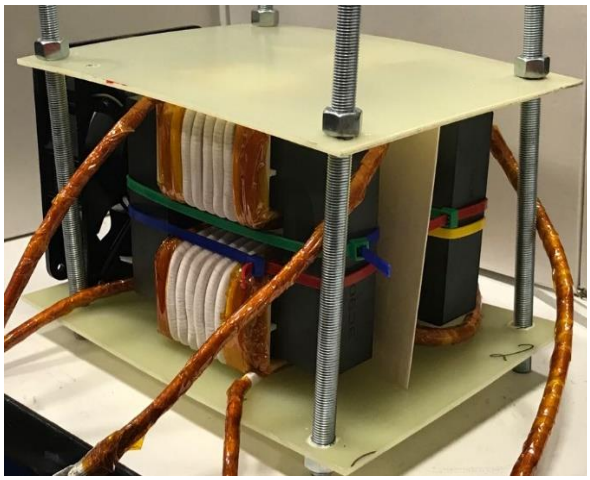

Figure 7.18. ES & Output Port Side Inductor(L2, L3).

Table 16.External Inductor Parameters

No of turns on RES, ES & Output side Inductors	N_1=12, N_2=12, N_3=18
Design Flux Density B_m	0.27
Maximum Design Current for B_m	I_{1max}=90, I_{2max}=90, I_{2max}=60
Measured value of Inductances	L_1 = 41µH, L_2 = 41µH, L_3 = 92µH
Self-capacitances across the each half portions of inductors	12~20pF
Measured ac resistances at 20kHz	R_1=10mΩ, R_2=12mΩ, R_3=28mΩ
Total air gap in each core	6mm

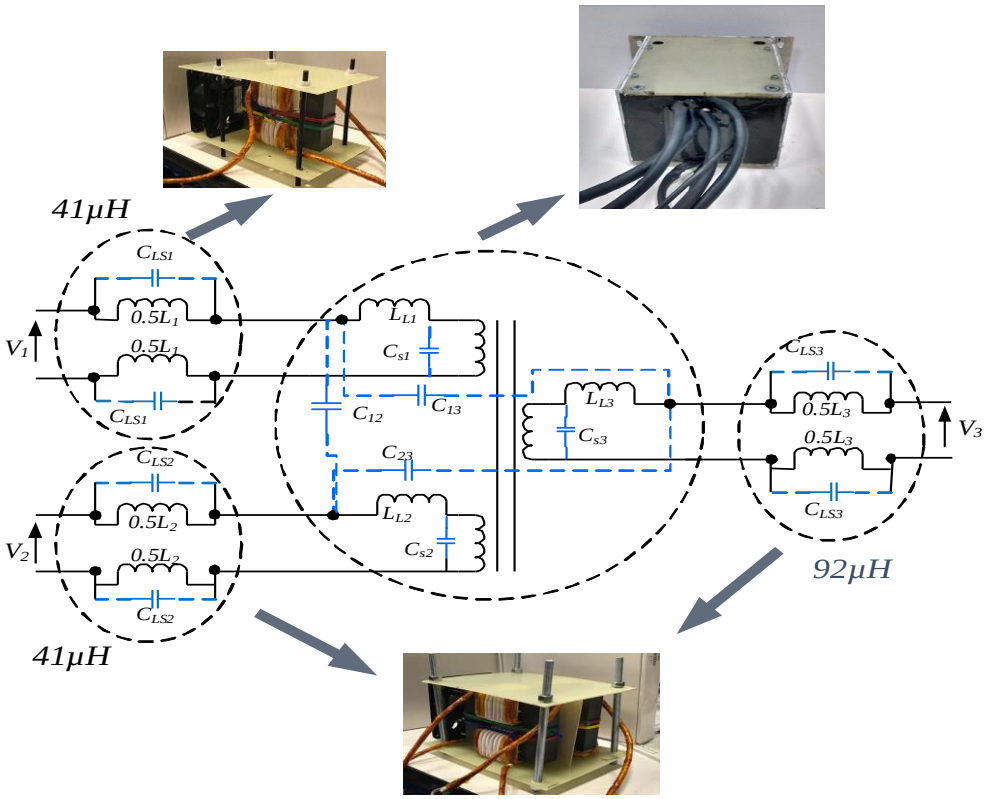

Figure 7.19. Circuit Schematic Using Series Inductors.

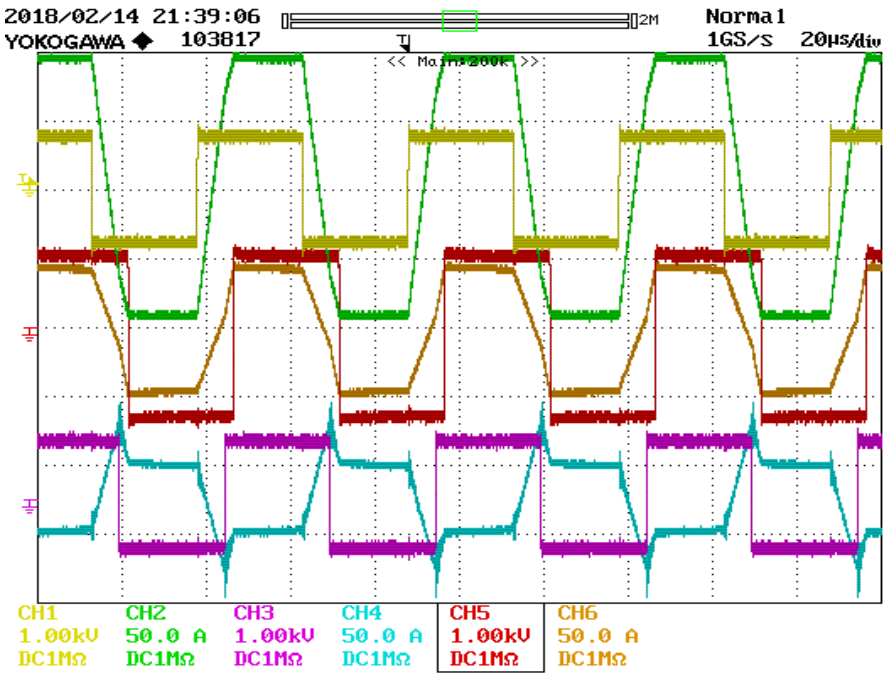

Figure 7.20. Waveforms for P_1 = 50kW, P_{out} = 38kW, P_2 =-12kW.

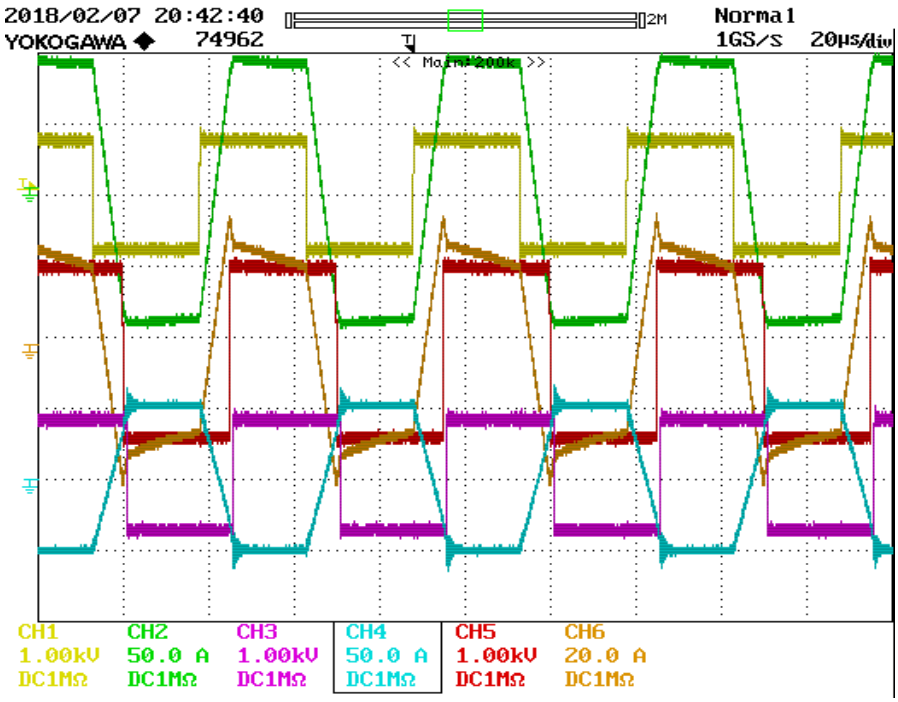

Figure 7.21. Waveforms for P_1 = 50kW, P_{out} = 20kW, P_2 =-30kW.

The three port converter system with nano-crystalline core and external ferrite inductors, as discussed in figure 7.19, can also be operated with two external series inductors. Figure 7.22 shows the equivalent circuit for the three port converter with two external inductors, which is similar to the equivalent circuit of three port converter with three external inductors with L_1=0. Figures 7.23-7.24 show the converter waveforms with two external inductors at different power conditions.

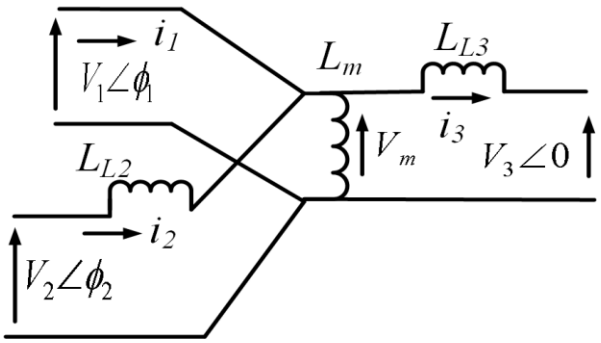

Figure 7.22. Equivalent Circuit with Two External Inductors.

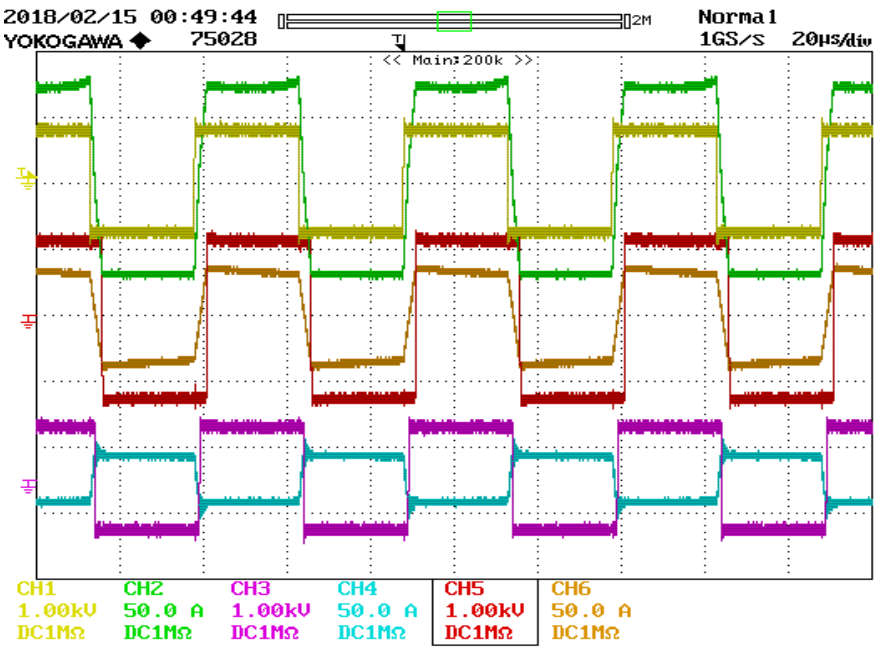

Figure 7.23. Waveforms for P_1 = 50kW, P_{out} = 30kW, P_2 =-20kW.

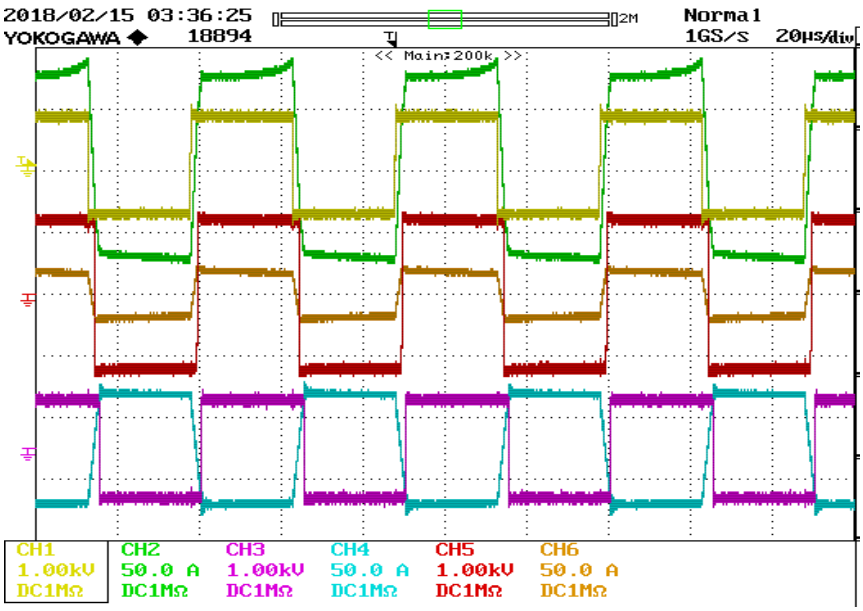

Figure 7.24. Waveforms for P_1 = 50kW, P_{out} = 20kW, P_2 =-30kW.

A comparison of efficiency analysis of the three port converter system is carried out. The measured quantities are the dc input power of each port. The converter efficiencies & total losses for the two converters are shown in figures 7.25-7.28. It can be observed that the efficiencies for both the converters are close to each other(around 98% to 99%) over the operating range and so are the total system losses.

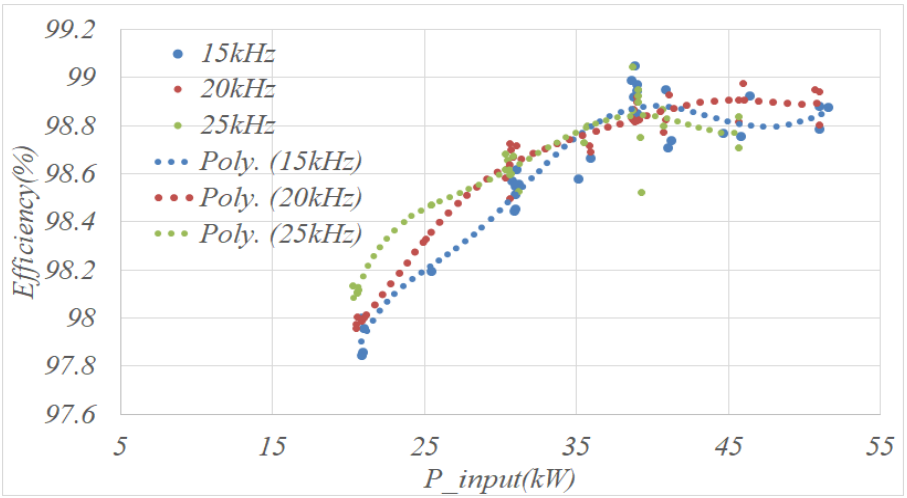

Figure 7.25. Efficiency Plots for TAB Converter with Three Series Inductors.

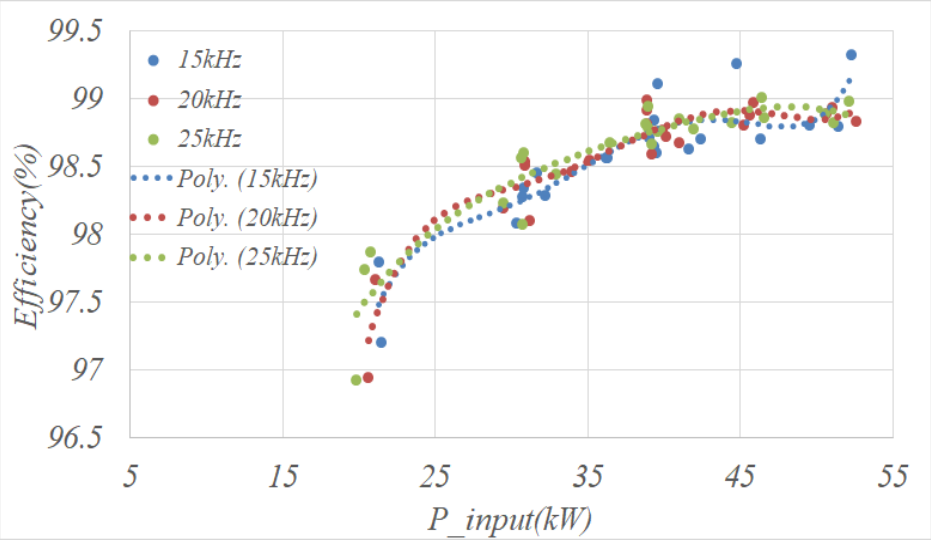

Figure 7.26. Efficiency Plots for TAB Converter with Two Series Inductors.

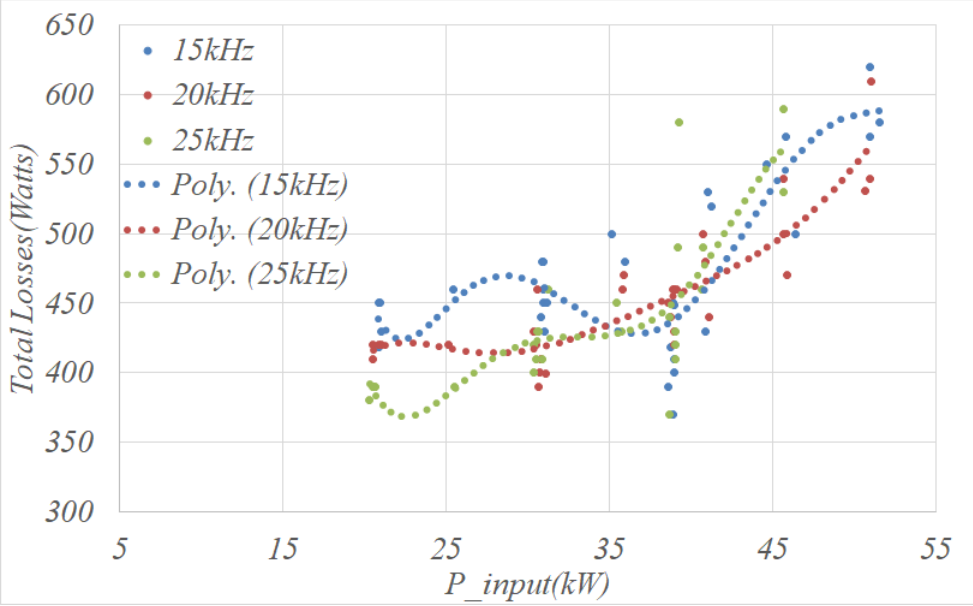

Figure 7.27. Losses for TAB Converter with Three Series Inductors.

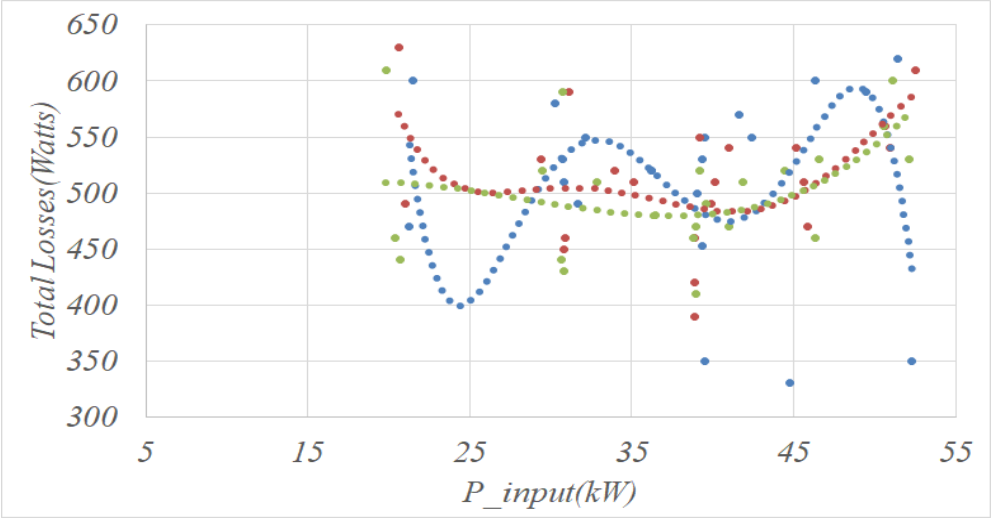

Figure 7.28. Losses for TAB Converter with Three Series Inductors.

A comparison of common mode current from PV terminal, are shown in figures 7.29-7.30 for the two systems, where it can be seen that using three inductors, the common mode current is much lower compared to common mode current using two inductors. Therefore use of three inductors provide an advantage in terms of common mode signals.

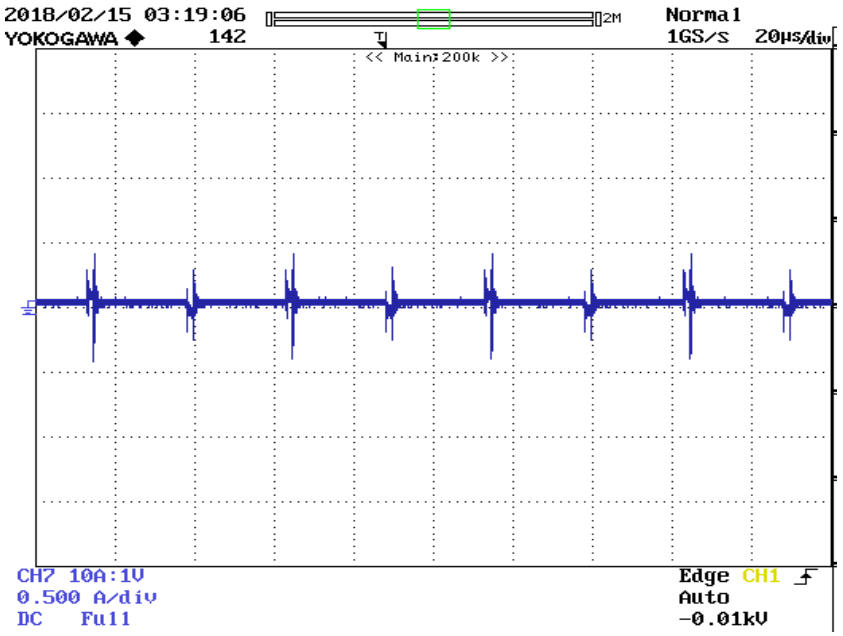

Figure 7.29. PV Winding Common Mode Current using Three Inductors.

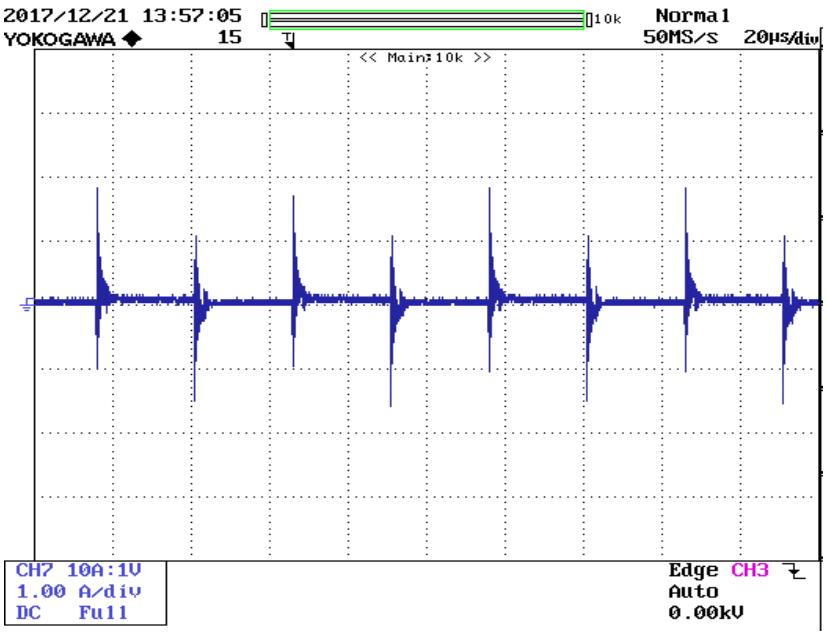

Figure 7.30. PV Winding Common Mode Current using Two Inductors.

7.3. Two Port Nano Crystalline Transformer with Integrated Leakage Inductance for Dual Active Bridge Converter

As explained in previous sections, using a tape wound core or nano-crystalline transformer leakage inductance as an energy transferring element in a power converter, results in eddy current losses in the laminations of the core material. Use of separate inductors for phase shifted three port dc-dc converter has been demonstrated in previous section. Integration of leakage inductor together with the nano-crystalline core has been an attractive solution for converter designers[69], which reduces the total converter volume and reduces winding copper requirement. In [69], different possible designs have been made to demonstrate two port designs with integrated leakage inductors for core-type two-limb transformers, where the windings on the two limbs enclose both the leakage layer and the magnetization core. Few of the design types demonstrated in [69], are shown below in figures 7.31-7.34.

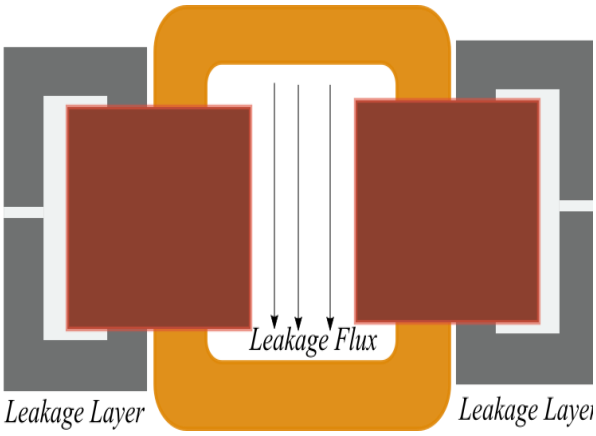

Figure 7.31. Leakage on the Limbs.

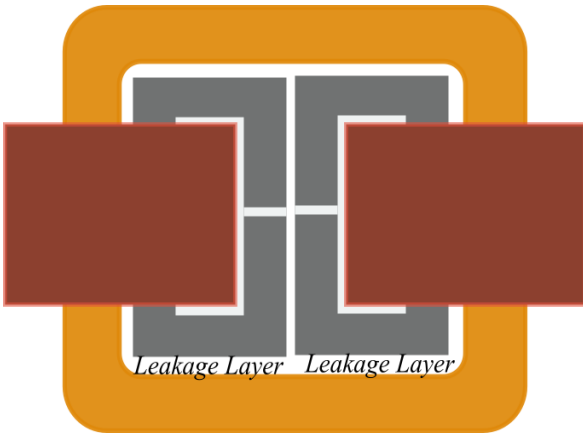

Figure 7.32. Leakage Inside Window.

Figure 7.33. Leakage Inside Window.

Figure 7.34. Leakage Between Cores.

The leakage integrated transformers shown in figures 7.31-7.34, are generally core-type transformers with leakage layers. In figure 7.31, in spite of leakage layers being placed on the two limbs, leakage flux is present in the window volume, which would cause eddy current losses in transformers. The transformer of figure 7.32, has the leakage layers inside the window volume, which requires a higher window area for the tape wound cores, thus increasing the cost of tape wound core transformer than that of figure 7.31. The transformer of figure 7.33 has the similar problem of flux cutting through the laminations near the leakage layer. The transformer of figure 7.34 has the leakage layer placed in between two separate cores. This arrangement

would reduce the eddy current losses but also reduces the total reluctance in the magnetization path of the tape wound transformer core. Here an arrangement for leakage integrated transformer is discussed for concentric winding type transformer with three limbs, similar to the concentric winding arrangement discussed in previous section. In the concentric winding arrangement, the leakage layers are placed in the front side and back side of the transformer., such that the leakage flux is reduced over the tape wound core window volume. The two possible arrangements of ferrite leakage layer integrated nano-crystalline core based transformer, are shown in figures 7.37-7.40. Figures 7.37-7.38 show the 3D view and top view of type 1 arrangement and figures 7.39-7.40 show the 3D view and top view of type 2 arrangement. The tape wound core of the transformers have the same dimension as the tape wound core for three port transformer of previous section. These two transformers have equal number of turns(8 each) for both inner and outer windings. The nano crystalline/tape wound core transformer details and ferrite leakage layer details are shown in table 17 and figures 7.35-7.36.

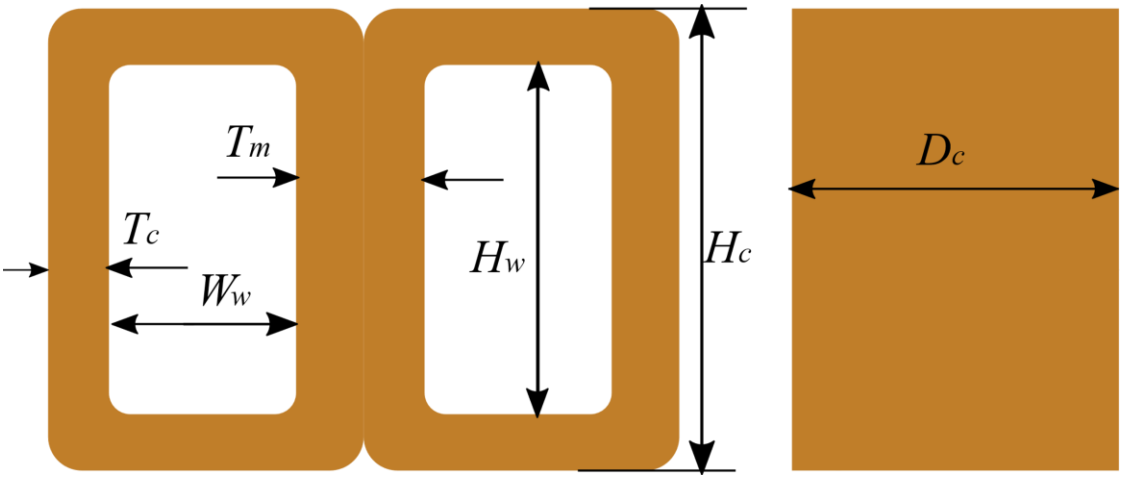

Figure 7.35. Tape Wound Core Front View & Side View.

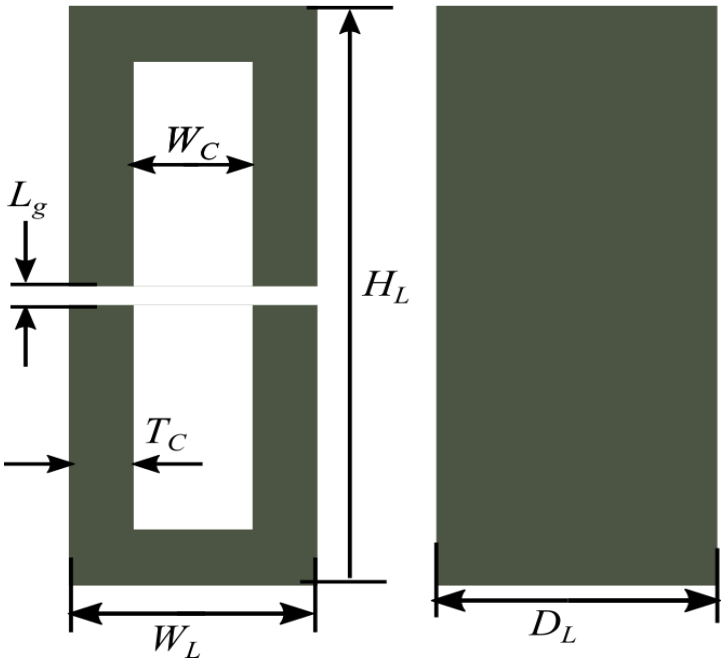

Figure 7.36. Leakage Layer Front View & Side View.

Table 17. Core Dimensions

T_c	13.5mm
T_m	27mm
H_w	78mm
W_w	32mm
H_c	105mm
D_c	96mm
W_c	12mm
T_c	18mm
W_L	48mm
H_L	103mm
D_L	45mm
L_g	3mm

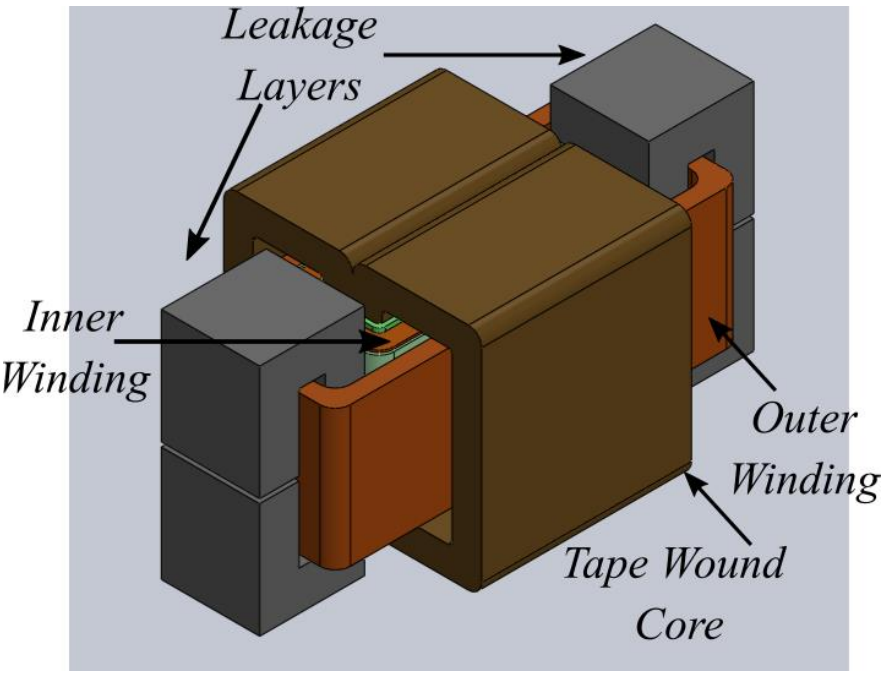

Figure 7.37. Type 1 Integrated Transformer.

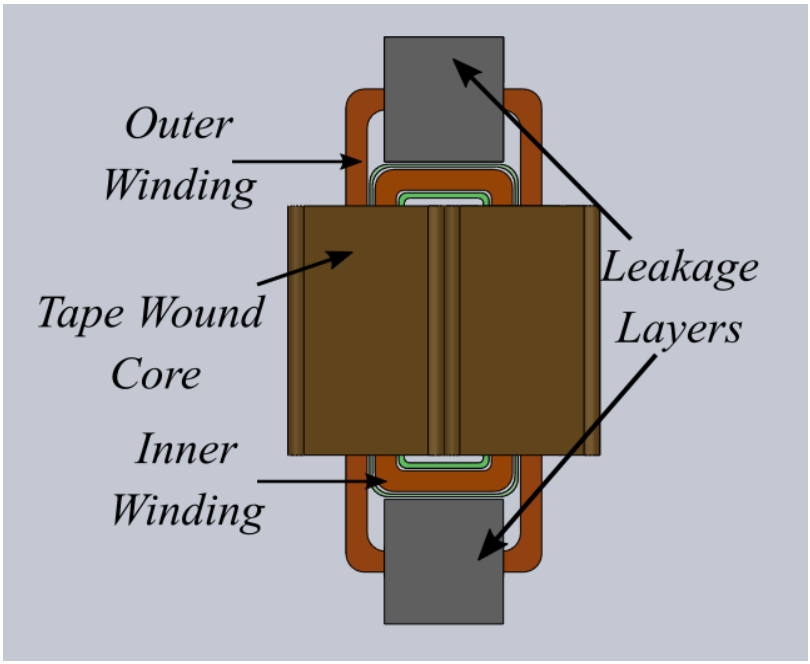

Figure 7.38. Type 1 Integrated Transformer(Top View).

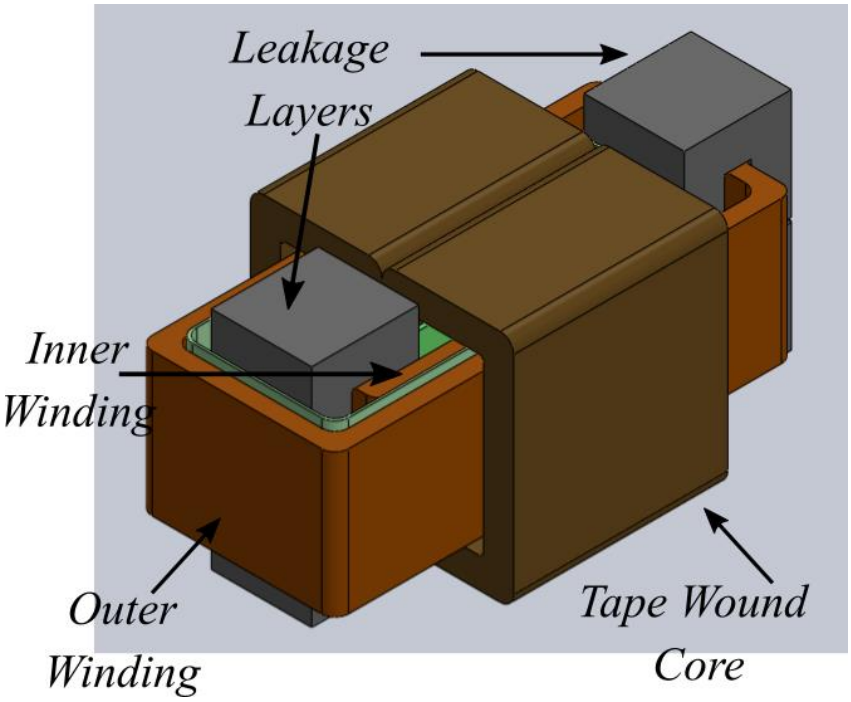

Figure 7.39. Type 2 Transformer.

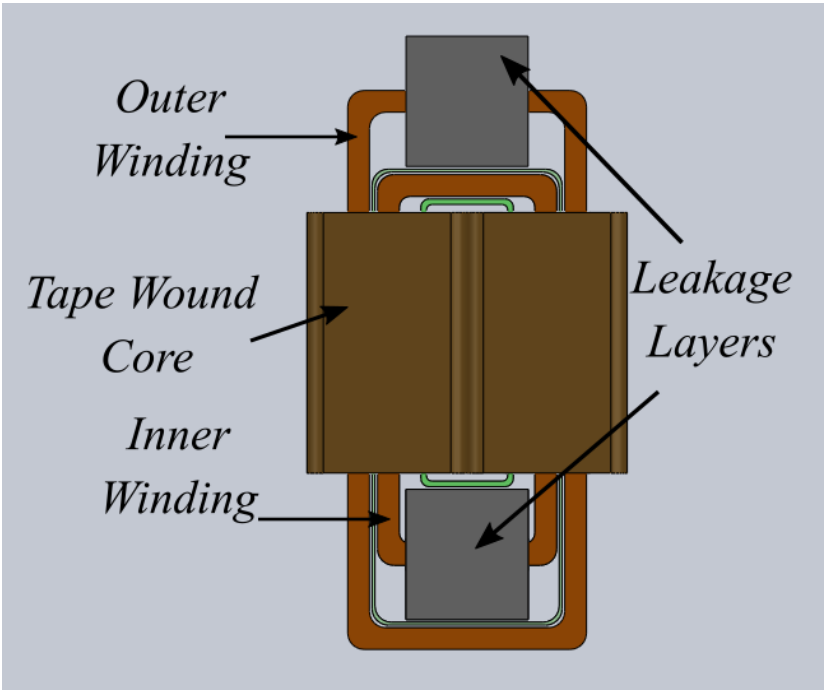

Figure 7.40. Type 2 Transformer(Top View).

In transformer type 1, the leakage layers are placed on only one winding, the outer winding. While in transformer type 2, the leakage layers are placed on both the windings. However, both the transformers have equal leakage due to same size of leakage layer, same air gap and same number of turns. The effect of placing the leakage layers in different manner, results in a difference in equivalent circuit. The equivalent circuits of the above two transformers are given below in figures 7.41-7.42. The effect of having the leakage inductances on one side or on both the sides, result in distribution of magnetizing current. In order to verify the effect on magnetizing current, Ansys Maxwell models for both the transformers have been created and FEA transient simulation have been performed to observe the magnetizing current effect and flux density in the transformer cores. The no-load winding currents, which is purely magnetizing in nature, for transformer type 1 and transformer type 2 are given in figures 7.43 and 7.44. The full load currents for the two transformer types are shown in figures 7.45 and 7.46, which are identical, thus the transformers have similar leakage inductances but their magnetizing current distribution is different. It can be observed that the magnetizing currents for type 2 transformer is shared by both the windings more equally than the magnetizing current being shared by both the windings for transformer type 1.

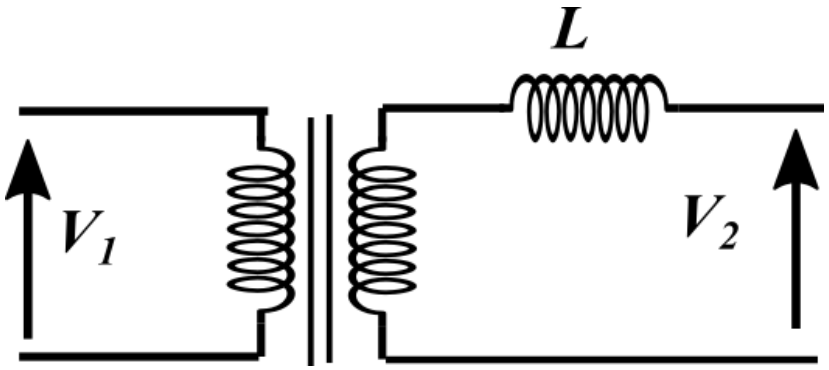

Figure 7.41. Equivalent Circuit for Type 1 Transformer.

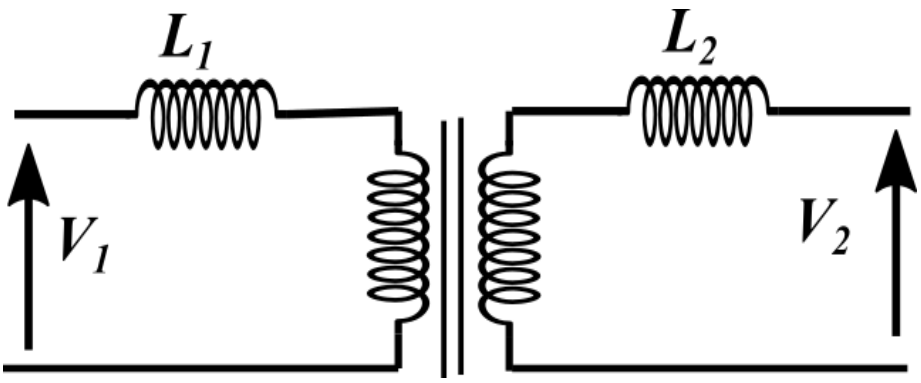

Figure 7.42. Equivalent Circuit for Type2 Transformer.

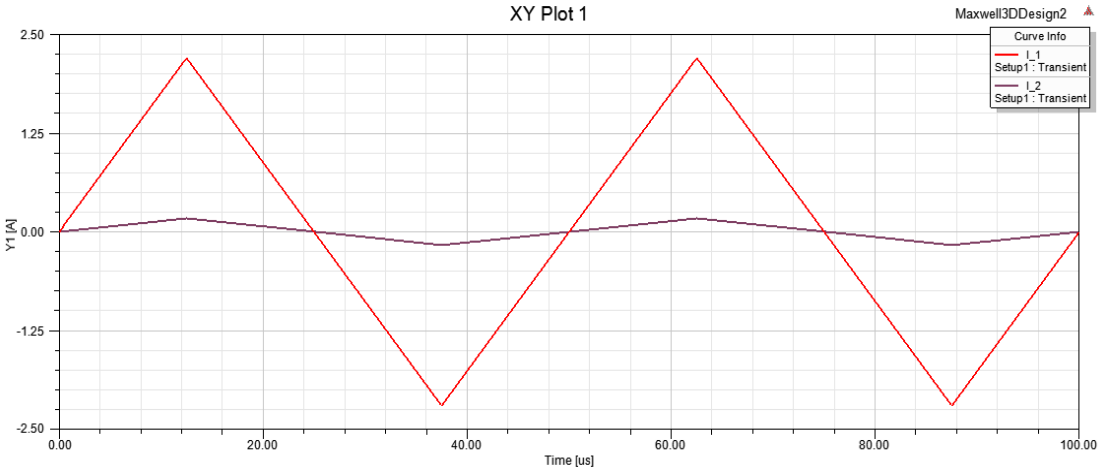

Figure 7.43. No-Load Winding Currents for Type 1 Transformers.

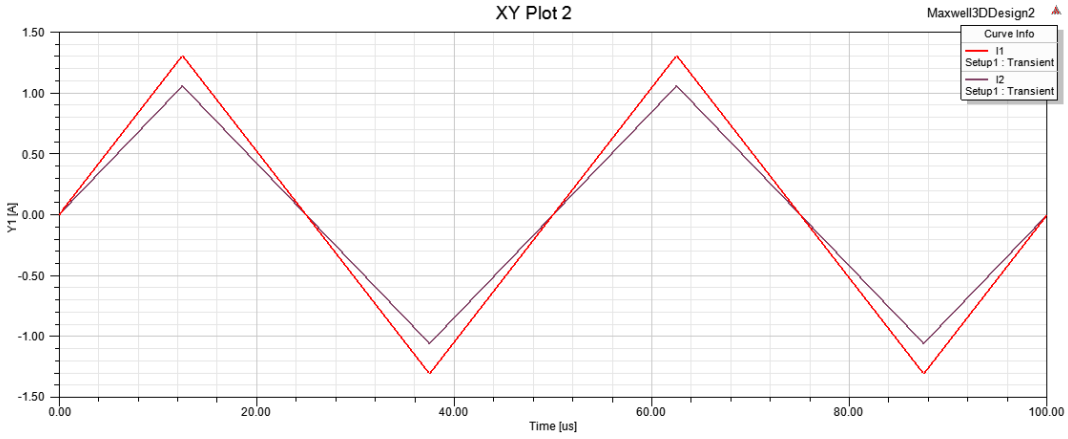

Figure 7.44. No-Load Winding Currents for Type 2 Transformers.

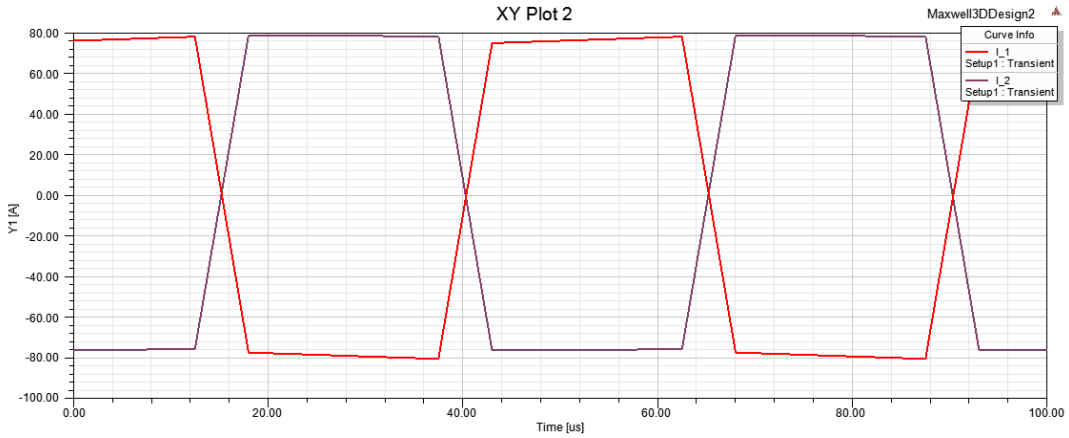

Figure 7.45. Full Load Winding Currents for Type 1 Transformers.

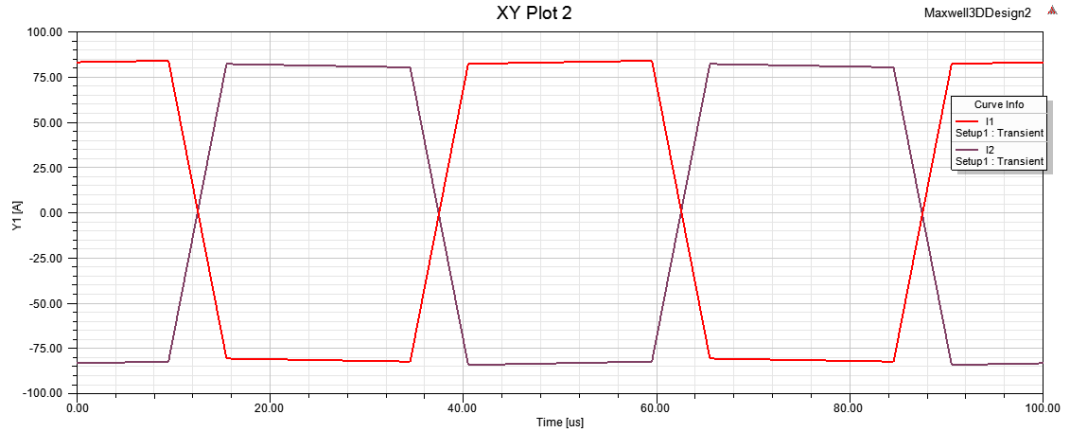

Figure 7.46. Full Load Winding Currents for Type 2 Transformers.

The comparison of total magnetizing currents for both the transformers at no-load and full load comparison is shown below in figures 7.47-7.50, it can be observed that though the no-load currents for both the transformers are equal(as shown in figures 7.47-7.48), there is a significant difference at full-load(as shown in figures 7.49-7.50) condition. The peak magnetizing current for transformer type 2 at full load condition is around 1.8A and for transformer type 1 is 2.4A, from figures 7.49-7.50. The reason for this is, as with increasing loading, the phase shift increases, the magnetizing voltage across magnetizing inductance reduces with increasing phase

shift angle, thus having lower magnetizing current. The effect of lower magnetizing current is to have lower loss at full load condition for type 2 transformer compared to type 1 transformer.

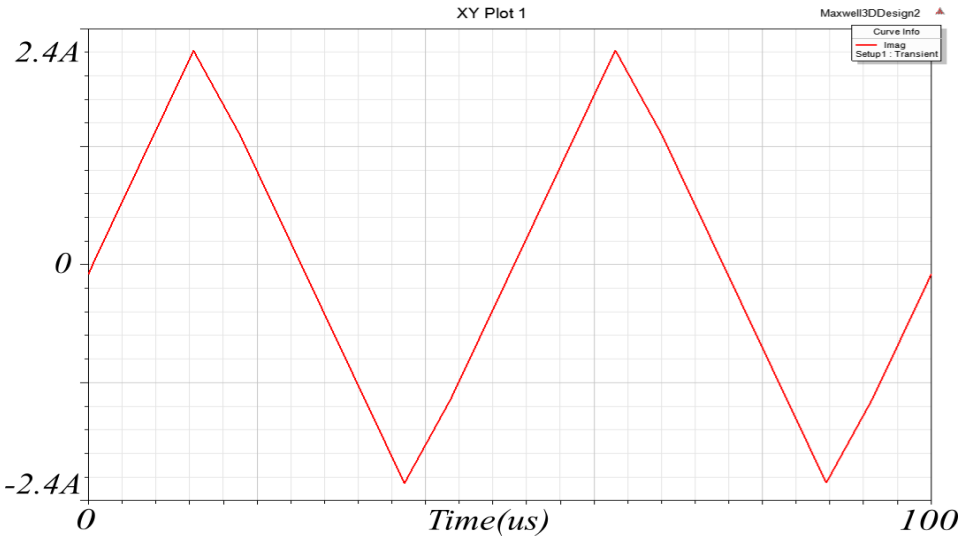

Figure 7.47. Magnetizing Current at No Load Current for Type 1 Transformer.

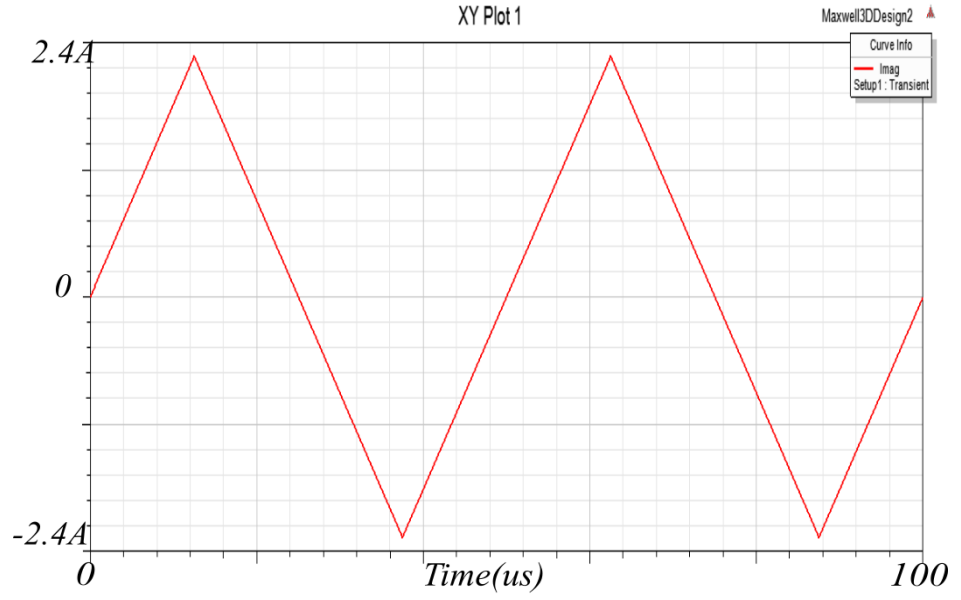

Figure 7.48. Magnetizing Current at No Load Current for Type 2 Transformer.

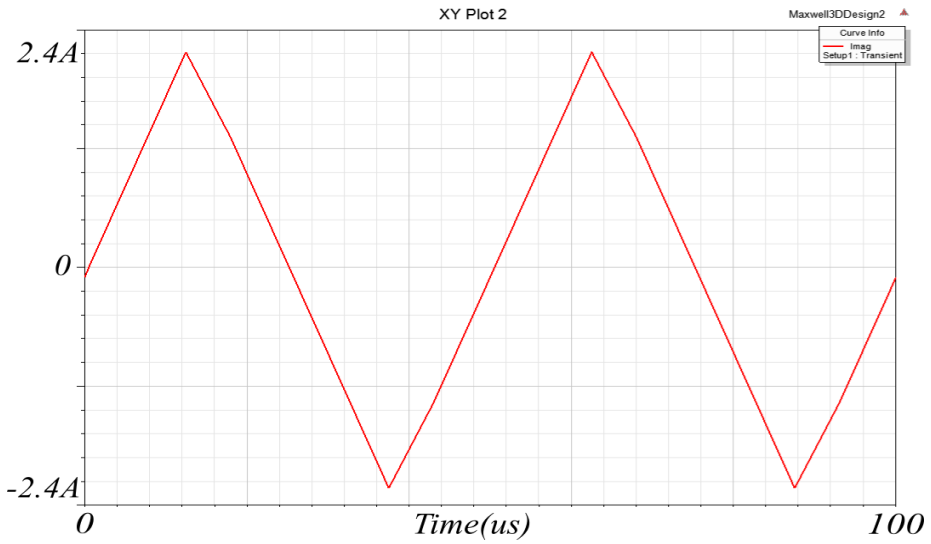

Figure 7.49. Magnetizing Current at Full Load Type 1 Transformer.

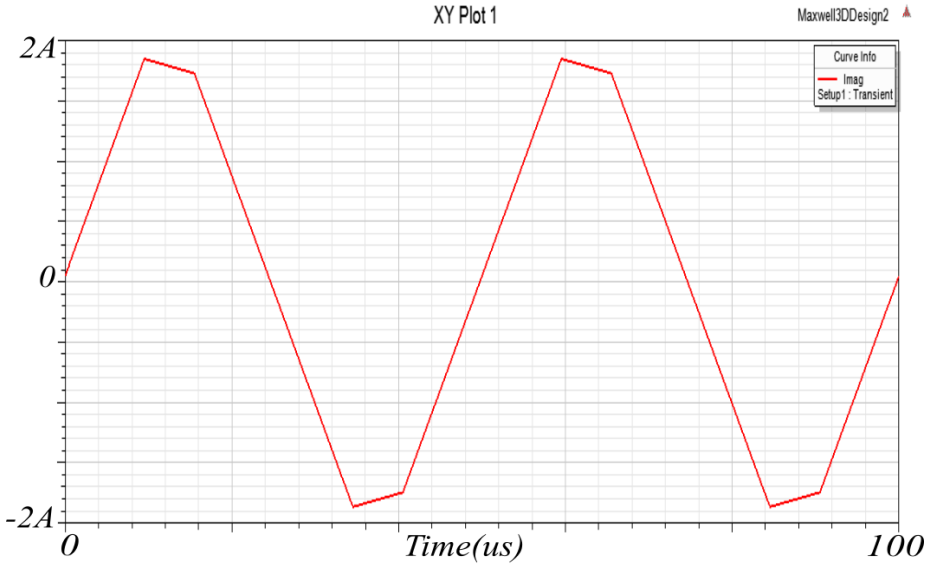

Figure 7.50. Magnetizing Current at Full Load for Type 2 Transformer.

The effect of reduced magnetizing current is also verified from the induced flux density in the tape-wound core. The peak flux densities for both the type 1 and type 2 transformers at no-load conditions and full-load conditions are shown in figures 7.51-7.54.

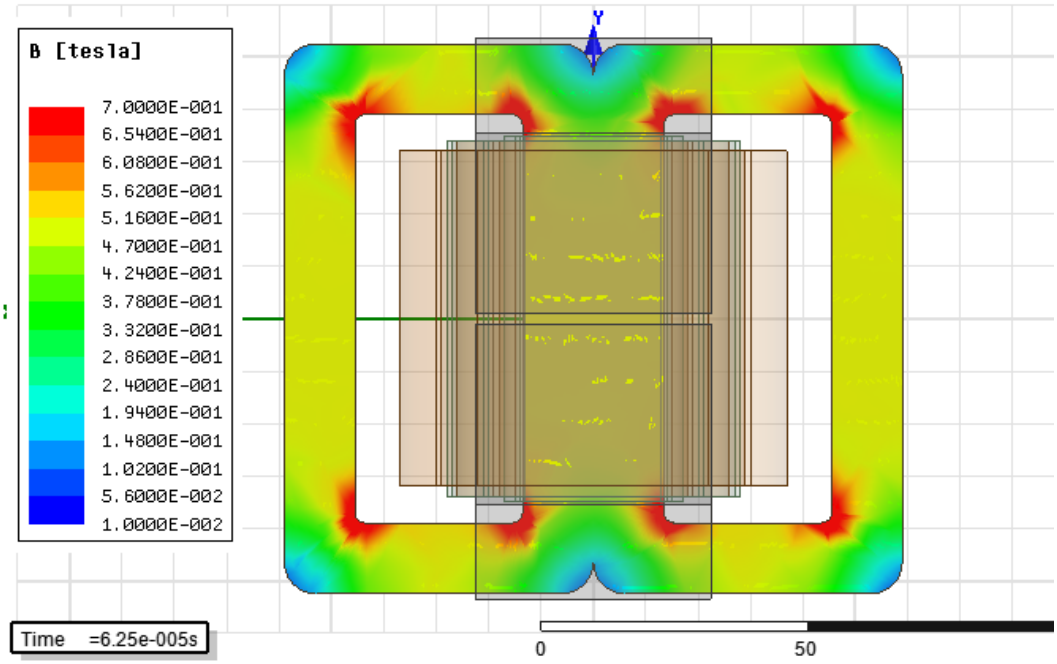

Figure 7.51. Peak Flux Density in Type 1 Transformer at No Load.

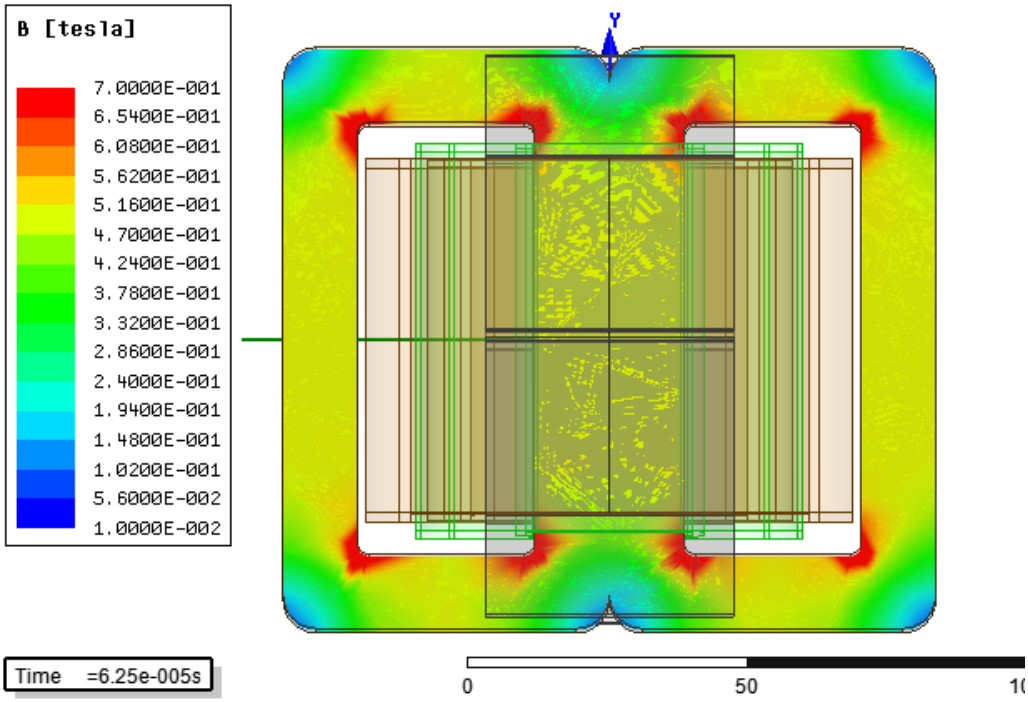

Figure 7.52. Peak Flux Density in Type 2 Transformer at No Load.

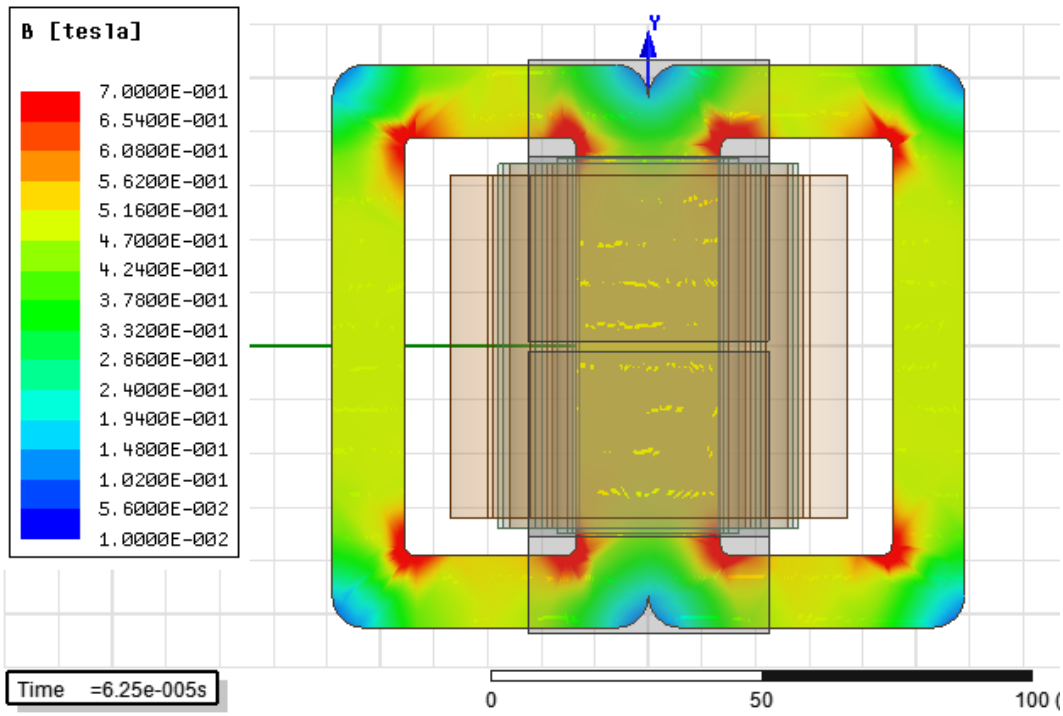

Figure 7.53. Peak Flux Density in Type 1 Transformer at Full Load.

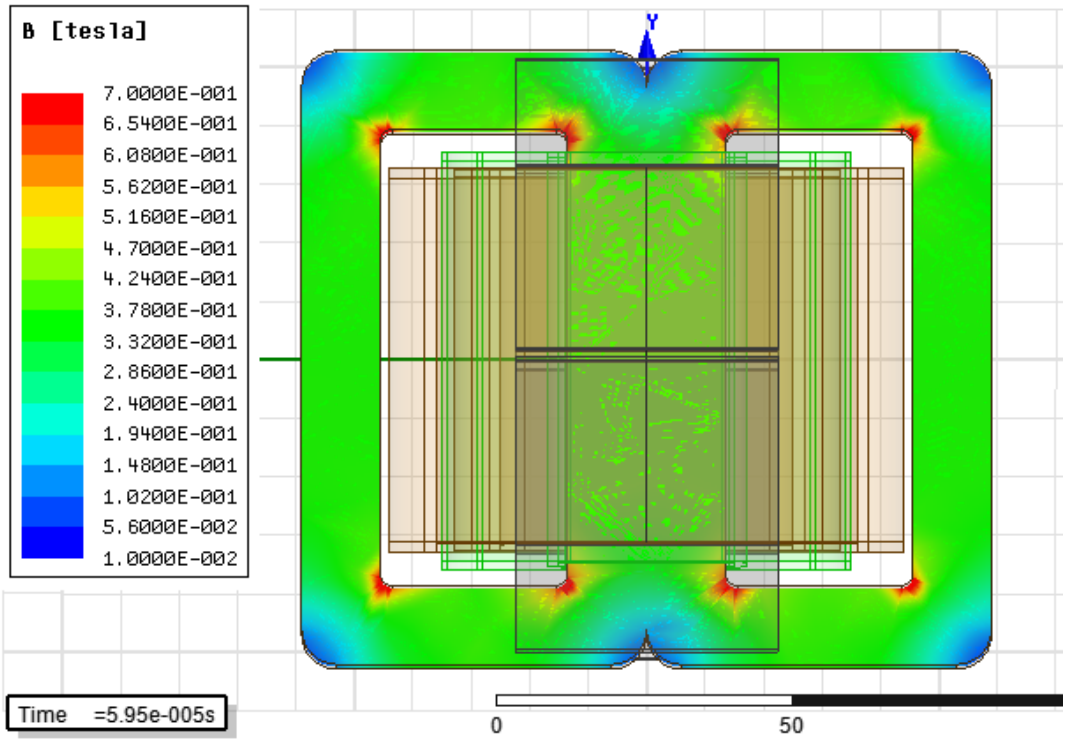

Figure 7.54. Peak Flux Density in Type 2 Transformer at Full Load.

It can be observed that the no-load peak flux density in the tape wound core is same(around 0.58T) for both the transformers but the full load peak flux density is much lower for type 2 transformer(around 0.4T) compared to type 1 transformer(around 0.56T). The variation of peak flux densities as a function of loading is shown in figure 7.55. The effect of the drop in peak flux density with increasing loading in type 2 transformer, results in lower core losses, which will be demonstrated with experimental results.

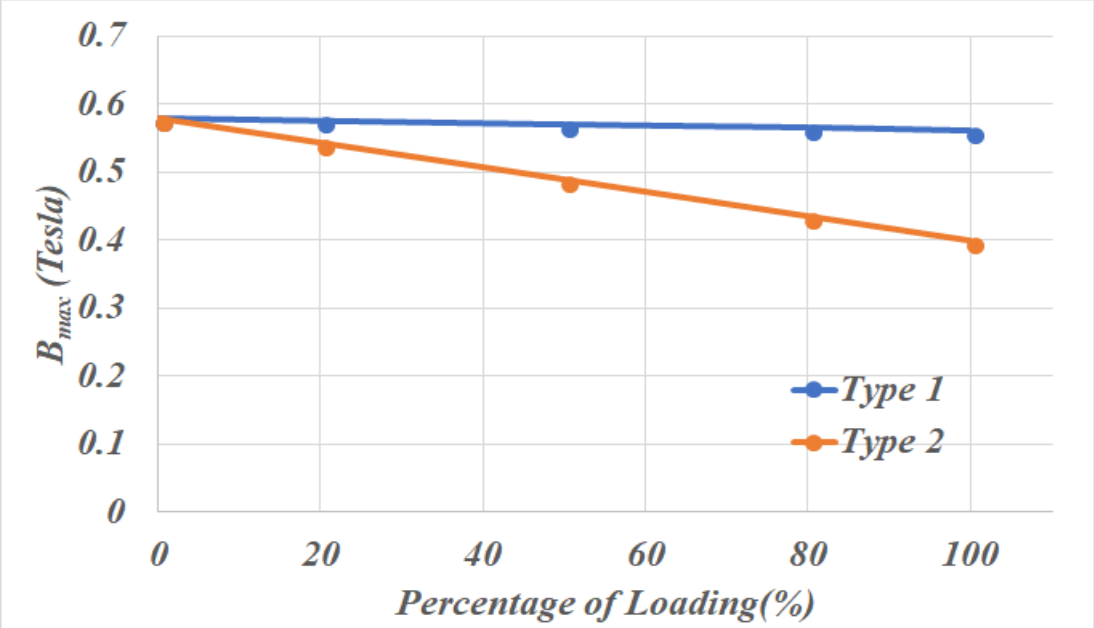

Figure 7.55. Variation of Core Peak Flux Density at 20kHz with Loading.

The inductance matrix obtained from FEA simulation are shown below in figures 7.56-7.57, to give an estimate of the leakage inductance distribution for the two transformers, the unit is in mH. It can be observed that for type 1 transformer, the self inductance L_{11} and mutual inductance L_{12} are much close to each other, compared to L_{21} and L_{22}, which indicates the leakage is mainly on the outer winding('2') side rather than inner winding. For type 2 transformer, both L_{11} and L_{22}

are almost equally deviant from L_{12} and L_{21}, thus indicating a more equal distribution of leakage inductances.

	Current1	Current2
Current1	4.2182	4.2143
Current2	4.2143	4.2651

Figure 7.56. Inductance Matrix for Type 1 Transformer.

	Current1	Current2
Current1	4.2446	-4.22
Current2	-4.22	4.2507

Figure 7.57. Inductance Matrix for Type 1 Transformer.

The FEA simulation of leakage layers, which are made of ferrite material in this case, are shown in figures 7.58 and 7.59. The FEA simulation has been performed for peak current of 100A, which is higher than estimated current of 90A for 50kW power flow of DAB converter. It can be observed that for both the type 1 and type 2 transformer, the peak flux densities are same around the core volume, except in the outer limb, having little lower peak flux density near the air gap due to fringing effect. The peak flux density in the ferrite leakage core are mainly around 0.25T to 0.3T, except near the edges of the cores, where it reached around 0.4T.

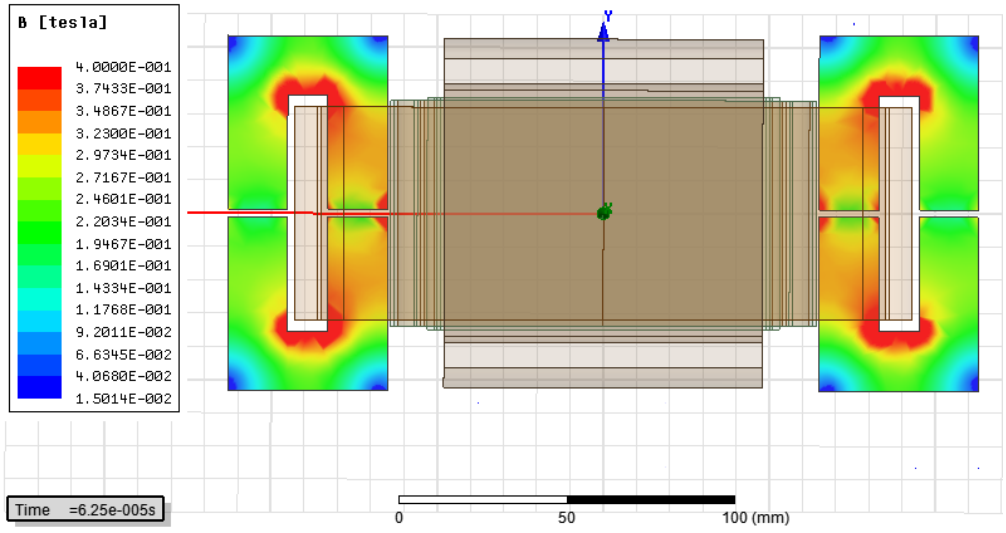

Figure 7.58. Leakage Layer Peak Flux Density for Type1 Transformer.

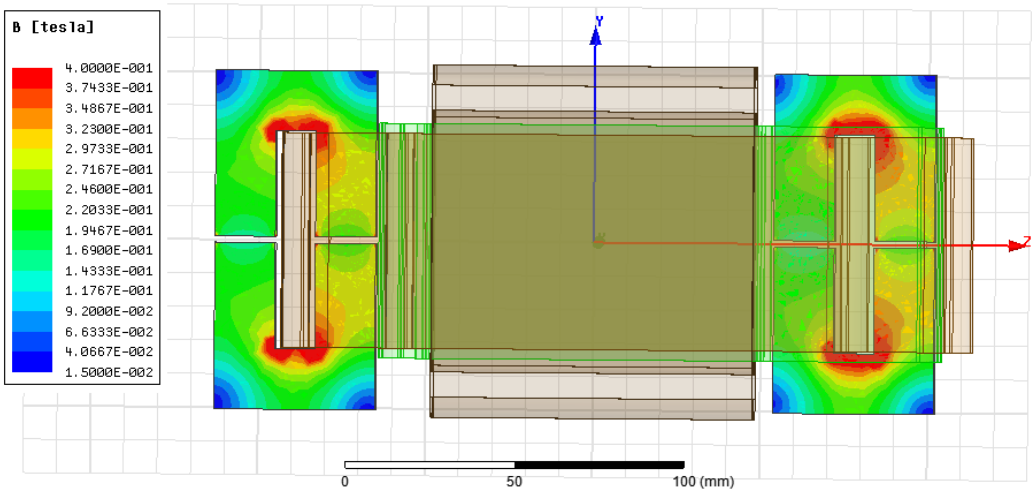

Figure 7.59. Leakage Layer Peak Flux Density for Type2 Transformer.

Given the benefits of core loss for type two transformer, where the leakage is distributed on two windings, a laboratory prototype of type 2 transformer has been developed for performing experimental studies. Figures 7.60 and 7.61 show different views of the laboratory prototype transformer. The transformer is rated at 50kW with switching frequency of 20kHz at a peak flux density of 0.58T. The winding is made of litz wire with construction 2500/38AWG.

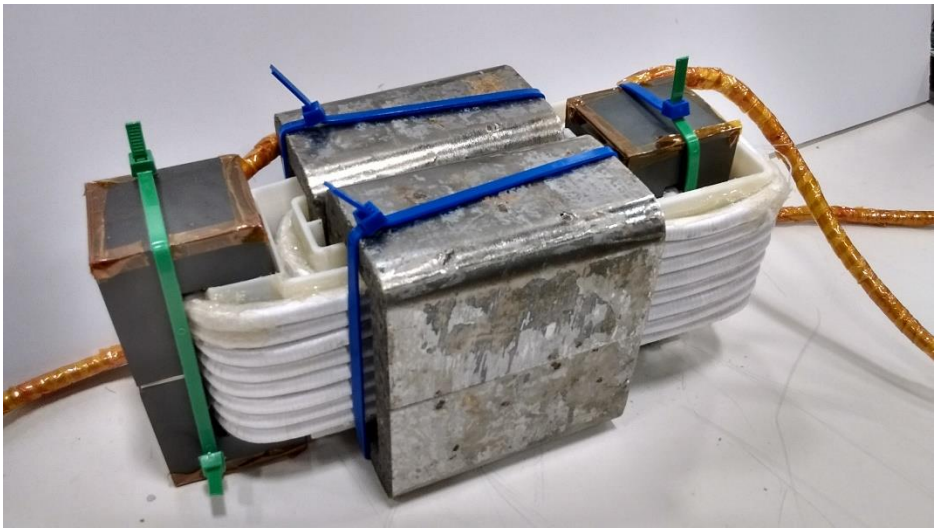

Figure 7.60. Laboratory Prototype of Integrated Transformer Type 2.

Figure 7.61. Laboratory Prototype of Integrated Transformer Type 2.

7.4. Experimental Study of Leakage Integrated Two Port Transformer

The aforementioned two port transformer with integrated nano-crystalline core and ferrite leakage layer is tested in a hardware prototype. The hardware prototype used for testing this transformer is same as the prototype used for the three port nano-crystalline transformer testing previously. The transformer is rated for 50kW power with operating frequencies around 20kHz. In this section, the transformer is run from 15kHz, 20kHz, 25kHz & 30kHz switching frequencies and the experimental results are analyzed. Schematic for the two port converter system prototype is shown in figure 7.62, where V_{dc1}=V_{dc2}=800V. Figures 7.63-7.64 show the transformer winding voltages & currents at 15kHz & 30kHz switching frequencies at 50kW power.

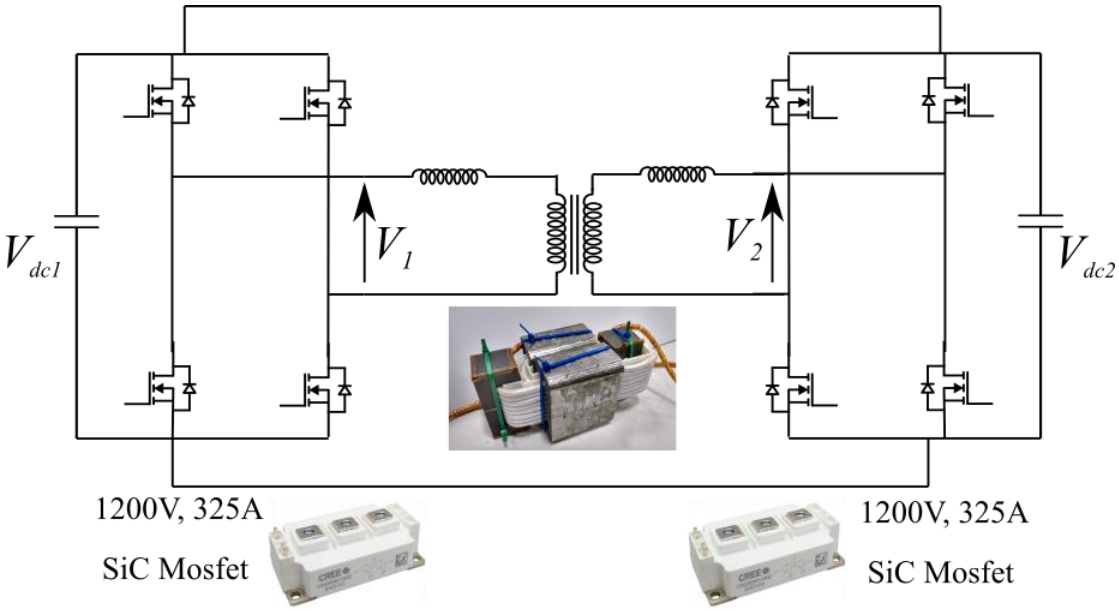

Figure 7.62. Schematic for test Setup of Two Port DAB Converter.

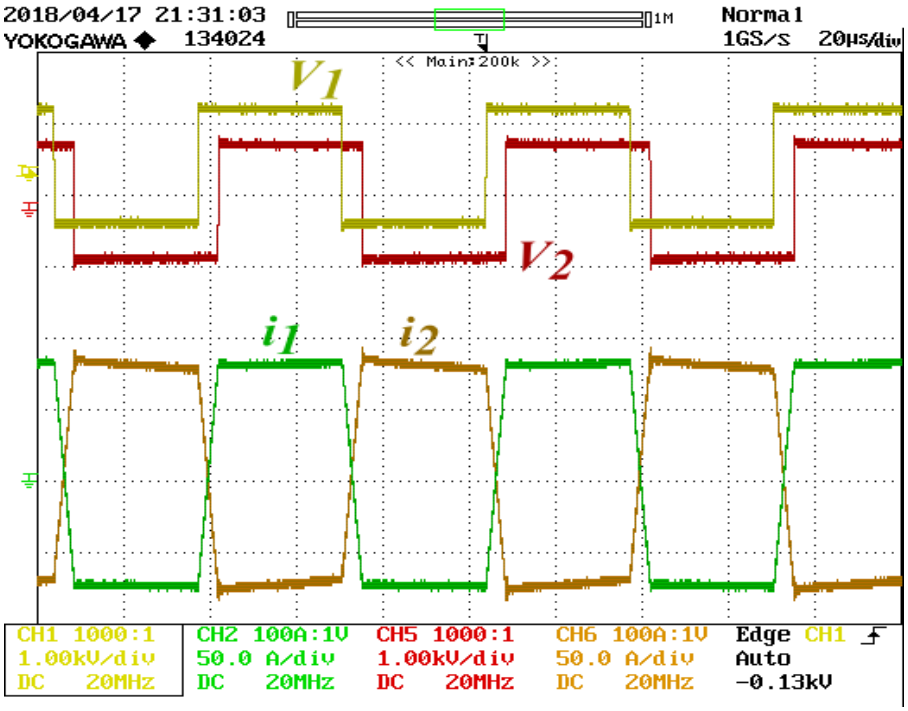

Figure 7.63. Transformer Waveforms at 15kHz.

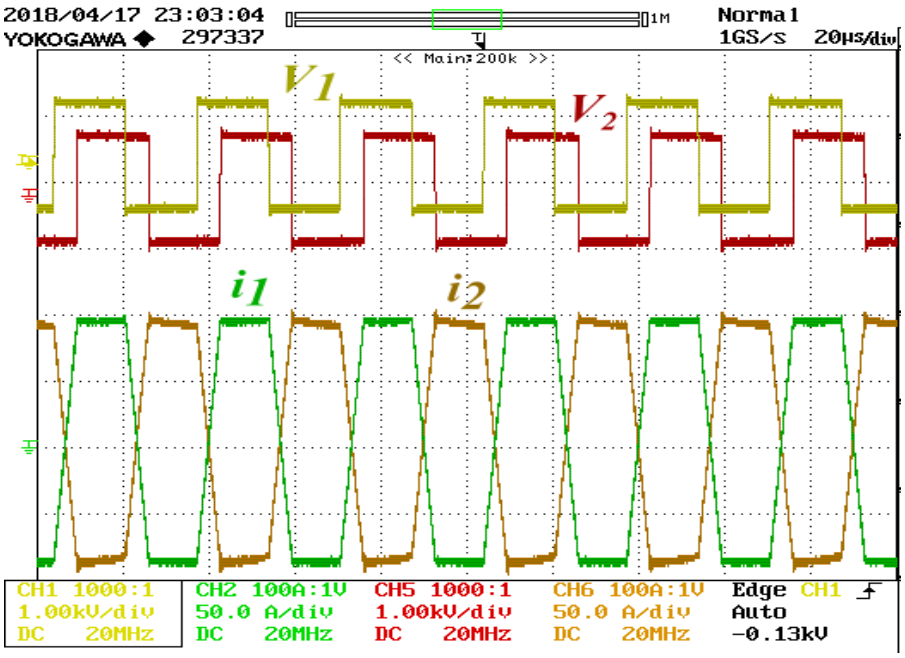

Figure 7.64. Transformer Waveforms at 30kHz.

The converter efficiency and the input & output powers are measured using a WT3000 power analyzer. The efficiency and losses, measured from power analyzer, for the whole converter system are shown in figures 7.65 and 7.66. The transformer core losses are measured by applying the same quasi square wave voltage across both the windings.

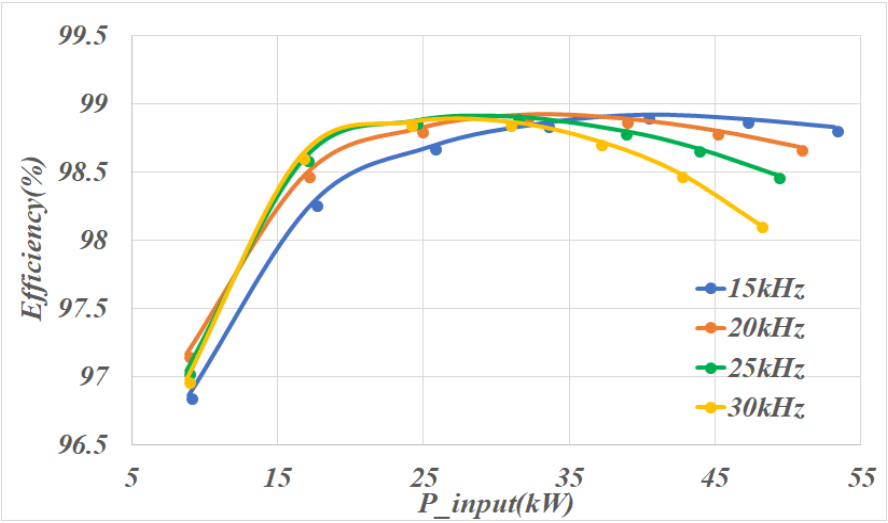

Figure 7.65. Efficiency of DAB Converter Over Full Operating Range.

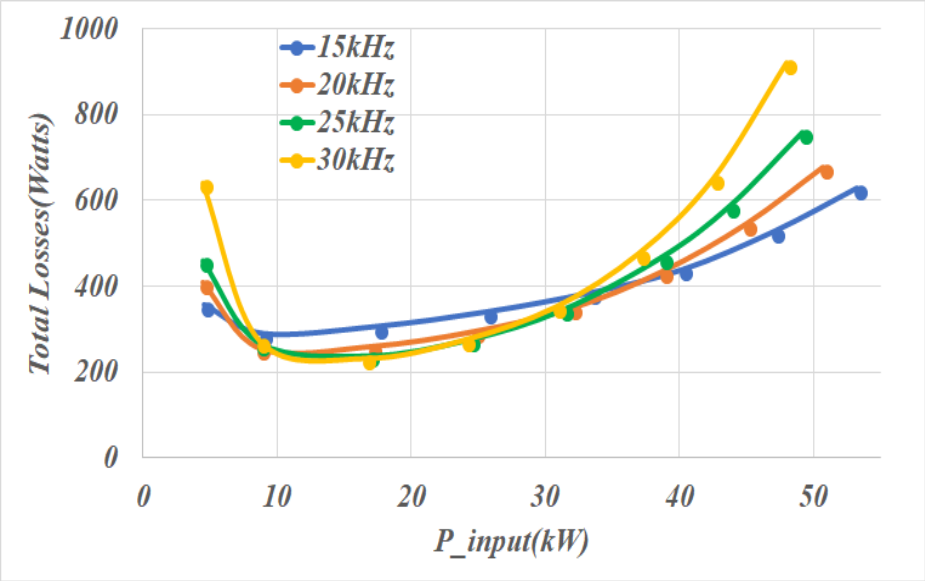

Figure 7.66. Total Loss Variation of Whole Converter.

The core loss for the nano-crystalline transformer for a particular operating point can be measured by applying the same quasi-square wave voltage(as shown in figure 7.67) for both V_1 and V_2 with no phase shift. From figure 7.42, if it is considered L_1=L_2, then the induced voltage across the magnetizing inductances can be derived as $V_m = \frac{V_1 + V_2}{2}$. Thus for a particular operating point with phase angle ϕ, the magnetizing voltage V_m can be recreated by introducing a zero voltage in the H-bridge converter output voltage. The duration of zero voltage in H-bridge converter output voltage is ϕ in half cycle π. A waveform of similar induced voltage across a sense coil on the core of the transformer is shown in figure 7.68.

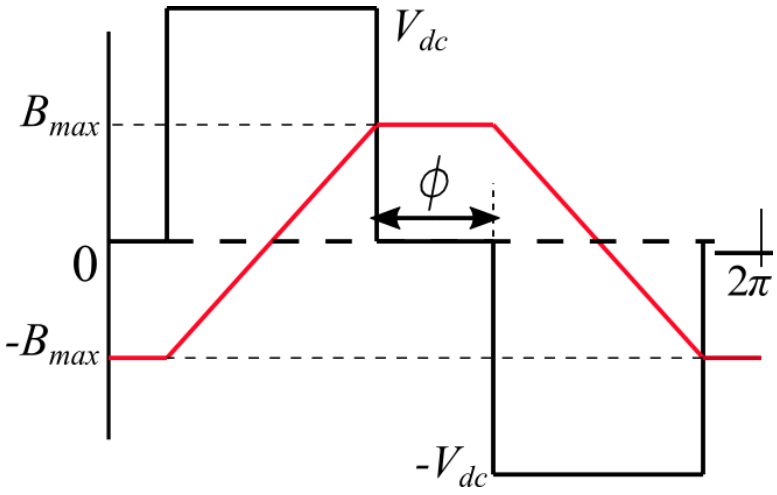

Figure 7.67. Magnetizing Voltage & Induced Flux pattern.

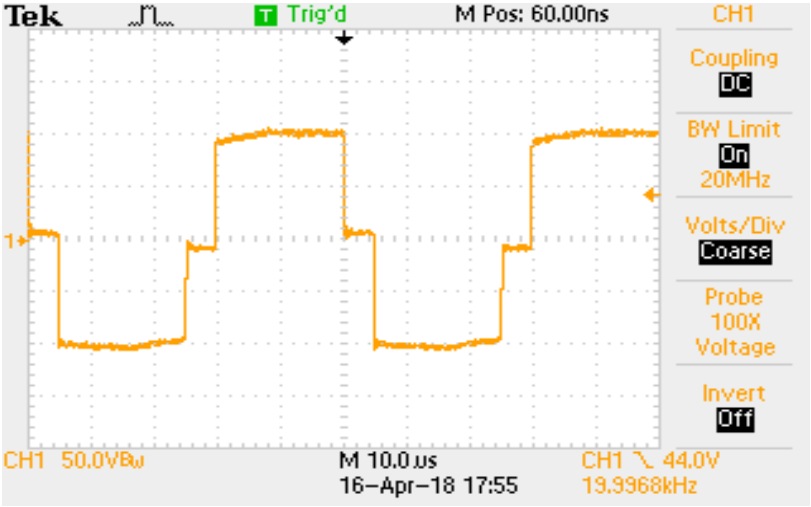

Figure 7.68. Induced Voltage Across Sense Coil.

The measured core losses at different frequencies for the nano-crystalline transformer is shown in figure 7.69, which also shows that the measured core losses drop with increasing loading or phase shift. Considering Zero Voltage Switching(ZVS) for Dual Active Bridge converter, the switching losses can be considered zero for SiC Mosfet devices, as the turn-on is soft-switched and the actual turn-off loss is negligible[70]. The conduction losses for SiC Mosfet devices are derived from PLECS simulation using conduction loss model and thermal model of

device package resistance and heatsink resistance. Therefore the total transformer loss and stray losses can be derived as $P_{Transformer\_total} = P_{Loss\_total} - P_{MOSFET\_conduction}$. The total transformer loss variation is shown in figure 70.

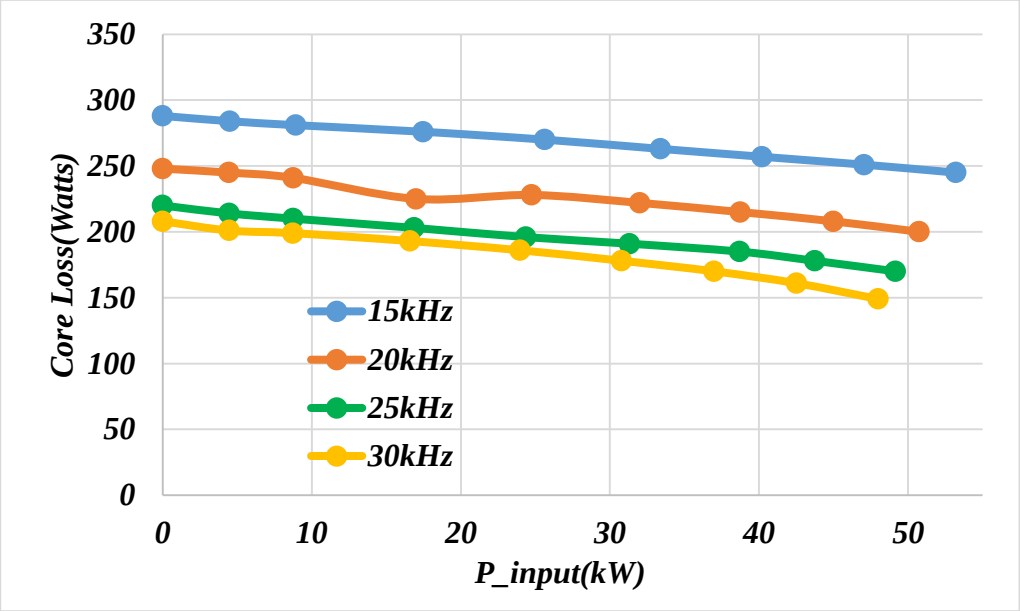

Figure 7.69. Measured Transformer Core Losses.

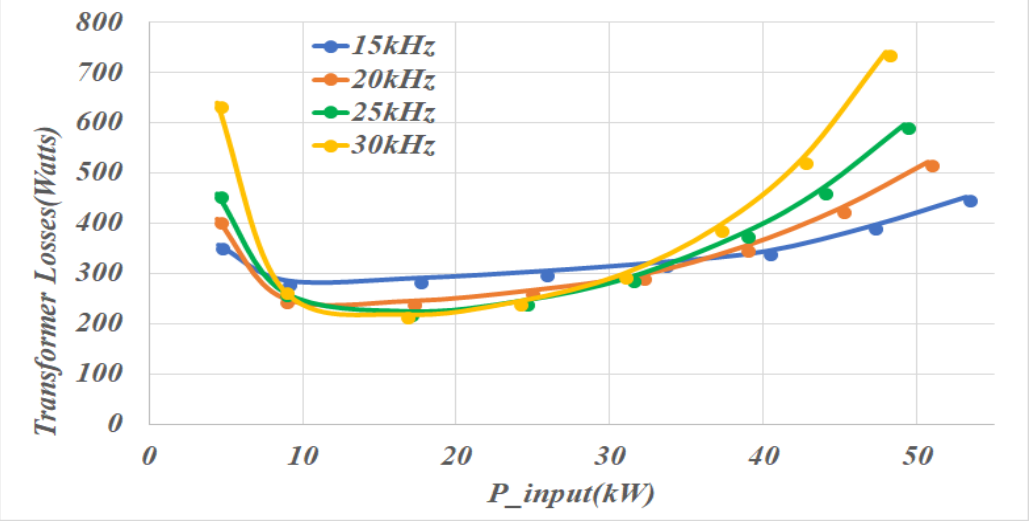

Figure 7.70. Transformer Loss Variation over Input Power.

It can be observed that at very low power, the losses are higher and as loading increases, the losses go down initially and then increases with loading again. This can be explained as due to very low loading at low power conditions, the converter does not have ZVS operation, due to insufficient energy in leakage inductance and has sufficient resulting switching losses, but as loading increases, the converter moves into ZVS operating region and switching losses become negligible. The losses in transformer winding and leakage layers can be estimated using conventional technique of estimating copper losses and inductor core losses(using iGSI method). In the above integrated transformer above, there is a significant amount of eddy current loss over the transformer window volume portion, where some portion of leakage flux cuts through the laminations onto the windings. This can also be explained as the difference between total leakage of the transformer(50μH) and leakage due to ferrite leakage layer(10μH). The eddy current loss over transformer window, can be estimated as difference between total transformer loss and sum of core loss, copper loss and leakage layer loss(shown in figure 7.71). In estimating the copper and leakage layer losses, the effect of temperature is not considered. The estimated winding losses and leakage layer losses are shown in figures 7.72 and 7.73.

$$P_{CU} = \sum_{n=1}^{9} {I_{rms,n}}^2 R_{ac\_total,n} \qquad P_L = \frac{1}{T}\int_0^T k_1 \left|\frac{dB}{dT}\right|^{\alpha} |B(t)|^{\beta-\alpha}$$

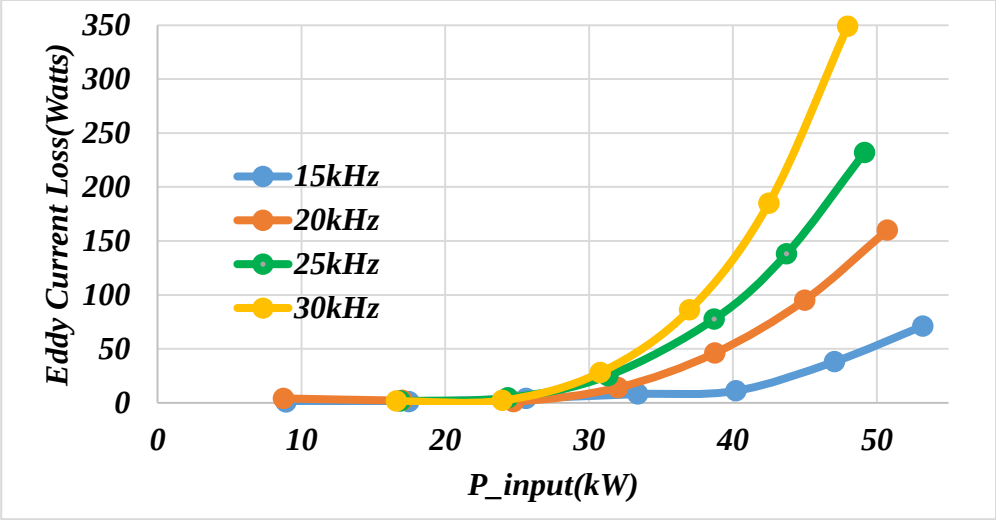

Figure 7.71. Eddy Current Loss Variation Over Input Power.

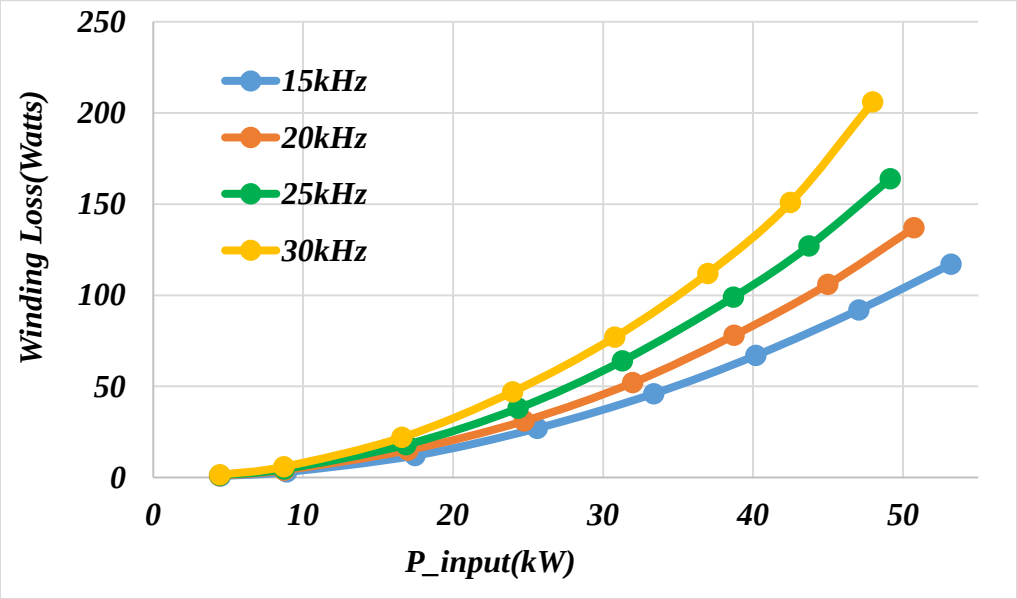

Figure 7.72. Winding Loss Variation.

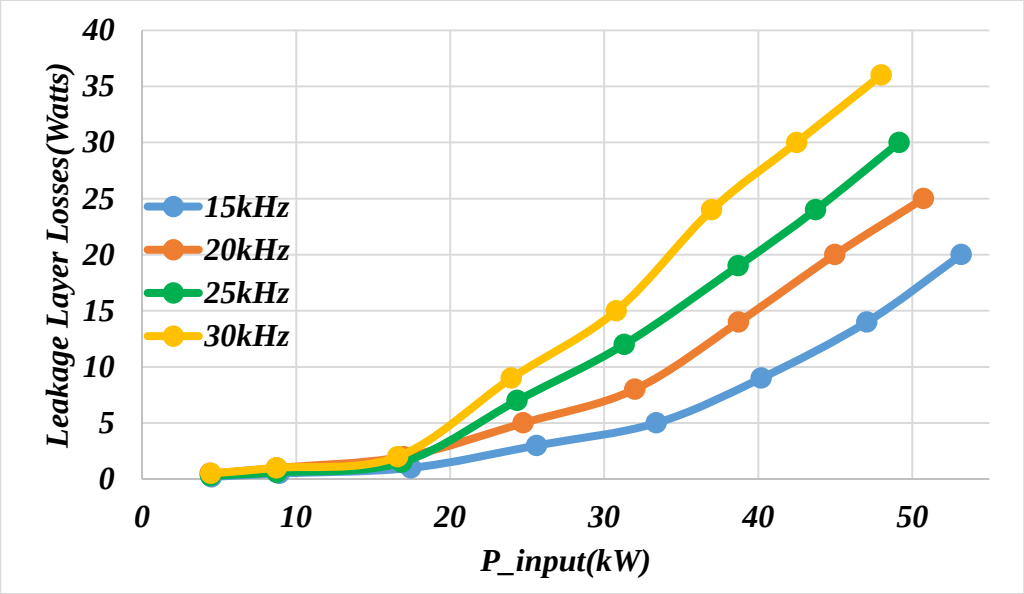

Figure 7.73. Ferrite Leakage Layer Loss Variation.

7.5. Conclusions

The leakage flux effect on tape wound core transformers create high losses and create heating of the tape wound core and cause fast temperature rise. The alternate methods of using external series inductors reduces the core loss and provide high efficiency, which has been demonstrated with the results of three port converter system. The integrated transformer+inductor topology also has provided high efficiencies over the operating region. The use of inductors on both primary & secondary windings reduces core losses significantly over the operating range & increases efficiency.

Chapter 8. High Frequency Transformer Current Control Strategy For Triple Active Bridge(TAB) Converter

The basic power flow operation of Dual Active Bridge(DAB) or Triple Active Bridge(TAB) converter is controlled by controlling the phase-shift angle between different winding voltages[56,60]. Different versions of phase shifted converters have been explained in detail in literature[50-62]. Few research efforts have focused on optimal operation focusing on optimum current stress on power semiconductor devices, optimum converter losses and optimum switching losses with ZVS modulation[61-62, 71-74]. The phase shifted DC-DC converters' control techniques are the key things required for optimum performance and operation, which requires the high frequency transformer to operate reliably. Using a conventional PI controller approach for dc power flow control or output dc voltage control, the phase angle control method causes transformer core saturation during high transients in the isolating high frequency transformer. Different current control approaches & flux control approaches for dc-dc converters have been proposed in [75]-[82]. A peak current control and peak-valley current control for the transformer winding current of two port DAB converter has been proposed in [79], which controls the transformer winding currents within one switching cycle by sampling the winding current twice in a single switching cycle. A similar method for two winding DAB has also been proposed in [78]. The methods proposed in [78],[79] use peak current sensing during device switching, which is highly sensitive to noise and EMI generated due to generated dv/dt from high speec switching of SiC Mosfet devices.

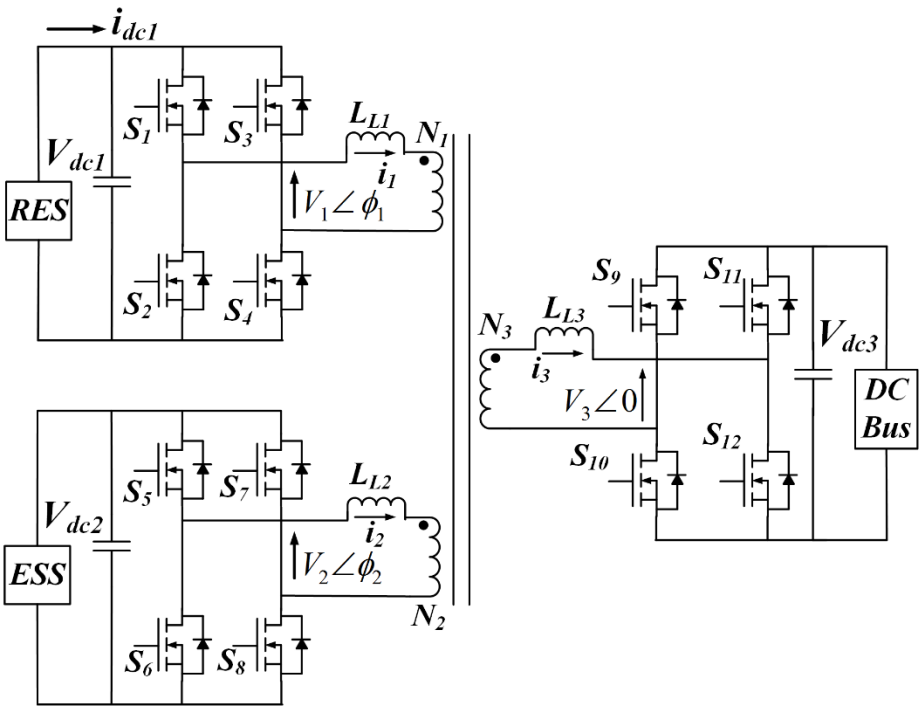

Figure 8.1. Triple Active Bridge(TAB) Phase-Shifted DC-DC Converter.

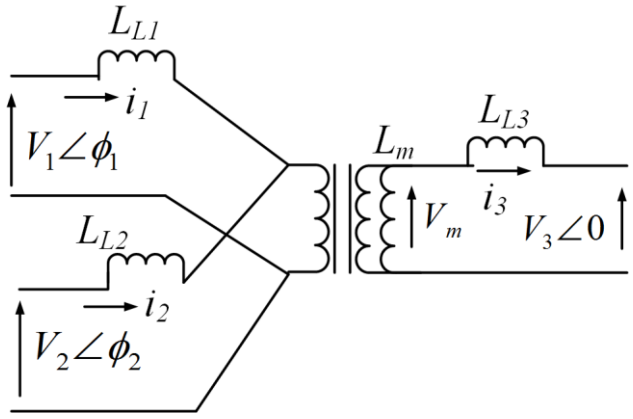

Figure 8.2. Equivalent Circuit of Transformer for TAB Converter.

In this section, the current control method discussed in [78-79] has been extended for three port phase shifted TAB converter(shown in figure 8.1), using high frequency current sensing method and updating the phase angle in each switching cycle. The objective of current control method is to control the high frequency transformer current in each cycle so that dc transients are

eliminated from transformer currents during any phase angle change from one cycle to the next. The transformer currents are sensed in each cycle and the phase shift angles for next switching cycle are calculated and updated based on the reference value for next cycle. The control methods discussed in this paper uses two methods for sensing the currents and updating the phase shift angles. The current control methods discussed in this chapter provide an inherent power decoupling for the three port TAB converter where currents from two ports can be individually & independently controlled. In the first current control method, the transformer currents are sensed in each half cycle and the phase angles are updated in the subsequent opposite half cycle, which is an extension of the current control method discussed in [78],[79]. In the second method, a new technique is proposed where the transformer currents are both sensed and updated only once in a switching cycle and they are controlled as per their references in a single switching cycle. The advantage of the second method is that, it allows higher time window to the digital controller for performing other complex calculations and allowing the designer for control implementation at higher switching frequencies. The second method also reduces the error in calculation due to any offset from the high frequency current sensor, which is present in first method for low power cases and it causes the phase angle values and steady state winding currents to oscillate around a stable value. The analysis of the proposed control methods is done in this paper based on the equivalent circuit for three port phase shifted TAB converter, which is shown in figure 8.2. The current control methods have been experimentally verified and satisfactory results have been obtained for verification. The implementation of the current control techniques have been done using digital controller.

8.1. Three Port Phase Shifted Converter Analysis

The leakage inductance of high frequency transformer for phase shifted converter acts as energy transferring element[56]. The three H-bridges in figure 8.1, produce square wave voltages across their respective windings, with phase differences among them, causing active power transfer from one port to the other. The power flow scenarios between the three ports of the transformer of figure 8.1, are functions of the phase differences between different windings[56]. In figure 8.1, the voltage V_3 is considered as the reference voltage and the other two winding voltages V_1,V_2 are referenced w.r.t. voltage V_3. The voltages V_1,V_2 have phase shift angles ϕ_1, ϕ_2 which are referenced w.r.t. V_3. The transformer winding currents for a TAB converter are piecewise linear in nature[56] and are functions of the phase shift angles ϕ_1, ϕ_2. For this thesis work, it is assumed that RES at port 1 acts as source and can only deliver power, while the ESS at port 2 can act as both source and sink. Therefore there are three possible scenarios based on the phase shift angles (a) $\phi_1 < \phi_2 < 0$, (b) $\phi_2 < \phi_1 < 0$, and (c) $\phi_1 < 0 < \phi_2$. The three possible cases of winding voltage positions are shown in figures 8.3-8.5.

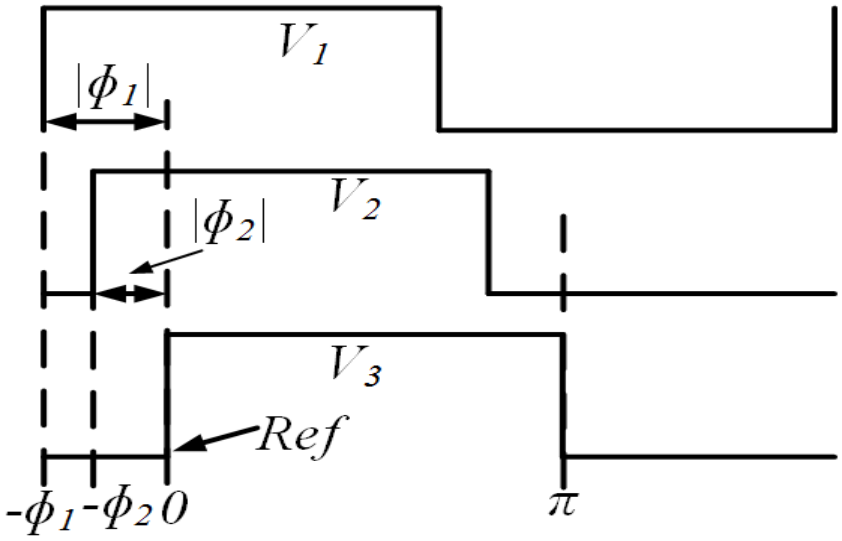

Figure 8.3. Mode 1: Winding Voltages when $\phi_1 < \phi_2 < 0$.

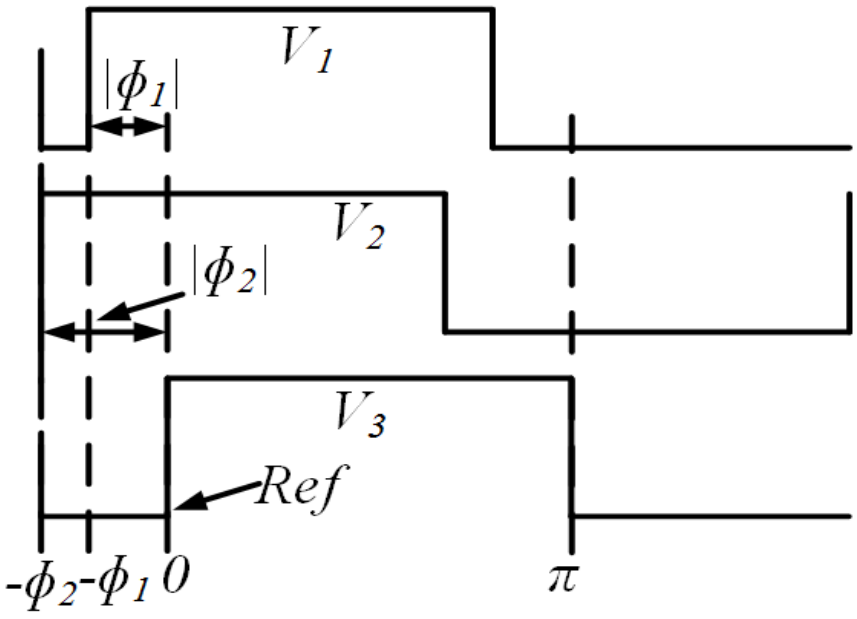

Figure 8.4. Mode 2: Winding Voltages when $\phi_2 < \phi_1 < 0$.

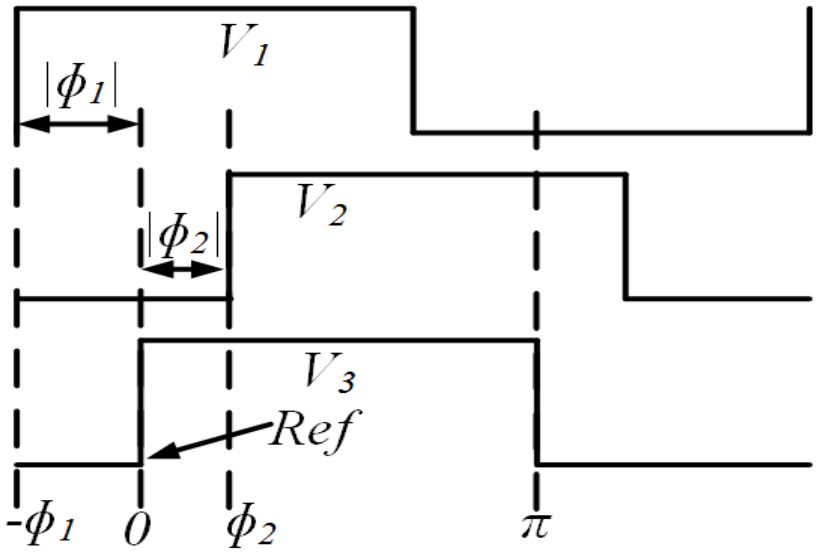

Figure 8.5. Mode 3: Winding Voltages when $\phi_1 < 0 < \phi_2$.

The voltage V_m across the magnetizing inductance L_m, referred to windings 1,2,3 are given in equations (1,2,3). The voltage term V_{xy} refers the voltage V_x of winding 'x' referred to winding 'y'. Similarly, inductance L_{Lxy} refers to inductance L_{Lx} of winding 'x' referred to winding y. The

piecewise linear nature of transformer winding currents for winding 1,2 and 3 are given in equations (8.7-8.9), where θ_0 is initial instant for the linear interval x and θ is any instant within that interval 'x' and m_x^y is slope of that interval 'x' for current in winding 'y'.

$$V_{m1} = \frac{(V_1 L_{L21} L_{L31} + V_{21} L_{L1} L_{L31} + V_{31} L_{L21} L_{L1}) L_{m1}}{L_{n1}{}^3} \quad (8.1)$$

$$V_{m2} = \frac{(V_2 L_{L12} L_{L32} + V_{12} L_{L2} L_{L32} + V_{32} L_{L2} L_{L12}) L_{m2}}{L_{n2}{}^3} \quad (8.2)$$

$$V_{m3} = \frac{(V_{13} L_{L23} L_{L3} + V_{23} L_{L13} L_{L3} + V_3 L_{L23} L_{L13}) L_{m3}}{L_{n3}{}^3} \quad (8.3)$$

where $$L_{n1}{}^3 = L_{L1} L_{L21} L_{L31} + L_{L1} L_{L21} L_{m1} + L_{L1} L_{L31} L_{m1} + L_{L21} L_{L31} L_{m1} \quad (8.4)$$

$$L_{n2}{}^3 = L_{L12} L_{L2} L_{L32} + L_{L12} L_{L2} L_{m2} + L_{L12} L_{L32} L_{m2} + L_{L2} L_{L32} L_{m2} \quad (8.5)$$

$$L_{n3}{}^3 = L_{L13} L_{L23} L_{L3} + L_{L13} L_{L23} L_{m3} + L_{L13} L_{L3} L_{m3} + L_{L23} L_{L3} L_{m3} \quad (8.6)$$

$$i_1(\theta) = i_1(\theta_0) + \frac{\{V_1(\theta) - V_{m1}(\theta)\}}{\omega L_{L1}} (\theta - \theta_0) = i_1(\theta_0) + m_x{}^1 (\theta - \theta_0) \quad (8.7)$$

$$i_2(\theta) = i_2(\theta_0) + \frac{\{V_2(\theta) - V_{m2}(\theta)\}}{\omega L_{L2}} (\theta - \theta_0) = i_2(\theta_0) + m_x{}^2 (\theta - \theta_0) \quad (8.8)$$

$$i_3(\theta) = i_3(\theta_0) + \frac{\{V_{m3}(\theta) - V_3(\theta)\}}{\omega L_{L3}} (\theta - \theta_0) = i_3(\theta_0) + m_x{}^3 (\theta - \theta_0) \quad (8.9)$$

The average dc power flow for each port are expressed by average value of the product of winding voltage and winding current for that particular port. The winding voltage for a square wave voltage waveform is constant over a half cycle. Therefore evaluating the average value of winding current over a half cycle provides the easy expression of average power flow associated with that port. The half cycle average currents are obtained using the equations (8.7-8.9). The

average dc power flow over a switching cycle for each port are given below in (8.10-8.12). The turns ratio term r_x^y are defined as $r_x^y = N_x/N_y$. The slopes for the currents i_1, i_2 and i_3 are defined in equations (8.13-8.21) where m_x^y is slope of winding current in winding 'y' during interval 'x'.

$$P_1 = \frac{1}{\pi\omega L_{n1}{}^3}(V_{dc1}r_{13}V_{dc3}\phi_1(\pi - |\phi_1|)L_{L21}L_{L31} + V_{dc1}r_{12}V_{dc2}(\phi_1 - \phi_2)(\pi - |\phi_1 - \phi_2|)L_{L31}L_{m1}) \quad (8.10)$$

$$P_2 = \frac{1}{\pi\omega L_{n2}{}^3}(V_{dc2}r_{23}V_{dc3}\phi_2(\pi - |\phi_2|)L_{L12}L_{L32} - r_{21}V_{dc1}V_{dc2}(\phi_1 - \phi_2)(\pi - |\phi_1 - \phi_2|)L_{L32}L_{m2}) \quad (8.11)$$

$$P_3 = \frac{1}{\pi\omega L_{n3}{}^3}(r_{31}V_{dc1}V_{dc3}\phi_1(\pi - |\phi_1|)L_{L23}L_{L3} + r_{32}V_{dc2}V_{dc3}\phi_2(\pi - |\phi_2|)L_{L13}L_{L3}) \quad (8.12)$$

During interval 1, when $V_1 < 0$, $V_2 < 0$, $V_3 < 0$

$$m_1^1 = (r_{12}V_{dc2} - V_{dc1})K_1^1 + (r_{13}V_{dc3} - V_{dc1})K_2^1 - V_{dc1}K_3^1 \quad (8.13)$$

$$m_1^2 = (r_{21}V_{dc1} - V_{dc2})K_1^2 + (r_{23}V_{dc3} - V_{dc2})K_2^2 - V_{dc2}K_3^2 \quad (8.14)$$

$$m_1^3 = (V_{dc3} - r_{31}V_{dc1})K_1^3 + (V_{dc3} - r_{32}V_{dc2})K_2^3 + V_{dc3}K_3^3 \quad (8.15)$$

During interval 1, when $V_1 > 0$, $V_2 < 0$, $V_3 < 0$

$$m_2^1 = (r_{12}V_{dc2} + V_{dc1})K_1^1 + (r_{13}V_{dc3} + V_{dc1})K_2^1 + V_{dc1}K_3^1 \quad (8.16)$$

$$m_2^2 = (-r_{21}V_{dc1} - V_{dc2})K_1^2 + (r_{23}V_{dc3} - V_{dc2})K_2^2 - V_{dc2}K_3^2 \quad (8.17)$$

$$m_2^3 = (V_{dc3} + r_{31}V_{dc1})K_1^3 + (V_{dc3} - r_{32}V_{dc2})K_2^3 + V_{dc3}K_3^3 \quad (8.18)$$

During interval 1, when $V_1 > 0$, $V_2 > 0$, $V_3 < 0$

$$m_3^1 = (-r_{12}V_{dc2} + V_{dc1})K_1^1 + (r_{13}V_{dc3} + V_{dc1})K_2^1 + V_{dc1}K_3^1 \quad (8.19)$$

$$m_3^2 = (-r_{21}V_{dc1} + V_{dc2})K_1^2 + (r_{23}V_{dc3} + V_{dc2})K_2^2 + V_{dc2}K_3^2 \quad (8.20)$$

$$m_3^3 = (V_{dc3} + r_{31}V_{dc1})K_1^3 + (V_{dc3} + r_{32}V_{dc2})K_2^3 + V_{dc3}K_3^3 \quad (8.21)$$

$$K_1^{\,1} = \frac{L_{L31}L_{m1}}{\omega L_{n1}^{\,3}}, \quad K_2^{\,1} = \frac{L_{L21}L_{m1}}{\omega L_{n1}^{\,3}}, \quad K_3^{\,1} = \frac{L_{L31}L_{L21}}{\omega L_{n1}^{\,3}} \quad (8.22)$$

$$K_1^{\,2} = \frac{L_{L32}L_{m2}}{\omega L_{n2}^{\,3}}, \quad K_2^{\,2} = \frac{L_{L12}L_{m2}}{\omega L_{n2}^{\,3}}, \quad K_3^{\,2} = \frac{L_{L12}L_{L32}}{\omega L_{n2}^{\,3}} \quad (8.23)$$

$$K_1^{\,3} = \frac{L_{L23}L_{m3}}{\omega L_{n3}^{\,3}}, \quad K_2^{\,3} = \frac{L_{L13}L_{m3}}{\omega L_{n3}^{\,3}}, \quad K_3^{\,3} = \frac{L_{L13}L_{L23}}{\omega L_{n3}^{\,3}} \quad (8.24)$$

The above power flow expressions clearly indicate that the systems are coupled to each other and average power flow of one port cannot be controlled using one phase angle. The non-linear decoupling method for this has been proposed in [56], but this requires pre-computation of all feasible operating points, and this method does not consider the dynamic phase angle change effects for the phase shifted converters. Moreover, using this method, the transformer current develops dc transients during phase angle change, which is not addressed in [56]. In the following sections, transformer current control methods to avoid dc transients during phase change is discussed. The control methods provide inherent power decoupling. In this paper, currents in windings 1 and 3 are controlled directly which automatically controls the current in winding 2.

8.2. Triple Active Bridge Converter Current Control

In the current control method discussed in this section, transformer winding currents are sampled in each switching cycle at a fixed instant. The phase shift angles for next switching cycles are calculated based on the sampled values and the corresponding reference currents. Similar current control has been proposed for Dual Active Bridge(DAB) converter in [78-79], where the transformer winding current is sensed twice in a switching cycle and the phase angle is updated twice in a switching cycle. In this section, the double sampling method has been

extended for three port triple active bridge converter and a single sampling method is proposed. The current control for the above TAB converter is implemented here by sensing and controlling currents i_1, i_3 in windings 1,3 and updating phase angles ϕ_1 and ϕ_2.

8.2.1. Double Sampling Method for Current Control

In the double sampling method, the current sampling and phase shift update takes place at the zero and peak of a triangular carrier wave, which is used for all the three ports' gating pulses generation or winding voltage generation, as shown in figure 8.6. The reference for the current sample sensed at zero, is at the zero of carrier for next switching cycle i.e., one switching cycle later. The controller then calculates the phase angles within half period of the current switching cycle and updates the new phase angles to PWM controller at the peak of the carrier wave for current switching cycle, i.e., at half switching cycle later. Similarly, for the currents sampled at peak of the carrier, their references are at the next peak and the phase angles are updated in next zero of the carrier wave. From the instantaneous current expressions from (8.7-8.9), it can be inferred that the winding currents' slopes change for every winding voltage polarity change. The current control is derived here for the voltage positioning scenario of figure 8.3, but it is applicable to all possible positioning of the voltage vectors. The current control is based on predictive method and the calculated phase angle expressions are same for all scenarios of voltage vectors' positions in figures 8.3-8.5.

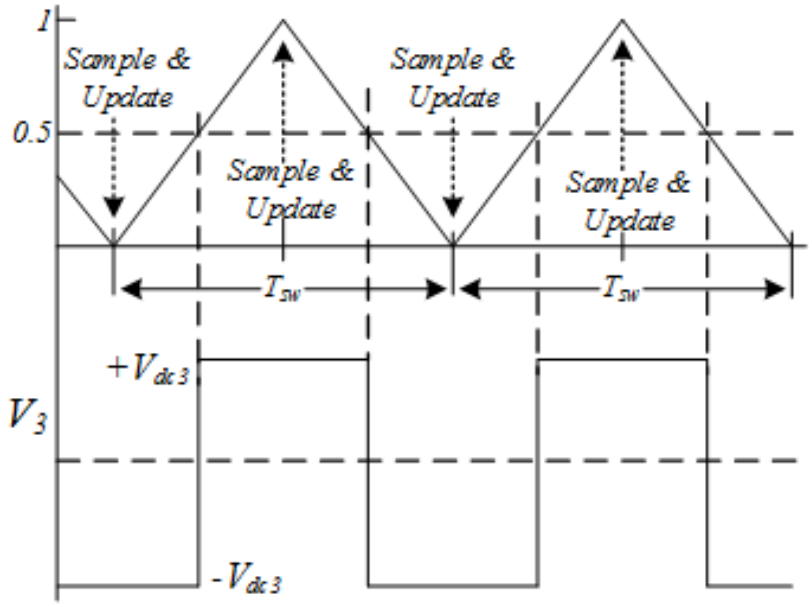

Figure 8.6. Sample and Update for Double Sampling Method.

The sample and update instants are shown in figure 8.7, i_1 and i_3 are sampled at the midpoint instant of the output winding voltage V_3 during both positive and negative half cycles, i.e. when the carrier of figure 8.7 reaches zero and peak. The references i_{1ref}, i_{3ref} for sampled currents i_{1sam}, i_{3sam} sample are at one switching cycle later, i.e. two Sample & Update(S&U) instant later. The references for sampled currents at $(n-1)^{th}$ S&U instant are at $(n+1)^{th}$ S&U instant. Similarly, the references for sampled currents at n^{th} S&U instant are at $(n+2)^{th}$ S&U instant.

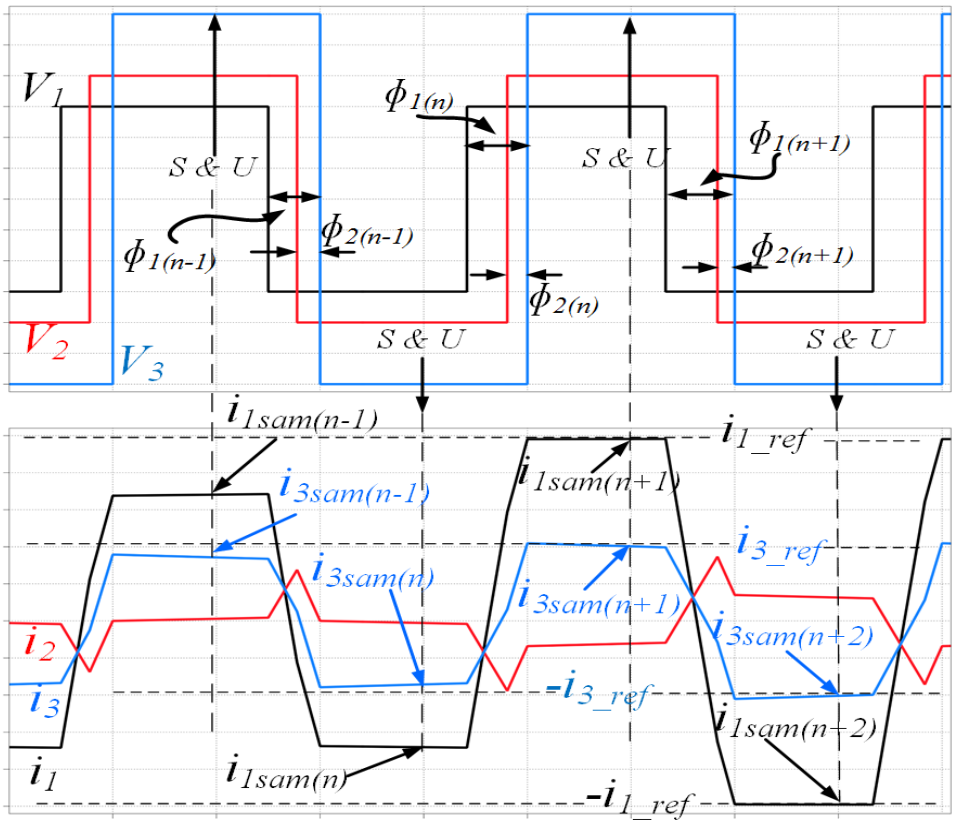

Figure 8.7. Current Control Action using Double Sampling Method.

The predictive control algorithm works in the manner that it samples at zero and peak of the carrier wave for V_3, calculates the new phase shift angle values ϕ_1 and ϕ_2, and updates the PWM generator at half switching cycle later from the sample instant. From figure 8.7, during positive half cycle, the controller samples at $(n-1)^{th}$ sampling instant while the reference is at $(n+1)^{th}$ sampling instant, and the PWM phase shift generator is updated at n^{th} sampling instant. Similarly, for negative half cycle, the controller samples at n^{th} sampling instant, the reference is at $(n+2)^{th}$ sampling instant, and the new phase shift angles ϕ_1 and ϕ_2 are updated into the PWM generator at $(n+1)^{th}$ sampling instant. The predictive controller uses the sampled winding currents' values i_{1sam}, i_{3sam} and calculates the phase shift angles ϕ_1, ϕ_2 based on previous half

switching cycle values of phase shift angles. The controller updates the PWM generator with new phase shift values at the midpoint of positive and negative polarity of winding voltage V_3.

From figure 8.7, starting from (n-1)th sampling instant, the winding 1 and 3 currents at (n+1)th sampling instant can be expressed using current slopes based on piecewise linear model of equations (8.7-8.9) and (8.13-8.18).

$$\begin{aligned} i_{1\_ref} &= i_{1sam(n+1)} = i_{1sam(n-1)} - m_1^{\,1}(\frac{\pi}{2} - \phi_1^{\,n-1}) - m_2^{\,1}(\phi_1^{\,n-1} - \phi_2^{\,n-1}) - m_3^{\,1}(\phi_2^{\,n-1}) \\ &+ m_1^{\,1}(\pi - \phi_1^{\,n}) + m_2^{\,1}(\phi_1^{\,n} - \phi_2^{\,n}) + m_3^{\,1}(\phi_2^{\,n}) - m_1^{\,1}(\frac{\pi}{2}) \end{aligned} \quad (8.25)$$

$$\begin{aligned} i_{3\_ref} &= i_{3sam(n+1)} = i_{3sam(n-1)} - m_1^{\,3}(\frac{\pi}{2} - \phi_1^{\,n-1}) - m_2^{\,3}(\phi_1^{\,n-1} - \phi_2^{\,n-1}) - m_3^{\,3}(\phi_2^{\,n-1}) \\ &+ m_1^{\,3}(\pi - \phi_1^{\,n}) + m_2^{\,3}(\phi_1^{\,n} - \phi_2^{\,n}) + m_3^{\,3}(\phi_2^{\,n}) - m_1^{\,3}(\frac{\pi}{2}) \end{aligned} \quad (8.26)$$

Rearranging equations (8.25)-(8.26), the following matrix form is generated.

$$\begin{bmatrix} (m_2^{\,1} - m_1^{\,1}) & (m_3^{\,1} - m_2^{\,1}) \\ (m_2^{\,3} - m_1^{\,3}) & (m_3^{\,3} - m_2^{\,3}) \end{bmatrix} \begin{bmatrix} \phi_1^{\,n} \\ \phi_2^{\,n} \end{bmatrix} = \begin{bmatrix} J_1 \\ J_2 \end{bmatrix} \quad (8.27)$$

where

$$J_1 = (i_{1\_ref} - i_{1sam(n-1)}) + (m_2^{\,1} - m_1^{\,1})\phi_1^{\,n-1} + (m_3^{\,1} - m_2^{\,1})\phi_2^{\,n-1} \quad (8.28)$$

$$J_2 = (i_{3\_ref} - i_{3sam(n-1)}) + (m_2^{\,3} - m_1^{\,3})\phi_1^{\,n-1} + (m_3^{\,3} - m_2^{\,3})\phi_2^{\,n-1} \quad (8.29)$$

The matrix elements are expressed in terms of circuit parameters as given below.

$$m_2^{\,1} - m_1^{\,1} = 2V_{dc1}(K_1^{\,1} + K_2^{\,1} + K_3^{\,1}) = 2V_{dc1}K_{sum}^{1} \quad (8.30)$$

$$m_3^{\,1} - m_2^{\,1} = -2r_{12}V_{dc2}K_1^{\,1} \quad (8.31), \quad m_2^{\,3} - m_1^{\,3} = 2r_{31}V_{dc1}K_1^{\,3} \quad (8.32),$$

$$m_3^{\,3} - m_2^{\,3} = 2r_{32}V_{dc2}K_2^{\,3} \quad (8.33)$$

Solving the equation (8.27), the required phase angles to be updated for n[th] sampling instant are obtained as follows.

$$\begin{bmatrix} \phi_1^{\,n} \\ \phi_2^{\,n} \end{bmatrix} = \begin{bmatrix} 2r_{32}V_{dc2}K_2^{\,3} & 2r_{12}V_{dc2}K_1^{\,1} \\ -2r_{31}V_{dc1}K_1^{\,3} & 2V_{dc1}K_{sum}^{1} \end{bmatrix} \times \begin{bmatrix} J_1 \\ J_2 \end{bmatrix} \times \frac{1}{D} \quad (8.34)$$

$$\text{Where} \quad D = 4r_{32}V_{dc1}V_{dc2}K_2^{\,3}K_{sum}^{1} + 4r_{31}r_{12}V_{dc1}V_{dc2}K_1^{\,3}K_1^{\,1} \quad (8.35)$$

Expanding equations (8.34)-(8.35), the following solutions for the phase angles are obtained

$$\phi_1^{\,n} = \phi_1^{\,n-1} + \frac{\Delta i_{1ref}(2r_{32}V_{dc2}K_2^{\,3}) + \Delta i_{3ref}(2r_{12}V_{dc2}K_1^{\,1})}{D} \quad (8.36)$$

$$\phi_2^{\,n} = \phi_2^{\,n-1} + \frac{\Delta i_{1ref}(-2r_{31}V_{dc1}K_1^{\,3}) + \Delta i_{3ref}(2V_{dc1}K_{sum}^{1})}{D} \quad (8.37)$$

$$\Delta i_{1ref} = (i_{1\_ref} - i_{1sam(n-1)}) \quad (8.38) \qquad \Delta i_{3ref} = (i_{3\_ref} - i_{3sam(n-1)}) \quad (8.39)$$

For the negative half cycle also, the same equations apply, only Δi_{1ref} and i_{3ref} change as given below.

$$\phi_1^{\,n+1} = \phi_1^{\,n} + \frac{\Delta i_{1ref}(2r_{32}V_{dc2}K_2^{\,3}) + \Delta i_{3ref}(2r_{12}V_{dc2}K_1^{\,1})}{D} \quad (8.40)$$

$$\phi_2^{\,n+1} = \phi_2^{\,n} + \frac{\Delta i_{1ref}(-2r_{31}V_{dc1}K_1^{\,3}) + \Delta i_{3ref}(2V_{dc1}K_{sum}^{1})}{D} \quad (8.41)$$

$$\text{Where} \quad \Delta i_{1ref} = (i_{1\_ref} + i_{1sam(n)}) \quad (8.42) \text{ and } \quad \Delta i_{3ref} = (i_{3\_ref} + i_{3sam(n)}) \quad (8.43)$$

The equations (8.36-8.43) define the current predictive control of triple active bridge converter using double sampling of winding currents. The above method has been derived using the case when both the winding voltages V_1 and V_2 lead V_3, however the derived expressions can still be applied for any of the possible lead-lag cases of winding voltages defined in figures (8.3-8.5).

8.2.2. Single Sampling Method for Current Control

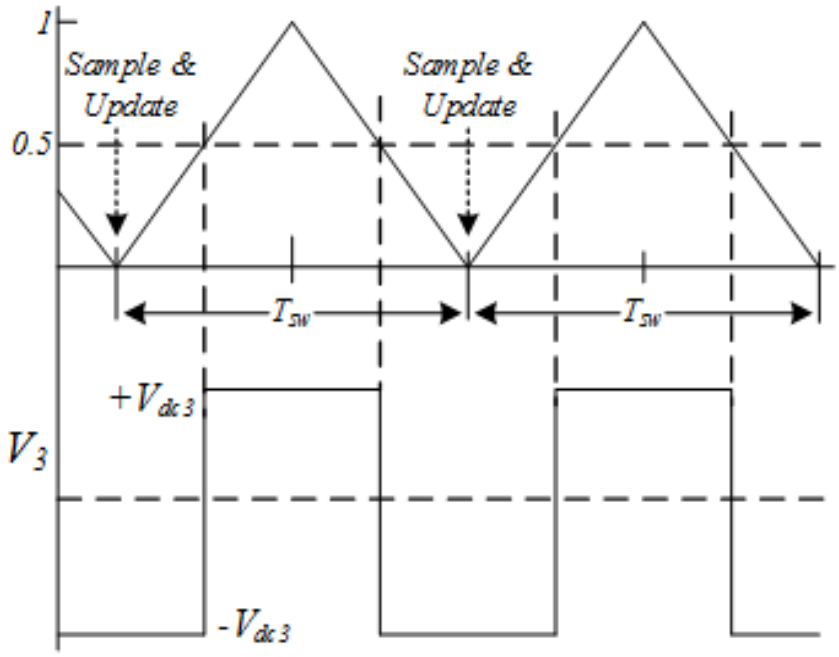

Figure 8.8. Sample and Update for Single Sampling Method.

In the single sampling method, the current sampling and phase shift update takes place only at the zero of triangular carrier wave for voltage V_3, as shown in figure 8.8. The references for the currents i_1 and i_3 are at the zero and peak of the carrier. The single sample and update method proposed here makes sure that during the peak and zero of the carrier wave, the winding currents reach their reference values. The single sampling method for triple active bridge converter is explained in figure 8.9. Here during negative to positive transition of voltages, the phase angles are defined as ϕ_{1u} and ϕ_{2u}. Similarly, during negative to positive transition of voltages, the phase angles are defined as ϕ_{1d} and ϕ_{2d}.

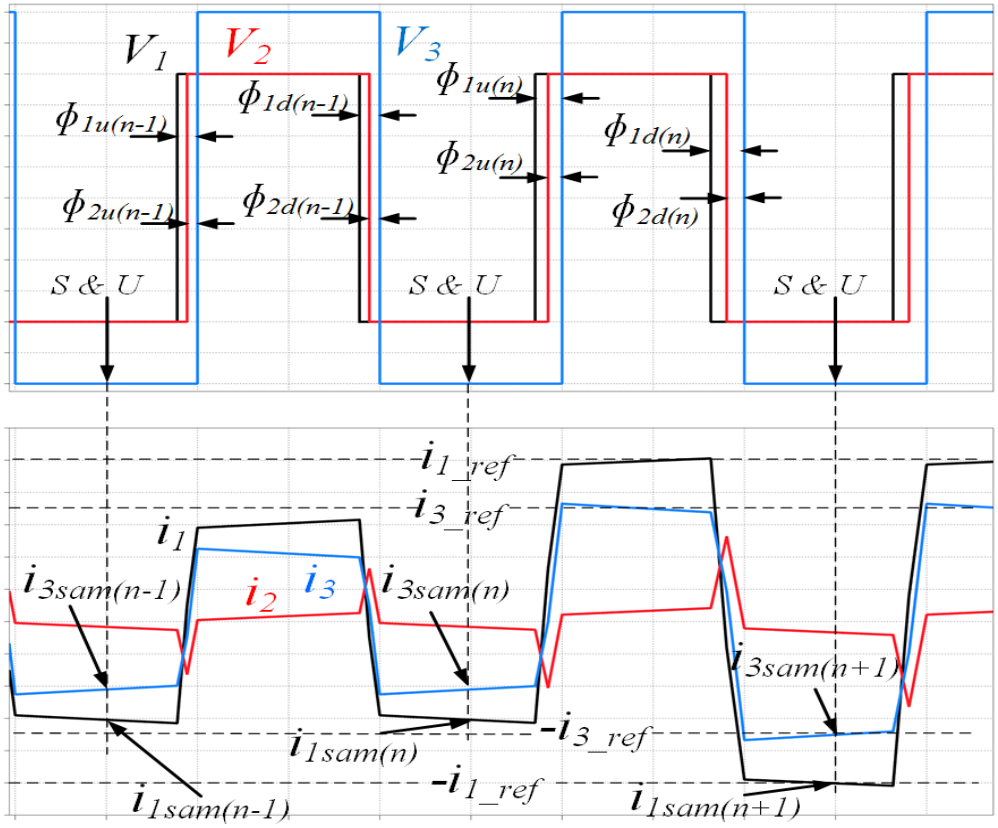

Figure 8.9. Current Control Action using Single Sampling Method.

$$i_{1\_ref} = i_{1sam(n)} + m_1^{\,1}(\frac{\pi}{2} - \phi_{1u(n)}) + m_2^{\,1}(\phi_{1u(n)} - \phi_{2u(n)}) + m_3^{\,1}\phi_{2u(n)} - m_1^{\,1}\frac{\pi}{2} \quad (8.44)$$

$$i_{3\_ref} = i_{3sam(n)} + m_1^{\,3}(\frac{\pi}{2} - \phi_{1u(n)}) + m_2^{\,3}(\phi_{1u(n)} - \phi_{2u(n)}) + m_3^{\,3}\phi_{2u(n)} - m_1^{\,1}\frac{\pi}{2} \quad (8.45)$$

$$\begin{aligned} i_{1sam(n)} &= i_{1sam(n-1)} + m_1^{\,1}(\frac{\pi}{2} - \phi_{1u(n-1)}) + m_2^{\,1}(\phi_{1u(n-1)} - \phi_{2u(n-1)}) + m_3^{\,1}\phi_{2u(n-1)} \\ &- m_1^{\,1}(\pi - \phi_{1d(n-1)}) - m_2^{\,1}(\phi_{1d(n-1)} - \phi_{2d(n-1)}) - m_3^{\,1}\phi_{2d(n-1)} + m_1^{\,1}\frac{\pi}{2} \end{aligned} \quad (8.46)$$

$$\begin{aligned} i_{3sam(n)} &= i_{3sam(n-1)} + m_1^{\,3}(\frac{\pi}{2} - \phi_{1u(n-1)}) + m_2^{\,3}(\phi_{1u(n-1)} - \phi_{2u(n-1)}) + m_3^{\,3}\phi_{2u(n-1)} \\ &- m_1^{\,3}(\pi - \phi_{1d(n-1)}) - m_2^{\,3}(\phi_{1d(n-1)} - \phi_{2d(n-1)}) - m_3^{\,3}\phi_{2d(n-1)} + m_1^{\,3}\frac{\pi}{2} \end{aligned} \quad (8.47)$$

Using the equations (8.46-8.47) in place of $i_{1sam(n)}$ & $i_{2sam(n)}$ in equations (8.44-8.45), a matrix similar to equation (8.27) is obtained. Repeating the steps in equations (8.27-8.35), the following expressions for $\phi_{1u(n)}$ and $\phi_{2u(n)}$ are obtained.

$$\phi_{1u(n)} = \phi_{1d(n-1)} - \phi_{1u(n-1)} + \frac{\Delta i_{1ref}(2r_{32}V_{dc2}K_2^{\,3}) + \Delta i_{3ref}(2r_{12}V_{dc2}K_1^{\,1})}{D} \quad (8.48)$$

$$\phi_{2u(n)} = \phi_{2d(n-1)} - \phi_{2u(n-1)} + \frac{\Delta i_{1ref}(-2r_{31}V_{dc1}K_1^{\,3}) + \Delta i_{3ref}(2V_{dc1}K_{sum}^{1})}{D} \quad (8.49)$$

$$\Delta i_{1ref} = (i_{1\_ref} + i_{1sam(n-1)}) \quad (8.50) \qquad \Delta i_{3ref} = (i_{3\_ref} + i_{3sam(n-1)}) \quad (8.51)$$

The phase shift angles $\phi_{1d(n)}$ and $\phi_{2d(n)}$ are calculated below.

$$\begin{aligned} -i_{1\_ref} &= i_{1sam(n)} + m_1^{\,1}(\frac{\pi}{2} - \phi_{1u(n)}) + m_2^{\,1}(\phi_{1u(n)} - \phi_{2u(n)}) + m_3^{\,1}\phi_{2u(n)} \\ &-m_1^{\,1}(\pi - \phi_{1d(n)}) - m_2^{\,1}(\phi_{1d(n)} - \phi_{2d(n)}) - m_3^{\,1}(\phi_{2d(n)}) + m_1^{\,1}\frac{\pi}{2} \end{aligned} \quad (8.52)$$

$$\begin{aligned} -i_{3\_ref} &= i_{3sam(n)} + m_1^{\,3}(\frac{\pi}{2} - \phi_{1u(n)}) + m_2^{\,3}(\phi_{1u(n)} - \phi_{2u(n)}) + m_3^{\,3}\phi_{2u(n)} \\ &-m_1^{\,3}(\pi - \phi_{1d(n)}) - m_2^{\,3}(\phi_{1d(n)} - \phi_{2d(n)}) - m_3^{\,3}(\phi_{2d(n)}) + m_1^{\,3}\frac{\pi}{2} \end{aligned} \quad (8.53)$$

Using the equations (8.44),(8.45) in places of $i_{1sam(n)}$ and $i_{3sam(n)}$ in equations (8.52),(8.53) the following expressions for $\phi_{1d(n)}$ and $\phi_{2d(n)}$ are obtained.

$$\phi_{1d(n)} = \frac{4i_{1\_ref}r_{32}V_{dc2}K_2^{\,3} + 4i_{3\_ref}r_{12}V_{dc2}K_1^{\,1}}{D} \quad (8.54)$$

$$\phi_{2d(n)} = \frac{4i_{1\_ref}r_{31}V_{dc1}K_1^{\,3} + 4i_{3\_ref}V_{dc1}K_{sum}^{1}}{D} \quad (8.55)$$

The derived equations (8.48-8.51) and (8.54-8.55) define the current control using single sampling methods to control the transformer current in each cycle. The current control equations have been derived using the case for voltage vectors' positions for $\phi_1 < \phi_2 < 0$ case(figure 8.3),

but the same set of equations are applicable to other two cases of $\phi_2 < \phi_1 < 0$ and $\phi_1 < 0 < \phi_2$, shown in figures 8.4 and 8.5. The current control equations have also been derived for the other two cases of figures 8.4 and 8.5, and the derived phase angle expressions for ϕ_1 and ϕ_2 have been found to be same for all the cases. Hence, the required new phase angle values for change in voltage vectors' positions from any of the cases in figures (8.3-8.5) to any of the other two cases can be achieved using the same equations for ϕ_1 and ϕ_2.

8.3. Effects of Inductance Variation on High Frequency Current Control

8.3.1. Effects of Inductance Variation for Double Sampling Method

The three port transformer current control methods discussed above, use the feedback signals from high frequency current sensors and are dependent on the transformer leakage inductance estimation and their variations. Transformer leakage inductances depend on transformer core & winding geometry, but in case of external series inductors being used for three port transformer, the inductances can vary depending on core temperature & saturation level. Various techniques for leakage inductance estimation exists and they can produce different results. The effect of variations of inductances and sensitivity analysis are studied here.

The effect of inductance variation is analyzed over here by considering the measured inductances to be like $L_{L1} = L_{L1,act} + \Delta L_{L1}$, $L_{L2} = L_{L2,act} + \Delta L_{L2}$, $L_{L3} = L_{L3,act} + \Delta L_{L3}$. With these variations of inductances. the estimated slope parameters of equations (8.22-8.30) vary from actual values and so as the solution set of equations (8.42-8.43) and (8.46-8.47) for the double sampling method. The solution set of equations for single sampling method given in equations (8.54-8.55) and (8.60-8.61) also vary with variation of inductances. While considering variation of inductances, all the slope parameters K_x^y in equations (8.22-8.30) are referred to as $K_{x,act}^y$.

$$
\begin{aligned}
& i_{1,sam(n+1)} = i_{1,ref} + \Delta i_{1,sam}^{n+1} \\
& = i_{1,sam(n)} + (m_2{}^1 - m_1{}^1)\phi_1{}^n + (m_3{}^1 - m_2{}^1)\phi_2{}^n \\
& = i_{1,sam(n)} + 2V_{dc1}K_{sum,act}^1\phi_1{}^n - 2r_{12}V_{dc2}K_{1,act}^1\phi_2{}^n \\
& = -i_{1,ref} + \Delta i_{1,sam}^n + 2V_{dc1}K_{sum,act}^1\phi_1{}^n - 2r_{12}V_{dc2}K_{1,act}^1\phi_2{}^n
\end{aligned} \tag{8.56}
$$

$$
\begin{aligned}
& i_{3,sam(n+1)} = i_{3,ref} + \Delta i_{3,sam}^{n+1} \\
& = i_{3,sam(n)} + (m_2{}^3 - m_1{}^3)\phi_1{}^n + (m_3{}^3 - m_2{}^3)\phi_2{}^n \\
& = i_{3,sam(n)} + 2r_{31}V_{dc1}K_{1,act}^3\phi_1{}^n + 2r_{32}V_{dc2}K_{2,act}^3\phi_2{}^n \\
& = -i_{3,ref} + \Delta i_{3,sam}^n + 2r_{31}V_{dc1}K_{1,act}^3\phi_1{}^n + 2r_{32}V_{dc2}K_{2,act}^3\phi_2{}^n
\end{aligned} \tag{8.57}
$$

$$
\begin{aligned}
& i_{1,sam(n+2)} = -i_{1,ref} + \Delta i_{1,sam}^{n+2} \\
& = i_{1,sam(n+1)} + (m_1{}^1 - m_2{}^1)\phi_1{}^{n+1} + (m_2{}^1 - m_3{}^1)\phi_2{}^{n+1} \\
& = i_{1,sam(n+1)} - 2V_{dc1}K_{sum,act}^1\phi_1{}^{n+1} + 2r_{12}V_{dc2}K_{1,act}^1\phi_2{}^{n+1} \\
& = i_{1,ref} + \Delta i_{1,sam}^{n+1} - 2V_{dc1}K_{sum,act}^1\phi_1{}^{n+1} + 2r_{12}V_{dc2}K_{1,act}^1\phi_2{}^{n+1}
\end{aligned} \tag{8.58}
$$

$$
\begin{aligned}
& i_{3,sam(n+2)} = -i_{3,ref} + \Delta i_{3,sam}^{n+2} \\
& = i_{3,sam(n+1)} + (m_1{}^3 - m_2{}^3)\phi_1{}^{n+1} + (m_2{}^3 - m_3{}^3)\phi_2{}^{n+1} \\
& = i_{3,sam(n+1)} - 2r_{31}V_{dc1}K_{1,act}^3\phi_1{}^{n+1} - 2r_{32}V_{dc2}K_{2,act}^3\phi_2{}^{n+1} \\
& = i_{3,ref} + \Delta i_{3,sam}^{n+1} - 2r_{31}V_{dc1}K_{1,act}^3\phi_1{}^{n+1} - 2r_{32}V_{dc2}K_{2,act}^3\phi_2{}^{n+1}
\end{aligned} \tag{8.59}
$$

$$
\text{Where } \phi_1{}^{n+1} = \phi_1{}^n + \frac{\Delta i_{1ref}(2r_{32}V_{dc2}K_{2,est}^3) + \Delta i_{3ref}(2r_{12}V_{dc2}K_{1,est}^1)}{D_{est}} \tag{8.60}
$$

$$
\text{and } \phi_2{}^{n+1} = \phi_2{}^n + \frac{\Delta i_{1ref}(-2r_{31}V_{dc1}K_{1,est}^3) + \Delta i_{3ref}(2V_{dc1}K_{sum,est}^1)}{D_{est}} \tag{8.61}
$$

$$
\Delta i_{1ref} = (i_{1\_ref} + i_{1sam(n)}) = \Delta i_{1,sam}^n \tag{8.62}
$$

$$
\text{and } \Delta i_{3ref} = (i_{3\_ref} + i_{3sam(n)}) = \Delta i_{3,sam}^n \tag{8.63}
$$

Using the equations (8.56-8.63) and expressing $\Delta i_{1,sam}^{n+2}$ & $\Delta i_{3,sam}^{n+2}$ in terms of $\Delta i_{1,sam}^{n}$ & $\Delta i_{3,sam}^{n}$, the following expressions are obtained. The K_x^y parameters involving actual inductances are expressed as $K_{x,act}^y$ and with estimated inductances, the terms are expressed as $K_{x,est}^y$.

$$\Delta i_{1,sam}{}^{n+2} = \Delta i_{1,sam}{}^{n} \frac{r_{32}K_{2,est}{}^{3}(K_{sum,est}{}^{1} - K_{sum,act}{}^{1}) + r_{12}r_{31}K_{1,est}{}^{3}(K_{1,est}{}^{1} - K_{1,act}{}^{1})}{r_{32}K_{2,est}{}^{3}K_{sum,est}{}^{1} + r_{31}r_{12}K_{1,est}{}^{3}K_{1,est}{}^{1}}$$
$$+\Delta i_{3,sam}{}^{n} \frac{r_{12}(K_{sum,act}{}^{1}K_{1,est}{}^{1} - K_{1,act}{}^{1}K_{sum,est}{}^{1})}{r_{32}K_{2,est}{}^{3}K_{sum,est}{}^{1} + r_{31}r_{12}K_{1,est}{}^{3}K_{1,est}{}^{1}} \quad (8.64)$$

$$\Delta i_{3,sam}{}^{n+2} = \Delta i_{3,sam}{}^{n} \frac{r_{32}K_{sum,est}{}^{1}(K_{2,est}{}^{3} - K_{2,act}{}^{3}) + r_{12}r_{31}K_{1,est}{}^{1}(K_{1,est}{}^{3} - K_{1,act}{}^{3})}{r_{32}K_{2,est}{}^{3}K_{sum,est}{}^{1} + r_{31}r_{12}K_{1,est}{}^{3}K_{1,est}{}^{1}}$$
$$+\Delta i_{1,sam}{}^{n} \frac{r_{31}r_{32}(K_{2,act}{}^{3}K_{1,est}{}^{3} - K_{1,act}{}^{3}K_{2,est}{}^{3})}{r_{32}K_{2,est}{}^{3}K_{sum,est}{}^{1} + r_{31}r_{12}K_{1,est}{}^{3}K_{1,est}{}^{1}} \quad (8.65)$$

The perturbations $\Delta i_{1,sam}^{n+2}$ & $\Delta i_{3,sam}^{n+2}$ can be expressed in terms of $\Delta K's$, which are changes in values of the parameters K for changes in values of inductances L.

$$\Delta i_{1,sam}^{n+2} = \Delta i_{1,sam}^{n}\left(\frac{\Delta K_{sum}^{1}}{C_{1a}} + \frac{\Delta K_{1}^{1}}{C_{1b}}\right) + \Delta i_{3,sam}{}^{n}\left(\frac{\Delta K_{sum}^{1}}{C_{1c}} + \frac{\Delta K_{1}^{1}}{C_{1d}} + \frac{\Delta K_{sum}^{1}\Delta K_{1}^{1}}{C_{1e}}\right) \quad (8.66)$$

$$\Delta i_{3,sam}^{n+2} = \Delta i_{3,sam}^{n}\left(\frac{\Delta K_{2}^{3}}{C_{3a}} + \frac{\Delta K_{1}^{1}}{C_{3b}}\right) + \Delta i_{3,sam}^{n}\left(\frac{\Delta K_{sum}^{1}}{C_{3c}} + \frac{\Delta K_{1}^{1}}{C_{3d}} + \frac{\Delta K_{sum}^{1}\Delta K_{1}^{1}}{C_{3e}}\right) \quad (8.67)$$

The perturbation $\Delta i_{j,sam}^{n+2}$ will be lower than the perturbation $\Delta i_{j,sam}^{n}$ one switching cycle earlier, only if $\Delta K_x^y < C_{ja,b}$, which are functions of all the K_x^y parameters. The effect of variation of inductances are verified here from simulation studies by varying the individual inductances by ±20%. Figures 8.10 and 8.11 show the transformer winding currents due to step changes in

references. It can be observed that with variation of inductances, the current has the pure ac nature but it takes few switching cycles to settle down to steady state.

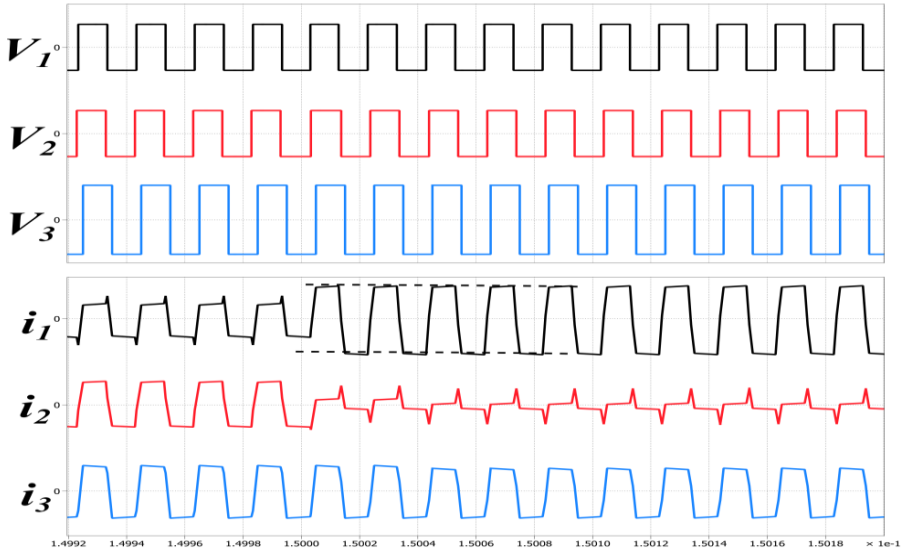

Figure 8.10. Transformer Current Control with No Variation in Inductances.

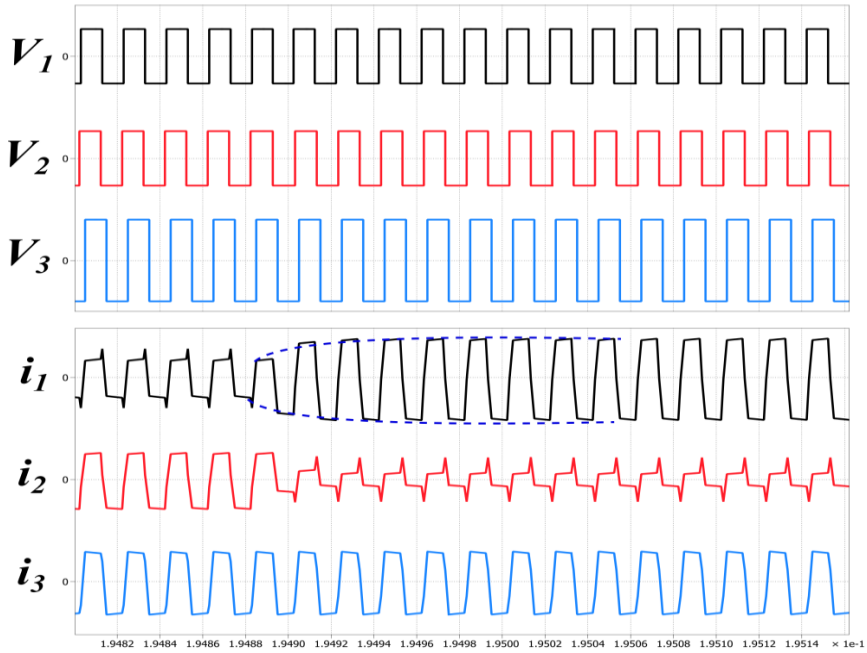

Figure 8.11. Transformer Currents with 20% Variation in Inductances.

8.3.2. Effects of Inductance Variation for Single Sampling Current Control Method

The effects of inductance variation has also been studied for single sampling current control method. The transformer winding currents are expressed below with inductance variation for single sampling method.

$$\begin{aligned} i_{1,u(n)} &= i_{1,ref} + \Delta i_{1,u}^{n} \\ &= i_{1,sam(n)} + (m_2^{\,1} - m_1^{\,1})\phi_{1u}{}^{n} + (m_3^{\,1} - m_2^{\,1})\phi_{2u}{}^{n} \\ &= i_{1,sam(n)} + 2V_{dc1}K_{sum,act}^{1}\phi_{1u}{}^{n} - 2r_{12}V_{dc2}K_{1,act}^{1}\phi_{2u}{}^{n}n \\ &= -i_{1,ref} + \Delta i_{1,sam}^{n} + 2V_{dc1}K_{sum,act}^{1}\phi_{1u}{}^{n} - 2r_{12}V_{dc2}K_{1,act}^{1}\phi_{2u}{}^{n} \end{aligned} \tag{8.68}$$

$$\begin{aligned} i_{3,u(n)} &= i_{3,ref} + \Delta i_{3,u}^{n} \\ &= i_{3,sam(n)} + (m_2^{\,3} - m_1^{\,3})\phi_{1u}{}^{n} + (m_3^{\,3} - m_2^{\,3})\phi_{2u}{}^{n} \\ &= i_{3,sam(n)} + 2r_{31}V_{dc1}K_{1,act}^{3}\phi_{1u}{}^{n} + 2r_{32}V_{dc2}K_{2,act}^{3}\phi_{2u}{}^{n} \\ &= -i_{3,ref} + \Delta i_{3,sam}^{n} + 2r_{31}V_{dc1}K_{1,act}^{3}\phi_{1u}{}^{n} + 2r_{32}V_{dc2}K_{2,act}^{3}\phi_{2u}{}^{n} \end{aligned} \tag{8.69}$$

$$\begin{aligned} i_{1,sam(n+1)} &= -i_{1,ref} + \Delta i_{1,sam}^{n+1} \\ &= i_{1,u(n)} + (m_1^{\,1} - m_2^{\,1})\phi_{1d}{}^{n} + (m_2^{\,1} - m_3^{\,1})\phi_{2d}{}^{n} \\ &= i_{1,u(n)} - 2V_{dc1}K_{sum,act}^{1}\phi_{1d}{}^{n} + 2r_{12}V_{dc2}K_{1,act}^{1}\phi_{2d}{}^{n} \\ &= i_{1,ref} + \Delta i_{1,sam}^{n} - 2V_{dc1}K_{sum,act}^{1}\phi_{1d}{}^{n} + 2r_{12}V_{dc2}K_{1,act}^{1}\phi_{2d}{}^{n} \end{aligned} \tag{8.70}$$

$$\begin{aligned} i_{3,sam(n+1)} &= -i_{3,ref} + \Delta i_{3,sam}^{n+1} \\ &= i_{3,u(n)} + (m_1^{\,3} - m_2^{\,3})\phi_{1d}{}^{n} + (m_2^{\,3} - m_3^{\,3})\phi_{2d}{}^{n} \\ &= i_{3,u(n)} - 2r_{31}V_{dc1}K_{1,act}^{3}\phi_{1d}{}^{n} - 2r_{32}V_{dc2}K_{2,act}^{3}\phi_{2d}{}^{n} \\ &= i_{3,ref} + \Delta i_{3,sam}^{n} - 2r_{31}V_{dc1}K_{1,act}^{3}\phi_{1d}{}^{n} - 2r_{32}V_{dc2}K_{2,act}^{3}\phi_{2d}{}^{n} \end{aligned} \tag{8.71}$$

where $$\phi_{1u(n)} = \phi_{1d(n-1)} - \phi_{1u(n-1)} + \frac{\Delta i_{1ref}(2r_{32}V_{dc2}K_{2,est}^{3}) + \Delta i_{3ref}(2r_{12}V_{dc2}K_{1,est}^{1})}{D_{est}} \tag{8.72}$$

$$\text{and } \phi_{2u(n)} = \phi_{2d(n-1)} - \phi_{2u(n-1)} + \frac{\Delta i_{1ref}(-2r_{31}V_{dc1}K_{1,est}^{3}) + \Delta i_{3ref}(2V_{dc1}K_{sum,est}^{1})}{D_{est}} \quad (8.73)$$

where $\Delta i_{1ref} = (i_{1\_ref} + i_{1sam(n)})$, $\Delta i_{3ref} = (i_{3\_ref} + i_{3sam(n)})$ and

$$\phi_{1d(n)} = \frac{4i_{1ref}r_{32}V_{dc2}K_{2,est}^{3} + 4i_{cref}r_{12}V_{dc2}K_{1,est}^{1}}{D_{est}} \quad (8.74)$$

$$\phi_{2d(n)} = \frac{-4i_{1ref}r_{31}V_{dc1}K_{1,est}^{3} + 4i_{cref}V_{dc1}K_{sum,est}^{1}}{D_{est}} \quad (8.75)$$

The effect of variation of inductances are verified here from simulation studies by varying the individual inductances by ±20%. Figures 8.12 and 8.13 show the transformer winding currents due to step changes in references. It can be observed that with variation of inductances, the current has a small dc component and takes few switching cycles to settle down.

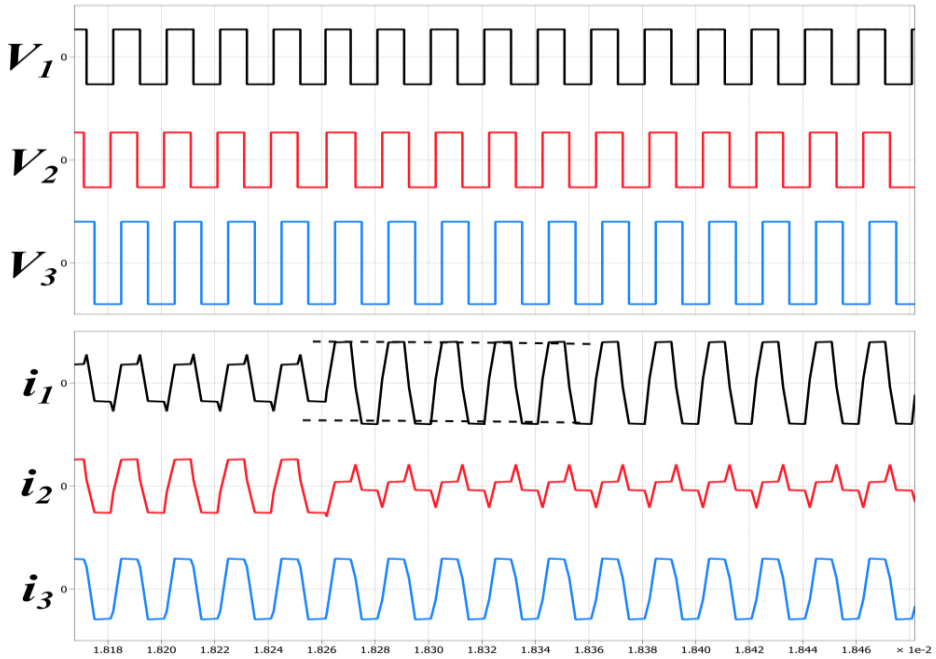

Figure 8.12. Transformer Currents with No Variation in Inductances.

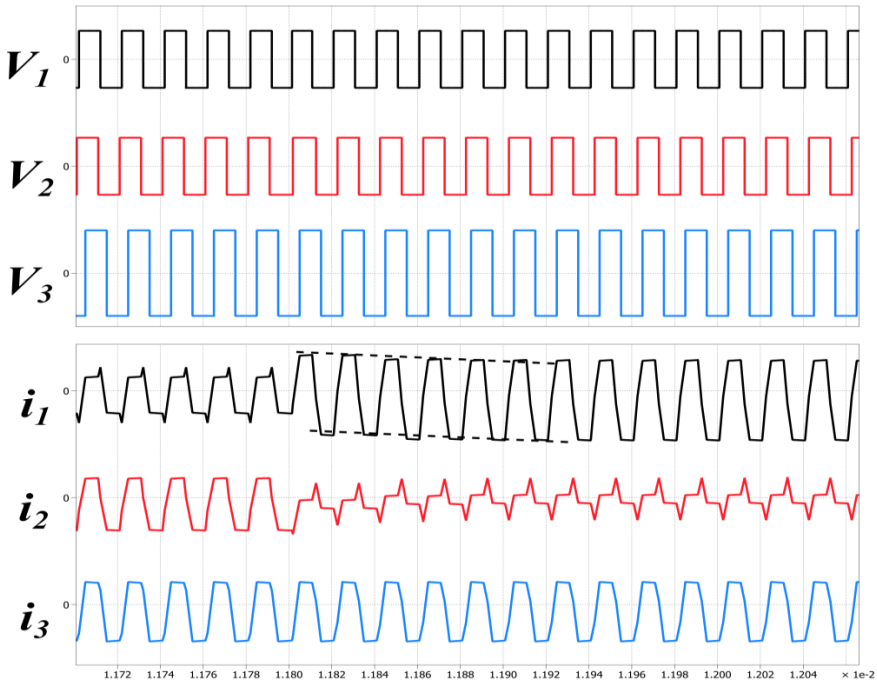

Figure 8.13. Transformer Currents with 20% Inductance Variation.

8.4. Experimental Results for Double Sampling & Single Sampling Current Control Methods

The aforementioned current control methods have been implemented in a laboratory scale hardware prototype using a three-port transformer with 1:1:1.5 turns ratio. The hardware prototype has three H-bridges built using SiC Mosfets. The experimental study has been carried out at lower dc bus voltages, 400V for V_{dc1}, V_{dc2} and 600V for V_{dc3}. The high frequency transformer has been made using ferrite material 3C97 and windings are made using litz wire. Figure 8.14 shows the high frequency transformer used for experimental study. The transformer details are from chapter 6. Figure 8.15 shows the 2MHz bandwidth Sensitec current sensor CMS3025ABA used for sensing high frequency transformer currents.

Figure 8.14. Three Port High Frequency Transformer.

Figure 8.15. High bandwidth Current Sensor.

The closed loop operation is performed by performing a dc voltage control at the output port at 600V and controlling the transformer winding currents. The block diagram for the closed loop control is shown in figure 8.16. The outer voltage loop generates the i_{3ref} , which is reference for the output port high frequency current i_3. The current reference i_{1ref} , which is reference for port 1 high frequency current i_1, can be generated from MPPT controller or from other current reference generator. For the experimental purpose in this purpose, the i_{1ref} has been fed externally into the controller. The controller used for the aforementioned current control methods is TI DSP TMS320F28335 with 150MHz clock.

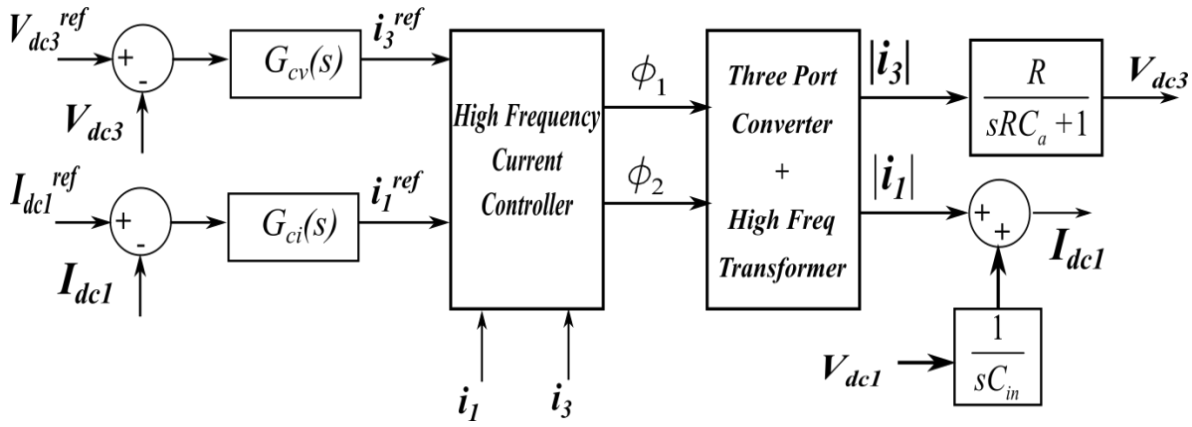

Figure 8.16. Closed Loop Power Control with Sampled Current Control.

The current control is verified in the hardware prototype by using a step change in the current reference i_{1ref} . The experimental results for double sampling method are shown in figures 8.17 and 8.18, where the effects of inductance variations are shown. Figure 8.17 shows the transient change in current waveforms during a step change decrease in i_{1ref} . As the control signal CS goes high, the i_{1ref} changes to a new value and the controller calculates the new phase shift angles for the next half cycle and updates the controller with new phase angle values at next S&U instant. The controller continuously updates the values for ϕ_1 and ϕ_2 at every half cycle. Using this technique, the i_1 settles at new reference value in both positive and negative half cycle within one switching cycle. As $V_{dc3-ref}$ does not change, i_{3ref} also does not change and the controller maintains the current at the same reference value. The port 2 current i_2 changes automatically to new value to show the reflected change in power level. Figure 8.18 shows the V_{dc3} control and i_{1ref} control when the reference for i_1 goes high. The controller performs

similar control actions in this case as in figure 8.17, to control i_1 and i_3 as per the new references and maintains the output voltage V_{dc3}.

It can be observed that for the case with 20% variation in leakage inductances, the winding currents undergo variations before settling in. Also, the effect of sensor offsets can be observed in figures 8.17-8.18, where oscillations can be observed in winding current i_2. Moreover, using double sampling current control method, continuous audible noise is observed from ferrite core transformer, which is a property of ferrite cores while the core is operating near saturation region.

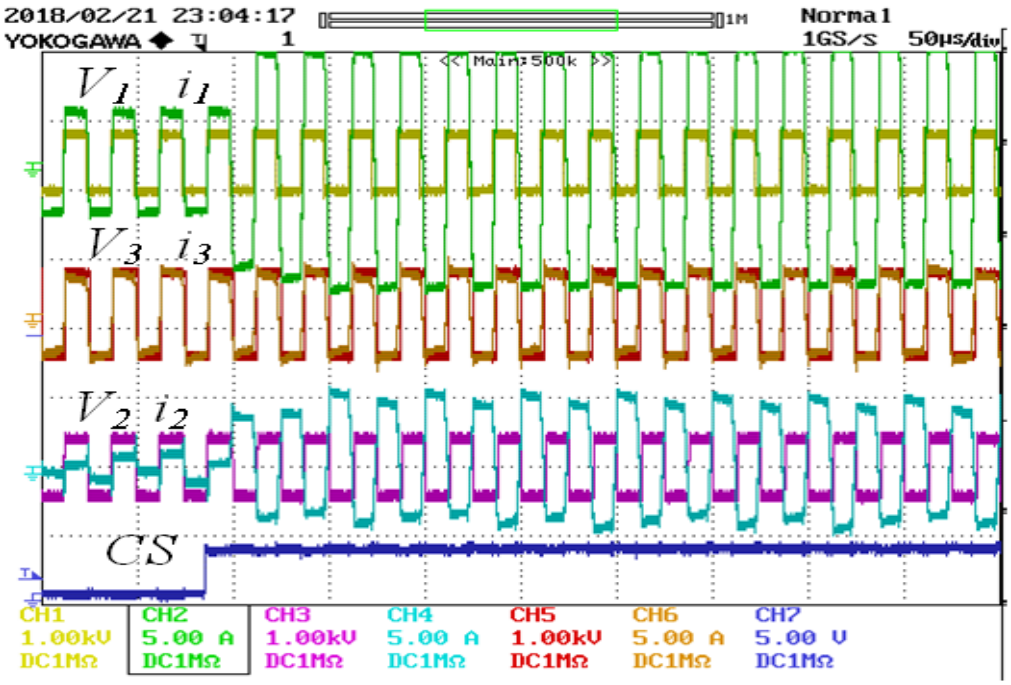

Figure 8.17. Double Sampling Current Control with Proper Inductances.

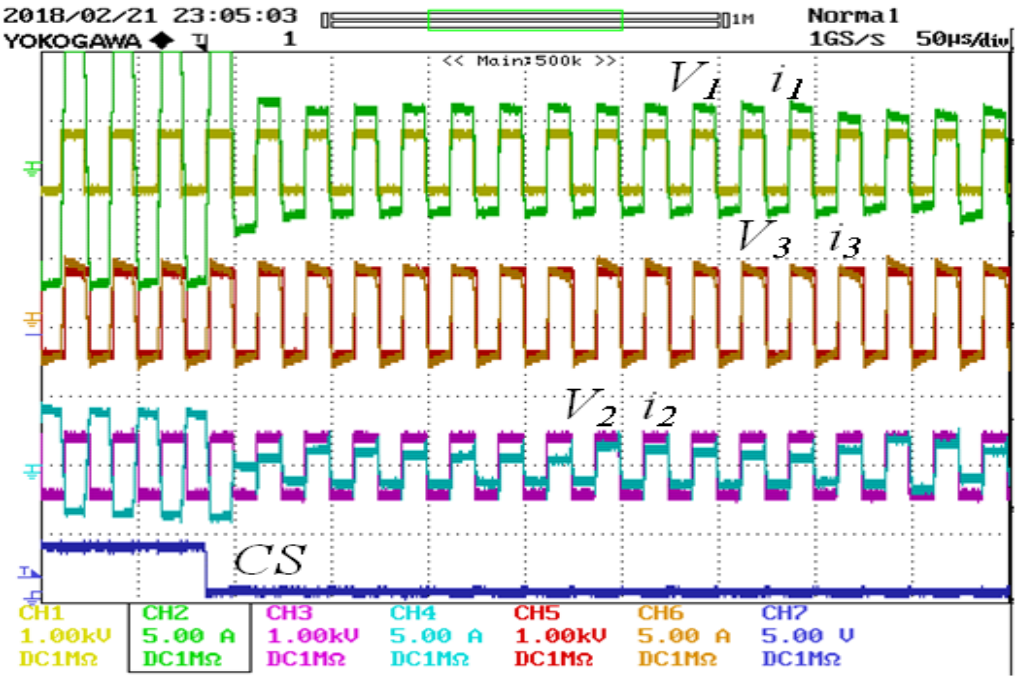

Figure 8.18. Double Sampling Current Control with 20% Deviant Inductances.

The high frequency current control method using single sampling method with properly estimated inductance values and with 20% variation in leakage inductance values are shown in figures 8.19-8.20. It is observed that for the case with 20% variation in leakage inductance, the winding currents undergo significant oscillations before settling in. However, the effect of sensor offsets on the current oscillations and continuous audible noise is absent in this case.

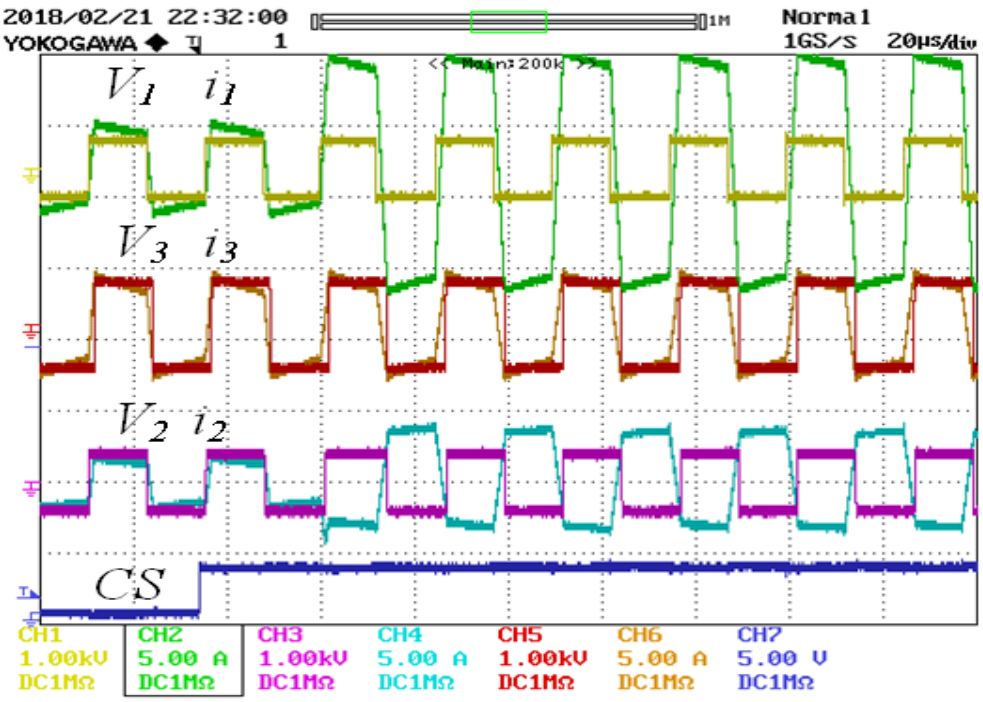

Figure 8.19. Single Sampling Current Control with Proper Inductances.

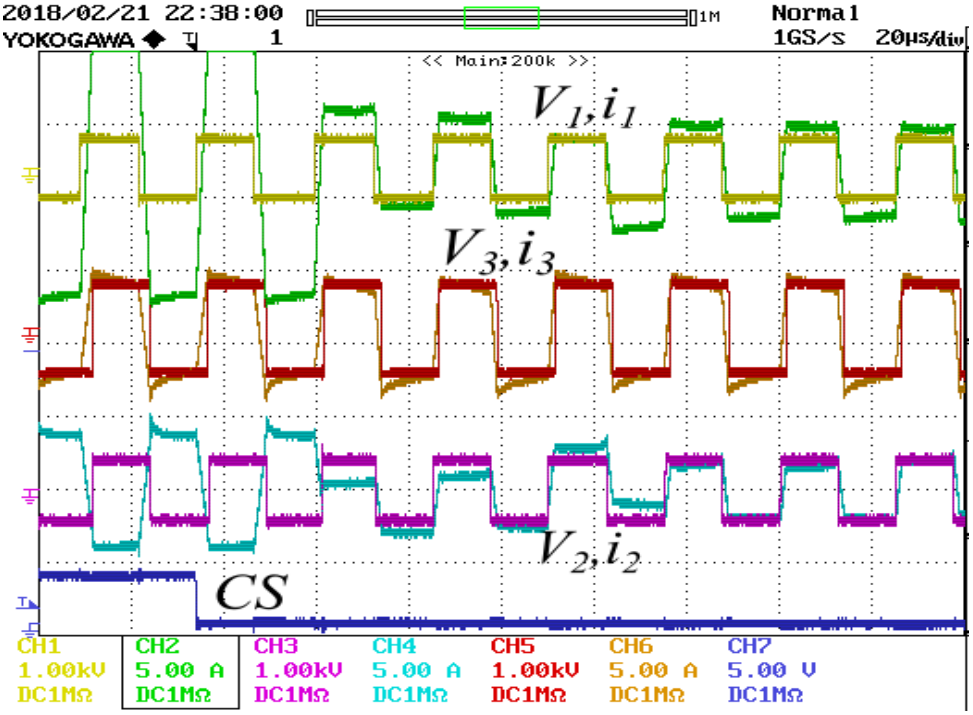

Figure 8.20. Single Sampling Current Control with 20% Deviation in Inductances.

8.5. Current Control without Sampling Transformer Currents

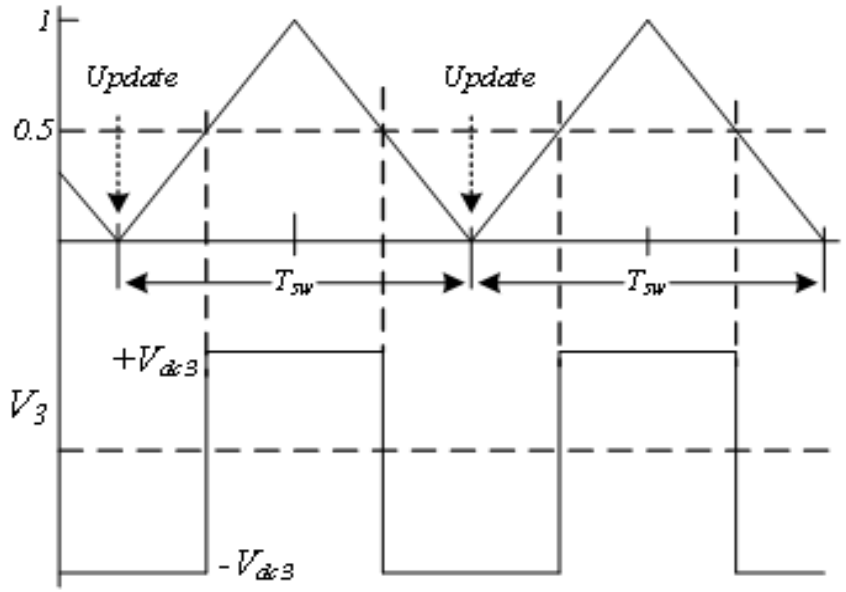

Figure 8.21. Phase Angle Update for Every Switching Cycle.

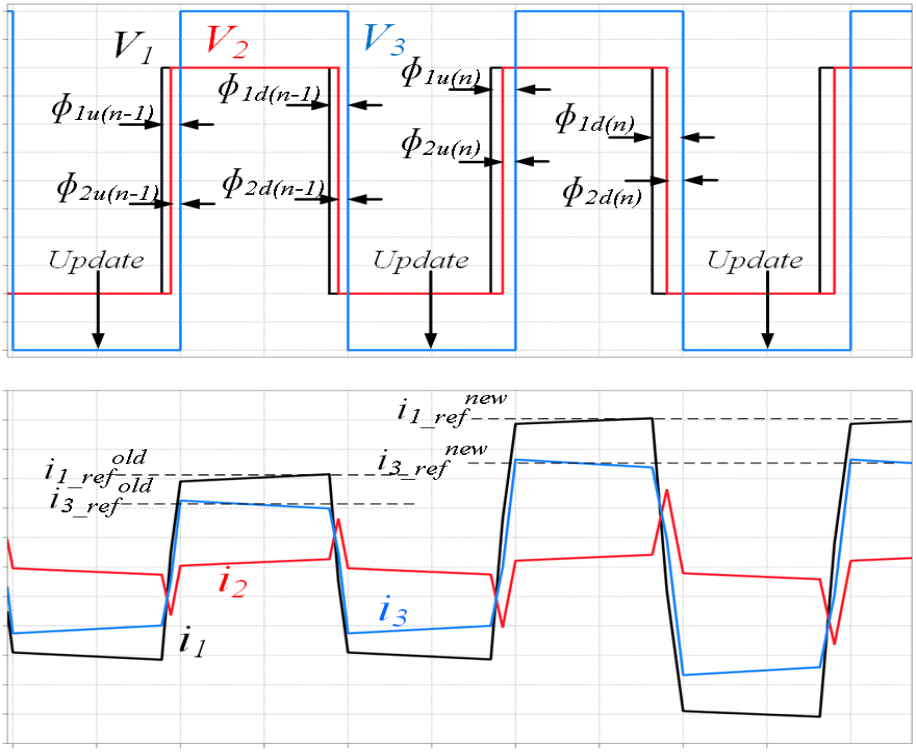

Figure 8.22. Current Control without Sensing Transformer Currents.

In order to eliminate the effects of inductance variation and effects of sensor, which result in oscillations in winding currents and decaying dc offsets, a current control method is proposed here which do not use sampled currents from sensor outputs, but estimate the phase angles for next switching cycle based on current reference inputs and estimated leakage inductance values. The figures 8.21 and 8.22 explain how the phase estimation method works. The controller generates the phase shift angles $\phi_{1u(n)}$, $\phi_{2u(n)}$, $\phi_{2d(n)}$ and $\phi_{2d(n)}$ for the next nth switching cycle and updates them and updates them at the zero crossing of carrier wave. The equations for calculating $\phi_{1u(n)}$, $\phi_{2u(n)}$, $\phi_{2d(n)}$ and $\phi_{2d(n)}$ are given below in 8.76-8.79. It can be observed that the calculated phase angles using no sampled current values, use only references for the winding currents and eliminate the effects of sensor output offsets. The effects of inductance variation also eliminate the chances of oscillations, as only reference values are used for transformer current control. However, with variation in estimated inductance values, the actual high frequency winding current is either lower or higher than reference value, but using the closed loop control of figure 8.23, the dc current tracking or voltage tracking is maintained.

$$\phi_{1u(n)} = \frac{({i_{1ref}}^{new} + {i_{1ref}}^{old})(2r_{32}V_{dc2}{K_2}^3) + ({i_{3ref}}^{new} + {i_{3ref}}^{old})(2r_{12}V_{dc2}{K_1}^1)}{D} \quad (8.76)$$

$$\phi_{2u(n)} = \frac{({i_{1ref}}^{new} + {i_{1ref}}^{old})(-2r_{31}V_{dc1}{K_1}^3) + ({i_{3ref}}^{new} + {i_{3ref}}^{old})(2V_{dc1}{K_{sum}}^1)}{D} \quad (8.77)$$

$$\phi_{1d(n)} = \phi_{1u(n)} + \frac{({i_{1ref}}^{new} - {i_{1ref}}^{old})(2r_{32}V_{dc2}{K_2}^3) + ({i_{3ref}}^{new} - {i_{3ref}}^{old})(2r_{12}V_{dc2}{K_1}^1)}{D} \quad (8.78)$$

$$\phi_{2d(n)} = \phi_{2u(n)} + \frac{({i_{1ref}}^{new} - {i_{1ref}}^{old})(-2r_{31}V_{dc1}{K_1}^3) + ({i_{3ref}}^{new} - {i_{3ref}}^{old})(2V_{dc1}{K_{sum}}^1)}{D} \quad (8.79)$$

8.6. Experimental Results for Current Control without Sampling Transformer Winding Currents

The experimental results for Triple Active Bridge converter current control without using any sampled currents are discussed over here. Figure 8.23 shows the closed loop converter control schematic without using any sampled value of transformer winding currents. The feedback signals sent to the converter control loops are the output dc voltage feedback and source(RES) current input. The output dc control loops produce the references for transformer winding currents. Based on the reference values and transformer leakage inductance information, the phase angles for the winding voltages are determined the high frequency current controllers.

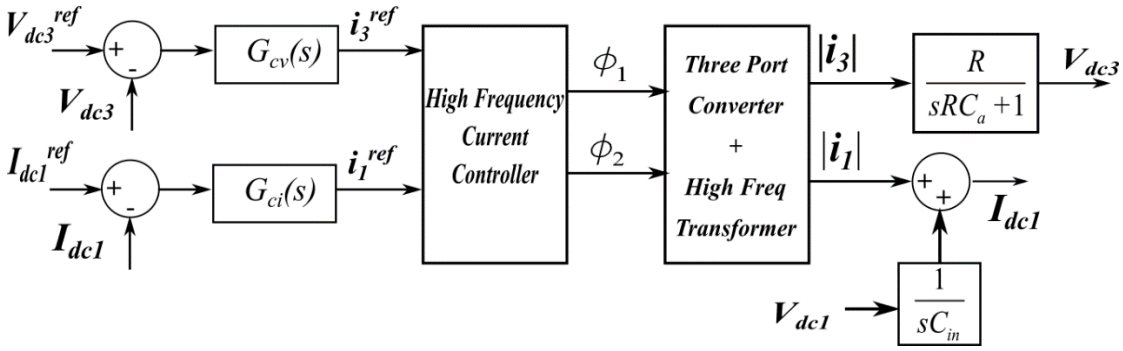

Figure 8.23. Closed Loop Power Control without Sampling Currents.

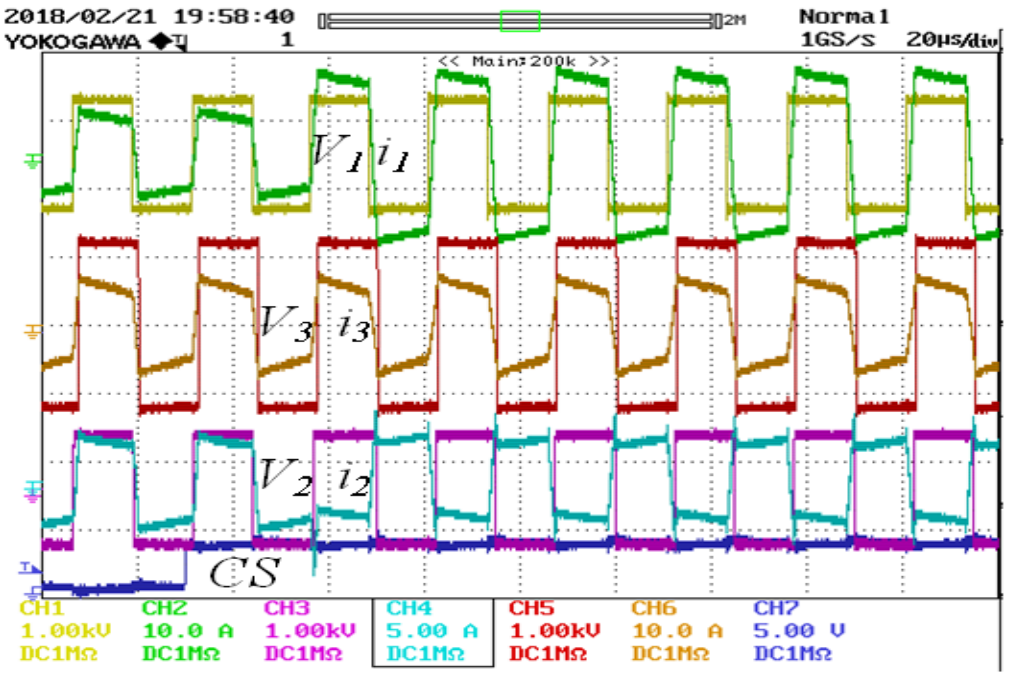

Figure 8.24. Step Change in Winding Current with No Sampling Current Control.

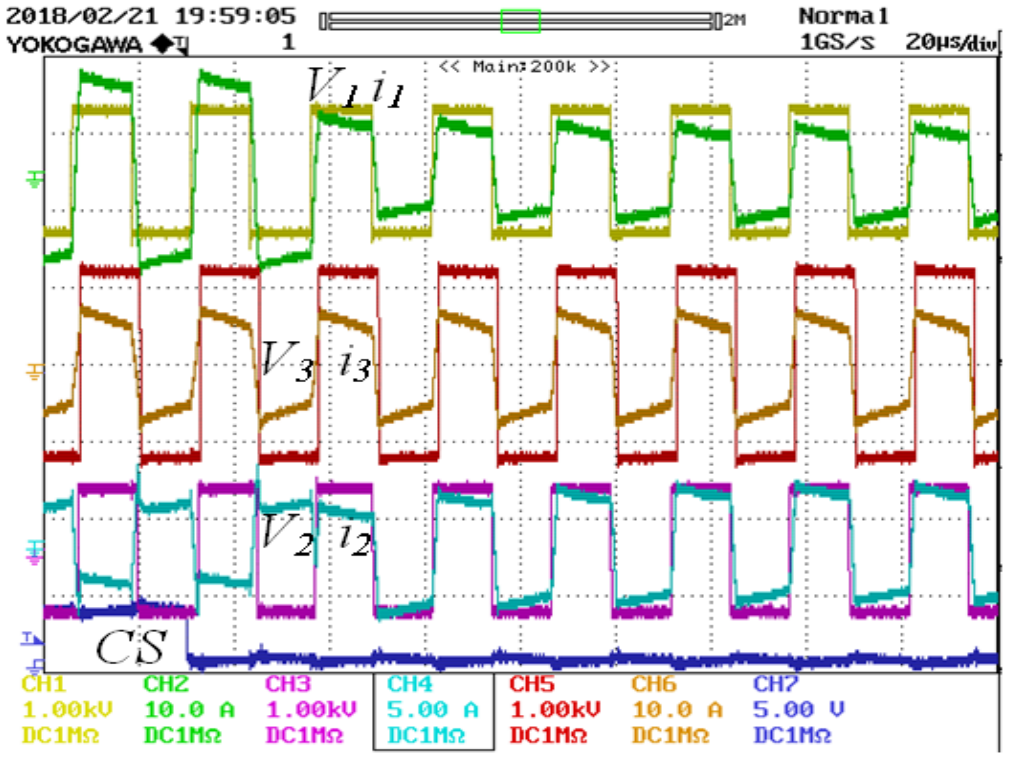

Figure 8.25. Step Change in Winding Current with No Sampling Current Control.

Figures 8.24 and 8.5 show the responses in transformer winding currents due to step changes in i_{1ref} and it is observed that the transformer winding currents have no oscillations or dc offsets using this method and attains the steady state within one switching cycle. In figures 8.24 and 8.25, the output dc voltage V_{dc3} is controlled at a steady state value of 1.2kV with a dc load while input voltages are at a voltage of 800V. The step change given in i_{1ref} is from 10A to 16A(fig 8.28) and again back from 16A to 10A(fig 8.29) is observed in figures 8.24 & 8.25. Responses of the converter due to step changes in I_{dc1}^{ref} are shown in figures 8.26-8.27. Transient changes in transformer winding voltages and currents, and transient changes in dc currents are given in figure 8.26-8.27 for a step change in I_{dc1}^{ref} from 4A to 12A is shown, which is approximately a jump in power P_1 from 3kW to 9.6kW. Similarly, figures 8.28-8.29 show the transient responses for step change in I_{dc1}^{ref} back from 12A to 4A. It can be observed that as I_{dc1} changes, I_{dc2} also changes to balance the output power going to output port 3 and maintain the output voltage at a fixed reference value.

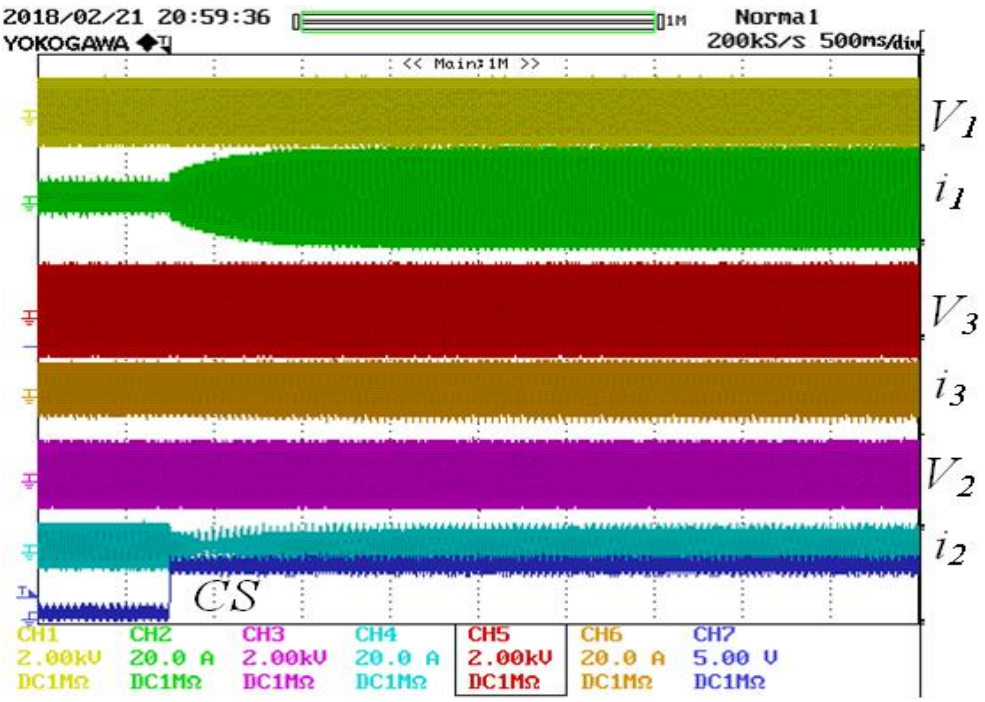

Figure 8.26. Transformer Winding Voltages and Currents under Transients.

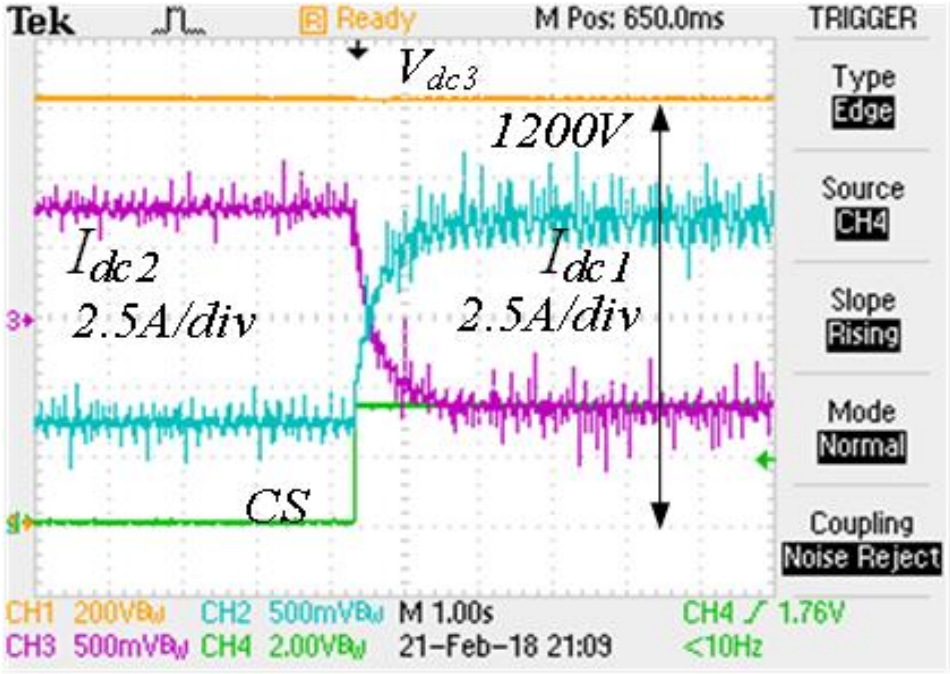

Figure 8.27. Converter Input Currents and Output Voltage under Transient.

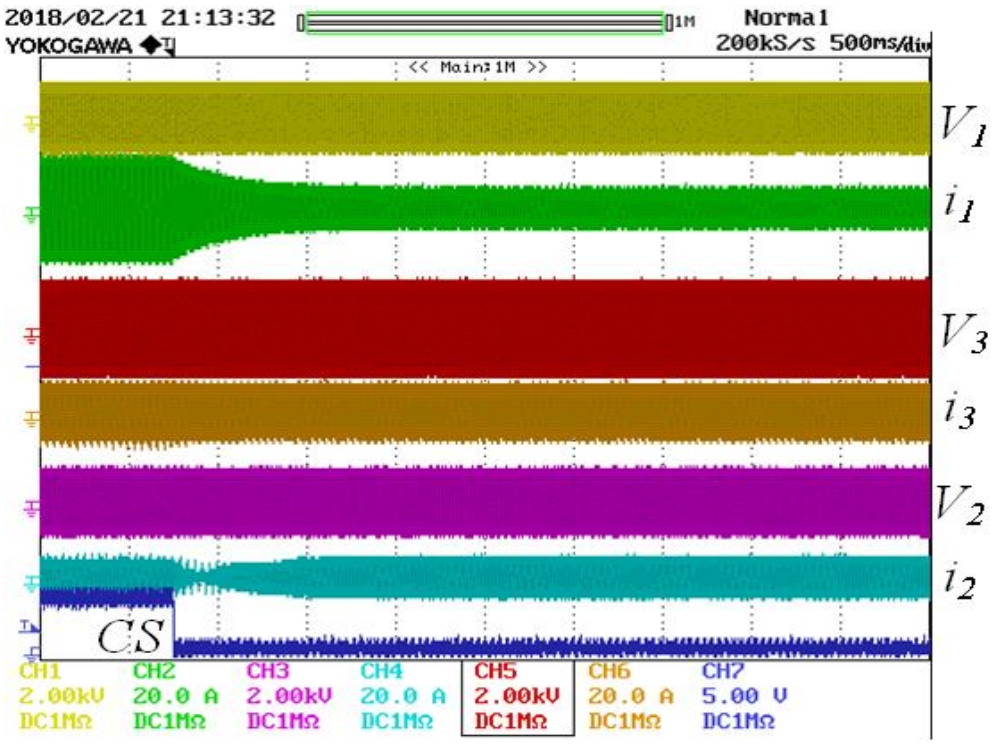

Figure 8.28. Transformer Winding Voltages and Currents under Transients.

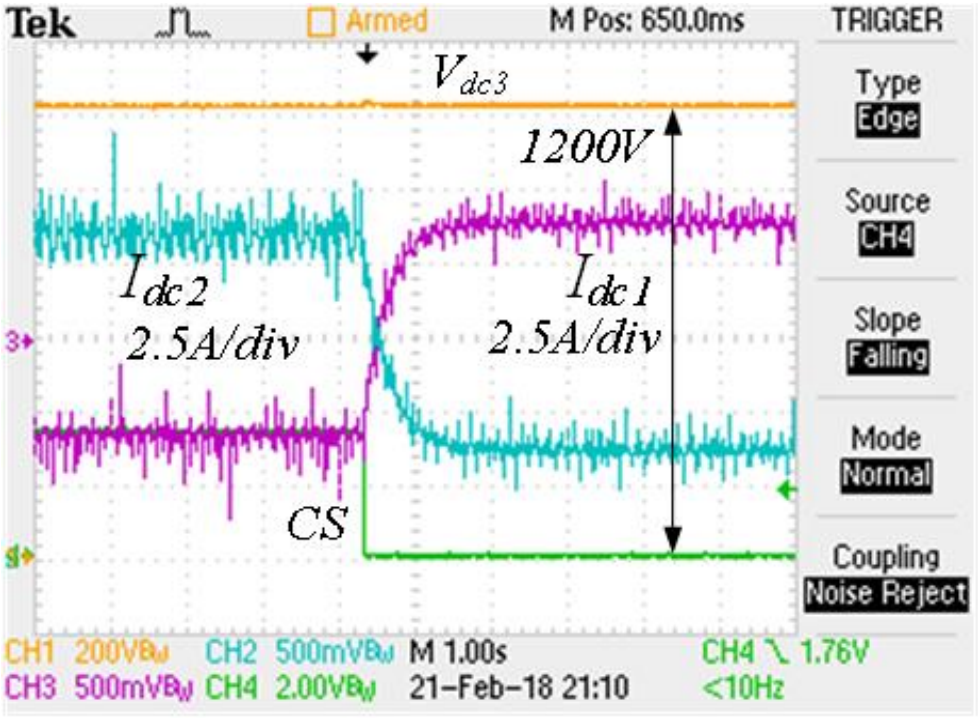

Figure 8.29. Converter Input Currents and Output Voltage under Transient.

8.7. Series Connection of Three Port DC-DC Converter Outputs for Higher DC Bus Voltage

The three port converter discussed in this thesis work, is aimed to work as a modular building block for large scale integration of PV and Energy Storage(ES). The three port converter can work as a input dc source to individual DC-AC converter module for cascaded medium voltage converter(Fig. 1.7 in chapter 1). The three port converter can also act as a modular building block for series connected MV dc bus of Figure 1.6 in chapter 1. In this section, series connection of the output voltages of the three port isolated dc-dc converters is demonstrated here to obtain a MV DC bus for converter architecture of figure 1.6. Series connection of the output voltages of multiple three port dc-dc converters can provide a medium voltage dc bus for a medium voltage grid integration of PV and ES. In this section, the output voltages of the individual dc buses of two modular three port dc-dc converters are series connected, while the input side voltages are kept independent or can be parallel connected. Schematic of the series connected system of three port dc-dc converter is shown in figure 8.30, where each of the output voltages are maintained around 1.1kV-1.2kV, while the input side PV and ES dc voltages are kept at 800V. The total series voltage obtained experimentally in this section is around 2.3kV dc. The control schematic for series connection of three port dc-dc converter outputs is shown in figure 8.31.

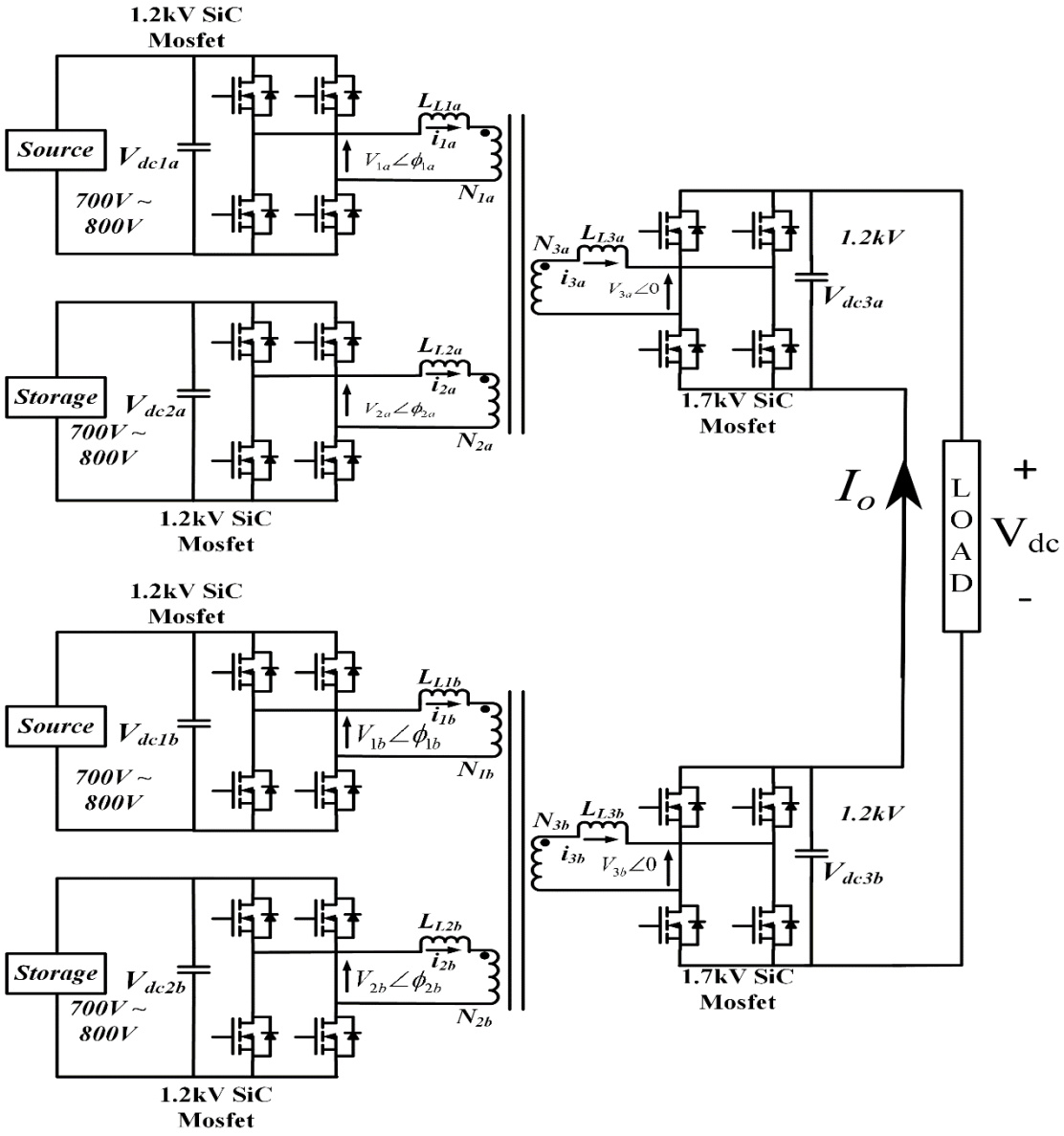

Figure 8.30. Series Connected DC-DC Converter.

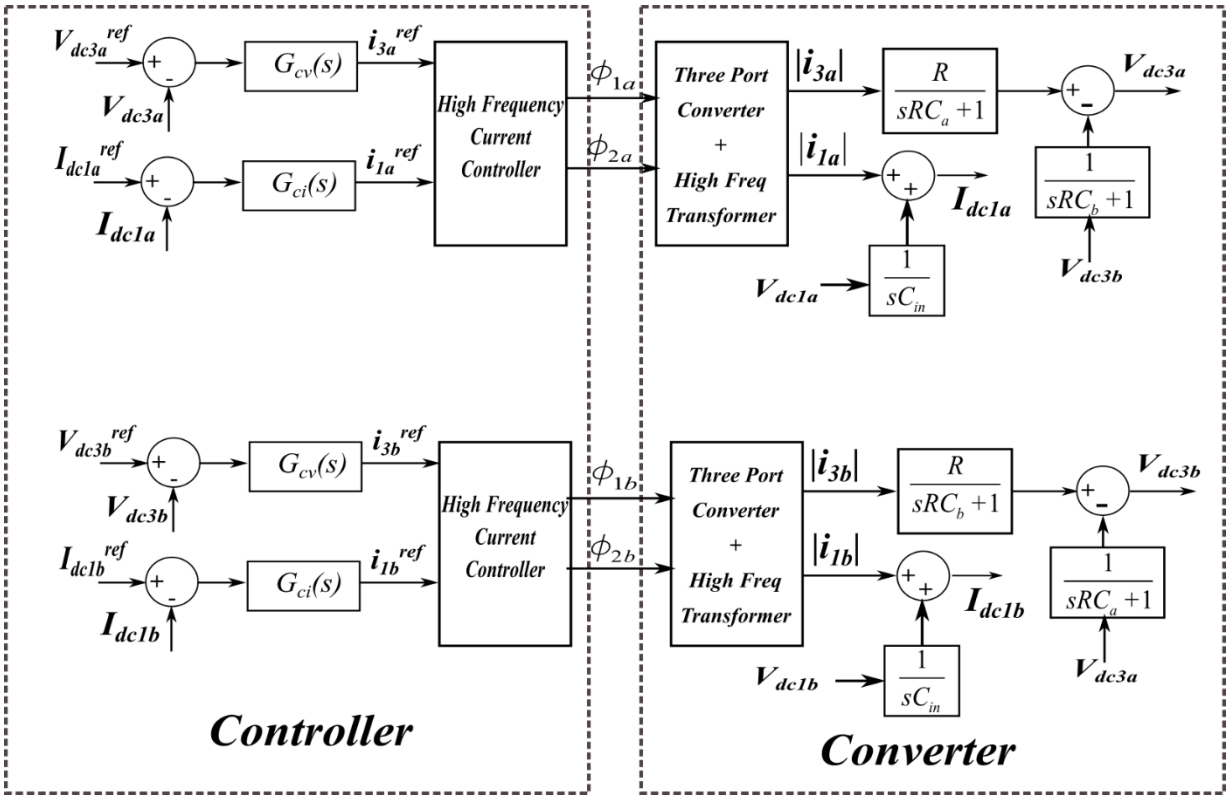

Figure 8.31. Closed Loop Control of Series Connected Converter.

The closed loop control for individual converters of figure 8.30 is identical to that demonstrated in previous section, where each converter output voltage is controlled along with the dc power input from one of the input ports. In the control diagram of figure 8.31, each three port dc-dc converter module of the series connected dc bus has independent control. The closed loop outer voltage control of once converter does not interact with closed loop control of other dc-dc converter modules. However, there is a feed forward coupling term present in the converter system block diagram, whose effect is nullified by the fact that feed forward terms do not influence the control regulation action of independent closed loop control.

For the series connected system of figure 8.30, the following equations at the output terminal can be derived from the figure 8.30,

$$\left|i_{1a}\right| + \frac{V_{dc1a}}{sC_{in}} = I_{dc1a} \text{ (8.80)}, \quad \left|i_{1b}\right| + \frac{V_{dc1b}}{sC_{in}} = I_{dc1b} \text{ (8.81)}$$

$$\left|i_{1a}\right| \frac{R}{sRC_{out}+1} + \frac{V_{dc3b}}{sRC_{out}+1} = V_{dc3a} \text{ (8.82)}$$

$$\left|i_{1b}\right| \frac{R}{sRC_{out}+1} + \frac{V_{dc3a}}{sRC_{out}+1} = V_{dc3b} \text{ (8.83)}$$

The 'High Frequency Current Controller' of the closed loop control of figure 8.31 is for the high frequency transformer current control, which is mentioned above in aforementioned sections of this chapters. Since the current control is a fast control method with a bandwidth of switching frequency, therefore gain of the current control loop seen by outer voltage control loop can be taken as 1. The closed loop control for the outer dc loop voltage control can be designed based on output load dynamics. The output voltage controllers from figure 8.31, are designed as PI controllers, having a pole placed close to the system pole $\frac{1}{RC_{out}}$ and the bandwidth chosen is 1kHz. The input current controller is designed as a PI controller with a bandwidth of 100Hz. The output voltage controller is given a faster response than input current controller. The steady state transformer winding currents under series connection are shown in figure 8.32 and the dc voltages and currents of the two converters are shown in figure 8.33.

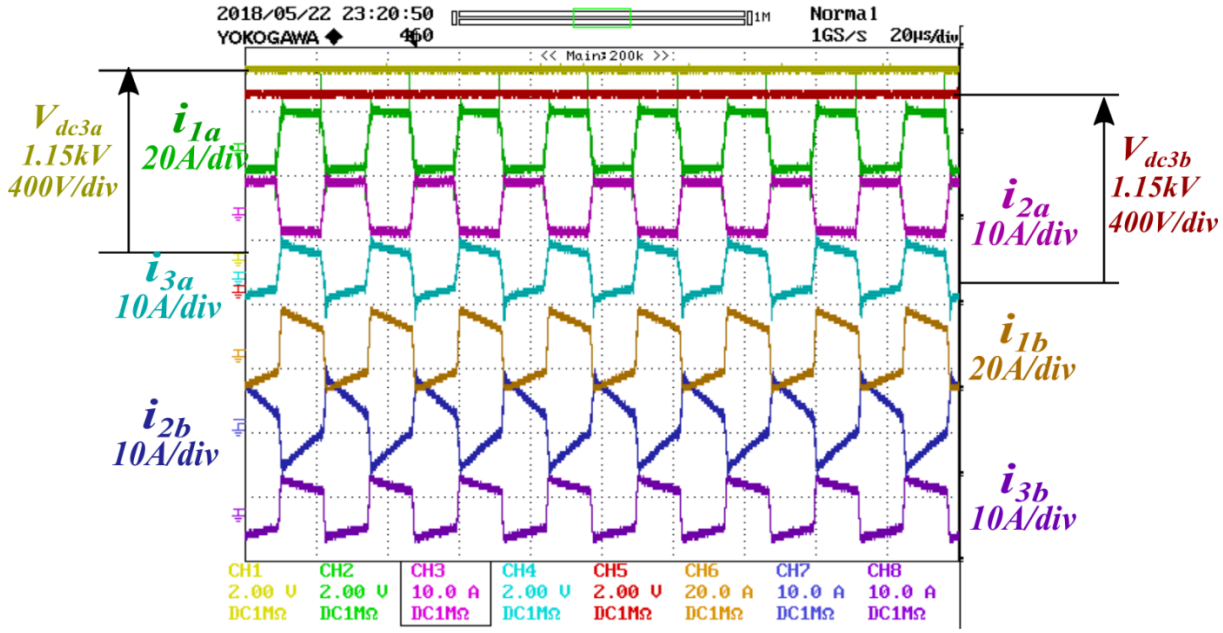

Figure 8.32. Transformer Currents and DC Voltages for Series Connection.

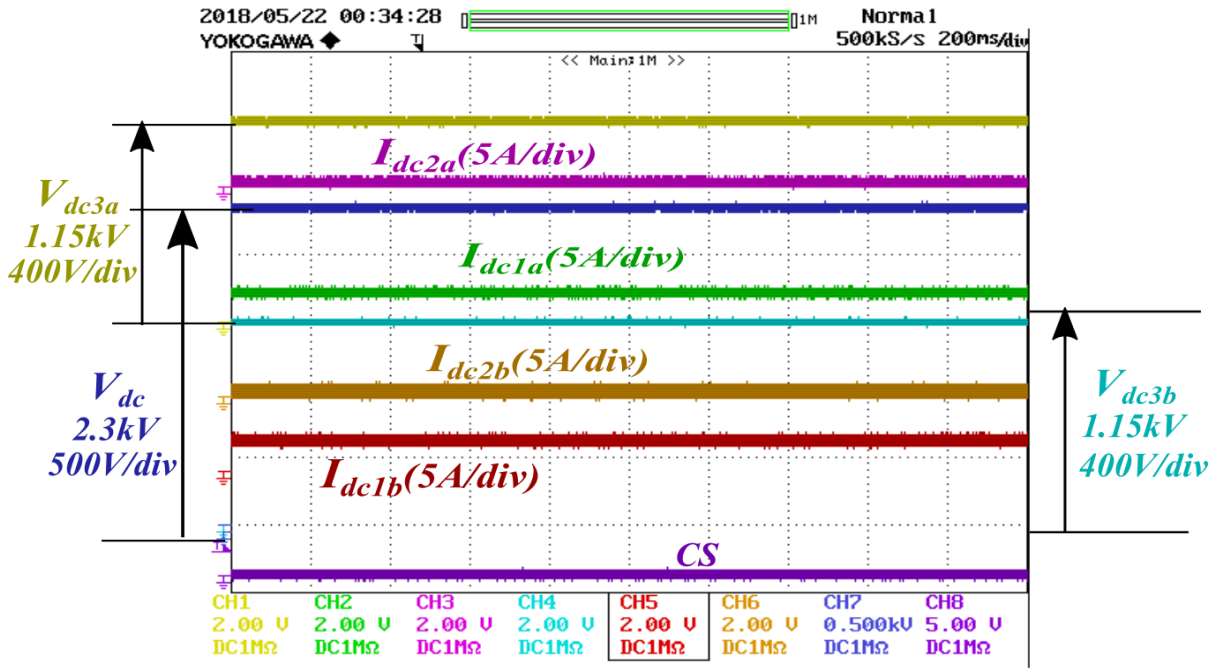

Figure 8.33. Input dc Currents & Output dcVoltages for Series Connection.

The transient response for the series connected converters of figure 8.30, using the closed loop control technique shown in figure 8.31, are shown below. Figures 8.34 and 8.35 show the

response in input dc currents and transformer winding currents for both the converters of figure 8.30, when a step change in I_{dc1a}^{ref} is given from 4A to 9A. It is observed that as the input PV current I_{dc1a} for the top converter changes, the ES port dc current I_{dc2a} changes in opposite direction to keep the output dc voltage V_{dc3a} constant at the reference voltage, caused by control action of figure 8.31. In this scenario, the lower converter's input dc currents I_{dc1b}, I_{dc2b} and the output dc voltage V_{dc3b} do not change, they are kept constant at their reference values by its own converter control action. This demonstrates the scenario when one converter module goes through a change in input PV power availability, the output voltage of that particular converter and operating conditions of the other converters in series connected dc, bus are unaltered and maintained constant. Figures 8.36 and 8.37 show the changes in input dc currents and transformer winding currents for both the converters when a step change is given in I_{dc1b}^{ref}. Similar phenomenon are observed in figures 8.36 and 8.37, when input PV power of converter 2 changes. Operating points for converter 1 are unaltered and maintained constant while converter 2 undergoes operating point changes.

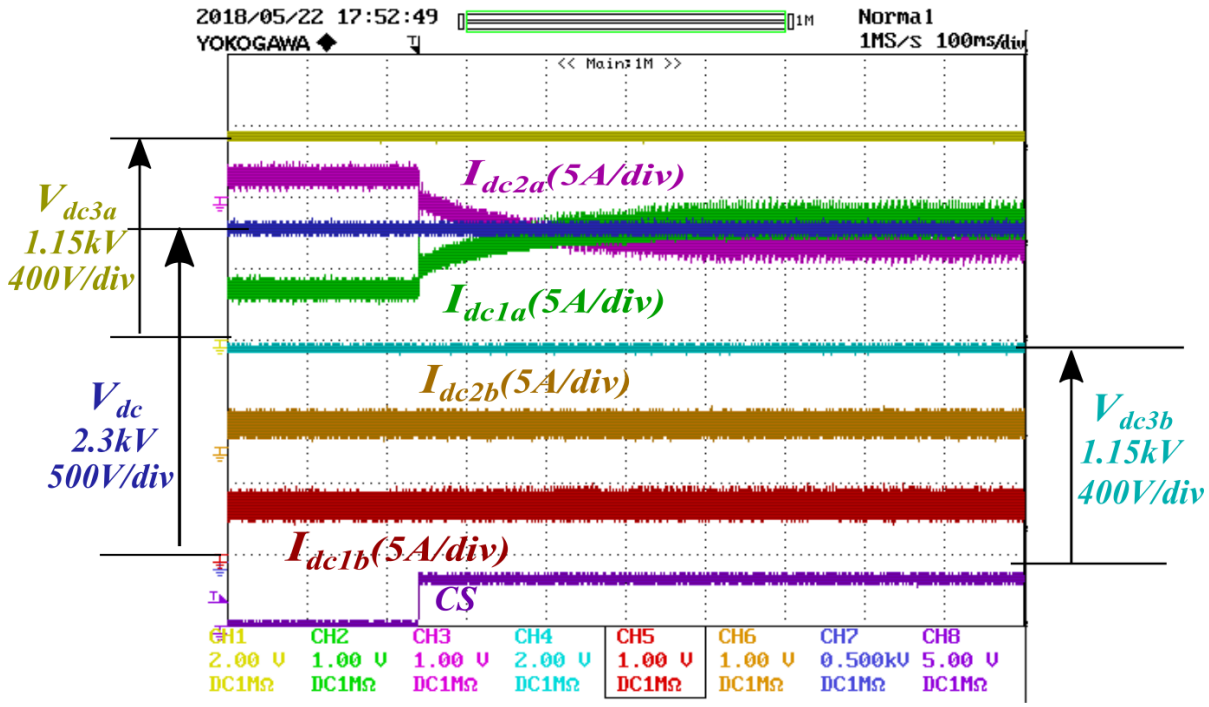

Figure 8.34. Changes in DC Currents of Both Converters for Step Change in I_{dc1a}^{ref}.

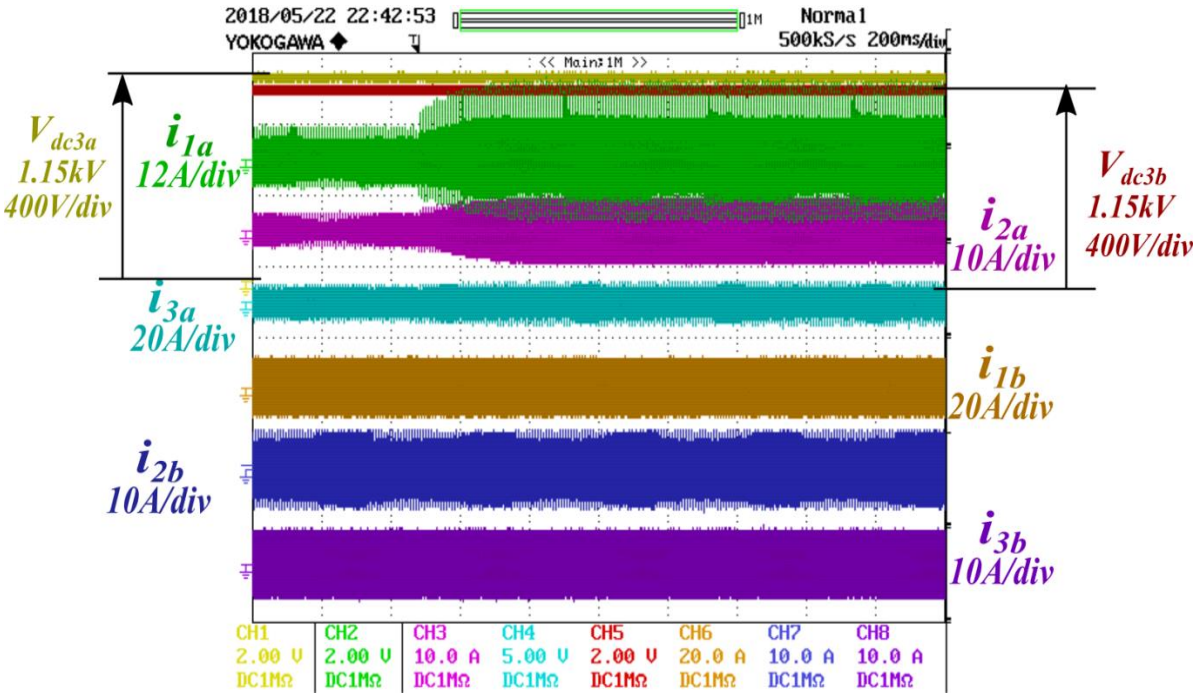

Figure 8.35. Changes in Transformer Currents of Converters for Step Change in I_{dc1a}^{ref}.

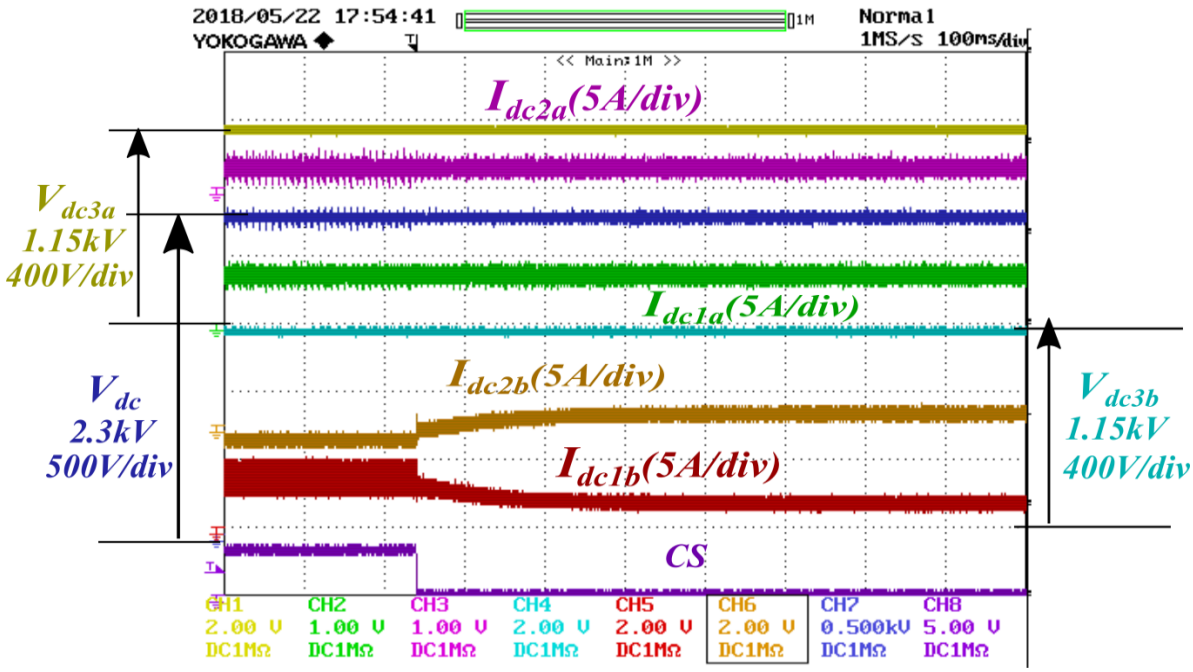

Figure 8.36. Changes in DC Currents of Both Converters for Step Change in I_{dc1b}^{ref}.

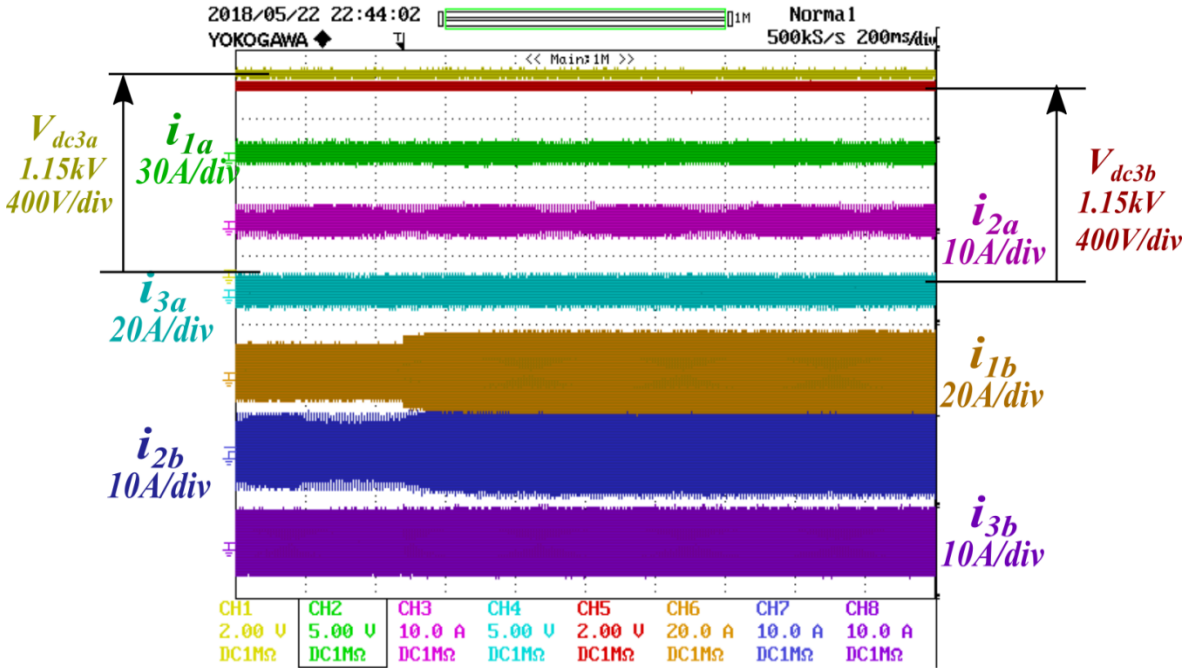

Figure 8.37. Changes in Transformer Currents of Converters for Step Change in I_{dc1b}^{ref}.

From the results shown in figures 8.34-8.37 and the discussion above, the two converters of figure 8.30 having independent dc voltage and current control loops can successfully operate independent of each other. Therefore, it can also be argued that the independent voltage controller should allow the converters to have unequal dc voltage across them. The verification of the concept of having unequal dc voltages across individual converter outputs of the series connected dc bus of figure 8.30, is carried out using experimental study. Figures 8.38 and 8.39 show the two converters operating with unequal dc voltages across converter output terminals. In figure 8.38, the converter 1 output reference voltage V_{dc3a}^{ref} is given change, which makes the output voltage V_{dc3a} to change to new steady state value, while the two series connected dc buses continue to operate at different voltages while carrying the same dc current. The same thing is demonstrated in figure 8.39, where converter 2 output voltage V_{dc3b} changes to a new steady state value and the two converters continue to operate with unequal dc bus voltages.

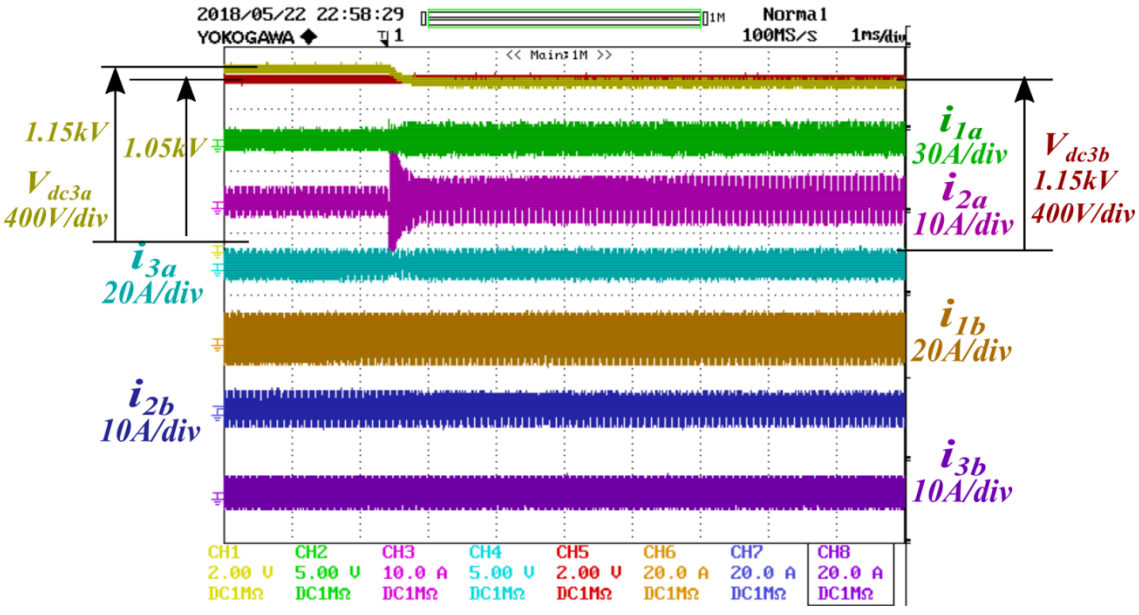

Figure 8.38. Transient Change in DC Voltage of Top Converter.

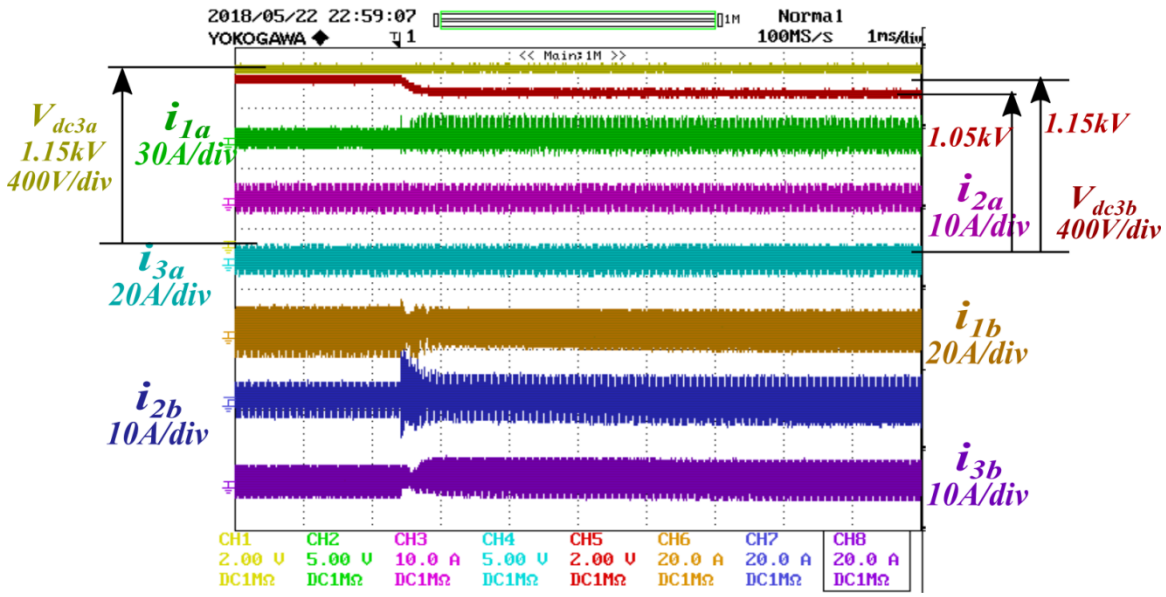

Figure 8.39. Transient Change in DC Voltage of Bottom Converter.

In figures 8.38-8.39, it can be observed that as one converter undergoes transient due to change in reference voltage, the other converter is undisturbed, except some changes in ripple for the transformer winding currents.

8.8. Conclusions

The high frequency current control techniques discussed in this section provide different aspects to the converter operation depending on the type of current control. The double sampling method provides quite a few disadvantages over the other two control methods, such as continuous oscillations and audible noise. The single sampling method is devoid of the continuous oscillations and audible noise, but some transient oscillations are observed during phase change due to sensitivity to inductance variation. The sensorless current control technique is devoid of all the drawbacks of double & single sampling current control methods, as it doesn't use any sampled currents from sensors. However, dc sensors are required for sensing dc current and voltage signals to use as feedback signals for closed loop power control. The series

connection of dc-dc converter out technique uses the sensorless current control method which enables the dc-dc converter outputs to be independently controlled. Different case studies with experimental results have been performed to validate the series connection of dc buses for checking the independency of power control for the series connected converters.

Chapter 9. Generalized Phase Shifted DC-DC Converter Control Techniques For Eliminating DC Transients From Transformer Winding Currents

The conventional phase shift control method of DAB or TAB converters(schematics shown in figures 9.1 & 9.2) produce large dc transients in transformer winding currents during operating phase angle change. The developed dc transients in transformer winding currents take quite a few cycles to dissipate depending on winding time constant. For continuous phase angle change operation, the transformer develops huge dc offsets in winding currents and in core magnetizing flux, which can cause transformer saturation leading to converter failure. Figures 9.3 and 9.4 show the dc transients that is observed in transformer winding currents due to changes in phase angles for DAB and TAB converters. In order to reduce effects of dc transients, techniques like controller bandwidth reduction and introduction of air-gaps in transformer cores are used to avoid saturation during transients. Phase shifted DC-DC converter current control methods, proposed in [71]-[74], has not addressed transformer saturation phenomenon. Direct current control methods proposed in [75]-[82], use different sensors for implementing dc bias removal for, but these methods are sensitive to changes leakage inductances.

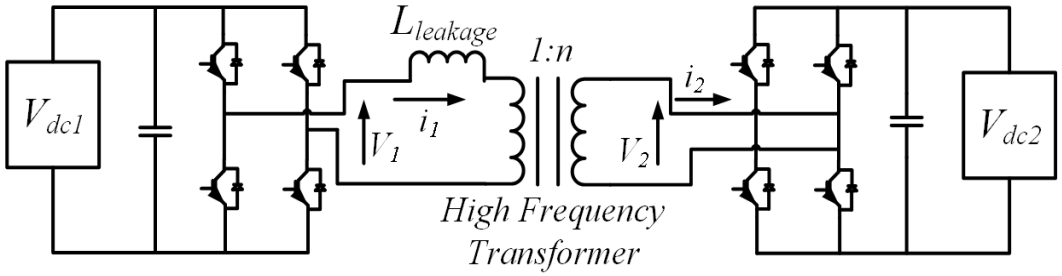

Figure 9.1. Two Port Dual Active Bridge Converter.

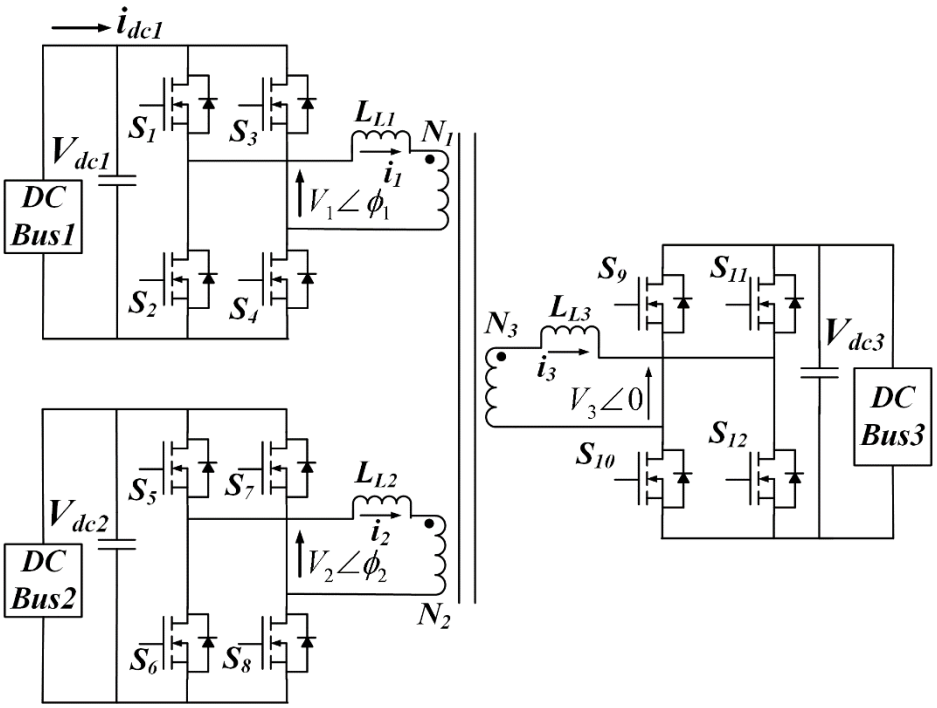

Figure 9.2. Three Port Triple Active Bridge Converter.

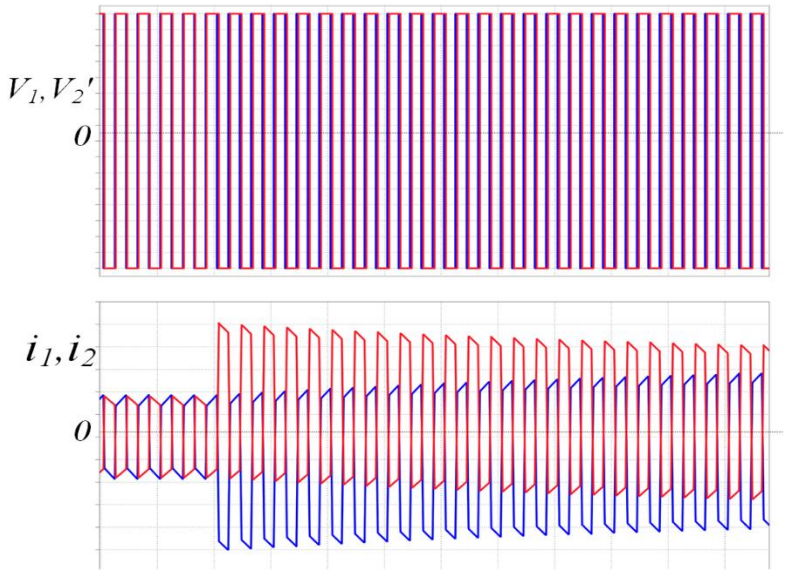

Figure 9.3. Transformer Currents During Transients in DAB Converter.

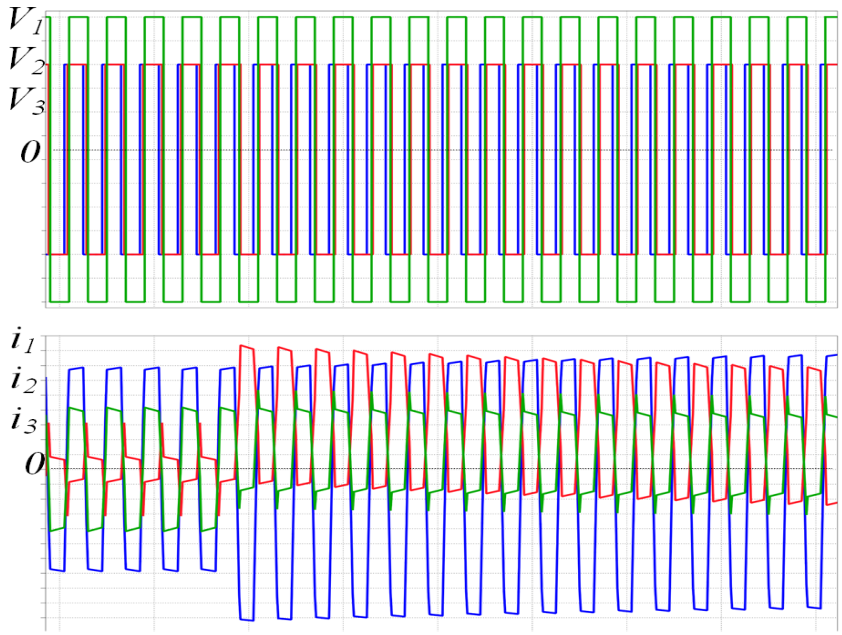

Figure 9.4. Transformer Currents During Transients in TAB Converter.

A novel two phase shift method is discussed in this chapter, which uses two different phase shift angles during transients for each half cycle to eliminate or reduce the dc transient currents to a minimum level. In this chapter, the proposed two phase shift method is applied to DAB and TAB converter transient operation for square wave winding voltages and quasi-square wave voltages. The two phase shift method is also applied for power reversal of DAB converter without dc transient currents, operating mode change from three port operation to two port operation and back to three port operation for TAB converter. The two phase shift method is verified using a laboratory hardware prototype made of 1200V and 1700V SiC Mosfets using a ferrite core based high frequency transformer. The DAB converter operation is tested at 400V/400V for V_{dc1} and V_{dc2} with a high frequency transformer. The three port TAB converter operation is tested at 400V/400V/600V voltage levels for V_{dc1}, V_{dc2} & V_{dc3}. The power level for

two phase shift control method is tested around 4kW-5kW power level for DAB & TAB converter with operating switching frequency of 25kHz.

9.1. Proposed Two Phase Shift Method for Dual Active Bridge(DAB) Converter

9.1.1. Two Phase Shift Method for Square Wave Voltages

In the proposed two phase shift method, the PWM generator of the controller uses two different phase shift angles during any change command in operating phase angle. The two phase shifts are applied during positive & negative half cycles of winding voltages. The two phase shift angles for the next switching cycle are generated in thee current switching cycle and are updated in the PWM controller. In order to derive and explain the two phase shift method, the equivalent circuit of DAB converter, neglecting magnetizing inductance of the transformer, is used which is given in figure 5. The proposed two phase shift method is explained in figure 6, where ϕ_{old} is the steady state phase angle for switching cycle $(n-1)$. When the command for steady state phase angle change occurs, the controller generates an intermediate phase angle ϕ_k for positive half cycle, which changes the transformer current to the steady state value of ϕ_{new}.

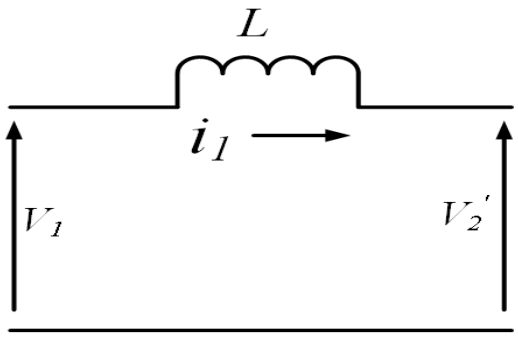

Figure 9.5. Equivalent Circuit for DAB Transformer.

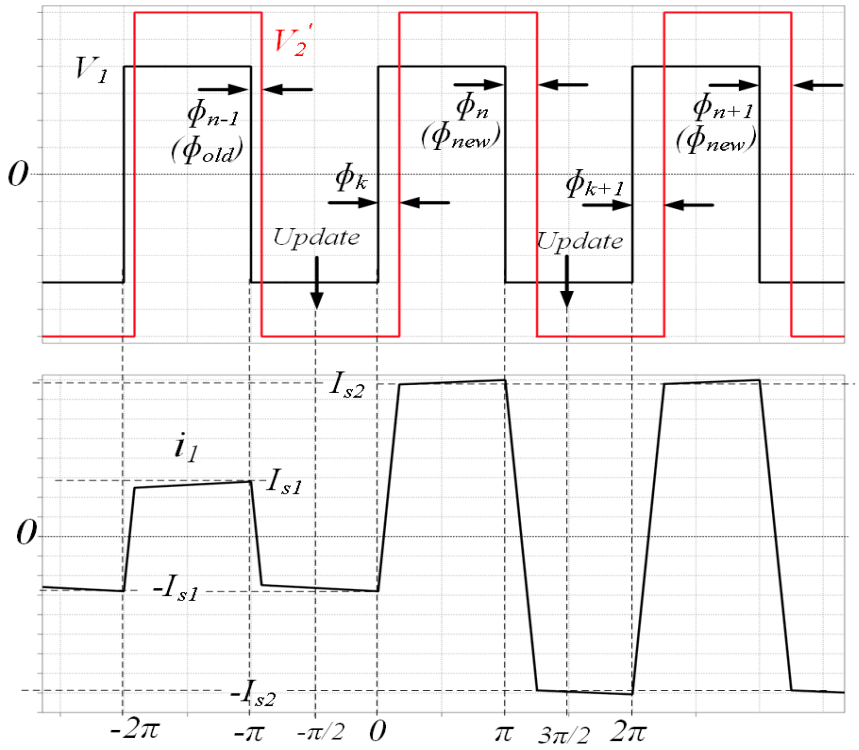

Figure 9.6. Two Phase Shift Method in DAB Converter.

In figure 9.6, the phase angle for the next switching cycle is updated in the PWM generator at the midpoint of each negative half cycle of V_1, i.e. at $\omega t = \frac{n\pi}{2}$ instant, where $n = -1, 3, 7$ etc. In this method, two phase angles are used between primary and secondary voltages. ϕ_k is the phase shift between the negative to positive transition($-V_{dc}$ to $+V_{dc}$) and ϕ_{new} is the phase shift between positive to negative transition($+V_{dc}$ to $-V_{dc}$). I_{s1} is the steady state peak line current at $m\pi$ (m=odd) instants when phase angle is ϕ_{old}, and I_{s2} is the steady state peak line current at $m\pi + \phi_{new}$(m=even) instant, when phase angle is ϕ_{new}. If phase angle needs to be changed in n^{th} switching cycle from ϕ_{old} to ϕ_{new}, the peak line current must reach from $-I_{s1}$ at $\omega t = 0$ to $+I_{s2}$ at $\omega t = \phi_{new}$. The intermediate phase shift ϕ_k is the required phase angle to eliminate dc transient

effect in winding current. Clearly the angle ϕ_k can be expressed as a function of ϕ_{old} and ϕ_{new}, which is derived below. From DAB operation, currents $-I_{s1}$ and $+I_{s2}$ are expressed as shown in (9.1) and (9.2). The currents $-I_{s1}$ and $+I_{s2}$ can be related to each other, as given in (9.3). Solving ϕ_k from (9.1)-(9.3), the expression for ϕ_k is given in (9.4). Following this method, the phase angle ϕ_{k+1} at $(n+1)^{th}$ switching cycle is equal to ϕ_{new}, as given in (9.5). The proposed control thus settles the winding current within one switching cycle during phase angle change.

$$-I_{s1} = -\frac{V_{dc1}}{\omega L}(\frac{\pi}{2}) + V_{dc2}{}'\omega L(\frac{\pi}{2} - \phi_{old}) \quad (9.1)$$

$$I_{s2} = -\frac{V_{dc1}}{\omega L}(\frac{\pi}{2} - \phi_{new}) + V_{dc2}{}'\omega L(\frac{\pi}{2}) \quad (9.2)$$

$$I_{s2} = -I_{s1} + \frac{V_{dc2}{}' + V_{dc1}}{\omega L}(\phi_k) \quad (9.3)$$

$$\phi_k = \frac{V_{dc1}\phi_{new} + V_{dc2}{}'\phi_{old}}{V_{dc1} + V_{dc2}{}'} \quad (9.4)$$

$$\phi_{k+1} = \frac{V_{dc1}\phi_{n+1} + V_{dc2}{}'\phi_n}{V_{dc1} + V_{dc2}{}'} = \frac{V_{dc1}\phi_{new} + V_{dc2}{}'\phi_{new}}{V_{dc1} + V_{dc2}{}'} = \phi_{new} \quad (9.5)$$

The proposed two phase shift method is verified using a laboratory hardware prototype for a 400V:400V DAB converter at 25kHz. Figure 9.7 shows the transformer winding voltages and currents without using two phase shift method control. Figures 9.8 and 9.9 show the transformer winding voltages and current waveforms during transient using two phase shift method. In order to verify the robustness of the method, the phase shift is varied as a low frequency sinusoid with

a dc value, as $\phi = \phi_{dc} + \phi_{ac} sin(\omega t)$. Figure 9.10 shows the transformer winding voltages and currents for continuously varying phase shift, where it is observed that with continuously changing phase shift angle, where steady state operating point changes in phase cycle, the two phase shift method provides robust control.

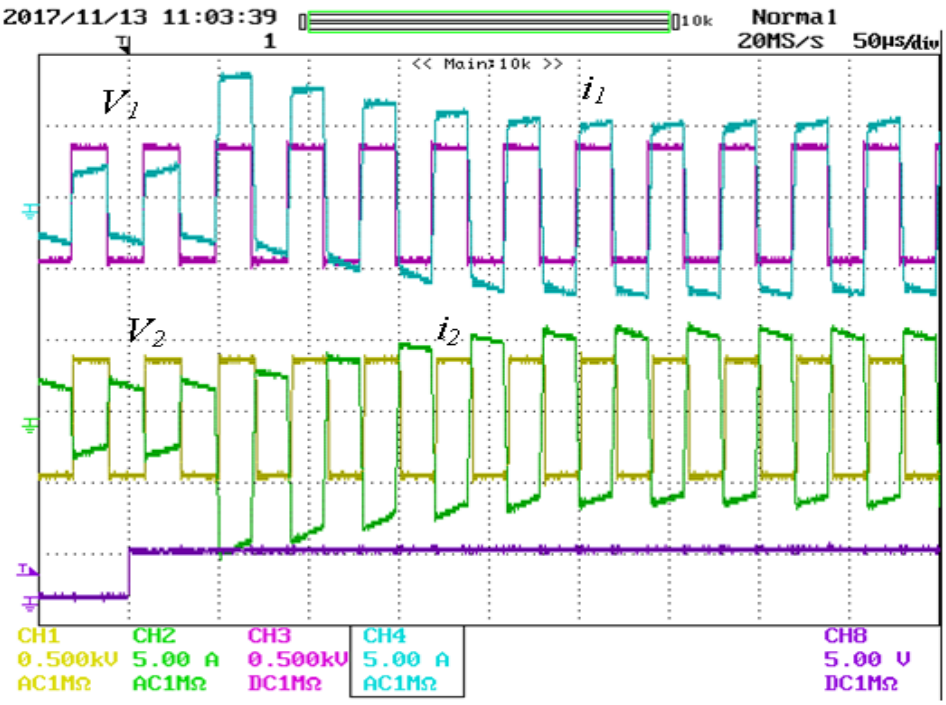

Figure 9.7. DC Transients in Transformer Currents without Two Phase Shift Control.

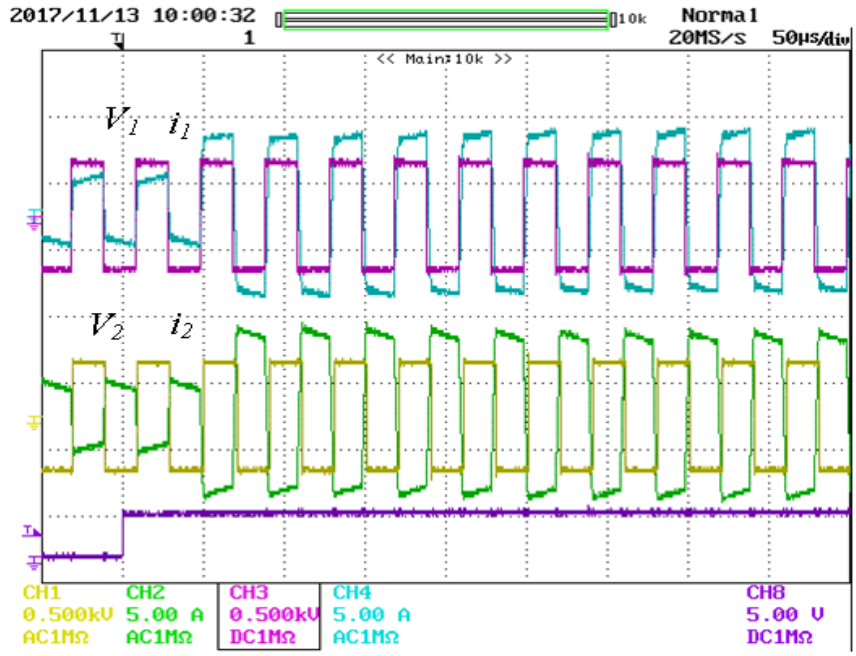

Figure 9.8. Transients in Transformer Currents Using Two Phase Shift Control.

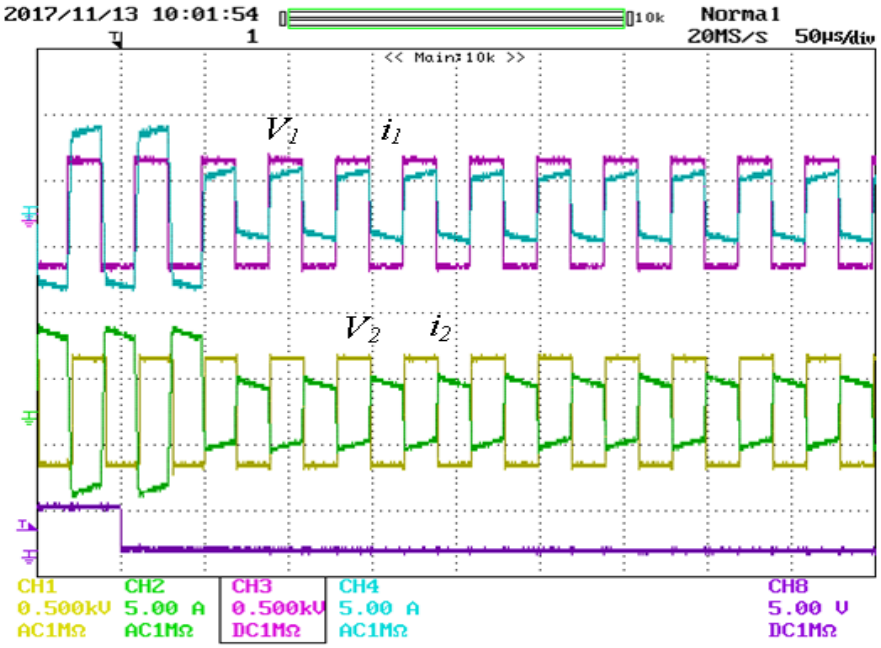

Figure 9.9. Transients in Transformer Currents Using Two Phase Shift Control.

Using the two phase shift method it is observed that the winding currents reach the new steady state within one switching cycle. There is a very small dc offset present which is due to the resistance of the winding, since the derived equations are based on ideal inductive circuit. One critical condition for successful two phase shift method is based on the condition that $\omega L >> R_s$. In this paper, all the derivations are based on ideal inductive circuit for DAB converter.

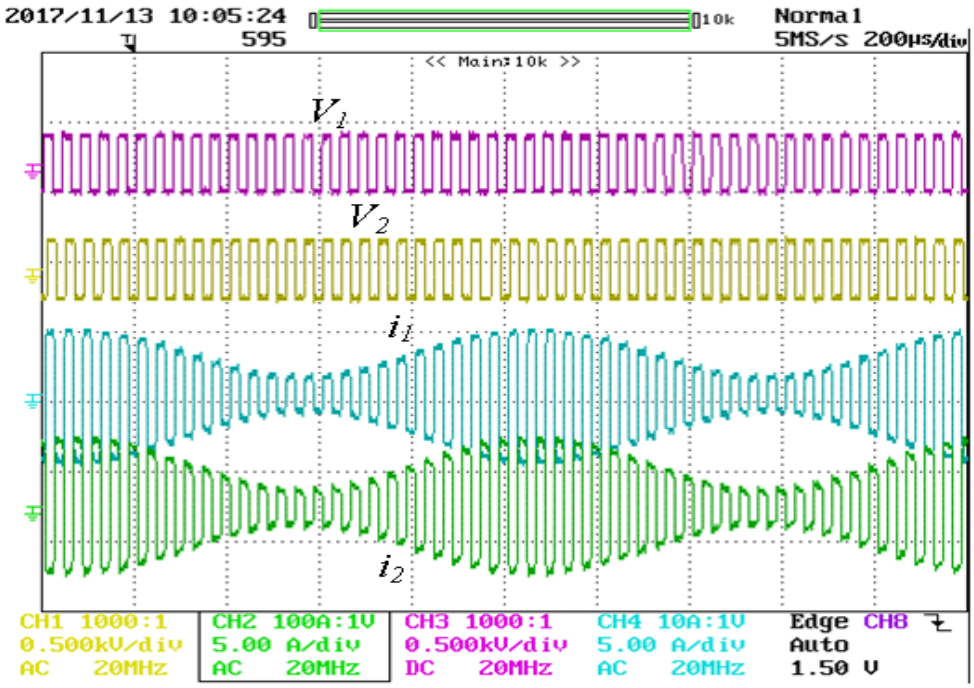

Figure 9.10. Transformer Currents with Varying Phase Shift Angle.

9.1.2. Two Phase Shift Method for Quasi-Square Wave Voltages

The aforementioned two phase shift method is extended to duty cycle modulated quasi-square wave voltages, i.e. square wave voltages with a zero duration. The quasi square wave voltage is necessary for DAB operation mainly to improve the soft-switching region for DAB converter and achieve higher efficiency at low power operating regions[71-74]. The number of control

parameters for DAB converter using quasi square wave voltages, changes from one(ϕ) to three(ϕ, D_1, D_2). Figures 9.11-9.16 show the six possible cases for duty cycle and phase shift combined modulation.

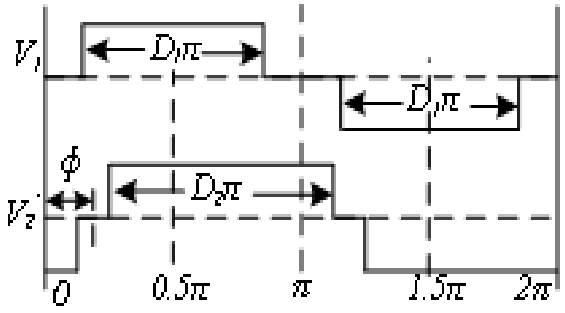

Figure 9.11. Case1.
$0 < 0.5(1-D_1)\pi < \phi - 0.5(1-D_2)\pi < \phi + 0.5(1-D_2)\pi$

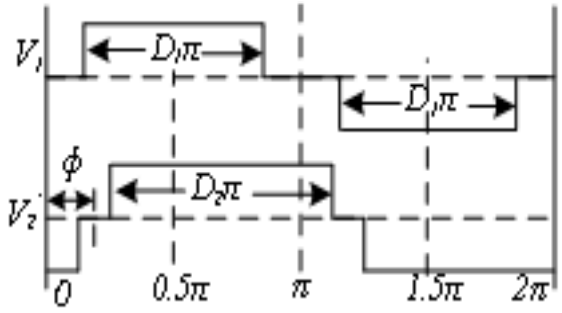

Figure 9.12. Case2.
$0 < \phi - 0.5(1-D_2)\pi < 0.5(1-D_1)\pi < \phi + 0.5(1-D_2)\pi$

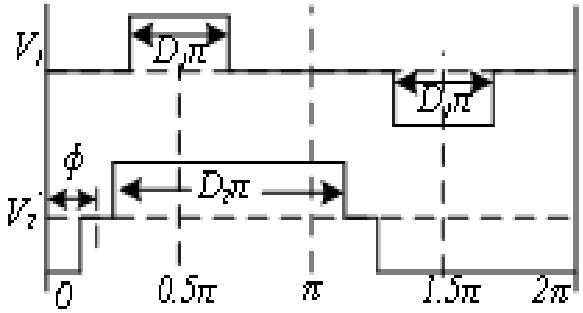

Figure 9.13. Case3.
$0 < \phi - 0.5(1-D_2)\pi < \phi + 0.5(1-D_2)\pi < 0.5(1-D_1)\pi$

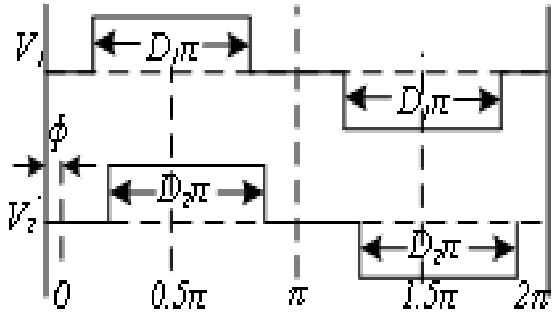

Figure 9.14. Case4.
$0 < 0.5(1-D_1)\pi < \phi + 0.5(1-D_2)\pi$
$< 0.5(1+D_1)\pi < \phi + 0.5(1+D_2)\pi$

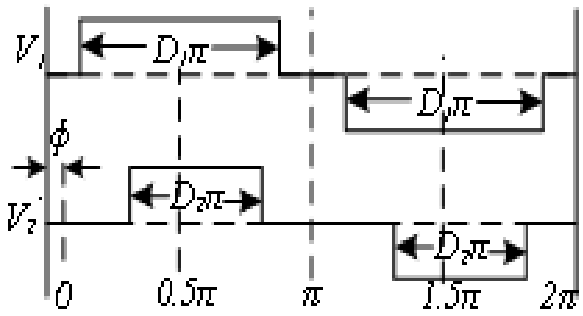

Figure 9.15. Case5.
$0 < 0.5(1-D_1)\pi < \phi + 0.5(1-D_2)\pi$
$< \phi + 0.5(1+D_2)\pi < 0.5(1+D_1)\pi$

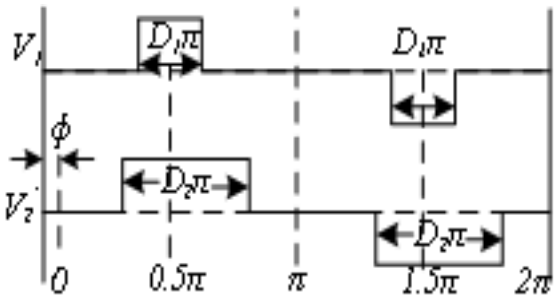

Figure 9.16. Case6.
$0 < \phi + 0.5(1-D_2)\pi < 0.5(1-D_1)\pi$
$< 0.5(1+D_1)\pi < \phi + 0.5(1+D_2)\pi$

In the combined phase shift and duty cycle method, the three variables under considerations are winding voltages' duty cycles D_1, D_2 and phase shift angle ϕ between the winding voltages. In this method, for any change in the values of parameters D_1, D_2, ϕ, the intermediate phase angle value ϕ_k is evaluated such that the dc transient from winding current, is removed. The phase angle ϕ_k is evaluated in such a manner that for a change of steady state operating points from old set of ($D_1^{old}, D_2^{old}, \phi_{old}$) to a new set of steady state operating point of ($D_1^{new}, D_2^{new}, \phi_{new}$) is achieved in half a switching cycle. In each switching cycle, the new set of values are updated at $\omega t = \frac{3\pi}{2}$ instant. The duty ratios D_1^{new}, D_2^{new} are same for both the positive half cycle and negative half cycle, whereas the angle ϕ_k is applied for positive half cycle and the angle ϕ_{new} is applied for negative half cycle. The winding current expressions at $\omega t = \frac{3\pi}{2}$ for current cycle with old sets of values of $D_1^{old}, D_2^{old}, \phi_{old}$ are given in equation (9.6). The winding current expressions at $\omega t = \frac{\pi}{2}$ for next cycle with new sets of values of $D_1^{new}, D_2^{new}, \phi_{new}$ are given in

equation (9.7). The intermediate phase angle ϕ_k is derived from the equation (9.8), where '*m*' is the slope for each intermediate sub-intervals and $\Delta\theta$ denotes each sub-interval duration. The intermediate phase angle ϕ_k is derived for each of the possible cases defined above and the expression for ϕ_k comes out to be same in all the three cases, as given in equation (9.9), same to that in equation (9.4). The negative half cycle phase angle is given by ϕ_{new}.

$$i_1(\frac{3\pi}{2}) = -\frac{V_2^{'}}{\omega L}\phi_{old} \quad (9.6) \qquad i_1(\frac{\pi}{2}) = \frac{V_2^{'}}{\omega L}\phi_{new} \quad (9.7)$$

$$i\{\frac{\pi}{2}\} = i(\frac{3\pi}{2}) + \sum m(V_1, V_2^{'}, \omega L, \phi_k, D_1^{new}, D_2^{new}) * \Delta\theta\phi_k \quad (9.8)$$

$$\phi_k = \frac{V_{dc1}\phi_{new} + V_{dc2}^{'}\phi_{old}}{V_{dc1} + V_{dc2}^{'}} \quad (9.9)$$

The experimental waveforms for two phase shift method combined with phase shift and duty cycle changes are shown in figures 9.17 & 9.18. In the figures, it can be observed that the winding current settles within one switching cycle. The control action is implemented in such a way that when the external command comes(represented by the signal CS), the controller takes one cycle to calculate the transition phase shift angle and it updates the phase angles at $\omega t = \frac{3\pi}{2}$.

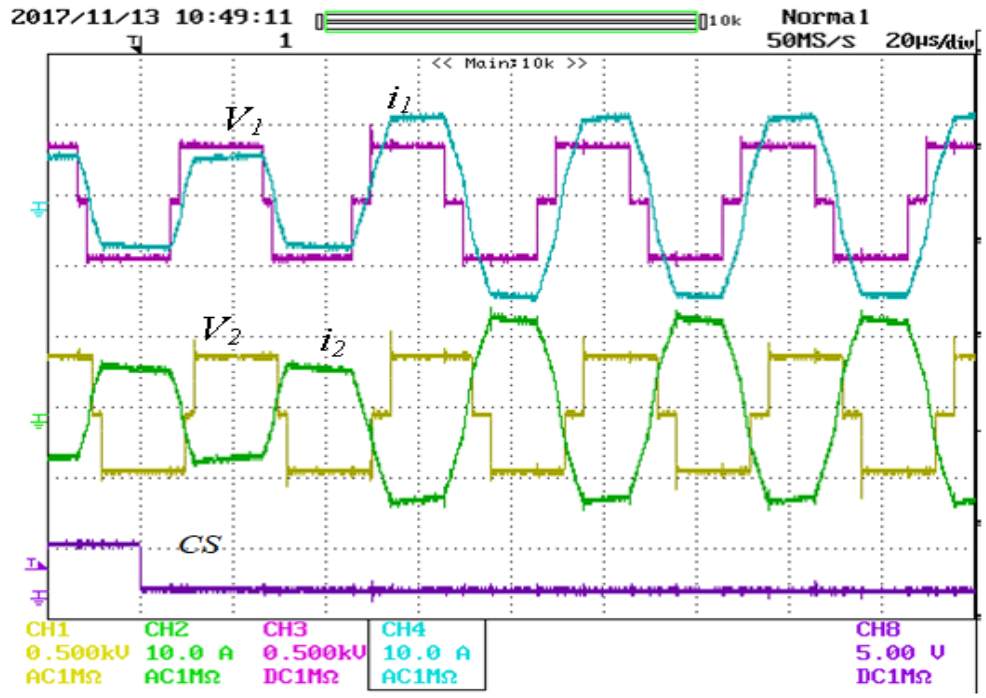

Figure 9.17. Transients for combined Phase Shift & Duty Cycle Change.

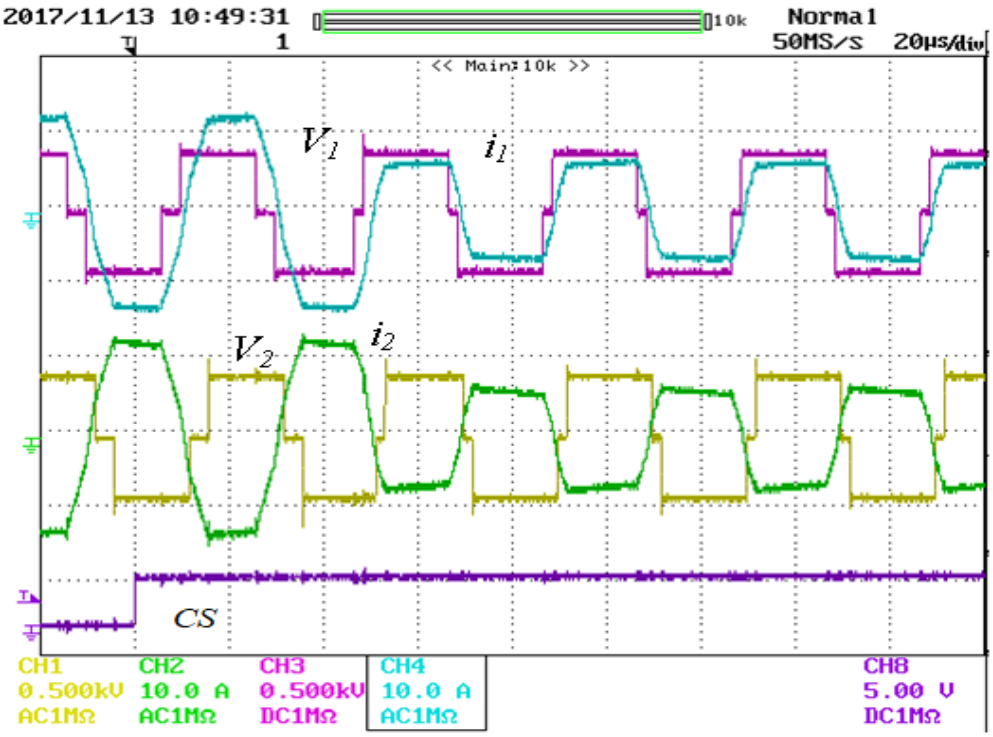

Figure 9.18. Transients for combined Phase Shift & Duty Cycle Change.

9.1.3. Two Phase Shift Method for Power Reversals of DAB Converter

The two-phase shift method is also applied for power direction reversal of Dual Active Bridge(DAB) converter. The two phase shift method, given by equations (9.4) and (9.5) when applied to a phase shift direction reversal, creates a dc shift in transformer winding currents as shown in figure 9.19. In order to avoid the transients during power reversals, an intermediate half switching cycle of zero power is created. When the phase shift angle changes from ϕ_{old} to $-\phi_{new}$ by making the positive half cycle phase shift as $\phi_k = 0.5\phi_{old}$ and by making the negative half cycle phase shift as $-0.5\phi_{new}$. Figures 9.20 and 9.21 show the two cases of power reversal, where power flow is changing from primary to secondary and vice versa. In figures 9.20 and 9.21, a small current flows in the transformer windings during the zero half cycle power, which is due to the magnetizing inductance of the windings.

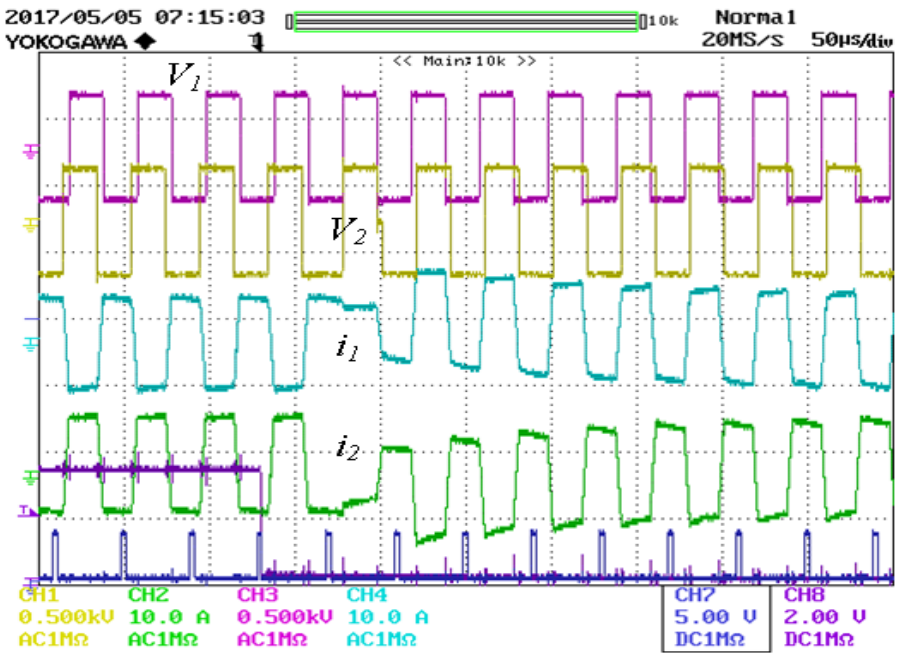

Figure 9.19. Transients During Power Reversal Under Normal Phase Direction Change.

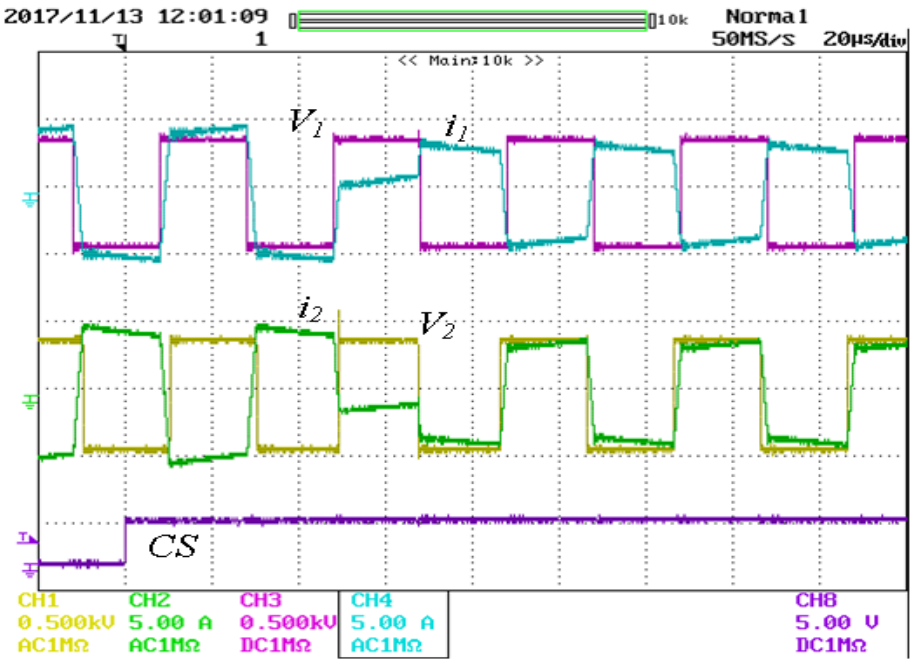

Figure 9.20. Transients During Modified Power Reversal Method.

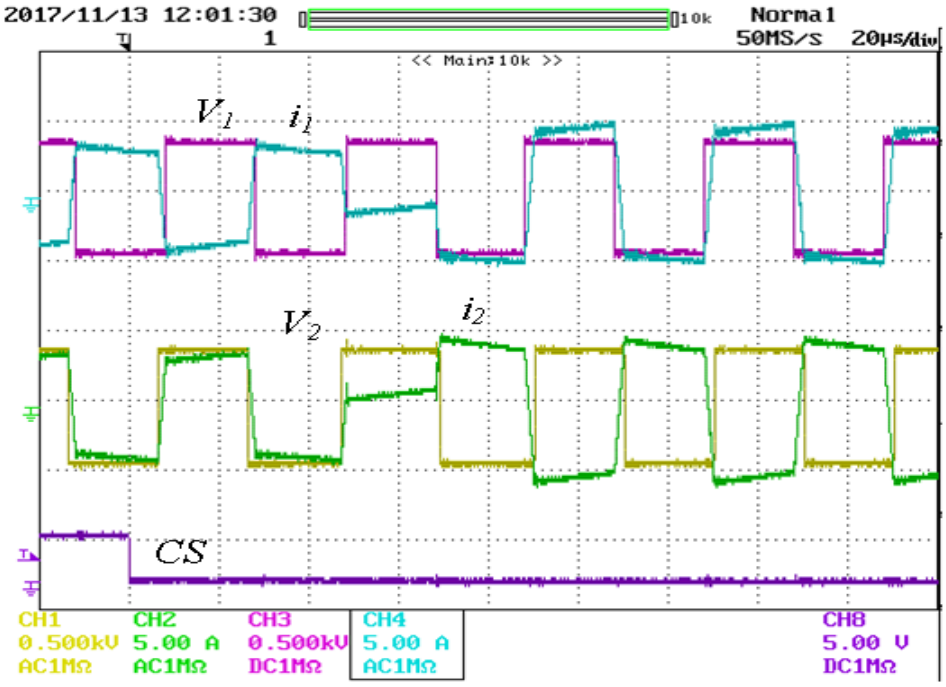

Figure 9.21. Transients During Modified Power Reversal Method.

9.2. Two Phase Shift Method for Triple Active Bridge(TAB) Converter

9.2.1. Two Phase Shift Method with Square Wave Voltages

The proposed two phase shift method has been extended to three port Triple Active Bridge(TAB) converter in this section. The approach for two phase shift method is similar to that implemented in previous section. The two phase shift method for three port TAB converter to eliminate dc transients from transformer winding currents is explained in figure 9.22.

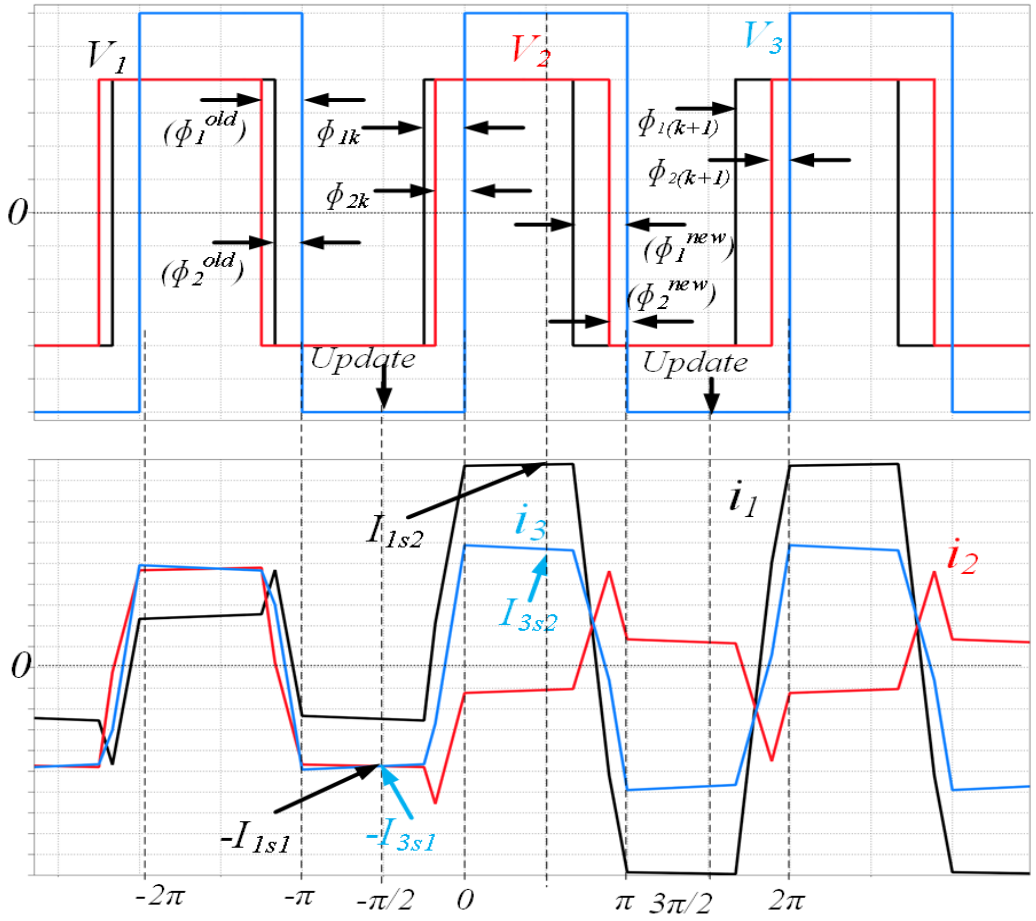

Figure 9.22. Two Phase Shift Method for TAB Converter.

The square wave winding voltage V_3 is taken as reference and the other two voltages V_1 and V_2 are phase shifted by ϕ_1 and ϕ_2 w.r.t V_3. The two phase shift method for eliminating dc

transient is explained in figure 9.22. The winding voltages V_1 and V_2 have phase angles ϕ_1 and ϕ_2 respectively w.r.t V_3. A typical winding voltage position for Triple Active Bridge(TAB) converter is shown in figure 9.22. The update of intermediate phase angle ϕ_k is done at $\omega t = \frac{3\pi}{2}$, i.e. at midpoint of V_3 during negative half cycle. The currents $-I_{1s1}$ and $-I_{3s1}$ are the steady state current values at instant $\omega t = \frac{3\pi}{2}$ for phase angles ϕ_1^{old} and ϕ_2^{old}. The currents I_{1s2} and I_{3s2} are the steady state current values at instant $\omega t = \frac{\pi}{2}$ for phase angles ϕ_1^{new} and ϕ_2^{new}. The currents $-I_{1s1}$, $-I_{3s1}$, I_{1s2}, I_{3s2} are related to each other as functions of current slopes & phase angles, as given in equations (9.10)-(9.11), where m_1^1, m_2^1, m_3^1 and m_1^3, m_2^3, m_3^3 are the slopes of winding currents during different intervals.

$$I_{1s2} = -I_{1s1} + m_1^1(\pi - \phi_{1k}) + m_2^1(\phi_{2k} - \phi_{1k}) + m_3^1(\phi_{2k}) \quad (9.10)$$

$$I_{3s2} = -I_{3s1} + m_1^3(\pi - \phi_{1k}) + m_2^3(\phi_{2k} - \phi_{1k}) + m_3^3(\phi_{2k}) \quad (9.11)$$

The current expressions $-I_{1s1}$, $-I_{3s1}$, I_{1s2}, I_{3s2} are expressed in terms of ϕ_1^{old}, ϕ_2^{old}, ϕ_1^{new}, ϕ_2^{new} in equations (9.12)-(9.15).

$$-I_{1s1} = 0.5\{-m_1^1(\pi - \phi_1^{old}) - m_2^1(\phi_2^{old} - \phi_1^{old}) - m_3^1(\phi_2^{old})\} \quad (9.12)$$

$$-I_{3s1} = 0.5\{-m_1^3(\pi - \phi_1^{old}) - m_2^3(\phi_2^{old} - \phi_1^{old}) - m_3^3(\phi_2^{old})\} \quad (9.13)$$

$$I_{1s2} = 0.5\{m_1^1(\pi - \phi_1^{new}) + m_2^1(\phi_2^{new} - \phi_1^{new}) + m_3^1(\phi_2^{new})\} \quad (9.14)$$

$$I_{3s2} = 0.5\{m_1^3(\pi - \phi_1^{new}) + m_2^3(\phi_2^{new} - \phi_1^{new}) + m_3^3(\phi_2^{new})\} \quad (9.15)$$

Using expressions (9.12)-(9.15) in equations (9.10),(9.11) and solving for ϕ_{1k} & ϕ_{2k}, the derived expressions are given in (9.16),(9.17). The phase shift angles used for negative half cycle are ϕ_1^{new} and ϕ_2^{new} respectively.

$$\phi_{1k} = 0.5(\phi_1^{old} + \phi_1^{new}) \quad (9.16) \qquad \phi_{2k} = 0.5(\phi_2^{old} + \phi_2^{new}) \quad (9.17)$$

The experimental study on the three port phase shifted converter control is performed using a 400V/400V/600V three port TAB converter. In this experimental study, the phase angles are changed from ϕ_1^{old}, ϕ_2^{old} to ϕ_1^{new}, ϕ_2^{new}. The angle values are chosen such that the power flowing into port 3 remains constant whereas the power flowing out of port 1 and 2 changes. Figures 9.23 and 9.24 show the TAB converter waveforms using two phase shift method control.

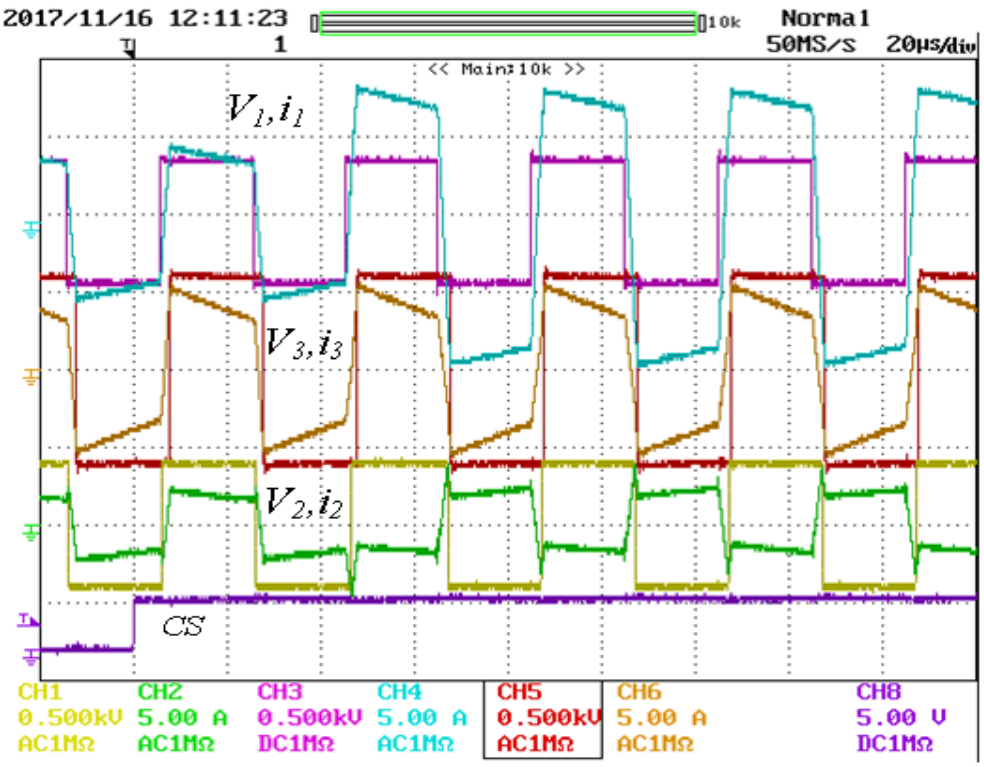

Figure 9.23. Two Phase Shift Method in TAB Converter.

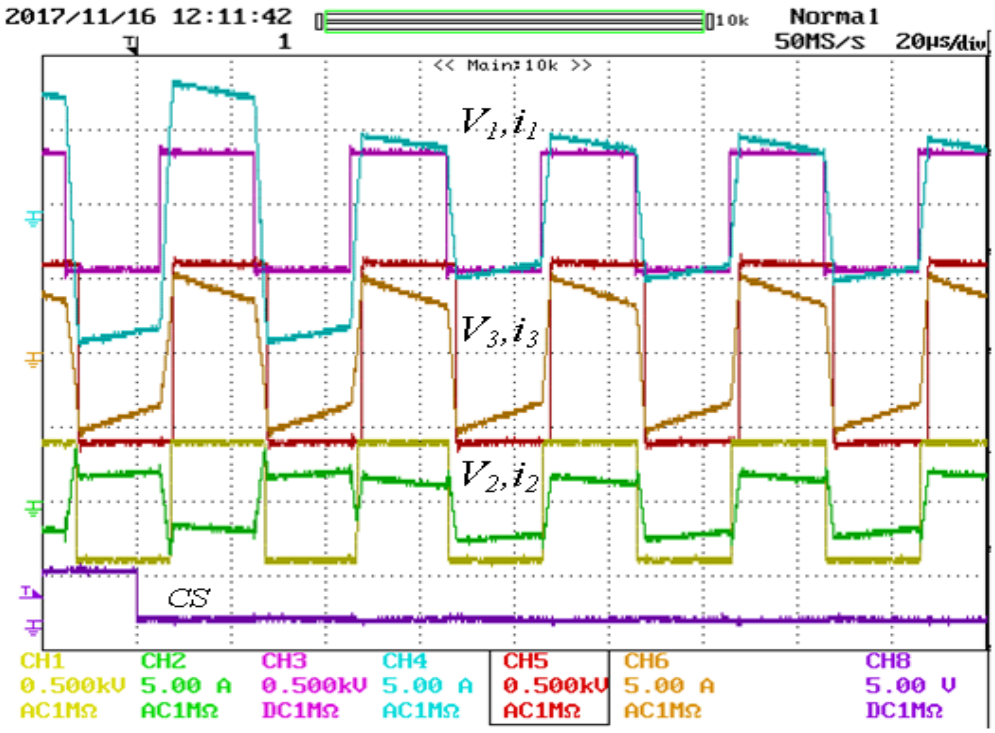

Figure 9.24. Two Phase Shift Method in TAB Converter.

It can be observed in figures 18 and 19 that the shape of current i_3 remains same before and after change of operating point, which is initiated by CS command. This indicates that the power flowing out of ports 1 and 2, change only in these cases while power flow of port 3 remains unchanged. In figure 9.23, as current i_1 increases, current i_2 changes direction to absorb extra power required to maintain constant power flowing into port 3. Similarly in figure 9.24, as current i_1 decreases, current i_2 changes direction to deliver extra power required for port 3.

9.2.2. Two Phase Shift Method with Quasi-Square Wave Voltages

The two phase shift method is implemented for quasi square wave voltages as well for three port phase shifted TAB converter. The implementation method is similar to that for DAB converter discussed before. In this case, there are five control parameters, ($D_1, D_2, D_3, \phi_1, \phi_2$). For

ease of implementation, only ϕ_1 and ϕ_2 are considered as control parameters. The values for duty cycles D_1, D_2, D_3 are updated with new values instantly. As an external command comes for changing from an old operating point of ($\phi_1^{old}, \phi_2^{old}, D_1^{old}, D_2^{old}, D_3^{old}$) to a new operating point of ($\phi_1^{new}, \phi_2^{new}, D_1^{new}, D_2^{new}, D_3^{new}$), the controller takes one cycle to calculate the new values of ϕ_{1k}, ϕ_{2k} for the positive half cycle and $\phi_1^{new}, \phi_2^{new}$ for negative half cycle phase angles and updates the new values at $\omega t = \frac{3\pi}{2}$. The expressions for ϕ_{1k}, ϕ_{2k} are same as given in equations (9.16),(9.17). Figures 9.25 and 9.26 show the experimental cases for two phase shift control implemented in TAB converter for quasi-square wave voltage waveforms, where controller commands a change from an old operating point of ($\phi_1^{old}, \phi_2^{old}, D_1^{old}, D_2^{old}, D_3^{old}$) to a new set of values ($\phi_1^{new}, \phi_2^{new}, D_1^{new}, D_2^{new}, D_3^{new}$). It can be observed that the winding currents change within one half cycle to their new steady state operating points to maintain the required power flow in both the cases.

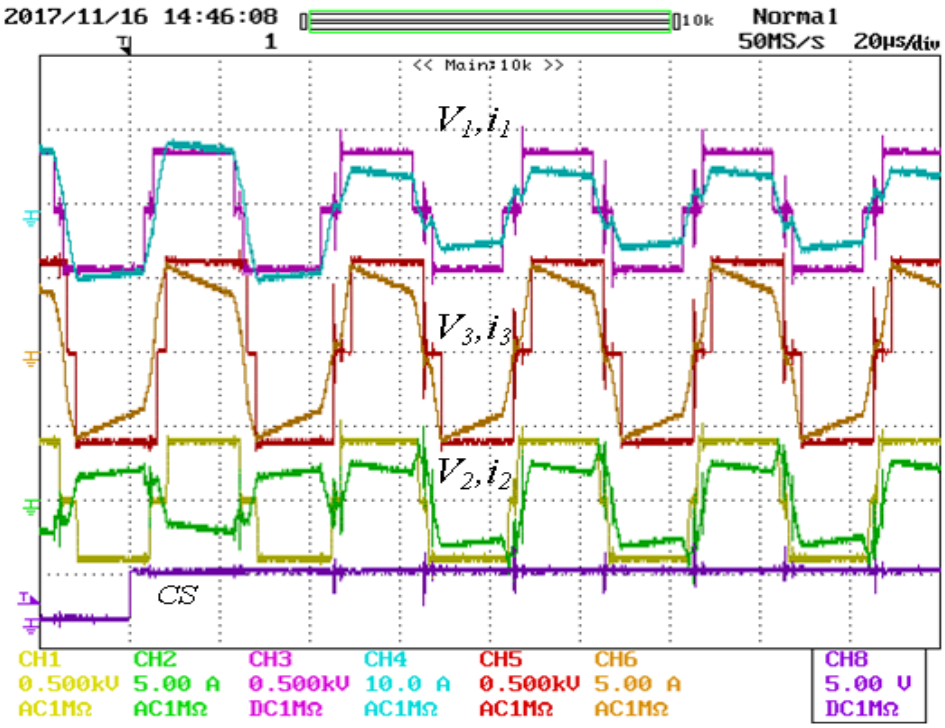

Figure 9.25. Two Phase Shift Method with Duty Cycle Change in TAB Converter.

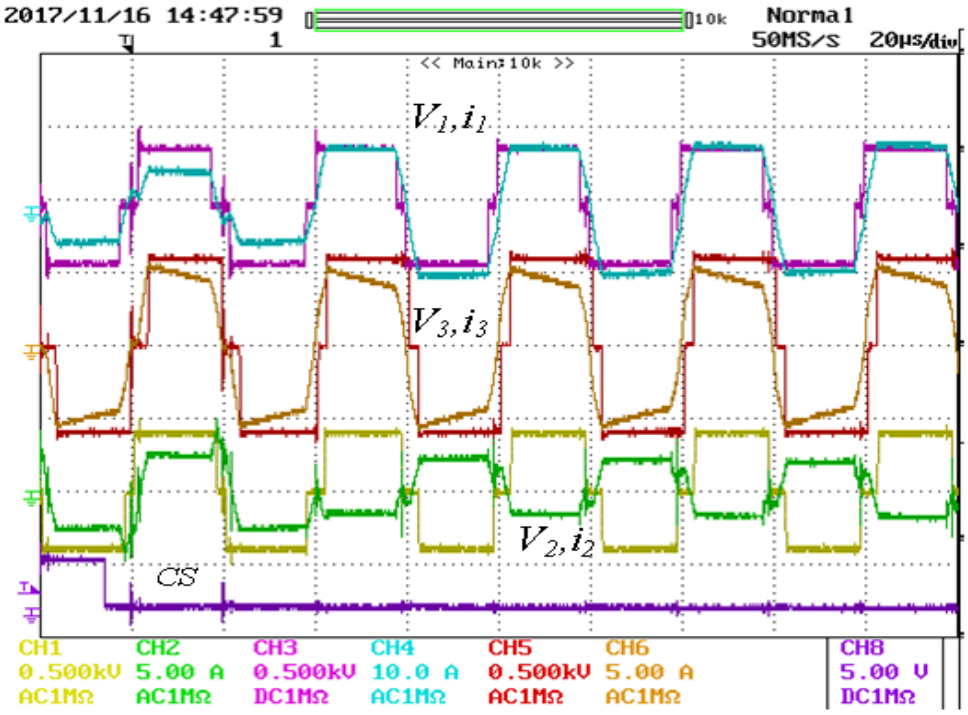

Figure 9.26. Two Phase Shift Method with Duty Cycle Change in TAB Converter.

9.2.3. Operating Mode Change for Three Port TAB Converter

One of the most important aspects of three port converter is to operate the converter while one port being idle. Smooth transition from three port operating mode to two port operating mode and vice versa, is an important feature for three port converter. In this section, the transition between two modes is achieved by using the concept of two phase shift method. In this paper, only port 1 is considered to switch ON & OFF depending on external commands. During two mode operation, port 2 is considered to supply the whole power requirement for port 3, therefore the required phase angle ϕ_{new} is considered the steady state phase angle for port 2. During three port active operation, when the external signal CS for mode change comes, the gate pulses for port 1 are turned off at $\omega t = \frac{3\pi}{2}$ and for the next switching cycle, ϕ_{2k} for positive half cycle is made equal to $0.5\phi_2^{new}$ and for negative half cycle phase angle ϕ_2^{new} is used. In figure 9.27, it can be observed that when signal CS goes high, port 1 gate pulses are turned off by the PWM generator, current i_1 decays to zero, and phase shift angle ϕ_2 is updated to new values for positive half cycle and negative half cycle. A small duration of voltage bump is seen in V_1 during current decaying of i_1. Current i_2 changes to new steady state operating value within one half switching cycle and port 3 power is kept unchanged. Similarly, for transition from two port to three port operation, when the external signal CS goes low, for the next switching cycle 'k', ϕ_{2k} is made equal to $0.5\phi_{2ss}$ (where ϕ_{2ss} is the steady state value of two port operating mode), and during negative half cycle all phase shift angles are made zero. In the next $(k+1)^{th}$ cycle, the

steady state values for ϕ_1, ϕ_2 are updated according to equations (9.15),(9.16) where $\phi_1^{old}, \phi_2^{old}$ are equal to zeros and $\phi_1^{new}, \phi_2^{new}$ are equal to the new steady state values.

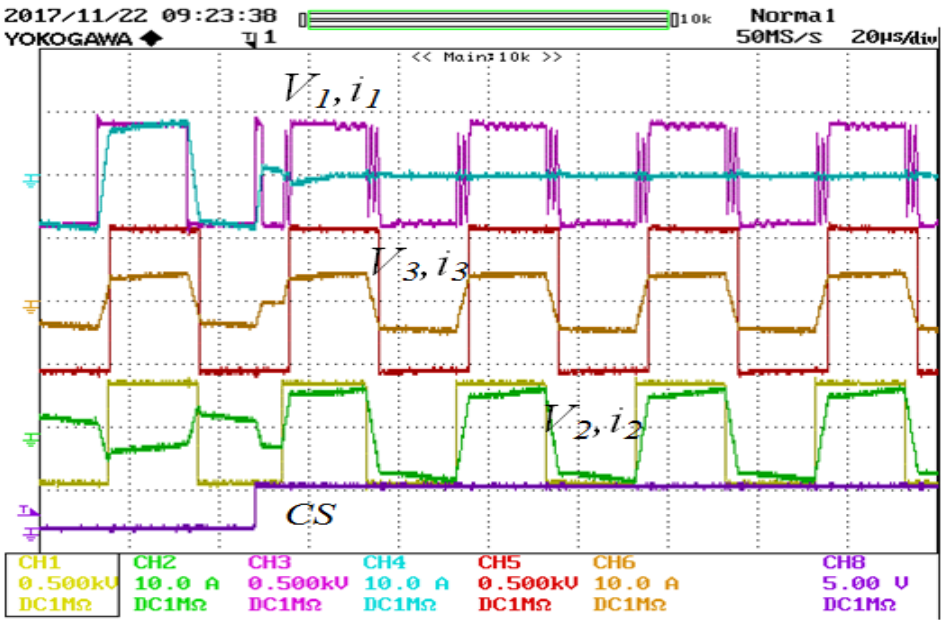

Figure 9.27. Three Port to Two Port Mode Change.

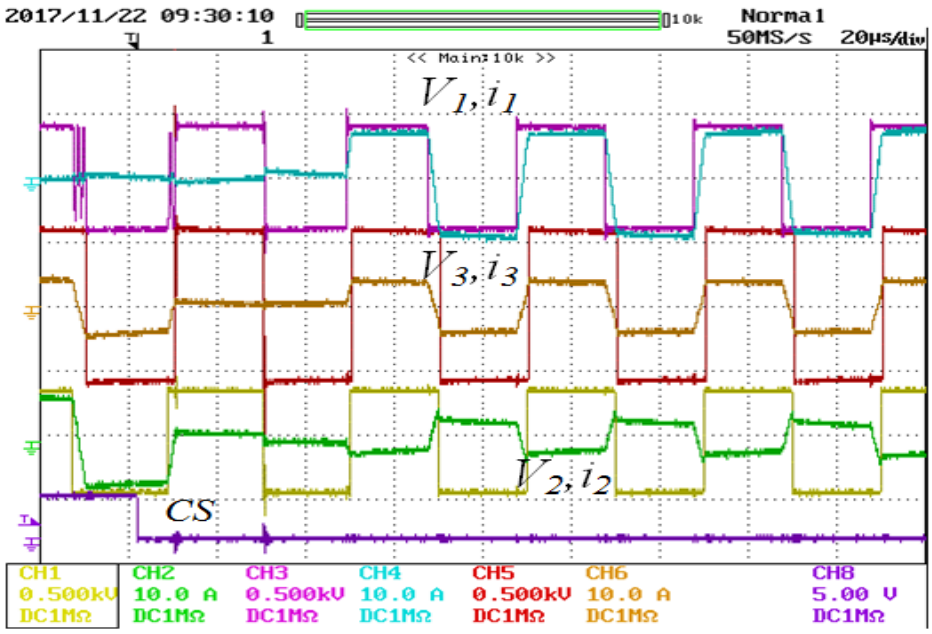

Figure 9.28. Two Port to Three Port Mode Change.

9.3. Conclusion

The two phase shift method proposed here in the paper for phase shifted dc-dc converters, has controlled the transformer currents within one switching cycle during any change in operating phase angle of the transformer. The proposed technique has provided considerably satisfactory results for two port Dual Active Bridge(DAB) converter and three port Triple Active Bridge(TAB) converter. The two phase shift technique also successfully operates for power flow direction reversal cases and three port to two port mode change cases. The two phase shift method also has the advantage of being independent of transformer leakage inductances and does not require any current sensor. Only requirements are dc voltage sensing for dc buses and information of transformer turns ratio. The proposed two phase shift method provides satisfactory, stable and robust performance for phase shifted dc-dc converters.

Chapter 10. Conclusions & Future Work

10.1. Conclusions

The work presented in this dissertation addresses three port phase shifted dc-dc converter with different transformer topologies, their shortcomings, advantages, properties etc. The focus of the research is to understand the operation of isolated three port phase shifted dc-dc converter for Renewable Energy Source(RES) and Energy Storage(ES) integration using high frequency transformer, along with suitable transformer topologies & their converter control. The dissertation also addresses key control techniques for high frequency transformer current control with dc power decoupling. The proposed power decoupling provides independent control for dc power at any two ports, which is utilized for series connection of dc-dc converter outputs. The key challenges for three port phase-shifted dc-dc converter has been the high frequency transformer, as the leakage inductance of the transformer is key element for power transfer. The leakage modelling of three winding transformer has been developed for having a closely accurate model of leakage inductances. The leakage inductance models are thus incorporated into transformer design so that optimum design of transformer for a specific power rating can be achieved. The tape wound core transformer designs along with their challenges due to leakage flux has been investigated and possible solutions has been proposed in this thesis work.

10.2. Scope for Future Research

The future scope for this research provides a whole lot of possible directions.

- The DC-DC three port converter architecture can be extended to develop a DC-AC converter architecture with transformer isolation in a single stage. The DC-AC

converter module can be used as a modular converter unit for Cascaded H-Bridge(CHB) converter.

- Moreover, the two port leakage integrated transformer of chapter 7 can be extended to a three port converter prototype for three port converter application. The design process can be optimized using several optimization techniques.
- The series connected converter system can be grid-tied to an utility grid and due to interaction of two converters, several converter stability related problems can be addressed.

BIBLIOGRAPHY

[1] ABB megawatt station PVS800-MWS 1 to 1.25 MW, *ABB Inc*.

[2] ABB megawatt station PVS800-MWS 1 to 2.4 MW, *ABB Inc*.

[3] Solar inverters SINVERT – Siemens, *w3.siemens.com*.

[4] LV5 Series Solar Central Inverters, GE Energy Connections.

[5] SINVERT 60 M – SINVERT 1700 M, Three-phase inverters for grid-connected photovoltaic systems. SINVERT PV Inverter, Siemens.

[6] Central Inverters, www.sma-america.com/products/solarinverters.html.

[7] Conext Core XC series central inverters, Schneider Electric.

[8] PVS800-57B_central_inverters, ABB.

[9] PVS800_central_inverters, ABB.

[10] SMA Utility Power Systems, SMA.

[11] ENERGY STAR Market and Industry Scooping Report Medium Voltage Distribution Transformers February 2014.

[12] Dry-Type Medium Voltage Distribution (Power) Transformer, 1.2 kV to 46 kV Class, 500kVA to 34 MVA, Hammond Power Solutions.

[13] Grid Connected Photovoltaic Central Inverter, SanRex.

[14] C. Rahmann, V. Vittal, J. Ascui, J. Haas, "Mitigation Control Against Partial Shading Effects in Large-Scale PV Power Plants," *IEEE Trans. Sustainable. Energy.*, vol. 7, Issue. 1, Year 2016. pp. 173-180.

[15] B. Crciun, T. Kerekes, D. Sera, R. Teodorescu, "Frequency Support Functions in Large PV Power Plants With Active Power Reserves," *IEEE Journal of Emerging and Selected Topics in Power Electronics,* vol.2, Issue. 4, Year 2014. pp. 849-858.

[16] M. Shawky El Moursi, W. Xiao, J. L. Kirtley, "Fault ride through capability for grid interfacing large scale PV power plants," *IET Generation, Transmission & Distribution,* vol. 7, Issue. 9, Year. 2013, pp.1027-1036.

[17] L. Liu, H. Li, Y. Xue, W. Liu, "Decoupled Active and Reactive Power Control for Large-Scale Grid-Connected Photovoltaic Systems Using Cascaded Modular Multilevel Converters," *IEEE Trans. Power. Elect.*, vol. 30, Issue. 1, Year 2015. pp. 176-187.

[18] C. D. Townsend, Y. Yu, G. Konstantinou, V. G. Agelidis, "Cascaded H-Bridge Multilevel PV Topology for Alleviation of Per-Phase Power Imbalances and Reduction of Second

Harmonic Voltage Ripple," *IEEE Trans. Power. Elect.*, vol. 31, Issue. 8, Year 2016. pp. 5574-5586.

[19] B. Xiao, L. Hang, J. Mei, C. Riley, L. M. Tolbert, B. Ozpineci, "Modular Cascaded H-Bridge Multilevel PV Inverter With Distributed MPPT for Grid-Connected Applications," *IEEE Trans. Ind. Elect.*, vol. 51, Issue. 2, Year 2015. pp. 1722-1731.

[20] X. Guo, X. Jia, "Hardware-Based Cascaded Topology and Modulation Strategy With Leakage Current Reduction for Transformerless PV Systems," *IEEE Trans. Ind. Elect.*, vol. 63, Issue. 12, Year 2016. pp. 7823-7832.

[21] G. Farivar, B. Hredzak, V. G. Agelidis, "A DC-Side Sensorless Cascaded H-Bridge Multilevel Converter-Based Photovoltaic System," *IEEE Trans. Ind. Elect.*, vol. 63, Issue. 7, Year 2016. pp. 4233-4241.

[22] F. Wu, X. Li, F. Feng, H. B. Gooi, "Modified Cascaded Multilevel Grid-Connected Inverter to Enhance European Efficiency and Several Extended Topologies," *IEEE Trans. Ind. Informatics.*, vol. 11, Issue. 6, Year 2016. pp. 1358-1365.

[23] Yifan Yu; Georgios Konstantinou; Branislav Hredzak; Vassilios G. Agelidis, "Operation of Cascaded H-Bridge Multilevel Converters for Large-Scale Photovoltaic Power Plants Under Bridge Failures," *IEEE Trans. Ind. Elect.*, vol. 62, Issue. 11, Year 2015. pp. 7228-7236.

[24] H. Nademi, A. Das, R. Burgos, L. E. Norum, "A New Circuit Performance of Modular Multilevel Inverter Suitable for Photovoltaic Conversion Plants," *IEEE Journal of Emerging and Selected Topics in Power Electronics*, vol. 4, Issue. 2, Year 2016. pp. 393-404.Alexander, M. Thathan, "Modelling and analysis of modular multilevel converter for solar photovoltaic applications to improve power quality," *IET Renewable Power Generation*, vol. 9, Issue. 1, Year 2015. pp. 78-88.

[25] J. Mei, B. Xiao, K. Shen, L. M. Tolbert, J. Y. Zheng, "Modular Multilevel Inverter with New Modulation Method and Its Application to Photovoltaic Grid-Connected Generator," *IEEE Trans. Power. Elect.*, vol. 62, Issue. 11, Year 2015. pp. 7228-7236.

[26] Y. Wang, X. Lin, Y. Kim, N. Chang, M. Pedram, "Architecture and Control Algorithms for Combating Partial Shading in Photovoltaic Systems," *IEEE Tran. Computer-Aided Design of Integrated Circuits and Systems*, vol. 33, Issue. 6, Year. 2014. pp. 917-930.

[27] N. Agarwal, A. Arya, M. W. Ahmad, S. Anand, “Lifetime Monitoring of Electrolytic Capacitor to Maximize Earnings From Grid-Feeding PV System,” *IEEE Trans. Ind. Elect.*, vol. 63, Issue. 11, Year 2016. pp. 7049-7058.

[28] C. D. Townsend, Y. Yu, G. Konstantinou, V. G. Agelidis, “Cascaded H-Bridge Multilevel PV Topology for Alleviation of Per-Phase Power Imbalances and Reduction of Second Harmonic Voltage Ripple,” *IEEE Trans. Power. Elect.*, vol. 31, Issue. 8, Year 2016. pp. 5574-5586.

[29] K. Kroics, J. Zakis, A. Suzdalenko, G. Gaigals, “A simplified approach to input voltage balancing for series connected isolated DC-DC converters,” *2016 18th European Conference on Power Electronics and Applications (EPE'16), 2016,* pp.1-10.

[30] Y. Lian, G. P. Adam, D. Holliday, S. J. Finney, “Active power sharing in input-series-input-parallel output-series connected DC/DC converters,” *2015 IEEE Applied Power Electronics Conference and Exposition (APEC),* pp. 2790-2797.

[31] Y. Lian, D. Holliday, S. J. Finney, “Dual-active bridge converter with input-series-input-parallel output-series connection,” *8th IET International Conference on Power Electronics, Machines and Drives (PEMD 2016),* pp. 1-6.

[32] R. Giri, V. Choudhary, R. Ayyanar, N. Mohan, “Common-duty-ratio control of input-series connected modular DC-DC converters with active input voltage and load-current sharing,” *IEEE Trans. Ind. Elect.*, vol. 42, Issue. 4, Year 2006. pp. 1101-1111.

[33] R. Ayyanar, R. Giri, N. Mohan, “Active input-voltage and load-current sharing in input-series and output-parallel connected modular DC-DC converters using dynamic input-voltage reference scheme,” *IEEE Trans. Ind. Elect.*, vol. 19, Issue. 6, Year 2004. pp. 1462-1473.

[34] J. W. Kimball, J. T. Mossoba, P. T. Krein, “Control Technique for Series Input-Parallel Output Converter Topologies,” *2005 IEEE 36th Power Electronics Specialists Conference,* pp. 1441-1445.

[35] H. Ertl, T. Wiesinger, J. W. Kolar, “Active voltage balancing of DC-link electrolytic capacitors,” *IET Power Electronics,* 2008, vol. 1. Issue. 4., pp.488-496.

[36] H. Choi, M. Ciobotaru, V. G. Agelidis, “Large-scale PV systems with energy storage utilizing high-gain DC/DC converters,” *2014 IEEE International Conference on Industrial Technology (ICIT),* 2014, pp. 484-490.

[37] Antonios Marinopoulos, Panagiotis Bakas, “Techno-economic evaluation of alternative configurations for very large scale PV power systems including energy storage,” *2014 Ninth International Conference on Ecological Vehicles and Renewable Energies (EVER),* 2014, pp. 1-7.

[38] D. I. Doukas, K. Papastergiou, P. Bakas, A. Marinopoulos, “Energy storage sizing for large scale PV power plants base-load operation - comparative study & results,” *38th IEEE Photovoltaic Specialists Conference*, 2012, pp. 570-574.

[39] A. Azidehak, R. Chattopadhyay, S. Acharya, A. K. Tripathi, M. G. Kashani, G. Chavan, S. Bhattacharya, “Control of modular dual active bridge DC/DC converter for photovoltaic integration,” *IEEE Energy Conversion Congress and Exposition (ECCE),* 2015, pp.3400-3406.

[40] K. Hatua, S. Dutta, A. Tripathi, S. Baek, G. Karimi, S. Bhattacharya, “Transformer less Intelligent Power Substation design with 15kV SiC IGBT for grid interconnection,” *IEEE Energy Conversion Congress and Exposition (ECCE), 2011,* pp. 4225 – 4232.

[41] D. Rothmund, G. Ortiz, Th. Guillod, J. W. Kolar, “10kV SiC-based isolated DC-DC converter for medium voltage-connected Solid-State Transformers,” *2015 IEEE Applied Power Electronics Conference and Exposition (APEC),* 2015, pp. 1096-1103.

[42] S. Madhusoodhanan, A. Tripathi, K. Mainali, A. Kadavelugu, D. Patel, “Three-phase 4.16 kV medium voltage grid tied AC-DC converter based on 15 kV/40 a SiC IGBTs,” *IEEE Energy Conversion Congress and Exposition (ECCE),* 2015, pp. 6675 - 6682.

[43] S. Hazra, A. De, L. Cheng, J. Palmour, M. Schupbach, B. Hull, S. Allen, S. Bhattacharya, “High Switching Performance of 1700V, 50A SiC Power MOSFET over Si IGBT/BiMOSFET for Advanced Power Conversion Applications,” *IEEE Trans. Power Elec.*, vol. 31, Issue. 16, pp. 4742-4754, Year. 2016.

[44] G. Wang, F. Wang, G. Magai, Y. Lei, A. Huang, M. Das, “Performance comparison of 1200V 100A SiC MOSFET and 1200V 100A silicon IGBT,” *2013 IEEE Energy Conversion Congress and Exposition,* 2013, pp. 3230-3234.

[45] A. Bolotnikov, P. Losee, K. Matocha, J. Glaser, J. Nasadoski, L. Wang, A. Elasser, S. Arthur, Z. Stum, P. Sandvik, Y. Sui, T. Johnson, J. Sabate, L. Stevanovic, “3.3kV SiC MOSFETs designed for low on-resistance and fast switching,” *24th International Symposium on Power Semiconductor Devices and ICs*, 2012, pp. 389-392.

[46] S. Madhusoodhanan, K. Hatua, S. Bhattacharya, S. Leslie, Sei-Hyung Ryu, M. Das, A. Agarwal, D. Grider, "Comparison study of 12kV n-type SiC IGBT with 10kV SiC MOSFET and 6.5kV Si IGBT based on 3L-NPC VSC applications," *IEEE Energy Conversion Congress and Exposition (ECCE),* 2012, pp. 310-317.

[47] H. Tao, A. Kotsopoulos, J. L. Duarte, M. A. M. Hendrix, "Family of multiport bidirectional DC-DC converters," *IEE Proceedings - Electric Power Applications,* 2006, vol. 153, Issue. 3, pp. 451-458.

[48] L. Solero, A. Lidozzi, J. A. Pomilio, "Design of multiple-input power converter for hybrid vehicles," *IEEE Tran. Power Elect.,* vol. 20, Issue. 5, Year. 2005, pp. 1007-1016.

[49] L. Solero, F. Caricchi, F. Crescimbini, O. Honorati, F. Mezzetti, "Performance of a 10 kW power electronic interface for combined wind/PV isolated generating systems," *proc. IEEE Power Electronics Specialists Conf. (PESC),* June 1996, pp. 1027–1032.

[50] A. Di Napoli, F. Crescimbini, S. Rodo, L. Solero, "Multiple input dc-dc power converter for fuel-cell powered hybrid vehicles," *proc. IEEE Power Electronics Specialists Conf. (PESC),* 2002, Vol. 4, pp. 1685–1690.

[51] B.G. Dobbs, P.L. Chapman, "A multiple-input dc-dc converter," *IEEE Power Electron. Lett., 2003,* vol. 1, Issue. 1, pp. 6–9.

[52] Y.M. Chen, Y.C. Liu, F.Y.Wu, "Multi-input dc/dc converter based on the multiwinding transformer for renewable energy applications," *IEEE Trans. Ind. Appl.,* 2002, 38, (4), pp. 1096–1104.

[53] H. Tao, A. Kotsopoulos, J.L. Duarte, M.A.M. Hendrix, "A soft-switched three-port bidirectional converter for fuel cell and supercapacitor applications," *proc. IEEE Power Electronics Specialists Conf. (PESC),* Recife, Brazil, June 2005, pp. 2487–2493.

[54] M. Michon, J.L. Duarte, M. Hendrix, M.G. Simoes, "A threeport bi-directional converter for hybrid fuel cell systems," *proc. IEEE Power Electronics Specialists Conf. (PESC),* Aachen, Germany, June 2004, pp. 4736–4742.

[55] D. Gunasekaran, L. Umanand, "Integrated magnetics based multi-port bidirectional DC-DC converter topology for discontinuous-mode operation," *Power Elect., IET, 2012,* vol. 5, Issue 7, 2012, pp. 935- 944.

[56] C. Zhao, S. D. Round, J. W. Kolar, “An Isolated Three-Port Bidirectional DC-DC Converter With Decoupled Power Flow Management,” *IEEE Tran. Power Elect.,* vol. 23, Issue. 5, Year. 2008, pp. 2443-2453.

[57] Wenjie Chen, Xu Yang, Weiping Zhang, Xiaomei Song, “Leakage Current Calculation for PV Inverter System Based on a Parasitic Capacitor Model,” *IEEE Tran. Power Elect.,* vol. 31, Issue. 12, Year. 2016, pp. 8205-8217.

[58] Lin Ma, T. Kerekes. R. Tedorescu, F. Tang, X. Jin, Y. Tong, J. Liang, “Leakage current analysis of single-phase transformer-less grid-connected PV inverters,” *41st Annual Conference of the IEEE Industrial Electronics Society(IECON),* 2015, pp. 887-892.

[59] A. Tripathi, S. Madhusoodhanan, K. Mainali, A. Kadavelugu, D. Patel, S. Bhattacharya, K. Hatua, “Grid connected CM noise considerations of a three-phase multi-stage SST,” *9th International Conference on Power Electronics and ECCE Asia (ICPE-ECCE Asia),* 2015, pp. 793 - 800.

[60] M. H. Kheraluwala, A. R. Schnore, R. L. Steigerwald, “Performance characterization of a high power factor power supply with a single power stage,” *Conference Record of the 1992 IEEE Industry Applications Society Annual Meeting,* 1992, vol.1. pp.659-665.

[61] J. Everts, F. Krismer, J. V. den Keybus, J. Driesen, J. W. Kolar, “Optimal ZVS Modulation of Single-Phase Single-Stage Bidirectional DAB AC–DC Converters,” *IEEE Transactions on Power Electronics,* 2014, Vol. 29, Issue. 8, pp. 3954 – 3970.

[62] F. Krismer, J. W. Kolar, “Closed Form Solution for Minimum Conduction Loss Modulation of DAB Converters,” *IEEE Transactions on Power Electronics,* 2012, Vol. 27, Issue. 1, pp. 174 – 188.

[63] M. Kaymak, Z. Shen, Rik W. De Doncker, “Comparison of analytical methods for calculating the AC resistance and leakage inductance of medium-frequency transformers,” *2016 IEEE 17th Workshop on Control and Modeling for Power Electronics (COMPEL),* 2016, pp. 1-8.

[64] M. Lambert, F. Sirois, M. Martinez-Duro, J. Mahseredjian, “Analytical Calculation of Leakage Inductance for Low-Frequency Transformer Modeling,” *IEEE Tran. Power Delivery,* vol. 28, Issue. 1, Year. 2013, pp. 507-515

[65] R. Doebbelin, M. Benecke, A. Lindemann, “Calculation of leakage inductance of core-type transformers for power electronic circuits,” *13th International Power Electronics and Motion Control Conference,* 2008, pp. 1280-1286.

[66] Roters, H. C., “Electromagnetic Devices”, 1st ed. John Wiley & Sons, New York, 1941.

[67] M.A. Juds, “Notes on Electromagnetics,” Eaton Corporation, Corporate Research & Technology.

[68] Francisco de Leon, Juan A. Martinez, “Dual Three-Winding Transformer Equivalent Circuit Matching Leakage Measurements,” *IEEE Trans. on Power Delivery,* 2009, vol. 24, Issue. 1, pp. 160-168.

[69] Bernardo Cougo, Johann W. Kolar, “Integration of Leakage Inductance in Tape Wound Core Transformers for Dual Active Bridge Converters”, *7th International Conference on Integrated Power Electronics Systems (CIPS),* 2012, pp. 1 – 6.

[70] G. Wang, A.Q. Huang, Chushan Li, “ZVS range extension of 10A 15kV SiC MOSFET based 20kW Dual Active Half Bridge (DHB) DC-DC converter,” *2012 IEEE Energy Conversion Congress and Exposition (ECCE),* pp. 1533-1539.

[71] Jun Huang, Yue Wang, Zhuoqiang Li, Wanjun Lei, “Unified Triple-Phase-Shift Control to Minimize Current Stress and Achieve Full Soft-Switching of Isolated Bidirectional DC–DC Converter,” *IEEE Trans. on Industrial Electronics,* 2016, vol. 63, Issue. 7, pp. 4169-4179.

[72] N. Hou, W. Song, M. Wu, “Minimum-Current-Stress Scheme of Dual Active Bridge DC–DC Converter With Unified Phase-Shift Control,” *IEEE Transactions on Power Electronics,* 2016, vol. 31, Issue. 12, pp. 8552-8561.

[73] C. Song, A. Chen, J. Chen, C. Du, C. Zhang, “Current-stress-optimized strategy of dual active bridge DC-DC converter with dead-time effect in single-phase-shift control,” *IECON 2017, 43rd Annual Conference of the IEEE Industrial Electronics Society,* pp. 1013-1018.

[74] Z. Li, Y. Wang, L. Shi, J. Huang, W. Lei, "Optimized modulation strategy for three-phase dual-active-bridge DC-DC converters to minimize RMS inductor current in the whole load range,” *2016 IEEE 8th International Power Electronics and Motion Control Conference (IPEMC-ECCE Asia),* pp. 2787-2791.

[75] S. Han, I. Munuswamy, D. Divan, “Preventing transformer saturation in bi-directional dual active bridge buck-boost DC/DC converters,” *2010 IEEE Energy Conversion Congress and Exposition,* pp. 1450-1457.

[76] B. P. Baddipadiga, M. Ferdowsi, “Dual loop control for eliminating DC-bias in a DC-DC dual active bridge converter,” *2014 International Conference on Renewable Energy Research and Application (ICRERA),* pp. 490-495.

[77] S. Dutta, S. Bhattacharya, “A method to measure the DC bias in high frequency isolation transformer of the dual active bridge DC to DC converter and its removal using current injection and PWM switching,” *2014 IEEE Energy Conversion Congress and Exposition (ECCE),* pp. 1134-1139.

[78] S. Dutta, S. Hazra, S. Bhattacharya, “A Digital Predictive Current-Mode Controller for a Single-Phase High-Frequency Transformer-Isolated Dual-Active Bridge DC-to-DC Converter,” *IEEE Transactions on Industrial Electronics,* vol. 63., Issue. 9, 2016, pp. 5943-5952.

[79] J. Huang, Y. Wang, Z. Li, W. Lei, “Predictive valley-peak current control of isolated bidirectional dual active bridge DC-DC converter,” *2015 IEEE Energy Conversion Congress and Exposition (ECCE),* pp. 1467-1472.

[80] S. Han, I. Munuswamy, D. Divan, “Preventing transformer saturation in bi-directional dual active bridge buck-boost DC/DC converters,” *2010 IEEE Energy Conversion Congress and Exposition,* pp. 1450-1457.

[81] Y. Panov, M. M. Jovanović, L. Gang, M. Yueyong, “Transformer-flux-balancing control in isolated bidirectional DC-DC converters,” *2014 IEEE Applied Power Electronics Conference and Exposition - APEC 2014*¸ pp. 49-56.

[82] Y. Panov, M. M. Jovanović, B.T. Irving, “Novel transformer-flux-balancing control of dual-active-bridge bidirectional converters,” *2015 IEEE Applied Power Electronics Conference and Exposition (APEC),* pp. 42-49.

[83] K. Venkatachalam, C.R. Sullivan, T. Abdallah, H. Tacca, “Accurate prediction of ferrite core loss with nonsinusoidal waveforms using only Steinmetz parameters,” in proc. IEEE Workshop on Computers in Power Electronics, 2002, pp. 36-41.

[84] R.P. Wojda, M.K. Kazimierczuk, “Winding resistance of litz-wire and multi-strand inductors,” in IET Power Electronics, 2012, vol. 5, Issue. 2, pp. 257-268.

[85] P. M. Shabestari, G. B. Gharehpetian, G. H. Riahy, Sh. Mortazavian, “Voltage controllers for DC-DC boost converters in discontinuous current mode,” *2015 International Energy and Sustainability Conference (IESC),* pp. 1-7.

[86] N. Ghanbari, H. Golzari, H. Mokhtari, M. Poshtan, “Optimum location for operation of small size distributed generators,” *2017 IEEE 6th International Conference on Renewable Energy Research and Applications (ICRERA),* pp. 300-303.

[87] W. Wang, P. Wang, T. Ma, H. Liu, H. Wu, “A simple decoupling control method for isolated three-port bidirectional converter in low-voltage DC microgrids,” 2015 *IEEE Energy Conversion Congress and Exposition (ECCE),* pp. 3192-3196.

[88] H. Tao, J. L. Duarte, M. A. M. Hendrix, “Three-Port Triple-Half-Bridge Bidirectional Converter With Zero-Voltage Switching,” *IEEE Trans. on Power Electronics,* 2008, vol. 23, Issue. 2, pp. 782-792.

[89] H. Tao, J. L. Duarte, M. A. M. Hendrix,, “High-Power Three-Port Three-Phase Bidirectional DC-DC Converter,” 2007 *IEEE Industry Applications Annual Meeting,* pp. 2022-2029.

[90] H. Krishnaswami, N. Mohan, “Three-Port Series-Resonant DC–DC Converter to Interface Renewable Energy Sources With Bidirectional Load and Energy Storage Ports,” *IEEE Trans. on Power Electronics,* 2009, vol. 24, Issue. 10, pp. 2289-2297.

[91] Y. Yu, K. Masumoto, K. Wada, Y. Kado, “Power flow control of a triple active bridge DC-DC converter using GaN power devices for a low-voltage DC power distribution system,” 2017 *IEEE 3rd International Future Energy Electronics Conference and ECCE Asia (IFEEC 2017 - ECCE Asia),* pp. 772--777.

[92] R. Yapa, A. Forsyth, “Extended soft switching operation of the triple active bridge convereter,” *6th IET International Conference on Power Electronics, Machines and Drives (PEMD 2012),* pp. 1-6.

[93] S. Nakagawa, J. Arai, R. Kasashima, K. Nishimoto, Y. Kado, K. Wada, “Dynamic performance of triple-active bridge converter rated at 400 V, 10 kW, and 20 kHz,” 2017 *IEEE 3rd International Future Energy Electronics Conference and ECCE Asia (IFEEC 2017 - ECCE Asia),* pp. 1090-1094.

[94] H. R. Mamede, W. M. dos Santos, D. C. Martins, “A new DC-DC power converter derived from the TAB for bipolar DC microgrids,” 2015 *IEEE Energy Conversion Congress and Exposition (ECCE),* pp. 6217-6222.

[95] V. N. S. R.Jakka, A. Shukla, G. D. Demetriades, “Dual-Transformer-Based Asymmetrical Triple-Port Active Bridge (DT-ATAB) Isolated DC–DC Converter,” *IEEE Trans. on Industrial Electronics,* 2017, vol. 64, Issue. 6, pp. 4549-4560.

[96] L. Jiang, D. Costinett, “A triple active bridge DC-DC converter capable of achieving full-range ZVS,” 2016 *IEEE Applied Power Electronics Conference and Exposition (APEC),* pp. 872-879.

[97] M. Neubert, S. P. Engel, J. Gottschlich, R. W. De Doncker, “Dynamic power control of three-phase multiport active bridge DC-DC converters for interconnection of future DC-grids,” *2017 IEEE 12th International Conference on Power Electronics and Drive Systems (PEDS),* pp. 639-646.